Universidade do Minho
Escola de Engenharia

Jorge de Araújo Rocha

Structural glass flexural strengthening with CFRP composites and Fe-SMA based on passive, active and hybrid techniques
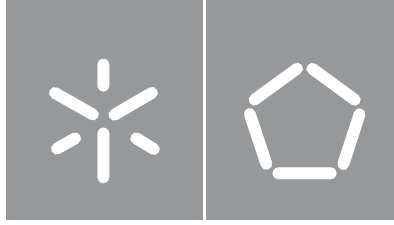
Structural glass flexural strengthening with CFRP composites and Fe-SMA based on passive, active and hybrid techniques

Jorge de Araújo Rocha

UMinho | 2022

October, 2022

Universidade do Minho
Escola de Engenharia

Jorge de Araújo Rocha

Structural glass flexural strengthening with CFRP composites and Fe-SMA based on passive, active and hybrid techniques

Doctoral Thesis
Civil Engineering

Work conducted under supervision of
Professor Eduardo Nuno Borges Pereira
Professor José Manuel de Sena Cruz

October, 2022

COPYRIGHT AND TERMS OF USE OF THIS WORK BY A THIRD PARTY

ACKNOWLEDGMENTS

I'd like to start by saying "thank you so much!" to Professors Eduardo Pereira and José Sena Cruz. This sentence is clearly too short to express my deepest gratitude for their guidance, constant encouragement, confidence and enthusiasm throughout the development of this work, as well as for their profuse wisdom and knowledge. In addition, I would also like to highlight their human qualities and friendship. This work would not be the same without the inspiration, interesting discussions and careful reading of my supervisors. I can never thank them for how much I learned from them.

I would like to thank all the staff of the Civil Engineering Department of University of Minho. I am especially grateful to all laboratory technicians of the Structural Laboratory of University of Minho, especially António Matos and Marco Peixoto. Also, I would like to acknowledge the Institute for Sustainability and Innovation in Structural Engineering (ISISE) for providing the facilities and resources to develop this thesis.

I could not forget to thank the contribution of all the companies that have been involved for the development of this work: (i) COVIPOR – Companhia Vidreira do Porto Lda., especially Francisco Ferreira and Mauricio Sousa; (ii) S&P Clever Reinforcement Iberica Lda.; (iii) Sika AG Company; and (iv) re-fer AG Company.

I would like to thank my peers and friends from the Civil Engineering Department of University of Minho, for the hours we spent together discussing the most varied topics with each other. I could not forget all my close friends, which supported and encouraged me throughout this work.
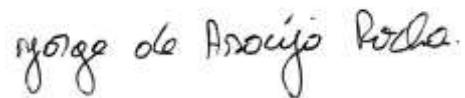
Finally, I would like to dedicate this work to my grandparents, parents, sister and girlfriend. To my grandparents Maria and Manuel, to my parents Eugénia and Carlos and to my sister Filipa, "obrigado" for your constant presence and unconditional love. Now, in particular to Filipa, my soulmate, thank you for your love, kindness, support, dedication and strength. I am grateful to have your company every day of my life. Thank you all, you are the best!!!

STATEMENT OF INTEGRITY

I hereby declare having conducted this academic work with integrity. I confirm that I have not used plagiarism or any form of undue use of information or falsification of results along the process leading to its elaboration.

I further declare that I have fully acknowledged the Code of Ethical Conduct of the University of Minho.

University of Minho, October 31, 2022

Jorge de Araújo Rocha

"NOTHING IN LIFE IS TO BE FEARED, IT
IS ONLY TO BE UNDERSTOOD. NOW IS
THE TIME TO UNDERSTAND MORE, SO
THAT WE MAY FEAR LESS."

Marie Curie

ABSTRACT

Contemporary architecture encourages the use of glass in structural applications. Glass industry has developed the thermal toughening to increase its tensile strength and lamination to prevent brittle failure. However, glass can still fail unexpectedly due to the growth of surface flaws. Recent studies have focused on glass composite systems, mainly using steel as reinforcement. Other reinforcement materials (e.g. CFRP and Fe-SMA) and application techniques (e.g. prestressing) need also to be explored, given their promising features to face the growing structural challenges.

This thesis aimed at covering two main topics related to structural glass: (i) post-cracking performance and (ii) mechanical post-tensioning. Its main objective was to evaluate the feasibility of using CFRP and Fe-SMA as reinforcement in flexure to obtain ductile failure modes, as well as the application of post-tensioning to reduce the unpredictability of the glass fracture strength. The experimental programs included (i) tensile tests on double-lap joints to assess the bond performance of glass-to-CFRP adhesive connections, (ii) flexural tests on small-scale monolithic glass beams with externally bonded CFRP or Fe-SMA reinforcements, and (iii) flexural tests on large-scale laminated glass beams with hybrid (EBR + NSM) strengthening. It was possible to obtain ductile failure modes when glass was strengthened with CFRP and Fe-SMA. The post-cracking performance was sensitive to the adhesive type, reinforcement material, strengthening system and, in the case of Fe-SMA reinforced glass, the activation temperature. Hybrid strengthening systems prevented premature debonding of the reinforcement and made better use of its tensile capacity. NSM-CFRP composite systems were safely prestressed and FRP peeling-off failure was avoided during load releasing.

Considering the importance of design rules for practitioners, numerical modelling was carried out to assess (i) the efficiency of different constitutive models to simulate the non-linear behaviour of glass in tension and (ii) the influence of design parameters on the numerical response of glass composite systems. Further numerical simulations were performed to better understand the structural performance of CFRP reinforced glass elements, including at the level of the glass-to-CFRP adhesive joint. The results obtained were promising, and although additional studies are needed, new perspectives were opened for a future safer and widespread use of glass as a structural material.

KEYWORDS: CFRP; Fe-SMA; Glass composite systems; Flexural response; Prestressing; Numerical modelling

RESUMO

A arquitetura contemporânea tem encorajado a aplicação estrutural do vidro. A indústria do vidro desenvolveu os processos de têmpera, de modo a aumentar a sua resistência à tração, e de laminação, com o propósito de evitar roturas frágeis. O vidro pode, ainda assim, romper inesperadamente devido à propagação de defeitos superficiais. Recentemente, os sistemas compósitos de vidro têm sido estudados como uma alternativa para prevenir roturas inesperadas, usando principalmente aço. Outros tipos de reforço recentes (ex: CFRP e Fe-SMA) e técnicas de aplicação (por exemplo, protensão) apresentam também características promissoras.

Esta tese aborda dois tópicos cruciais no contexto do vidro estrutural: (i) o comportamento pós-fissuração e (ii) o pré-esforço mecânico. A obtenção de modos de rotura dúcteis por via do reforço com CFRP e Fe-SMA e a redução da imprevisibilidade da resistência à tração do vidro por via da aplicação de pré-esforço foram os principais objetivos deste estudo. Os programas experimentais incluíram (i) ensaios em juntas de sobreposição dupla para caracterizar o desempenho de ligações adesivas vidro-CFRP, (ii) ensaios de flexão em vigas de vidro monolítico de pequena dimensão, reforçadas externamente com CFRP e Fe-SMA, e (iii) ensaios de flexão em vigas de vidro laminado de grande dimensão com sistemas de reforço híbridos (EBR + NSM). Foi possível obter roturas dúcteis em elementos estruturais de vidro reforçados com CFRP e Fe-SMA. O desempenho pós-fissuração mostrou ser sensível ao tipo de adesivo, ao material de reforço, ao sistema de reforço e, no caso de vidro reforçado com Fe-SMA, à temperatura de ativação. Os sistemas de reforço híbridos mostraram bons resultados na prevenção do destacamento prematuro do reforço.

Considerando a importância das regras de projeto para os sistemas em estudo, realizaram-se simulações numéricas para avaliar (i) a eficácia de diferentes modelos constitutivos para simular o comportamento não-linear do vidro e (ii) a influência de parâmetros de projeto na resposta numérica de sistemas compósitos de vidro. Posteriormente realizaram-se ainda simulações numéricas adicionais para aprofundar o conhecimento sobre o desempenho estrutural de elementos de vidro reforçados com CFRP, incluindo simulações ao nível das juntas adesivas entre vidro e CFRP. Os resultados obtidos foram promissores e, embora sejam necessários estudos adicionais, abriram-se novas perspetivas para que a aplicação estrutural do vidro seja mais segura e generalizada no futuro.

PALAVRAS-CHAVE: CFRP; Fe-SMA; Pré-esforço; Reposta à flexão; Simulação numérica; Sistemas compósitos de vidro

TABLE OF CONTENTS

LIST OF TABLES

LIST OF FIGURES

LIST OF ABBREVIATIONS AND SYMBOLS

Abbreviations

AB	Adhesively bonded reinforcement
AFRP	Aramid fibre reinforced polymers
Al_2O_3	Aluminium oxide
B_2O_3	Boron trioxide
BSG	Borosilicate glass
CaO	Calcium oxide
CC	Consequence class
Cd-Au	Cadmium-Gold (alloy)
CEN	European Committee for Standardization
CFRP	Carbon fibre reinforced polymers
C-G	Cohesive failure in glass
CLS	Collapse limit state
CNR	Italian National Research Council
CoV	Coefficient of variation
CS-G	Glass substrate failure
Cu-SMA	Copper-based shape memory alloy
DCB	Double Cantilever Beam
Di	Ductility index
DIC	Digital image correlation
DMA	Dynamic mechanical analysis
DPM	Damage plasticity model
EB	Elastic behaviour (approach)
Empa	Swiss Federal Laboratories for Materials Science and Technology
EBR	Externally bonded reinforcement
EN	European Norm
ENF	End Notched Flexure
EVA	Ethylene Vinyl Acetate

FCC	Fracture consequence class
FEA	Finite element analysis
Fe-Mn-Si	Iron-Manganese-Silicon (alloy)
Fe-SMA	Iron-based shape memory alloys
FLS	Fracture limit state
FRP	Fibre reinforced polymers
FT-L	Fibre-tear failure in CFRP laminate
GFRP	Glass fibre reinforced polymers
I-AG	Adhesive failure by debonding at the interface adhesive
IB	Interface behaviour (approach)
INNOGLAST	Innovative Steel-Glass-Structures (research project)
ISO	International Organization for Standardization
K_2O	Potassium oxide
LEB	Linear elastic behaviour (approach)
LVDT	Linear variable differential transformer
MA	Mechanically anchored reinforcement
Mg	Magnesia
Na_2O	Sodium oxide
NiS	Nikel-sulfite (inclusions)
Ni-Ti	Nikel-Titanium (Nitinol)
NLB	Non-linear behaviour (approach)
NS	Numerical simulations
NSM	Near surface mounted
PB	Perfect bond (approach)
PFLS	Post fracture limit state
PTFE	Polytetrafluoroethylene
PVB	Polyvinyl Butyral
ROI	Region of interest
RSi	Residual strength index
SCM	Smeared crack model

SG	Strain gauge
SGP	SentryGlass
SiO_2	Silicon dioxide
SLS	Serviceability limit state
SLSG	Soda lime silicate glass
SMA	Shape memory alloys
ULS	Ultimate limit state
UV	Ultra-violet (radiation)

Symbols

A_a	Beam's equivalent cross-section area during Fe-SMA activation
A_f	Austenite finish temperature
A_r	Reinforcement's cross-section area
A_s	Austenite start temperature
C	Viscous damping matrix
$E; E_i$	Modulus of elasticity
E_{adh}	Adhesive's modulus of elasticity
E_{CFRP}	Modulus of elasticity of CFRP
E_{EBR}	Modulus of elasticity of the EBR reinforcement
E_g	Modulus of elasticity of glass
E_{GFRP}	Modulus of elasticity of GFRP
E_{NSM}	Modulus of elasticity of the NSM reinforcement
E_k	Kinetic energy
$E_{r,a}$	Fe-SMA's modulus of elasticity during activation
$E_{r,rec}$	Equivalent modulus of elasticity after Fe-SMA activation
E_r	Reinforcement's modulus of elasticity
E_t	Internal energy / Strain energy
E_v	Viscous energy
E_w	Work done by external forces

F	Applied load
$F_{c,g}$	Compression force in the uncracked glass zone
F_{cr}	Cracking load
$F_{cr,a}$	Analytical cracking load
F_{EBR}	Final prestressing force applied in the EBR reinforcement
$F_{max}; F_p$	Maximum load reached during the structural response (post-cracking stage for flexural tests)
F_{NSM}	Final prestressing force applied in the NSM reinforcement
F_p	Post-tensioning force
$F_{t,r}$	Tensile force in the reinforcement element
F_{ult}	Applied load at failure
$G_f; G_{min}$	Minimum mode-I fracture energy
G_g	Mode-I fracture energy of glass
G_m	Mode-II fracture energy
I_a	Moment of inertia assuming no composite action (Fe-SMA activation)
I_{el}	Moment of inertia in elastic stage
L_s	Span length
K	Stiffness matrix
K_c	Shape of yield surface
$K_{el,a}$	Analytical initial stiffness (elastic stage)
$K_{el}; K$	Initial stiffness
K_n	Linear elastic normal stiffness
$K_s; K_t$	Linear elastic tangential stiffnesses
K_τ	Shear stiffness of the adhesive joint
$K_{\tau,eff}$	Effective shear stiffness of the adhesive joint
L_b	Bond length
L_{min}	Smallest finite element dimension
M	Mass matrix
M_{cr}	Bending moment corresponding to cracking load
M_f	Martensite finish temperature
M_s	martensite start temperature

P_b	Reinforcement-to-glass bonding perimeter
T	Temperature
T_1	Period of the fundamental vibration mode
T_a	Activation temperature
b	Shape of the tension-softening diagram
c_d	Dilatational wave speed
d	Displacement
$\dot{d}$	Velocity
$\ddot{d}$	Acceleration
$d_{CFRP,le\text{-}s}$	Displacement of the CFRP laminate at the loaded end section
d_{exp}	Vertical displacement at the mid-span section after Fe-SMA activation
$d_{g,le\text{-}s}$	Displacement of the glass internal surface at the loaded end section
$d_{g,LVDT\text{-}s}$	Displacement of the glass external surface at the LVDT section
$d_{max}; s_{le,p}$	Displacement / relative slip at peak load
d_{num}	Numerical vertical displacement caused by the Fe-SMA activation
d_t	Parameter for damage law
e	Eccentricity
f_{adh}	Adhesive's tensile strength
f_{bc}	Initial biaxial compressive yield stress
f_c	Uniaxial compressive yield stress
$f_{g,c}$	Compression strength of glass
$f_{g,eff}$	Effective tensile strength of glass
$f_{g,t}$	Tensile strength of glass
$f_{r,t}$	Reinforcement's tensile strength
f_t	Tensile strength
h	Crack band width
h_{CFRP}	GFRP profile heigth
h_{GFRP}	Glass panel heigth
$h_i; b_i$	Dimentions of each component

h_t	Total heigth of the specimen
l_1	Length of the shear span
l_2	Length of the pure bending span
l_a	Activated length in Fe-SMA strips
$l_{b,d}$	Adhesive bond length damaged by Fe-SMA activation
l_{eff}	Effective bond length
p	Constant value for shear retention factor
s	Relative slip between the bonded interfaces
$s(x)$	Relative slip curve along the bond length
$s_{DIC}(x)$	Relative slip curve along the bond length extracted from DIC
s_{eff}	Effective Loaded end slip
s_{fe}	Free end slip
s_{le}	Loaded end slip
s_m	Slip at bond strength
$s_{NS}(x)$	Numerical relative slip curve along the bond length
t_a	Adhesive layer thickness
u_{max}	Maximum total displacement for mode-I fracture
y_a	Neutral axis position during the Fe-SMA activation
y_{el}	Neutral axis position in elastic stage
y_{ult}	Neutral axis position at failure
z_i	Distance from the centroid of each component to the neutral axis
$z_{i,t}$	Distance from the centroid of each component and the glass top edge
ΔF_{cr}	Increment of cracking load due to the post-tensioning
Δt	Maximum stable time increment
Δs_s	Increment of displacement in the tangential direction to the interface
Δu_n	Increment of displacement in the normal direction to the interface
$\Delta \sigma_n$	Increment of stress in the normal direction to the interface
$\Delta \tau_s$	Increment of stress in the tangential direction to the interface
ϵ	Shape of plastic flow

α	Shape of the pre-peak curve
α'	shape of the post-peak curve
α_0	Mass-proportional damping
β	Shear retention factor
β_0	Stiffness-proportional damping
δ	Mid-span deflection
δ_{cr}	Mid-span deflection at inital cracking
$\delta_{cr,a}$	Analytical mid-span deflection at inital cracking
δ_{num}	Numerical mid-span deflection
δ_{ult}.	Ultimate mid-span deflection
$\varepsilon_{adh,ult}$	Adhesive's ultimate strength
$\varepsilon_{b,ult}$	Axial strain at the beams's bottom edge (reinforcement) at failure
$\varepsilon_{CFRP}(x)$	Axial strain distribution in the CFRP laminate
$\varepsilon_{CFRP,DIC}(x)$	Axial strain distribution in the CFRP laminate derived from DIC
ε_{exp}	Experimental measured axial strain
$\varepsilon_{g,t}$	Axial strain at the glass top edge
ε_{inc}	Incremental strain due to the bending effect
ε_{lin}	Analytical axial strain
ε_{pre}	Fe-SMA pre-strain
ε_n^{cr}	Crack normal strain
$\varepsilon_{n,ult}^{cr}$	Ultimate crack normal strain
ε_r	Axial strain in reinforcement
ε_{rem}	Permanent remaining deformation
ε_{rev}	Reversal stress
$\varepsilon_{r,p}$	Pre-strain adopted for prestressing the reinforcement
$\varepsilon_{r,ult}$	Reinforcement's ultimate strength
ε_t^{el}	Elastic strain
ε_t^{pl}	Plastic strain
$\varepsilon_{t,ult}$	Axial strain at the beam's top edge (glass) at failure
ε_{ult}	Ultimate strain

ε_y	Yield strain
$\hat{\lambda}; \hat{\mu}$	Lamé's constants
ρ	Density
ρ_r	Reinforcement percentage
$\sigma_{g,b}$	Axial stress at the glass bottom edge
$\sigma_{g,t}$	Axial stress at the glass top edge
σ_m	Normal strength
σ_n	Stress in the normal direction to the interface
σ_{pre}	Axial stress corresponding to the Fe-SMA pre-strain
$\sigma_{rec,cr}$	Recovery stresses developed in Fe-SMA from cracking loads
$\sigma_{rec,max}$	Maximum recovery stress
$\sigma_{rec,sg}$	Recovery stress developed in Fe-SMA from strain gauge measurements
σ_y	Yield stress
τ_m	Bond strength
$\tau_s; \tau_t$	Stress in both tangential directions to the interface
$\tau_{s,max}; \tau_{t,max}$	Shear strengths
$\tau(s)$	Shear stress at the bonded interfaces
$\tau(x)$	Shear stress curve on the bond length
υ	Poisson's ratio
υ_{CFRP}	Poisson's ratio of CFRP
υ_g	Poisson's ratio of glass
υ_{GFRP}	Poisson's ratio of GFRP
ψ	Dilation angle
ω_1	Angular frequency of the fundamental vibration mode
ω_j	Angular frequency
ω_{max}	Highest angular frequency

CHAPTER 1

INTRODUCTION

1.1. MOTIVATION

The development of new materials has always been responsible for great advancements throughout the history of Humanity. Some of them were even used to name time periods, such as the Stone Age, Bronze Age and Iron Age [1]. Although glass has never named any period in the history, it has been used by humans for centuries. Today, glass is a symbol of the contemporary architecture due to its transparency, which is a unique characteristic that other traditional building materials (e.g. concrete, steel and timber) do not have. Due to its versatility, glass has been widely used throughout history for a variety of purposes, from fibres to large-scale structures, from decorative elements to structural applications and from the automotive industry to construction and communications [1].

In the construction industry, glass was used for centuries as a non-structural material in windows and building envelopes to create interior spaces without blocking the entrance of visible light into the buildings [2]. Nowadays there is an increasing demand for transparency. Thus, glass has been increasingly used as a load-bearing material to produce structural elements (e.g. beams and even columns) for roof and façade structures, footbridges and staircases. Furthermore, glass can take countless aesthetical possibilities and, taking into account the concerns related to building sustainability and the use of resources, it may be 100 % recyclable. As an example, improved delamination techniques, such as the wet method, are being developed to separate the glass from the interlayer and in turn recycle both materials [3–5].

Although glass has interesting properties for structural applications (e.g. very high compression strength), like concrete its behaviour in tension is brittle and unpredictable due to the unavoidable mechanical flaws induced during the production and handling operations. These small mechanical flaws grow when the glass is subjected to long-term loads and moisture. Consequently, even if glass does not break at load application, it may break after a certain period of time which is a function of the loading history, surface characteristics and environmental conditions [6].

Glass industry has introduced several technological innovations in the glass production process, namely the thermal toughening and the lamination. While the former reduces the unpredictability of glass and increases its tensile strength due to the residual stress state generated after being reheated, the latter introduces relatively safe failure mechanisms, guaranteeing the structural integrity of the glass element after cracking due to the interlayer action. Both processing methods have contributed to promote the use of glass as a load-bearing material in a wide spectrum of structural applications. On the other hand, glass industry has developed new manufacturing plants with the aim of extending the maximum size of glass elements, hitherto limited to the standard size of 6.00×3.21 [m] [7]. Given the increasing structural relevance of glass elements, stiffer interlayers (e.g. ionomers) have also been developed to enhance the pre- and post-failure performance of the laminated glass, as well as its resistance to moisture and UV radiation [8].

The latest technological advances in the glass industry have attracted the interest of the international research community, which has been addressing numerous concerns about glass structural applications. This investigation has been translated into the development and improvement of existing guidelines and standards (e.g. [9–13]). Nonetheless, the most challenging structural applications (e.g. beams) are not covered by existing standards. Most design methodologies for structural glass mainly focus on (i) the shear interaction at the bonded interfaces of laminated glass panes, (ii) the flexural behaviour of glass panels subjected to out-of-plane loads, (iii) the buckling behaviour of glass elements under compression (e.g. glass fins) and in-plane shear stresses, as well as on (iv) the connection technologies between glass elements.

Adopting the design methodologies commonly used in the aeronautics, glass structural systems have been designed according to the concepts of hierarchy, robustness and redundancy [11]. However, these methodologies are certainly not economical and, whatever the type of glass, laminated glass breaks without showing warning signs. Furthermore, whatever the interlayer material, laminated glass does not have sufficient post-fracture strength and ductility for structural applications [14,15]. A

secondary load carrying mechanism is therefore essential to comply with the structural redundancy requirements.

Following the philosophy employed in reinforced concrete, safety concepts have been developed combining glass with reinforcement materials, such as concrete, timber, steel and Carbon (CFRP) and Glass (GFRP) Fibre Reinforced Polymers [15–18]. When glass breaks, collapse is avoided by transferring tensile stress from the glass to the reinforcement through shear stresses in the adhesive joint. Subsequently, the applied load is transferred to the supports by means of a resisting mechanism formed by an uncracked glass zone in compression and the reinforcement element in tension. As a result, composite glass systems can still carry load after the first glass cracking. Besides the reinforcement material, the post-failure performance is a function of several aspects, and some of them have been addressed in recent investigations, such as (i) the reinforcement percentage (e.g. [19]), (ii) the cross-section geometry (e.g. [20]), (iii) the type of bonding agent (e.g. [20,21]) and (iv) the type of glass (e.g. [22]).

Multiple aesthetical possibilities can be obtained by assembling individual glass sheets through interlayers and transparent adhesives. Hence, besides the traditional rectangular sections, box-, I- and T-sections have also been investigated to prevent lateral-torsional buckling, since glass structural elements are typically slender compared to reinforced concrete [23,24]. Like in concrete structures strengthened with composite materials, epoxy adhesives are commonly used as bonding agent because these ensure superior bond performance compared with other types of adhesive (e.g. polyurethane and acrylate). However, soft adhesives have also been used to increase ductility [20]. Glass composite systems manufactured with annealed glass sheets have shown better post-failure performance than those with thermally toughened glass [22]. Although the latter shows much higher tensile strength than annealed glass, the former is better at providing residual strength because it breaks into larger fragments than fully tempered glass and heat-strengthened glass. On the other hand, glass composite systems with passive reinforcement have successfully achieved sufficient robustness and safety after cracking, but the tensile strength of glass is still unreliable.

In recent years, as an alternative to the thermal toughening, mechanical post-tensioning has been investigated with the aim of improving the fracture strength of glass. Unlike tempering, mechanical post-tensioning does not modify the nature of the glass fracture and, in addition, it can be adjusted as a function of the glass element. Steel, CFRP and GFRP have been used as prestressed reinforcement materials in post-tensioned glass systems [18]. The principle of such systems is similar to prestressed

concrete. Different systems are used to introduce prestress in concrete elements, such as (i) the cambered prestressing systems; (ii) the prestressing against an external support; and (iii) the prestressing against the target element [25,26]. The last two strategies have been used for post-tensioning of glass (e.g. [27–31]), but the prestressing against an external support is the most prominent. The second method consists of prestressing the reinforcement against an independent and external reaction steel frame before bonding it to the target element [25]. When the adhesive is fully cured, the reinforcement is released and the prestress is transferred to the glass, thus introducing a compression pre-stress state in tensile glass zones to prevent the growth of small surface flaws under service loading. On the other hand, the last method requires the use of anchorages. These are fixed at the ends of the target element, providing reaction force while the prestress is applied by pulling the reinforcement with hydraulic jacks [25]. When the adhesive is fully cured, all temporary elements are removed [26].

CFRPs have been widely used in recent decades for the strengthening of existing concrete structures, mainly due to their relatively high stiffness and tensile strength, low relaxation, lightness and high resistance to corrosion [32]. However, few works are found in the literature focusing on CFRPs as reinforcement material for glass composite systems, both experimentally (e.g. [30,33–35]) and numerically (e.g. [34,36]). Two strengthening techniques are commonly used for the application of CFRPs [26,37–40]: (i) the Externally Bonded Reinforcement (EBR) technique, which consists of bonding the CFRP laminate on the tensile surfaces of the structural element to be strengthened; and (ii) the Near Surface Mounted (NSM) technique, which consists of introducing the CFRP laminate or bar inside pre-opened grooves located in the tensile region of the target structural element. In glass elements, the reinforcement is typically applied according the EBR technique (e.g. [27,31,41]). However, its performance strongly depends on the resistance of the substrate material [42]. As a consequence, over the last decades, the NSM technique has been increasingly used as an effective alternative to the classical approach of applying externally bonded CFRPs [40]. Compared to EBR, the NSM technique is less prone to premature debonding due to the larger bonding surface area between the adherends, as well as the confinement effect created by the grooves, thus allowing a more efficient use of the tensile capacity of the reinforcement material. Furthermore, the surrounding glass protects the reinforcement against corrosion, fire, vandalism actions, mechanical damage and aging [43]. As a result, an increasing number of investigations have been addressing the feasibility of strengthening glass elements according to the NSM technique (i) by laminating the reinforcement together with the

glass sheets and using the interlayer as a bonding agent (e.g. [22,44]) or (ii) by designing recessed grooves on the glass edges for the subsequent insertion of the reinforcement element (e.g. [33,45]).

Lately, Shape Memory Alloys (SMA) have been used for the strengthening of existing concrete structures. Unlike traditional materials (e.g. steel and FRPs), (i) mechanically deformed SMAs can recover their initial shape by heating, the well-known shape memory effect; and, (ii) under certain temperature conditions, they can also recover from high imposed mechanical deformations after unloading and without heating, the so-called superelasticity [46,47]. SMAs have been employed in different engineering fields due to their unique properties, such as (i) the post-tensioning of structural elements (e.g. [48–53]) and (ii) the energy dissipation in structures subjected to dynamic loads (e.g. [54,55]). When the SMA reinforcement is properly anchored to the target element prior to its activation (e.g. adhesively bonded and mechanically anchored), post-tensioning forces are generated by heating the SMA. This simple procedure has encouraged the application of SMAs in the construction industry, whose conventional procedure of prestressing with hydraulic jacks is often difficult to implement due to the lack of space [47,56]. Among the other SMAs, iron-based alloys (Fe-SMA) present essential characteristics for the construction industry, such as: (i) reasonably low cost, (ii) relatively high modulus of elasticity and low activation temperature, as well as (iii) good workability, (iv) machinability and (v) weldability [47,57]. Due to the novelty of the glass as a load-bearing material and SMAs as a reinforcement material, to the best of the author's knowledge only four studies (e.g. [58–61]) are found in the literature addressing this topic.

Glass contains mechanical flaws randomly distributed on its surfaces and edges and, therefore, high stress concentrations should be avoided to prevent these flaws from growing over time [62,63]. If relatively high prestressing levels are adopted, glass breakage may be an unavoidable event while loading starts (e.g. [64]). On the other hand, the use of mechanical anchorages can be technically and aesthetically inappropriate, as they cannot be fastened to the substrate material like in concrete or metallic structures. In this context, SMAs may be a promising candidate to be used as reinforcement material for the fabrication of post-tensioning glass systems that are safer than those produced with traditional reinforcement materials. If SMAs are adhesively bonded to the glass, their activation damages the adhesive joint, mobilizing longer bond lengths and creating damage gradients that smoothen the transfer of the post-tensioning force from the reinforcement to the glass. Furthermore, the shape memory effect could be used in two different contexts: (i) before glass rupture, to improve the tensile strength of glass by creating favourable stresses in the glass tensile zone; and (ii) after

glass rupture, to enhance the post-failure performance until the glass element is replaced, reducing the deformation, preventing the crack progression and, eventually, closing existing cracks.

1.2. OBJECTIVES AND RESEARCH METHODOLOGY

Despite the most recent developments, there are still significant gaps in the glass composite systems knowledge for structural applications, namely on the following topics: (i) the post-failure behaviour of reinforced glass systems; and, (ii) the mechanical post-tensioning of glass.

The present work aims at contributing to the existing knowledge on glass composite systems. Thus, the main objectives of this PhD thesis are two-fold: (i) to develop strengthening systems capable of guaranteeing safe failure modes in glass structures; and (ii) to develop reliable post-tensioning methodologies to reduce the unpredictability of the glass fracture strength. It is expected that this research work contributes to the existing knowledge on the composite glass systems, providing analytical and numerical methodologies for predicting the post-failure performance. The development of post-tensioning methodologies capable of increasing the fracture strength of glass and reducing the risk of peeling-off failure due to stress concentrations is also expected. Finally, and due to its importance, this work contributes for the definition and development of design guidelines, as to better accounting for the robustness of glass composite systems.

Therefore, the first objective set for this thesis, related to the development of strengthening systems to introduce ductile failure modes in structural glass elements, was achieved by addressing the following tasks:

- The assessment of the influence of the type of adhesive on the bond behaviour of glass-to-CFRP adhesively bonded connections. It includes tensile tests on double-lap joint specimens to characterize the shear interaction at the bonded interfaces, calibration of local bond stress-slip relationships by using an existing computational tool and numerical modelling to better understand the observed phenomena in the experiments, using the derived local bond stress-slip relationships as input;
- The assessment of the post-failure performance of annealed glass beams reinforced with externally bonded CFRP laminates, and to study the influence of the adhesive type by testing small-scale specimens until failure in a four-point-bending configuration;
- The development of finite element models to simulate the experimental results obtained from experiments, and to evaluate the efficiency of different mechanical constitutive models to

simulate the non-linear behaviour of glass in tension. These are important for a better understanding the observed phenomena in the tests, as well as to extend the studies carried out and to assess the applicability and efficiency of different modelling strategies to simulate the bond behaviour of glass-to-CFRP adhesively bonded joints.

The second objective set for this thesis, related to the development of reliable methodologies for post-tensioning glass, was achieved by carrying out the following topics:

- The fabrication of post-tensioned glass beams by prestressing CFRP laminates and by activating Fe-SMA strips, both externally bonded to the glass substrate. It includes a study about the influence of different types of adhesive on the transfer of prestressing force from the reinforcement to the glass, in case of CFRP-reinforced specimens;

- The assessment of the post-failure performance of annealed glass beams reinforced with externally bonded Fe-SMA strips and study the benefits of activating Fe-SMA strips on the fracture strength of glass and post-failure performance of such systems, as well as the study of the influence of the Fe-SMA activation temperature on the post-tensioning level and adhesive damage propagation. It includes four-point bending tests until failure with passive and post-tensioned small-scale specimens, as well as an analytical model to determine the maximum post-tensioning level to ensure a relatively safe failure;

- The development and assessment of the feasibility of a hybrid strengthening system capable of preventing premature debonding of the reinforcement element due to critical shear crack and, in case of post-tensioning of the glass, peeling-off at load introduction (release of the prestressed reinforcement), in order to take advantage of the full tensile capacity of the reinforcement material. Large-scale specimens were tested until failure adopting a four-point bending configuration.

Based on the above-mentioned objectives, the overall research methodology that was followed is schematically depicted in **Figure 1.1**.
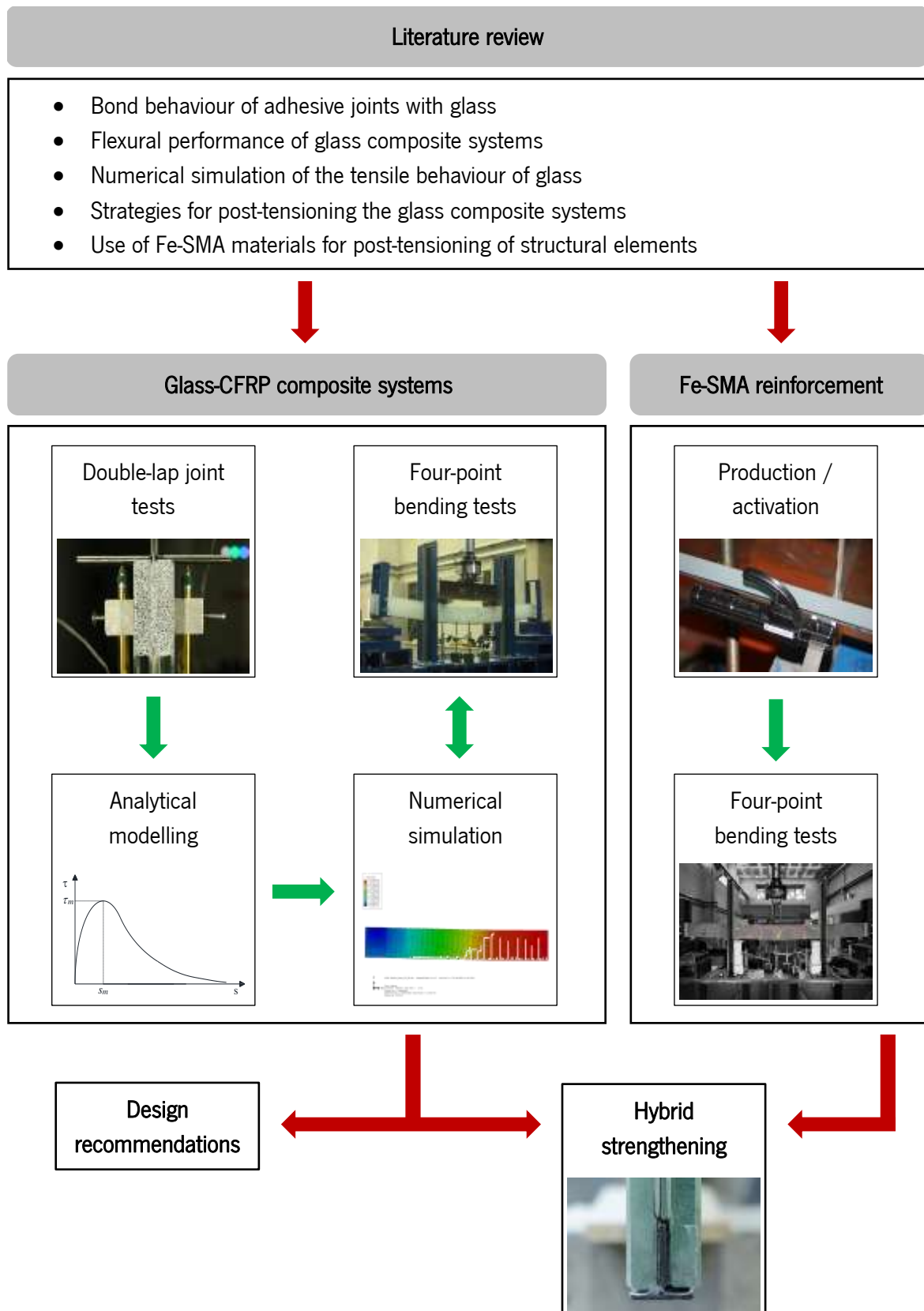
Figure 1.1: Research methodology

1.3. OUTLINE OF THE DISSERTATION

The content of this work, which is presented as a collection of five papers published or submitted to peer-review international journals, is organized in five chapters as follows:

- **Chapter 1** provides a general introduction to the research topic, describes the general objectives and overall methodology and, finally, presents the outline of the present work;

- **Chapter 2** focuses on the fundamental aspects of glass as a building material, such as the production process and the main material properties, the processing methods developed by the glass industry to improve its overall performance and the current requirements and methodologies for the design of glass structures. Few examples of glass structures are presented in this chapter, providing a general overview of the most common glass structural applications;

- **Chapter 3** concerns the premises behind the reinforced glass concept and gives an overview of the available literature on glass composite systems with passive or post-tensioned steel, timber, GFRP and CFRP reinforcements, covering aspects such as the bond behaviour of adhesively bonded connections and the post-failure performance of composite elements. A critical discussion on the feasibility of using SMAs as reinforcement in glass composite systems is carried out at the end of the chapter, as well as a brief description of the phase behaviour of the most important SMAs for civil engineering applications;

- **Chapter 4** presents a brief summary of the papers that constitute this PhD thesis. Four of these papers have been already published in scientific journals (Q1), while fifth has been submitted;

- **Chapter 5** summarizes the main conclusions of the developed work and presents recommendations for future work.

1.4. REFERENCES

[1]   Soler X. Structural glass in buildings : study of the deflection, durability, and breakage of laminated glass elements and polymeric interlayers. PhD thesis. University of Lleida, Spain, 220AD.

[2]   Ritchie I. Aesthetics in glass structures. Structural Engineering International: Journal of the International Association for Bridge and Structural Engineering (IABSE) 2004;14:73–5. https://doi.org/10.2749/101686604777964062.

[3]   Dyer T. Glass Recycling. Elsevier Inc.; 2014. https://doi.org/10.1016/B978-0-12-396459-5.00014-3.

[4]   Šooš L, Matúš M, Pokusová M, Čačko V, Bábics J. The Recycling of Waste Laminated Glass through Decomposition Technologies. Recycling 2021;6. https://doi.org/10.3390/recycling6020026.

[5]   Tupý M, Meřinská D, Svoboda P, Zvoníček J. Influence of Water and Magnesium Ion on the Optical Properties in Various Plasticized Poly(vinyl butyral) Sheets. Journal of Applied Polymer Science 2010;118:2100–8. https://doi.org/10.1002/app.32555.

[6]   Haldimann M, Luible A, Overend M. Structural use of glass. LABSE - Lanka Association of Building Services Engineers; 2008.

[7]   O'Callaghan J, Bostick C. The Apple Glass Gube: Version 2.0. Challenging Glass 3: Conference on Architectural and Structural Applications of Glass, CGC 2012, 2012, p. 57–65. https://doi.org/10.3233/978-1-61499-061-1-57.

[8]   Callewaert D. Stiffness of Glass / Ionomer Laminates in Structural Applications. PhD thesis. Faculty of Engineering and Architecture, Ghent University, Belgium, 2012.

[9]   Abeln B, Preckwinkel E, Yandzio E, Heywood M, Eliášová M, Netušil M, et al. Development of innovative steel-glass structures in respect to structural and architectural design (Innoglast). Report EUR 25316 EN. Luxembourg: Publications Office of the European Union; 2013. https://doi.org/10.2777/91697.

[10]   Feldmann M, Kasper R, Abeln B. Guidance for European Structural Design of Glass Components. Report EUR 26439 EN. Report EUR. Luxembourg: 2014. https://doi.org/10.2788/5523.

[11]   CNR-DT 2010/2013. Guide for the Design, Construction and Control of Buildings with Structural Glass Elements. CNR - Advisory Committee on Technical Recommendations for Construction, Rome: National Research Council of Italy; 2013.

[12]   DIN 18008-1:2020. Glass in Building – Design and construction rules – Part 1: Terms and general bases. Deutsches Institut für Normung, Deutsches Institut fur Normung E.V. (DIN); 2020.

[13]   prCEN/TS 19100-1:2021. Structural glass – Design and construction rules – Part 1: Basis ofdesign and materials. CEN - European Committee for Standardization, 2021.

[14]   Belis J, Depauw J, Callewaert D, Delincé D, Van Impe R. Failure mechanisms and residual capacity of annealed glass/SGP laminated beams at room temperature. Engineering Failure Analysis 2009;16:1866–75. https://doi.org/10.1016/j.engfailanal.2008.09.023.

[15]   Martens K, Caspeele R, Belis J. Development of composite glass beams - A review. Engineering Structures 2015;101:1–15. https://doi.org/10.1016/j.engstruct.2015.07.006.

[16]   Kozlowski M. Hybrid glass beams. Review of research projects and applications. Architecture Civil Engineering Environment 2012;3:53–62.

[17] Freytag B. Glass-concrete composite technology. Structural Engineering International: Journal of the International Association for Bridge and Structural Engineering (IABSE) 2004;14:111–7. https://doi.org/10.2749/101686604777963991.

[18] Martens K, Caspeele R, Belis J. Development of Reinforced and Posttensioned Glass Beams: Review of Experimental Research. Journal of Structural Engineering 2016;142:4015173. https://doi.org/10.1061/(asce)st.1943-541x.0001453.

[19] Louter C, Veer F, Hobbelman G. Reinforcing glass, effects of reinforcement geometry and bonding technology. Glass Processing Days, 2007, p. 2–6.

[20] Correia J, Valarinho L, Branco F. Post-cracking strength and ductility of glass-GFRP composite beams. Composite Structures 2011;93:2299–309.

[21] Valarinho L, Correia JR, Branco F. Experimental study on the flexural behaviour of multi-span transparent glass-GFRP composite beams. Construction and Building Materials 2013;49:1041–53. https://doi.org/10.1016/j.conbuildmat.2012.11.024.

[22] Louter C, Belis J, Veer F, Lebet J. Structural response of SG-laminated reinforced glass beams; experimental investigations on the effects of glass type, reinforcement percentage and beam size. Engineering Structures 2012;36:292–301. https://doi.org/10.1016/j.engstruct.2011.12.016.

[23] Belis J, Louter C, Verfaillie K, Van Impe R, Callewaert D. The Effect of Post-Tensioning on the Buckling Behaviour of a Glass T-Beam. International symposium on the application of architectural glass ISAAG 2006: conference proceedings, Munich: Universität Der Bundeswehr: 2006, p. 129–36.

[24] Louter C. Adhesively bonded reinforced glass beams. Heron 2007;52:31–57.

[25] El-Hacha R, Wight R, Green M. Prestressed fibre-reinforced polymer laminates for strengthening structures. Progress in Structural Engineering and Materials 2001;3:111–21. https://doi.org/10.1002/pse.76.

[26] Pellegrino C, Sena-Cruz J, editors. Design Procedures for the Use of Composites in Strengthening of Reinforced Concrete Structures: State-of-the-Art Report of the RILEM Technical Committee 234-DUC, Springer Science and Business Media; 2016.

[27] Cupać J, Louter C, Nussbaumer A. Flexural behaviour of post-tensioned glass beams: Experimental and analytical study of three beam typologies. Composite Structures 2021;255. https://doi.org/10.1016/j.compstruct.2020.112971.

[28] Bos F, Veer F, Hobbelman G, Louter C. Stainless steel reinforced and post-tensioned glass beams. 12th International Conference on Experimental Mechanics, Bari, Italy: 2004, p. 1–9.

[29] Engelmann M, Weller B. Post-tensioned glass beams for a 9 m Spannglass Bridge. Structural Engineering International 2016;26:103–13.

https://doi.org/10.2749/101686616X14555428759000.

[30] Louter C, Cupać J, Debonnaire M. Structural glass beams prestressed by externally bonded tendons. GlassCon Global Conference Proceedings, Philadelphia, EUA: 2014, p. 450–9. https://doi.org/10.14296/deeslr.v5i0.1848.

[31] Louter C, Cupać J, Lebet J. Exploratory experimental investigations on post-tensioned structural glass beams. Journal of Facade Design and Engineering 2014;2:3–18. https://doi.org/10.3233/FDE-130012.

[32] Belarbi A, Dawood M. Sustainability of fiber-reinforced polymers (FRPs) as a construction material. Houston, USA: Woodhead Publishing; 2016. https://doi.org/10.1016/b978-0-08-100370-1.00020-2.

[33] Cagnacci E, Orlando M, Spinelli P. Experimental campaign and numerical simulation of the behaviour of reinforced glass beams. Glass Performance Days, Tempere, Finland: 2009.

[34] Bedon C, Louter C. Structural glass beams with embedded GFRP, CFRP or steel reinforcement rods: Comparative experimental, analytical and numerical investigations. Journal of Building Engineering 2019;22:227–41. https://doi.org/10.1016/j.jobe.2018.12.008.

[35] Palumbo M. A New Roof for the XIIIth Century 'Loggia de Vicari' (Arquà Petrarca – PD Italy) Based on Structural Glass Trusses: A Case Study. Glass Processing Days, Tempere, Finland: 2005.

[36] Bedon C, Louter C. Numerical analysis of glass-FRP post-tensioned beams – Review and assessment. Composite Structures 2017;177:129–40. https://doi.org/10.1016/j.compstruct.2017.06.060.

[37] ACI 440.2R-02. Guide for the Design and Construction of Externally Bonded FRP Systems for Strengthening Concrete Structures. ACI - American Concrete Institute, Farmington Hills, USA: 2008. https://doi.org/10.1061/40753(171)159.

[38] Bilotta A, Ceroni F, Di Ludovico M, Nigro E, Pecce M, Manfredi G. Bond Efficiency of EBR and NSM FRP Systems for Strengthening Concrete Members. Journal of Composites for Construction 2011;15:757–72. https://doi.org/10.1061/(asce)cc.1943-5614.0000204.

[39] CNR-DT 200 R1/2013. Guide for the Design and Construction of Externally Bonded FRP Systems for Strengthening Existing Structures. CNR - Advisory Committee on Technical Recommendations for Construction, Rome: National Research Council of Italy; 2013.

[40] De Lorenzis L, Teng JG. Near-surface mounted FRP reinforcement: An emerging technique for strengthening structures. Composites Part B: Engineering 2007;38:119–43. https://doi.org/10.1016/j.compositesb.2006.08.003.

[41] Neto P, Alfaiate J, Valarinho L, Correia J, Branco F, Vinagre J. Glass beams reinforced with GFRP laminates: Experimental tests and numerical modelling using a discrete strong

discontinuity approach. Engineering Structures 2015;99:253–63. https://doi.org/10.1016/j.engstruct.2015.04.002.

[42] Sena-Cruz J, Barros J, Coelho M, Silva L. Efficiency of different techniques in flexural strengthening of RC beams under monotonic and fatigue loading. Construction and Building Materials 2012;29:175–82. https://doi.org/10.1016/j.conbuildmat.2011.10.044.

[43] Dias SJE, Barros JAO. Performance of reinforced concrete T beams strengthened in shear with NSM CFRP laminates. Engineering Structures 2010;32:373–84. https://doi.org/10.1016/j.engstruct.2009.10.001.

[44] Cupać J, Martens K, Nussbaumer A, Belis J, Louter C. Experimental investigation of multi-span post-tensioned glass beams. Glass Structures and Engineering 2017;2:3–15. https://doi.org/10.1007/s40940-017-0038-5.

[45] Cagnacci E, Orlando M, Salvatori L, Spinelli P. Four-point bending tests on laminated glass beams reinforced with FRP bars adhesively bonded to the glass. Glass Structures and Engineering 2021;6:211–32. https://doi.org/10.1007/s40940-021-00147-9.

[46] Jani JM, Leary M, Subic A, Gibson MA. A review of shape memory alloy research, applications and opportunities. Materials and Design 2014;56:1078–113. https://doi.org/10.1016/j.matdes.2013.11.084.

[47] Cladera A, Weber B, Leinenbach C, Czaderski C, Shahverdi M, Motavalli M. Iron-based shape memory alloys for civil engineering structures: An overview. Construction and Building Materials 2014;63:281–93. https://doi.org/10.1016/j.conbuildmat.2014.04.032.

[48] Hosseini A, Michels J, Izadi M, Ghafoori E. A comparative study between Fe-SMA and CFRP reinforcements for prestressed strengthening of metallic structures. Construction and Building Materials 2019;226:976–92. https://doi.org/10.1016/j.conbuildmat.2019.07.169.

[49] Izadi M, Hosseini A, Michels J, Motavalli M, Ghafoori E. Thermally activated iron-based shape memory alloy for strengthening metallic girders. Thin-Walled Structures 2019;141:389–401. https://doi.org/10.1016/j.tws.2019.04.036.

[50] Michels J, Shahverdi M, Czaderski C. Flexural strengthening of structural concrete with iron-based shape memory alloy strips. Structural Concrete 2017;19:876–91. https://doi.org/10.1002/suco.201700120.

[51] Shahverdi M, Michels J, Czaderski C, Motavalli M. Iron-based shape memory alloy strips for strengthening RC members: Material behavior and characterization. Construction and Building Materials 2018;173:586–99. https://doi.org/10.1016/j.conbuildmat.2018.04.057.

[52] Shin M, Andrawes B. Experimental investigation of actively confined concrete using shape memory alloys. Engineering Structures 2010;32:656–64. https://doi.org/10.1016/j.engstruct.2009.11.012.

[53]   Rojob H, El-Hacha R. Self-prestressing using iron-based shape memory alloy for flexural strengthening of reinforced concrete beams. ACI Materials Journal 2017;114:523–32. https://doi.org/10.14359/51689455.

[54]   Asgarian B, Moradi S. Seismic response of steel braced frames with shape memory alloy braces. Journal of Constructional Steel Research 2011;67:65–74. https://doi.org/10.1016/j.jcsr.2010.06.006.

[55]   Dieng L, Helbert G, Chirani SA, Lecompte T, Pilvin P. Use of shape memory alloys damper device to mitigate vibration amplitudes of bridge cables. Engineering Structures 2013;56:1547–56. https://doi.org/10.1016/j.engstruct.2013.07.018.

[56]   Izadi MR, Ghafoori E, Shahverdi M, Motavalli M, Maalek S. Development of an iron-based shape memory alloy (Fe-SMA) strengthening system for steel plates. Engineering Structures 2018;174:433–46. https://doi.org/10.1016/j.engstruct.2018.07.073.

[57]   Kajiwara S. Characteristic features of shape memory effect and related transformation behavior in Fe-based alloys. Materials Science and Engineering A 1999;273–275:67–88. https://doi.org/10.1016/s0921-5093(99)00290-7.

[58]   Bedon C, Amarante dos Santos F. FE Exploratory Investigation on the Performance of SMA-Reinforced Laminated Glass Panels. Advanced Engineering Materials 2016;18:1478–93. https://doi.org/10.1002/adem.201600096.

[59]   Deng Z, Silvestru V, Michels J, Li L, Ghafoori E, Taras A. Performance of Glass to Iron-based Shape Memory Alloy Adhesive Shear Joints with Different Geometry. In: Belis B& L (Eds. ., editor. Challenging Glass Conference Proceedings, vol. 8, Ghent, Belgium: 2022, p. 1–12. https://doi.org/10.47982/cgc.8.397.

[60]   Silvestru V, Deng Z, Michels J, Li L, Ghafoori E, Taras A. Application of an iron-based shape memory alloy for post-tensioning glass elements. Glass Structures and Engineering 2022;7:187–210. https://doi.org/10.1007/s40940-022-00183-z.

[61]   Silvestru V, Deng Z, Michels J, Taras A. Enabling a Ductile Failure of Laminated Glass Beams with Iron-Based Shape Memory Alloy (Fe-SMA) Strips. The International Colloquium on Stability and Ductility of Steel Structures, Aveiro, Portugal: Ernst & Sohn GmbH; 2022. https://doi.org/https://doi.org/10.1002/cepa. 1839.

[62]   Veer F, Riemslag T, Romein T. The failure strength of glass, a non transparent value. Glass Performance Days, Tempere, Finland: 2007, p. pages 610–614.

[63]   Yankelevsky DZ. Strength prediction of annealed glass plates - A new model. Engineering Structures 2014;79:244–55. https://doi.org/10.1016/j.engstruct.2014.08.017.

[64]   Cupać J, Louter C, Nussbaumer A. Post-tensioning of glass beams: Analytical determination of the allowable pre-load. Glass Structures and Engineering 2021;6:233–48. https://doi.org/10.1007/s40940-021-00150-0.

CHAPTER 2

GLASS AS A BUILDING MATERIAL

Glass has been used for centuries for its aesthetic potential and transparency, but never before has it assumed such relevance in contemporary architecture. As a result, the glass is today one of the most interesting and attractive materials in construction industry. Compared to other building materials, glass has high compression strength and relatively high modulus of elasticity and tensile strength. In recent decades, glass has been increasingly used for structural purposes, such as floors, roofs, beams, columns and walls. In addition, recent improvements introduced by the glass industry with regard to (i) the production of large glass elements, (ii) the thermal toughening of glass and (iii) the development of interlayers with superior structural performance have allowed the construction of all-glazed structures. However, despite all of these improvements, laminated glass continues to show brittle behaviour and reduced post-fracture resistance and ductility, not complying with the traditional design philosophies and the most recent structural standards. The present chapter discusses the production of float glass, its chemical and mechanical properties, the different types of glass and structural applications of glass in recent decades, as well as the current standards that support the design of glass elements.

2.1. PRODUCTION OF GLASS

Depending on the purpose of the final product (e.g. glass panes, wool, fibres or lamps), several manufacturing processes are available in the glass industry, such as drawing, blowing, pressing, casting, rolling, extracting and floating [1]. Currently, the float method, introduced commercially by Pilkington Brothers Ltd in 1959, is the most common process used to produce flat glass, accounting

for 90 % of the world's flat glass production [2,3]. Compared to previous production methods of flat glass (e.g. Fourcault and Pittsburgh), this method (i) is less expensive, (ii) allows to obtain glass panels with constant thickness and (iii) allows to produce of larger glass panels under safe conditions [2].

The production of float glass is schematically presented in **Figure 2.1**, being possible to distinguish three main stages: (i) melting, (ii) forming and (iii) cooling. Initially, the raw materials are introduced in a furnace at a temperature of 1500 °C. Subsequently, at a temperature of 1200 °C, the molten glass is poured into an enclosed box where it floats on a bath of molten tin. This is the phase responsible for providing glass panels with very smooth surfaces, eliminating the need for any polishing to obtain satisfactory transparency. The thickness of the glass sheet is assigned at this phase and, depending on the speed of the rollers of the annealing *lehr* (next phase), it can vary between 2.0 and 25.0 mm. After that, at a temperature of approximately 600 °C, the glass sheet enters an oven called annealing *lehr*, where it is slowly cooled up to approximately 100 °C in order to avoid residual stresses. Finally, the glass is inspected and subsequently cut into panels of 6.00 × 3.21 [m]. The glass obtained from the float process is commonly called as annealed glass because the last stage of the manufacturing process occurs in an annealing *lehr* [2,3].
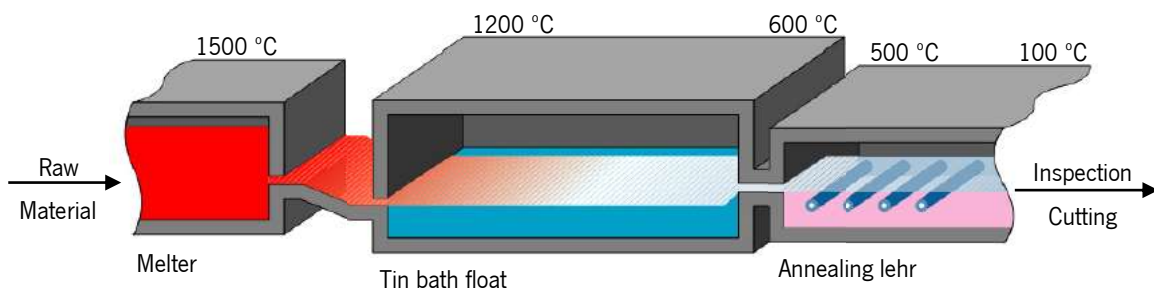
Figure 2.1: Schematic representation of the production process of float glass. Adapted from Henriques [4].

The float production process is not perfect and induces small deficiencies in glass during its manufacture. As a result, the surfaces of glass panels are not completely identical due to (i) the diffusion of tin atoms into the bottom surface, which influences the bond behaviour of adhesive joints applied to this surface; and, (ii) the superficial defects caused by the transport rolls of the annealing *lehr* on the bottom surface, which decrease its mechanical strength [2,5]. It should be noted that the glass surface in contact with the molten tin can be identified when exposed to ultraviolet radiation.

2.2. MATERIAL PROPERTIES

2.2.1. Chemical composition

In the production of glass, the fusion of the chemical ingredients is followed by its rapid cooling, which occurs without crystallization of the minerals. Depending on the chemical composition, the glass can be classified into two different categories: (i) the soda lime silicate glass (SLSG) and (ii) borosilicate glass (BSG). The borosilicate glass offers very high resistance to temperature changes, as well as a very high hydrolytic and acid resistance. This is only used in special applications (e.g. fire protection glazing, heat resistant glazing and chemical laboratory devices) because of its high cost [2]. **Table 2.1** shows the chemical composition of both glass types previously mentioned.

Table 2.1: Chemical composition of the soda lime silicate glass and borosilicate glass according to standards EN 572-1:2004 [6] and EN 1748-1-1:2004 [7], respectively.

Components		Soda lime silica glass [%]	Borosilicate glass [%]
Silica sand	SiO_2	69 - 74	70 - 87
Lime (calcium oxide)	CaO	5 - 14	-
Soda	Na_2O	10 - 16	0 - 8
Boron trioxide	B_2O_3	-	7 - 15
Potassium oxide	K_2O	-	0 - 8
Magnesia	M_g	0 - 6	-
Aluminium oxide	Al_2O_3	0 - 3	0 - 8
others	-	0 - 5	0 - 8

The chemical composition of glass has an important influence on its viscosity, melting temperature and thermal expansion. The glass transition temperature of the soda lime silicate glass is about 530 °C. According to Haldimann [8], the solidification of the glass (transition between liquid and solid states) does not occur for a precise temperature but over a temperature range, in contrast to crystalline materials. The best performance of the borosilicate glass in some applications comes from boron (B_2O_3) and potassium (K_2O) oxides. Besides the chemical composition listed in **Table 2.1**, these two glass types also have other components, such as iron, cobalt and titanium oxides and others, which are responsible for their coloration.

2.2.2. Physical and mechanical properties

For the contemporary architecture, the transparency within the visible spectrum (wavelengths between 380 and 750 nm) is the most important physical property of glass. The optical properties of glass (e.g.

absorbed and transmitted radiation spectrum) depend on its thickness, chemical composition and applied coatings. The infrared radiation with a wavelength exceeding 5000 nm is absorbed by the glass, as well as the ultraviolet radiation [2].

Glass is an isotropic material with elastic behaviour until failure. Such as concrete, glass presents a brittle failure, without plastic deformation. At molecular level, the tensile strength of glass is exceptionally high, ranging from 6000 to 10000 MPa [1,2]. However, due to the manufacturing process and handling of glass sheets, flaws are always present at the glass surfaces and its effective tensile strength is therefore much lower than the theoretical value [3]. The tensile strength of annealed glass for structural applications (macroscopic scale) varies between 30 and 80 MPa [9]. It is influenced by several aspects, namely (i) the size of the glass element, (ii) the loading history (intensity and duration), (iii) the residual stress and (iv) the environmental conditions, as well as the conditions of the glass surfaces (size and depth of flaws) [2].

Loading history directly influences the conservation of glass surfaces. The deterioration of surfaces flaws occurs when glass is subjected to long-term loads under humidity conditions [1,2]. Consequently, the higher the load and the severity of environmental conditions, longer the load duration and deeper the initial surface flaws, the lower the effective tensile strength of the glass. In general, the literature indicates values of tensile strength between 45 and 55 MPa [2,10]. According to EN 16612:2020 [11], both soda lime silicate glass and borosilicate glass have a characteristic flexural strength of 45 MPa. **Table 2.2** shows the other mechanical properties of these glass types.

2.3.   TYPES OF GLASS

After production, annealed glass can undergo secondary processing methods (e.g. edge treatment, coatings and thermal treatment) depending on the purpose of the glass product. Among these processing methods, thermal treatment (tempering) stands out. The structural application of annealed glass has been limited by the uncertainty involving its tensile strength, due to the growth of surface flaws over time. In addition, in the construction industry, the annealed glass is seen as an extremely dangerous material. When it breaks, it creates large, irregular and sharp fragments, compromising the people's safety [1]. In this context, tempering is clearly the most important processing method to meet the current structural requirements.

Table 2.2: Physical and mechanical properties of the soda lime silicate glass and borosilicate glass according to standards EN 572-1:2004 [6] and EN 1748-1-1:2004 [7], respectively.

Properties	Units	Soda lime silica glass	Borosilicate glass
Density	kg/m^3	2500	2200 - 2500
Knoop hardness	GPa	6.0	4.5 - 6.0
Thermal conductivity	Wm^{-1}K^{-1}	1	1
Specific thermal capacity	Jkg^{-1}K^{-1}	720	800
Coefficient of thermal expansion	K^{-1}	9×10^{-6}	Glass 1: 3.1 - 4.0 Glass 2: 4.1 - 5.0 Glass 3: 5.1 - 6.0
Average refractive index within the visible spectrum	–	1.52 [a]	1.50
Modulus of elasticity	MPa	70000	60000 - 70000
Shear Modulus	MPa	28455 [b]	–
Poisson ratio	–	0.23 [c]	0.20
Characteristic bending strength	MPa	45	–

Notes:

[a] A value of 1.52 is commonly used in studies on structural glass, although the standard EN 572-1:2004 indicates 1.50

[b] This value is proposed by Huveners [1]

[c] The standard EN 572-1:2004 indicates a values of 0.20: however, 0.23 is the most commonly used value in studies on structural glass

Tempering is widely used in the glass industry to improve its resistance against mechanical loads and changes in temperature. It creates a residual stress field in the glass consisting of tensile stresses in the core and compression stresses on the external surfaces and edges. As the glass core does not contain flaws, it can still withstand a significant tensile stress and hence the tensile strength of the glass increases due to the favourable compressive pre-stress on the outer surfaces and surroundings. On the other hand, the undesirable flaws can only grow when a tensile stress higher than the residual compressive pre-stress is induced by external loading, thus reducing the unpredictability of the glass. As long as the applied tensile stress is lower than the residual compressive pre-stress, there is no effective tensile stress and consequently no crack growth [2].

Thermal toughened glass is obtained by reintroducing the float glass into a furnace and by heating it above the glass transition temperature ($T_g = 650$ °C). Subsequently, jets of cold air are used to cool the heated float glass, first solidifying the outer glass regions while the core region remains soft [3]. When the glass core cools, thermal contraction is prevented by the solidified outer surfaces, generating tensile stresses in the core region and, by internal equilibrium reasons, compression stresses in the outer regions. Thereby, the residual stress level depends on the cooling speed rate. Typically, the residual stress field presents an approximately parabolic distribution over the glass thickness. The

ratio between the maximum tensile (core) and compression (surface) stresses is approximately 1:2 (see **Figure 2.2**).
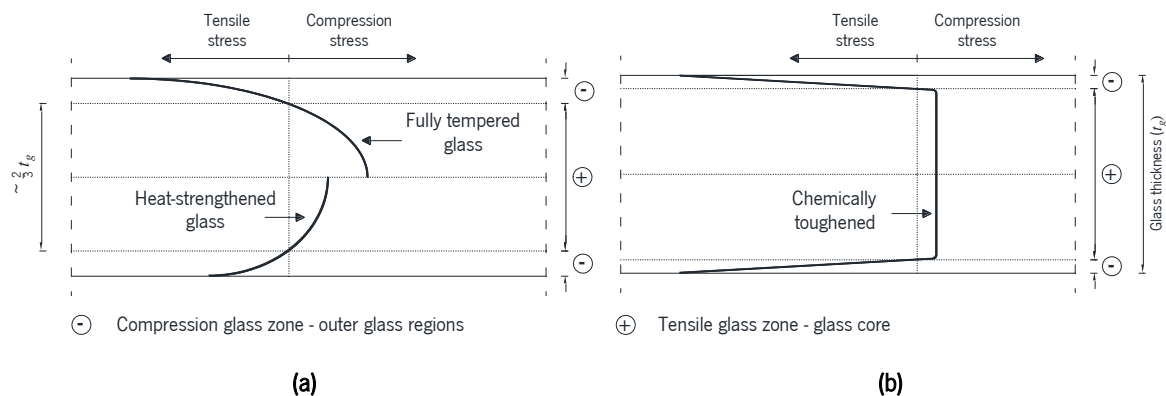
Figure 2.2: Comparison between the distributions of residual stress in (a) thermally toughened glass and (b) chemically toughened glass. Adapted from Huveners [1].

Two types of thermally toughened glass are commonly mentioned in the literature: the heat-strengthened glass and the fully tempered glass. The latter has a higher cooling rate than the former. Typically, the residual compressive pre-stress in fully tempered glass varies between 80 and 150 MPa while in heat-strengthened glass it ranges from 40 to 80 MPa [2,10]. According to the European standard EN 16612:2013 [11], the characteristic values of bending strength for heat-strengthened and fully tempered glass are respectively equal to 70 and 120 MPa, much higher than the 45 MPa found for annealed glass. After the tempering process, the glass cannot be cut or drilled because the stress state (energy balance) would be disturbed and the glass would crack immediately.

Chemical tempering can be an alternative to increase the tensile strength of glass. Residual stresses are induced through a chemical reaction in which sodium ions are exchanged by potassium ions (approximately 30 % larger in volume) [2]. This chemical process occurs only in a very thin glass zone near the surfaces and edges (see **Figure 2.2**). In contrast to thermally toughened glass, chemically tempered glass can be cut and/or drilled after tempering. Even so, its structural application is rare because this tempering process is expensive and time-consuming and, on the other hand, surface flaws can be deeper than the thin compression glass zone, causing spontaneous failure without external loading.

The fracture pattern depends on the amount of strain energy stored in the glass, i.e. the level of residual stress derived from the thermal treatment and the tensile stresses induced by external loads [12]. While annealed glass (negligible residual stress) usually breaks into relatively large fragments, heat-strengthened glass breaks into medium-to-small fragments and fully tempered glass (with the

highest residual stress among the glass types) breaks into even smaller and generally harmless fragments (e.g. dice), minimizing the risk of injury of loss of human life when they fall (see **Figure 2.3**). Given the above, fully tempered glass is commonly known as "safety glass" and is therefore used for a wide range of applications. However, due to the high amounts of strain energy, fully tempered glass shatters in an explosive manner when the residual stress equilibrium is disturbed.

(a)   (b)   (c)
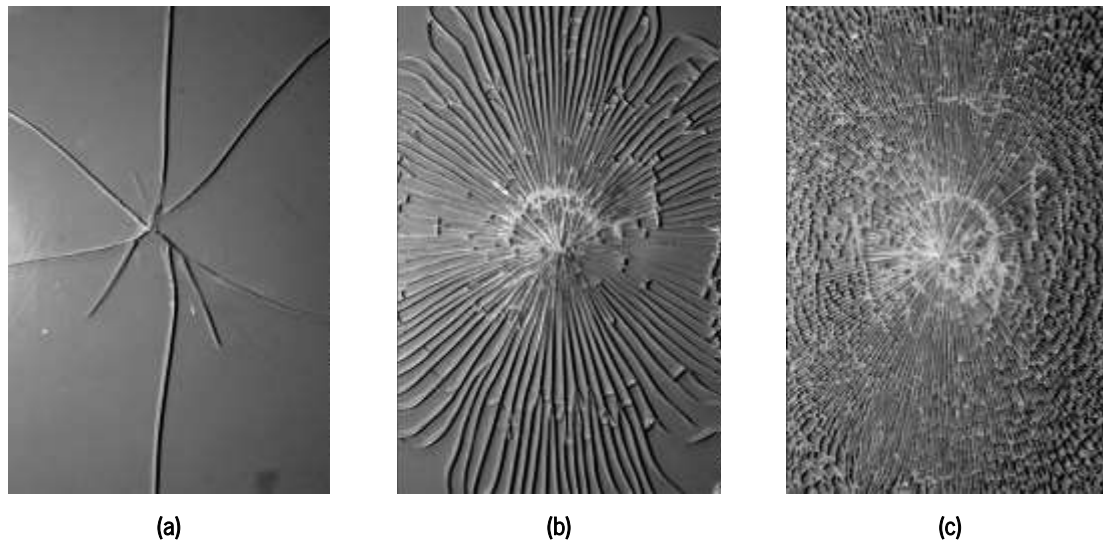
Figure 2.3: Comparison between the fracture patterns of (a) annealed glass, (b) heat-strengthened glass and (c) fully tempered glass. Adapted from Haldimann [2].

The fracture pattern influences both the post-failure safety and the post-failure performance [13]. Although fully tempered glass is the safest and has the highest tensile strength of all types of glass, it shows the poorest post-failure performance due to the lack of integrity of the tiny fragments as well. Concerning the heat-strengthened glass, it provides an interesting compromise between relatively high tensile strength and sufficiently large fragmentation for good post-failure performance [2].

Fully tempered glass can spontaneously break due to nickel-sulfite (NiS) inclusions, which penetrate the glass during its manufacturing process [14]. NiS particles expand in volume due to temperature variations, inducing high stress concentrations. As the core of fully tempered glass is subjected to a relatively high residual tensile pre-stress, the volume expansion of the NiS particles can cause spontaneous breakage [1–3].

Different topics have been focused in some studies addressing the glass tempering, namely (i) the fragmentation mechanism (e.g. [15–17]), (i) the residual stress state, either performing numerical simulations (e.g. [18,19]) or applying the principle of the photo-elasticity (e.g. [20]), and (iii) the influence of NiS inclusions (e.g. [21]).

2.4. LAMINATED GLASS

Although the thermal toughening of the annealed glass improves its mechanical performance and reduces its unpredictability, monolithic glass panels still exhibit brittle behaviour, with no plastic deformation before collapse and no load carrying capacity after glass cracking. Like annealed glass, thermally toughened glass fails suddenly and without any warning sign, posing a significant safety risk when applied as a structural material [13]. In this sense, the lamination process was developed in 1909 by Edouard Benedictus [22] to overcome this challenge, since it provides stability to the fragments after glass cracking.

The lamination process consists of joining at least two glass plies by means of a transparent and polymeric interlayer. It should be noted that laminated glass can comprise glass plies with the same thickness, or not, and with different residual stress levels – from annealed glass to fully tempered glass. Based on the concept of redundancy, when one of the glass plies breaks, the interlayer holds the fragments in place, preventing injury and damage property, and the external load is transferred for the surviving glass sheets through shear stresses in the interlayer [23]. As the fragments remain bonded to the interlayer after cracking, the interlocking effect between them results in residual structural capacity. This capacity depends on the fragmentation level. The larger the fragments the better the post-failure performance of the laminated glass (see **Figure 2.4**).

As depicted in **Figure 2.5**, after glass cracking, the interlayer can carry tensile stress while the glass fragments can still carry compression stress, creating a resisting mechanism capable of providing a certain level of residual strength and ductility, mainly for out-of-plane loads [24]. The cracking mechanism in laminated glass panes is schematically represented in **Figure 2.5** and can be divided into three stages: (i) the uncracked stage, without glass cracking; (ii) the cracking stage, in which the load carrying capacity is provided by the surviving glass sheets; and (iii) the post-cracking stage, with all glass plies cracked. For this reason, laminated glass is used for structural applications rather than monolithic glass.

The interlayer can be either an adhesive foil or an adhesive resin, but the former is the most used to produce laminated glass. Adhesive resins are commonly applied to join glass sheets at the construction site and the polymerization requires UV-radiation [14], e.g. acrylate adhesives. According to Callewaert [22], the lamination process involves three main stages: (i) first, the glass sheets are washed and introduced in a clean room; (ii) then, the glass sheets are stacked onto each other and adhesive foils are inserted between them, creating a "sandwich" panel; and (iii) finally, laminated glass

is produced by moving the glass sheets to an autoclave at a temperature between 130 and 150 °C, where they remain under a pressure of 14 bar for 2 to 3 hours.
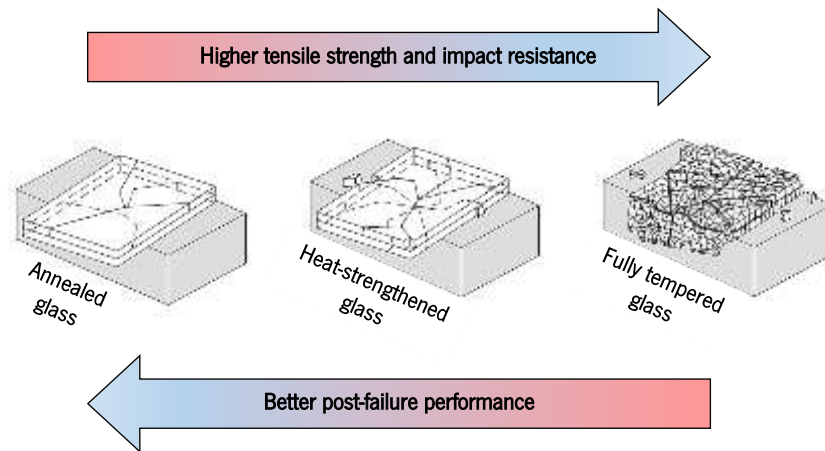
Figure 2.4: Evolution of the initial fracture strength and post-failure performance of glass as a function of the tempering level. Adapted from Sedlacek *et al.* [5]
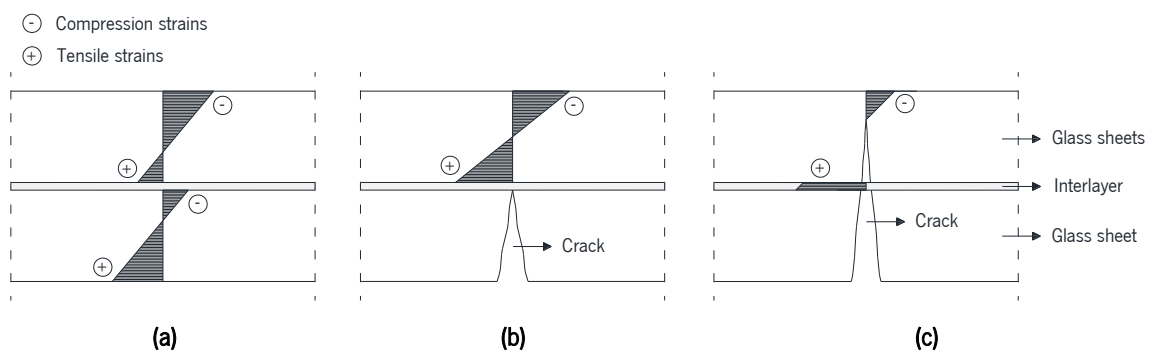
Figure 2.5: Redistribution of normal strains during the cracking process of two-layer laminated glass panel: (a) uncracked stage; (b) cracking stage; and (c) post-cracking stage. Adapted from Molnár *et al.* [25].

The interlayer (e.g. stiffness and strength properties) plays a key role in the post-failure performance of laminated glass, as well as the type of glass (e.g. size of the broken glass fragments) [26]. As mentioned, the interlayer is a polymeric material with a non-linear and viscoelastic response. As a consequence, laminated glass presents a time-dependent response, i.e. its flexural stiffness is a function of the loading history (duration and intensity) and temperature [27]. Therefore, the flexural stiffness of laminated glass can vary between two distinct scenarios: (i) the layered limit, with shear stiffness (G) → 0, in which the composite panel behaves like superimposed glass sheets without any composite action between them; and, (ii) the monolithic limit, with G → ∞, in which the interlayer ensures perfect bond between the glass sheets without relative displacement between them [28,29]. The stiffer and thinner the interlayer, the higher the shear interaction at the bonded interfaces and the more the laminated glass resembles the monolithic glass [24] (see **Figure 2.6**).

Polyvinyl Butyral (PVB), *Ionoplast* (e.g. SentryGlass - SGP) and *Ethylene Vinyl Acetate* (EVA) are the most suitable interlayers for structural glass applications. **Table 2.2** presents the main material properties of these interlayers. PVB has been the most used interlayer in the construction industry since the 1960s. This is based on several reasons: (i) firstly, PVB has high transmittance within the visible spectrum, similar to that of glass; (ii) secondly, it filters most of the UV radiation; (iii) thirdly, there are many manufacturers producing PVB, making it an economical interlayer for large-scale applications; and (iv) finally, it shows a good acoustic performance [30,31]. However, it has low shear stiffness and is highly viscoelastic even at room temperature [2,9]. Lately, stiffer interlayers (e.g. ionomer polymers and thermoplastic polyurethane) have been applied with the aim of increasing the structural application of glass by improving the shear interaction between the bonded interfaces.
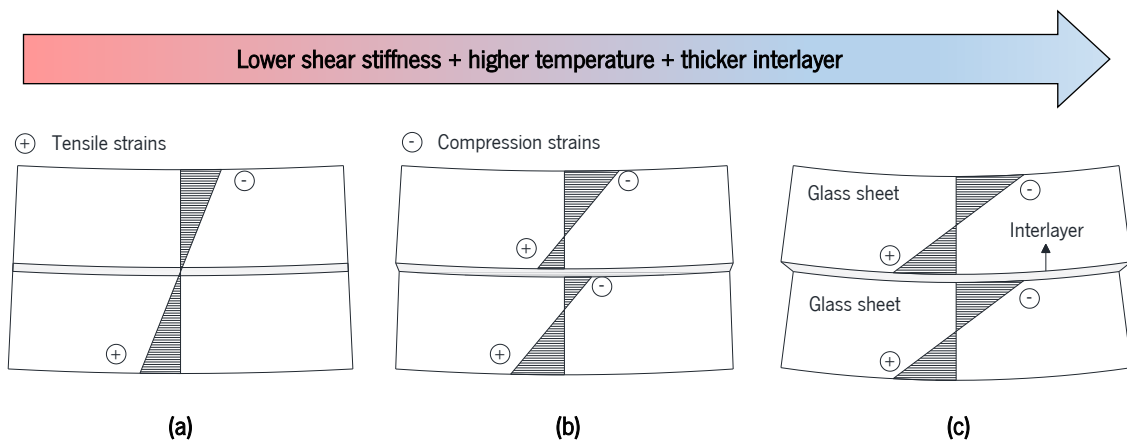
Figure 2.6: Distribution of normal strains over the cross-section of a two-layer laminated glass: (a) monolithic limit; (b) intermediate stage; and (c) layered limit. Adapted from Molnár *et al.* [25].

Focusing on the PVB and on the Ionoplasts, the most used interlayers in the construction industry today, the application of interlayer materials is briefly described next. PVB was first used as an interlayer to produce laminated glass for windshields, which took place in the 1930s [24]. After its great success in the automotive industry, the PVB has been widely used for the last 40 years in the construction industry [22]. Its chemical composition has been modified over time to meet new requirements, improving physical and aesthetic characteristics. To increase the load carrying capacity of glass facades, the SGP was developed in the 1990s by DuPont. It features high stiffness over a wide temperature range, making it suitable for structural applications. Like PVB, the chemical composition of SentryGlass has also been modified in recent decades to improve its performance.

Glass structures can be subjected to various load conditions, whose duration varies from few seconds to several years, as well as to various thermal conditions. Depending on these aspects, a polymer can

show an elastic, viscoelastic or viscous response. Hence, the mechanical properties of interlayers are usually presented as a reduction master curve, which is commonly derived by applying the time-temperature superposition principle. Each curve describes the evolution of a material property over time at a reference temperature. Based on the Maxwell-Weichert viscoelastic model, the reduction master curves are analytically represented using Prony series. The number of terms in the Prony series depends on the time period of interest and on the experimental data available for curve fitting. In general, such curves are extracted using different experimental setups, such as uniaxial tensile tests (e.g. [32]), dynamic mechanical analysis (DMA) tests on interlayer samples (e.g.[28]), pull-out tests (e.g. [33]) or torsional and flexural creep/relaxation tests on small-scale laminated glass specimens ([34]). Giovanna *et al.* [27] provide an overview of the test methods used to determine interlayer properties in laminated glass.

Table 2.3: Physical and mechanical properties of the most popular interlayer materials for structural glass applications [22].

Properties	Units	PVB	PVB Structural	Ionoplast	EVA
Density	kg/m^3	1070	1080	950	930
Tensile strength	MPa	25 to 27	33	34.5	9 to 31
Elongation at failure	%	200 to 250	190	> 500	> 415
Glass transition temperature	K	28 to 32	40 to 45	50 to 55	-60 to -31
Coefficient of thermal expansion	°C	468	155	100 to 150	98

Note: These mechanical and physical properties may slightly change depending on the producer

Based on DMA tests, **Figure 2.7** illustrates, for a reference temperature of 20 °C, the shear modulus of the commercial interlayers PVB *Butacite* and SGP *SentryGlass*, both produced by Kuraray Co. Ltd. [35]. As expected, both interlayers present similar shear modulus for short-term loads (e.g. shock loads) due to its viscoelastic behaviour. However, great differences between them are observed for medium- and long-term loads, the most of the applied loads in common structures. Both PVB and SGP exhibit viscoelastic response within the temperature range for common structural applications, from -20 to 80 °C [36], as well as a similar shear modulus at low temperatures (< 0 °C). However, these interlayers present significantly different glass transition temperatures, which for PVB is 20 °C while for SGP it is 55 °C [37].

The structural response of laminated glass has attracted the interest of several authors, either by simulating it numerically (e.g. [25,38]) and analytically (e.g. [29,39]) or performing experimental tests (e.g. [22,26,34,40–42]). In this context, the influence of the interlayer on the flexural stiffness (e.g.

25

[26,34]), lateral-torsional buckling behaviour (e.g.[22]) and post-failure behaviour (e.g. [41]) are the main topics addressed in literature, as well as the influence of the temperature (e.g. [42]) and type of glass (e.g. [40]).
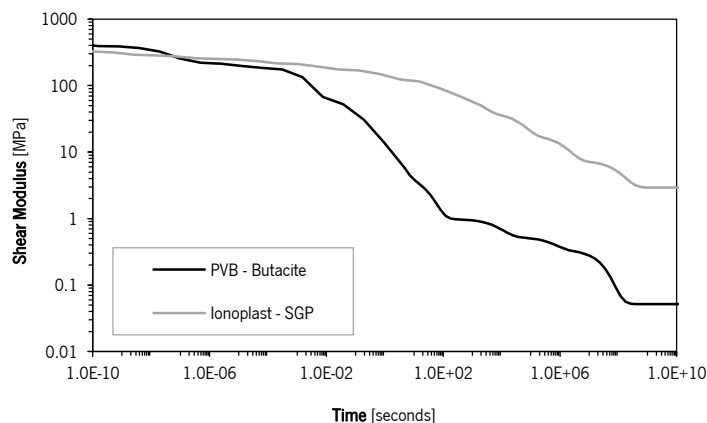
Figure 2.7: Evolution of the shear modulus of the interlayers PVB *Butacite* [43] and SGP *SentryGlass* [44] for a reference temperature of 20 °C.

2.1. CURRENT REQUERIMENTS

The standards applied to glass can be classified as (i) product certification standards, (ii) mechanical characterization standards and (iii) design standards. The former are aimed at ensuring the quality of glass products based on parameters set by regulator (e.g. European Committee for Standardization, CEN). The second ones present test methods to determine the main mechanical properties of glass (e.g. flexural strength and impact resistance). Finally, the latter are focused on the design of glass structures, indicating appropriate design methods and formulations based on the principles of safe design [45].

Unlike other building materials (e.g. reinforced concrete, steel, timber and aluminium), the lack of appropriate European standardization – Eurocodes – for glass has posed major challenges for the design of glass structures. However, national standards (e.g. [46–48]) and guidelines and recommendations (e.g. [9,49]) have been proposed in the last years to support the design of glass components. Furthermore, the second generation of Eurocodes will also include the Eurocode 10: "Design of Structural Glass", which will probably be available at the beginning of 2024 [50]. For the sake of simplicity, only the design standard CNR-DT 210/2013 [48] and the technical specification prCEN/TS 19100-1:2021 [46] will be focused below.

The design procedures proposed for glass structures are based on three concepts: (i) hierarchy, (ii) robustness and (iii) redundancy [9,48,51]. Thereby, like in any other structure (e.g. reinforced

concrete), glass structures must be able to redistribute stresses by providing alternative load paths after spontaneous and/or accidental failure of certain glass elements or part of them (e.g. glass plies from a laminated panel) [48].

Following the principle of design hierarchy and based on the classification system of consequence classes of European Standard EN1990 [52], both CNR-DT 210/2013 and prCEN/TS 19100-1:2021 classify the glass components according to the consequences of failure in economic, social and environmental terms, as well as in loss of human life. Both standards use a classification system with four levels, using the nomenclature (i) Consequence Class (CC) in CNR-DT 210/2013 and (ii) Fracture Consequence Class (FCC) in prCEN/TS 19100-1:2021.

Structural robustness is the ability to prevent excessive damage propagation caused by local failure. It can be achieved (i) by protecting the glass from impacts and (ii) by increasing the structural redundancy [51]. Due to the brittle behaviour of glass and risk of spontaneous breakage, redundancy is a crucial parameter in glass structures. It can be introduced at the level of the cross-section (e.g. laminated glass) or the entire structure (e.g. hyperstatic structures). The former concerns the ability of a glass component to carry load after its (partial) failure [9]. As a result, monolithic glass will never be considered structurally redundant. Therefore, laminated glass is typically used for structural applications because it satisfies the concept of redundancy by dividing the glass panel into thinner glass plies joined by an interlayer and/or adding additional glass plies to those required by the design procedure (i.e. over-designing methodologies). In the event of accidental failure, the surviving glass plies can still carry load. Redundancy can also be achieved by adopting structural systems able to mobilize alternative load transfer paths after failure of a glass component.

In contrast to other load-bearing materials, glass can fail unexpectedly and without any fault in the design procedure (e.g. NiS inclusions) [50]. Furthermore, local cracking can, in fact, trigger the collapse of the entire structure even at load levels lower than those anticipated for Ultimate Limit State (ULS) [48]. Thus, the design approach proposed by EN 1990, based on the Serviceability Limit State (SLS) and ULS, is not adequate to guarantee the safe fail of glass components. Thereby, CNR-DT 210/2013 introduced the Collapse Limit State (CLS), an additional analysis scenario. On the other hand, two additional limit state scenarios were also introduced by prCEN/TS 19100-1:2021: (i) the Fracture Limit State (FLS) and (ii) the Post Fracture Limit State (PFLS). Depending on the structural importance of the glass component, **Table 2.4** summarizes the design methodologies proposed by prCEN/TS 19100-1:2021.

Table 2.4: Glass design methodology according to prCEN/TS 19100-1:2021 [46].

State Limits	Failure Consequence Classes			
	FCC-0	FCC-1	FCC-2	FCC-3
SLS	✓	✓	✓	✓
ULS	✓	✓	✓	✓
FLS	✗	✓	✓	✓
PFLS	✗	✗	✓	✓
Examples	Infill panels	Balustrades Point-fixed walls	Horizontal roofs Façades	Floors Beams

While SLS concerns service requirements (e.g. deflections and vibrations), the ULS guarantees that the stress induced by anticipated actions at each point is lower than the glass strength [53]. Both the CLS and the PFLS consider the glass component to be fully or partially cracked. They aim to ensure that the glass components can still carry a portion of the actions anticipated for ULS and/or SLS (residual load-carrying capacity). Finally, the FLS is a limit state proposed only by prCEN/TS 19100:2021. It seeks to ensure that the glass structural elements break in an acceptable way, in order to provide safety and protection of people and/or structure during the cracking event (e.g. without falling fragments) [53].

2.2. STRUCTURAL APPLICATION OF GLASS

Glass has been used in the construction industry for centuries, primarily for non-structural applications (e.g. windows and decorative elements). However, since second half of the 20th century, glass has played a very important role in contemporary architecture due to its main characteristic: transparency. The demand for increasingly transparency and challenging buildings is encouraging the structural application of glass, such as in floors (see **Figure 2.8a** and **Figure 2.8b**), roofs (see **Figure 2.8c**) and façades (see **Figure 2.8d**). In addition, the recent development of reliable and advanced numerical tools for the design of glass, as well as the improvements introduced by the glass industry at the production/processing level (e.g. large-size elements and stiffer interlayers), allowed to overcome old psychological barriers and made glass an attractive building material. Due to the scope of this thesis, this section mainly focuses on some examples of structural glass beam applications.

During centuries, the use of glass in building was limited to windows or similar application where its brittle behaviour and variable tensile strength were not relevant. With the development of lightweight steel structures in the 19th century, glass was widely used as infill material in roofs. In this case, glass panes were mainly subjected to shell and membrane stresses (see **Figure 2.8c**). Nowadays, glass is

still used as infill material in floors, roofs and façades, the three most popular glass applications in construction industry. However, to maximize transparency inside buildings, efforts have been made over the last decades to replace traditional metallic load-bearing fames by glass elements (e.g. beams and/or columns) capable of carrying loads and transferring them to the foundations. One of the most important structural applications of glass today are the so-called glass fins (see **Figure 2.8d**). Glass fins are vertical glass beams that are used for the construction of all-glazed façades and are designed to support out-of-plane loads (e.g. wind). It should be noted that glass fins can also behave as columns, carrying vertical loads to the supports.

| (a) | (b) |
| (c) | (d) |
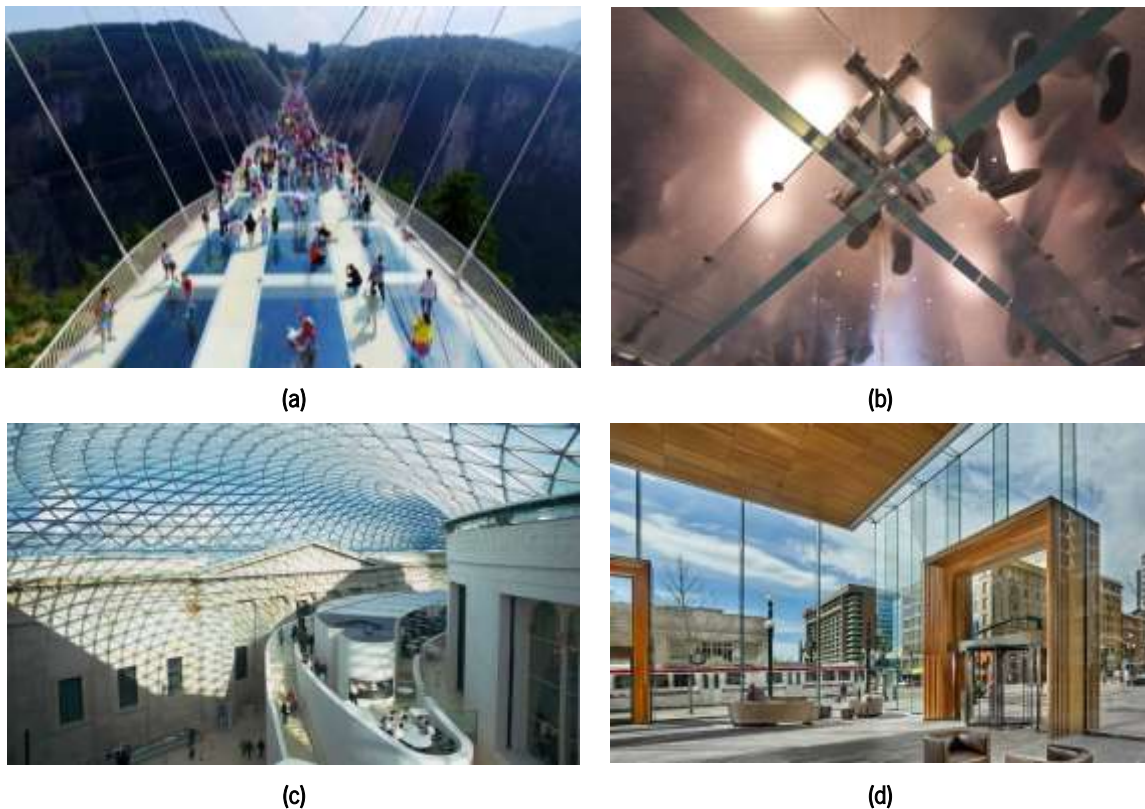
Figure 2.8: Structural glass applications: (a) pedestrian bridge designed by China Railway Major Bridge Reconnaissance & Design Institute Co Ltd. for Zhangjiajie Natural Park, China; (b) glazed floor at Apple Store in Paris, France [54]; (c) glazed roof at British Museum in London, UK [55]; and (d) glazed façade at 111 Main building in Salt Lake City, USA [54].

Glass beams can be divided into three categories: (i) continuous glass beams, (ii) segmented glass beams; and (iii) spliced laminated glass beams. The former consist of beams that are produced using one single and continuous (laminated) glass panel to span their entire length (see **Figure 2.9a**). Due to size restrictions on the production and lamination processes, the maximum length of such beams was limited to 6.0 m for a long time. However, this initial limit is being pushed forward due to recent improvements in both processes. As an alternative, segmented and spliced technologies have been

developed to produce beams with ever-large span lengths. While the former consists of screwing together two or more beam segments (see **Figure 2.9b**), the latter consists of overlapping three or more individual glass plies during the lamination process – the so-called splice-lamination technique. Individual glass plies can be arranged in different ways to form a spliced glass beam.

| (a) | (b) |

Figure 2.9: Types of glass beams: (a) continuous beams applied in a historic house in Ireland [54]; and (b) segmented-bolted beams designed by Arup for the Medical School building in Glasgow, UK [14].

Although the application of glass as a load-bearing material is still insufficiently popularized, the latest developments on this topic are encouraging architects to increasingly maximize the use of glass and reduce the use of traditional materials (e.g. steel, timber). As a result, all-glazed structures such as staircases (see **Figure 2.10a**), building envelops (see **Figure 2.10b** and **Figure 2.10c**) and pedestrian bridges (see **Figure 2.10b**) are now a reality. Glass can be found in the main structural components, such as in panels, beams, columns and shear walls. Metallic elements are commonly used to join adjacent glass structural elements, although there are some investigations on the feasibility of non-metallic connections for glass structures.

One of the best and most challenging examples of all-glazed structures are the iconic Apple Stores around the world, namely on 5th Avenue in New York (see **Figure 2.10b**) and on Pudong district in Shanghai (see **Figure 2.10c**). The main purpose of this design concept was to find an appealing way for people to be encouraged to shop below ground [56]. Regarding the Apple Store on 5th Avenue (commonly called as glass cube in literature), the larger and the older of both Apple Stores, three different versions have been built on the same location since 2006. The glass cube was rebuilt in 2011 and 2019 keeping the original dimensions but, at the same time, always applying the latest developments in manufacturing techniques and methods of connecting the glass panels [56]. A total of 164 glass units were used to build the first version of the glass cube. These glass units were produced with a maximum size of 6.0 m due to the standard size of flat glass panels on the market

at the time (see **Figure 2.11a**). In contrast, only 35 glass units with a maximum size of 15.0 m were used to build the second version. As a result, this abrupt decrease in panels and subsequent joints/connections created a much more transparent glass structure (see **Figure 2.11b**). In addition, metallic connectors were introduced inside the glass panel during the lamination process in order to create entirely embedded joints between panels.

(a)

(b)

(c)

(d)

Figure 2.10: Examples of all-glazed structures: (a) glazed staircase at Apple Leidseplain in Amsterdam, Netherlands [54]; (b) Apple Pudong in Shanghai, China [54]; (c) Apple Story on 5th Avenue in New York, USA [56]; and (d) glass bridge at CORE Shopping Centre in Calgary, Canada [57].
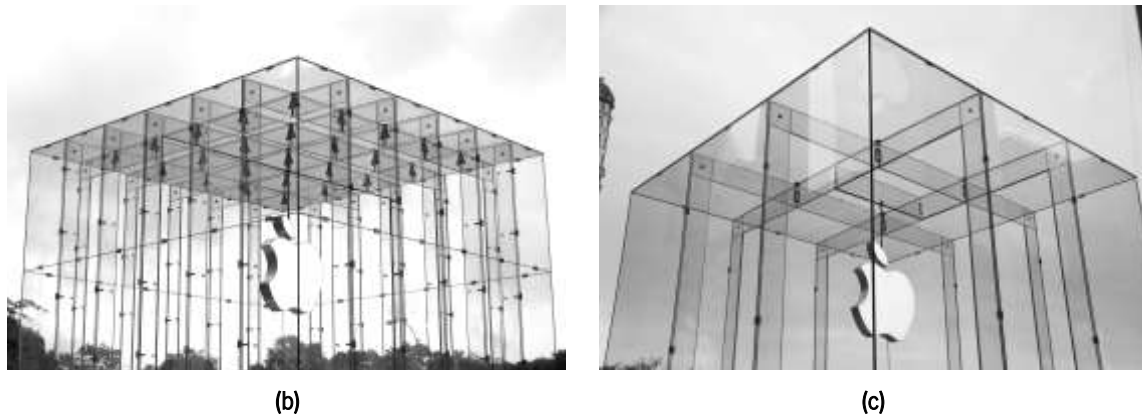
Figure 2.11: Difference between the transparency levels of (a) the original glass cube and (b) the glass cube rebuild in 2011 [56].

2.3. FINAL CONSIDERATIONS

One of the main challenges when glass is used as a structural material is its brittle behaviour. Its tensile strength is unreliable and time-dependent. Failure can occur without any warning in a catastrophic manner once the critical fracture toughness is attained. Thermal toughening is an effective solution to prevent the growth of surface flaws over time, but both fully tempered glass and heat-strengthened glass exhibit undesirable fragmentation patterns for structural applications. The tensile strength of glass and its fragmentation pattern seem to be two incompatible properties by applying tempering.

Glass lamination was developed based on the redundancy concept, but the collapse of entire glass structures can never be overlooked. Although the interlayer action is successful in preventing injuries or even loss of human life due to the fall of glass shards, laminated glass can barely support its own self-weight after cracking. Thus, safety concepts (e.g. glass composite systems) capable of withstanding load after cracking should be urgently developed, either to obtain ductile failure modes or reduce the cost of glass structures by improving over-designed methodologies used today.

2.4. REFERENCES

[1]   Huveners E. Circumferentially Adhesive Bonded Glass Panes for Bracing Steel Frames in Façades. PhD thesis. Eindhoven University of Technology, the Netherlands, 2009.

[2]   Haldimann M, Luible A, Overend M. Structural use of glass. LABSE - Lanka Association of Building Services Engineers; 2008.

[3]   Nielsen JH. Tempered Glass: Bolted Connections and Related Problems. PhD thesis. Technical University of Denmark (DTU), Denmark, 2009.

[4]   Henriques P. Comportamento ao fogo do vidro estrutural. MSc thesis [In Portuguese]. Univeristy of Aveiro, 2010.

[5]   Sedlacek G, Blank K, Laufs W, Gusgen J. Glas im konstruktiven Ingenieurbau. Berlim: 1999.

[6]   EN 572-1:2004. Glass in building – Basic soda lime silicate glass products – Part 1: Definitions and general physical and mechanical properties. CEN - European Committee for Standardization, 2004.

[7]   EN 1748-1-1:2004. Glass in building – Special basic products – Borosilicate glasses – Part 1-1: Definitions and general physical and mechanical properties. CEN - European Committee for Standardization, 2004.

[8]   Haldimann M. Fracture Strength of Structural Glass Elements - Analytical and Numerical Modelling, Testing and Design. PhD thesis. École Polytechnique Fédérale de Lausanne, Switzerland, 2006.

[9]   Feldmann M, Kasper R, Abeln B. Guidance for European Structural Design of Glass Components. Report EUR 26439 EN. Report EUR. Luxembourg: 2014. https://doi.org/10.2788/5523.

[10]   Schittich C, Staib G, Balkow D, Schuler M, Sobek W. Glass Construction Manual. 2nd revised and expanded edition. Munich: Birkhäuser; 2007. https://doi.org/10.11129/detail.9783034615532.

[11]   EN 16612:2020. Glass in building - Determination of the lateral load resistance of glass panes by calculation. CEN - European Committee for Standardization, 2019.

[12]   Nielsen JH, Bjarrum M. Deformations and strain energy in fragments of tempered glass: experimental and numerical investigation. Glass Structures and Engineering 2017;2:133–46. https://doi.org/10.1007/s40940-017-0043-8.

[13]   Valarinho L. Construction in Structural Glass: Flexural Behaviour of Laminated Glass Members and Development of Glass-GFRP Composite Beams. PhD thesis. University of Lisbon - Instituto Superior Técnico, 2016.

[14]   Louter C. Fragile yet Ductile: Structural Aspects of Reinforced Glass Beams. PhD thesis. Delft University of Technology, the Netherlands, 2011.

[15]   Nielsen JH, Olesen JF, Stang H. The fracture process of tempered soda-lime-silica glass. Experimental Mechanics 2009;49:855–70. https://doi.org/10.1007/s11340-008-9200-y.

[16]   Mognato E, Barbieri A, Schiavonato M, Pace M. Thermally Toughened Safety Glass: Correlation Between Flexural Strength, Fragmentation and Surface Compressive Stress. Glass Performance Days Proceedings 2011:115–8.

[17]   Pourmoghaddam N, Kraus MA, Schneider J, Siebert G. Relationship between strain energy and fracture pattern morphology of thermally tempered glass for the prediction of the 2D macro-

scale fragmentation of glass. Glass Structures and Engineering 2019;4:257–75. https://doi.org/10.1007/s40940-018-00091-1.

[18]   Nielsen JH, Olesen JF, Poulsen PN, Stang H. Finite element implementation of a glass tempering model in three dimensions. Computers and Structures 2010;88:963–72. https://doi.org/10.1016/j.compstruc.2010.05.004.

[19]   Pourmoghaddam N, Schneider J. Finite-element analysis of the residual stresses in tempered glass plates with holes or cut-outs. Glass Structures and Engineering 2018;3:17–37. https://doi.org/10.1007/s40940-018-0055-z.

[20]   Lohr K, Weller B. Residual stress distribution in tempered glass with reground edges. Glass Structures and Engineering 2019;4:99–115. https://doi.org/10.1007/s40940-018-0084-7.

[21]   Kasper A. Spontaneous cracking of thermally toughened safety glass. Part one: Properties of nickel sulphide inclusions. Glass Structures and Engineering 2019;4:279–313. https://doi.org/10.1007/s40940-018-0083-8.

[22]   Callewaert D. Stiffness of Glass / Ionomer Laminates in Structural Applications. PhD thesis. Faculty of Engineering and Architecture, Ghent University, Belgium, 2012.

[23]   Louter C, Belis J, Veer F, Lebet J. Durability of SG-laminated reinforced glass beams: Effects of temperature, thermal cycling, humidity and load-duration. Construction and Building Materials 2012;27:280–92. https://doi.org/10.1016/j.conbuildmat.2011.07.046.

[24]   Martín M, Centelles X, Solé A, Barreneche C, Fernández AI, Cabeza LF. Polymeric interlayer materials for laminated glass: A review. Construction and Building Materials 2020;230. https://doi.org/10.1016/j.conbuildmat.2019.116897.

[25]   Molnár G, Vigh L, Stocker G, Dunai L. Finite element analysis of laminated structural glass plates with polyvinyl butyral (PVB) interlayer. Periodica Polytechnica Civil Engineering 2012;56:35–42. https://doi.org/10.3311/pp.ci.2012-1.04.

[26]   Serafinavičius T, Lebet J, Louter C, Lenkimas T, Kuranovas A. Long-term laminated glass four point bending test with PVB, EVA and SG interlayers at different temperatures. Procedia Engineering 2013;57:996–1004. https://doi.org/10.1016/j.proeng.2013.04.126.

[27]   Giovanna R, Zulli F, Andreozzi L, Fagone M. Test Methods for the Determination of Interlayer Properties in Laminated Glass. Journal of Materials in Civil Engineering 2017;29:4016268. https://doi.org/10.1061/(asce)mt.1943-5533.0001802.

[28]   Andreozzi L, Briccoli Bati S, Fagone M, Ranocchiai G, Zulli F. Dynamic torsion tests to characterize the thermo-viscoelastic properties of polymeric interlayers for laminated glass. Construction and Building Materials 2014;65:1–13. https://doi.org/10.1016/j.conbuildmat.2014.04.003.

[29]   Galuppi L, Manara G, Royer Carfagni G. Practical expressions for the design of laminated glass.

Composites Part B: Engineering 2013;45:1677–88. https://doi.org/10.1016/j.compositesb.2012.09.073.

[30] Pyper J. Use of PVB in laminated side glass for passenger vehicle interior noise reduction. Society of Automotive Engineers - SAE Transactions 2000;109:1016–21. https://doi.org/10.4271/2000-01-2728.

[31] Foraboschi P. Behavior and Failure Strength of Laminated Glass Beams. Journal of Engineering Mechanics 2007;133:1290–301. https://doi.org/10.1061/(asce)0733-9399(2007)133:12(1290).

[32] Santarsiero M, Louter C, Nussbaumer A. The mechanical behaviour of SentryGlas ® ionomer and TSSA silicon bulk materials at different temperatures and strain rates under uniaxial tensile stress state. Glass Structures and Engineering 2016;1:395–415. https://doi.org/10.1007/s40940-016-0018-1.

[33] Biolzi L, Cagnacci E, Orlando M, Piscitelli L, Rosati G. Long term response of glass-PVB double-lap joints. Composites Part B: Engineering 2014;63:41–9. https://doi.org/10.1016/j.compositesb.2014.03.016.

[34] Valarinho L, Correia JR, Garrido M, Sá M, Branco F. Flexural Creep Behavior of Full-Scale Laminated Glass Panels. Journal of Structural Engineering 2017;143:4017139. https://doi.org/10.1061/(ASCE)ST.1943-541X.0001841.

[35] Web site of 'Kuraray Europe GmbH' 2021.

[36] EN 1991-1-1:2002. Eurocode 1: Actions on structures - Part 1-1: General actions - Densities, self-weight, imposed loads for buildings. CEN - European Committee for Standardization, 2002.

[37] Bennison S, Qin M, Davies P. High-performance laminated glass for structurally efficient glazing. Innovative Light-weight Structures and Sustainable Facades, Hong Kong: 2008, p. 1–12.

[38] Pelayo F, Lamela-Rey MJ, Muniz-Calvente M, López-Aenlle M, Álvarez-Vázquez A, Fernández-Canteli A. Study of the time-temperature-dependent behaviour of PVB: Application to laminated glass elements. Thin-Walled Structures 2017;119:324–31. https://doi.org/10.1016/j.tws.2017.06.030.

[39] Bedon C, Belis J, Luible A. Assessment of existing analytical models for the lateral torsional buckling analysis of PVB and SG laminated glass beams via viscoelastic simulations and experiments. Engineering Structures 2014;60:52–67. https://doi.org/10.1016/j.engstruct.2013.12.012.

[40] Zhao C, Yang J, Wang X, Azim I. Experimental investigation into the post-breakage performance of pre-cracked laminated glass plates. Construction and Building Materials 2019;224:996–1006. https://doi.org/10.1016/j.conbuildmat.2019.07.286.

[41]   Biolzi L, Cattaneo S, Orlando M, Piscitelli LR, Spinelli P. Post-failure behavior of laminated glass beams using different interlayers. Composite Structures 2018;202:578–89. https://doi.org/10.1016/j.compstruct.2018.03.009.

[42]   Samieian MA, Cormie D, Smith D, Wholey W, Blackman BRK, Dear JP, et al. Temperature effects on laminated glass at high rate. International Journal of Impact Engineering 2018;111:177–86. https://doi.org/10.1016/j.ijimpeng.2017.09.001.

[43]   Bennison SJ, Jagota A, Smith CA. Fracture of Glass/Poly(vinyl butyral) (Butacite) Laminates in Biaxial Flexure. Journal of the American Ceramic Society 1999;82:1761–70. https://doi.org/10.1111/j.1151-2916.1999.tb01997.x.

[44]   Belis J. Kipsterkte van Monolithische en Gelamineerde Glazen Liggers. [In Dutch]. PhD thesis. Ghent University. Belgium, 2006.

[45]   Bedon C, Amadio C. Comparative Assessment of Analytical models for the ULS Resistance Verification of Structural Glass Elements under Variable Loads. American Journal of Engineering and Applied Sciences 2017;10:229–42. https://doi.org/10.3844/ajeassp.2017.229.242.

[46]   prCEN/TS 19100-1:2021. Structural glass – Design and construction rules – Part 1: Basis ofdesign and materials. CEN - European Committee for Standardization, 2021.

[47]   DIN 18008-1:2020. Glass in Building – Design and construction rules – Part 1: Terms and general bases. Deutsches Institut für Normung, Deutsches Institut fur Normung E.V. (DIN); 2020.

[48]   CNR-DT 2010/2013. Guide for the Design, Construction and Control of Buildings with Structural Glass Elements. CNR - Advisory Committee on Technical Recommendations for Construction, Rome: National Research Council of Italy; 2013.

[49]   Abeln B, Preckwinkel E, Yandzio E, Heywood M, Eliášová M, Netušil M, et al. Development of innovative steel-glass structures in respect to structural and architectural design (Innoglast). Report EUR 25316 EN. Luxembourg: Publications Office of the European Union; 2013. https://doi.org/10.2777/91697.

[50]   Feldmann M, Di Biase P. The CEN-TS 'Structural Glass - Design and Construction Rules' as pre-standard for the Eurocode. Ce/Papers 2018;2:71–80. https://doi.org/10.1002/cepa.911.

[51]   Höier J, Lago S. Numerical Analysis of Point-Fixed Glass Balustrades. Halmstad University, 2019.

[52]   EN 1990:2002. Eurocode - Basis of structural design. CEN - European Committee for Standardization, 2005.

[53]   Wüest T, Luible A. Glass Design in Switzerland. Challenging Glass 7 - Conference on

Architectural and Structural Applications of Glass, Ghent, Belgium: 2021.

[54]   Web site of 'Eckersley O'Callaghan - Engineers' 2022. https://www.eocengineers.com.

[55]   Web site of 'Waagner Biro steel and glass' 2022. https://wb-sg.com.

[56]   O'Callaghan J, Bostick C. The Apple Glass Gube: Version 2.0. Challenging Glass 3: Conference on Architectural and Structural Applications of Glass, CGC 2012, 2012, p. 57–65. https://doi.org/10.3233/978-1-61499-061-1-57.

[57]   Wellershoff F, Sendelbach M, Schmitt F. Glass Bridges and Blass Walls. Challenging Glass 2 - Conference on Architectural and Structural Applications of Glass, CGC 2010 2010:217–26.

CHAPTER 3

STRENGTHENING OF GLASS

Glass is still an extremely fragile material. Therefore, based on the philosophy employed in reinforced concrete, glass has been combined with other materials in order to improve its post-failure performance. Furthermore, different concepts have been studied with respect to (i) type of glass, (ii) type of adhesive, (iii) reinforcement percentage; (iv) relative position of the reinforcement element, and (v) post-tensioning level. As a consequence, further investigations are focusing (i) on the bond behaviour of glass-to-reinforcement adhesive joints, which plays a crucial role in the overall response of glass composite systems; and (ii) on the numerical modelling of glass composite systems, which is essential to use this new technology at an industrial level for large scale applications. Reinforcement materials recently applied in civil engineering, such as SMAs, seem to be a promising alternative for the post-tensioning of glass structures. In addition, SMAs have self-sensing attributes that can be exploited to develop continuous monitoring techniques for glass structures. The present chapter presents and discusses some of the most important investigations on glass composite beams strengthened with steel, timber, GFRP and CFRP reinforcement materials, ranging from the bond behaviour of adhesive joints to the structural behaviour of composite systems and its numerical simulation, as well as the phase behaviour of SMAs.

3.1. STRUCTURAL AND SAFETY CONCEPT

Despite the improvements introduced by glass industry in the last decades (e.g. production and lamination processes), the behaviour of glass is still fragile regardless of its residual stress level, interlayer properties and structural options adopted. As a consequence, the safety of glass structures

is commonly ensured by adopting over-designing techniques, either by adding sacrificial glass sheets (e.g. glass floors) and/or by adopting thicker glass panes [1]. However, over-designed glass structures are certainly not cost-effective and the failure of the entire structure cannot be ruled out (e.g. unexpected loads – vandalism and accidental loads).

Like concrete, glass combines high compression strength with relatively low tensile strength. Therefore, it is reasonable to adapt the commonly accepted design philosophy of reinforced concrete to the glass, by bonding and/or anchoring reinforcement at the tensile region of the glass elements [2], thus creating glass composite systems. Even if glass is broken, they can still carry load due to the transfer of tensile stress from the cracked glass to the reinforcement element through shear stresses in the adhesive joint, creating a resisting mechanism formed by a compression force in the uncracked glass zone and a tensile force in the reinforcement (see **Figure 3.1**). The reinforcement acts as a crack bridge, thus preventing uncontrolled crack propagation and transferring the tensile force over the crack to the supports/foundations.
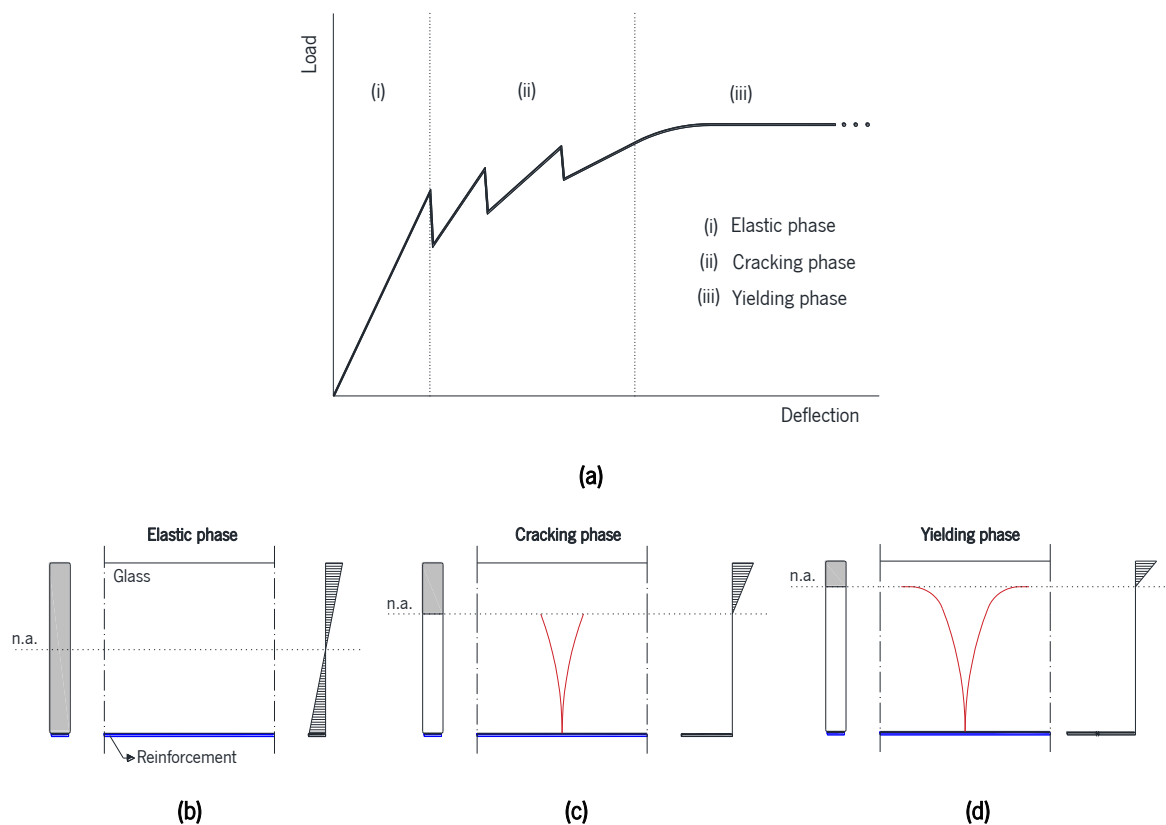
Figure 3.1: Structural behaviour of composite glass systems: (a) load *vs.* deflection diagram; and distribution of normal strains over the cross-section at the (b) elastic phase, (c) cracking phase and (d) yielding phase, as well as the crack growth. Note: the neutral axis (n.a.) is displayed as a horizontal dotted line.

Glass composite systems with timber (e.g. [3,4]), steel (e.g. [5–8]), CFRP (e.g. [9,10]) and GFRP (e.g. [11–16]) have been investigated as an alternative means of ensuring post-failure strength capacity and ductility in glass structures. Timber, GFRP and CFRP show brittle behaviour until failure, such as glass. However, the sequential failure of these materials and/or connections allows the glass composite systems to exhibit non-linear inelastic behaviour, with progressive decrease in stiffness with increasing load [17]. On the other hand, the ductility in glass-steel composite systems is a consequence of the yielding of the reinforcement material, which causes an increase in deformation under an approximately constant load.

3.2. BOND BEHAVIOUR OF GLASS JOINTS

Bolted connections are still extensively used by glass industry. However, they lack structural efficiency and reliability, as the drilling/cutting required may introduce flaws and discontinuities on the glass surfaces [18]. In contrast, adhesively bonded joints seem to minimize the development of stress concentrations and, consequently, avoid the formation of additional surface flaws, besides the clear aesthetic advantages compared to mechanic connections [18]. Soft gap-filling adhesives have been widely used in glazing systems. However, they are not able to transfer significant stress due to their low tensile strength. Lately, stiffer and stronger adhesives, based on epoxy and acrylate resins, are being study for this purpose.

The composite action between adherends, materialized by an adhesive joint, is crucial for the structural behaviour of composite systems. The bond behaviour of adhesive connections depends strongly on the adhesive type. This aspect is particularly relevant in glass structures because they do not have the ability to redistribute stress concentrations due to the yielding. Thus, it is particularly important to characterize the bond behaviour of adhesive connections, with respect to the substrate materials, the thickness of the adhesive layer, the effect of environmental conditions and the duration and rate of the load [19].

Some studies are found addressing the bond behaviour of glass composite systems. Glass-to-steel (e.g. [19–21]), glass-to-GFRP (e.g. [15,22]), glass-to-timber (e.g. [3,23]) and, very recently, glass-to-SMA (e.g. [24,25]) adhesively bonded connections have been investigated, using different types of adhesive (e.g. epoxy, acrylate, structural polyurethane and polyurethane gap-filing) to assess their influence on the shear interaction between adherends. Moreover, the interlayer has also been studied as a bonding agent when the reinforcement is introduced within the laminated glass panel before the lamination process (e.g. [20]). Different test setups have been adopted, such as single lap joint tests

(e.g. [21]), double-lap joint tests (e.g. [15]) and pull-out tests (e.g. [20]), as well as interface characterization tests such as Double Cantilever Beam (DCB) for mode-I fracture and End Notched Flexure (ENF) for mode-II fracture (e.g. [26]).

Although most studies have focused on the experimental characterization of glass composite systems, the development of analytical (e.g. [22]) or numerical (e.g. [27]) tools have also been addressed. Local bond stress – slip laws are calibrated to match experimental responses and are used as an input in numerical models, where adhesive damage is typically modelled using interface models, which in turn use energetic criteria (e.g. traction-separation laws) to govern the crack growth.

3.3. GLASS COMPOSITE SYSTEMS IN LITERATURE

3.3.1. Glass-steel composite systems

Glass-steel composite systems have been investigated since 2003 (e.g. [28–30]). Besides the experimental validation of the structural concept, these studies have focused on the influence of additional aspects on the structural response, such as the cross-section geometry, the bonding strategy for joining the reinforcement and the glass, the reinforcement percentage, the type of glass and the adhesive stiffness.

One of the largest investigations focusing on glass-steel composite systems was carried out at Delft University of Technology (TU Delft), as part of a wide research project to build a fully transparent pavilion using glass as a load-bearing material [31], as shown in **Figure 3.2**. The production of an 18 m long steel-reinforced glass beam capable of supporting load after glass cracking and, in turn, presenting a relatively safe and ductile failure mechanism [6,32–36] was a major milestone of this project. Before that, small scale models were manufactured and tested, assessing the influence of different cross-section geometries (see **Figure 3.3**) on the overall response of glass-steel composite systems [31,37]. Beams with most complex geometries were obtained by assembling the glass panels using an interlayer or a transparent structural adhesive. Based on the results, box- I- and T-section beams are better at preventing the lateral-torsional buckling of the compression glass zone [32]. I-section beams were extensively studied as a part of another large research project on glass-steel composite systems: the European project Innovative Steel-Glass-Structures (INNOGLAST) [38]. As glass composite systems are a relatively recent development in the construction industry and there are no specific design guidelines, a general design guidance was created by summarizing the main results of INNOGLAST [38]. This beam geometry is relatively easy to produce in comparison with box-

and T-sections and, furthermore, the steels flanges provide lateral stability, additional bending resistance and enhanced post-failure response.

Figure 3.2: Fully transparent pavilion built at Delft University using steel-reinforced glass beams [31].

As observed in **Section 3.2**, the composite action between the adherends plays a very important role on the structural performance of glass composite elements. Thus, another aspect investigated by the Glass & Transparency research group from TU Delft was the bonding strategy between the reinforcement and glass, mainly the adhesive type and the bonding surface area. Louter *et al.* [39] evaluated the influence of three distinct reinforcement configurations (see **Figure 3.4**) on the structural response of glass-steel composite beams. The reinforcement area was the same in all series to directly compare their structural responses. Following the most common strategies for strengthening existing concrete structures, the steel reinforcement was externally bonded to the glass panel ($1F$ and $2F$ series), according to the EBR technique, while for the $3F$ series it was introduced inside the glass panel, resembling the NSM technique. As expected, the specimens with a larger steel-to-glass contact area ($3F$ series) were more efficient in preventing the premature failure of glass composite systems by debonding of the reinforcement element, generating a stiffer post-cracking response, as well as a higher residual strength reserve (see **Table 3.1**). On the other hand, the strategy adopted in the $2F$ series can be useful to prevent a sudden failure of the strengthening system. Following the same principle (redundancy) of the laminated glass, when multiple reinforcement elements are used to achieve a certain reinforcement percentage, the premature debonding and/or failure of one of them can be offset by the others, thus preventing a sudden collapse of the glass composite system.
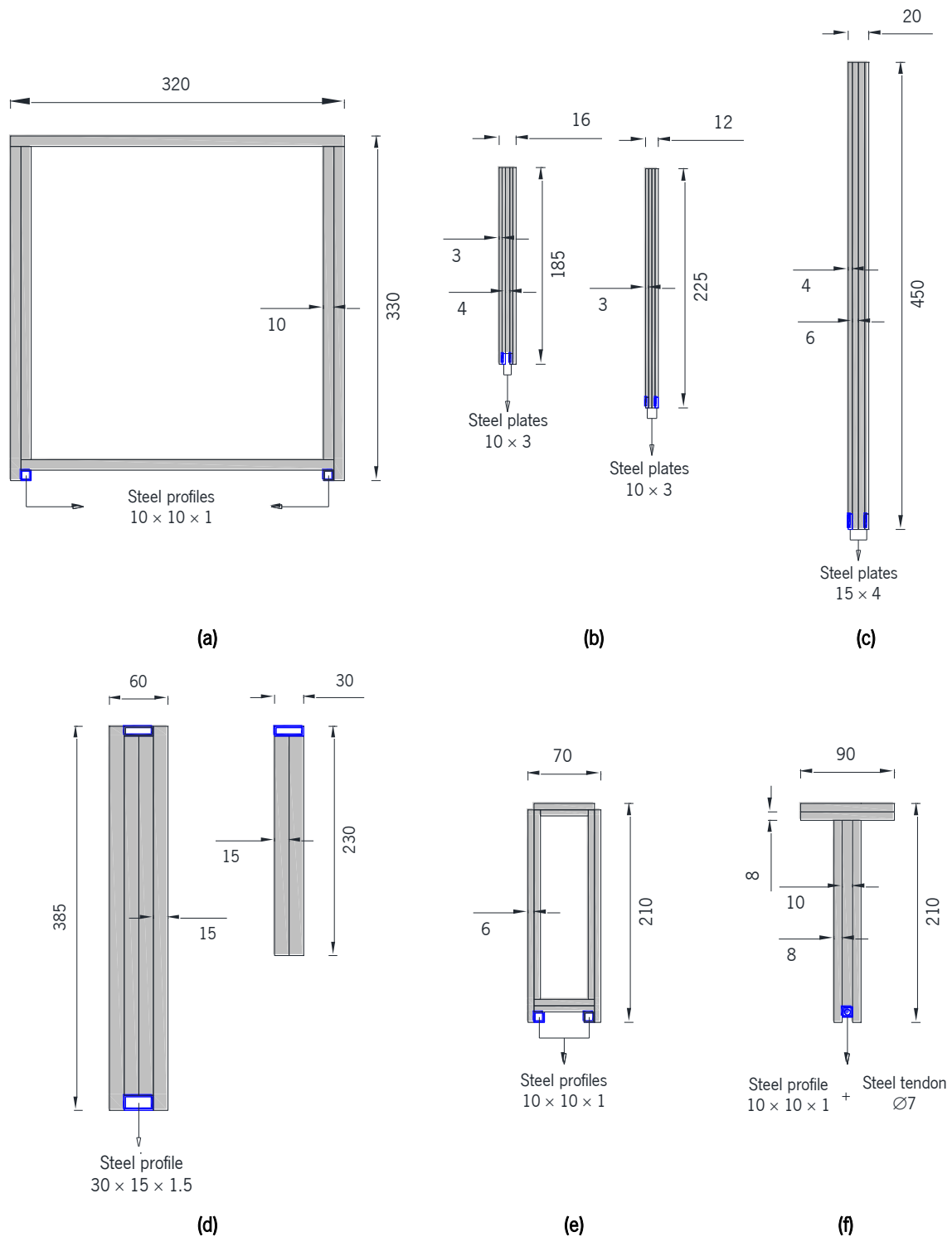
Figure 3.3: Cross-section geometry of steel-reinforced glass beams manufactured and tested as part of research projects developed at Delft University of Technology: (a) Veer *et al.* [28]; (b) and (c) Bos *et al.* [6]; (d) Louter *et al.* [31]; (e) Louter [37]; and (f) Louter *et al.* [36]. Note: units in [mm].

Premature debonding of externally bonded reinforcement (EBR technique) has been often observed in the literature, either in concrete (e.g. [40]) and glass (e.g. [41]) reinforced beams. This aspect is extremely important in glass structures because they are not strengthened with transversal

reinforcement (e.g. stirrups), unlike reinforced concrete. As a consequence, high interfacial stresses are induced at the bonded interfaces when shear cracks are formed, leading to an inevitable detachment of the reinforcement towards the supports, since there are no stirrups to restrain the cracks from opening. Some studies (e.g. [36]) have addressed the feasibility of mechanically anchoring the steel reinforcement at the beam ends, aiming to ensure a residual load-carrying capacity even when the adhesive connection no longer provides composite action between adherends or after a premature detachment of the reinforcement due to unpredictable actions, such as fire [42]. Mechanical anchorages are mainly used when reinforcement is prestressed (see **Section 3.4**).
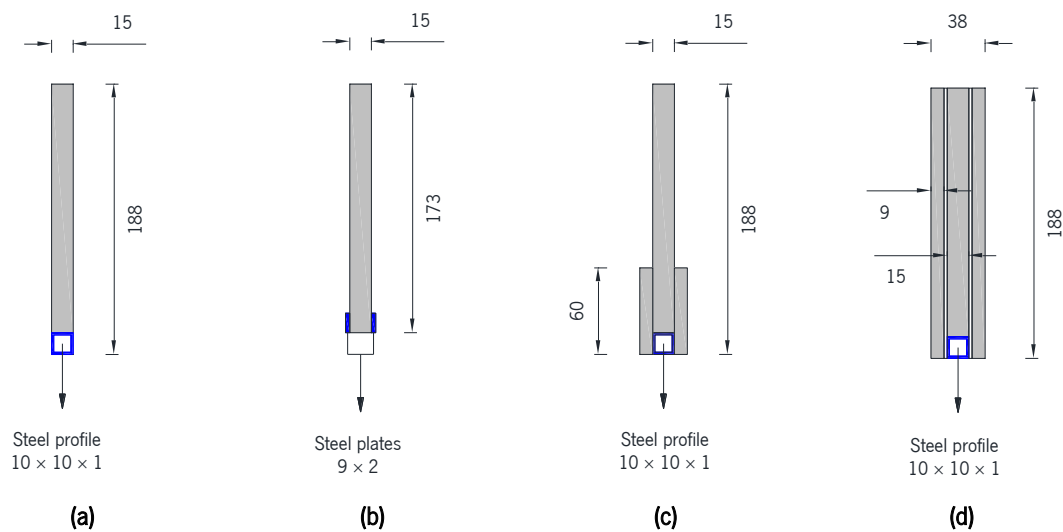
Figure 3.4: Cross-section geometry of steel-glass composite beams tested by (a-c) Louter *et al.* [39] – (a) geometry 1*F*; (b) geometry 2*F*; and (c) geometry 3*F* – and (d) Louter *et al.* [7]. Note: units in [mm].

Louter and Veer [36] tested three distinct mechanical anchorage solutions (see **Figure 3.5**): (i) in specimen #1, anchor plates were laterally bonded on the steel reinforcement and on the outer glass surface; (ii) in specimen #2, the steel reinforcement was directly screwed to "anchor heads" previously bonded at the beam ends; and (iii) in specimen #3, threaded rods were first welded to the steel reinforcement and then bolted to the "anchor heads". It should be noted that acrylate (specimens #1 and #2) and epoxy (specimen #3) adhesives were used to bond the steel reinforcement to the glass. As proven by experimental tests, the mechanical anchorage of steel reinforcement provides additional redundancy, since it can still transfer tensile forces to the supports after debonding, creating the so-called *tie-effect* [43]. Furthermore, the stiff adhesive generated superior composite action between adherends and, in turn, higher load carrying capacity before debonding.

Depending on the residual stress distribution, the glass shows distinct fracture patterns. Thus, Louter *et al.* [7] evaluated the influence of different types of glass on the structural response of steel-reinforced

glass beams (see **Figure 3.4d**), using annealed glass (*ANG* series), heat-strengthened glass (*HSG* series) and fully tempered glass (*FTG* series). Using the interlayer as a bonding agent, the steel reinforcement was introduced inside the laminated glass panel, resembling the NSM technique. As expected, the *FTG* series presented the highest initial failure strength among the three series, while *ANG* specimens presented the highest residual strength capacity and ductility. On the other hand, *HSG* series showed an intermediate behaviour between the other two specimen series, both in the pre- and post-cracking stages. In contrast to the *ANG* series, where the crack propagation was a function of the equilibrium of internal forces to withstand an external action, in the *HSG* and *FTG* series, it was highly influenced by dynamic cracking processes resulting from the high amounts of strain energy stored in the glass after tempering. Heat-strengthened glass may be interesting for structural applications, but fully tempered glass does not provide sufficient integrity after rupture to obtain safe and ductile post-cracking responses.
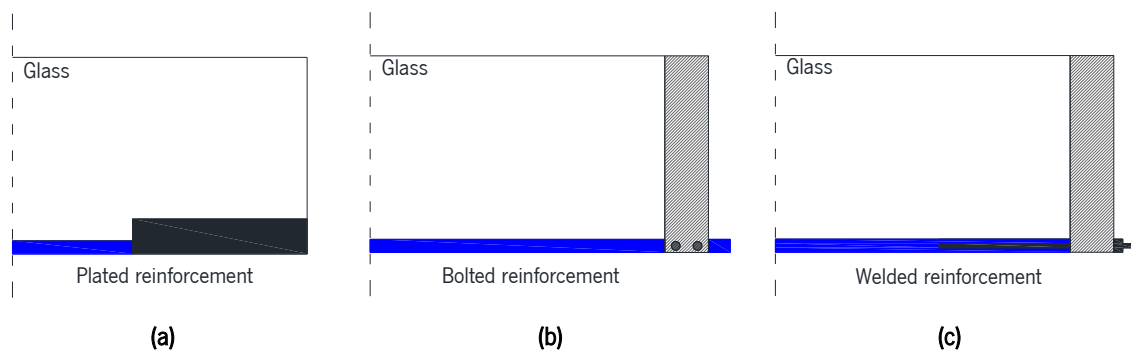
Figure 3.5: Anchorage of the reinforcement element at the beam ends studied by Louter and Veer [36]: (a) system #1; (b) system #2; and (c) system #3.

Currently, the demand for ever-larger structural glass elements is increasing, encouraging the glass industry to invest in new technologies (e.g. autoclave) to overcome this challenge. However, the maximum size of glass elements depends on the transport conditions and on-site manoeuvrability, since they are not cast *in situ* like concrete structures. Furthermore, the production of flat glass by float method (panel size equal to 6.00×3.21 [m] – see **Section 2.1**) is today a non-stop process and therefore the production of non-standard glass elements (> 6 m) is expensive because it requires modifications to the production process [44]. Attempts have been made (e.g. [33,37,45]) to manufacture large-span glass beams by overlapping standard glass sheets, producing the so-called spliced laminated glass beams. Although this strategy can be employed at the construction site to reach large-span beams, the lamination process requires specific conditions to be successful and

effective, such as a clean environment, and these conditions are normally very difficult to guarantee at the construction site.

Table 3.1: Overview of investigated concepts of steel-reinforced glass beams, indicating the most relevant parameters related to the specimen geometry and its post-failure performance.

Reference: Louter *et al.* [39]

Series	Adhesive	ρ_r [%]	P_b/A_r [mm^{-1}]	h_t/L_s [mm/m]	F_{max}/F_{cr} [%]	δ_{ult}/δ_{cr} [%]
1*F*	Epoxy vs. Acrylate	3.1	0.28	89.29	75 - 194	127 - 325
2*F*		3.1	0.50	82.14	85 - 164	314 - 775
3*F*		2.2	0.83	89.29	126 - 184	340 - 510

Reference: Louter and Veer [36]

Series	Adhesive	ρ_r [%]	P_b/A_r [mm^{-1}]	h_t/L_s [mm/m]	F_{max}/F_{cr} [%]	δ_{ult}/δ_{cr} [%]
#1	Acrylate				115	530
#2		1.35	0.32	104.6	80	548
#3	Epoxy				120	205

Reference: Louter et al. [7]

Series	Adhesive	ρ_r [%]	P_b/A_r [mm^{-1}]	h_t/L_s [mm/m]	F_{max}/F_{cr} [%]	δ_{ult}/δ_{cr} [%]
ANG	SG-interlayer				150	> 4472
HSG		1.36	0.83	89.29	50	< 1606
FTG					40	< 526

Note:
ρ_r = tensile reinforcement percentage; P_b = reinforcement-to-glass bonding perimeter; A_r = reinforcement cross-section area; h_t = total height of the specimen; L_s = span length; F_{max} = peak load registered after glass cracking; F_{cr} = cracking load; δ_{ult} = mid-span deflection at failure; and δ_{cr} = mid-span deflection correponding to F_{cr}.

As an alternative, the feasibility of an embedded steel reinforcement system has been explored in some investigations (e.g. [46–48]). Before the lamination process, steel plates are inserted between glass sheets, as schematized in **Figure 3.6a**. Thereafter, beam units can be easily joined on-site by bolting or welding these steel plates together to obtain longer spans (see **Figure 3.6b**). Experimental tests on specimens using this technology have shown promising results concerning the load transfer behaviour between glass units. Notwithstanding, as the interlayer is a viscoelastic material, the response of the glass-steel connection is a function of the temperature and loading rate. Embedded steel plates can play an active role in providing post-failure robustness when extended across the full beam length. With this in mind, Cruz *et al.* [48] developed a new concept of steel-reinforced glass beams by joining an inner perforated steel plate and two outer annealed glass sheets. PVB and SGP interlayers were used to join the components and their influence on the structural response was assessed as well. All specimens were tested until failure adopting a four-point bending configuration.

In addition, they were subjected to temperatures ranging from 20 to 80 °C during the tests. The *SGP* series always exhibited a higher residual strength than the *PVB* series and, at a temperature of 20 °C, showed a relatively distributed crack pattern, similar to the ones obtained in steel-reinforced glass beams with common bonding strategies (resembling the EBR and NSM techniques). One of the main disadvantages of using an embedded steel reinforcement system may be the visual impact, as maximum transparency is the primary objective in most of the glass structural applications.

Steel-framed glass beams have been another concept employed to manufacture ever-larger structural glass elements (e.g. [5,49]). They consist of introducing the glass panel into an enveloping steel frame, using a structural adhesive to join both components. Glass acts as an in-plane stiffener. After cracking, the resisting mechanism of steel-framed glass beams is similar to a truss. While the diagonal struts under compression are formed in glass, tensile forces are transferred to the supports by the surrounding steel frame. Belis *et al.* [5] investigated a steel-framed glass beam developed by Absoluut Glastechniek, in the Netherlands, which was especially designed so that framed units could be bolted together to produce large structural elements (see **Figure 3.7**). In such a system, an adhesive sealant to avoid direct steel-glass contact and the surrounding steel frame reduces the possibility of unexpected glass rupture due to stress concentrations, since in-plane loads are always applied on the surrounding steel frame. After an extensive characterization of the flexural behaviour, this new solution was adopted in real cases, with emphasis on the roof and facade structures of the Dutch Ministry of Finance in The Hague. The façade structure consisted of 21 m long continuous beams on three supports.

1- Glass sheets
2- Interlayers
3- Embedded steel plate

(a)   (b)
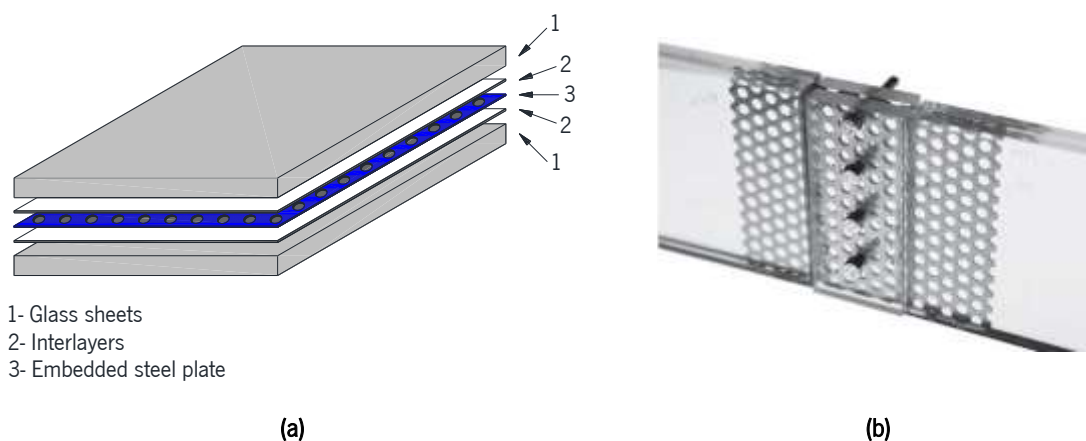
Figure 3.6: Embedded reinforcement system: (a) assemblage of the laminated glass panel; and (b) embedded reinforcement acting as a connecting element.
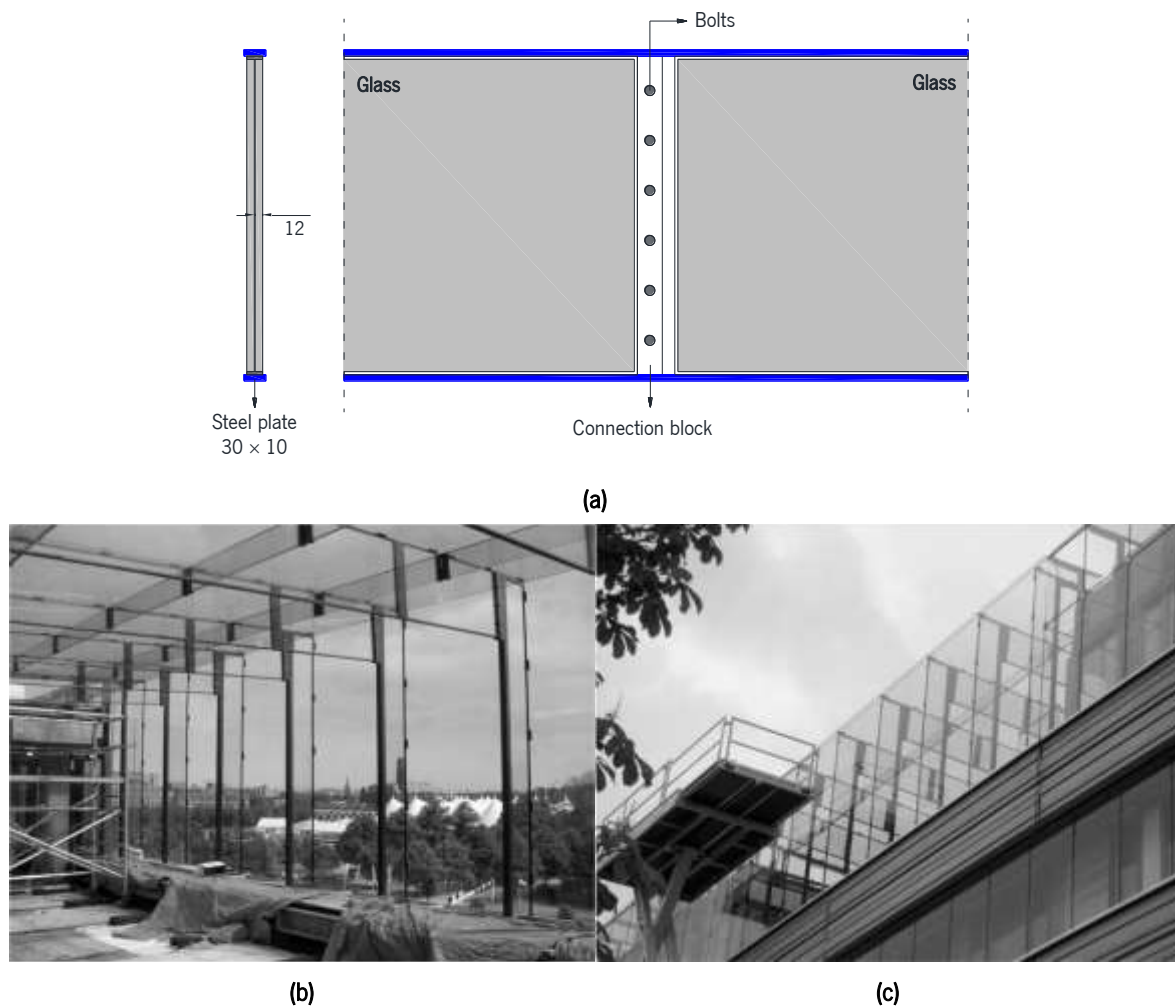
Figure 3.7: Steel-framed glass beam developed by Belis *et al.* [5]: (a) cross-section-geometry and schematic representation of the connection between beam segments; and (b-c) Dutch Ministry of Finance in The Hague. Note: units in [mm].

3.3.2. Glass-timber composite systems

Solutions including glass and timber are used for a long time (e.g. windows), but glass is mostly applied as an infill. Since the 2000s, some studies have addressed the possibility of strengthening glass with timber (e.g. [4,50–55]). Like glass, timber is one of the most important materials in contemporary architecture due to its mechanical and aesthetical features. Timber is a natural and environmentally friendly material. Its high strength-to-weight ratio and relatively low thermal conductivity make it an attractive alternative compared to other construction materials [53].

I-section beams formed by a glass web and timber flanges (see **Figure 3.8a**) were the first concept studied using both materials together [51]. It was concluded that timber reinforcement can be successful in providing load carrying capacity after glass breakage. After that, for the application of glass-timber composite beams at the Palafitte hotel, in Switzerland, Kreher [55] carried out an

extensive experimental campaign on I-section beams (see **Figure 3.8b**), varying both the glass type and the cross-section geometry. As expected, the higher the tempering level, the poorer the post-failure response, since thermally toughened glass has higher tensile strength and lower integrity after cracking in comparison with annealed glass. Moreover, the authors highlighted that such concept is aesthetically advantageous and capable of fulfilling the most recent design requirements, namely those regarding the structural performance under fire.

(a)   (b)   (c)
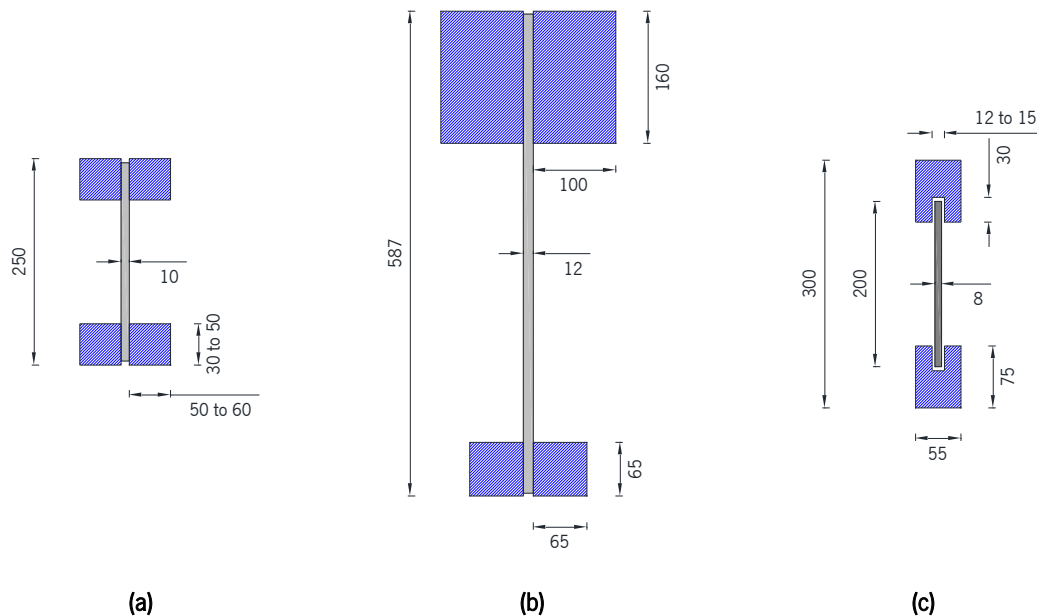
Figure 3.8: Cross-section geometry of glass-timber composite beams tested by (a) Hamm [51], (b) Kreher [55] and (c) Kozlowski [53]. Note: units in [mm].

In these mentioned studies, I-section beams were always manufactured by bonding timber bars on the side faces of the glass panel, similar to the EBR technique. However, in order to increase the bonding area between the adherends, Kozlowski [53] investigated another concept in which the glass pane was introduced into pre-cut groves in the timber flanges (see **Figure 3.8c**). First, adopting this novel concept, the influence of the adhesive layer thickness on the post-cracking behaviour of timber-reinforced glass beams was assessed by Hulimka and Kozlowski [52]. Then, Kozlowski *et al.* [54] tested I-section beams manufactured with three types of adhesive (silicone, acrylate and epoxy) and heat-strengthened glass panes. Probably due to the high amounts of strain energy released after glass rupture, none of the specimens showed post-cracking response. Notwithstanding, specimens with stiffer adhesives presented almost full composite action, in contrast to the softer silicone ones.

3.3.3. Glass-GFRP composite systems

In the last few decades, FRPs have been widely used in the construction industry, mainly as a reinforcement material in new structures or for the strengthening of existing concrete structures [56,57]. FRPs are available as unidirectional strips made by pultrusion or as sheets or fabrics with unidirectional or multidirectional fibres. The former, which are the FRPs commonly used as reinforcement in civil engineering applications, consist of long, unidirectional and continuous fibres embedded in a resin matrix. In this sense, FRPs are a heterogeneous and anisotropic material. While fibres govern the mechanical response of FRPs, which usually present a linear elastic response until failure, the matrix protects them from environmental agents (e.g. moisture) and redistributes stresses along the fibres. FRPs are commonly manufactured using thermosetting resins, such as polyester, vinylester and epoxy resins [56]. FRPs produced with carbon (CFRP), glass (GFRP), and aramid (AFRP) fibres are the most used for structural applications [58].

In construction, GFRPs are commonly used due to their low-cost [58]. This material presents high strength/weight and stiffness/weight ratios, as well as high durability. Like glass, GFRPs present a brittle failure and although they have high strength, commonly ranging from 200 to 500 MPa, their modulus of elasticity is relatively low compared to steel, CFRP or even glass. Furthermore, GFRP profiles can assume a variety of forms and shapes [59].

GFRP-reinforced glass beams are one of the most investigated glass composite concepts (e.g. [11,12,14,15,60–63]). Research on this topic have mainly focused on the influence of the adhesive type (e.g. [12,15]) and cross-section geometry (e.g. [15]), as well as the efficiency of different application alternatives for the GFRP reinforcement, such as (i) GFRP rods embedded within the interlayer (e.g. [60]), (ii) GFRP pultruded profiles externally bonded (e.g. [11]) and (iii) GFRP plates introduced between glass sheets in laminated glass (e.g. [62]).

Louter *et al.* [60] evaluated the feasibility of producing SG-laminated glass beams reinforced with embedded round (series #1) or flat (series #2) GFRP rods (see **Figure 3.10**). Promising results were obtained from both series through four-point bending tests. For short-term loading and at room temperature, the interlayer was able to provide sufficient shear interaction between both adherends. Furthermore, specimens with flat GFRP rods presented a stiffer post-fracture response than those reinforced with round GFRP rods, with a smaller GFRP-to-glass contact area than the first ones (see **Table 3.2**). Therefore, the series #1 were unloaded after significant slippage of the reinforcement, while the series #2 failed explosively by lateral-torsional buckling. Despite slight differences between

both specimen series (e.g. tensile capacity, modulus of elasticity and geometry), it was concluded that the reinforcement-to-glass bonding area plays an important role in the post-failure response, even when embedded reinforcement systems are adopted.
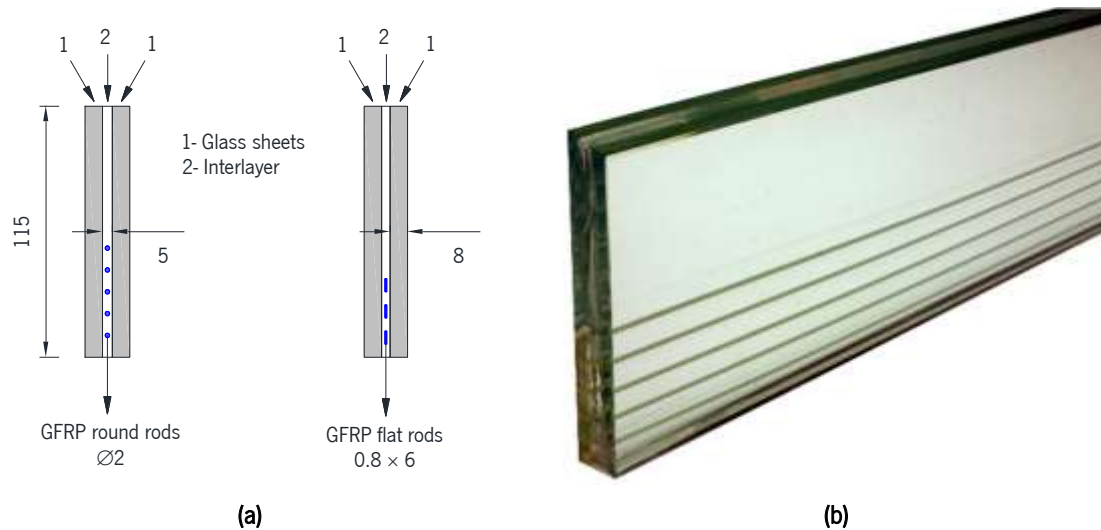
Figure 3.9: SG-laminated glass beams with embedded GFRP reinforcement tested by Louter *et al.* [60]: (a) cross-section geometry; and (b) specimen. Note: units in [mm].

Later, I-section beams formed by a glass web and GFRP flanges (series *I*) were tested by Correia *et al.* [12], as well as reference beams reinforced at the bottom edge with an externally bonded GFRP laminate (series *R*), as shown in **Figure 3.10a**. For bonding both components, an elastic gap-filling polyurethane adhesive (*PU*) and an epoxy adhesive (*EP*) were used. Based on four-point bending tests, I-section beams exhibited a higher residual strength capacity than those from the *R* series, in part because a much higher reinforcement percentage was adopted in the former (see **Table 3.2**). On the other hand, L-shaped GFRP plates were also used to join the GFRP flanges to the glass web, significantly increasing the bonding area between adherends. As a result and taking the *R* series as a reference, the I-section beams were able to (i) avoid premature detachment of the reinforcement by preventing high interfacial stresses at the tip of delamination cracks when the stiff adhesive was used and (ii) produce superior residual strength capacity by promoting greater shear interaction between adherends when the flexible adhesive was used. As observed in steel-reinforced glass beams, the reinforcement percentage and the bonding surface area were also important here.

Like in glass-steel composite systems (see **Section 3.3.1**), the type of adhesive remains a key parameter when GFRP replaces steel as reinforcement material. In this sense, Valarinho *et al.* [15] tested I-section GFRP-reinforced glass beams (cross-section geometry depicted in **Figure 3.10b**), adopting both isostatic and hyperstatic test configurations. In order to cover a wide range of shear

stiffness, three different adhesives were used to join the components: (i) an elastic gap-filling polyurethane adhesive (*SFlex* series), with the lowest modulus of elasticity; (ii) an epoxy adhesive (*SDur* series), the stiffest one; and (iii) a structural polyurethane adhesive (*SForce* series), with a moderate modulus of elasticity. With a focus on the isostatic tests, the stiffest adhesive was the best in providing residual strength, as expected, while *SFlex* series showed the highest values of deflection at failure, as well as the lowest values of residual strength and post-failure stiffness (see **Table 3.2**). The high post-cracking deformation observed in the *SFlex* series derived from a significant slip between the adherends due to the high deformability and low stiffness of the gap-filling polyurethane adhesive. Accordingly, the *SForce* and *SDur* series showed much denser crack patterns than the *SFlex* series, whose post-failure response was mainly governed by the damage propagation towards the supports at the adhesive joint level and the consequent horizontal crack propagation, i.e. crack branching, in the glass panel, as shown in **Figure 3.11**.

Table 3.2: Overview of investigated concepts of GFRP-reinforced glass beams, indicating the most relevant parameters related to the specimen geometry and its post-failure performance.

Reference: Louter *et al.* [60]						
Series	Adhesive	ρ_r [%]	P_b/A_r [mm^{-1}]	h_t/L_s [mm/m]	F_{max}/F_{cr} [%]	δ_{ult}/δ_{cr} [%]
#1	SG-interlayer	0.85	2.00	82.14	119	> 1250
#2		0.78	2.83		213	> 2349
Reference: Correia *et al.* [12]						
Series	Adhesive	ρ_r [%]	P_b/A_r [mm^{-1}]	h_t/L_s [mm/m]	F_{max}/F_{cr} [%]	δ_{ult}/δ_{cr} [%]
R-PU	Polyurethane	10.00	0.10	74.00	< 100	438
R-EP	Epoxy				104	394
I-PU	Polyurethane	139.5 [a)]	0.04	82.67	153	883
I-EP	Epoxy				199	426
Reference: Valarinho *et al.* [15]						
Series	Adhesive	ρ_r [%]	P_b/A_r [mm^{-1}]	h_t/L_s [mm/m]	F_{max}/F_{cr} [%]	δ_{ult}/δ_{cr} [%]
SDur	Epoxy				282	569
SForce	Polyurethane	90.32 [a)]	0.06	85.71	224	297
SFlex	Non-structural				165	1825

Notes:

ρ_r = tensile reinforcement percentage; P_b = reinforcement-to-glass bonding perimeter; A_r = reinforcement cross-section area; h_t = total height of the specimen; L_s = span length; F_{max} = peak load registered after glass cracking; F_{cr} = cracking load; δ_{ult} = mid-span deflection at failure; and δ_{cr} = mid-span deflection correponding to F_{cr}.

[a)] These values were determined considering the total amount of reinforcement. However, tensile forces were only supported by the bottom GFRP flange.
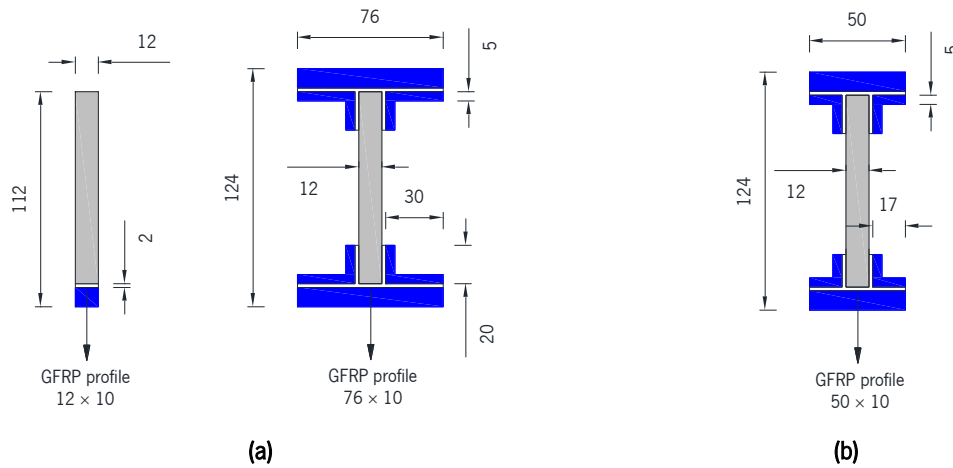
Figure 3.10: Cross-section geometry of GFRP-reinforced glass beams tested by (a) Correia *et al.* [12] and (b) Valarinho *et al.* [15]. Note: units in [mm].
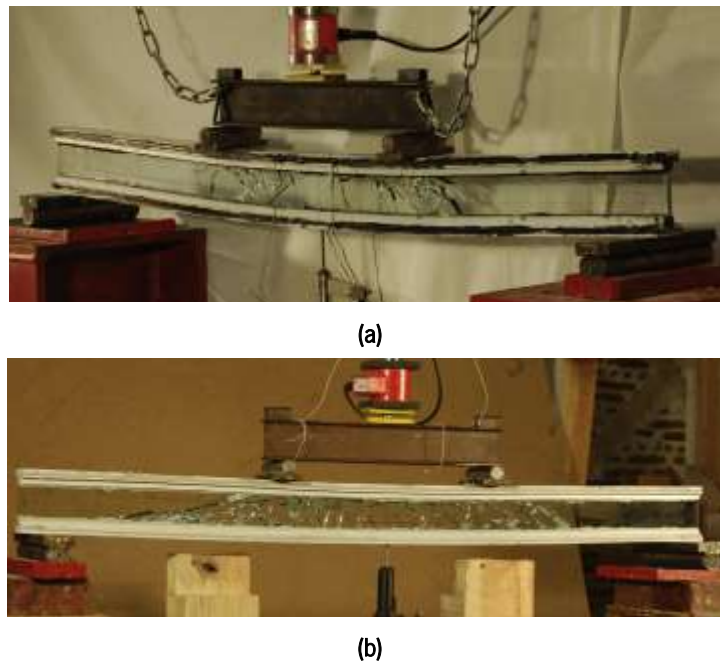
Figure 3.11: Crack patterns of GFRP-reinforced glass beams tested by Valarinho *et al.* [15]: (a) *SFlex* beams; and (b) *SDur* beams.

3.3.4.   Glass-CFRP composite systems

Today, CFRPs are one of the first choices for the strengthening of existing concrete structures [58]. Compared to steel, they are a lighter material and have higher stiffness and tensile strength, lower relaxation, no creep deformation and longer fatigue life, as well as higher resistance to chemical, thermal and aggressive environmental effects. With advance in technology, the cost of CFRPs is

decreasing and nowadays they are a viable and competitive solution for structural applications as a reinforcement material [58,64].

The structural behaviour of glass beams reinforced with CFRP has been addressed by few studies (e.g. [9,65,66,10]). In a general analysis, different strategies for applying CFRP reinforcement are found in the literature, such as: (i) CFRP laminates externally bonded to the glass [10]; (ii) CFRP rods embedded into the interlayer [66]; and (iii) CFRP rods introduced into previously designed grooves in laminated glass [65], resembling the NSM technique.

For the application of large CFRP-reinforced glass beams in the roof structure of the Loggia dei Vicari in Italy (see **Figure 3.12a**), Palumbo *et al.* [10] carried out the first study on glass-CFRP composite beams to the best of the author's knowledge. A small-scale prototype was tested adopting a three-point bending configuration. The specimen was manufactured by bonding a CFRP laminate to the bottom edge of an SG-laminated glass panel (see **Figure 3.12b**). Experimental results showed the ability of the CFRP reinforcement to generate stress distribution mechanisms after glass cracking, providing a significant post-cracking load carrying capacity (see **Table 3.3**).

Table 3.3: Overview of investigated concepts of CFRP-reinforced glass beams, indicating the most relevant parameters related to the specimen geometry and its post-failure performance.

Reference: Palumbo *et al.* [10]						
Series	Adhesive	ρ_r [%]	P_b/A_r [mm^{-1}]	h_t/L_s [mm/m]	F_{max}/F_{cr} [%]	δ_{ult}/δ_{cr} [%]
-	Epoxy	-	-	100	179	-

Reference: Louter *et al.* [66]						
Series	Adhesive	ρ_r [%]	P_b/A_r [mm^{-1}]	h_t/L_s [mm/m]	F_{max}/F_{cr} [%]	δ_{ult}/δ_{cr} [%]
-	SG-interlayer	0.26	2.67	82.1	96	> 3061

Reference: Cagnacci *et al.* [65,67]						
Series	Adhesive	ρ_r [%]	P_b/A_r [mm^{-1}]	h_t/L_s [mm/m]	F_{max}/F_{cr} [%]	δ_{ult}/δ_{cr} [%]
S-EP	Epoxy				22	-
S-PO	Polyester	1.15 [a]	0.50	107.1	21	-
H-EP	Epoxy				55	-
H-PO	Polyester				80	-

Notes:

ρ_r = tensile reinforcement percentage; P_b = reinforcement-to-glass bonding perimeter; A_r = reinforcement cross-section area; h_t = total height of the specimen; L_s = span length; F_{max} = peak load registered after glass cracking; F_{cr} = cracking load; δ_{ult} = mid-span deflection at failure; and δ_{cr} = mid-span deflection correponding to F_{cr}.

[a] This value was determined considering the total amount of reinforcement. However, tensile forces were only supported by the bottom CFRP bar after glass rupture.
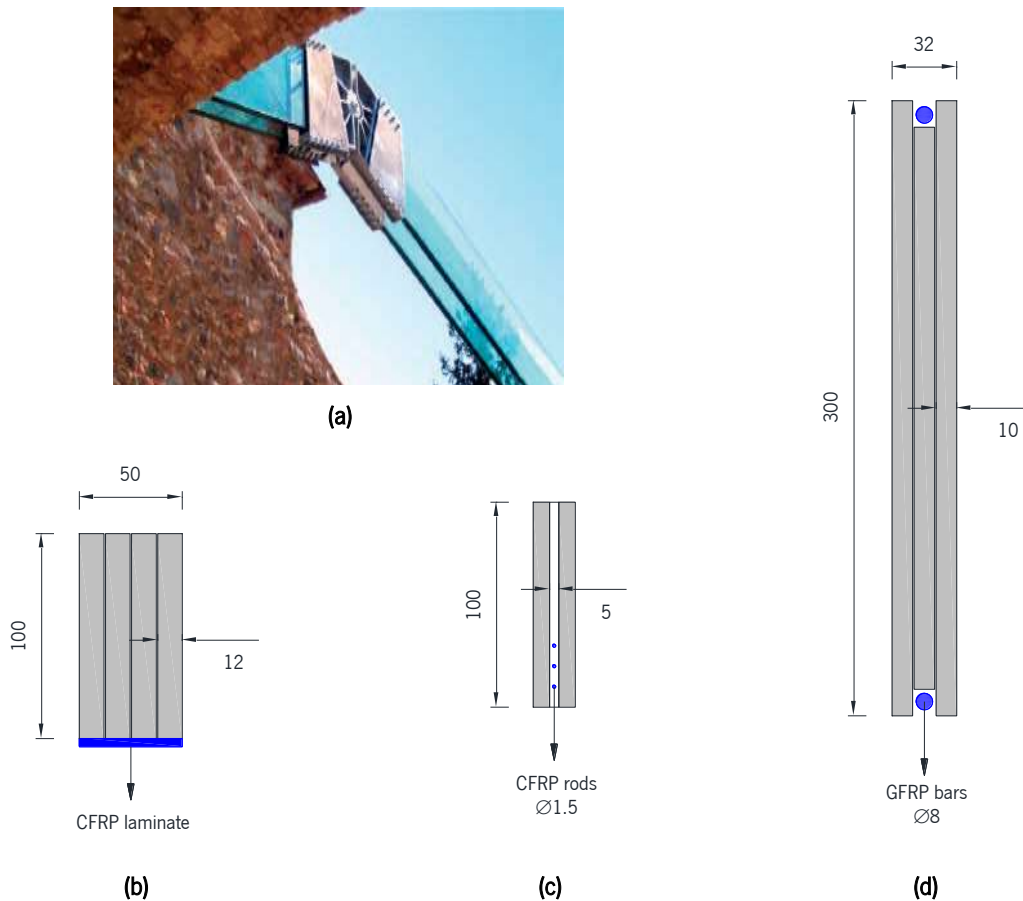
Figure 3.12: Glass-CFRP composite beams: (a) roof structure of the Loggia dei Vicari, in Italy [10]; and cross-section geometry of specimens tested by (b) Palumbo *et al.* [10], (c) Louter *et al.* [66] and (d) Cagnacci *et al.* [65,67]. Note: units in [mm].

Following the philosophy employed in glass-GFRP composite beams (see **Section 3.3.3**), Louter *et al.* [66] introduced round CFRP rods into the interlayer of two-layer laminated glass panels during the lamination process, as schematized in **Figure 3.12c**. On the other hand, Cagnacci *et al.* [65,67] developed a novel concept of CFRP-reinforced glass beams which consists of inserting round CFRP rods into U-shaped recessed grooves on both longitudinal edges of a three-layer laminated glass panel (see **Figure 3.12d**). The specimens were manufactured with CFRP bars with smooth (S) and helical wrapped (H) surfaces, as well as epoxy (EP) and polyester (PO) adhesives for bonding the components. As observed in concrete structures (e.g. [68]), the surface properties of CFRP bars strongly influenced the shear interaction level at the reinforcement/adhesive interface. Higher residual strength was achieved replacing smooth CFRP bars by helical wrapped ones (see **Table 3.3**). As a result, the specimen failure was no longer governed by adhesive failure at the CFRP/adhesive interface, but by tensile failure in CFRP (specimens with polyester adhesive) or damage propagation at the adhesive joint and glass substrate (specimens with epoxy adhesive). This difference between

failure modes was probably a result of the shear stiffness provided by each adhesive. In contrast to the polyester adhesive, the epoxy adhesive was not able to mobilize long bond lengths to transfer the shear stresses between adherends, thus inducing high interfacial stresses at the tip of delamination cracks. Given the above, some improvements would be necessary to achieve greater post-failure strength, such as the adoption of a higher reinforcement percentage.

3.4. POST-TENSIONING OF GLASS

As noticed in passively reinforced glass beams, the annealed glass is better at providing structural integrity after cracking due to the interlocking between the resulting large shards. However, its tensile strength is time-dependent because surface flaws grow when subjected to tensile stress and humidity. Tempering has been successful in avoiding this unpredictability, but when fully tempered glass breaks, it results in small shards, compromising the structural integrity of glass elements and, consequently, the post-failure load-carrying capacity and ductility of composite systems [12,15,69]. Heat-strengthened glass provides an interesting compromise between fairly tensile strength and sufficiently large fragmentation patterns, but annealed glass has obvious economic and structural benefits for the construction industry [1]. In addition, heat-strengthened glass subjected to in-plane loads can break into tiny fragments, like fully tempered glass.

Resembling the prestressing methodologies employed to concrete structures, post-tensioned composite systems have been recently investigated with the aim of improving the performance of glass structural elements, both before and after glass cracking. Like tempering, post-tensioning induces beneficial compressive stress in the glass to prevent existing flaws from growing under service load, making it safer for large-scale applications. Compared to tempering, the mechanical prestressing of glass can be advantageous in several aspects, such as: (i) the post-failure performance of glass remains virtually unchanged after post-tensioning; (ii) the glass can theoretically be drilled and/or cut after post-tensioning to overcome unexpected geometric challenges; (iii) both the prestressing level and the layout can be adapted to each structural element and its loading conditions, unlike the thermally toughened glass available on the market; and (iv) after glass rupture, the reinforcement acts as a crack bridge, transferring the tensile force to the supports and providing residual load carrying capacity.

A limited number of researches have addressed the post-tensioning of glass composite systems. Steel (e.g. [6,8,41,70]) is the most commonly used material as prestressed reinforcement, and recently CFRP (e.g. [9]) and GFRP (e.g. [62]) as well. These exploratory studies have mainly focused on the

post-tensioning setup and on the anchorage system to transfer the post-tensioning force from the reinforcement to the glass. Regarding the first aspect, the reinforcement can be introduced within the laminated glass panel (e.g. [6,8]) or placed externally (e.g. [9,71]) and, on the one hand, can be positioned as a straight line along the glass element (e.g. [9]) or adopting a layout similar to the shape of the bending moment diagram (e.g. [71]), on the other hand. Concerning the anchorage strategy, the reinforcement can be mechanically anchored at the beam ends (e.g. [8]) and/or adhesively bonded to the glass (e.g. [9]).

One of the first studies on post-tensioned glass systems was performed by Bos *et al.* [6]. A T-section beam was post-tensioned using a steel tendon mechanically anchored at the beam ends (see **Figure 3.3c**). After that, it was bonded to the glass using a UV-curing acrylate adhesive. The glass web consisted of a SG-laminated glass panel with three glass layers and the steel tendon was introduced between the outer glass layers, adopting a parabolic layout. Based on the experimental results, the initial failure strength of glass can be significantly increased by applying prestress. Post-tensioning reduces the tensile strength reserve of the reinforcement material, wherefore safety measures must be taken to ensure sufficient residual strength after glass cracking. Furthermore, prestressing can triggers or magnifies the torsional-lateral buckling in the compression glass zone, and therefore changes in cross-section geometry may be necessary to prevent or delay it.

Louter *et al.* [9] developed and tested two post-tensioning setups. One of the specimen series (MECH-PT) consisted of post-tensioning SG-laminated glass beams by stretching steel tendons placed in recessed grooves on the top and bottom sides (see **Figure 3.13a**). These steel tendons were not bonded to the glass. They were mechanically anchored at the beam ends. In addition, the post-tensioning force was approximately the same in both tendons, thus imposing a uniform compressive pre-stress on the cross-section. Another series (*ADH-PT*) consisted of prestressing a steel plate before bonding it to the bottom edge of the glass panel (see cross-section geometry in **Figure 3.13b**). In this case, the post-tensioning force generated an axial force (P) and a bending moment ($P \times e$) due to the eccentricity of the steel reinforcement in relation to the neutral axis. Compared to unreinforced reference series, both post-tensioning setups were successful in increasing the failure strength of glass, between 47.5 (*MECH-PT* series) and 128.4 % (*ADH-PT* series), as presented in **Table 3.4**. Regarding the post-cracking response, *ADH-PT* beams exhibited much higher ductility values than the *MECH-PT* beams. Furthermore, while the former failed by detachment of the steel plate after extensive crack propagation towards the supports, the latter failed explosively due to lateral instability of the

compression glass zone. Taking the *MECH-PT* series as a reference, it was concluded that the *ADH-PT* configuration (i) was more efficient in increasing the initial fracture load because it requires a lower post-tensioning force to attain the target failure strength, (ii) was better at preventing lateral instability after cracking, since the eccentricity of the steel plate induced favourable tensile stresses on the upper glass zone, and (iii) was better at improving the post-cracking response (both the residual strength capacity and the ductility) of glass beams, increasing the tensile strength reserve of the reinforcement before yielding/failure.

In a similar research, Cupác *et al.* [41] examined three different setups for post-tensioning steel-reinforced glass beams (see **Figure 3.13c** and **Figure 3.13d**): (i) in the *AS* series, a prestressed steel plate was bonded to the bottom edge of the glass panel, according to the EBR technique; (ii) in the *MD* series, two steel plates positioned on the bottom and top sides of the specimen were stretched and then mechanically anchored at the beam ends; and (iii) in the *AMS* series, two prestressed steel plates were mechanically anchored at the beam ends and bonded to the bottom and top edges of the glass panel. Three main conclusions can be extracted from experimental results. First, AS beams ($P + P \times e$) required a lower post-tensioning force to attain the same initial fracture strength observed in *AMS* beams ($2P$). Second, *AS* and *AMS* beams showed superior post-fracture response compared to *MD* beams, which failed due to lateral-torsional buckling. Finally, the post-cracking performance (e.g. lateral stability) of the beams reinforced on both sides (uniform compressive pre-stress on the cross-section) was significantly improved by bonding the steel plates to the glass, as expected (see **Table 3.4**).

One of the most commonly seen failure modes in post-tensioned glass systems is lateral-torsional buckling, since the post-tensioning induces unfavourable pre-stresses in compression glass zones (e.g. top sides). Moreover, post-tensioning can produce small out-of-plane deformations due to minor deviations between component alignments components, slightly reducing buckling resistance. Concerning this last topic, Weller and Engelmann [72] assessed the influence of distinct post-tensioning setups on out-of-plane flexural behaviour (see **Figure 3.13e**). It was concluded that geometric imperfections have no significant influence on the buckling strength of the specimens.
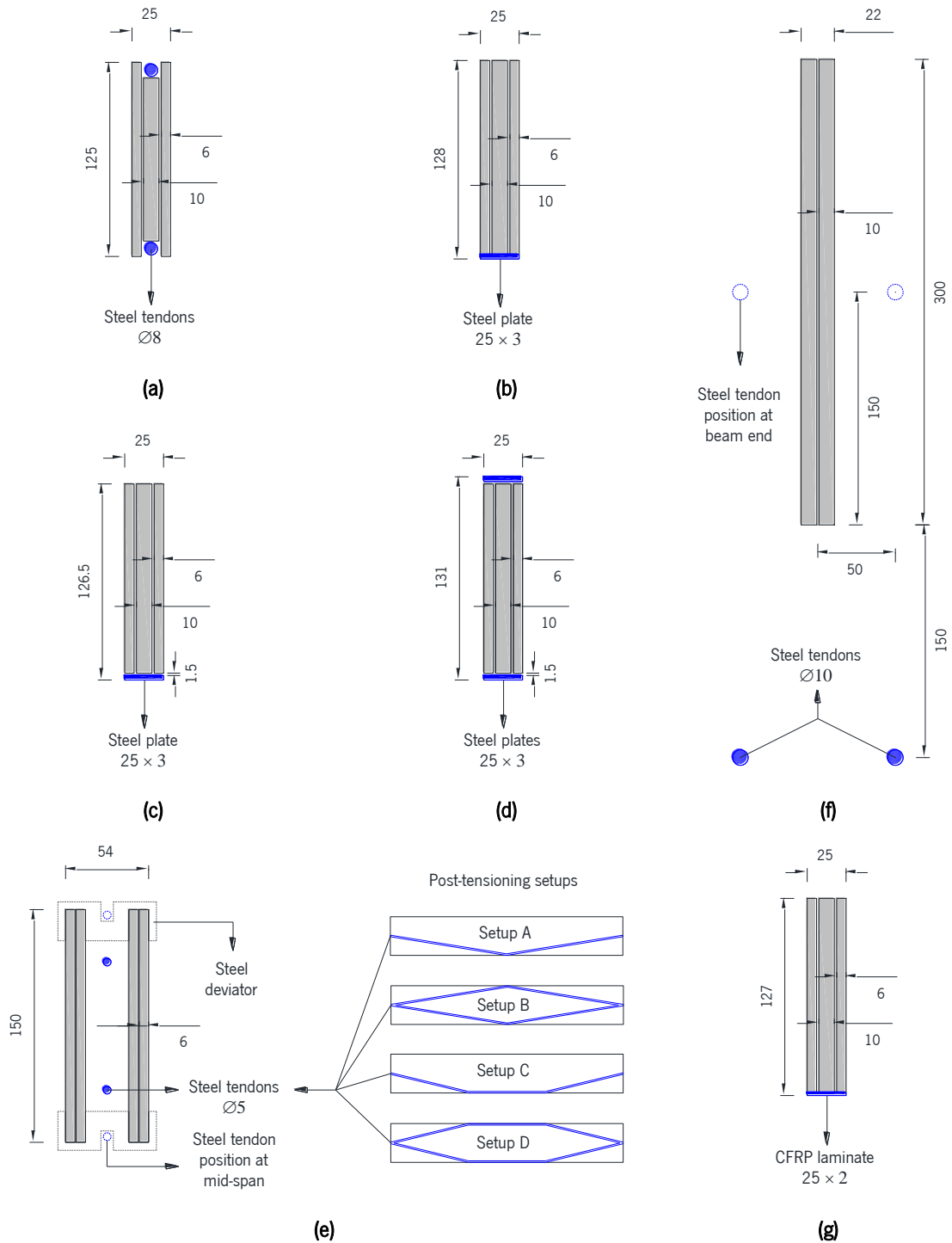
Figure 3.13: Post-tensioned glass beams tested by (a and b) Louter *et al.* [9], (c and d) Cupác *et al.* [41], (e) Weller and Engelmann [72], (f) Jordão *et al.* [71] and (g) Louter *et al.* [9]. Note: units in [mm].

The post-tensioning force required to achieve a certain initial failure strength can be reduced by increasing the eccentricity of the reinforcement element. The benefits of this strategy are two-fold: (i) it increases the tensile strength reserve of the reinforcement after glass cracking and (i) it minimizes/suppresses the undesirable compressive pre-stress in compression zones by increasing

59

the resulting bending moment ($P \times e$). In this sense, Jordão *et al.* [71] tested a new post-tensioning setup in which mechanically anchored steel tendons where positioned up to 150 mm below the bottom edge of the glass panel, adopting a layout similar to the bending moment curve shape (see **Figure 3.13f**). These steel tendons were mechanically anchored at the beam ends and, at the load point sections, steel deviators were installed at the bottom edge to redirect the steel tendons. This layout was able to produce tensile pre-stress at the top glass zone and, in turn, significantly reduce the likelihood of lateral instability after glass cracking. On the other hand, the specimen presented significant post-fracture strength (see **Table 3.4**). However, the steel deviators seem to have induced high peek stresses at the bottom edge, causing the crack-to-crack sooner. Due to the steel elements used to produce the beam (reinforcement, deviators and anchorage heads), this strategy may not meet aesthetic and transparency requirements.

Table 3.4: Overview of investigated concepts of post-tensioned glass beams, indicating the most relevant parameters related to the specimen geometry and its post-failure performance.

Reference: Louter *et al.* [9]						
Series	Connection	ρ_r [%]	h_t/L_s [mm/m]	F_p [kN]	ΔF_{cr} [%]	F_{max}/F_{cr} [%]
MECH-PT	MA	3.66	89.3	50.0	47	138
ADH-PT	AB	2.72		26.8	128	178
Reference: Cupác *et al.* [41]						
Series	Connection	ρ_r [%]	h_t/L_s [mm/m]	F_p [kN]	ΔF_{cr} [%]	F_{max}/F_{cr} [%]
AS	AB	2.72		15	96	220
MD	MA	5.45	89.3	30	53	145
AMD	AB + MA			50	131	194
Reference: Jordão *et al.* [71]						
Series	Connection	ρ_r [%]	h_t/L_s [mm/m]	F_p [kN]	ΔF_{cr} [%]	F_{max}/F_{cr} [%]
-	MA	2.61	103.4	17.5	87	177
Reference: Louter *et al.* [9]						
Series	Connection	ρ_r [%]	h_t/L_s [mm/m]	F_p [kN]	ΔF_{cr} [%]	F_{max}/F_{cr} [%]
-	AB	1.82	89.3	13.6	88	222

Notes:
MA = machanically anchored reinforcement; AB = adhesively bonded reinforcement; ρ_r = tensile reinforcement percentage; h_t = total height of the specimen; L_s = span length; F_p = post-tensioning force; ΔF_{cr} = increase in cracking load due to the post-tensioning; and F_{max} = peak load registered after glass cracking.

Recently, CFRP materials have been used for post-tensioning glass structural elements. Louter *et al.* [9] tested SG-laminated glass panels reinforced at the bottom edge with prestressed CFRP laminates (see **Figure 3.13g**). As a result, the initial fracture strength increased by approximately 90 % in

comparison with unreinforced reference beams (see **Table 3.4**). This study showed the ability of the CFRP to be used as a passive or prestressed reinforcement material in glass structures. Furthermore, CFRP materials have higher tensile strength compared to steel and therefore post-tensioning can be easily adopted without compromising post-failure strength or requiring a higher reinforcement percentage for this purpose.

In spite of mechanically prestressing is an effective strategy to increase the initial failure strength of glass, transferring the post-tensioning force from the reinforcement to the glass is still a major challenge, as the glass cannot redistribute peak stresses by yielding. Appropriate safety measures must be taken to ensure that the post-tensioning force is smoothly transferred from the reinforcement to the glass, in order to prevent premature failure of the glass due to the growth of surface flaws over time [73].

Louter *et al.* [34] examined four alternative mechanical anchorages to transfer the post-tensioning force between components (see **Figure 3.14**). In Anchorages I and II, where the post-tensioning force was directly transferred from the anchorage head to the beam ends, an aluminium plate was placed between these two elements to reduce stress concentrations. As glass edges are typically weaker than glass surfaces, in Anchorages III and IV, the post-tensioning force was transferred by means of aluminium wedges adhesively bonded to the sides of the glass panel. Compression tests on specimens showed that misalignment between the components is more likely in more complex the anchorage systems. As a consequence, Anchorage I exhibited the best performance among all the strategies tested. However, if proper strategies are adopted to avoid misalignments, the remaining strategies can be advantageous for smoothing the stress transfer. Notwithstanding, the load carrying capacity of mechanical anchorages subjected to long-term loads must also be estimated, since the tensile strength of glass strongly depends on surface conditions and loading history [74].

Unlike the concrete industry, where the structural elements are commonly cast *in situ*, this does not occur in the glass industry. Typically, the glass structural elements are prepared at the factory and then assembled at the construction site using mechanical and/or adhesive connections. Therefore, solutions involving mechanically anchored reinforcement can pose significant challenges in connecting adjacent glass elements.
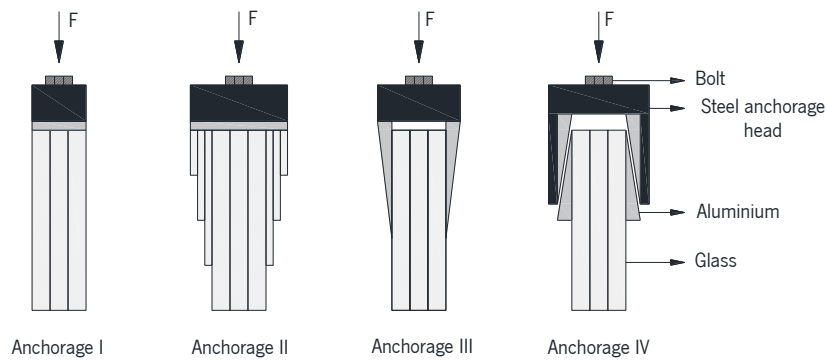
Figure 3.14: Different anchoring systems studied by Louter *et al.* [34] for transferring the post-tensioning force from the reinforcement to the glass.

SHAPE MEMORY ALLOYS

3.5.1. A brief history

SMAs are a group of metallic alloys that undergo solid-to-solid phase transformations at the atomic level when exposed to temperature and/or stress variations [75,76]. Such behaviour produces the shape memory effect, in which mechanically deformed SMAs can still recover its initial shape after heating them above a certain temperature by external or internal (Joule effect) heating. Some SMAs can still show superelasticity, which is the material's capability to recover its initial shape after unloading and without any heating. It is noteworthy that such behaviour occurs under specific temperature conditions.

The development of SMAs started in the 1930s, when Ölander [77] first discovered the shape memory effect in a Cd-Au alloy. Nevertheless, the significance of SMAs was not well understood until the beginning of the 1960s, when Buehler *et al.* [78] created the nickel-titanium (Ni-Ti) alloy, commonly known as Nitinol. Since then, SMAs have been used in a wide range of industrial fields, such as in consumer products and industrial applications (e.g. [79–81]), structures and composites (e.g. [82,83]), automotive (e.g. [84,85]), aerospace (e.g. [76,86,87]), robotics (e.g. [88,89]), biomedical (e.g. [90,91]) and even in fashion (e.g. [[92]). However, the Ni-Ti alloy is not suitable for the construction industry due to its expensive nature [93]. In the construction industry, due to its specificities, low-cost SMAs are required, such as the iron-based (Fe-SMAs) and copper-based (Cu-SMAs) alloys, especially the former. When compared to the Ni-Ti alloy, the Fe-SMAs present (i) lower cost, (ii) easier manufacturing process, (iii) higher modulus of elasticity, and (iv) relatively lower activation temperature [94].

The shape memory effect in Fe-Mn-Si alloys was first discovered by Sato *et al.* [95] in 1982. Subsequently, the transformation behaviour, the microstructural and crystallography characteristics and the mechanical properties of Fe-SMAs were investigated in detail at the National Institute for Material Science, Japan. New Fe-SMAs with better behaviour and lower cost were subsequently developed. Fe-Mn-Si alloys have received special attention in recent decades due to their low cost, good workability, machinability and weldability, making them the most promising candidates for the application of Fe-SMAs in the construction industry, whether for the repairing existing structures or the reinforcing of new ones [96,97]. In addition, different constituents have been added to the parent Fe-Mn-Si alloys to improve their features in terms of corrosion resistance, training effect, cyclic deformation and strength [98].

SMAs have recently been used in civil engineering applications (e.g. buildings and bridges), reducing both the effort and the time involved in post-tensioning compared to conventional reinforcement materials (e.g. steel and CFRP). While the superelasticity is used to increase the damping and energy dissipation of reinforced concrete structures for shock loads, such as earthquakes (e.g. [99,100]), the shape memory effect is used for post-tensioned strengthening of structural elements (e.g. [93,101–105]). The recent development of Fe-SMAs, with relatively inexpensive constituent materials, have enhanced the applications of this type of materials in the construction industry. Promising results have been obtained from studies where the post-tensioned strengthening with Fe-SMAs has been investigated (e.g. [96,101,103,105,106]).

3.5.2. Phase behaviour

At atomic level, SMAs have two distinct phases: (i) the high-symmetry austenite phase, which is stable at high temperatures, and (ii) the low-symmetry martensite phase, which is stable at lower temperatures [107]. Therefore, the martensitic transformation, also called forward transformation, is the crystallography transformation at atomic level from the austenite phase to the martensite one. During the martensitic transformation, which occurs by mechanical deformation or changes in temperature, atoms move in an organized manner relatively to their neighbours. Unlike plastic deformation, martensitic transformation does not involve diffusion of atoms, it just creates a new crystalline structure due to shear distortion [107]. Plastic deformation of SMAs occurs when shear distortion of the crystalline structure is replaced by irreversible slip of the atoms. Although these atoms change their neighbours, the crystalline structure remains intact and, therefore, the plastic deformation cannot be reversed by heating.

When SMAs are first subjected to load-unload cycles, in a process called "training", unrecoverable plastic strains are generated [108]. However, they stabilize after sufficient cycling and the hysteresis response of the SMA becomes consistent. Depending on the training process, SMAs can show a one-way or two-way shape memory effect. The former is the SMA's capability to memorize its original shape in austenite phase (higher temperatures), while the latter is the SMA's capability to memorize the original shape in both austenite and martensitic phases [109].

The phase diagram of the Ni-Ti alloy is schematized in **Figure 3.15**. In the absence of mechanical loading, the martensite phase is called twinned martensite. For temperatures below M_f (martensite finish temperature), the detwinned martensite phase is induced by external loading, causing a macroscopic deformation that remains after unloading. In the absence of mechanical loading, the reverse transformation is induced by heating the material above A_s (austenite start temperature) and the detwinned martensite material starts to recover the permanent deformation previously induced, in a process called shape memory effect, which is entirely completed when the material is heated to A_f (austenite finish temperature).
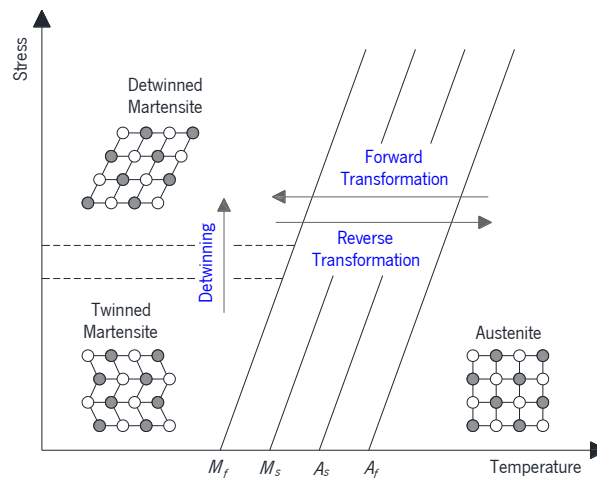
Figure 3.15: Schematic phase diagram of Ni-Ti alloys, adapted from Rojob and El-Hacha [105].

The main difference between the Ni-Ti alloy and Fe-SMAs is associated to the mechanism of martensitic transformation. As shown in **Figure 3.16a**, the detwinning process in Fe-SMAs takes place at temperatures between M_s (martensite start temperature) and A_s, while in Ni-Ti alloys takes place at temperatures below M_f. Furthermore, unlike the Ni-Ti alloys, the superelasticity effect is not exhibited by Fe-SMAs because they deform irreversibly when they are mechanically loaded under temperatures above A_f [96]. At low temperatures, the austenite-martensite transformation occurs before plastic deformation, while at high temperatures, only irreversible deformation occurs. The procedure for post-

tensioned strengthening by activation Fe-SMA materials can be summarized into three main steps: (i) pre-straining; (ii) activation; and, (iii) service loading [101]. **Figure 3.16b** illustrates the stress-strain and stress-temperature relationships during the two first steps required for the post-tensioning of Fe-SMA reinforcement. Based on **Figure 3.16**, the Fe-SMA strip is first mechanically loaded at room temperature – phase (1) – and, after the transformation phase from austenite to detwinned mastensite is reached, it is completely unloaded – phase (2). Then, the Fe-SMA strip is mechanically anchored or adhesively bonded to the structural element to be strengthened. Subsequently, the Fe-SMA strip is activated through resistive heating – phase (3). When the temperature reaches A_s, the reverse transformation from the detwinned martensite phase to austenite phase begins and the Fe-SMA tends to shrink. As the longitudinal deformation of the Fe-SMA strip is previously restrained, recovery stresses are developed due to the reverse transformation from martensite to austenite – phase (3.1) – and thermal contraction of the Fe-SMA reinforcement – phase (3.2).
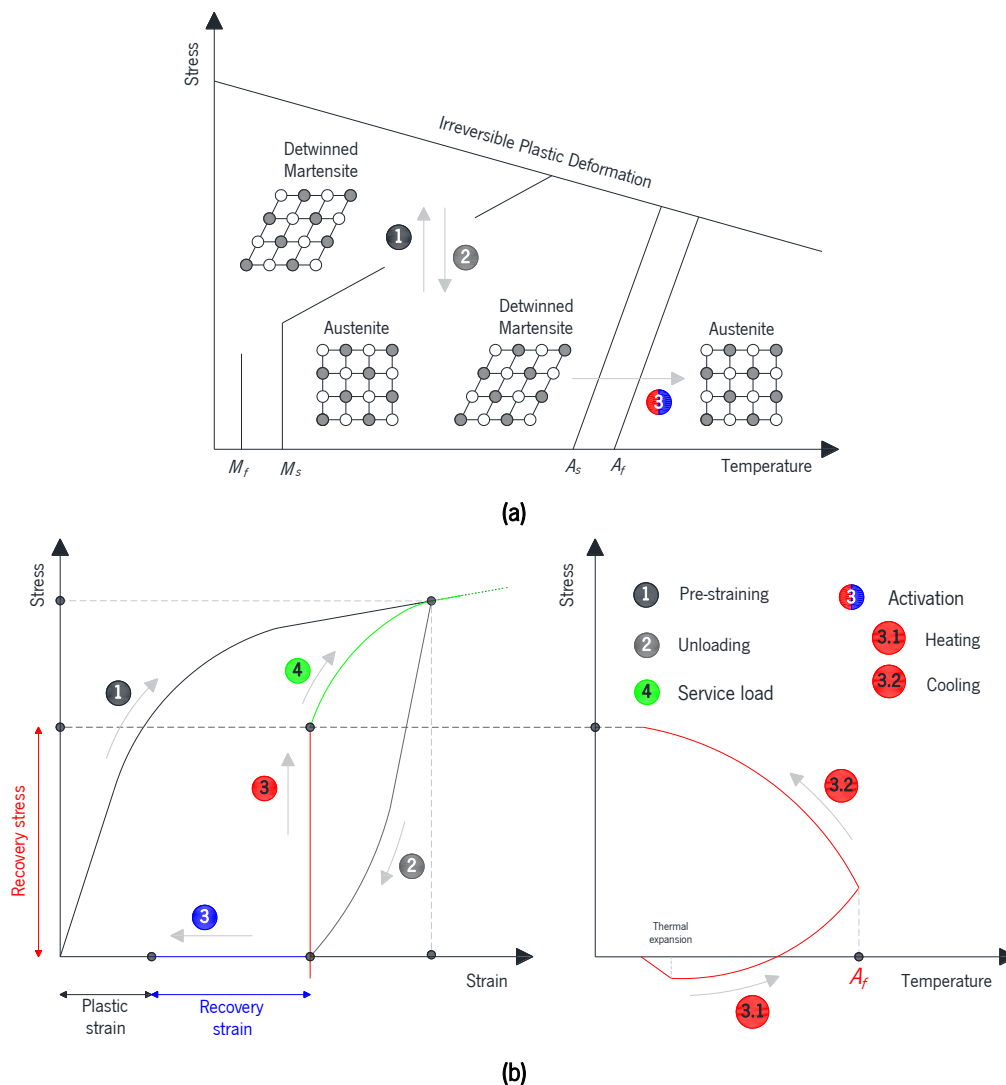
Figure 3.16: Behaviour of Fe-SMAs: (a) phase diagram [105] and (b) schematic activation procedure [93].

If SMA reinforcement is adhesively bonded to the glass and a proper activation strategy is adopted, then its activation could ensure a smooth and safe transfer of post-tensioning force from the reinforcement to the glass due to the adhesive damage caused by heating. Given the above, SMA materials can be a promising solution for the post-tensioned strengthening of glass structural elements. In addition, their shape memory effect could be used in two distinct contexts: (i) before glass rupture, to improve the tensile strength of glass by creating favourable pre-stresses in the tensile zone; or (ii) after glass rupture, to enhance the post-failure performance until the glass element to be replaced, reducing the deformation, preventing the crack progression and, eventually, closing existing cracks.

On the other hand, SMAs can still be used for structural health monitoring (e.g. [110,111]). Their self-sensing properties provide automated damage detection capabilities for civil engineering structures without external sensors, resulting in less complex systems. Structural health monitoring is typically based on the relationship between the electrical resistivity of the SMA and their deformability. As the tensile strength of glass is unpredictable, the risk of catastrophic collapses can be significantly reduced using the self-sensing functionality of the SMAs for identifying stress concentrations.

One of the most important properties in SMA materials is the temperature hysteresis, which measures the difference between the transition temperatures for martensitic and reverse transformations. Depending on the chemical composition of the SMAs, they may have narrow or wide hysteresis. Accordingly, for a wide range of engineering applications, the hysteresis must require careful consideration during the SMA material selection. SMAs with a wide hysteresis are required for post-tensioning, in order to maintain the pre-defined shape within a large temperature range. In other words, in order to avoid significant losses in post-tensioning force after activation and during the structure lifetime, M_s must always be lower than the ambient temperature in any case [96].

Glass-SMA composite systems have been addressed by few studies (e.g. [25,112,24,113]). Deng *et al.* [25] and Silvestru *et al.* [24] developed an extensive experimental campaign to characterize the influence of different adhesives on the bond behaviour of glass-to-SMA adhesive connections. In a later stage, aiming to develop SMA reinforced glass elements for structural applications, Silvestru *et al.* [112] conducted an exploratory study to assess the feasibility of strengthening laminated glass beams with externally bonded Fe-SMA strips. Results showed that the Fe-SMA reinforcement is able to prevent the glass brittleness and, when activated, to increase its initial fracture strength. Furthermore, Bedon *et al.* [113] performed an exploratory investigation on the flexural behaviour of laminated glass panels

reinforced with Ni-Ti wires embedded in the interlayer. The numerical study was based on two premises: (i) at lower temperatures, the Ni-Ti wires would provide further flexural stiffness because the interlayer would be able to guarantee sufficient shear interaction between the glass plies, while (ii) at higher temperatures, with the decrease in shear stiffness of the interlayer, the Ni-Ti wires would be activated, preventing out-of-plane deformations in the laminated glass panel.

3.6. FINAL CONSIDERATIONS

Current research is mainly focused on the experimental validation of the structural concept of glass composite systems, addressing aspects such as the reinforcement material, the type of glass and the bonding strategy. As a consequence, further topics for understanding the structural behaviour of glass composite systems are still insufficiently studied, such as the bond behaviour of glass-reinforcement adhesively bonded connections. However, in both cases, most studies have focused on the experimental characterization of glass composite systems, neglecting the development of reliable analysis and design tools.

Although CFRPs are widely used in the construction industry for strengthening existing concrete structures, the experimental research on glass composite systems has been mostly devoted to the flexural behaviour of steel-reinforced and GFRP-reinforced glass beams. Compared to other reinforcement materials (e.g. steel), CFRPs present higher tensile stiffness and tensile strength. Thus, they can be adopted to reduce the reinforcement percentage and improve the aesthetic characteristics of glass composite systems.

Post-tensioning is an effective strategy to solve the mismatch between glass fragmentation and tensile strength created by thermal tempering. However, post-tensioning force transfer mechanisms should be carefully designed to prevent high stress concentrations because glass has time-dependent strength. SMAs emerge as promising candidates for the post-tensioning of glass structures. SMA activation can be used to smoothly transfer the post-tensioning force from the reinforcement to the glass, taking advantage of the adhesive damage caused by heating the SMA reinforcement. In addition, its self-sensing properties can be used for monitoring glass structures over time.

3.7. REFERENCES

[1]   Martens K, Caspeele R, Belis J. Development of composite glass beams - A review. Engineering Structures 2015;101:1–15. https://doi.org/10.1016/j.engstruct.2015.07.006.

[2]   Achintha M, Balan B. Mechanical prestressing of annealed glass beams using pretensioned

GFRP: Characterisation and potentiality. Structures 2019;20:11–9. https://doi.org/10.1016/j.istruc.2019.02.017.

[3]   Cruz P, Pequeno J. Structural Timber-Glass Adhesive Bonding. Challenging Glass, 2008, p. 205–14.

[4]   Cruz P, Pequeno J. Timber-Glass Composite Beams: Mechanical Behaviour & Architectural Solutions. Challenging Glass, 2008, p. 439–48.

[5]   Belis J, Callewaert D, Delincé D, Impe R Van. Experimental failure investigation of a hybrid glass / steel beam. Engineering Failure Analysis 2009;16:1163–73. https://doi.org/10.1016/j.engfailanal.2008.07.011.

[6]   Bos F, Veer F, Hobbelman G, Louter C. Stainless steel reinforced and post-tensioned glass beams. 12th International Conference on Experimental Mechanics, Bari, Italy: 2004, p. 1–9.

[7]   Louter C, Belis J, Veer F, Lebet J. Structural response of SG-laminated reinforced glass beams; experimental investigations on the effects of glass type, reinforcement percentage and beam size. Engineering Structures 2012;36:292–301. https://doi.org/10.1016/j.engstruct.2011.12.016.

[8]   Louter C, Cupać J, Lebet J. Exploratory experimental investigations on post-tensioned structural glass beams. Journal of Facade Design and Engineering 2014;2:3–18. https://doi.org/10.3233/FDE-130012.

[9]   Louter C, Cupać J, Debonnaire M. Structural glass beams prestressed by externally bonded tendons. GlassCon Global Conference Proceedings, Philadelphia, EUA: 2014, p. 450–9. https://doi.org/10.14296/deeslr.v5i0.1848.

[10]   Palumbo M. A New Roof for the XIIIth Century 'Loggia de Vicari' (Arquà Petrarca – PD Italy) Based on Structural Glass Trusses: A Case Study. Glass Processing Days, Tempere, Finland: 2005.

[11]   Achintha M, Balan B. Characterisation of the mechanical behaviour of annealed glass – GFRP hybrid beams. Construction and Building Materials 2017;147:174–84. https://doi.org/10.1016/j.conbuildmat.2017.04.086.

[12]   Correia J, Valarinho L, Branco F. Post-cracking strength and ductility of glass-GFRP composite beams. Composite Structures 2011;93:2299–309.

[13]   Bedon C, Louter C. Numerical investigation on structural glass beams with GFRP-embedded rods, including effects of pre-stress. Composite Structures 2018;184:650–61. https://doi.org/10.1016/j.compstruct.2017.10.027.

[14]   Neto P, Alfaiate J, Valarinho L, Correia J, Branco F, Vinagre J. Glass beams reinforced with GFRP laminates: Experimental tests and numerical modelling using a discrete strong discontinuity approach. Engineering Structures 2015;99:253–63.

https://doi.org/10.1016/j.engstruct.2015.04.002.

[15]   Valarinho L, Correia JR, Branco F. Experimental study on the flexural behaviour of multi-span transparent glass-GFRP composite beams. Construction and Building Materials 2013;49:1041–53. https://doi.org/10.1016/j.conbuildmat.2012.11.024.

[16]   Valarinho L, Sena-Cruz J, Correia J, Branco F. Numerical simulation of the flexural behaviour of composite glass-GFRP beams using smeared crack models. Composites Part B: Engineering 2017;110:336–50. https://doi.org/10.1016/j.compositesb.2016.10.035.

[17]   Keller T, De Castro J. System ductility and redundancy of FRP beam structures with ductile adhesive joints. Composites Part B: Engineering 2005;36:586–96. https://doi.org/10.1016/j.compositesb.2005.05.001.

[18]   Katsivalis I, Thomsen O, Feih S, Achintha M. Strength evaluation and failure prediction of bolted and adhesive glass/steel joints. Glass Structures and Engineering 2018;3:183–96. https://doi.org/10.1007/s40940-018-0070-0.

[19]   Machalická K, Eliášová M. Adhesive joints in glass structures: effects of various materials in the connection, thickness of the adhesive layer, and ageing. International Journal of Adhesion and Adhesives 2017;72:10–22. https://doi.org/10.1016/j.ijadhadh.2016.09.007.

[20]   Louter C, Belis J, Veer F, Lebet J. Durability of SG-laminated reinforced glass beams: Effects of temperature, thermal cycling, humidity and load-duration. Construction and Building Materials 2012;27:280–92. https://doi.org/10.1016/j.conbuildmat.2011.07.046.

[21]   Nhamoinesu S, Overend M. The mechanical performance of adhesives for a steel-glass composite façade system. Challenging Glass 3: Conference on Architectural and Structural Applications of Glass, CGC 2012, Delft, Netherlands: 2012, p. 293–306. https://doi.org/10.3233/978-1-61499-061-1-293.

[22]   Speranzini E, Agnetti S, Corradi M. Experimental analysis of adhesion phenomena in fibre-reinforced glass structures. Composites Part B: Engineering 2016;101:155–66. https://doi.org/10.1016/j.compositesb.2016.06.074.

[23]   Rodacki K. The Load-Bearing Capacity of Timber-Glass Composite I-Beams Made with Polyurethane Adhesives. Civil and Environmental Engineering Reports 2017;27:105–20. https://doi.org/10.1515/ceer-2017-0054.

[24]   Silvestru V, Deng Z, Michels J, Li L, Ghafoori E, Taras A. Application of an iron-based shape memory alloy for post-tensioning glass elements. Glass Structures and Engineering 2022;7:187–210. https://doi.org/10.1007/s40940-022-00183-z.

[25]   Deng Z, Silvestru V, Michels J, Li L, Ghafoori E, Taras A. Performance of Glass to Iron-based Shape Memory Alloy Adhesive Shear Joints with Different Geometry. In: Belis B& L (Eds. ., editor. Challenging Glass Conference Proceedings, vol. 8, Ghent, Belgium: 2022, p. 1–12. https://doi.org/10.47982/cgc.8.397.

[26]   Katsivalis I, Thomsen OT, Feih S, Achintha M. Development of cohesive zone models for the prediction of damage and failure of glass/steel adhesive joints. International Journal of Adhesion and Adhesives 2020;97:102479. https://doi.org/10.1016/j.ijadhadh.2019.102479.

[27]   Bedon C, Machalická K, Eliášová M, Vokáč M. Numerical modelling of adhesive connections including cohesive damage. Challenging Glass 6: Conference on Architectural and Structural Applications of Glass, CGC 2018 - Proceedings, 2018, p. 309–20. https://doi.org/10.7480/cgc.6.2155.

[28]   Veer F, Gross S, Hobbelman G, Vredeling M, Janssen M, van den Berg R, et al. Spanning Structures in Glass. Glass Processing Days 2003:78–81.

[29]   Flinterhoff A. Load carrying behaviour of hybrid steel-glass beams in bending. [Master dissertation]. University of Dortmund. Institute of Steel Construction, 2003.

[30]   Wellershoff F, Sedlacek G. Structural use of glass in hybrid elements: steel-glass-beams, glass-GFRP-plates. Glass Processing Days, Tempere, Finland: 2003, p. 268–70.

[31]   Louter C, Belis J, Bos F, Veer F, Hobbelman G. Reinforced Glass Cantilever Beams. Glass Processing Days, 2005, p. 429–33.

[32]   Belis J, Louter C, Verfaillie K, Van Impe R, Callewaert D. The Effect of Post-Tensioning on the Buckling Behaviour of a Glass T-Beam. International symposium on the application of architectural glass ISAAG 2006: conference proceedings, Munich: Universität Der Bundeswehr: 2006, p. 129–36.

[33]   Trösch E, Kassnel-Henneberg B. Load-bearing behaviour of splice-laminated glass beams for wide spans. In: Louter C, Bos F, Belis J, Lebet J-P, editors. Challenging Glass 4 & COST Action TU0905 Final Conference, Lausanne, Switzerland: 2014, p. 531–539.

[34]   Louter C, Heusden J, Veer F, Vambersky J, Boer H, Versteegen J. Post-tensioned Glass Beams. ECF, 2006. https://doi.org/10.1007/1-4020-4972-2.

[35]   Louter C, Veer F. Large span reinforced glass beams, prototype research. IASS 2007 Shell and Spatial Structures Conference 2007:1–10.

[36]   Louter C, Veer F. Experimental research on scale 1:4 models of an 18m reinforced glass beam, part I. Glass Performance Days, Tempere, Finland: 2007, p. 87–92.

[37]   Louter C. Adhesively bonded reinforced glass beams. Heron 2007;52:31–57.

[38]   Abeln B, Preckwinkel E, Yandzio E, Heywood M, Eliášová M, Netušil M, et al. Development of innovative steel-glass structures in respect to structural and architectural design (Innoglast). Report EUR 25316 EN, 2013. https://doi.org/10.2777/91697.

[39]   Louter C, Veer F, Hobbelman G. Reinforcing glass, effects of reinforcement geometry and bonding technology. Glass Processing Days, 2007, p. 2–6.

[40] Sena-Cruz J, Barros J, Coelho M, Silva L. Efficiency of different techniques in flexural strengthening of RC beams under monotonic and fatigue loading. Construction and Building Materials 2012;29:175–82. https://doi.org/10.1016/j.conbuildmat.2011.10.044.

[41] Cupać J, Louter C, Nussbaumer A. Flexural behaviour of post-tensioned glass beams: Experimental and analytical study of three beam typologies. Composite Structures 2021;255. https://doi.org/10.1016/j.compstruct.2020.112971.

[42] Valarinho L. Construction in Structural Glass: Flexural Behaviour of Laminated Glass Members and Development of Glass-GFRP Composite Beams. PhD thesis. University of Lisbon - Instituto Superior Técnico, 2016.

[43] Firmo JP, Correia JR, França P. Fire behaviour of reinforced concrete beams strengthened with CFRP laminates: Protection systems with insulation of the anchorage zones. Composites Part B: Engineering 2012;43:1545–56. https://doi.org/10.1016/j.compositesb.2011.09.002.

[44] Martens K, Caspeele R, Belis J. Load-carrying behaviour of interrupted statically indeterminate reinforced laminated glass beams. Glass Structures and Engineering 2016;1:81–94. https://doi.org/10.1007/s40940-016-0017-2.

[45] Ringli R, Vogel T. Load-bearing behavior of spliced glass beams under bending action. Glass Structures and Engineering 2016;1:61–80. https://doi.org/10.1007/s40940-016-0006-5.

[46] Trajanoska B, Gavriloski V, Bogatinoski Z, Zdraveski F. Glass - steel hybrid elements under four point bending test. Istrazivanja I Projektovanja Za Privredu 2015;13:141–6. https://doi.org/10.5937/jaes13-8806.

[47] Carvalho P, Cruz P, Veer F. Connecting through the reinforcement - design, testing and construction of a folded reinforced glass structure. Journal of Facade Design and Engineering 2 2014;1–2:109–22. https://doi.org/doi:10.1201/b16499-35.

[48] Cruz P, Valente I, Carvalho P, Marinho B, Ribeiro S. Experimental analysis on steel reinforced glass beams at different temperatures. COST Action TU0905 Mid-term Conference on Structural Glass, 2013, p. 261–8. https://doi.org/10.1201/b14563-37.

[49] Englhardt O, Bergmeister K. Hybrid structural elements an innovative high filigree glass-steel-system. Glass Performance Days, Tempere, Finland: 2007, p. 134–7.

[50] Furtak K, Rodacki K. Experimental investigations of load-bearing capacity of composite timber-glass I-beams. Archives of Civil and Mechanical Engineering 2018;18:956–64. https://doi.org/10.1016/j.acme.2018.02.002.

[51] Hamm J. Tragverhalten von Holz und Holzwerkstoffen im statischen Verbund mit Glas. PhD thesis. Ecole Polytechnique Fédérale de Lausanne, 2000.

[52] Hulimka J, Kozlowski M. Mechanism of failure and post-breakage strength of hybrid timber-glass beams. In: Faculty of Civil Engineering STU Bratislava, editor. Proceedings of the 10th

International Conference on New Trends in Statics and Dynamics of Buildings, Bratislava: 2012, p. 7.

[53]   Kozłowski M. Experimental and numerical analysis of hybrid timber-glass beams. PhD thesis. Silesian University of Technology, 2014.

[54]   Kozłowski M, Serrano E, B. E. Experimental investigation on timber-glass composite I-beams. Challenging Glass 4 & COST Action TU0905 Final Conference, Taylor & Francis Group; 2014, p. 261–8.

[55]   Kreher K, Natterer J, Natterer J. Timber-Glass-Composite Girders for a Hotel in Switzerland. Structural Engineering International: Journal of the International Association for Bridge and Structural Engineering (IABSE) 2004;14:149–51. https://doi.org/10.2749/101686604777963964.

[56]   Naser MZ, Hawileh RA, Abdalla JA. Fiber-reinforced polymer composites in strengthening reinforced concrete structures: A critical review. Engineering Structures 2019;198:109542. https://doi.org/10.1016/j.engstruct.2019.109542.

[57]   Hollaway LC. A review of the present and future utilisation of FRP composites in the civil infrastructure with reference to their important in-service properties. Construction and Building Materials 2010;24:2419–45. https://doi.org/10.1016/j.conbuildmat.2010.04.062.

[58]   Belarbi A, Dawood M. Sustainability of fiber-reinforced polymers (FRPs) as a construction material. Houston, USA: Woodhead Publishing; 2016. https://doi.org/10.1016/b978-0-08-100370-1.00020-2.

[59]   Correia JR. GFRP Pultruded Profiles in Civil Engineering: Hybrid Solutions, Bonded Connections and Fire Behaviour. PhD thesis. Technical University of Lisbon, Portugal, 2008.

[60]   Louter C, Leung C, Kolstein H, Vamberský J. Structural glass beams with embedded glass fibre reinforcement. Challenging Glass 2 - Conference on Architectural and Structural Applications of Glass, CGC 2010 2010:439–48.

[61]   Balan B, Achintha M. Experimental and Numerical Investigation of Float Glass-GFRP Hybrid Beams. In: Belis, Bos, Louter, editors. Challeging Glass 5 - Conference on Architectural and Structural Applications of Glass, vol. 97, Ghent: 2016, p. 281–96. https://doi.org/10.2514/6.2009-5462.

[62]   Speranzini E, Agnetti S. Flexural performance of hybrid beams made of glass and pultruded GFRP. Construction and Building Materials 2015;94:249–62. https://doi.org/10.1016/j.conbuildmat.2015.06.008.

[63]   Valarinho L, Correia JR, Branco F. Experimental Investigations on Continuous Glass-GFRP Beams. Preliminary Non- linear Numerical Modelling. In: Delf University Technology, editor. Challenging Glass 3 - Conference on Architectural and Structural Applications of Glass, Delft: 2012, p. 14.

[64]   Pendhari SS, Kant T, Desai YM. Application of polymer composites in civil construction: A general review. Composite Structures 2008;84:114–24. https://doi.org/10.1016/j.compstruct.2007.06.007.

[65]   Cagnacci E, Orlando M, Spinelli P. Experimental campaign and numerical simulation of the behaviour of reinforced glass beams. Glass Performance Days, Tempere, Finland: 2009.

[66]   Bedon C, Louter C. Structural glass beams with embedded GFRP, CFRP or steel reinforcement rods: Comparative experimental, analytical and numerical investigations. Journal of Building Engineering 2019;22:227–41. https://doi.org/10.1016/j.jobe.2018.12.008.

[67]   Cagnacci E, Orlando M, Salvatori L, Spinelli P. Four-point bending tests on laminated glass beams reinforced with FRP bars adhesively bonded to the glass. Glass Structures and Engineering 2021;6:211–32. https://doi.org/10.1007/s40940-021-00147-9.

[68]   Mazaheripour H, Barros JAO, Sena-Cruz JM, Pepe M, Martinelli E. Experimental study on bond performance of GFRP bars in self-compacting steel fiber reinforced concrete. Composite Structures 2013;95:202–12. https://doi.org/10.1016/j.compstruct.2012.07.009.

[69]   Biolzi L, Orlando M, Piscitelli LR, Spinelli P. Static and dynamic response of progressively damaged ionoplast laminated glass beams. Composite Structures 2016;157:337–47. https://doi.org/10.1016/j.compstruct.2016.09.004.

[70]   Engelmann M, Weller B. Post-tensioned glass beams for a 9 m Spannglass Bridge. Structural Engineering International 2016;26:103–13. https://doi.org/10.2749/101686616X14555428759000.

[71]   Jordão S, Pinho M, Martin J, Santiago A, Neves L. Behaviour of laminated glass beams reinforced with pre-stressed cables. Steel Construction 2014;7:204–7. https://doi.org/10.1002/stco.201410027.

[72]   Weller B, Engelmann M. Spannglasträger - Glasträger mit vorgespannter Bewehrung. Stahlbau 2014;83:193–203. https://doi.org/10.1002/stab.201490059.

[73]   Cupać J, Louter C, Nussbaumer A. Post-tensioning of glass beams: Analytical determination of the allowable pre-load. Glass Structures and Engineering 2021;6:233–48. https://doi.org/10.1007/s40940-021-00150-0.

[74]   Haldimann M, Luible A, Overend M. Structural use of glass. LABSE - Lanka Association of Building Services Engineers; 2008.

[75]   Teh Y. Fast , Accurate Force and Position Control of Shape Memory Alloy Actuators. PhD thesis. Australian National University, 2008.

[76]   Hartl D, Lagoudas D. Aerospace applications of shape memory alloys. Proceedings of the Institution of Mechanical Engineers, Part G: Journal of Aerospace Engineering, vol. 221, 2007, p. 535–52. https://doi.org/10.1243/09544100JAERO211.

[77]   Ölander A. An Electrochemical Investigation of Solid Cadmium-Gold Alloys Solid. Journal of the American Chemical Society 1932;54:3819–33. https://doi.org/https://doi.org/10.1021/ja01349a004.

[78]   Buehler W, Gilfrich J, Wiley R. Effect of Low-Temperature Phase Changes on the Mechanical Properties of Alloys near Composition TiNi. Journal of Applied Physics 1963;34:1475–7. https://doi.org/10.1063/1.1729603.

[79]   Wu M, Schetky L. Industrial Applications for Shape Memory Alloys. Proceedings of the International Conference on Shape Memory and Superelastic Technolgies, Pacific Grove, California, USA: 2000, p. 171–82.

[80]   Chiodo J, Jones N, Billett E, Harrison D. Shape memory alloy actuators for active disassembly using 'smart' materials of consumer electronic products. Materials and Design 2002;23:471–8. https://doi.org/10.1016/s0261-3069(02)00018-3.

[81]   Czechowicz A, Langbein S, editors. Shape Memory Alloy Valves: Basics, Potentials, Design. Springer Science and Business Media; 2015. https://doi.org/10.1007/978-3-319-19081-5.

[82]   Cohades A, Michaud V. Shape memory alloys in fibre-reinforced polymer composites. Advanced Industrial and Engineering Polymer Research 2018;1:66–81. https://doi.org/10.1016/j.aiepr.2018.07.001.

[83]   Lester B, Baxevanis T, Chemisky Y, Lagoudas D. Review and perspectives: shape memory alloy composite systems. Acta Mechanica 2015;226:3907–60. https://doi.org/10.1007/s00707-015-1433-0.

[84]   Williams E, Shaw G, Elahinia M. Control of an automotive shape memory alloy mirror actuator. Mechatronics 2010;20:527–34. https://doi.org/10.1016/j.mechatronics.2010.04.002.

[85]   Jani J, Leary M, Subic A. Shape memory alloys in automotive applications. Applied Mechanics and Materials, vol. 663, Switzerland: Trans Tech Publications Ltd; 2014, p. 248–53. https://doi.org/10.4028/www.scientific.net/AMM.663.248.

[86]   Costanza G, Tata M. Shape memory alloys for aerospace, recent developments, and new applications: A short review. Materials 2020;13. https://doi.org/10.3390/MA13081856.

[87]   Prasad N, Wanhill R, editors. Aerospace Materials and Material Technologies. vol. 1. Singapore: Springer International Publishing; 2017. https://doi.org/10.1007/978-981-10-2134-3.

[88]   Sreekumar M, Nagarajan T, Singaperumal M, Zoppi M, Molfino R. Critical review of current trends in shape memory alloy actuators for intelligent robots. Industrial Robot 2007;34:285–94. https://doi.org/10.1108/01439910710749609.

[89]   Kheirikhah M, Rabiee S, Edalat M. A Review of Shape Memory Alloy Actuators in Robotics. In: Ruiz-del-Solar J, Chown E, Plöge P, editors. RoboCup 2010: Robot Soccer World Cup XIV, Berlin Heidelberg, Germany: Springer; 2011, p. 206–17.

[90]   Biesiekierski A, Wang J, Gepreel M, Wen C. A new look at biomedical Ti-based shape memory alloys. Acta Biomaterialia 2012;8:1661–9. https://doi.org/10.1016/j.actbio.2012.01.018.

[91]   Petrini L, Migliavacca F. Biomedical Applications of Shape Memory Alloys. Journal of Metallurgy 2011;2011:1–15. https://doi.org/10.1155/2011/501483.

[92]   Langenhove L, Hertleer C. Smart clothing: A new life. International Journal of Clothing Science and Technology 2004;16:63–72. https://doi.org/10.1108/09556220410520360.

[93]   Shahverdi M, Michels J, Czaderski C, Motavalli M. Iron-based shape memory alloy strips for strengthening RC members: Material behavior and characterization. Construction and Building Materials 2018;173:586–99. https://doi.org/10.1016/j.conbuildmat.2018.04.057.

[94]   Leinenbach C, Kramer H, Bernhard C, Eifler D. Thermo-mechanical properties of an Fe-Mn-Si-Cr-Ni-VC shape memory alloy with low transformation temperature. Advanced Engineering Materials 2012;14:62–7. https://doi.org/10.1002/adem.201100129.

[95]   Sato A, Chishima E, Soma K, Mori T. Shape memory effect in $\gamma \rightleftarrows \epsilon$ transformation in Fe-30Mn-1Si alloy single crystals. Acta Metallurgica 1982;30:1177–83. https://doi.org/10.1016/0001-6160(82)90011-6.

[96]   Cladera A, Weber B, Leinenbach C, Czaderski C, Shahverdi M, Motavalli M. Iron-based shape memory alloys for civil engineering structures: An overview. Construction and Building Materials 2014;63:281–93. https://doi.org/10.1016/j.conbuildmat.2014.04.032.

[97]   Kajiwara S. Characteristic features of shape memory effect and related transformation behavior in Fe-based alloys. Materials Science and Engineering A 1999;273–275:67–88. https://doi.org/10.1016/s0921-5093(99)00290-7.

[98]   Sato A, Kubo H, Maruyama T. Mechanical properties of Fe-Mn-Si based SMA and the application. Materials Transactions 2006;47:571–9. https://doi.org/10.2320/matertrans.47.571.

[99]   Asgarian B, Moradi S. Seismic response of steel braced frames with shape memory alloy braces. Journal of Constructional Steel Research 2011;67:65–74. https://doi.org/10.1016/j.jcsr.2010.06.006.

[100] Dieng L, Helbert G, Chirani SA, Lecompte T, Pilvin P. Use of shape memory alloys damper device to mitigate vibration amplitudes of bridge cables. Engineering Structures 2013;56:1547–56. https://doi.org/10.1016/j.engstruct.2013.07.018.

[101] Hosseini A, Michels J, Izadi M, Ghafoori E. A comparative study between Fe-SMA and CFRP reinforcements for prestressed strengthening of metallic structures. Construction and Building Materials 2019;226:976–92. https://doi.org/10.1016/j.conbuildmat.2019.07.169.

[102] Izadi M, Hosseini A, Michels J, Motavalli M, Ghafoori E. Thermally activated iron-based shape memory alloy for strengthening metallic girders. Thin-Walled Structures 2019;141:389–401.

https://doi.org/10.1016/j.tws.2019.04.036.

[103] Michels J, Shahverdi M, Czaderski C. Flexural strengthening of structural concrete with iron-based shape memory alloy strips. Structural Concrete 2017;19:876–91. https://doi.org/10.1002/suco.201700120.

[104] Shin M, Andrawes B. Experimental investigation of actively confined concrete using shape memory alloys. Engineering Structures 2010;32:656–64. https://doi.org/10.1016/j.engstruct.2009.11.012.

[105] Rojob H, El-Hacha R. Self-prestressing using iron-based shape memory alloy for flexural strengthening of reinforced concrete beams. ACI Materials Journal 2017;114:523–32. https://doi.org/10.14359/51689455.

[106] Izadi MR, Ghafoori E, Shahverdi M, Motavalli M, Maalek S. Development of an iron-based shape memory alloy (Fe-SMA) strengthening system for steel plates. Engineering Structures 2018;174:433–46. https://doi.org/10.1016/j.engstruct.2018.07.073.

[107] Montoya-Coronado LA, Ruiz-Pinilla JG, Ribas C, Cladera A. Experimental study on shear strengthening of shear critical RC beams using iron-based shape memory alloy strips. Engineering Structures 2019;200:109680. https://doi.org/10.1016/j.engstruct.2019.109680.

[108] Brinson L, Huang M, Boller C, Brand W. Analysis of controlled beam deflections using SMA wires. Journal of Intelligent Material Systems and Structures 1997;8:12–25. https://doi.org/10.1177/1045389X9700800103.

[109] Ansari M, Fahimi P, Baghani M, Golzar M. An Experimental Investigation on Training of NiTi-Based Shape Memory Alloys. International Journal of Applied Mechanics 2018;10:1–17. https://doi.org/10.1142/S1758825118500400.

[110] Abdullah EJ, Soriano J, Garrido I, Abdul Majid DL. Accurate position control of shape memory alloy actuation using displacement feedback and self-sensing system. Microsystem Technologies 2020;0. https://doi.org/10.1007/s00542-020-05085-0.

[111] Song G, Mo Y, Otero K, Gu H. Health monitoring and rehabilitation of a concrete structure using intelligent materials. Smart Materials and Structures 2006;15:309–14. https://doi.org/10.1088/0964-1726/15/2/010.

[112] Silvestru V, Deng Z, Michels J, Taras A. Enabling a Ductile Failure of Laminated Glass Beams with Iron-Based Shape Memory Alloy (Fe-SMA) Strips. The International Colloquium on Stability and Ductility of Steel Structures, Aveiro, Portugal: Ernst & Sohn GmbH; 2022. https://doi.org/https://doi.org/10.1002/cepa. 1839.

[113] Bedon C, Amarante dos Santos F. FE Exploratory Investigation on the Performance of SMA-Reinforced Laminated Glass Panels. Advanced Engineering Materials 2016;18:1478–93. https://doi.org/10.1002/adem.201600096.

CHAPTER 4

SUMMARY OF APPENDED PAPERS

This chapter presents a summary of the papers that constitute this PhD thesis.

This research began with a numerical study on FRP reinforced glass beams. As mentioned in **Section 3.1**, due to the novelty of glass composite systems, most studies focusing on this topic aim at experimentally validating the structural concept behind this new solution. However, the development of reliable analyses and design tools are essential to better understand the resisting and failure mechanisms generated in glass composite systems and support the design of such systems, as well as to use this new technology at an industrial level for large scale applications. In this context, **PAPER I** focus on the ability of different constitutive models available in commercial finite element analysis (FEA) softwares to simulate the glass behaviour in tension. Such simulations are the basis for studying how aspects such as the adhesive type, the reinforcement percentage, the cross-section geometry and the reinforcement material influence the post-cracking performance of glass composite systems.

As described in **Section 3.2**, the bond behaviour of adhesive connections is the basis for understanding the behaviour of composite systems. The bond behaviour is affected by different factors, such as the environmental and load conditions, the adhesive type, the substrate materials and the surface properties. A wide range of adhesives, from gap-filling polyurethane adhesives to epoxy adhesives, have been used in previous investigations to manufacture glass composite systems. In most of these studies, they are used without an experimental characterization of the bond performance of glass-to-reinforcement adhesive connections. However, the assessment of the bond performance is a very important aspect, as it governs the ultimate load-carrying capacity of composite systems. Thus, the

effectiveness of composite systems is intrinsically dependent on the bond performance between the adherends. A study on the bond behaviour of glass-to-CFRP adhesively bonded connections is presented in **PAPER II**. Furthermore, local bond stress-slip laws were derived for each adhesive type in order to provide reliable analytical tools for simulating the observed experimental behaviour.

Given the brittle behaviour of glass, redundancy is a crucial attribute to avoid catastrophic collapses in glass structures in the event of local/partial failures, and glass composite systems are probably the best strategy to comply with this requirement. Although CFRPs are the first option for strengthening of concrete structural elements, they are not being used as much as steel or GFRPs as a reinforcement material in glass composite systems, as noted in **Section 3.3**. CFRPs exhibit higher stiffness and strength than other reinforcement materials and, therefore, the amount of reinforcement to reach a certain ultimate load-carrying capacity can be significantly reduced, thus increasing the transparency of glass structures, which is the main purpose of building such structures. In this sense, taking into account the assumptions of **PAPER I** and **PAPER II**, an investigation on the flexural behaviour of CFRP-reinforced glass beams is presented in **PAPER III**, assessing the influence of the adhesive type on the post-cracking performance and establishing reliable approaches for the numerical simulation of such composite systems.

Post-tensioning is essential both to increase the tensile strength of glass and to reduce its unpredictability but, as pointed out in **Section 3.4**, the post-tensioning force transfer between adherends poses major challenges to its application. Mechanical anchorage systems are nowadays not considered as a good solution to be used at an industrial level, as they are quite complex and, in case of small design/manufacture errors, they can even produce deleterious effects. Therefore, **PAPER IV** assesses the feasibility of post-tensioning annealed glass beams by activating part of Fe-SMA reinforcement. Prior to activation, the Fe-SMA strips were previously adhesively bonded to the tensile edge of monolithic glass beams. Fe-SMAs are currently used in construction industry for strengthening existing concrete structures, as mentioned in **Section 3.5**. Fe-SMAs can be easily activated and, by adopting a proper activation strategy, also the resulting adhesive damage can be used to create adhesive damage gradient at the bonded interfaced and smooth the transfer of post-tensioning force between adherends.

It is noteworthy to state that at the beginning of this research, the strategy outlined consisted of developing a strengthening system (i) capable of promoting safe failure modes in glass structural elements and (ii) suitable to be widely used at an industrial level for large scale applications (e.g. all-

glazed structures). Due to the novelty of glass composite systems with CFRPs and SMAs, it was decided that it would be of greater value for this research to characterize the structural behaviour of large-scale laminated glass beams with hybrid strengthening systems, combining two reinforcement materials (CFRP and Fe-SMA) and two strengthening methods (EBR and NSM). **PAPER V** presents the results of this study. They show the advantages of applying reinforcement according to the NSM technique as opposed to traditional EBR systems, with respect to the post-tensioning and the ultimate load-carrying capacity.

4.1. PAPER I

- Rocha J, Pereira E, Sena-Cruz J, Valarinho L, Correia JR. Numerical simulation of GFRP-reinforced glass structural elements under monotonic load. Engineering Structures 2021; 234:111968. https://doi.org/10.1016/j.engstruct.2021.111968
  Impact factor: 5.582

This paper presents a study on the efficiency of mechanical constitutive models most used in the literature to simulate the tensile behaviour of glass, namely (i) the smeared crack models available in the finite elements software FEMIX [1] and ABAQUS 6.14 [2] and (ii) the damage plasticity model available in the latter. Depending on the FEA software, these material models may require static or dynamic numerical approaches. A comparative analysis between the results extracted from all numerical approaches was carried out based on the (i) initial stiffness, (ii) cracking load, (iii) post-cracking stiffness, (iv) crack pattern and (v) failure mechanism. Furthermore, these approaches were compared regarding the (i) computation cost, (ii) input parameters and (iii) dynamic effects, in case of ABAQUS/Explicit analyses. In general, this paper identifies the most critical input design parameters on the numerical responses, such as the threshold angle and the mode-I fracture energy, and proposes strategies to obtain quasi-static analysis minimizing the computational effort. Numerical simulations were based on the experimental results obtained from the flexural tests conducted by Valarinho *et al.* [3] on glass-GFRP composite beams.

Based on the numerical results, three main conclusions were reached: (i) dynamic approaches (ABAQUS FEA software) require much higher computational effort but, on the other hand, they capture in greater detail the effects of cracking on the structural responses because, unlike static approaches (FEMIX FEA software), much smaller load steps can be easily implemented without compromising the convergence during crack formation; (ii) damage plasticity models require input parameters that are very difficult to calibrate experimentally; and (iii) a minimum mode-I fracture energy must be adopted

instead of the values reported in the literature after experimental testing, to avoid convergence problems (e.g. snap-back instabilities) and reduce deleterious dynamic effects.

4.2. PAPER II

- Rocha J, Sena-Cruz J, Pereira E. Tensile behaviour of CFRP-glass adhesively bonded connections: double-lap joint tests and numerical modelling. Engineering Structures 2022; 260:114212. https://doi.org/10.1016/j.engstruct.2022.114212

  Impact factor: 5.582

This paper first presents and discusses the results of an experimental study involving tensile tests on double-lap joint specimens, in order to characterize the bond behaviour of glass-to-CFRP adhesive connections. For this purpose, three different adhesives were selected to assess the influence of the adhesive's nature on the behaviour of glass-to-CFRP adhesive connections. Furthermore, two overlap lengths were tested, the second being twice as long as the first. Based on the experimental results, flexible adhesives seem to be better at promoting stress redistribution mechanisms, mobilizing longer bond lengths to transfer shear stresses between adherends. Adhesives showing an extremely stiff response induce high stress concentrations in the glass substrate, promoting premature failure of bonding systems due to cohesive shear debonding at the glass substrate.

In the second part of this paper, local bond stress – slip laws were derived for each of the adhesive types used to manufacture glass-to-CFRP adhesive connections. Using a second order differential equation in terms of slip, this analytical study was performed based on a computational application developed by Sena-Cruz and Barros [4]. It finds the parameters required by the chosen local bond stress – slip laws using an inverse analysis strategy complemented with numerical fitting tools. Furthermore, in order to determine the effective bond length for each adhesive type, the maximum load was plotted as a function of the anchorage length of the CFRP laminate. Compared to stiff, the flexible adhesives require longer bond lengths to mobilize the full load-carrying capacity of glass-to-CFRP adhesive connections. Finally, a numerical study was also carried out to show how the response of glass-to-CFRP adhesively bonded connections can be accurately simulated by applying the analytically derived bond stress – slip laws.

4.3. PAPER III

- Rocha J, Sena-Cruz J, Pereira E. Influence of adhesive stiffness on the post-cracking behaviour of CFRP-reinforced structural glass beams. Composites Part B Engineering 2022; 247:110293. https://doi.org/10.1016/j.compositesb.2022.110293
  Impact factor: 11.322

This paper was aimed at assessing the influence of the adhesive type on the post-cracking performance of glass-CFRP composite beams under flexure. The three adhesives previously used for double-lap joint specimens were also used in this case. The CFRP reinforcement was adhesively bonded to the bottom edge of annealed glass elements. In the first part of this paper, the experimental procedures are detailed and the experimental results obtained from four-point bending tests are presented and discussed. They show that CFRP-reinforced glass beams can exhibit ductile failure modes. Furthermore, depending on the type of adhesive, the cracking load can be sometimes attained or surpassed during the post-cracking phase, improving significantly the structural safety. Adhesives with high toughness and moderate stiffness seem to be the best for manufacturing glass-CFRP composite systems because they prevent high stress concentrations at the glass substrate while being sufficiently stiff.

Reliable approaches for the modelling of reinforced glass structures are investigated in the second part of this paper, which focuses on the best approach to numerically simulate the glass-to-CFRP adhesive connections depending on the adhesive type. They were well simulated assuming (i) perfect bond between components, neglecting the physical existence of the adhesive layer, for the stiffest adhesive; (ii) perfect bond at the glass/adhesive/CFRP interfaces, simulating the adhesive as a linear elastic material, for the moderate stiffness adhesive; and (iii) non-linear behaviour of the adhesive connection, adopting interface elements governed by the local bond stress – slip laws derived from double-lap joint tests, for the softest adhesive.

4.4. PAPER IV

- Rocha J, Pereira E, Sena-Cruz J. Feasibility of mechanical post-tensioning of annealed glass beams by activating externally bonded Fe-SMA reinforcement. Construction and Building Materials 2022; 365:129953. https://doi.org/10.1016/j.conbuildmat.2022.129953
  Impact factor: 7.693

This paper investigates for the first time, to the best of the author's knowledge, the feasibility of post-tensioning annealed glass beams by activating Fe-SMA strips adhesively bonded to the bottom edge. To estimate the benefits of the post-tensioning on the flexural response of such glass composite beams, post-tensioned glass beams are compared to reference ones (with passive Fe-SMA reinforcement). Fe-SMA strips were activated by heating them to temperatures between 120 and 160 °C. In order to prevent premature debonding of the Fe-SMA strips due to the inevitable adhesive damage caused by heating, these were not activated throughout their full extension. Fe-SMA strips zones near the beam ends were left without being activated in order to act as anchorage zones during the heating phase, while composite action is partially lost. Based on four-point bending tests, it has been shown that Fe-SMA reinforced glass beams were observed to exhibit a significant load-carrying capacity after glass cracking, as well as extremely ductile failure modes due to the Fe-SMA yielding. Post-tensioning reduced the possibility of an unexpected glass breakage due to the growth of initial surface flaws, and post-tensioned beams showed up to 30 % higher cracking loads than reference beams. The activation strategy proved to be appropriate to avoid both the premature debonding of the reinforcement element and high stress concentrations at the glass substrate. In general, the Fe-SMA can be a promising reinforcement material to be used in glass composite systems, either passive or post-tensioned.

4.5. PAPER V

- Rocha J, Pereira E, Sena-Cruz J. Flexural behvaiour of post-tensioned laminated glass beams with hybrid strengthening systems using CFRP and Fe-SMA reinforcements. In subimition to Construction and Building Materials.

  Impact factor: 7.693

The feasibility of strengthening glass structural elements with hybrid strengthening systems is assessed in this paper. Tailored Laminated glass beams were fabricated by joining three annealed glass layers using PVB interlayers. Each specimen was strengthened with CFRP and/or Fe-SMA reinforcements applied according to the EBR and NSM techniques. It should be noted that (i) two epoxy adhesives were used to bond both reinforcement materials to the glass; (ii) CFRP laminates were prestressed when inserted into the groove pre-designed before the glass lamination, according to the NSM technique; and (iii) Fe-SMA strips were always activated regardless of their position. Fe-SMA strips were not activated near the beam ends to preserve the full mechanical characteristics of the adhesive near the supports and act as anchorage zones. The experimental results showed that

NSM CFRP composite systems can be safely prestressed, preventing the premature FRP peeling-off failure during the prestress application. In addition, hybrid strengthening systems are more efficient than the EBR systems in preventing the premature debonding of the reinforcement element due to a critical shear crack, taking better advantage from the tensile capacity of the reinforcement materials. In general, hybrid strengthening systems are good for improving the overall flexural behaviour of glass beams because the Fe-SMA reinforcement can always be activated and the CFRP reinforcement remains providing post-cracking stiffness after the yielding of the Fe-SMA.

4.6. REFERENCES

[1]   Sena-Cruz J, Barros J, Azevedo A, Ventura-Gouveia A. Numerical Simulation of the Nonlinear Behavior of RC Beams Strengthened With NSM CFRP Strips. CMNE 2007 - Congress on Numerical Methods in Engineering and XXVIII CILAMCE - Iberian Latin-American Congress on Computational Methods in Engineering, Porto: 2007, p. 13–5.

[2]   Simulia. ABAQUS computer software and Online Documentation. v6.12. 2012.

[3]   Valarinho L, Sena-Cruz J, Correia J, Branco F. Numerical simulation of the flexural behaviour of composite glass-GFRP beams using smeared crack models. Composites Part B: Engineering 2017;110:336–50. https://doi.org/10.1016/j.compositesb.2016.10.035.

[4]   Sena-Cruz J, Barros J. Modeling of bond between near-surface mounted CFRP laminate strips and concrete. Computers and Structures 2004;82:1513–21. https://doi.org/10.1016/j.compstruc.2004.03.047.

CHAPTER 5

CONCLUSIONS AND FUTURE WORK

5.1. CONCLUSIONS

Recently, the structural glass applications are among the most prominent breakthroughs in civil engineering. Glass is currently seen as the greatest symbol of the contemporary architecture. Following the philosophy behind reinforced concrete, glass composite systems emerge as the main approach to overcome the glass brittleness and, in turn, boost its structural application. However, (i) the bond behaviour of glass-to-reinforcement adhesive connections, (ii) the structural performance of glass composite systems, (iii) the unpredictability of the glass tensile strength and (iv) the numerical simulation of glass composite systems are still open topics, and their development is essential for the acceptance and recognition by the construction industry. The main objective of the research conducted in this PhD thesis was, on the one hand, to develop, test, analyse and evaluate appropriate strengthening strategies for preventing catastrophic failures in glass structures and, on the other hand, to reduce the unpredictability of the glass fracture strength. Annealed glass was used in all experiments due to its obvious benefits after cracking, as mentioned before. Two different reinforcement materials were studied: (i) CFRP, which is widely used in the construction industry for the strengthening of existing concrete structures; and, (ii) Fe-SMA, which is emerging as a competitive alternative to CFRP in the post-tensioned strengthening of existing concrete structures. Monolithic glass elements (a single glass sheet) were firstly tested to measure the effective contribution of the reinforcement on the post-cracking performance, while laminated glass elements were then selected with the aim of developing and applying a hybrid strengthening system capable of delaying the premature debonding of the

reinforcement element and preventing peeling-off failure during the release of the prestressed reinforcement.

After the completion of this work, the objectives initially defined for this PhD thesis were fully accomplished. Specific conclusions related to the research carried out and the recommendations for future developments are presented in the following sections.

5.1.1.   Glass-CFRP composite systems

In this first research domain, experimental, analytical and numerical studies were performed about the structural performance of glass-CFRP composite systems. It was assessed by means of an extensive experimental campaign aiming at the characterization of (i) the bond behaviour of glass-to-CFRP adhesive connections by carrying out tensile tests on double-lap joint specimens and (ii) the overall behaviour of CFRP reinforced glass beams.

5.1.1.1.   *Preliminary numerical study on FRP reinforced glass beams*

Based on previous experimental results found in the literature (glass-GFRP composite beams), a preliminary numerical study was carried out to assess the efficiency of different constitutive models commonly used for glass modelling, namely the smeared crack models (SCM) available in the finite elements software FEMIX and ABAQUS and the damage plasticity model (DPM) from ABAQUS. Furthermore, the influence of some parameters required by material models on the numerical responses were assessed through a parametric study.

Preliminary numerical simulations on glass-GFRP composite beams showed that all mechanical constitutive models were adequate to simulate the non-linear behaviour of glass in tension. Unlike FEMIX, ABAQUS/Explicit requires a dynamic-based numerical approach to obtain convergence, which implies a much higher computational effort. Even performing quasi-static analyses, through a proper prescription of the loading time, mass scaling factor, loading scheme and the damping ratio, the undesirable dynamic effects seem to have influenced the cracking load, since in a dynamic-based numerical approach, the force – deflection curve does not depend only on stiffness (displacement), but also on mass (acceleration) and damping (velocity) properties. The damping ratio played a key role in reducing the significant of the dynamic response, but experimental calibration is very difficult. On the other hand, both ABAQUS models showed great ability to capture in greater detail all the effects of cracking on the structural response because, as opposed to FEMIX model, much smaller load steps were easily implemented without compromising stability during crack formation.

Focusing on ABAQUS models, the SCM was more efficient than the DPM at simulating the post-cracking behaviour of glass, as the latter does not allow considering a maximum absolute damage factor of 1.0, with residual stress in cracks. In addition, the DPM required as input parameters the dilation angle and the shape of the yield surface, which are two parameters typically used for simulating concrete but not so much in glass. The DPM showed greater difficulties in capturing the mode-II fracture at the glass-to-GFRP interfaces due to the assumptions inherent to this constitutive model.

ABAQUS models required finer mesh patterns to capture phenomena (e.g. cracking at the glass bottom edge) than SCM-FEMIX. On the other hand, numerical results showed that a minimum mode-I fracture energy should adopted, which are typically higher than the experimental values found in the literature, in order to avoid convergence problems (e.g. snap-back instabilities). Other deleterious effects may be excessive dynamic effects or lack of convergence,

5.1.1.2.   *Bond behaviour of glass-to-CFRP adhesively bonded connections*

Concerning the bond behaviour of glass-to-CFRP adhesive connections, double-lap joint specimens with bond lengths of 25 mm (L25 series) and 50 mm (L50 series) were produced using three different adhesives: (i) SikaForce L100 7100 (SF series), a flexible polyurethane adhesive with non-linear behaviour; (ii) SikaDur 330 (SD series), a stiff epoxy adhesive with linear elastic behaviour; and (iii) 3M DP490 (3M series), an epoxy adhesive with moderate stiffness and non-linear behaviour.

Double-lap joint tests showed that the bond behaviour and failure mode of glass-to-CFRP adhesive connections strongly depend on the adhesive type. Unlike the SD series, which presented linear behaviour until failure, a remarkable loss of shear stiffness occurred in SF series due to the highly non-linear behaviour of the SikaForce adhesive. On the other hand, 3M series exhibited an intermediate performance. Unlike the SF and 3M series, in which the maximum load increased respectively 54.9 % and 11.6 % when the bond length was extended from 25 mm to 50 mm, this did not occur in the SD series. This reflects the inability of stiffer/brittle adhesives to mobilize relatively long bond lengths and smoothen stress concentrations at the substrates. Such behaviour promoted premature glass breakage due to the growth of existing surface flaws. Furthermore, the 3M series presented 23.5 % – 42.8 % higher cracking loads than those obtained from the corresponding SD series. Unlike the SikaDur, the 3M and SikaForce adhesives developed an extended plastic zone capable of smoothening local stress concentrations, confirmed with higher values of slip at maximum load in the corresponding series, varying between 1.25 – 8.33 times for L25 series and 1.04 – 4.26

times for L50 series. The adhesive ductility played a critical role in the failure mode of double-lap joint specimens, with SD series exhibiting distinct failure modes from the other specimen series, mainly dominated by fibre-tear failure in CFRP and glass substrate failure

When using stiffer adhesives, the maximum load may not be a function of the tensile strength of glass or the shear strength of the adhesive because local mechanical properties become more relevant (e.g. edge treatment quality, density of surface flaws) on the performance of glass-CFRP composite systems. In this case, the maximum load and the failure mechanism is mainly governed by a dynamic phenomenon related to the sudden release of strain energy when initial cracks appeared in the substrate. Such behaviour mainly depends on the load level at crack initiation. This is very important in glass structures, as glass contains countless flaws randomly distributed on its surfaces. The performance observed in each series fundaments this idea: among the adhesives that meet the required specifications (e.g. shear strength), the one with the greatest deformation capacity should be adopted.

To solve the 2nd order equation of bond, the local bond stress (τ) – slip (s) laws were derived for each specimen series. A linear $\tau - s$ law was adopted for SD series due to the absence of any adhesive damage propagation before failure. To account for the non-linear behaviour exhibited by the SF and 3M series, the Dimande's exponential $\tau - s$ relationship was adopted in both cases. Taking SF joints as a reference, 3M joints are up to 3.0 times stronger and, theoretically, SD joints have no bond strength limit.

Then, additional numerical simulations were performed to assess the efficiency of using the $\tau - s$ relationships to simulate glass-to-CFRP adhesive connections. The results showed that mixed-mode I+II occurred due to the lateral deflection of glass plates. Numerical simulations were successfully used to recalibrate the $\tau - s$ relationships to account for this unanticipated effect. While the shear stress distribution along the bond length was almost constant in SF joints, it presented a quadratic distribution in SD joints, with shear stress at the loaded end 2 times higher than at the free end.

5.1.1.3.   *Post-cracking performance of glass-CFRP composite beams*

Following the premises of the EBR technique, a CFRP laminate was bonded to the bottom edge of monolithic glass panels using the three adhesives previously adopted for manufacturing double-lap joint specimens. The specimens produced with SikaForce L100 7100, SikaDur 330 and 3M DP490,

respectively identified as the S*Force*, S*Dur* and 3M series, were tested until failure adopting a four-point bending configuration.

The experimental campaign showed the advantages and feasibility of using CFRP to produce glass composite systems. It was shown that glass structures can exhibit safe and relatively ductile failure mechanisms when CFRP materials are bonded to the glass using structural adhesives. Before cracking, the flexural behaviour was clearly linear elastic. Since the glass panel has a much higher flexural stiffness than any other component, all series exhibited similar values of initial stiffness and cracking load, with differences between series of less than 6.7 %. After crack initiation, all composite beams maintained their integrity due to the contribution of reinforcement, exhibiting a post-cracking stage that was strongly influenced by the adhesive type.

Excluding the S*Dur* series, all the others presented residual strength ratios above 100 %. This occurred due to the brittle behaviour of SikaDur and its low strain energy release (i.e. damping capacity). In S*Dur* beams, the crack propagation was mainly governed by mode-II fracture and dynamic effects (e.g. sudden load drops), which seem to have contributed for the growth of existing surface flaws at the glass substrate, reducing the tensile stress required for the formation of new cracks and promoting an asymmetric progression of cracks towards the supports. Although the residual strength reached in S*Force* series is 1.35 times higher than that obtained from S*Dur* series due to the SikaForce's ability to smoothen stress concentrations, both presented similar ductility ratios due to the low toughness of the SikaForce adhesive, as a result of its reduced capacity to withstand the shock loads induced by new cracks. Consequently, the flexural cracks in S*Force* beams were predominantly V-shaped, which apparently provided additional load-bearing capacity and flexural stiffness at the beginning of the post-cracking stage.

Due to the brittle nature of the glass, the elastic strain energy absorption capacity of the adhesive plays a key role. While the SikaForce adhesive showed insufficient resistance to withstand shock loads, the SikaDur adhesive showed insufficient sufficient ductility and damping capacity to smoothen stress concentrations, the 3M adhesive seemed to be able to meet these requirements simultaneously. Accordingly, compared to the S*Force* and S*Dur* series, 3M series presented a much better post-cracking performance, with a 17.9 % – 58.6 % higher residual strength index and a 51.1 % – 61.2 % higher ductility index.

Numerical modelling was performed and aimed at finding the best approach to simulate the adhesive joint (shear interaction level) in glass-CFRP composite systems. The adhesive joint was simulated

considering (i) perfect bond (*PB* hypothesis), (ii) linear elastic behaviour (*EB* hypothesis) and (iii) adhesive damage propagation (*IB* hypothesis). Numerical simulations captured well the overall performance and crack patterns of glass-CFRP composite beams. Material properties obtained from simple mechanical characterization tests (*PB* and *EB* hypotheses) or adhesion tests (*IB* hypothesis) were shows to be sufficient to successfully predict the behaviour of complex glass structural systems. The *IB* hypothesis was better at capturing the flexural behaviour of the S*Force* series, while the S*Dur* and 3M series were better simulated using the *PB* and *EB* hypotheses, respectively.

5.1.2. Mechanical post-tensioning of Fe-SMA reinforced glass beams

Fe-SMA strips were bonded to the bottom edge of monolithic glass panels using the 3M DP490 adhesive. Excluding the reference beams (R_T0 series), all Fe-SMA strips were pre-strained before bonding. After the adhesive cured, they were heated at 120 °C (P_T120 series), 140 °C (P_T140 beam) and 160 °C (P_T160 beam) to create post-tensioning. As the polymeric adhesives do not perform well at high temperatures, only the middle region of Fe-SMA strips was heated, in order to preserve the properties near the beam ends. Then, the specimens were tested until failure in a four-point bending configuration.

Relatively safe and ductile failure mechanisms were observed in all specimens, showing the efficiency of strengthening glass beams with Fe-SMA to avoid catastrophic failures. Moreover, the experimental program also demonstrated the great potential of post-tensioning glass elements by activating externally bonded Fe-SMA reinforcement. Mechanical post-tensioning with Fe-SMA materials may be a promising strategy to prevent the growth of existing surface flaws under service load.

The pre-cracking stage was dominated by a linear elastic behaviour. All specimens were able to maintain their integrity during the cracking process, exhibiting a post-cracking response that was strongly influenced by the activation temperature. The R_T0 series showed a post-cracking response significantly distinct from that observed in glass-CFRP composite beams (3M series). Due to the non-linear behaviour of the Fe-SMA, the R_T0 series presented a ductility capacity at least 1.75 times higher than the one of the 3M series. On the other hand, the yielding of the Fe-SMA prevented the R_T0 series from reaching residual strength ratio higher than the one in the 3M series, which was approximately 20.0 % lower.

The activation strategy adopted, which consisted on heating only the middle region of the Fe-SMA strips, proved to be a suitable as an alternative to avoid the use of metallic elements (e.g. mechanical

anchorages) and to avoid the concentration of shear stresses in weaker zones of the glass panel (e.g. beam ends). In addition, the adhesive damage induced within the activated region and nearby adhesive joint zones reduced the likelihood of premature glass rupture due to stress concentrations at the glass substrate, due to the resulting smoothening effect on the shear transfer between the reinforcement and the glass substrate.

Compared to the R_T0 series, the activation of Fe-SMA strips increased the cracking load of post-tensioned beams between 17 % and 30 %. However, activation also influenced the post-cracking behaviour. The higher the activation temperature, the lower the residual strength ratio, since the activation of the Fe-SMA strips reduced the tensile strength reserve before occurring the austenite-martensite transformation. As structures are loaded under load control during their lifetime, a maximum recovery stress (activation temperature) must be estimated to guarantee a minimum residual strength capacity after cracking and avoid catastrophic collapses.

Special attention must be paid to the stress relaxation behaviour of the Fe-SMA, which resulted in a loss of post-tensioning force between 4.9 % and 10.1 %.

5.1.3. Hybrid strengthening systems

In order to avoid/delay premature debonding of the reinforcement by critical shear crack, three-ply laminated glass panels with a recessed groove were produced to assess the efficiency of hybrid strengthening systems. A reinforcement element was introduced into the pre-designed groove, according to the NSM technique, and another reinforcement element was externally bonded to the bottom edge. Five specimens were tested in flexure adopting different strengthening systems. NSM reinforcement was always pre-stressed/activated in all specimens. On the other hand, only externally bonded SMA strips were activated.

All specimens exhibited relatively safe and ductile failure modes. In addition, all of them failed by crushing of the compression glass zone due to shear-compression failure. This shows the efficiency of the hybrid strengthening system at preventing the progressive debonding of the reinforcement when shear cracks appeared. Focusing on the R_CFRP_CFRP beam, the residual strength and ductility ratios are approximately 2 times higher in relation to the ones obtained from the monolithic glass beams (SD series), despite a slightly reduction of the reinforcement ratio from 1.17 % to 0.96 %. At failure, the axial strain in the reinforcement was 38.1 % higher in the R_CFRP_CFRP beam. The performance observed allowed to conclude that, when hybrid strengthening systems are adopted, a

better post-cracking behaviour can be obtained even with reduced reinforcement percentage and, in turn, increasing the transparency. This shows that the influence of the adhesive type on the post-cracking performance is not so significant in hybrid strengthening systems, as is the case in EBR strengthening systems.

NSM-CFRP reinforcement could be safely prestressed without premature peeling-off failure at load introduction. The NSM technique minimized the probability of premature failure at load introduction because it increased the bonded surface area between adherends and, also because, the CFRP reinforcement is only bonded to the glass surfaces, which show higher strength than glass edges. Post-tensioning the reinforcement increased the glass fracture strength between 22.7 % and 94.7 %. Mechanical post-tensioning of annealed glass by prestressing NSM-CFRP laminates or activating Fe-SMA materials was showed to be feasible and effective on preventing the growth of surface flaws.

The CFRP_SMA hybrid strengthening system showed to have a good compromise between the pre- and post-cracking performances. The most stiff reinforcement material must always be introduced into the pre-designed groove to guarantee sufficient post-failure stiffness, even after premature debonding of the externally bonded reinforcement. Accordingly, as the Fe-SMA reinforcement can always be activated, the fracture strength of glass can be maximized by strengthening glass applying NSM-CFRP and EBR-SMA composite systems.

5.2. FUTURE DEVELOPMENTS

The experimental, analytical and numerical investigations conducted within this research aim at contributing for the knowledge on the structural performance of glass composite systems with passive and prestressed CFRP reinforcement and SMAs. However, this topic is still relatively recent in the structural glass field and, therefore, further investigation should be carried out to better understand the behaviour of glass composite systems and to develop reliable solutions with commercial prospects. This section presents some recommendations for a deeper research on these subjects, mainly:

i. The long-term and durability behaviour of adhesive connections involving glass adherends should be investigated (accelerated aging in laboratory and/or real exposure conditions) to fully understand how different environmental agents (e.g. temperature cycles and humidity) influence the bond behaviour. This will provide valuable information for the design of reinforced glass beams;

ii.   Another critical aspect that deserves special attention is the influence of the adhesive type (e.g. stiffness, strength and overall behaviour) on the structural performance and failure models of adhesively bonded joints with glass adherends. Further investigation about this topic is needed, and focus should be placed on the viscoelastic properties of the adhesives (elastic energy absorption capacity) to prevent significant dynamic effects and improve the structural safety of glass structures;

iii.   The study presented in Paper III showed that the adhesive type plays a key role on the structural response of glass-CFRP composite systems. Therefore, in order to obtain an optimized post-cracking performance in terms of load-carrying reserve and ductility, the influence of distinct aspects should be also addressed to understand how glass composite systems depend on the type of glass (e.g. annealed or heat-strengthened glass), the bonding agent (e.g. structural adhesives or interlayer), the reinforcement percentage and the cross-section geometry (e.g. I- or T-sections);

iv.   Given the well-known time and temperature dependency of adhesives and fibre reinforced polymers, further experimental investigation is needed to characterize the structural behaviour of glass composite systems under fire exposure;

v.   The exploratory study presented in Paper IV showed that the activation of Fe-SMAs can be successfully used for the post-tensioned strengthening of glass structures. As with any composite system, the investigation of glass-SMA composite systems at the level of the adhesive joint is fundamental to better understand their post-cracking performance and should be included in future works;

vi.   The influence of the temperature on the mechanical properties of adhesives (e.g. stiffness) is not well-known and, consequently, experimental and numerical studies about the activation process of Fe-SMA reinforcement should be conducted, focusing on the adhesive behaviour at different temperatures and on the heat flow during the activation process;

vii.   Losses in post-tensioning force occurred after activating Fe-SMA strips, decreasing the expected cracking load of the Fe-SMA reinforced glass beams. This indicates that the long-term behaviour of Fe-SMA reinforced glass elements may be an important issue to be investigated, mainly focusing on the relaxation behaviour of Fe-SMA materials and on the stress concentrations at the ends of the activation region;

viii. The study presented in Paper V showed that hybrid strengthening systems were efficient in delaying the premature debonding of the reinforcement by critical shear crack. In addition,

the NSM-CFRP reinforcement was safely prestressed for relatively high prestressing levels, avoiding a premature FRP peeling-off failure at load introduction. However, in order to take better advantage of the full tensile capacity of CFRP materials and increase the fracture strength of annealed glass to the levels registered in heat-strengthened or tempered glass, further investigation is required to study end-anchorage systems capable of transferring smoothly the high shear stresses from the reinforcement to the glass substrate;

ix.   Good correlation between the numerically predicted responses and the ones experimentally obtained was achieved. An attempt to numerically simulate the post-cracking behaviour of Fe-SMA reinforced composite beams should be included in future works, with emphasis on the activation process and the subsequent tensile behaviour of the activated Fe-SMA material. Another topic that needs further investigation is the development of numerical tools to model the fracture behaviour of thermally toughened glass.

PAPER I

PRELIMINARY NUMERICAL STUDY ON FRP REINFORCED GLASS BEAMS

ABSTRACT: Several reinforcing strategies have recently been developed to overcome glass brittleness and numerical simulations are essential to investigate the structural behaviour of such hybrid systems. Based on previous experimental results from monotonic quasi-static tests, this paper presents a numerical study about the flexural behaviour of glass beams reinforced with glass fibre reinforced polymer (GFRP) laminates bonded with two different adhesives: polyurethane and epoxy. The main objective of this study is to evaluate the efficiency of different constitutive models to simulate the non-linear behaviour of glass, considering the following factors: initial stiffness, cracking load, post-cracking stiffness, crack pattern and progressive failure. The glass is simulated using smeared crack (SCM) and damaged plasticity (DPM) models with static and dynamic numerical approaches. Particular attention is paid to the influence of the several parameters that influence the structural behaviour of glass (e.g. threshold angle), as well as to the interfaces between all the materials involved (e.g. thickness of the adhesive layer). In relation to static numerical approaches, dynamic numerical

approaches require more computational effort and their dynamic effects may influence the structural responses obtained; however, they also show to be able to capture all the stages of cracking in greater detail, because stability during cracking formation is guaranteed even at smaller loading stages. Since DPM models do not allow considering a maximum absolute damage factor of 1.0, the smeared crack models simulate better the non-linear behaviour of glass.

KEYWORDS: Damaged plasticity model; Dynamic effects; Glass-GFRP composite beams; Numerical analysis; Smeared crack model; Structural behaviour.

1   INTRODUCTION

Structural glass is nowadays of great relevance in contemporary architecture, due to its aesthetic and functional virtues [1, 2]. However, the structural behaviour of glass is substantially different from other building materials, such as steel and reinforced concrete [3]. The brittle behaviour of glass and the difficulties in anticipating its failure require the adoption of suitable safety measures.

To improve the structural performance of annealed glass, the industry has developed glass toughening to increase its tensile strength and glass lamination to overcome its brittleness [1,4] In the first method creates compressive stresses on outer surfaces, closing flaws and, therefore, increasing its tensile strength. However, the breakage of tempered glass creates smaller fragments, which reduces the residual strength. On the other hand, the second method consists of joining two or more glass sheets using an interlayer. The glass lamination prevents the failure of the entire element (redundancy) and, due to the interlayer action, the fragments will remain in place. The structural performance of laminated glass elements has been addressed in several experimental (e.g. [4]) and numerical (e.g. [5]) studies, evaluating the influence of different interlayers, loading conditions and temperatures. In order to improve the post-cracking performance of laminated glass with fully tempered glass plies, interlayers with embedded reinforcement have also been studied (e.g. [6]). However, the brittle behaviour of glass is not eliminated by either method.

In recent years, several reinforcing strategies have been developed to overcome glass brittleness [7], particularly the hybrid glass systems with timber (e.g. [8,9]), steel (e.g. [10–13]), Carbon Fibre Reinforcement Polymers, CFRP (e.g. [14,15]) and Glass Fibre Reinforcement Polymers, GFRP (e.g. [1,2,16–19]). Therefore, the selection of the type of adhesive to use is also critical, considering that there is a wide range of adhesives with different properties before and after hardening [20].

Numerical simulations are essential to investigate the structural behaviour of hybrid glass systems, or to design more complex or structurally demanding cases. However, the brittle behaviour of glass poses great challenges to the numerical simulations of structures comprising glass components, as well as the calibration of the material constitutive models adopted. Different authors have shown that the major challenges associated to the numerical simulation of structural glass behaviour, besides the calibration of the non-linear constitutive models used for glass simulation, are (i) the realistic definition of the structural interaction between materials and (ii) the assessment of the post-cracking behaviour [19,21]. Several approaches have been used to study critical aspects related to laminated glass and/or hybrid glass structural elements: (i) the type of interlayer representation and factors that influence its stiffness, such as temperature and load duration; (ii) the type of interaction between materials, mainly glass and reinforcement; and (iii) the type of constitutive models used to describe the non-linear behaviour of the glass and interlayer, as well as the behaviour of the reinforcement.

Different constitutive models suitable for representing brittle or quasi-brittle behaviour have been used to simulate the non-linear behaviour of glass. While Neto *et al.* [18] have used a discrete crack approach, Valarinho *et al.* [19], Bedon and Louter [21–24] and Louter *et al.* [25] have used a smeared crack approach. Damaged plasticity approach was also used by Bedon and Louter [26]. The numerical simulations in Bedon and Louter [21–24] were performed in the ABAQUS finite elements software, by employing the Rankine failure criterion for cracks detection. The "brittle failure" option was adopted to model cracking evolution in Bedon and Louter [21,22], while the "brittle shear" option was adopted in Bedon and Louter [23,24]. Finally, the study performed by Bedon and Louter [26] included the numerical simulation of post-tensioned glass beams using ABAQUS, by means of the "concrete damaged plasticity" model, commonly used for modelling concrete.

Because glass is an extremely fragile material, which has low fracture energy, some studies have adopted strategies to overcome problems related to the convergence of numerical models, such as linear sequential elastic analysis. The aim was to avoid a possibly negative tangential stiffness, which is the main cause for convergence problems found in non-linear analysis [25]. However, all these strategies require additional regularization procedures to obtain mesh objective results [18].

Considering the importance of developing accurate approaches for the simulation of glass structures, and the challenges that normally are associated to the simulation of the behaviour of brittle materials such as glass, this study is aimed at assessing the in-depth details associated to the numerical simulation of reinforced structural glass, including both the force-deflection response and the cracking

evolution. This work presents a numerical study of the structural behaviour of glass beams reinforced with GFRP laminates, which were simulated using different Smeared Crack (SCM) and Damaged Plasticity (DPM) models, available in FEMIX [27] and ABAQUS 6.14 [28], as well as different static and dynamic numerical approaches. In order to evaluate the efficiency of these models for the simulation of the post-cracking behaviour, the different numerical responses were analysed and compared considering the following factors: initial stiffness, cracking load, post-cracking stiffness, crack pattern and progressive failure. For this purpose, the material parameters derived by Valarinho *et al.* [19], based on experimental tests of glass-GFRP composite beams, were used. In this context, the present work addresses two main novel aspects, (i) concerning the comparison of different approaches for the numerical simulation of reinforced structural glass, since existing literature is absent in such critical analysis; (ii) on the other hand, literature often refers ABAQUS/Explicit analyses without addressing the influence of dynamic effects; both factors are critical for accurate simulations. The paper identifies the most critical factors and possible strategies to obtain quasi-static analysis without excessive computational effort.

2   TESTS ON GLASS-GFRP COMPOSITE SYSTEMS

The numerical simulations of glass-GFRP composite beams were based on an exploratory experimental study carried out by Valarinho et al. [19]. These beams were tested following the four-point bending setup. The glass-GFRP composite beam specimens, as shown in **Figure I.1**, consisted of annealed glass panels, with cross-section of 12×100 [mm], reinforced at the bottom face with a GFRP pultruded laminate with a cross-section of 12×8 [mm]. These materials were joined using two different adhesives, with a 2.0 mm thick layer: (i) a polyurethane adhesive, Sikaflex 265, with low Young's modulus and considered as a flexible adhesive, and (ii) an epoxy adhesive, SikaDur 31-fc, with high Young's modulus and considered as a stiff adhesive.

Double-lap joint specimens were also tested in tension by Valarinho *et al.* [19], in order to characterize the bond behaviour between GFRP and glass. From these tests the following main conclusions were obtained: (i) in the specimens with flexible adhesive, which exhibited an initial linear behaviour, a significant loss of stiffness before collapse was observed (see **Figure I.2a**), with failure characterized by debonding at the glass-adhesive interface; (ii) the specimens with stiff adhesive exhibited a practically linear behaviour until the collapse (see **Figure I.2b**), eventually with glass failure.
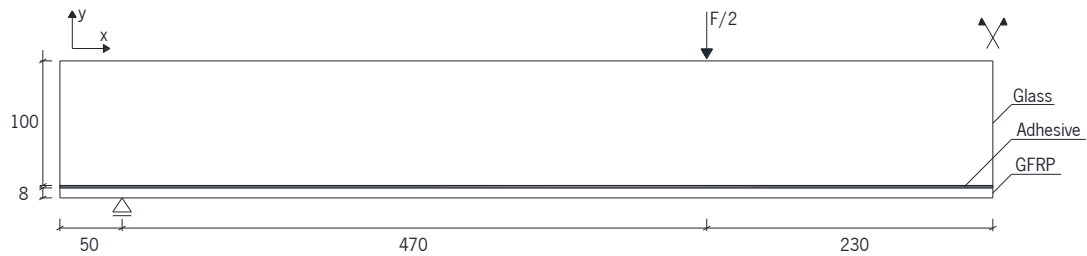
(a)
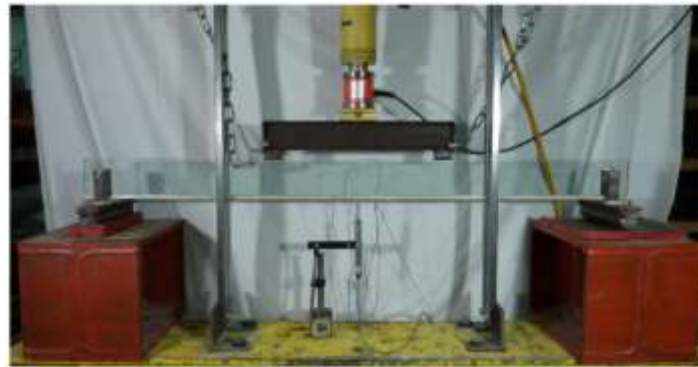
(b)

Figure I.1: Four-point bending tests of the glass-GFRP composite beams: (a) schematic representation; (b) experimental setup [19]. Note: units in [mm].
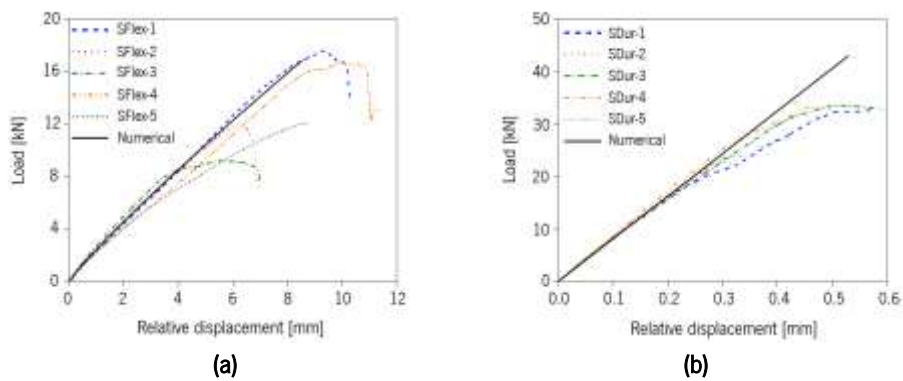
| (a) | (b) |

Figure I.2: Load *vs.* relative displacement obtained from tensile tests on double-lap joints with (a) polyurethane and (b) epoxy adhesives [19].

Figure I.3 presents the structural behaviour of the glass-GFRP composite beams with polyurethane (S*Flex* beams) and epoxy (S*Dur* beams) adhesives obtained from four-point bending tests [19]. These composite beams presented linear elastic behaviour until the first crack appeared in the glass panel. Due to the brittle nature of glass failure and the inherent variability of its tensile strength, the cracking loads reached during testing have shown some scatter, as well as the post-cracking responses. This variability is associated to the numerous flaws contained by glass, which are randomly distributed in the material – such flaws, which are very small in size (not distinguishable by the naked eye) result

mainly from the production process, and also from cutting and handling operations [29]. This inherent characteristic of glass explains not only the relatively high scatter of its tensile strength (e.g. Veer and Rodichev [30]), but also the occurrence of relevant size effects [31]. In the post-crack phase, a progressive loss of stiffness was observed after the development of a single crack in the case of the glass-GFRP composite beams made with polyurethane adhesive (see **Figure I.4b**). In the case of the composite beams made with epoxy adhesive, several cracks have developed, propagating towards the supports (see **Figure I.4a**). According to Valarinho *et al.* [19], the deflection increment before cracking (pre-cracking stage) ranged from 0.95 mm/min to 1.52 mm/min and then, during the post-cracking stage, between 1.70 mm/min and 3.21 mm/min. In these tests, both the applied load and the mid-span deflection were measured at an average acquisition frequency of 5 Hz. All glass-GFRP beams were tested at an average temperature of 24 °C and 60 % of relative humidity.

(a)   (b)
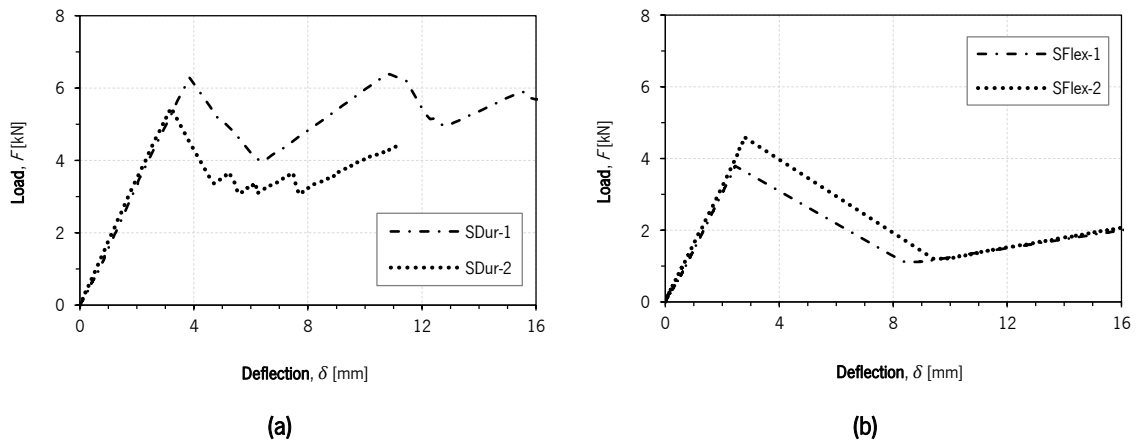
Figure I.3: Structural responses (load *vs.* deflection) obtained from the experimental tests: (a) S*Dur* beams; (b) S*Flex* beams [19].

(a)   (b)

Figure I.4: Experimental crack patterns: (a) S*Dur* beams; (b) S*Flex* beams [19].

The double-lap joint specimens have shown significant relative displacements between the glass pane and the GFRP laminate when flexible adhesives were used (about 20 times higher than for the stiff

adhesives). For this reason, four strain gauges (SG1 to SG4) were installed at different locations of the S*Flex*-1 beam at its mid-span section: (i) SG1 was placed at the top edge of the glass panel; (ii) SG2 was placed at the bottom/bonded edge of the glass panel; (iii) SG3 was placed at the top/bonded edge of the GFRP laminate; and (iv) SG4 was placed at the bottom edge of the GFRP laminate. As depicted in **Figure I.5**, a significant slippage occurred at the bonded interfaces of S*Flex*-1, both before and after the first crack was formed. Therefore, Bernoulli's hypothesis was not observed for these beams.
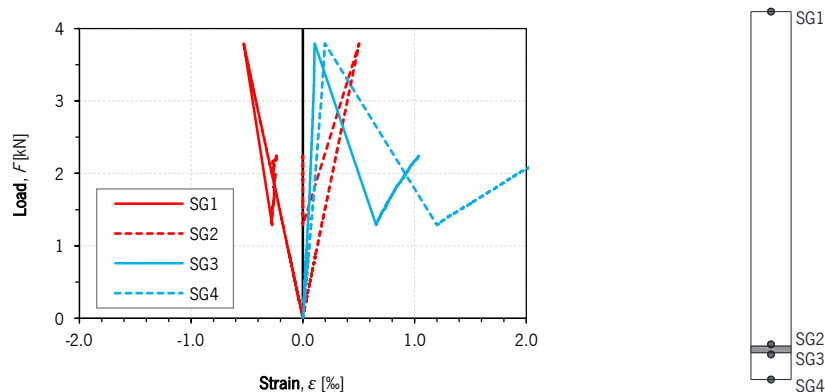
Figure I.5: Axial strains *vs*. load measured at different depths of the S*Flex*-1 beam mid-span section.

3   NUMERICAL SIMULATON

Based on an initial estimation of the material non-linear parameters derived in Valarinho *et al*. [19], different material models, based in smeared crack and damaged plasticity approaches, were studied to simulate the non-linear behaviour of glass, as detailed in the following sections.

3.1.   Smeared crack approach

The smeared crack approach has been used by different researchers to describe the non-linear behaviour of brittle and quasi-brittle materials, e.g. concrete, masonry and glass. This approach can be categorized into fixed and rotating [32]. With the fixed concept, the orientation of the cracks is fixed during the entire computational process, whereas the rotating concept allows the orientation of the cracks to co-rotate with the axes of principal stress [32]. The multi-fixed crack concept provides an intermediate option.

The multi-fixed concept, used by FEMIX [27], is suitable for tension-shear conditions, which is typical of fracture propagation problems [32]. The cracks start only under tension conditions, in mode-I, and subsequently propagate in tension-shear conditions. In the described behaviour, the maximum principal stress directions rotate after crack formation, which leads to increasing discrepancy relatively

to the fixed crack directions. After the first crack, a new crack may appear when: (i) the maximum principal stress of an integration point exceeds the defined tensile strength, and (ii) the angle between the direction of the existing cracks and the direction of the maximum principal stress exceeds the value of a predefined threshold angle.

The smeared crack approach contributes to describe the structural behaviour of the material when the maximum principal stress exceeds the uniaxial tensile strength. The main assumptions of this numerical approach are: (i) the damaged area is distributed by a specific crack band width, h, and (ii) the constitutive law of the damaged material is characterized by a tension-softening diagram, which, together with the fracture energy, G_f, are considered as material properties [33]. The type of tension-softening diagram and the number of cracks in each integration point are parameters required by the multi-fixed smeared crack approach [34].

Bazant and Oh [33], Sena-Cruz [34] and Rots *et al.* [35] proposed different ways to estimate the crack band width: (i) equal to the square root of the area of the finite element, (ii) equal to the square root of the area of the integration point, and (iii) equal to a constant value. The mesh objectivity must be ensured by the relationship between the crack band width and mesh size [32,34]. According to de Borst [36], the computational instabilities and convergence problems (e.g. snap-back instabilities) are avoided when the **Eq. (I.1)** is fulfilled. Therefore, the crack band width must be controlled to guarantee the stability and convergence of the smeared crack models. The other parameters are assumed to be constant properties of the material. The minimum facture energy required for a stable numerical process is given by **Eq. (I.2)**, obtained from the manipulation of **Eq. (I.1)**.

$$h \leq \frac{G_f E}{f_t^2 b} \tag{I.1}$$

$$G_f \geq \frac{f_t^2 b h}{E} \tag{I.2}$$

The smeared crack approach was formulated in such a way that not only tension-softening but also crack shear can be taken into account through the shear retention factor, β [35]. This can be defined in two different ways [32,34]: (i) a constant value, and (ii) a non-constant value using the **Eq. (I.3)**, where p is a constant value (e.g. 1, 2 or 3), ε_n^{cr} and $\varepsilon_{n,ult}^{cr}$ are the crack normal strain and the ultimate crack normal strain, respectively.

$$\beta = \left(1 - \frac{\varepsilon_n^{cr}}{\varepsilon_{n,ult}^{cr}}\right)^p \tag{I.3}$$

The constant shear retention factor implies a linear ascending relation between shear stress and shear strain across the crack, as well as a constant crack shear modulus [32]. In addition to the arbitrariness in choosing this value, the shear stress can increase indefinitely with a constant shear retention factor and, consequently, the maximum principal stress directions in cracked elements rotate ceaselessly [32].

The ABAQUS uses a smeared crack approach with fixed concept (orthogonal cracks). Therefore, the maximum number of cracks at an integration point is limited by the number of stress components, e.g. 3 cracks in 3D models and 2 cracks in 2D models. According to ABAQUS [28], although the fixed concept has the orthogonally limitation, it is considered superior to the rotating concept when the effect of multiple cracks is important, since the last concept is restricted to a single crack at each integration point. The shear retention factor is defined as a non-constant value through the **Eq. (I.3)**.

3.2. FEMIX smeared crack model (SCM-FEMIX)

This Section presents the assumptions adopted in the numerical simulation of the glass, GFRP and adhesives for the simulation of the beams with the FEMIX software. Three different strategies were considered to simulate the adhesive joint of composite beams: (i) the *Perfect Bond* (*PB*) between the glass and GFRP laminate, neglecting the physical existence of the adhesive; (ii) the *Linear Elastic Behaviour* (*LEB*) of the adhesive, using plane stress elements for 2D models or solid elements for 3D models, and assuming perfect bond at the GFRP/adhesive and adhesive/glass interfaces; and (iii) the *Non-Linear Behaviour* (*NLB*) of the joint, using interface elements, simulating the non-linear behaviour of the interfaces (GFRP/adhesive and adhesive/glass) and the adhesive itself.

3.2.1. Annealed glass

According to the Guideline for European Structural Design of Glass Components [37], in the simulation the linear elastic behaviour of annealed glass a Young's modulus, E_g, of 70 GPa, a Poisson's ratio, v_g, of 0.23 and a tensile strength, $f_{g,t}$, which ranges from 30 MPa to 80 MPa, were adopted. In composite beams models, the glass was simulated by linear elastic behaviour in compression and in tension, before cracking. Rankine failure criterion was used for the crack detection. After the cracking, non-linear behaviour of the glass was simulated by the smeared crack model.

After a parametric study, in which the experimental and the numerical results were compared in terms of initial stiffness, cracking load, post-cracking stiffness, crack pattern and progressive failure of the composite beams, Valarinho *et al.* [19] defined the glass linear features required by this mechanical constitutive model. The following properties were adopted: (i) tensile strength of 50 MPa, (ii) tension-softening diagram with linear shape, (iii) quadratic shear retention factor law, (iv) minimum mode-I fracture energy, G_f, to avoid snap-back instabilities, according to **Eq. (I.2)**, and (v) crack band width equal to the square root of the finite elements area. A threshold angle of 30° was also defined for the development of new cracks, as well as the maximum number of two and three cracks in each element in 2D and 3D models, respectively.

3.2.2. GFRP

The GFRP was modelled as linear elastic material, for both compression and tension, assuming the following mechanical properties (obtained from tests): Young's modulus, E_{GFRP}, of 28.7 GPa, Poisson's ratio, υ_{GFRP}, of 0.28.

3.2.3. Interface

Based on the parametric study described in Valarinho *et al.* [19], where three strategies were tested for the numerical modelling of the adhesive bonded joint, the perfect bond (*PB*) strategy was adopted to simulate the composite beam with epoxy adhesive (stiff adhesive). Previous numerical simulations showed that the two alternative strategies (*LEB* and *NLB*) did not accurately capture the experimental response after cracking, in terms of stiffness and ultimate load.

The polyurethane adhesive of the S*Flex* beam was described by the non-linear behaviour (*NLB*) strategy using a non-linear bond-slip relationship, as suggested in Valarinho *et al.* [19]. The *PB* strategy was initially excluded because it neglected the physical existence of the adhesive layer. On the other hand, previous simulations using the *LEB* strategy showed higher post-cracking stiffness than the one observed in the experimental responses, since it was not able to simulate the adhesive failure. Assuming a bilinear bond-slip relationship, **Table I.1** presents the used properties: (i) the linear elastic tangential stiffness, K_t, (ii) the shear strength, τ_m, and (iii) the mode-II fracture energy, G_m. The linear elastic tangential stiffness was assumed to be the same in both directions of the adhesive layer. Finally, according to Sena-Cruz [34], a high value of the linear elastic normal stiffness, K_n, was adopted in order to avoid any influence on the shear behaviour of the interface elements.

Table I.1: Mechanical properties used to simulate the polyurethane adhesive using the bilinear bond-slip relationship (*NLB* strategy).

K_n [MPa/mm]	K_t [MPa/mm]	τ_m [MPa]	G_m [N/mm]
10^6	0.4048	1.70	3.50

The non-linear bond-slip relationship used in Valarinho *et al.* [19] is governed by the **Eq. (I.4)**, where τ_m and s_m are the maximum shear stress and the corresponding maximum slip, respectively, and the shape of the pre- and post-peak curves are defined respectively by the parameters α and α' [34]. The mechanical properties used to model the polyurethane adhesive are presented in **Table I.2**. The mode-II fracture energy, G_m, was calculated as the integral of the post-peak curve, according to **Eq. (I.5)**.

$$\tau(s) = \begin{cases} \tau_m \left(\dfrac{s}{s_m}\right)^{\alpha} & if \ s \ \leq \ s_m \\ \tau_m \left(\dfrac{s}{s_m}\right)^{-\alpha'} & if \ s \ \geq \ s_m \end{cases} \tag{I.4}$$

$$G_m = \int_{s_m}^{\infty} \tau_m \left(\frac{s}{s_m}\right)^{-\alpha'} ds \tag{I.5}$$

Table I.2: Mechanical properties used in [19] to describe the polyurethane adhesive joint of the S*Flex* beam.

K_n [N/m³]	τ_m [MPa]	s_m [mm]	α [-]	α' [-]
10^6	1.70	4.20	0.90	3.00

3.2.4.   Mesh strategy

Taking into account the real geometry and the symmetry conditions of the glass-GFRP composite beams (see **Figure I.1**), only half span was numerically simulated (*l* = 700 mm). In the S*Dur* beams, 8-node plane stress elements, with 2 × 2 Gauss-Legendre integration scheme, were used to simulate the glass panel and GFRP laminate (2D models). However, to compare the results obtained in the three material models (reasons are given in **Section 3.3.3**), 20-node solid elements were also used to simulate the different structural materials (GFRP laminate and glass panel) of the S*Flex* beams (3D models).

In the *NLB* strategy, in agreement with the previously presented assumptions, the adhesive layer was simulated by 16-node interface elements with 3 (height) × 2 (thickness) using Gauss-Lobatto integration rule. The thickness of the adhesive joint was reproduced by positioning the glass panel at a distance of 2 mm from the GFRP laminate, which was then filled by the interface elements.

Based on the sensitivity of mesh analysis carried out in Valarinho *et al.* [19], elements of 10×10 [mm] yield sufficiently accurate simulations. In the 3D models, only one layer of finite elements was used to describe the beam thickness (10 (width) $\times$ 10 (height) $\times$ 12 (thickness) [mm]). In order to avoid out-plane displacements, the z-direction displacements of the nodes located at the middle-thickness were prevented.

3.3. ABAQUS smeared crack model (SCM-ABAQUS)

As for the FEMIX smeared crack model (see **Section 3.2**), similar assumptions and mechanical properties were adopted when using ABAQUS commercial package. The GFRP laminate was modelled as a linear elastic material with the same mechanical properties presented in **Section 3.2.2**. In the case of the simulation of the annealed glass, the smeared crack model available in ABAQUS/Explicit is suitable for quasi-static and dynamic analyses [28]. The computational effort required by ABAQUS/Explicit depends on the density of the materials [28]. Thus, a density of 2500 kg/m^3 and 1600 kg/m^3 was adopted for the annealed glass and GFRP, respectively. By default, ABAQUS/Explicit considers the geometric non-linearity through the "Nlgeom" setting. However, this option was ignored for the sake of simplicity because the influence of the geometric non-linearity on the structural responses would be very small.

3.3.1. Annealed glass

The compressive behaviour of annealed glass was assumed as linear elastic. The brittle failure in tension was properly considered by adopting the "Brittle Cracking" mechanical model, using the "Brittle Shear" option to model crack evolution. This constitutive model is suitable for concrete brittle and quasi-brittle materials, and it was also adopted for glass [19,21–23,25,26]. Before the tensile strength is reached, the linear elastic behaviour was assumed.

In the "Brittle Cracking" model, a Rankine failure criterion is used for the crack detection. The main parameters introduced in this material model are: (i) the tensile strength, (ii) the mode-I facture energy, and (iii) shear retention factor law (in "Brittle Shear" option). Similarly to the FEMIX models (see **Section 3.2**), the following properties were adopted: the tensile strength, $f_{g,t}$, of 50 MPa, minimum mode-I facture energy, G_f, and the quadratic shear retention law. The ABAQUS approach adopts, by default, a crack band width, h, equal to the square root of the finite elements area, as well as a linear tension-softening diagram when the "GFI" option (facture energy cracking criterion) is selected [28].

Therefore, the maximum crack opening strain, $\varepsilon_{n,ult}^{cr}$, required by the "*Brittle Shear*" option to define the quadratic shear retention law is given by **Eq. (I.6)**, and was set to 8.0×10^{-4}.

$$\varepsilon_{n,ult}^{cr} = \frac{2G_f}{hf_{g,t}}$$

(I.6)

3.3.2.   Interface

The *PB* and *NLB* strategies were used to simulate the S*Dur* and S*Flex* beams, respectively. The interface GFRP/glass was modelled by adopting the "*Surface-Based Cohesive Behaviour*" with "*Progressive Damage and Failure*". This interface model is suitable for situations where the interface thickness is negligible [28], so the thickness of the adhesive layer was not considered in the simulations.

The constitutive model of the interface was described by the linear elastic normal stiffness, K_n, the linear elastic tangential stiffness in each direction of the adhesive layer, K_t, the normal strength, σ_m, the shear strength, τ_m, and the mode-II facture energy, G_m, assuming a linear softening law. The interface material models used in FEMIX and ABAQUS were characterized by similar parameters, defined in **Table I.1**.

3.3.3.   Mesh strategy

Like in SCM-FEMIX, in these numerical models only half span of the composite beams was discretized. Considering the interface model adopted (see **Section 3.3.2**), ABAQUS/Explicit does not allow the edge-to-edge contact. Therefore, three-dimensional (3D) simulations of the S*Flex* beams was performed using 8-node solid elements with reduced integration (C3D8R).

On the other hand, 4-node plane stress elements with reduced integration (CPS4R) were used to simulate the S*Dur* beams (2D models). The 2×2 integration scheme in 4-node elements is not supported by ABAQUS/Explicit, as well as 8-node elements with 3×3 or 2×2 integration schemes [28]. The adhesive layer was simulated by 4-node zero thickness surface elements (SFM3D4), with 4 integration points (surface-to-surface).

A mesh of 5 (width) $\times$ 5 (height) [mm] finite elements was adopted for S*Dur* beam, in order to maintain a consistent number of degrees of freedom with respect to SCM-FEMIX (see **Section 3.3.4**), where the finite elements were assigned with a 2×2 integration scheme. Two layers of finite elements of 10 (width) $\times$ 10 (height) $\times$ 6 (thickness) [mm] were used to describe the thickness of the S*Flex* beam.

This approach was adopted in order to avoid out-plane displacements, and the z-direction displacements of the nodes located at the middle-thickness, which are shared by the two layers of finite elements that describe the thickness of the beam, were prevented. The adoption of finite elements of 5 (width) × 5 (height) × 6 (thickness) [mm] would require a high computational effort and, in the case of the S*Flex* beam, would not significantly improve the capturing of its post-cracking behaviour, as verified by preliminary simulations.

Linear elements (e.g. CPS4R and C2D8R) with reduced integration tend to be too flexible due to the hourglass problem. The distortions may be such that the deformations calculated at the integration point are all zero, leading to uncontrolled distortion of the mesh [28]. Hourglass is usually controlled by introducing counteracting internal nodal forces. The ABAQUS/Explicit provide five different hourglass controls: (i) relax stiffness (by default); (ii) enhanced; (iii) stiffness; (iv) viscous; and (v) combined (stiffness and viscous) [28]. According to Mostafawi [38], the viscous and combined hourglass controls give very large artificial energy and are not appropriate for quasi-static problems. On the other hand, the enhanced hourglass control is not appropriate for non-linear problems, since it provides increased resistance and may yield overly stiff responses [28]. In the present study the stiffness relax was adopted to control hourglass.

3.3.4. Dynamic effects

According to Chen *et al.* [39], (i) the loading time, (ii) the loading scheme, (iii) the damping ratio, (iv) the time increment size and (v) the time integration method are factors that affect the accuracy of quasi-static simulations with models that are intrinsically dynamic. The correct combination of these factors allows to reduce the dynamic effects of the models and obtain quasi-static responses. In ABAQUS, the viscous damping is defined as Rayleigh Damping, where the viscous damping matrix, C, is expressed as a linear combination of the mass matrix, M, and the stiffness matrix, K (see **Eq. (I.7)**). The damping ratio for the jth mode of the system can be expressed by **Eq. (I.8)**.

$$C = \alpha_0 M + \beta_0 K \tag{I.7}$$

$$\xi_j = \frac{\alpha_0}{2\omega_j} + \frac{\beta_0 \omega_j}{2} \tag{I.8}$$

The α_0 and β_0 parameters of **Eq. (I.7)** and **Eq. (I.8)** are constants for mass and stiffness-proportional damping, respectively. On the other hand, ω_j is the angular frequency corresponding to the jth mode. The period, T_1, and the angular frequency, ω_1, of the fundamental vibration mode of the S*Dur* beams,

which were determined using the "linear perturbation procedures" available in ABAQUS/Standard, are equal to 0.255 s and 24.63 rad/s, respectively. According to Chen *et al.* [39], the loading time should be in the range of $50T_1$ to $100T_1$ (14 s to 28 s, approximately). As the S*Flex* beams have a lower stiffness than the S*Dur* beams, since the polyurethane adhesive is flexible, a loading time of 17.5 s and 12.5 s was used for the S*Dur* and S*Flex* beams, respectively.

The application of loading induces large dynamic effects, due to the initial velocity and acceleration [39]. A linear loading scheme was adopted because, as the loading rate is constant during the process, the acceleration is null during most of the loading process and its influence on the structural response is negligible. The adoption of a smooth loading scheme in general requires longer loading time or, to complete the process within the predefined time, a higher loading rate. However, the increase of these two parameters could increase the dynamic effects [39].

In ABAQUS/Explicit, by default, the time increment scheme is fully controlled by the stability limit of the central difference method and requires no user intervention, which would always adopt a non-optimized value [28]. Therefore, an automatic time increment size was used. According to ABAQUS/Explicit [28] a small damping is introduced to control high frequency oscillations. The maximum stable time increment (Δt) with damping is given by the **Eq. (I.9)**, where ξ_{max} is the ratio of critical damping of the vibration mode with the highest frequency, ω_{max}. In this way, the damping reduces the stable time increment and, consequently, increases the computational cost.

$$\Delta t \leq \frac{2}{\omega_{max}}\left(\sqrt{1 + \xi_{max}^2} - \xi_{max}\right)$$
(I.9)

Considering the numerical models presented in Chen *et al.* [39], the mass-proportional damping may become unstable and fail. On the other hand, to create the same level of critical damping in the lowest vibration mode, the stiffness-proportional damping requires more computational cost, since it causes a larger decrease in the maximum stable time. Thus, the mass-proportional damping, which has a higher damping efficiency for the low frequency vibration modes, was applied in this work.

According to ABAQUS [28], an approximation to the stability limit is given by the **Eq. (I.10)**, where L_{min} is the smallest element dimension in the mesh and c_d is the dilatational wave speed, calculated from the **Eq. (I.11)**, where ρ is the density. In an isotropic and elastic material (e.g. glass), the effective Lamé's constants $\hat{\lambda}$ and $\hat{\mu}$ can be computed based on the Young's Modulus, E, and Poisson's ratio, υ, using **Eq. (I.12)** and **Eq. (I.13)**, respectively.

$$\Delta t = \frac{L_{min}}{c_d} \tag{I.10}$$

$$c_d = \sqrt{\frac{\hat{\lambda} + 2\hat{\mu}}{\rho}} \tag{I.11}$$

$$\hat{\lambda} = \lambda_0 = \frac{Ev}{(1+v)(1-2v)} \tag{I.12}$$

$$\hat{\mu} = \mu_0 = \frac{E}{2(1+v)} \tag{I.13}$$

Analysing **Eq. (I.10)**, **Eq. (I.11)**, **Eq. (I.12)** and **Eq. (I.13)**, the computational effort can be reduced by increasing the material density, using the mass scaling, which reduces the dilatational wave speed, or increasing the dimensions of the finite elements. As all finite elements have the same dimensions, the last option was not adopted because it would decrease the number of degrees of freedom of the mesh.

3.4. ABAQUS damaged plasticity model (DPM-ABAQUS)

The assumptions and mechanical properties adopted in the previous models (see **Section 3.3**) were also used in case of the simulations with the Damaged Plasticity Model (*DPM*), mainly: (i) the GFRP was modelled as a linear elastic material (mechanical properties presented in **Section 3.2.2**); (ii) the *PB* and *NLB* strategies were used in S*Dur* and S*Flex* beams, respectively; (iii) the "*Surface-Based Cohesive Behaviour*" with "*Progressive Damage and Failure*" were used to describe the interface GFRP/glass (mechanical properties presented in **Table I.1**); and (iv) the finite elements CPS4R, C3D8R and SFM3D4 were used to simulate the S*Dur* and S*Flex* beams. Although the *DPM* is available in ABAQUS/Standard, the simulations were performed in ABAQUS/Explicit for the sake of comparison and to avoid snap-back instabilities, mainly in the simulation of the S*Flex* beam that, comparing with S*Dur* beam, has a more brittle behaviour.

As stated before, the glass was model with the "*Concrete Damage Plasticity*" model. This model was originally used in the simulation of reinforced concrete elements [40–42], and then extended to the simulation of other quasi-brittle materials, e.g., glass [26] and masonry. The inelastic compressive and tensile behaviours are described by multi-hardening plasticity and a scalar isotropic damaged elasticity, respectively [28]. Thereby, the definition of the yield surface and the plastic flow are required by DPM-ABAQUS through the following parameters: (i) the dilation angle, ψ; (ii) the eccentricity, ϵ, which defines the shape of plastic flow; (iii) the ratio between the initial biaxial compressive yield stress, f_{bc}, and the initial uniaxial compressive yield stress, f_c; and (iv) the shape of yield surface, defined by

K_c. The dilation angle was set to 1°. According to the recommendations in ABAQUS [28] for quasi-brittle materials, such as concrete, values of 0.1, 2/3 and 1.16 were considered for ϵ, K_c and f_{bc}/f_c ratio, respectively.

The mechanical parameters required to simulate the tensile behaviour of glass are: (i) the yield stress, σ_t, (ii) the mode-I facture energy, G_f, and (iii) the damage law, defined by the d_t parameter [28]. The minimum mode-I facture energy was adopted to avoid snap-back instabilities, such as in the case of smeared crack models (see **Section 3.2** and **Section 3.3**). As mentioned in **Section 3.3.1**, when the GFI option is selected, the ABAQUS software assumes a linear tension-softening diagram. Therefore, the maximum total displacement, u_{max}, which also includes the elastic deformation, was determined by **Eq. (I.14)** and its value is equal to 1.514×10^{-2} mm.

As glass has a brittle nature, the plastic strain, ε_t^{pl}, is essentially null ($\varepsilon_t^{el} = \varepsilon_t$). According to ABAQUS [28], an excessive damage factor may have a critical effect on the rate of convergence. A damage factor of 0.99 was assigned to the maximum total displacement, which corresponds to a 99 % reduction of the stiffness, taking into account recommendations given in [28]. Based on these aspects, the damage law adopted is presented in **Figure I.6**, as well as the corresponding mechanical constitutive model.

$$u_{max} = \frac{h f_{g,t}}{E_g} + \frac{2 G_f}{f_{t,g}} \tag{I.14}$$
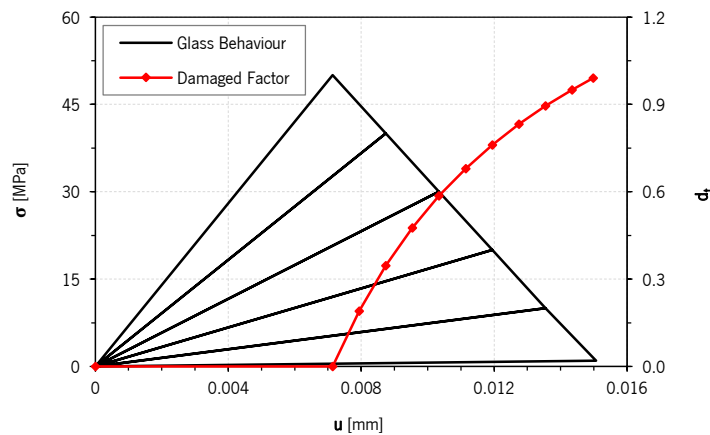
Figure I.6: Damage law adopted for simulating glass behaviour.

3.5. Parametric study

The structural behaviour of glass composite systems can be divided in two stages, separated by the appearance of the first crack: the pre- and post-cracking stages. Initially, during the pre-cracking stage, glass behaves as a linear elastic material until the maximum principal stress exceeds its tensile strength, regardless of the numerical model adopted. Therefore, the pre-cracking response (e.g. stiffness and cracking load) is controlled only by elastic properties, such as Young's modulus and tensile strength. On the other hand, during the post-cracking stage, the behaviour of annealed glass is controlled by the constitutive models, through the material parameters required by each model to define the post-peak response (softening branch).

However, the input parameters required to define the cracked behaviour of glass involve higher uncertainty, either due to the difficulty of measuring these material properties in glass (e.g. fracture energy) or because these constitutive models were not specifically developed to simulate glass (e.g. DPM-ABAQUS). Thus, a parametric study was carried out concerning these input parameters, namely the threshold angle in SCM-FEMIX, the fracture energy in SCM-ABAQUS and DPM-ABAQUS and, finally, the dilation angle and the shape of the yield surface in DPM-ABAQUS. For the sake of simplicity, only SDur beams were considered for this parametric study, due to their extensive cracking during the post-cracking behaviour. The results will be presented and compared in **Section 4.1.2**, in terms of structural response and crack pattern.

As previously mentioned in **Section 3.1**, while a multi-fixed concept is used by SCM-FEMIX, SCM-ABAQUS uses, by default, a fixed concept (orthogonal cracks). At integration points close to the bottom edge of the glass panel, large rotations in their maximum principal stresses are expected due to the shear stresses induced by the GFRP/glass interface. Thereby, special attention was given to the influence of the threshold angle on the post-cracking response of SDur beams. For this purpose, a threshold angle of 90° (fixed concept) was also considered in SCM-FEMIX, later called SCM-FEMIX-90°.

As glass is extremely brittle, its fracture energy is close to zero. However, according to **Eq. (I.2)**, a minimum mode-I fracture energy should be used to avoid numerical instabilities in static analysis, taking into account the mesh pattern and the mechanical properties of the material, that is, the tensile strength and the Young's modulus. In contrast, when adopting dynamic approaches, such as the one adopted by ABAQUS/Explicit [28], lower values than the minimum mode-I fracture energy can be used ensuring the convergence of models. In previous numerical studies on glass [21–24,26,43], a value

of 3 J/m^2 (0.003 N/mm) [44] has been used to define the fracture energy of annealed glass, regardless of the mesh size. Therefore, this value was also considered in this parametric study.

On the other hand, the dilatancy is the physical phenomenon that describes the increase in volume of the material microstructure caused by shear stresses. This phenomenon is mainly associated with soils and quasi-brittle materials (heterogeneous materials). Compared to concrete, smooth surfaces are created when the glass breaks. Therefore, the dilation angle in glass is likely lower than in concrete, which is usually greater than 30°, according to Coronado and Lopez [41]. Values of 1°, 10° and 20° were considered.

As the S*Dur* beams were numerically simulated neglecting the physical existence of the adhesive layer, according to *PB* strategy (see **Section 3.2.3**), considerable shear stresses were expected near the bottom edge of the glass panel. Thereby, the influence of the yield surface shape was considered in this parametric study. Values of 0.5 (Rankine yield surface), 0.67 (recommended value in ABAQUS [28]), and 1.0 (Von Mises yield surface) were considered for the crack detection criteria.

In addition to the material parameters required by the constitutive models, the post-cracking behaviour of glass-GFRP composite systems is influenced by the mesh pattern, which determines whether a numerical model is capable of capturing in detail all the failure processes that were observed experimentally. Thus, the ability to capture localized phenomena, such as the progressive detachment of the GFRP laminate towards the supports, can be substantially influenced by the mesh pattern adopted, both the mesh size and the number of integration points per finite element. In the present research 8-node plane stress elements of 10×10 [mm] with 2×2 Gauss-Legendre integration scheme were used in SCM-FEMIX, while 4-node plane stress elements of 5×5 [mm] with reduced integration (CPS4R) were used in ABAQUS models to simulate S*Dur* beams. In order to assess the influence of the mesh pattern on each ABAQUS model, a sensitivity analysis was carried out considering two additional mesh sizes: 2.5×2.5 and 10×10 [mm].

4 RESULTS AND DISCUSSION

Figure I.7, **Figure I.8** and **Figure I.9** show the load (F) *vs.* deflection at mid-span (δ) responses of S*Dur* and S*Flex* beams obtained from the numerical simulations, as well as the crack patterns obtained at relevant phases: (i) onset and end of the post-cracking stage of S*Dur* beams, and (ii) after cracking for the S*Flex* beams. In S*Dur* beams, the crack patterns are also presented at an intermediate stage of the post-cracking response to show the evolution of the cracking processes. The S*Dur* beam analysis

was stopped when the initial cracking load was fully recovered. On the other hand, in the simulation of S*Flex* beam, the analysis was stopped when the deflection of 12 mm was attained, since the post-cracking stage of these composite beams showed an almost linear steady recovery of the load carrying capacity. Additionally, the further computation was difficult due to pronounced numerical instabilities after this displacement was attained, most likely due to the large opening of the cracks already formed.

Figure I.10 shows the load *vs*. deflection responses obtained by using the three numerical models, as well as the experimental results obtained for the composite beams made with epoxy (S*Dur*) and polyurethane (S*Flex*) adhesives (two test results are presented for each type of beam). **Table I.3** summarizes, for the simulated beams, the main parameters characterizing their structural behaviour: elastic stiffness, K_{el}, cracking load, F_{cr}, and corresponding deflection, δ_{cr}.

S*Dur* beam
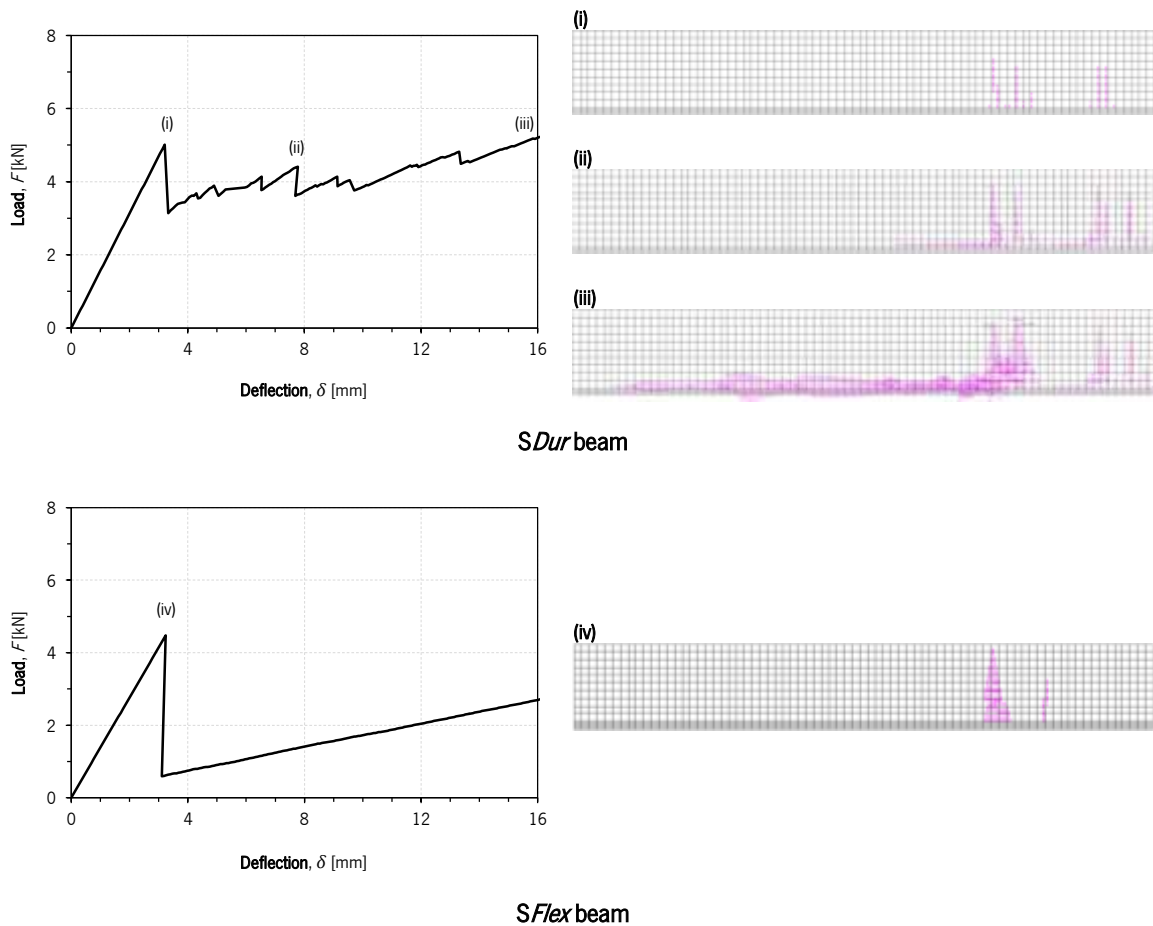
S*Flex* beam

Figure I.7: Load *vs*. deflection curves of the S*Dur* and S*Flex* beams obtained from the SCM-FEMIX, and corresponding crack pattern at different phases, (i), (ii), (iii) and (iv).

113

S*Dur* beam
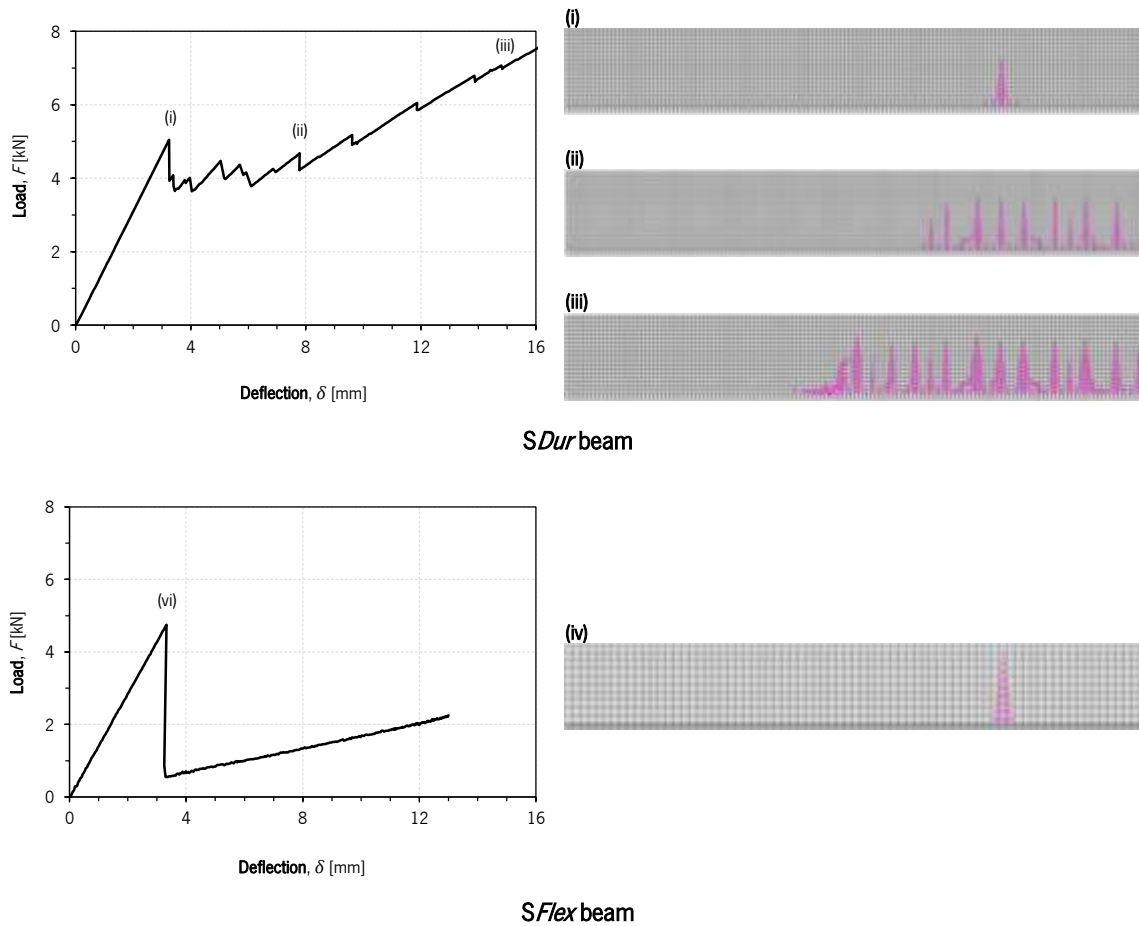
S*Flex* beam

Figure I.8: Load *vs*. deflection curves of the S*Dur* and S*Flex* beams obtained from the SCM-ABAQUS, and corresponding crack pattern at different phases, (i), (ii), (iii) and (iv).

Table I.3: Elastic properties of the S*Dur* and S*Flex* beams defined from the experimental and numerical responses, as well as the difference of the numerically obtained properties in relation to the respective experimental values.

	S*Dur* beams			S*Flex* beams		
	K_{el} [kN/mm]	F_{cr} [kN]	δ_{cr} [mm]	K_{el} [kN/mm]	F_{cr} [kN]	δ_{cr} [mm]
S*Dur*-1	1.63	6.28	3.85	-	-	-
S*Dur*-2	1.70	5.45	3.20	-	-	-
S*Flex*-1	-	-	-	1.55	3.80	2.45
S*Flex*-2	-	-	-	1.66	4.60	2.77
SCM-FEMIX	1.57 (-5.7%)	5.02 (-14.4%)	3.20 (-9.2%)	1.38 (-14.0%)	4.40 (4.8%)	3.18 (21.8%)
SCM-ABAQUS	1.55 (-6.9%)	5.04 (-14.1%)	3.25 (-7.8%)	1.41 (-12.1%)	4.76 (13.3%)	3.33 (27.6%)
DPM-ABAQUS	1.56 (-6.3%)	5.11 (-12.9%)	3.27 (-7.2%)	1.43 (-10.9%)	4.79 (14.0%)	3.36 (28.7%)
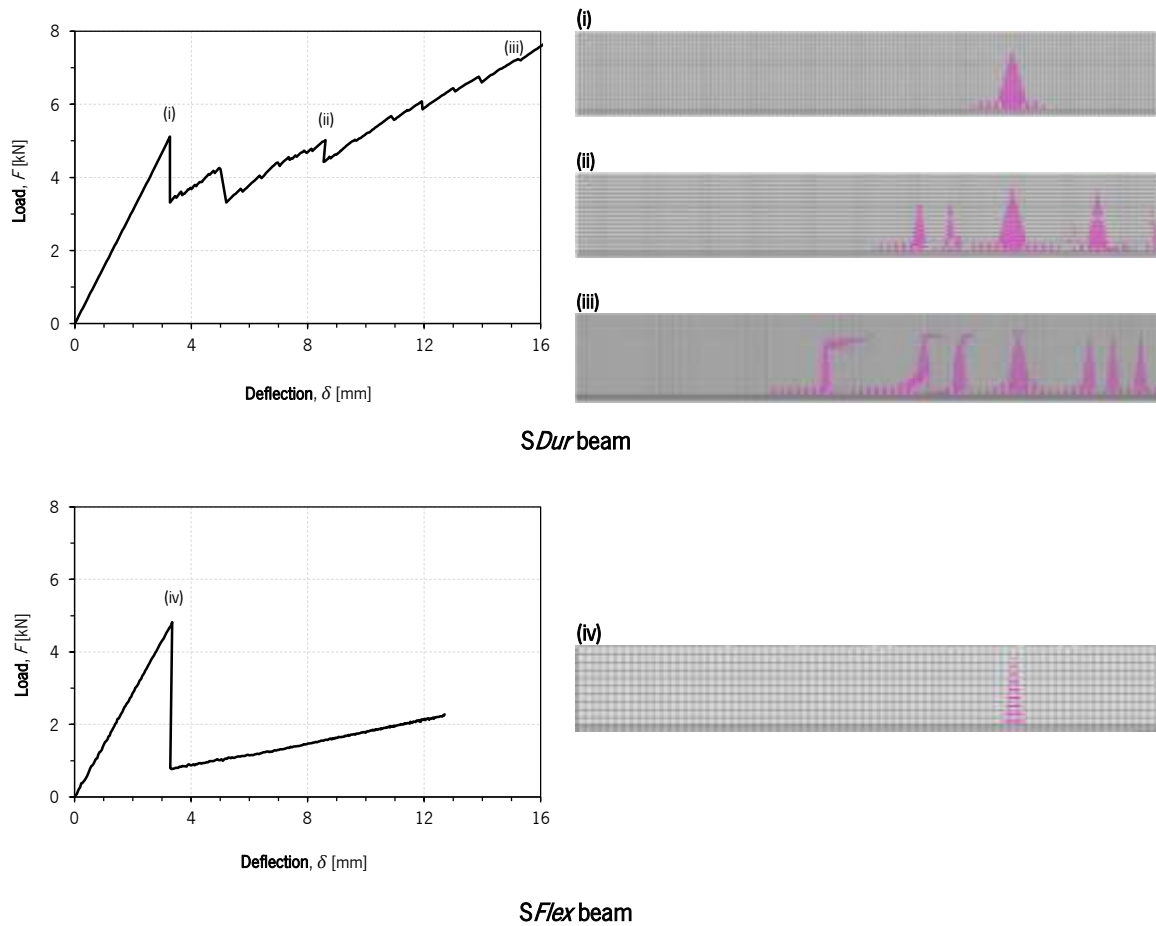
Figure I.9: Load *vs*. deflection curves of the S*Dur* and S*Flex* beams obtained from the DPM-ABAQUS, and corresponding crack pattern at different phases, (i), (ii), (iii) and (iv).

4.1. S*Dur* beams

4.1.1. Pre-cracking stage

In the pre-cracking stage, the assumptions of the *PB* strategy (perfect bond between the GFRP laminate and the glass) resulted in a slight difference between the numerical and the experimental stiffness of the response in the elastic domain, since the physical absence of the epoxy adhesive layer caused a small decrease in the section height (108 mm) and, consequently, in its flexural stiffness.

While the load *vs*. deflection curve obtained from the SCM-FEMIX (static analysis) remains perfectly linear during the pre-cracking stage, in the ABAQUS models this does not occur. The equation of motion of a dynamic structural problem is described by **Eq. (I.15)**, where: (i) F is the applied external force; (ii) M, C and K are the mass, damping and stiffness matrix of the structural element, respectively; and (iii) d, $\dot{d}$ and $\ddot{d}$ are, respectively, the displacement, velocity and acceleration vectors.

$$F = M\ddot{d} + C\dot{d} + Kd \tag{I.15}$$
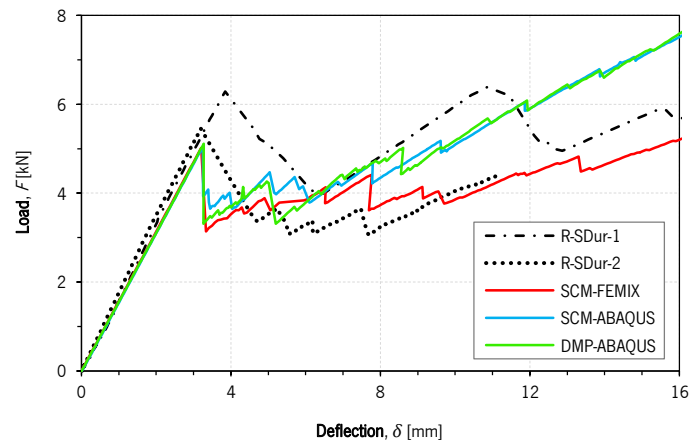
(a)
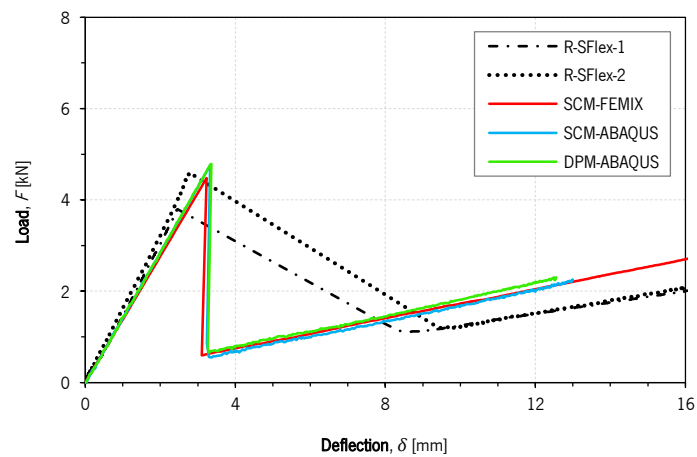
(b)

Figure I.10: Load *vs.* deflection curves obtained from the experimental tests and distinct numerical models: (a) S*Dur* beams; (b) S*Flex* beams.

In order to evaluate the influence of the dynamic effects on the structural responses, **Figure I.11** presents, step-by-step (0.05 s), the relationship between the slope of the tangent line of the load *vs.* deflection curves obtained from the ABAQUS models and elastic stiffness derived from the SCM-FEMIX (1.566 kN/mm). This relation, later designated R_k, is represented against the mid-span deflection in **Figure I.11**. The dynamic effects (inertial forces) are clearly visible at the beginning of the load *vs.* deflection curves obtained from the ABAQUS models, as shown by the rapid growth observed in R_k. The small perturbations of R_k caused by the high frequency vibration modes could be avoided by adopting stiffness-proportional damping, but the computational effort of the numerical models would increase and its accuracy would not significantly improve, namely regarding the cracking load.
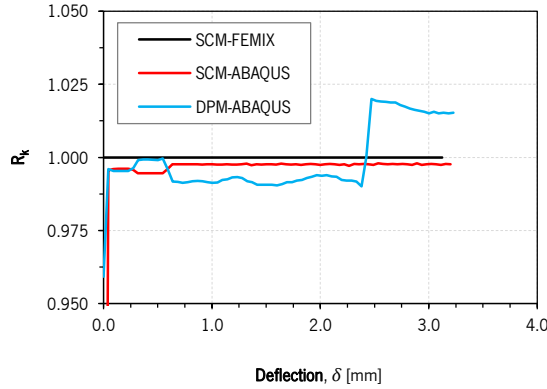
Figure I.11: Ratio between the slope of the load *vs*. deflection curves and the elastic stiffness for the S*Dur* beams obtained from the ABAQUS models.

In all numerical models the same mechanical properties of the materials have been adopted, but R_k is generally less than 1.0 throughout the pre-cracking stage (see **Figure I.11**). This was expectable, because while the equation of motion of a static structural problem depends only on the displacement, in a dynamic structural problem it depends also on the velocity and acceleration, as defined by **Eq. (I.15)**. The tangent line to the load *vs.* deflection curve obtained from the DMP-ABAQUS increases unexpectedly before cracking. In order to evaluate the influence of the dynamic effects in this artefact, **Figure I.12** presents the ratio between the viscous energy, E_v, and work of the external forces, E_w, being the viscous energy the energy dissipated by damping mechanisms, including bulk viscosity damping and material damping. The E_v/E_w ratio shows that dynamic effects are not responsible for the oscillations in the R_k ratio of the DPM-ABAQUS.
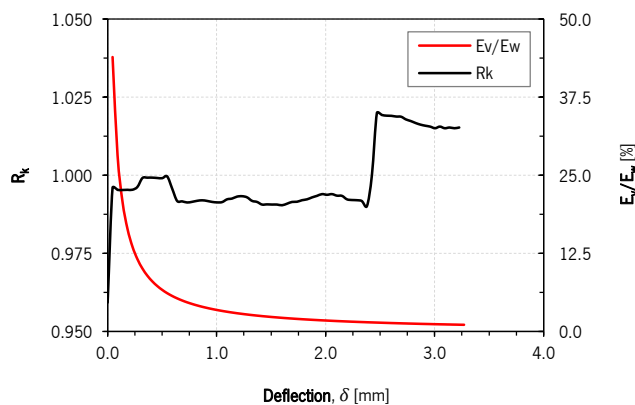
Figure I.12: Ratio E_v/E_w along the tangent line of the load *vs.* displacement curves of the DPM-ABAQUS.

The first crack appears in the central region of the beam between the loading points in all models, inside the pure bending area. Taking into account this information, for the S*Dur* beams, which were modelled assuming the perfect bond between glass and GFRP laminate (*PB* strategy), the analytical

117

cracking load, $F_{cr,a}$, is given by Eq. (I.16), where $I_{el} = 1.111 \times 10^6$ mm^4 (homogenized cross-section), $y_{el} = 56.285$ mm, $l_1 = 470$ mm and $h_{GFRP} = 8.0$ mm. On the other hand, considering the elastic integration method and neglecting the shear effects, the analytical deflection at mid-span corresponding to the cracking load, $\delta_{cr,a}$, is provided by Eq. (I.17), where $l_2 = 230$ mm and $EI_{el} = 7.779 \times 10^{10}$ N.mm^2. In the numerical modelling the crack initiation occurs when the stress at the integration points located right above the bottom edge of the glass sheet reach the tensile strength. Table I.4 shows the elastic properties of SDur beams, computed from Eq. (I.16) and Eq. (I.17), considering the assumptions mentioned previously.

$$F_{cr,a} = \frac{2f_{g,t} \cdot I_{el}}{(y_{el} - h_{GFRP}) \cdot l_1} \qquad (I.16)$$

$$\delta_{cr,a} = \frac{1}{EI_{el}} \left(\frac{F_{cr}l_1}{4} l_2^2 - \frac{F_{cr}l_1 l_2}{2} l_2 + \frac{F_{cr}}{12} l_1^3 - \left(\frac{F_{cr}l_1^2}{4} + \frac{F_{cr}l_1 l_2}{2} \right) l_1 \right) \qquad (I.17)$$

Table I.4: Mechanical properties of the elastic behaviour of SDur beams analytically calculated.

$K_{el,a}$ [kN/mm]	$F_{cr,a}$ [kN]	$\delta_{cr,a}$ [mm]
1.59	4.90	3.08

In general, the numerical and analytical results have shown a good agreement. The small differences observed may be due to: (i) the analytical approach, which omits the shear deformation effects and, consequently, may slightly underestimate the vertical deformations; and (ii) the distance between the first integration point at which cracking occurs and the surface between the glass and the laminate, where cracking initiates. Additionally, the deflection immediately before and immediately after cracking, which should be approximately similar as captured by the numerical models, were observed to be different in the experimental responses. However, in this case this was probably due to the relatively low rate of the data acquisition system used during the experiments (mean value of 5 Hz) when compared to the very rapid development of cracking (not captured by the transducers readings), as well as the difficulty usually associated with the control of tests where abrupt losses of stiffness or load carrying capacity occur.

4.1.2. Post-cracking stage

Comparing the numerical and experimental results, it is generally observed that all the numerical models captured reasonably well the post-cracking behaviour of SDur beams. However, the final crack patterns of the three models show significant differences. The failure caused by the excessive damage

on the bottom edge of the glass panel was satisfactorily represented by SCM-FEMIX, through the formation of several cracks at the glass/GFRP interface, starting at the loading points and propagating towards the supports. However, these cracks, which eventually lead to the laminate detachment, are not clearly visible in the case of ABAQUS models, resulting in higher stiffness of the load *vs.* deflection responses during the entire post-cracking stage when compared to SCM-FEMIX (see **Figure I.10**). The type of smeared crack approach may justify this difference. While the SCM-FEMIX uses a multi-fixed concept, with a maximum of two cracks in each integration point and a threshold angle of 30° (see **Section 3.2.1**), the SCM-ABAQUS uses, by default, a fixed crack concept (orthogonal cracks), which in general leads to a stiffer response.

The final crack pattern of SCM-FEMIX-90° (see **Figure I.13**), with predominantly vertical and more distributed cracks, resembles better the SCM-ABAQUS crack patterns and the experimental results (see **Figure I.4a**). As shown in **Figure I.14**, the smeared crack approach mainly influences the propagation of cracks and, consequently, the post-cracking behaviour. SCM-FEMIX 90° and SCM-ABAQUS correctly simulated the distribution of cracks between loading points, although they were unable to reproduce the increasing slope of the cracks towards the supports, as was the case with DPM-ABAQUS (see **Figure I.9**). Considering the higher stiffness of the epoxy adhesive, the GFRP/glass interface induces high shear stresses in the integration points near the interface. Consequently, the maximum principal stresses experience large rotations. As result, SCM-FEMIX 90° shows higher post-cracking stiffness than SCM-FEMIX.
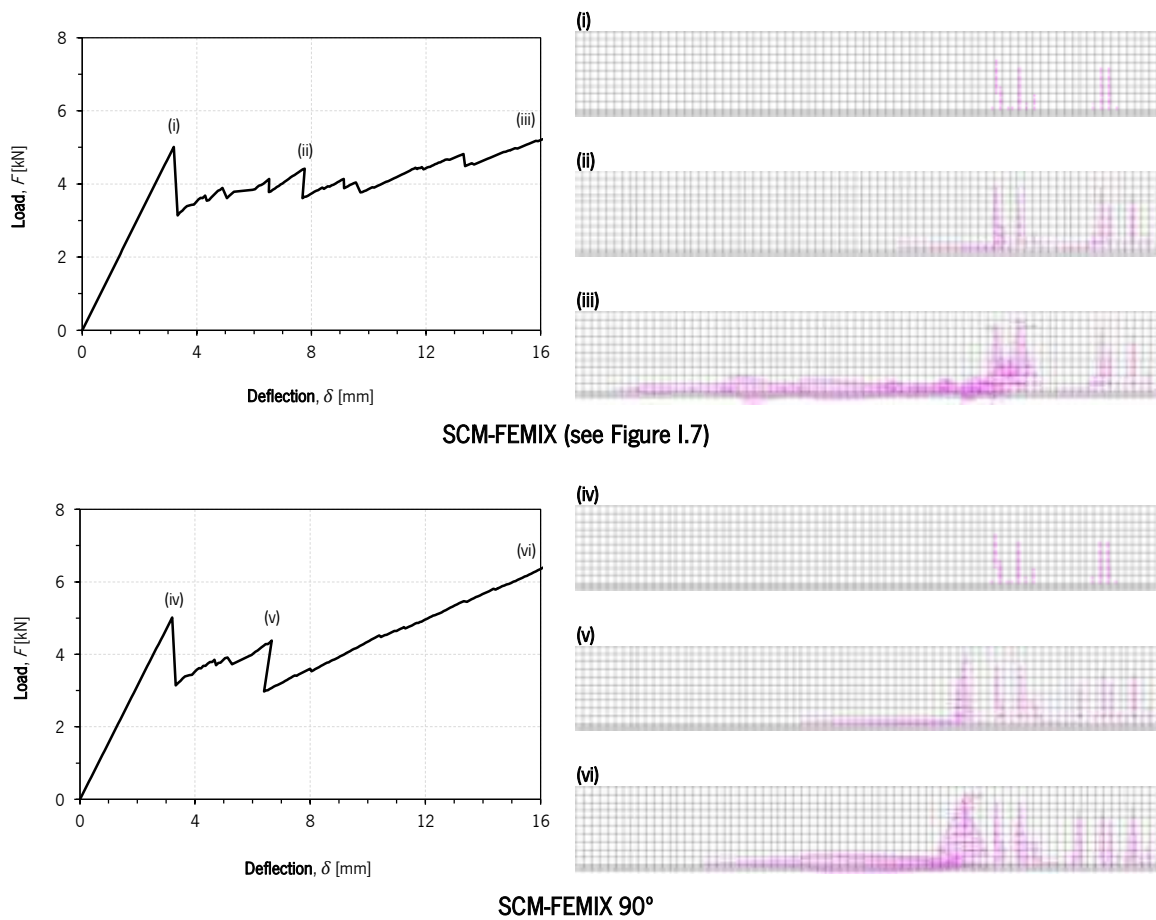
Figure I.13: Load *vs.* deflection curves of the S*Dur* beams obtained from SCM-FEMIX and SCM-FEMIX 90°, and corresponding crack pattern at different phases, (i), (ii), (iii), (iv), (v) and (vi).
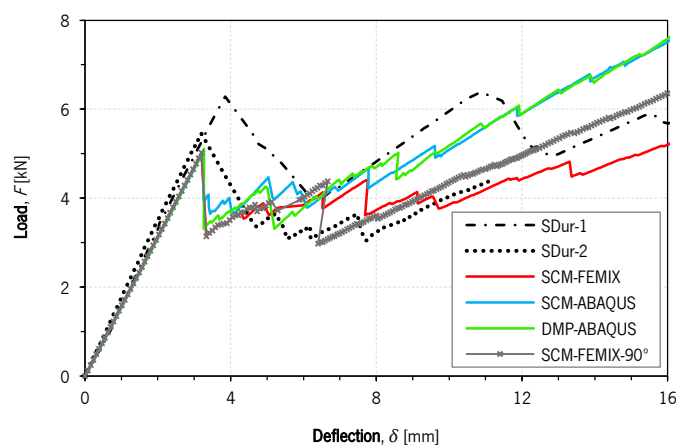
Figure I.14: Load *vs.* displacement curves of S*Dur* beams obtained from the three initial material models and the SCM-FEMIX 90°.

Figure I.15 presents the structural response and the final crack pattern obtained from different mesh patterns (see **Section 3.5**). Like in SCM-FEMIX, SCM-ABAQUS with a fine mesh was able to capture the cracking at the GFRP/glass interface towards the support, resulting in lower stiffness during the

post-cracking stage compared to the models with coarse meshes (5×5 and 10×10 [mm]). Therefore, the post-cracking behaviour of S*Dur* beams obtained from SCM-ABAQUS is mesh dependent. According to ABAQUS [28], the smeared crack models inherently induce mesh sensitivity in the results. In opposition to SCM-FEMIX, SCM-ABAQUS requires an extremely fine mesh to obtain similar post-cracking behaviour, due to the lower sensitivity of the finite elements with reduced integration and the fixed smeared crack approach (orthogonal cracks). On the other hand, unlike SCM-ABAQUS, similar post-cracking responses were obtained from DPM-ABAQUS with different mesh patterns. As the maximum damage factor recommended by ABAQUS is 0.99 (see **Section 3.4**), all cracks retained a residual stress roughly corresponding to 1.0 % of the glass's tensile strength. However, regardless of that, DPM-ABAQUS was unable to capture the cracking at the GFRP/glass interface, possibly due to the limitations previously discussed, which are inherent to the constitutive model adopted.
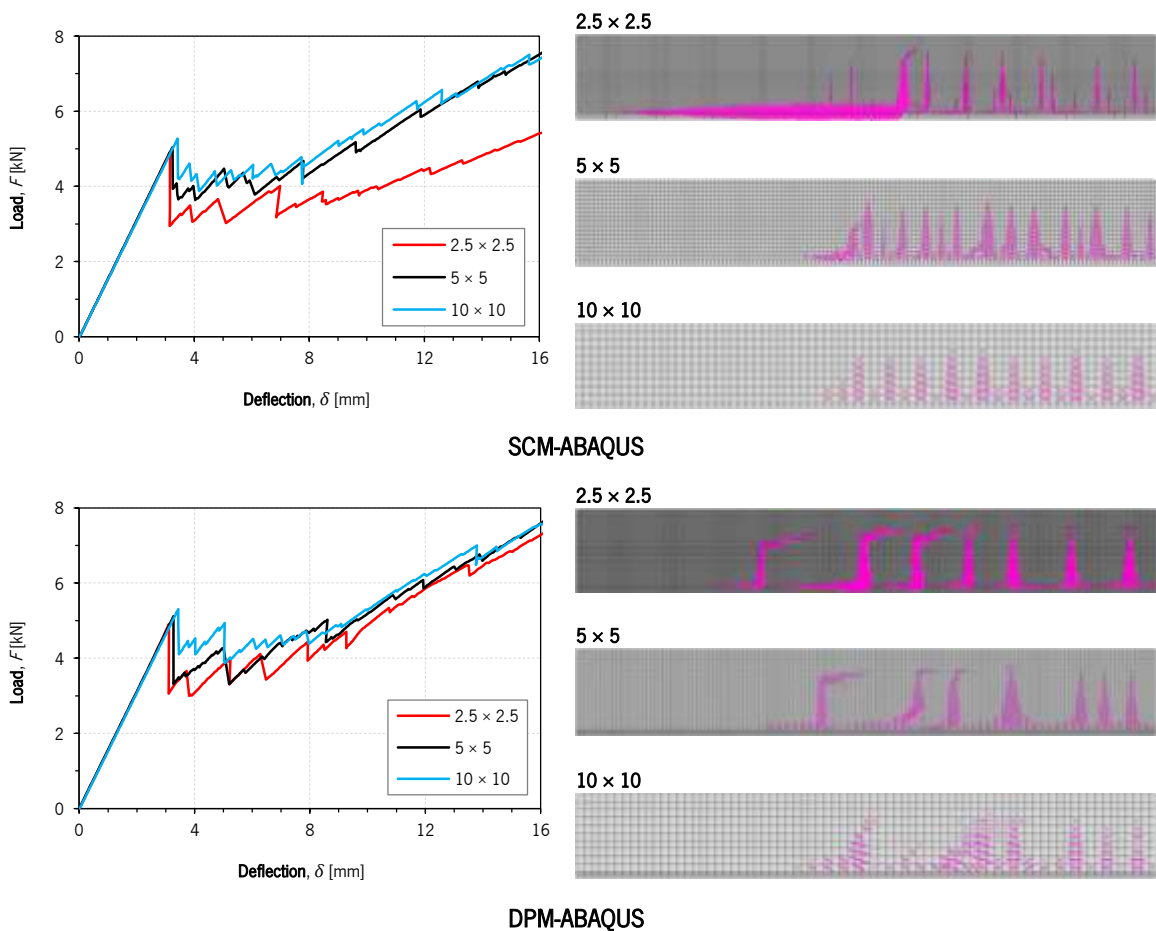
Figure I.15: Sensitivity of both ABAQUS material models in relation to the mesh pattern.

While in DMP-ABAQUS the cracked behaviour of glass is simulated through the progressive loss of material stiffness, in SCM-ABAQUS the cracked behaviour of glass is divided into two components: (i)

the elastic deformation of un-cracked material and (ii) the contribution of cracking. According to Jirásek [45], stiffness degradation modeling can be considered only as a first approximation when the damage derives from the initiation and propagation of micro-cracks, since the damage models are more appropriate to simulate materials weakened by micro-voids (e.g. concrete). Regarding the crack pattern, the shear cracks experimentally observed (see **Figure I.4a**) were captured by DPM-ABAQUS, unlike SCM-ABAQUS.

According to **Figure I.16**, when the fracture energy of 3 J/m^2 was considered, SCM-ABAQUS was able to capture the cracking at the GFRP/glass interface, in agreement with the SCM-FEMIX results, providing lower post-cracking stiffness in relation to the model with the minimum fracture energy and, in turn, better resembling the experimental results. Considering the numerical simulations previously performed by Valarinho *et al*. [19] using SCM-FEMIX, the absolutely accurate definition of fracture energy was not essential to capture the post-cracking behaviour with precision. However, due to the dynamic nature of ABAQUS/Explicit, the more suddenly the glass breaks (less fracture energy), the greater the dynamic effects which, in turn, influence the crack propagation and the structural response. In static analyses, like SCM-FEMIX, an extremely refined mesh of 0.15×0.15 [mm] would be required to avoid convergence problems in the model with fracture energy of 3 J/m^2, since the minimum mode-I fracture energy depends on the tensile strength and Young's modulus of the material. Therefore, only in ABAQUS/Explicit it is possible to use a fracture energy lower than the minimum value given by **Eq. (I.2)**, due to its dynamic nature.

On the other hand, the DPM-ABAQUS model with fracture energy of 3 J/m^2 provided a worse response than the model with the minimum mode-I fracture energy given by **Eq. (I.2)**, both in terms of post-cracking behaviour and in terms of crack pattern. As mentioned in **Section 3.4**, DPM-ABAQUS is suitable to simulate concrete and other quasi-brittle materials. Therefore, although the ABAQUS/Explicit dynamic approach was used, DPM-ABAQUS showed difficulties to simulate materials with low fracture energy, like glass, resulting in crack patterns significantly different from those obtained experimentally. As shown in **Figure I.16**, when the lower fracture energy was used, the glass broke so suddenly that the zone comprised by the loading points was completely cracked. Thus, like in SCM-FEMIX, the minimum mode-I fracture energy given by **Eq. (I.2)** must also be used in DPM-ABAQUS. In addition, to avoid convergence problems during the analysis, a substantially longer loading time was required by the model with a fracture energy of 3 J/m^2, thereby increasing the associated computational cost.
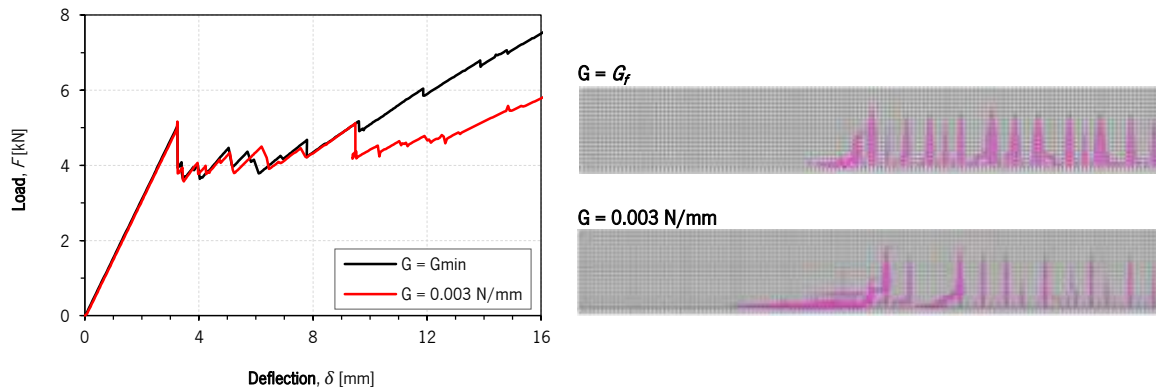
SCM-ABAQUS
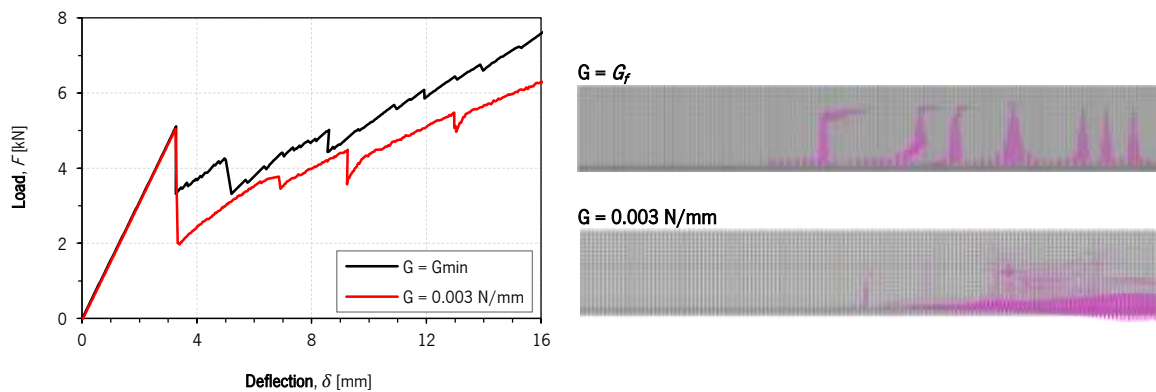
DPM-ABAQUS

Figure I.16: Sensitivity of both ABAQUS model in relation to the fracture energy.

As shown in **Figure I.17**, the post-cracking behaviour of S*Dur* beams is not influenced by the dilation angle. As dilatancy describes the increase in material volume caused by shear stresses, the dilation angle would only significantly influence the post-cracking behaviour if the crack propagation was dominated by mode-II (shear stresses). Although the mixed-mode I+II occurred close to the GFRP/glass interface, due to the shear stresses induced by the reinforcement, the crack propagation was mainly controlled by mode-I fracture (tensile stresses). On the other hand, irrelevant differences were also found between the models in terms of crack pattern, namely the bottom edge of the glass panel, although more distributed vertical cracks have been obtained with a dilation angle of $1°$, better resembling to the experimental crack pattern. However, to ensure the convergence of the numerical models with larger values of the dilation angle, longer loading times were required, increasing in turn the computational cost. Furthermore, according to Malm [46], for dilation angles close to $0°$, the material's behaviour is brittle, like glass, while for values close to the friction angle, the material's behaviour is ductile.

123
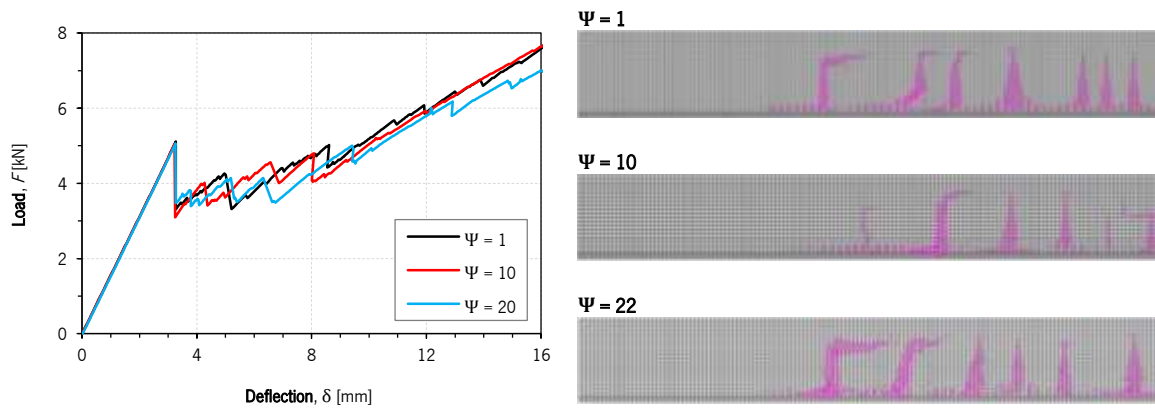
Figure I.17: Sensitivity of DPM-ABAQUS in relation to the dilation angle.

Regarding the shape of the yield surface, no significant differences are observed between the results provided by the distinct models (see **Figure I.18**), both in terms of post-cracking behaviour and crack pattern. When the crack initiation is controlled by mode-I (tensile behavior), which is typical of brittle materials, the shape of the yield surface does not influence the material behavior.
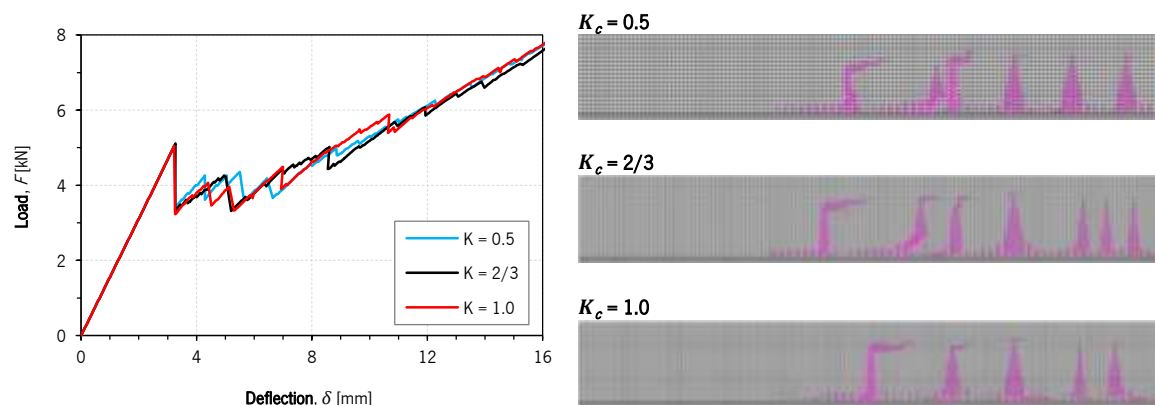
Figure I.18: Sensitivity of DPM-ABAQUS in relation to the shape of the yield surface.

4.1.3. Dynamic effects

The dynamic effects in ABAQUS/Explicit can be evaluated by comparing the kinetic energy, E_k, and internal energy, E_t [28]. **Figure I.19** shows the E_k / E_t ratio for SCM-ABAQUS and DPM-ABAQUS during the entire numerical responses obtained. The E_k / E_t ratio should typically be less than 10 % in quasi-static analyses [28]. At the beginning of the pre-cracking stage there is a kinetic energy peak (inertial forces), but during the remaining numerical response it is negligible, including during the entire post-cracking stage.

(a)

(b)
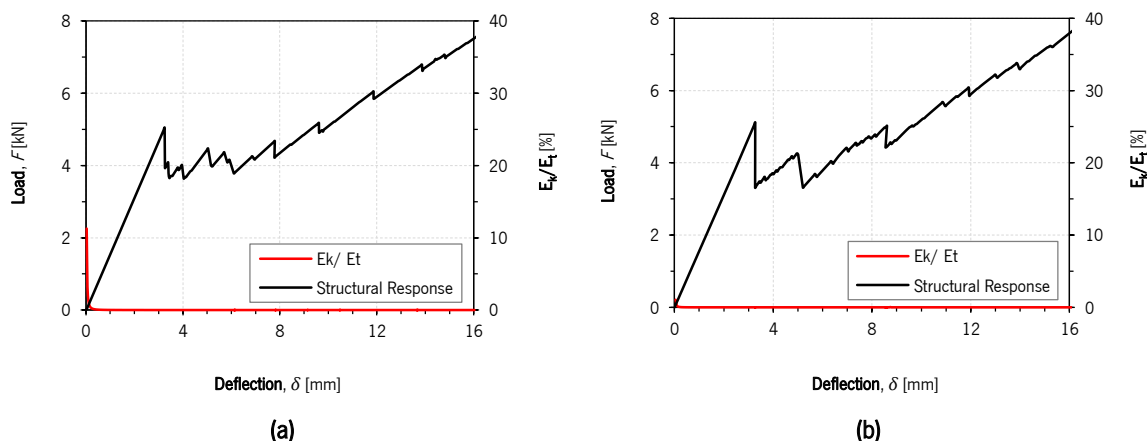
Figure I.19: E_k / E_t ratio along the load *vs.* deflection curves of the (a) SCM-ABAQUS and (b) DPM-ABAQUS.

4.2.   S*Flex* beams

4.2.1.   Pre-cracking stage

As shown in **Figure I.10**, during the pre-cracking stage, a slight difference was obtained between experimental and numerical elastic stiffness. This difference may have been due to some discrepancies between the material parameters used to define the models and the real material parameters, as well as, although less likely, to the inherent experimental uncertainty, given that the displacements are small and the test is fast at this stage. **Figure I.20** presents the crack pattern and numerical response of SCM-FEMIX-A, which is compared with the previously obtained numerical responses in **Figure I.21**. The elastic stiffness of the S*Flex* beam is slightly higher when the thickness of the adhesive joint is not simulated, SCM-FEMIX-A (1.393 kN/mm). As the polyurethane adhesive is more flexible, during the pre-cracking stage the behaviour of the S*Flex* beam is influenced mainly by the glass panel (approximately 90 % of the total beam cross-section). Therefore, the effect of neglecting the adhesive thickness on the numerical response is not significant.

Figure I.22 presents the $R_k – R_\delta$ relationship for each numerical model: R_k is the ratio between the slope of the responses obtained from SCM- and DPM-ABAQUS, calculated step-by-step (0.25 s), and the elastic stiffness derived from the SCM-FEMIX (constant value of 1.384 kN/mm), while R_δ is the ratio between the deflection during the pre-cracking stage and the deflection when the first crack occurred. Regarding the ABAQUS models, the S*Flex* beams showed to be more susceptible to high frequency vibration modes than the S*Dur* beams, probably due to the three-dimensional simulation and to the explicit simulation of the adhesive joint (flexible). This could be mitigated adopting a higher stiffness-proportional damping, but the computational effort of the numerical models would increase.

125
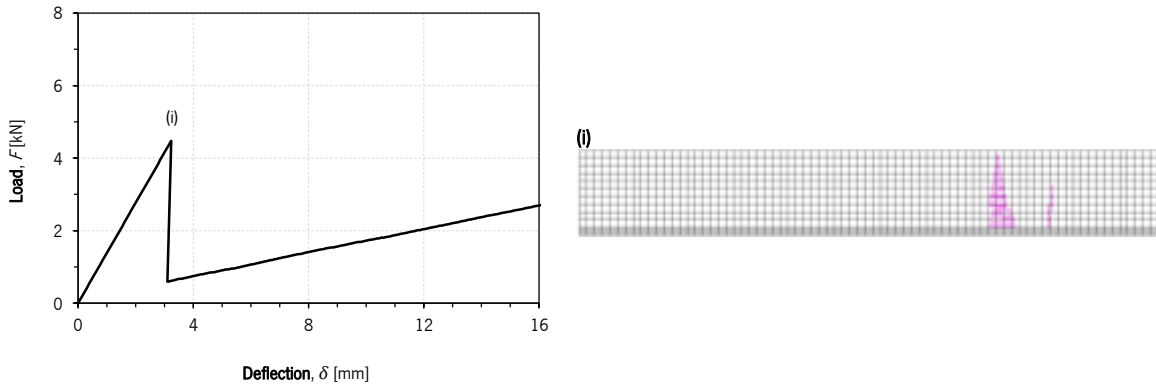
SCM-FEMIX (see Figure I.7)
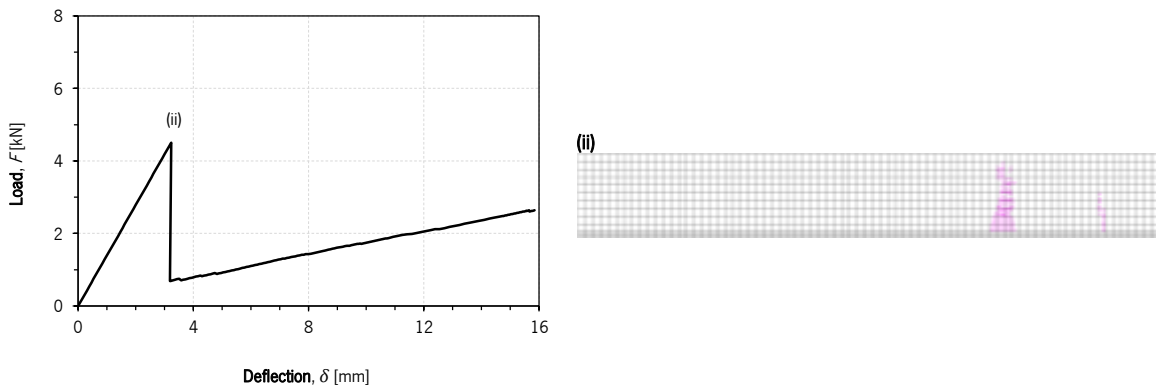
SCM-FEMIX-A

Figure I.20: Load vs. deflection curves of the S*Flex* beams obtained from SCM-FEMIX and SCM-FEMIX-A, and corresponding crack pattern at different phases, (i) and (ii).
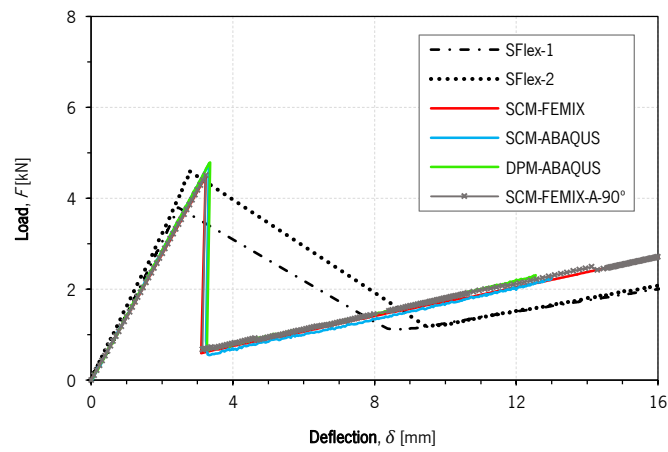
Figure I.21: Load *vs*. deflection curves of the S*Flex* beams obtained from the three material models and the SCM-FEMIX A.
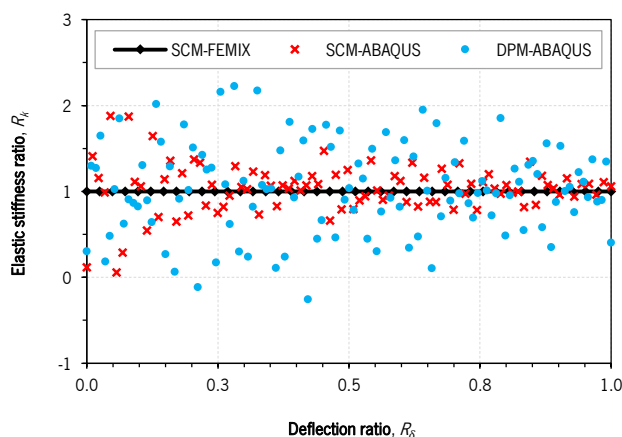
Figure I.22: Elastic stiffness *vs.* deflection diagrams of the S*Flex* beams.

SCM-ABAQUS and DPM-ABAQUS show higher cracking loads than SCM-FEMIX (see **Table I.3**). In addition to neglecting the adhesive joint thickness, in the case of both ABAQUS models the integration scheme used may also explain this difference. As **Figure I.22** shows, neglecting the adhesive joint thickness has marginal influence on the cracking load.

Similarly to what was observed for S*Dur* beams, also for the tests of the S*Flex* beams there seems to be a displacement jump right after cracking, which is probably due to the relatively low acquisition rate considering the velocity of the process involved, as well as the difficulty in controlling tests where abrupt losses of stiffness or load carrying capacity occur.

4.2.2. Post-cracking stage

All three numerical responses obtained are essentially similar when the post-cracking stage is considered. However, while the ABAQUS models show only a single vertical crack in the final crack patterns, SCM-FEMIX shows two cracks (see **Figure I.7**, **Figure I.8** and **Figure I.9**). Besides the smaller sensitivity of the finite elements of the ABAQUS models, this difference can also be explained by the smeared crack approach used by each mechanical constitutive model, similarly to what was observed in the S*Dur* beams. A multi-fixed concept with a maximum number of three cracks at each integration point and a threshold angle of 30° was used by the SCM-FEMIX, while the SCM-ABAQUS uses, by default, a fixed concept (orthogonal cracks), with a maximum number of three cracks at each integration point (3D models) and a threshold angle of 90°. The SCM-FEMIX-A-90° (see **Figure I.23** and **Figure I.24**) corresponds to the structural response of SCM-FEMIX with interface elements of zero thickness and a threshold angle fixed at 90°.
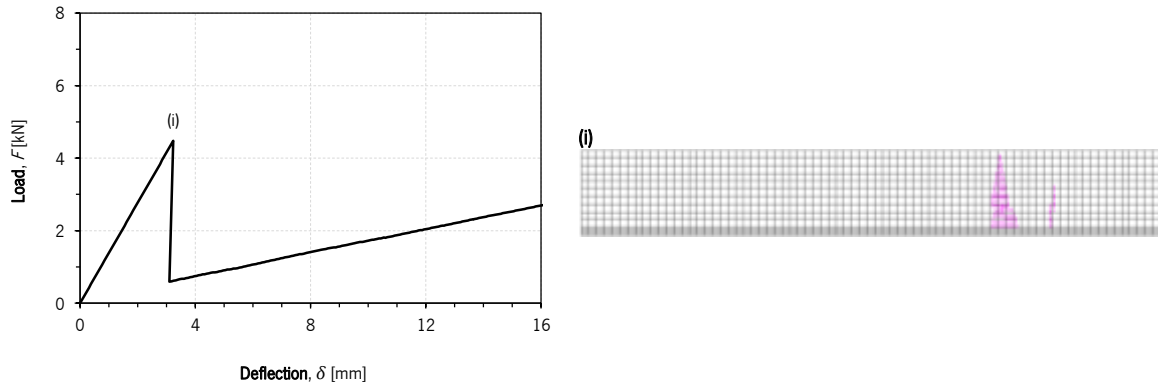
SCM-FEMIX (see Figure I.7)
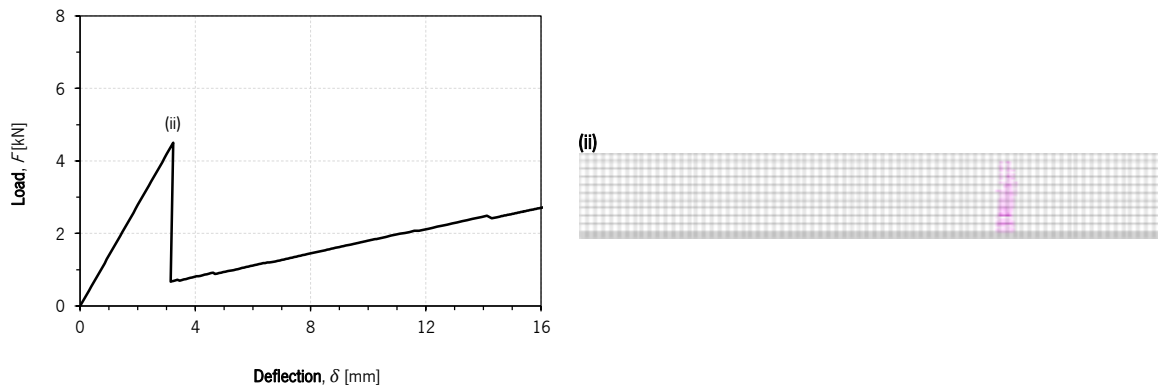
SCM-FEMIX-A-90°

Figure I.23: Load *vs*. deflection curves of the S*Flex* beams obtained from SCM-FEMIX and SCM-FEMIX A/90°, and corresponding crack pattern at different phases, (i) and (ii).
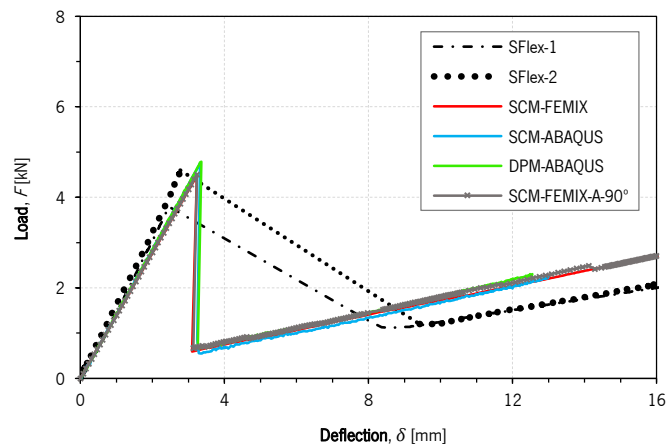
Figure I.24: Load *vs*. deflection curves of the S*Flex* beams obtained from the three material models and the SCM-FEMIX A/90°.

Unlike the epoxy adhesive, the polyurethane adhesive induces low shear stresses at the integration points above the bottom edge of the glass panel. Therefore, after the first crack, the maximum principal stresses experience small rotations in relation to the initial direction of the crack. As the polyurethane

adhesive allowed the GFRP reinforcement to slip due to its flexibility, the formation of a failure mechanism at the bottom edge of the glass panel that could cause the detachment of the GFRP laminate did not occur in the S*Flex* beams. In this way, although the threshold angle seems to have influenced the crack pattern of the S*Flex* beams, especially in relation to the appearance of a second crack, it has negligibly influenced the post-cracking load-deflection numerical response of the S*Flex* beams.

The slightly higher post-cracking load obtained in DPM-ABAQUS may result from a slightly higher residual stress in the crack response, which is a consequence of the difficulty that plasticity models experience when dealing with strong localization of deformations, such as cracks. Additionally, the DPM-ABAQUS was not assigned with an absolute damage factor of 1.0 at the maximum crack opening displacement, as mentioned in **Section 3.4**, retaining in the crack a residual stress of 1.0 % of the tensile strength of glass.

Table I.5 compares the strain gauge measurements for the S*Flex*-1 beam with the values obtained from the three numerical models. **Figure I.25** shows the experimental and numerical axial strain distributions along the mid-span cross-section of that beam at the crack initiation load (F_{cr}) and at the ultimate load (F_{ult}).

In general, the numerical models captured well the distribution of axial strains for F_{cr}, with relatively low differences between numerical and experimental results. Moreover, the significant slippage at the bonded interface was properly captured by the three numerical models. This provides further validation of the numerical models, namely of the constitutive model used to simulate the bond behaviour of the adhesive layer (*NLB* strategy), as well as of the elastic properties of the glass and GFRP laminate.

Table I.5: Comparison between the numerical and experimental axial strains in glass (SG1) and GFRP (SG4) corresponding to F_{cr} and F_{ult}, as well as the relative difference of the numerical strains in relation to the respective experimental values.

	F = F_{cr}		F = F_{ult}	
	SG1 [‰]	SG4 [‰]	SG1 [‰]	SG4 [‰]
SFlex-1	-0.53	0.20	-0.24	2.20
SCM-FEMIX	-0.59 (10.9%)	0.24 (20.1%)	-0.26 (7.9%)	1.76 (-19.2%)
SCM-ABAQUS	-0.57 (7.2%)	0.22 (15.5%)	-0.24 (-1.2%)	1.67 (-23.5%)
DPM-ABAQUS	-0.57 (7.2%)	0.22 (12.8%)	-0.25 (4.4%)	1.56 (-28.6%)
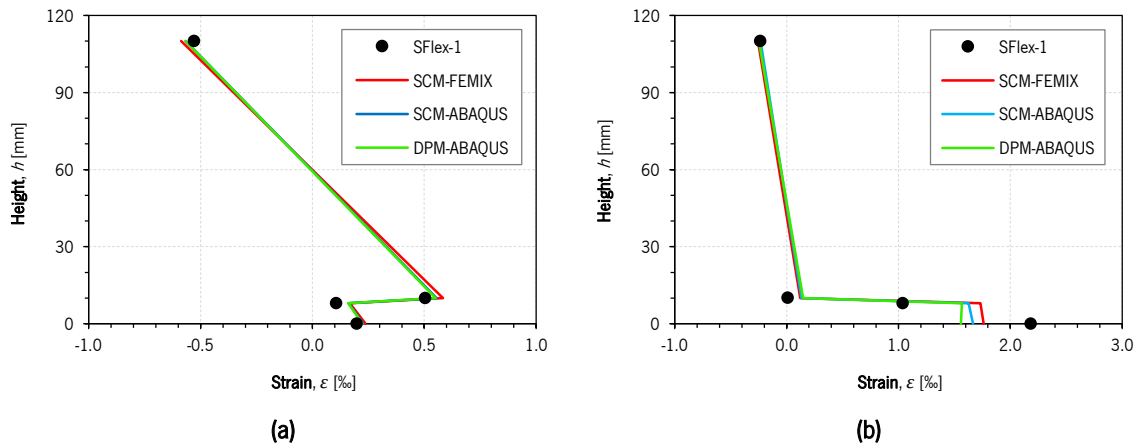
Figure I.25: Comparison between the numerical and experimental normal strains obtained at the mid-span section of the SFlex-1 beam corresponding to (a) cracking load F_{cr} and (b) ultimate load F_{ult}.

When F_{ult} is approached, in general the evolution of the axial strains observed in the numerical models resemble well the ones measured at the mid-span section of the SFlex-1 beam (see **Figure I.25b**). All numerical models seem to indicate that the GFRP laminate is mostly subjected to an almost constant axial strain along the thickness, with the exception of the section where the crack localizes. The experimental measurements show that besides a predominant extension deformation of the laminate (constant strain throughout the thickness), there is also a visible rotation component (see SG3 and SG4), suggesting that in the experiments a crack occurred in the vicinity of the mid-span section, where the strain gauges are located, and caused this localized bending effect on the laminate. Additionally, the measured axial strain at the bottom edge of the glass panel (SG2) for F_{ult} is approximately zero (see **Figure I.25b**), which is the likely result of the stress release caused by the formation of a nearby crack. Furthermore, the low interaction between the GFRP reinforcement and the glass substrate as a result of the low stiffness of the adhesive promoted large crack opening displacements that, in turn, induced a significant rotation effect on the GFRP laminate close to the cracked section (see **Figure I.26**), leading to compressive stresses at the top edge of the GFRP laminate and tensile stresses at its bottom edge. Nevertheless, the GFRP average axial strain obtained from the numerical model is quite close to the experimental one (1.61 ‰), providing further validation to the numerical models. On the other hand, the crack branching observed experimentally (see **Figure I.4b**) was not captured entirely by the numerical models. This resulted in a slight increase of the simulated flexural stiffness of the SFlex beams, which in turn reduced the flexural stresses in the GFRP laminate. The numerical models presented some difficulty in capturing all features of the crack branching, which seems to have resulted in a stiffer numerical behaviour and in slightly higher ultimate loads (F_{ult}) compared to the experimental data.
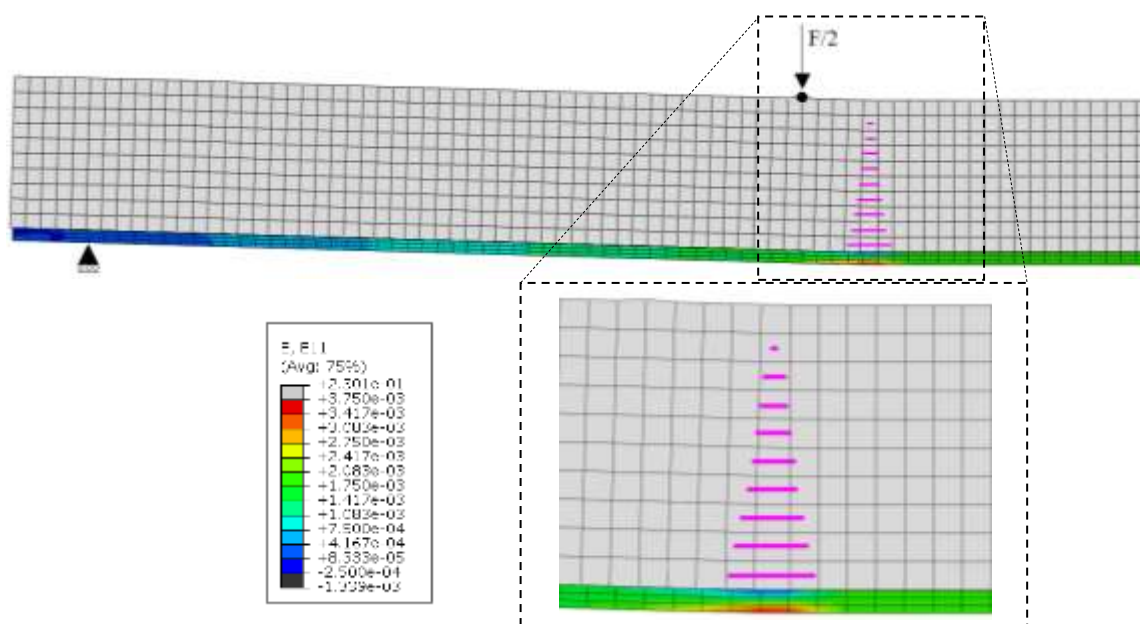
Figure I.26: Localized bending effect at the GFRP reinforcement caused by the formation and propagations of a nearby

4.2.3. Dynamic effects

Figure I.27 shows the E_k / E_t ratio (kinetic energy/internal energy) for SCM-ABAQUS and DPM-ABAQUS together with the numerical load-deflection responses. As mentioned in **Section 4.1.3**, the E_k / E_t ratio should typically be less than 10 % in quasi-static analyses [28]. At the beginning of the pre-cracking stage a kinetic energy peak occurs, but after cracking the dynamic effects on the structural response are not significant. The damping introduced was sufficient to mitigate the dynamic effects during cracking, although the S*Flex* beams are very brittle. The kinetic energy reached high values at the beginning of the pre-cracking stage, exceeding the limit of 10 % suggested in ABAQUS [28]. This could be avoided by adopting a smooth loading scheme, as mentioned in **Section 3.3.4**, but this would require a longer loading time or greater loading speed during the post-cracking stage to complete the process within the predefined time (12.5 s). A longer loading time would increase the computational cost (hours), while a greater loading speed during the post-cracking stage would compromise the convergence of the numerical models. Despite the peak kinetic energy at the beginning of the pre-cracking stage, the analyses are quasi-static, since this phenomenon occurred during a very short period and was immediately mitigated by the damping introduced in the model.
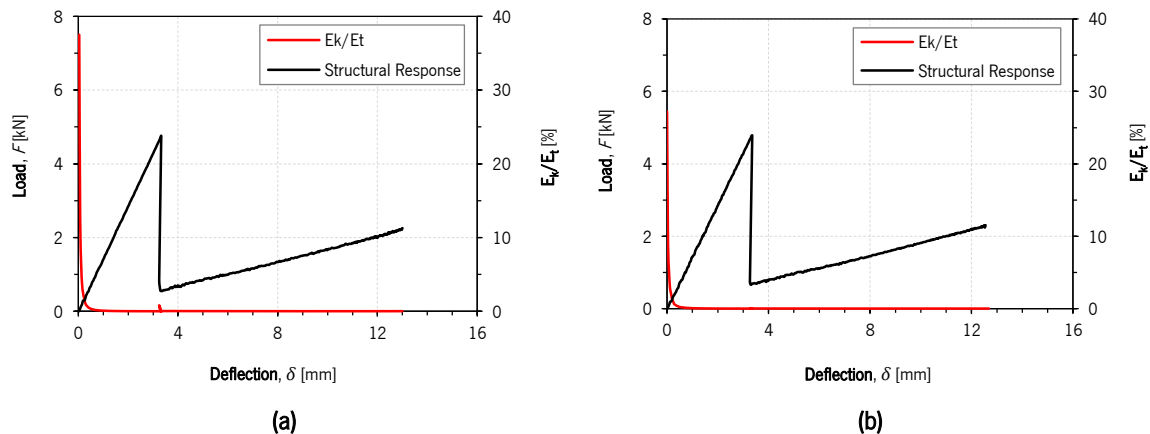
Figure I.27: E_k / E_t ratio along the load *vs.* deflection curves of the (a) SCM-ABAQUS and (b) DPM-ABAQUS.

5 CONCLUSIONS

In this paper, an extensive numerical study was carried out in order to assess the performance of the constitutive models currently available to simulate the behaviour of glass structural elements reinforced with GFRP, in particular the smeared crack and the damaged plasticity models. For this purpose the experimental results obtained in a previous study were considered, that involved four-point bending tests of glass beams reinforced with GFRP laminates adhesively bonded with two different adhesives: polyurethane (S*Flex* beams) and epoxy (S*Dur* beams).

The main conclusions may be summarized as follows:

- All mechanical constitutive models showed to be suitable to conveniently simulate the non-linear behaviour of glass structural beams. The cracking patterns formed and the progressive loss of stiffness observed in the experiments were correctly captured by the numerical models, particularly in the case of the S*Flex* beams, which have an extremely brittle behaviour. The different material models adopted have been essentially influenced by a common set of non-linear parameters: tensile strength, mode-I fracture energy, shape of the tension-softening diagram, and type of shear retention factor, which, in the case of the Damaged Plasticity Model, was replaced by the damage evolution law.

- When compared to SCM-FEMIX, the computational effort required by ABAQUS models was very high, especially in the case of the 3D models of S*Flex* beams. The ABAQUS/Explicit, which is a dynamic-based numerical approach, can also be used for quasi-static analysis by properly prescribing the loading time, the mass scaling factor, the loading scheme and, especially, the damping ratio. Although the damping ratio reduces the undesirable dynamic

effects of the structural responses, its influence on the results obtained requires special attention. Considering the brittle nature of glass, the damping ratio is a numerical parameter that is very difficult to calibrate by experimental means.

- SCM-FEMIX results were more accurate mostly due to the absence of dynamic effects related to the loading time, the damping ratio and others. As a result, during the pre-cracking stages of S*Dur* beams, SCM-FEMIX did not show the same non-linearity of the numerical responses obtained from ABAQUS models. In different situations these dynamic effects can result in the under or overestimation of the cracking loads of the ABAQUS models.

- The Damaged Plasticity Model is suitable for simulating the non-linear behaviour of glass structural elements. In comparison to the Smeared Crack Models (SCM), the structural responses obtained also represented well the post-cracking stage of glass-GFRP composite beams. However, the damaged plasticity model does not allow considering a maximum absolute damage factor of 1.0, which limits the reduction of the initial elastic stiffness to a maximum of 99 %. Therefore, the effects of these residual stresses are present in the post-cracking response and they were mostly visible in the S*Flex* beams.

- The numerical models performed in ABAQUS/Explicit, of a dynamic nature, showed to be able to capture in greater detail all stages of the effects of cracking on the structural responses because, as opposed to FEMIX models, much smaller load steps are easily implemented and this results in better stability during crack formation.

- In the case of S*Dur* beams, unlike the S*Flex* beams, the threshold angle showed to have a greater influence on the structural response throughout the entire post-crack stage, mostly regarding the crack patterns obtained. A threshold angle of 90° (ABAQUS models) seems to provide crack patterns which are more similar to experimental results at the initial stages of cracking. However, as cracking progresses, the difficulties in simulating the rotation of the principal directions become evident. The multi-fixed crack approach (SCM-FEMIX) becomes more efficient in describing the progress of the cracking in the lower part of the beam towards the supports, which ultimately leads to failure by detachment of the GFRP reinforcement.

- In SCM-ABAQUS, refined meshes should be used to capture localized phenomena (e.g. cracking at the GFRP/Glass interface) which, due to the lower sensitivity of finite elements with reduced integration and the threshold angle of 90° (fixed concept), showed not to be fully

captured by medium or coarse meshes. Due to the assumptions inherent to the constitutive model, DPM-ABAQUS showed difficulties in capturing the cracking processes at the GFRP/Glass interface in S*Dur* beams, regardless of the mesh size.

- The minimum mode-I fracture energy should be used in opposition to values referred in literature, since convergence problems (e.g. snap-back instabilities) were avoided in SCM-FEMIX and, in DPM-ABAQUS, structural responses and crack patterns resemble better the experimental ones. In SCM-ABAQUS, models with fracture energy below the minimum value and medium size meshes seemed to provide responses and crack patterns similar to the ones obtained with the models with minimum fracture energy and fine meshes. However, also in SCM-ABAQUS, at least the minimum mode-I fracture energy must be used, because the lower the fracture energy, the greater the deleterious dynamic effects. In addition, if the dynamic effects excessively influence the crack propagation, better results can be obtained by changing either the loading scheme or the loading time.

For quasi-static analysis, both ABAQUS material models showed to be suitable to simulate the non-linear behaviour of glass. In addition, these constitutive models provided better stability during crack propagation in relation to SCM-FEMIX, allowing to capture cracking in more detail by adopting small loading steps. However, the ABAQUS material models showed the following limitations: (i) the finite elements with reduced integration required by ABAQUS/Explicit, which implies the adoption of fine mesh patterns to capture localized phenomena (e.g. cracking at the GFRP/glass interface); (ii) the fixed crack approach used by default, which reduces the sensibility of finite elements close to the reinforcement; and (iii) the maximum damage factor of 0.99 allowed by DPM-ABAQUS, which leads to the retention of residual stress in cracks corresponding to 1% of the glass's tensile strength.

The numerical simulations carried out showed that the post-cracking behaviour of S*Flex* beams have less sensitivity to the mesh pattern and to the smeared crack approach, since one single vertical crack constitutes the crack pattern and the shear stresses at the GFRP/glass interface are negligible. Thus, the structural behaviour of glass-GFRP composite systems with flexible adhesives are mainly influenced by the tensile strength of glass and the interface model used to simulate the adhesive layer. On the other hand, in S*Dur* beams, where higher shear stresses at the GFRP/glass interface develop, the smeared crack approach and, mainly, the mesh pattern have a greater influence on structural responses.

6   ACKNOWLEDGEMENTS

7   REFERENCES

[1]   Correia J, Valarinho L, Branco F. Post-cracking strength and ductility of glass-GFRP composite beams. Composite Structures 2011;93:2299–309.

[2]   Valarinho L, Correia JR, Branco F. Experimental study on the flexural behaviour of multi-span transparent glass-GFRP composite beams. Construction and Building Materials 2013;49:1041–53. https://doi.org/10.1016/j.conbuildmat.2012.11.024.

[3]   Balan B, Achintha M. Experimental and Numerical Investigation of Float Glass-GFRP Hybrid Beams. In: Belis, Bos, Louter, editors. Challeging Glass 5 - Conference on Architectural and Structural Applications of Glass, vol. 97, Ghent: 2016, p. 281–96. https://doi.org/10.2514/6.2009-5462.

[4]   Biolzi L, Orlando M, Piscitelli LR, Spinelli P. Static and dynamic response of progressively damaged ionoplast laminated glass beams. Composite Structures 2016;157:337–47. https://doi.org/10.1016/j.compstruct.2016.09.004.

[5]   Yuan Y, Tan PJ, Li Y. Dynamic structural response of laminated glass panels to blast loading. Composite Structures 2017;182:579–89. https://doi.org/10.1016/j.compstruct.2017.09.028.

[6]   Biolzi L, Cattaneo S, Orlando M, Piscitelli LR, Spinelli P. Post-failure behavior of laminated glass beams using different interlayers. Composite Structures 2018;202:578–89. https://doi.org/10.1016/j.compstruct.2018.03.009.

[7]   Martens K, Caspeele R, Belis J. Development of composite glass beams - A review. Engineering Structures 2015;101:1–15. https://doi.org/10.1016/j.engstruct.2015.07.006.

[8]   Cruz P, Pequeno J. Structural Timber-Glass Adhesive Bonding. Challenging Glass, 2008, p. 205–14.

[9]   Cruz P, Pequeno J. Timber-Glass Composite Beams: Mechanical Behaviour & Architectural Solutions. Challenging Glass, 2008, p. 439–48.

[10]   Belis J, Callewaert D, Delincé D, Impe R Van. Experimental failure investigation of a hybrid glass / steel beam. Engineering Failure Analysis 2009;16:1163–73. https://doi.org/10.1016/j.engfailanal.2008.07.011.

[11]   Bos F, Veer F, Hobbelman G, Louter C. Stainless steel reinforced and post-tensioned glass beams. ICEM12 - 12th International Conference on Experimental Mechanics, Bari, Italy: 2004,

p. 1–9.

[12]   Louter C, Belis J, Veer F, Lebet J. Structural response of SG-laminated reinforced glass beams; experimental investigations on the effects of glass type, reinforcement percentage and beam size. Engineering Structures 2012;36:292–301. https://doi.org/10.1016/j.engstruct.2011.12.016.

[13]   Louter C, Cupać J, Lebet J. Exploratory experimental investigations on post-tensioned structural glass beams. Journal of Facade Design and Engineering 2014;2:3–18. https://doi.org/10.3233/FDE-130012.

[14]   Louter C, Cupać J, Debonnaire M. Structural glass beams prestressed by externally bonded tendons. GlassCon Global Conference Proceedings, Philadelphia, EUA: 2014, p. 450–9. https://doi.org/10.14296/deeslr.v5i0.1848.

[15]   Palumbo M. A New Roof for the XIIIth Century 'Loggia de Vicari' (Arquà Petrarca – PD Italy) Based on Structural Glass Trusses: A Case Study. Glass Processing Days, Tempere, Finland: 2005.

[16]   Achintha M, Balan B. Characterisation of the mechanical behaviour of annealed glass – GFRP hybrid beams. Construction and Building Materials 2017;147:174–84. https://doi.org/10.1016/j.conbuildmat.2017.04.086.

[17]   Bedon C, Louter C. Numerical investigation on structural glass beams with GFRP-embedded rods, including effects of pre-stress. Composite Structures 2018;184:650–61. https://doi.org/10.1016/j.compstruct.2017.10.027.

[18]   Neto P, Alfaiate J, Valarinho L, Correia J, Branco F, Vinagre J. Glass beams reinforced with GFRP laminates: Experimental tests and numerical modelling using a discrete strong discontinuity approach. Engineering Structures 2015;99:253–63. https://doi.org/10.1016/j.engstruct.2015.04.002.

[19]   Valarinho L, Sena-Cruz J, Correia J, Branco F. Numerical simulation of the flexural behaviour of composite glass-GFRP beams using smeared crack models. Composites Part B: Engineering 2017;110:336–50. https://doi.org/10.1016/j.compositesb.2016.10.035.

[20]   Pye A, Ledbetter S. The selection of an adhesive for the construction of a glass-adhesive T-beam. International Journal of Adhesion and Adhesives 1998;18:159–65. https://doi.org/10.1016/S0143-7496(98)00055-4.

[21]   Bedon C, Louter C. Exploratory numerical analysis of SG-laminated reinforced glass beam experiments. Engineering Structures 2014;75:457–68. https://doi.org/10.1016/j.engstruct.2014.06.022.

[22]   Bedon C, Louter C. Numerical analysis of glass-FRP post-tensioned beams – Review and assessment. Composite Structures 2017;177:129–40. https://doi.org/10.1016/j.compstruct.2017.06.060.

[23]   Bedon C, Louter C. Finite Element analysis of post-tensioned SG-laminated glass beams with adhesively bonded steel tendons. Composite Structures 2017;167:238–50. https://doi.org/10.1016/j.compstruct.2017.01.086.

[24]   Bedon C, Louter C. Finite-Element Numerical Simulation of the Bending Performance of Post-Tensioned Structural Glass Beams with Adhesively Bonded CFRP Tendons. American Journal of Engineering and Applied Sciences 2016;9(3):680–91. https://doi.org/10.3844/ajeassp.2016.680.691.

[25]   Louter C, Graaf A, Rots J. Modeling the Structural Response of Reinforced Glass Beams using an SLA Scheme. In: Bos, Louter, Veer, editors. Challenging Glass 2 - Conference on Architectural and Structural Applications of Glass, Delft: 2010.

[26]   Bedon C, Louter C. Finite-element analysis of post-tensioned SG-laminated glass beams with mechanically anchored tendons. Glass Structures & Engineering 2016;1:39–59. https://doi.org/10.1007/s40940-016-0020-7.

[27]   Sena-Cruz J, Barros J, Azevedo A, Ventura-Gouveia A. Numerical Simulation of the Nonlinear Behavior of RC Beams Strengthened With NSM CFRP Strips. CMNE 2007 - Congress on Numerical Methods in Engineering and XXVIII CILAMCE - Iberian Latin-American Congress on Computational Methods in Engineering, Porto: 2007, p. 13–5.

[28]   Simulia. ABAQUS computer software and Online Documentation. v6.12. 2012.

[29]   Yankelevsky DZ. Strength prediction of annealed glass plates - A new model. Engineering Structures 2014;79:244–55. https://doi.org/10.1016/j.engstruct.2014.08.017.

[30]   Veer FA, Rodichev YM. The structural strength of glass: Hidden damage. Strength of Materials 2011;43:302–15. https://doi.org/10.1007/s11223-011-9298-5.

[31]   Yankelevsky DZ. Size effect of the modulus of rupture in float glass plates. Structures 2020;27:1637–45. https://doi.org/10.1016/j.istruc.2020.08.006.

[32]   Rots J, Blaauwendraad J. Cracks Models for Concrete: Discrete or Smeared? Fixed, Multi-directional or Rotating? Heron 1989;34.

[33]   Bazant Z, Oh B. Crack band theory of concrete. Materials and Structures 1983;16:155–77. https://doi.org/10.1007/BF02486267.

[34]   Sena-Cruz J. Strengthening of concrete structures with near-surface mounted CFRP laminate strips. [PhD thesis]. Minho University, 2005.

[35]   Rots J, Nauta P, Kusters G, Blaauwendraad J. Smeared Crack Approach and Fracture Localization in Concrete. Heron 1985;30.

[36]   de Borst R. Computational methods in non-linear solid mechanics. Part 2: physical non-linearity. Netherlands: 1991.

[37]   Feldmann M, Kasper R, Abeln B. Guidance for European Structural Design of Glass

Components. Report EUR 26439 EN. Report EUR. Luxembourg: 2014. https://doi.org/10.2788/5523.

[38]   Mostafawi H. Experimental and Numerical Analysis of the Shear Ring. Royal Institute of Technology, 2014. https://doi.org/10.1007/s00603-014-0560-6.

[39]   Chen G, Teng J, Chen J, Xiao Q. Finite element modeling of debonding failures in FRP-strengthened RC beams : a dynamic approach. Computers and Structures 2015;158:167–83. https://doi.org/10.1016/j.compstruc.2015.05.023.

[40]   López-Almansa F, Alfarah B, Oller S. Numerical simulation of RC frame testing with damaged plasticity model comparison with simplified models. 2nd European Conference on Earthquake Engineering and Seismology, Istanbul: 2014, p. 1–12. https://doi.org/10.13140/2.1.3457.2169.

[41]   Coronado C, Lopez M. Sensitivity analysis of reinforced concrete beams strengthened with FRP laminates. Cement and Concrete Composites 2006;28:102–14. https://doi.org/10.1016/j.cemconcomp.2005.07.005.

[42]   Tao Y, Chen J. Concrete Damage Plasticity Model for Modeling FRP-to-Concrete Bond Behavior. Journal of Composites for Construction 2015;19. https://doi.org/10.1061/(ASCE)CC.1943-5614.0000482.

[43]   Kozłowski M, Kadela M, Hulimka J. Numerical Investigation of Structural Behaviour of Timber-Glass Composite Beams. Procedia Engineering 2016;161:990–1000. https://doi.org/10.1016/j.proeng.2016.08.838.

[44]   Haldimann M, Luible A, Overend M. Structural use of glass. LABSE - Lanka Association of Building Services Engineers; 2008.

[45]   Jirásek M. Damage and smeared crack models. CISM International Centre for Mechanical Sciences, Courses and Lectures 2011;532:1–49. https://doi.org/10.1007/978-3-7091-0897-0_1.

[46]   Malm R. Shear cracks in concrete structures subjected to in-plane stresses. Trita-Bkn Bulletin 2006:136. https://doi.org/10.1016/S0009-2614(00)00726-0.

PAPER II

BOND BEHAVIOUR OF GLASS-TO-CFRP ADHESIVELY BONDED CONNECTIONS

ABSTRACT: Within the context of glass structures, reinforcement strategies have been recently developed to prevent catastrophic failures by promoting the composite action between components. In this regard, the behaviour of adhesively bonded connections between glass and the reinforcement plays a crucial role. This paper presents an experimental, analytical and numerical study focussing on the bond behaviour of glass-to-CFRP adhesively bonded joints, comprising annealed glass sheets and CFRP laminates bonded with two stiff adhesives and one flexible adhesive. The experimental programme included (i) mechanical characterization tests and (i) tensile tests on glass-to-CFRP double-lap joints, evaluating the influence of the type of adhesive and the overlap length. Digital image correlation (DIC) method, analytical investigations and numerical modelling were performed to determine the local bond stress-slip laws for each adhesive, aiming at providing the required information to subsequently support the design of glass structural elements. Compared to the flexible adhesive, the stiff adhesives seem to promote more favourable interaction between the adherends;

however, the former is better at promoting stress redistribution mechanisms, therefore, mobilizing longer bond lengths to transfer the tensile force between adherends. Adhesives with an extremely stiff response induce high stress concentrations in small areas and, consequently, the bonding system may fail prematurely at the glass adherend governed by localized phenomena, such as the low quality of glass processing methods, the high density of surfaces flaws and localized damage during handling.

KEYWORDS: Analytical model; Annealed glass; Bond behaviour CFRP composite materials; Numerical simulations; Stiff and flexible adhesives;

1   INTRODUCTION

In recent years, structural glass has gained great relevance in contemporary architecture due to its aesthetic possibilities and transparency [1,2]. However, the structural behaviour of glass is substantially different from other traditional building materials, such as steel and reinforced concrete [3], requiring the adoption of appropriate safety measures to prevent catastrophic collapses due to its brittle behaviour. These safety measures must ensure that the failure of any structural element does not cause the unexpected collapse of the entire structure (fail-safe), ensuring an adequate load carrying capacity to allow the evacuation of people or, if possible, to proceed to the replacement of the damaged element [4].

With the aim of improving the structural performance of annealed glass, the industry has also developed glass toughening to increase its tensile strength, and glass lamination to overcome its brittleness [1,4]. In the first technique, the glass is subjected to thermal treatment, called "tempering", which creates compressive stresses on its surfaces and surroundings, closing flaws and, therefore, increasing its tensile strength. However, the tempering effect leads to undesirable features for structural applications, since the breakage of tempered glass creates smaller fragments, which reduces the residual strength [1,2,4]. Glass lamination is based on joining two or more sheets of glass by means of a polymeric interlayer. Therefore, the lamination method is based on structural redundancy. If one glass sheet breaks, the additional sheets will prevent the failure of the entire element and the fragments will remain in place due to the interlayer action. However, the brittle behaviour of glass is also not eliminated by this method.

Therefore, several safety approaches have been studied recently to mitigate the brittle behaviour of glass through the composite action between glass and an integrated reinforcement material, namely glass hybrid systems with timber (e.g. [5,6]), stainless steel (e.g. [7–10]), Carbon Fibre Reinforced

Polymers – CFRP (e.g. [11,12]) and Glass Fibre Reinforced Polymers – GFRP (e.g. [1,2,13–15]). This concept, somewhat similar to the one found in reinforced concrete or composite construction systems, provides residual strength and stiffness after glass cracking by promoting the transfer of tensile stresses from the glass to the reinforcement through the intermediary adhesive layer [2]. Although some of the reinforcements used have a brittle behaviour, such as glass, the sequential failure of these materials and/or connections allows the glass hybrid systems to exhibit non-linear inelastic behaviour, with progressive decrease in stiffness with increasing load [16]. This behaviour is commonly designated as pseudo-ductility because it can only develop at the system level.

The composite action between glass and reinforcement, materialized by an adhesive joint, is crucial for the structural behaviour of composite glass systems. Thus, for composite elements it is particularly important to determine the mechanical properties of the adhesives used and the structural behaviour of joints under loading, with respect to the substrate materials, the thickness of the adhesive layer, the effect of environmental conditions and the duration and rate of the load [17]. Some studies are found addressing the bond behaviour of glass hybrid systems. Steel-to-glass (e.g. [17–19]) and GFRP-to-glass (e.g. [2,20]) connections have been investigated recently, using different types of adhesive to assess their influence on the shear interaction between adherends. Moreover, the interlayer has also been studied as a bonding agent when the reinforcement is introduced within the laminated glass panel before the lamination process (e.g. [18]). Different test setups have been adopted, such as single lap joint tests (e.g. [19]), double-lap joint tests (e.g. [2]) and pull-out tests (e.g. [18]). Most studies have focused on the experimental assessment of the composite action of glass hybrid systems. Additional studies are required to accurately characterize such composite systems, namely towards the development of reliable design tools, whether analytical (e.g. [20]) or numerical (e.g. [21]).

Few studies have been addressing the bond behaviour of glass hybrid systems, and the experimental research in this topic has been mostly dedicated to the flexural behaviour of steel reinforced (e.g. [7–10]) and GFRP reinforced glass composite systems (e.g. [1,2,13–15]). Although CFRP materials are widely used in the construction industry (e.g. strengthening of existing concrete structures), only a limited number of studies have focused on the behaviour of glass-CFRP composite systems (e.g. [11,12]). Furthermore, to the best of the authors' knowledge, there are no studies in the literature related to the bond behaviour of glass-to-CFRP connections. Therefore, this research is important to support the future development of design guidelines and approaches for glass reinforced structures.

Given the lack of studies focusing on the composite action and on the flexural behaviour of glass-CFRP composite systems, this research aimed to study these systems at the level of the adhesive joint, based on an experimental and analytical/numerical research on glass-to-CFRP adhesively bonded joints. The experimental programme included the mechanical characterization tests of the different materials and the tensile testing of double-lap joints. Three different adhesives were selected taking into account the technical specifications provided by the suppliers, in order to assess the influence of the adhesive's nature on the behaviour of the glass-CFRP connections. In addition, the Digital Image Correlation (DIC) method was used to support the analysis of the results obtained from double-lap joint tests, capturing the propagation of adhesive damage with increasing load, as well as the stress concentration near the loaded end section [22]. DIC processing was performed by using the GOM Correlate 2019 software [23]. The second part of this paper presents the analytical/numerical studies considering the double-lap joint test results obtained. The analytical studies were based on solving the 2nd order equation of bond, while for the numerical studies ABAQUS commercial package v6.14 [24] was used.

2   MATERIALS AND METHODS

As stated in the introductory section, this work includes an experimental investigation on the bond behaviour of glass-to-CFRP adhesively bonded joints using adhesives of different stiffness. The study comprised (i) the characterization of the involved materials and (ii) tensile tests on double-lap joint specimens. The material characterization tests provided the mechanical properties of the CFRP laminates and the adhesives used, namely their tensile modulus of elasticity and corresponding tensile strength. On the other hand, the double-lap joint tests allowed comparing the performance of the different adhesives in terms of (i) their feasibility to be used as bond agent in structural glass joints and (ii) their influence on the structural behaviour of glass-to-CFRP connections, namely the overall response, stiffness and strength. This section summarizes the experimental procedures adopted in both tests.

2.1.   Materials characterization

The CFRP laminates used in the experimental campaign, with a cross-section of 50×1.2 [mm], were produced by S&P® Clever Reinforcement Company. These laminates are composed of unidirectional carbon fibres agglutinated with an epoxy vinyl ester resin matrix, presenting a smooth surface and a fibre fraction of about 70% in volume. The mechanical properties of the CFRP laminates have been characterized according to ISO 527-5:2009 [25]. Thus, samples of $250 \times 50 \times 1.2$ [mm] (length $\times$

width × thickness) were extracted. Metallic tabs of 50 mm length were glued to the ends to avoid premature failure of the specimens due to stress concentrations introduced by the griping system of the testing machine. A clip gauge (type: MFA 12; linearity: 0.1 %; sensitivity: 2.0 mV/V; resolution: 1.0 p.m.; precision: ±1.5 μm) with 50 mm of gage length was placed at the central region of each specimen to allow assessing the modulus of elasticity (E_{CFRP}), which was determined from the linear portion of the stress-strain response between strain values of 0.05 % and 0.25 % [25].

The adhesives for bonding the reinforcement to the glass were selected based on the literature on hybrid glass systems and taking into account their technical characteristics and the materials to be joined (glass and CFRP). In addition, these adhesives showed different stiffness in order to allow the assessment of its influence on the structural behaviour of glass-CFRP composite systems. Therefore, to cover the wide range of commercial adhesives suitable for glass-CFRP connections, three adhesives were tested: (i) the two-component polyurethane adhesive SikaForce®-7710 L100 [26], with low modulus of elasticity; (ii) the two-component epoxy resin-based adhesive SikaDur®-330 [27], with high modulus of elasticity; and the two-component epoxy resin-based adhesive 3M Scotch-Weld DP490 [28], with an intermediate modulus of elasticity in comparison to the two previous adhesives. It should be noted that concerns about long-term performance or particular exposure conditions were not taken into account when these adhesives were selected. Based on their technical data sheets [26–28], **Table II.1** summarizes the most important characteristics of the adhesives used in this study, namely mechanical properties, viscosity, service temperature and application areas. All adhesives, later called as SikaForce, SikaDur and 3M for the sake of simplicity, were characterized according to EN ISO 527-2:2012 [29]. Therefore, five dumbbell shape specimens of each adhesive were casted and tested in tension at a constant speed of 1.0 mm/min until failure. A clip gauge (the same used for the characterization of the CFRP laminate) with stroke of 50 mm was placed at the central region of each specimen to measure its longitudinal deformation and, thereafter, to calculate the modulus of elasticity from the slope of the secant line between strain values of 0.05 % and 0.25 % of the stress-strain curve, according to EN ISO 527-1:2012 [30].

This study is included in a wider research project aiming at developing CFRP-annealed glass composite beams. Tempered glass was not considered suitable for this research, since the increase in tensile strength is associated with a severe decrease in the residual strength after crack initiation, which is undesirable for structural applications. Although heat-strengthened glass provides an interesting compromise between a relatively high tensile strength and a sufficiently large fragmentation pattern,

this study is exclusively directed to the study of annealed glass applications. The annealed glass has been showing important economical (e.g. cheaper) and technical (e.g. it can be drilled or cut to accommodate unexpected changes in geometry) benefits to glass industry, particularly considering structural applications. On the other hand, laminated glass was also not considered since the study was focussed on the interaction between CFRP reinforcement and the glass substrate. Taking into account that the direct tension tests performed induce essentially pure tensile stresses in the glass sheets, the mechanical characterization of glass according to ISO 1288-3:2016 [31] was also not considered since it is based on bending tests which induce flexural stresses in the glass sheets.

Table II.1: Main characteristics of the three adhesives used in this study according to their technical data sheets.

	Adhesives		
	SikaForce®-7710 L100 [26]	SikaDur®-330 [27]	3M DP490 [28]
Resin type	Polyurethane	Epoxy	Epoxy
Application	Adhesive for producing sandwich panels with low density materials (e.g. polyurethane foam) enclosed by structural materials (e.g. GFRP)	Adhesive for bonding CFRP materials to different substrates (e.g. concrete and glass)	Gap-filling adhesive for assembling different materials (e.g. CFRP and glass)
Curing time	21 days (+23 °C / 50 % RH)	7 days (+23 °C / 50 % RH)	7 days (+23 °C / 50 % RH)
Shear strength	9.0 MPa [1]	> 4.0 MPa [2]	30.2 MPa [1]
Tensile strength	13.0 MPa	30 MPa	-
Service temperature	-	-40 °C to +45 °C	-80 °C to +120 °C
Viscosity	10000 mPas	6000 mPas	90000 mPas
Colour	Beige	Light grey	Black

Notes:
[1] Values determined from tensile tests on aluminium-to-aluminium single-lap joints – failure mode: cohesive failure in the adhesive
[2] Value determined from pull-off tests on adhesive-concrete joints – failure mode: concrete fracture on the sandblasted substrate
All mechanical properties shown were determined after the adhesive curing.

2.2. Double-lap joint testing

The double-lap joint test configuration was adopted for the study of the bonded connections, since it minimizes the peel and cleavage stresses induced by shear stresses observed in the single-lap joint test configuration [17,32]. Therefore, this type of specimen geometry is beneficial for both brittle substrates (e.g. glass) and polymeric materials reinforced with unidirectional fibres (e.g. CFRP). Moreover, all glass sheets used in the double-lap joints were subjected to a grinding treatment of the edges, in order to eliminate flaws and defects derived from the cutting process and to avoid any accidents during their handling.

Figure II.1 shows the double-lap joint test configuration adopted. The specimens comprised two outer glass sheets $450 \times 50 \times 12$ [mm] (length $\times$ width $\times$ thickness) and two inner CFRP laminates $450 \times 50 \times 1.2$ [mm] (length $\times$ width $\times$ thickness), which were bonded together using the different adhesives under investigation (see **Section 2.1**). The bond test region was located at the connection between the glass sheet and the laminate of smaller length, designated as CFRP_I in **Figure II.1**. In order to avoid directly clamping the glass sheets to the gripping system of the testing machine, a bond rigid connection between the glass sheet and the laminate of larger length, CFRP_II, was used. In this rigid bond connection a considerably larger bond length between the CFRP and the glass was adopted (200 mm, at least four times higher than the maximum bond length studied), while in the bond test region the different bond lengths were studied. Furthermore, the two epoxy adhesives mentioned in **Section 2.1** were used in the rigid bond connection to bond the components.
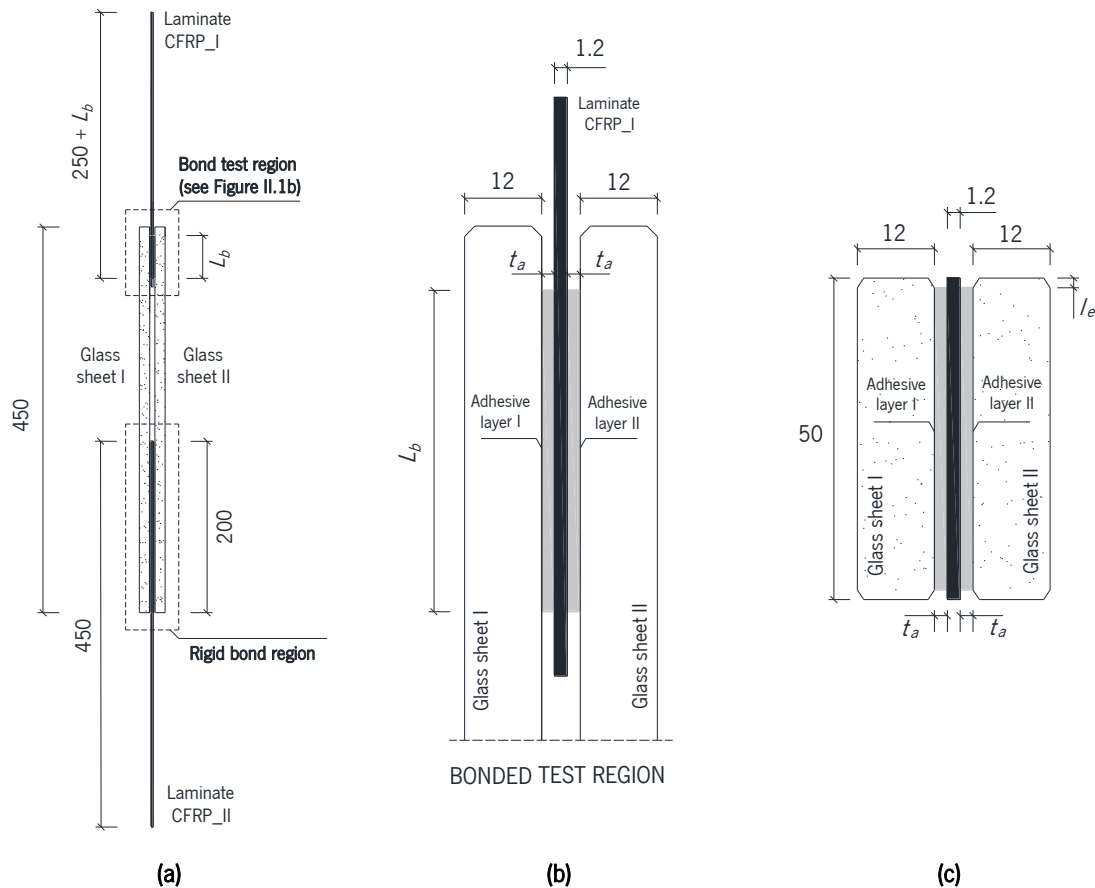
Figure II.1: Double-lap joint tests: (a) specimen's geometry, (b) studied connection and (c) connection cross-section. Units in [mm].

Regardless of the test configurations adopted, overlap lengths (bond length) of 15 mm (e.g. [33]), 25 mm (e.g. [19]) and 100 mm (e.g. [1,2]) were used in previous researches. Considering that the overlap length should be large enough to (i) be representative of the system and (ii) to neglect

unavoidable defects, bond lengths of 25 mm and 50 mm were studied for all adhesives. The unavoidable defects previously mentioned may be related to porosity and voids in the adhesive, laminate end shape and spew fillet geometry [34], which increase the scatter of the measured properties if the bond length is reduced. In agreement with the recommendations of the technical data sheets of the adhesives, an adhesive layer thickness (t_a) of 0.3 mm and 1.0 mm was adopted for the adhesives Sikaforce and SikaDur, respectively (see **Figure II.1c**). The technical data sheet of the adhesive 3M DP490 does not provide any information regarding the recommended adhesive layer thickness to be used. A thickness of 0.3 mm was adopted in this case, according to the suggestion provided by the supplier.

The preparation of the specimens involved several steps. First, the CFRP laminates and glass sheets were cut. Subsequently, the bonding surfaces were carefully cleaned and degreased with acetone before bonding. After that, the adhesives were prepared according to the technical specifications and, then, they were applied with the assistance of a spatula. Then, both adherends were carefully assembled taking into account the alignment between them. In order to guarantee the correct bonding conditions during the application of the adhesive and the reinforcement, a constant pressure of 240 g/cm^2 was applied as a minimum bonding pressure [26]. Finally, the adhesives were subjected to post-cure conditions that comprised three stages: (i) a 12 h heating cycle, between 20 °C and 50 °C; (ii) a 24 h plateau at a constant temperature of 50 °C; and (iii) a 12 h cooling cycle, between 50 °C and 20 °C. The post-curing protocol was aimed at (i) avoiding possible problems of testing specimens at slightly different ambient temperatures on the response of the glass-to-CFRP adhesively bonded joints; (ii) achieving further cure of the adhesives and, therefore, higher mechanical properties; and, (iii) minimizing the effect of testing specimens at different days. Furthermore, post-curing reproduces the long-term curing process that adhesives normally experience during their lifetime.

A total of 24 double-lap joints were prepared to be tested, with the following nomenclature: (i) SF-L25-i and SF-L50-i, for the i-th specimen with SikaForce adhesive and bond lengths of 25 mm and 50 mm, respectively; (ii) SD-L25-i and SD-L50-i, for the i-th specimen with SikaDur adhesive and bond lengths of 25 mm and 50 mm, respectively; and (iii) 3M-L25-i and 3M-L50-i, for the i-th specimen with 3M DP490 adhesive and bond lengths of 25 mm and 50 mm, respectively.

All tests were conducted in laboratory environment conditions at an average temperature and relative humidity of 18 °C and 60 %, respectively. All test specimens were loaded in tension, under displacement control at a constant displacement rate of 1.0 mm/min (displacement between grips)

until failure. All specimens were tested between 21 and 28 days after their production. The relative displacements between the laminate CFRP_I and the two glass sheets (slips) were measured using displacement transducers – Linear Variable Differential Transformer (LVDT) – with a stroke of 8 mm (linearity of 0.15 %), placed on the outer faces of both glass sheets, approximately 20 mm below the loaded end section (see **Figure II.2**). A Microtest PB2-F/200 kN load cell with precision of 0.01 kN was used to measure the load. Strain gauges (type: BFLA-5-3-3L by TML; gauge length: 5 mm; gauge factor: 2.08 ± 1 %) were installed on one specimen per series, on the outer faces of the glass sheets, at mid-length between the studied and rigid bond regions (see **Figure II.2**). The use of these sensors has two-fold objective: (i) verifying possible non-symmetric load distribution between the two glass sheets and (ii) determining the modulus of elasticity of the annealed glass (E_g), by inverse analysis.

(a)   (b)
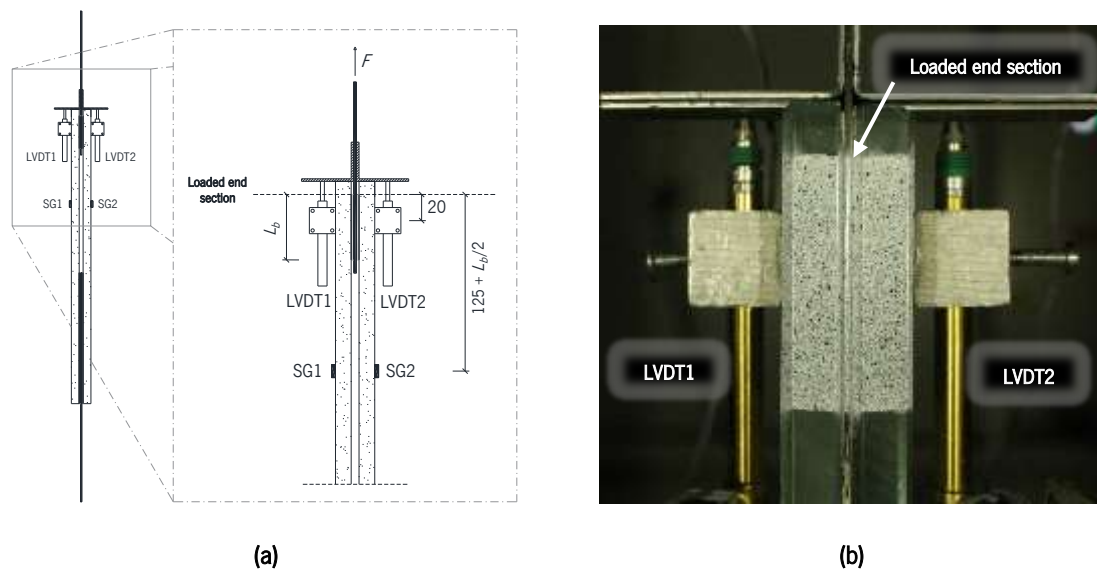
Figure II.2: Double-lap joint tests: (a) schematic representation and (b) image showing the measuring systems adopted. Units in [mm].

In some of the specimens, Digital Image Correlation (DIC) technique was also used to document the evolution of the resistant mechanisms of the glass-CFRP hybrid systems, as well as to complement the understanding of the structural behaviour obtained from the double-lap joint tests. For this, a thin coating of white matt paint was applied over the region of interest, followed by the application of distributed black dots using spray paint. Only the adhesive connection was included in the region of interest. A Canon EOS 450D camera coupled with a Canon Zoom-EF 28-80mm $f/3.5$-5.6 IS lens was used to capture the images. A working distance (distance between the external face of the camera and the target surface) of 250 mm was adopted. Data was analysed with Correlate 2019 software [23]. For this purpose, the region of interest (ROI) shown in **Figure II.3** was defined to perform the DIC

analysis. The applied load and the relative displacements were measured at an average frequency of 100 Hz. Due to limitations on the acquisition system, the longitudinal strains in glass were measured at average frequency of 3 Hz. On the other hand, the images of the ROI were captured every 5 s during testing.
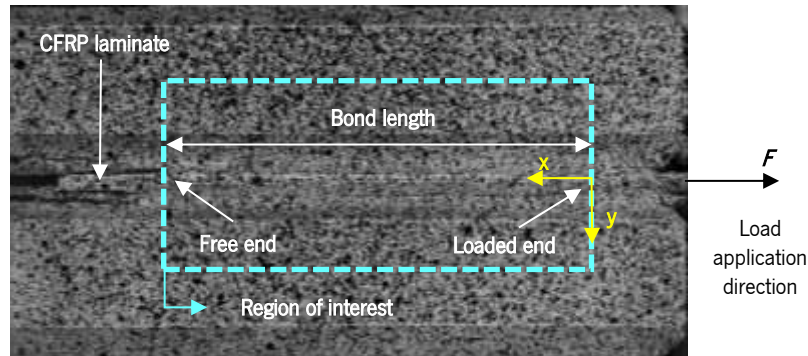
Figure II.3: Region of interest defined to the DIC analysis of the double-lap joints.

3   EXPERIMENTAL RESULTS

In this section, the experimental results derived from the mechanical characterization of the involved materials and from the double-lap joint tests are presented, analysed and discussed. Regarding the double-lap joint tests, in addition to the individual analysis of each series, the main advantages and disadvantages of each adhesive used are also discussed.

3.1.   Glass, CFRP and adhesives

Table II.2 shows the values of the mechanical properties obtained per material, namely the annealed glass, the CFRP laminate and the adhesives.

Table II.2: Average values of the mechanical properties obtained for the involved materials: modulus of elasticity (E), tensile strength (f_t), yield strain (ε_y) and ultimate strain (ε_{ult}), along with the respective coefficient of variations (CoV) in parenthesis.

Material	E [MPa]	f_t [MPa]	ε_y [‰]	ε_{ult} [‰]
Annealed glass	74000.0 (2.6%)	–	–	–
CFRP laminate	165200 (3.4%)	2418 (1.5%)	–	14.6 (2.5%)
SikaDur	4325.3 (3.1%)	32.34 (3.9%)	–	8.4 (5.4%)
SikaForce	48.4 (1.3%)	6.13 (1.7%)	205.6 (5.4%)	250.5 (7.7%)
3M	1728.1 (3.3%)	32.8 (4.2%)	–	30.7 (2.8%)

As previously described, the modulus of elasticity of the annealed glass was derived from the experimental results of double-lap joint tests through inverse analysis, and not directly obtained

through experimental testing for example adopting the procedure suggested by ISO 1288-3:2016 [23]. Initially the tensile stress in glass (σ_g) was calculated assuming that the force imposed by the testing machine was equally distributed by both glass sheets ($F/2$). Then, the relationship $\sigma_g - \varepsilon_g$ was defined using the strain gauge measurements at the glass sheets. Finally, the modulus of elasticity of the annealed glass was calculated from the slope of the experimental response $\sigma_g - \varepsilon_g$ for glass sheets between strain values of 0.05 ‰ and 0.15 ‰. A Young's modulus (E_g) of 74 GPa was determined, which is consistent with the literature [35].

Regarding the CFRP laminates, all specimens tested showed linear elastic behaviour until failure, as expected. From these tests, a modulus of elasticity of 165.2 GPa and a tensile strength of 2418 MPa were obtained (see **Table II.2**).

Regarding the adhesives, Sikaforce exhibited a significant non-linear behaviour showing a clear tensile force plateau before the failure and, therefore, also a high deformation capacity (see **Figure II.4a**). On the other hand, SikaDur presented an essentially linear elastic behaviour until failure (see **Figure II.4b**), as well as stiffness and strength much greater than the ones previously shown by the polyurethane adhesive SikaForce (about 100 and 5 times, respectively). Finally, the 3M adhesive showed an intermediate behaviour between the two previously mentioned adhesives, with high tensile strength, similar to the SikaDur adhesive, and progressive loss of stiffness, resembling SikaForce, which guaranteed greater deformation capacity in comparison with SikaDur. The Poisson's ratios have not been experimentally determined in the present study. Values of 0.44, 0.30 and 0.38 are referred by Rodrigues [36], Haghani and Al-Emrani [37] and Nhamoinesu and Overend [19] for the Sikaforce, SikaDur and 3M, respectively. These values were adopted in the present study.
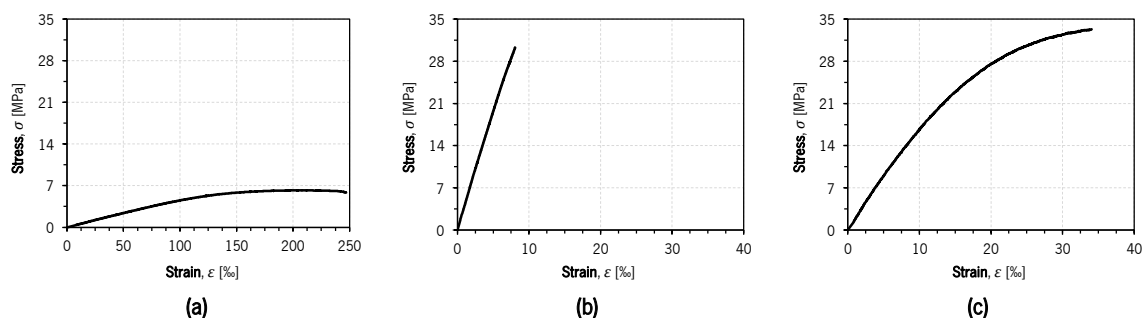
Figure II.4: Typical tensile stress-strain curves of the tested adhesives: (a) SikaForce; (b) SikaDur; and (c) 3M.

3.2. Double-lap joints

Figure II.5 shows the load (F) – loaded end slip (s_{le}) curves obtained from each series of double-lap joint tests. The bond responses obtained for each series differ significantly, as a result of the distinct

behaviours of the different adhesives used and the bond lengths (L_b) adopted. On the other hand, **Table II.3** summarizes the results in terms of initial stiffness (K), maximum load (F_{max}) and corresponding displacement (d_{max}), as well as the observed failure modes. The initial stiffnesses of 3M and SD specimens were not significantly influenced by L_b. On the other hand, the 3M and SD series presented similar values of K, which were significantly higher than the values obtained from the SF series. The $F - s_{le}$ curves and the strain gauge measurements are compared in **Figure II.6**. As mentioned in **Section 2.2**, only one specimen per series was monitored using strain gauges. The two strain gauges of the SF-L25-I specimens captured an unexpected decrease in ε_{exp} without any decrease in F being recorded (see **Figure II.6a**). Regarding the other specimens, the tensile load (F) vs. longitudinal strain (ε_{exp}) relationship was linear until failure. Geometrical differences between the glass sheets (e.g. width) created small differences between the values measured by the two strain gauges of the same specimen.

Figure II.7 also shows the typical failure modes of each series observed during the present experimental programme. Four types of failure modes were clearly identified, which are related to the mechanical behaviour of the adhesive and the bond length, as well as the strength of the glass sheets. **Table II.3** also provides information about the failure modes of the experiments using the following nomenclature: I-AG, for adhesive failure by debonding at the interface adhesive/glass (see **Figure II.8a**); FT-L, for fibre-tear failure in CFRP laminate (see **Figure II.8b**); CS-G, for cohesive shear debonding in glass (see **Figure II.8b**); and C-G, for cohesive failure in glass.

As mentioned previously in **Section 2**, representative specimens of SD and SF series were monitored by documenting the surface of the specimens using digital images during the tests. Then, DIC method was used to extract the deformation fields at the surface of the specimens, in order to document unexpected phenomena and compare the differences in the behaviour of glass-CFRP composite systems when stiff and flexible adhesives are used. For the sake of simplicity, this paper presents only the results of one specimen per series. Furthermore, in order to perform more in-depth analyses, only specimens monitored with strain gauges were selected. In this sense, the specimens SF-L25-I and SF-L50-I (from flexible adhesive series) and SD-L25-I and SD-L50-I (from stiff adhesive series) were considered for the DIC analysis.
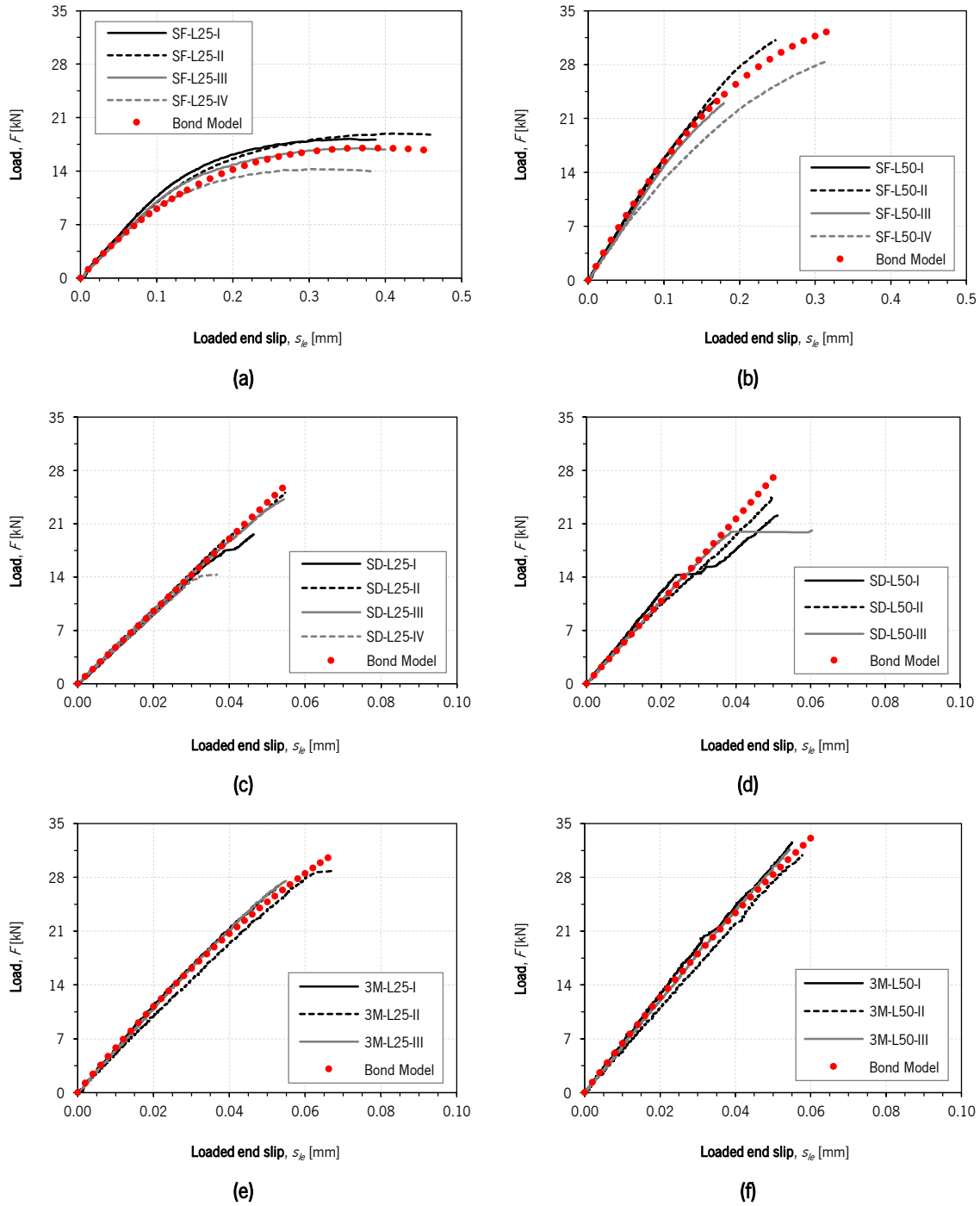
Figure II.5: Experimental and numerical load (F) – loaded end slip (s_{le}) responses obtained from the series of double-lap joints (a) SF-L25 and (b) SF-L50 with the SikaForce adhesive, (c) SD-L25 and (d) SD-L50 with the SikaDur adhesive, and (e) 3M-L25 and (f) 3M-L50 with the 3M adhesive. Note: 'Bond Model' is the analytical F – s_{le} response obtained from the local τ – s laws calibrated in **Section 4** for each type of adhesive.

Table II.3: Main tensile test results of double-lap joints with SikaDur, SikaForce and 3M adhesives, indicating in parentheses the coefficient of variation (CoV) for each series. The following failure modes were identified: C-G, cohesive failure in glass when its tensile failure was achieved; I-AG, for adhesive failure by debonding at the interface adhesive/glass; FT-L, for fibre-tear failure in CFRP laminate; and CS-G, for cohesive shear debonding in glass.

	K [kN/mm]	F_{max} [kN]	d_{max} [mm]	Failure mode
SF-L25-I	109.70	18.2	0.39	I-AG
SF-L25-II	101.40	18.9	0.46	I-AG
SF-L25-III	98.70	17.0	0.37	I-AG
SF-L25-IV	100.40	14.3	0.38	I-AG
SF-L25	**102.6 (4.1%)**	**17.1 (10.4%)**	**0.40 (8.8%)**	**-**
SF-L50-I	162.89	23.44	0.17	C-G
SF-L50-II	157.55	31.17	0.25	C-G
SF-L50-III	146.17	22.97	0.18	C-G
SF-L50-IV	143.52	28.45	0.32	C-G
SF-L50	**152.5 (5.2%)**	**26.5 (13.0%)**	**0.23 (25.2%)**	**–**
SD-L25-I	452.3	19.6	0.046	FT-L + CS-G
SD-L25-II	486.4	25.1	0.055	FT-L + CS-G
SD-L25-III	483.7	24.2	0.054	C-G
SD-L25-IV	451.7	14.3	0.037	C-G
SD-L25	**468.5 (3.7%)**	**23.0 (10.5%)**	**0.048 (15.3%)**	**–**
SD-L50-I	599.1	22.1	0.051	FT-L + CS-G
SD-L50-II	533.8	24.5	0.049	FT-L + CS-G
SD-L50-III	543.9	20.1	0.060	FT-L + CS-G
SD-L50	**558.9 (5.1%)**	**22.2 (7.9%)**	**0.054 (8.9%)**	**–**
3M-L25-I	564.4	26.9	0.0531	C-G
3M-L25-II	502.2	28.8	0.067	C-G
3M-L25-III	544.8	29.3	0.060	C-G
3M-L25	**523.5 (4.9%)**	**28.4 (3.6%)**	**0.060 (9.4%)**	**–**
3M-L50-I	639.2	32.6	0.055	C-G
3M-L50-II	549.7	30.9	0.058	C-G
3M -L50-III	599.8	31.7	0.054	C-G
3M-L50	**596.2 (6.1%)**	**31.7 (2.2%)**	**0.056 (2.7%)**	**–**

(c)

(d)

(c)

(d)
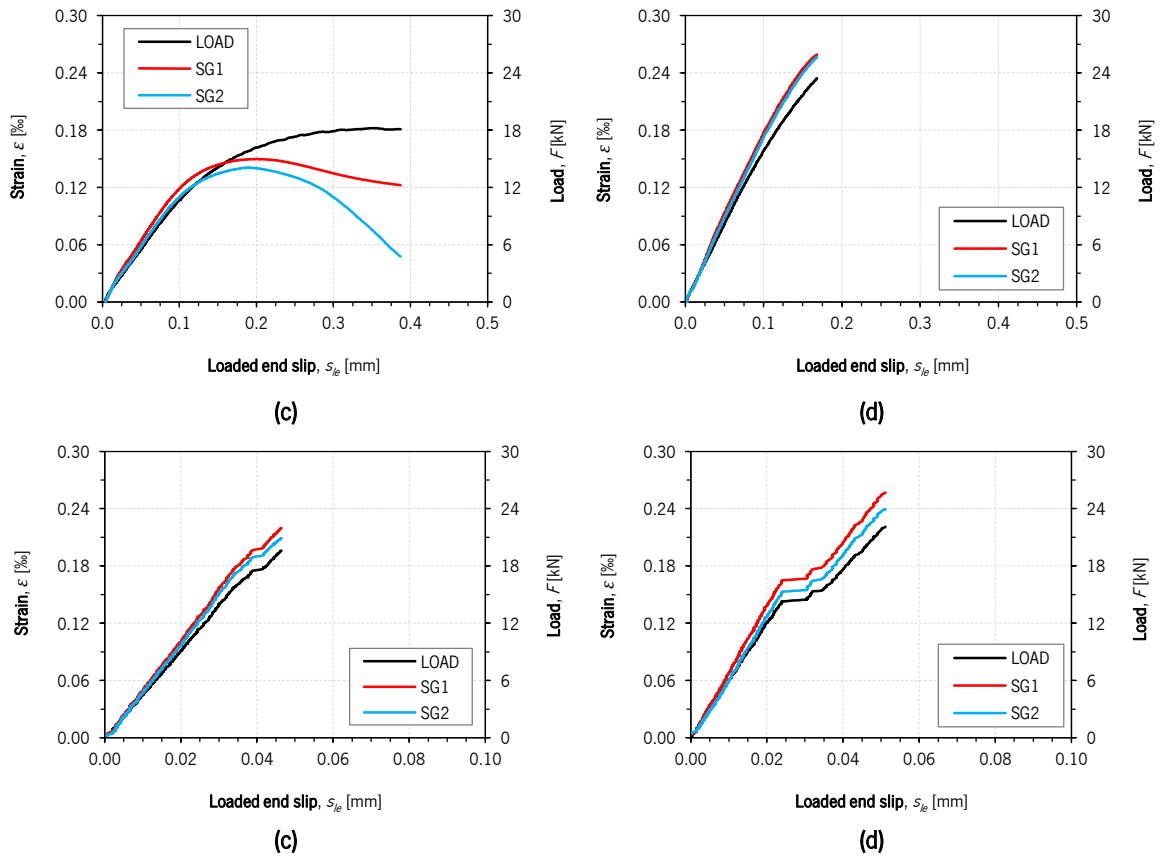
Figure II.6: Longitudinal strain in glass measured by strain gauges placed on the outer faces of both glass sheets, ε, and tensile load, F, *versus* the loaded end slip, s_{le}, for (a) SF-L25-I, (b) SF-L50-I, (c) SD-L25-I and (d) SD-L50-I.
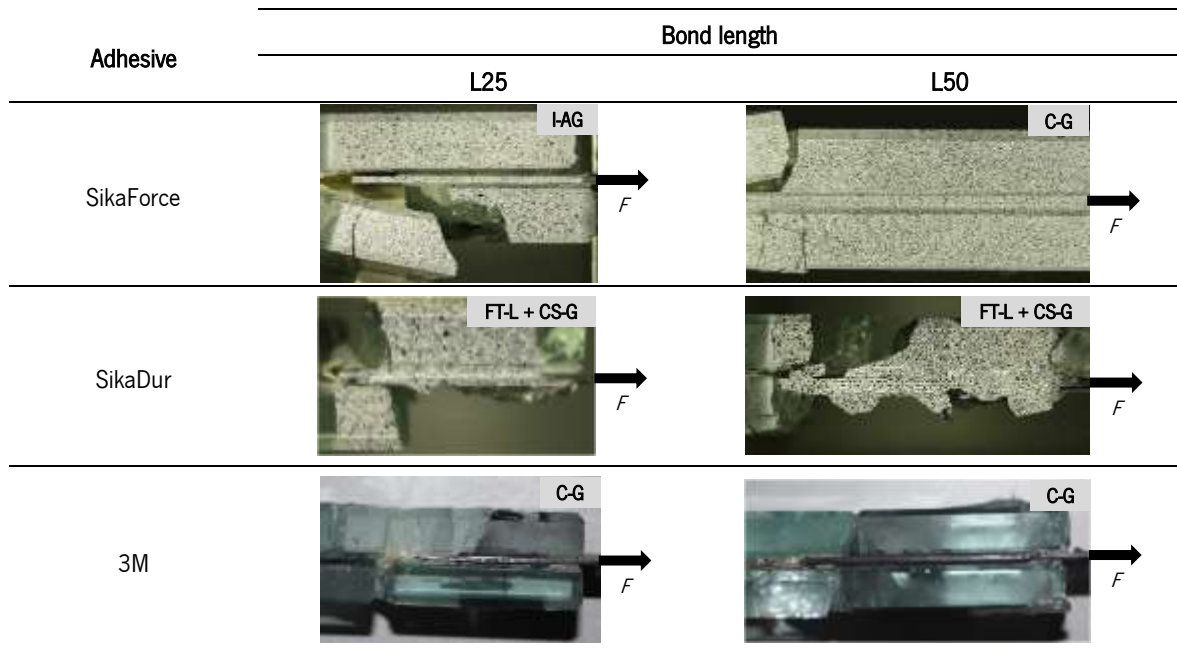
Figure II.7: Bond test region after collapse of double-lap joints, indicating the typical failure modes observed in each series, as well as the direction of load application.

(a)   (b)
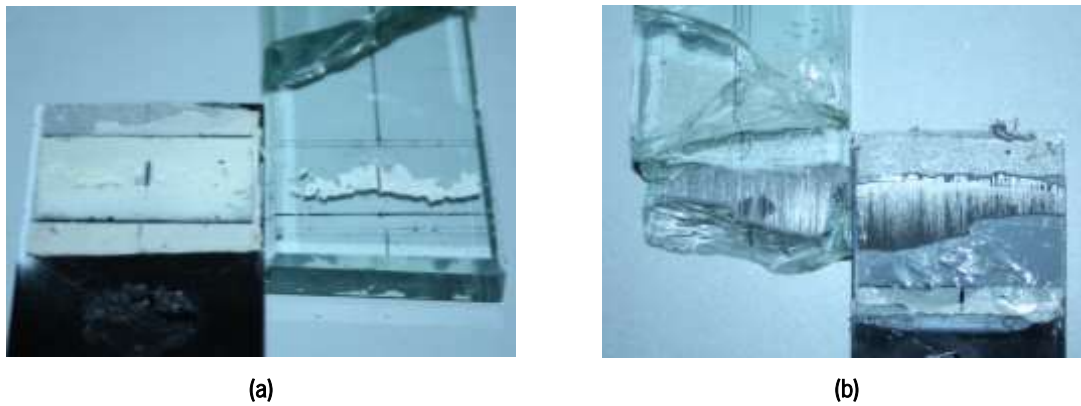
Figure II.8: Debonding at the glass/adhesive interface (a) in SF-L25 specimens and cohesive shear debonding in adherends (b) in SD-L25 specimens. In each case both images show the two opposite faces of the bonded connection after failure.

First, in order to verify the effectiveness of the DIC method in the scope of the present study, $F - s_{le}$ curves were extracted from the DIC analysis for one specimen per series and, subsequently, compared with the respective experimental curves (see **Figure II.9**). In line with the experimental monitoring setup shown in **Figure II.2**, s_{le} was determined measuring the displacement of the CFRP laminate at the loaded end section and the displacement of the glass sheets at 20 mm below this section, as close as possible to the outer faces. Similar $F - s_{le}$ curves were obtained from the DIC and LVDTs measurements (see **Figure II.9**). Considering s_{le} corresponding to F_{max}, relative differences between 1.6 % (SF-L50-I) and 18.8 % (SF-L25-I) were observed when comparing the DIC and LVDTs measurements. Minor deviations related to software calibration and image capture are the most likely reasons for the discrepancy observed between the two measurement strategies, as well as deformations induced by the loading procedure in the supports of the LVDTs, which are very small but noticeable at this scale. In addition, three-dimensional effects certainly contributed to the difference between DIC and LVDTs measurements.

Finally, relative slip curves, $s(x)$, along the bond length (L_b) were extracted from the DIC results, in order to identify differences between the bond behaviour of glass-CFRP composite systems when flexible and stiff adhesives are used (see **Figure II.10** and **Figure II.11**). For the sake of simplicity, the $s(x)$ curves were extracted only using the last image captured before failure.

(a)

(b)

(c)

(d)
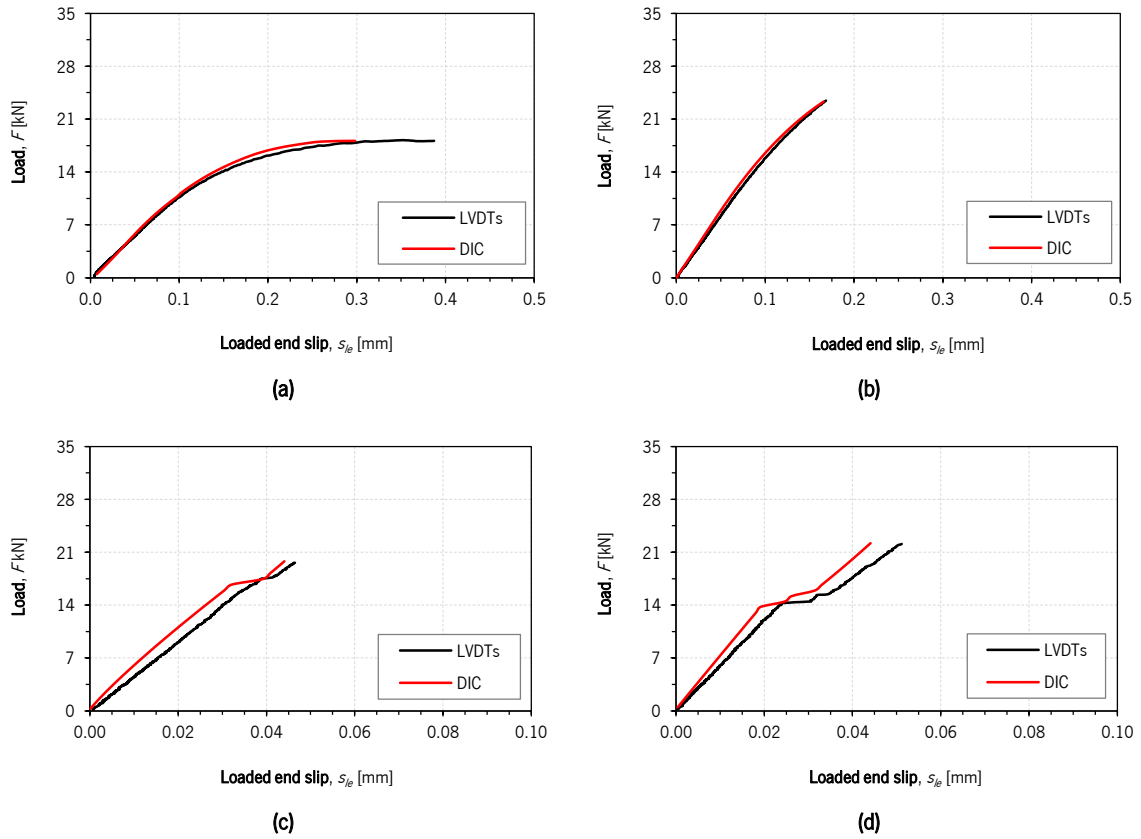
Figure II.9: Comparison between $F - s_{le}$ curves extracted from the LVDTs and the DIC technique for (a) SF-L25-I, (b) SF-L50-I, (c) SD-L25-I and (d) SD-L50-I.

(a)

(b)
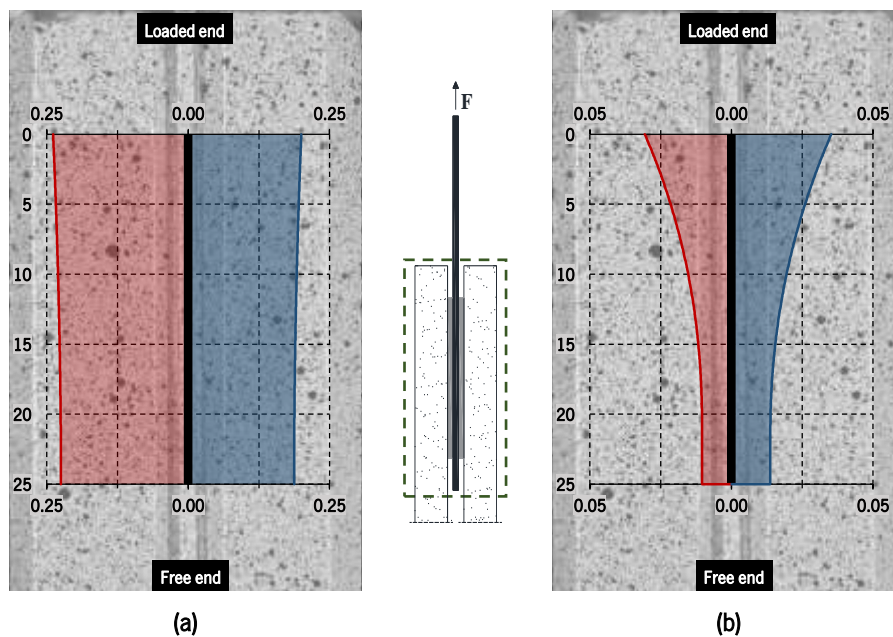
Figure II.10: Slip between the CFRP laminate and the glass sheets along L_b in (a) SF-L25-I and (b) SD-L25-I, extracted from the DIC method for the last image captured before the failure. Note: all values in millimetres.

(a)   (b)
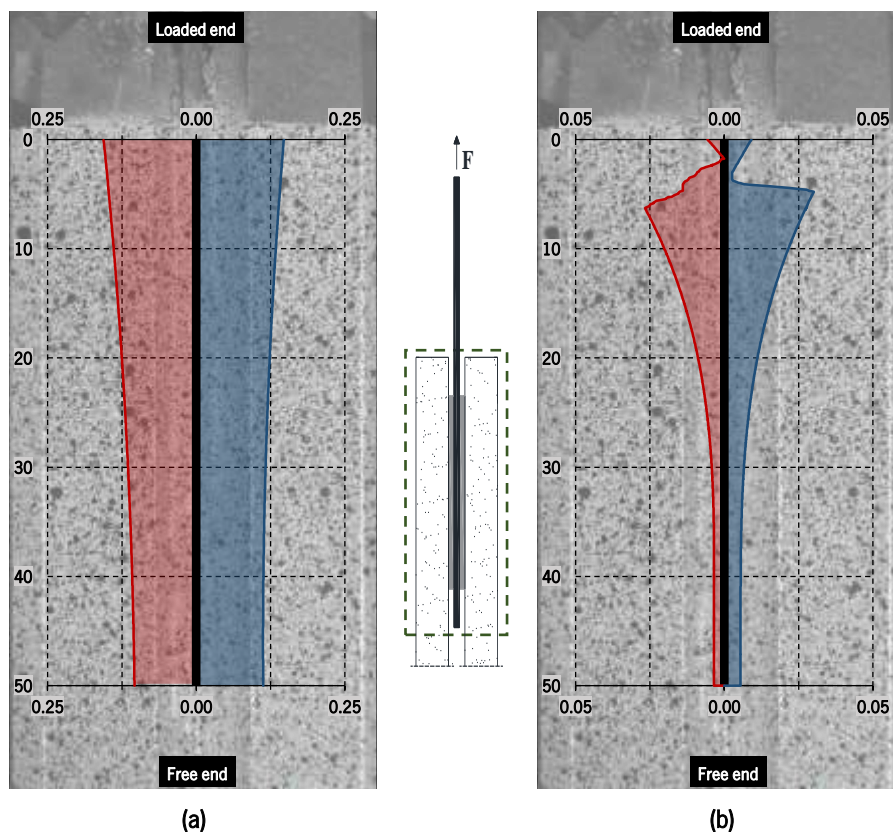
Figure II.11: Slip between the CFRP laminate and the glass sheets along L_b in (a) SF-L50-I and (b) SD-L50-I, extracted from the DIC method for the last image captured before the failure. Note: all values in millimetres.

3.3.   Discussion of results

3.3.1.   Structural behaviour

Both series SF-L25 and SF-L50 showed an almost linear behaviour at early stages of the bond response (see **Figure II.5a** and **Figure II.5b**), as a result of the chemical bond between the involved adherends (glass and CFRP). By increasing the bond length (from 25 mm to 50 mm) the initial stiffness increased $\approx$ 50 %. All the SF-L25 specimens failed by adhesive failure at the interface adhesive/glass, while SF-L50 specimens collapsed by cohesive failure in glass. A noticeable loss of stiffness was observed before the SF-L25 specimens reached their ultimate load. Two reasons can explain this: (i) first, the expectable degradation of the chemical bond at increasing loads in all interfaces, mainly at the glass/adhesive interface; and, (ii) secondly, the non-linear behaviour of the SikaForce adhesive (see **Figure II.4a**). In the case of SF-L50 series, the non-linear behaviour near the peak load was less pronounced since the failure was controlled by the glass rupture.

Regarding the SD-L25 and SD-L50 series (see **Figure II.5c** and **Figure II.5d**), in general, all specimens presented linear elastic behaviour until the failure, in line with the mechanical behaviour of the SikaDur

156

adhesive (see **Figure II.4b**). Due to its high strength (5.3 times higher than in SikaForce), the progressive damage propagation from the loaded end to the free end was not significant. Nevertheless, regardless of the bond length, small plateaus were observed in the $F - s_{le}$ responses of some specimens. However, their bond stiffness remained essentially unchanged, excluding SD-L50-I. In these series, more complex failure modes were observed, always involving glass rupture (see also next section). SD-L50-I presented greater initial stiffness than other SD-L50 specimens (see **Table II.3**). **Figure II.12** shows the maximum principal strains at different stages of SD-L50-I $F - s_{le}$ response. The initiation of diagonal cracks is clearly identified. These cracks appeared at the vicinity of the loaded end section and progressively propagated towards the free end section during loading, creating short plateaus on the $F - s_{le}$ response of the SD-L50-I specimen. As referred previously, in contrast to other specimens, the bond stiffness of SD-L50-I decreased after the appearance of the first cracks (see **Figure II.12c**), resembling values displayed by the remaining SD-L50 specimens. By comparing SD-L50-I with SD-L50-II and SD-L50-III, higher initial stiffness is observed in the former. This can be explained by possible defects of the specimen (incorrect bond length and eventual misalignment of adherends). Apparently, the premature cracking pattern of glass sheets in the SD-L50-I specimen doesn't suggest the influence of geometric defects. Thereby, these unexpected cracks seem to have resulted from the combination of two aspects: (i) first, the high stiffness and strength of the SikaDur adhesive, which prevented the progressive damage propagation from the loaded end to the free end and, in turn, the gradual transfer of tensile stresses from the CFRP laminate to the glass sheets, unlike the specimens with SikaForce; and, (ii) the lower strength of the glass close to the loaded end section, caused by the manufacturing process and handling of the glass pieces.

Regarding the 3M-L25 series (see **Figure II.5e**), all specimens presented a slight non-linear behaviour prior to failure, in line with the mechanical behaviour of the 3M adhesive (see **Figure II.4c**). By increasing the bond length (from 25 mm to 50 mm) this slight non-linear behaviour was not visible in 3M-L50 specimens (see **Figure II.5f**), since similar maximum loads were achieved in both series because the failure was controlled by the glass rupture. Due to the high strength of the 3M adhesive (similar to SikaDur), the progressive damage propagation from the loaded end to the free end and its impact in the shear response were not significant.

Comparing the 3M and SD series, both epoxy adhesives (SikaDur and 3M DP490) yielded similar initial stiffness (see **Table II.3**), despite the more flexible response of the 3M adhesive when compared to the SikaDur (about 2.5 times – see **Table II.2**). The difference between adhesive layer thicknesses

adopted for each epoxy, which was about 3 times higher in SD series (1.0 mm) than in 3M series (0.3 mm), may explain this result. In contrast to the SD-L25 series, a slight loss of stiffness was observed in specimens of the 3M-L25 series, in line with the mechanical behaviour of the respective adhesive (see **Figure II.4c**). Due to the high strength of the 3M adhesive, the glass sheets failed before the theoretical peak-load of the adhesive connection was reached and, consequently, the possible post-peak curve of the response was not captured.
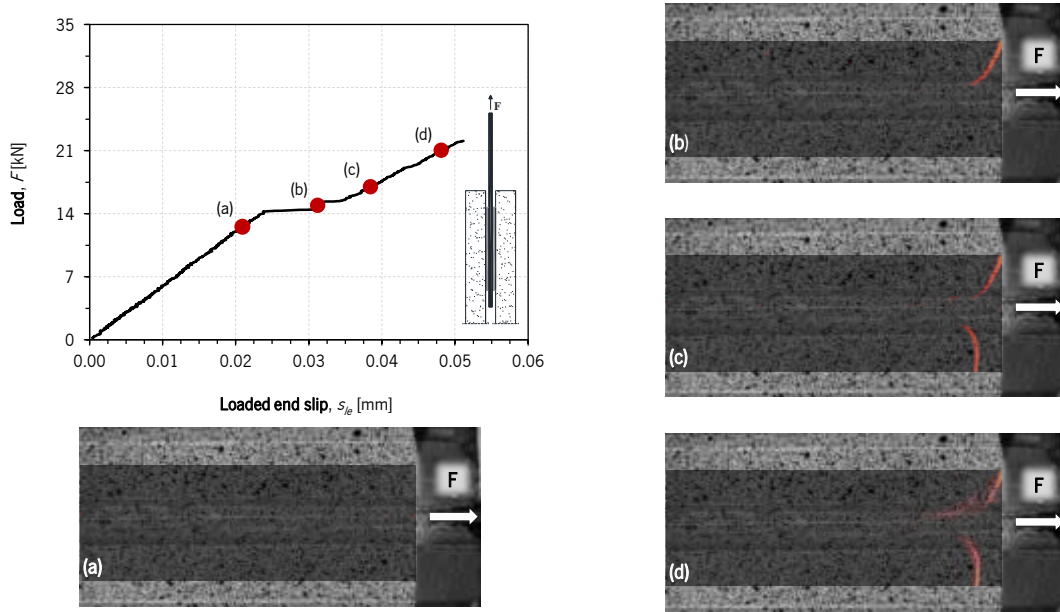
Figure II.12: Load (F) *vs.* slip (s_{le}) response obtained for the SD-L50-I specimen, together with the maximum principal strain fields obtained with DIC at the ROI, showing the cracks formed at stages (a), (b), (c) and (d).

Regarding the maximum load, the values obtained from the SF-L25 specimens were significantly influenced by the adhesive behaviour and the bond length, since the glass-to-CFRP connection failed by debonding at the adhesive/glass interface (adhesive failure). The SF-L25 specimens showed the lowest average maximum load (17 kN) because they were produced using the adhesive with the lowest shear strength, as well as the shortest bond length among all tested bond lengths. In all other series, the specimens failed by cohesive failure in glass and/or fibre-tear failure in CFRP laminate and/or cohesive shear debonding in glass (see **Figure II.7**). Therefore, the average maximum loads reached in the specimen series produced with epoxy adhesives were mainly influenced by the mechanical properties of glass and CFRP.

Glass rupture was observed in all the specimens where 3M and SikaDur adhesives were used. However, substantial differences between the 3M and SD series were observed (see **Table II.3**). In 3M series, the average maximum load increased from 28.4 kN to 31.7 kN (+11.6 %) when L_b was

increased from 25 mm to 50 mm. In contrast, the maximum load remained almost unchanged in the case of the SD series (SD-L25 *versus* SD-L50). On the other hand, considering similar bond lengths, both 3M series exhibited values of F_{max} significantly higher than the respective SD series, approximately 30 % and 40 % for bond lengths of 25 mm and 50 mm, respectively. The differences found are explained by the higher stiffness of the SikaDur adhesive, despite the natural scatter of the tensile strength of glass.

DIC analysis revealed that the bond test region of SD specimens that exhibited cracks close to the loaded end was completely shattered. Due to the brittle nature of the annealed glass, the formation of these cracks occurred very suddenly, releasing large amounts of energy and, in turn, increasing the dynamic response of the specimens. For high loading levels (>20 kN), the glass was unable to accommodate the energy released by the crack propagation from the loaded end to the free end and, consequently, the glass sheets failed in an uncontrolled manner, shattering the entire bond test region (see **Figure II.7**). Due to the brittle nature of the annealed glass which shows no softening, similar maximum loads were achieved in both SD series, where the failure was governed by the loading level at the instant corresponding to the initiation of new cracks near the loaded end. Although a smoothing of the stress concentration near the loaded end section was expected with increasing bond length, the SD-L50 series presented a slightly lower maximum load in comparison with the SD-L25 series, probably due to the high scatter of the tensile strength of glass.

Comparing the $F - s_{le}$ curves of SD-L25 and 3M-L25 series with the corresponding responses of SF-L25 series, significantly higher values of the initial stiffness and maximum load were obtained with the stiff adhesives, while significantly higher values of s_{le} corresponding to F_{max} were achieved with the polyurethane adhesive. The results also show that the increase in L_b from 25 mm to 50 mm resulted in higher values of K of the glass-to-CFRP adhesive connections. The SF-L50, SD-L50 and 3M-L50 series showed initial stiffness values 48.6 %, 19.3 % and 13.9 % higher than the counterpart series with L_b of 25 mm, respectively.

3.3.2.   Failure modes

Regardless of the bond length, 3M adhesive specimens always failed by cohesive failure in glass (see **Table II.3**). In the case of SF specimens, all SF-L50 specimens failed by cohesive failure in glass as well, while SF-L25 specimens always failed due to debonding at the adhesive/glass interface (see **Figure II.8a**) after facing an extensive loaded end slip. Regarding the SD specimens, cohesive shear

debonding in glass and fibre-tear failure in CFRP (see **Figure II.8b**) was observed in all specimens excluding SD-L25-III and SD-L25-IV, where the glass failed due to cohesive failure.

While the glass sheets of the SF-L50 specimens failed outside the bond test region (tensile failure), the SF-L25 specimens always failed by debonding at the adhesive/glass interface (see **Figure II.8a**). In all SF-L25 specimens one glass sheet failed immediately after the peak-load was achieved. Therefore, SF-L25 specimens did not show post-peak response (softening). As discussed subsequently, this can be explained by two distinct effects: (i) the asymmetric behaviour of the bond test region and (ii) the eccentric loading at the glass sheets.

The asymmetric behaviour of the bond test region was observed in all specimens. However, due to the low stiffness of SikaForce and progressive damage at the adhesive/glass interface, it was more evident in structural responses of SF-L25 specimens. The loss of symmetry in double-lap joints can be explained by several factors, namely: (i) deviations in the width of glass sheets related to their manufacturing process; (ii) variations in the edges' treatment of the glass elements, causing small differences between the bonding surfaces; and, (iii) finally, the adhesive thickness adopted in SF specimens was very thin (0.3 mm), and small differences between the thicknesses of both adhesive joints may have caused a considerable difference between their stiffnesses.

As shown in **Figure II.6a**, the loss of stiffness in SF-L25-I ($F > 5.0$ kN) seems to have resulted in a decrease in the longitudinal strain of the glass (ε_{exp}) captured by the strain gauge measurements. It should be noted that this effect only occurred in specimens with flexible adhesive (low stiffness) and L_b equal to 25 mm. Therefore, the lower the adhesive stiffness and the bond length, the higher the non-linearity observed in the $F - \varepsilon_{exp}$ responses. On the other hand, when SF-L25-I started to show stiffness decay, the slip at the loaded end measured by LVDTs was consistently greater than the values captured by DIC (see **Figure II.9a**). This effect may be explained by an increasing rotation of the LVDTs supports relatively to the loading axis (see **Figure II.13a**).

Taking into account the double-lap joint geometry (see **Figure II.1**), the load was transferred from the CFRP laminate to the glass sheets through shear stresses in the adhesive joints, inducing an eccentric loading in the glass sheets with eccentricity (e) approximately equal to 6.9 mm. The eccentricity effect yielded tensile stresses at the inner faces and compression stresses at the outer faces (lateral bending). In this sense, relative horizontal displacement curves between the two glass sheets and the CFRP laminate were extracted using the DIC method (see **Figure II.13**). For the sake of simplicity, only the last image captured before the SF-L25-I failure was considered. According to **Figure II.13**, when

SF-L25-I achieved F_{max}, the average horizontal displacement at the loaded end section was 18 % of s_{le}. For each glass sheet, the incremental strain (ε_{incr}) caused by the eccentricity effect was calculated according to the double integration method from the relative horizontal displacement curves shown in **Figure II.13**. On the other hand, the longitudinal strain (ε_{lin}) that would be expected without flexural stresses was calculated assuming E_g equal to 74 GPa and considering the symmetrical behaviour of the bond test region. According to **Table II.4**, the difference between ε_{exp} and ε_{lin} was entirely caused by the eccentricity effect. As the asymmetric behaviour of the bond test region is common to all specimens, regardless of the adhesive, it is reasonable to assume that the significant lateral bending of the glass sheets in SF-L25-I resulted from the flexible behaviour of the SikaForce adhesive and its low strength. The lateral bending of the glass sheets induced cleavage stresses in the adhesive joints, increasing the progressive damage from the loaded end to the free end. The higher the adhesive damage, the higher the flexural stresses in the glass sheets and, in turn, the cleavage stresses in the adhesive joints.

In the case of the 3M and SD series, although similar values of initial stiffness were observed in both cases, the two epoxy adhesives showed distinct failure modes. While the 3M specimens failed due to the glass rupture below the bond region (tensile failure), the SD specimens failed by cohesive shear debonding in substrates. Excluding SD-L25-II and SD-L25-IV, which failed by cohesive failure in glass, the bond region of the specimens with SikaDur was completely shattered (see **Figure II.7**). As inferred in **Section 3.3.1**, this resulted from the higher stiffness of the SD adhesive (when compared to 3M). Regardless of the bond length, the failure of SD specimens was mainly induced by dynamic effects resulting from the initial cracking of the glass sheets near the loaded end section.

Table II.4: Comparison between the longitudinal strains induced by the lateral deflection of glass sheets in SF-L25-I, as measured using the strain gauges and the DIC (percentage difference in parenthesis).

	ε_{exp} [‰]	DIC method – Lateral bending		
		ε_{lin} [‰]	ε_{incr} [‰]	$\varepsilon_{lin} + \varepsilon_{incr}$ [‰]
SG1	0.127	0.205	-0.077	0.128 (1.2%)
SG2	0.076	0.208	-0.134	0.075 (-2.1%)
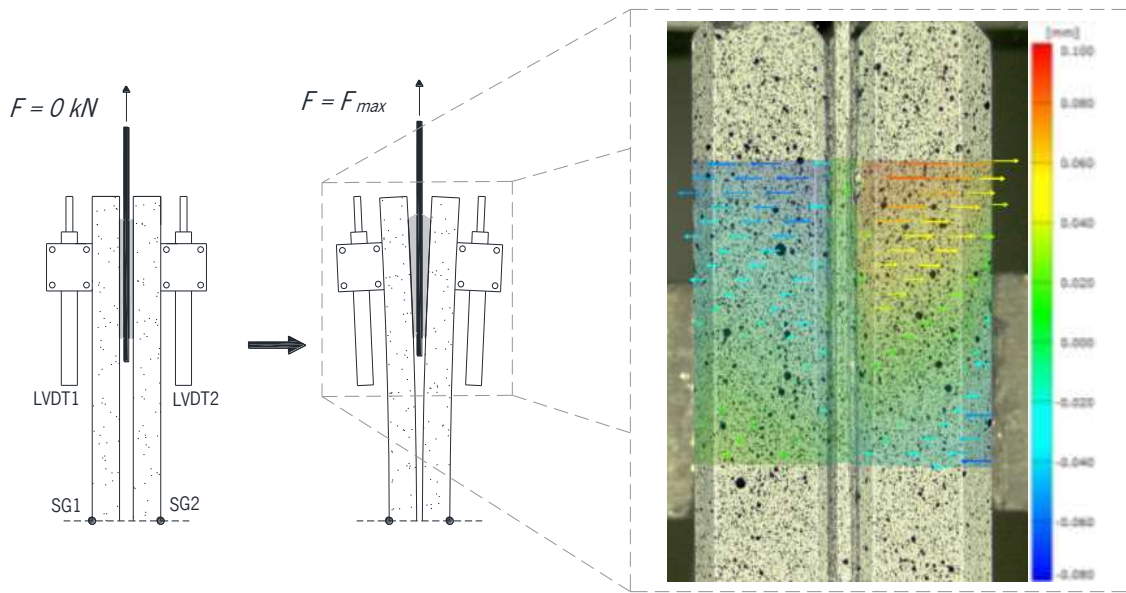
(a)
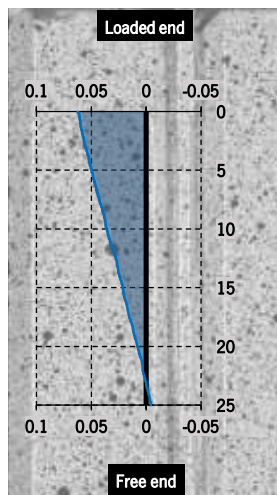
(b)
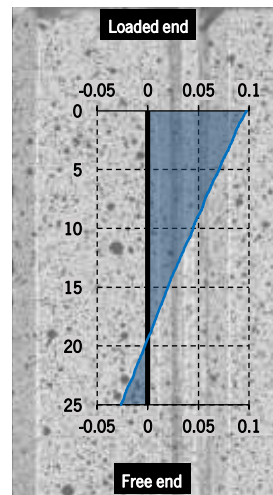
(c)

Figure II.13: Cleavage effect in SF-L25-I (a) showing the lateral deflection of the glass sheet I (b) and in the glass sheet II (c) in relation to the CFRP laminate. Note: nomenclature presented in **Figure II.1** and all values in mm.

3.3.3. Stiff *vs.* flexible adhesives

Figure II.10 and **Figure II.12** compare the slip profiles along the bond length between SF and SD series extracted from the DIC analysis. When SD adhesive is used for glass-to-CFRP connections, the damage progression affects also the surrounding glass (cracking from the loaded end to the free end). On the other hand, the application of SF results in concentration of damage mainly at the adhesive. A significant slip at the free end section (s_{fe}) was observed in both specimens with SF, the most flexible adhesive. This is the result of a more uniform distribution of bond stresses along L_b when flexible adhesives are applied, due to the lower stiffness of the material. In contrast, the values of s_{fe} in SD

162

specimens were substantially lower when compared to s_{le}. This is likely the result of the high stiffness of stiff adhesives, which led to high bond stresses near the loaded end section and very low bond stresses near the free end section, creating a non-uniform distribution of bond stresses along L_b. Due to the significantly higher stiffness of the CFRP laminate when compared to the polyurethane adhesive, the transmission of the tensile force from the CFRP to the glass sheets occurs in a smoother way. In contrast, the high stiffness of SikaDur adhesive leads to a greater stress concentration at the glass sheets, which may have led to the initiation of cracking in glass even before the L_b was entirely mobilized.

4   ANALYTICAL MODELLING

This section is dedicated to the study carried out to analytically estimate the local bond stress-slip ($\tau - s$) law and the maximum load (F_{max}) vs. bond length (L_b) response for each adhesive type, considering the experimental results obtained from the double-lap joint tests.

4.1.   Description of the method

Despite the three-dimensional character of glass-to-CFRP adhesive bond, in order to decrease the level of complexity of the theoretical formulations [38], 1D strategy is usually adopted to analytically model the bond behaviour. According to e.g. Focacci *et al.* [39], Russo *et al.* [40] and Sena-Cruz and Barros [41], the local bond phenomenon between the CFRP laminate and the glass can be characterized mathematically by a second order differential equation in terms of slip (see **Eq. (II.1)**). According to Sena-Cruz [38] and Sena-Cruz and Barros [41], **Eq. (II.1)** was derived assuming that CFRP laminate behaves linearity in its longitudinal direction and neglecting the substrate (in this case glass) and adhesive deformability. Despite the flexibility of SikaForce when compared to epoxy adhesives, for the sake of simplicity, the deformability of the adherends was neglected.

$$\frac{d^2 s}{dx^2} = \frac{P_b}{E_r A_r} \tau(x)$$

(II.1)

A computational application previously developed by Sena-Cruz and Barros [41] was used to define the $\tau - s$ relationships for the three adhesives. Using an inverse analysis strategy complemented with numerical fitting tools, this computational application performs several iterations until it finds the parameters required by the $\tau - s$ relationship that satisfy **Eq. (II.1)**, where $\tau(x) = \tau(s(x))$ is the shear stress between the CFRP laminate and adhesive as a function of the relative slip along the bond length.

Moreover, E_r and A_r are the Young's modulus and the cross-section area of the reinforcement element, respectively, and P_b is the perimeter of the reinforcement in contact with adhesive.

A brief description about the iterative procedure used by the computational application to determine the best parameters that define the $\tau - s$ relationship is given, as follows: (i) first, based on the experimental responses, the user sets a range of values for each required parameter by the $\tau - s$ relationship adopted; (ii) then, the computed $F - s$ response is determined for the free and loaded ends; (iii) later, the difference between the computed and experimental responses is calculated in terms of the peak load and the corresponding slip and the area difference between both curves (experimental and computed); and (iv) finally, this process is repeated until an acceptable accuracy is obtained, according to a pre-defined residual criteria defined by the user. More details about this algorithm may be found in Sena-Cruz [38] and Cunha *et al.* [42].

A glass-to-CFRP bonded joint is shown in **Figure II.14**, where L_b is the bond length, F is the load and s_{fe} and s_{le} are the slips at the free and loaded end sections, respectively. By using this tool, the following involved parameters can be access along the bond length: the slip, $s(x)$; the shear stress at the interface, $\tau(x)$; the axial strain in CFRP, $\varepsilon_r(x)$; and the axial force at the CFRP, $F(x)$. Finally, F is calculated using **Eq. (II.2)**, which was obtained by equating the internal work due to the elastic deformation of the CFRP and the external work produced by the shear stress profile created at the interface [42].
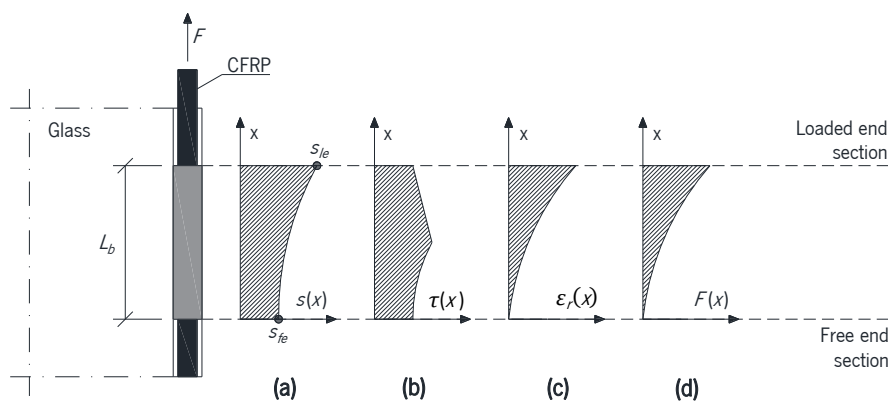
Figure II.14: Parameters involved in the analytical model [41]: (a) slip; (b) bond stress; (c) CFRP strain and (d) CFRP axial force.

$$F = \sqrt{\left(2E_r A_r P_b \int_{s_f}^{s(s=\widetilde{L_b})} \tau(s)ds\right)} \tag{II.2}$$

4.2. Local bond stress-slip relationship

Several authors (e.g. [43–46]) have evaluated the efficiency of different $\tau - s$ laws in the simulation of the local behaviour for FRP-to-concrete interfaces. Given the lack of specific $\tau - s$ relationships to simulate the debonding of glass-to-CFRP interfaces, several bond stress-slip laws that exist in the literature were considered in this study. The local $\tau - s$ laws were selected considering the following criteria: (i) the behaviour of adhesive; (ii) the type of response of the double-lap joints before the peak load is reached; (iii) the typically smooth surfaces of both adherends, suggesting the absence of friction stresses at the CFRP/adhesive or glass/adhesive interfaces; and (iv) the amount of interfacial fracture energy, which should be as low as possible for conservative reasons, taking into account the last two criteria.

As the stiffness of double-lap joints with SikaDur remained unchanged until they failed, their adhesive interfaces were modelled analyticcally considering a linear $\tau - s$ relationship, defining only the shear stiffness (K_τ). On the other hand, considering the abovementioned criteria, for the SikaForce and 3M adhesives, which showed non-linear behaviour in direct tension tests (see **Figure II.4c**) and in double-lap joints (see **Figure II.5e**), the $\tau - s$ exponential law proposed by Dimande [47] (see **Eq. (II.3)**) was used to solve **Eq. (II.1)**. According to **Eq. (II.3)**, two parameters are required to define the $\tau - s$ relationship proposed by Dimande [47]: the bond strength, τ_m, and its corresponding slip, s_m. These parameters were calibrated for the average experimental curve of each series with the L_b of 25 mm. Regarding the CFRP laminate, values of 92 mm (46 mm with each glass sheet) and 60 mm^2 for P_b and A_r were adopted, respectively.

$$\tau(s) = \tau_m \frac{s}{s_m} e^{1-\frac{s}{s_m}} \tag{II.3}$$

In 3M series, the glass sheets ruptured before the failure of the glass-to-CFRP interfaces was reached. Consequently, the $\tau - s$ relationship proposed by Dimande [47] could not be determined for the 3M adhesive, since an infinite number of $\tau_m - s_m$ combinations could be calibrated for each $F - s_{le}$ curve. To overcome this, the finite element software ABAQUS/Explicit [24] was used to determine τ_m. For this purpose, the 3M adhesive was simulated as an isotropic elastic material. Its non-linear behaviour (see **Figure II.4c**) was taken into account using a VUSDFLD subroutine, developed to redefine the

Young's modulus at each material point as a function of its maximum principal strain. Other assumptions adopted in these numerical simulations can be found later in **Section 5**. **Figure II.15** shows the diagram of shear stresses along L_b when the maximum principal stress at the loaded end section reaches the tensile strength of the 3M adhesive (32.8 MPa). From **Figure II.15**, the value of 19.6 MPa was adopted for τ_m.

(a)   (b)
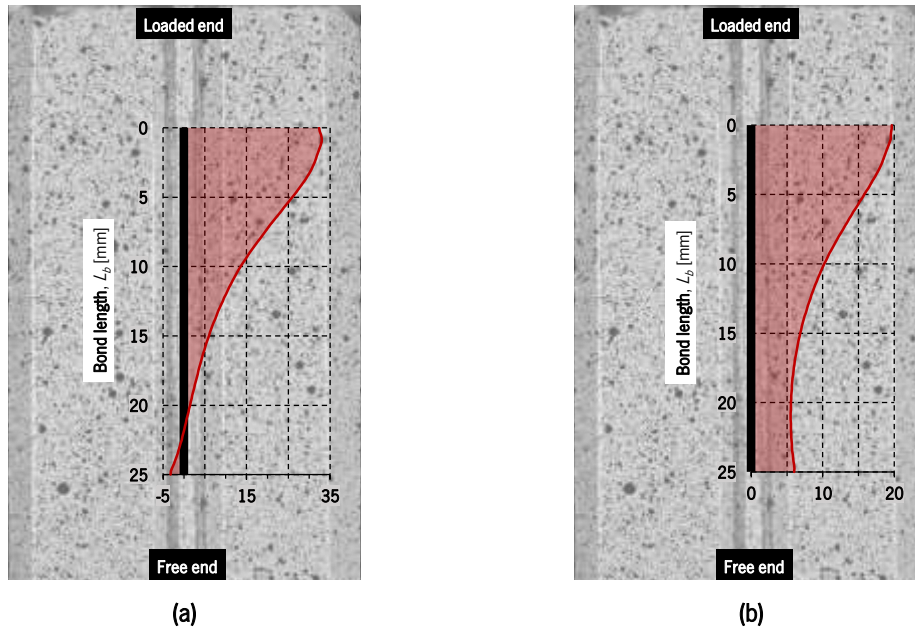
Figure II.15: Distribution of (a) maximum principal stress and (b) shear stress along the bond length obtained for the 3M adhesive from numerical simulations, at the instant when the tensile strength of the 3M adhesive at the loaded end section was reached and the adhesive failure was initiated. Note: values of stress in MPa.

Table II.5 presents the parameters that define the $\tau - s$ relationship for each adhesive, as well as the normalized error, *Err*, i.e. the ratio between the area limited by the experimental and computed responses. The experimental and computed $F - s_{le}$ responses are compared in **Figure II.5**, for both 25 mm and 50 mm bond lengths. The bond behaviour of glass-CFRP composite systems was well described by the analytical models adopted: (i) the Dimande's $\tau - s$ relationship when flexible (e.g. SikaForce) and stiff (e.g. 3M) adhesives with non-linear behaviour are used; and (ii) the linear $\tau - s$ relationship for stiff adhesives (e.g. SikaDur) with linear behaviour until failure and high strength. **Figure II.5** also demonstrate that parameters found for the $\tau - s$ relationships are independent of the bond length (the laws were calibrated for L_b = 25 mm and used for L_b = 50 mm).

Table II.5: Values of the parameters defining the $\tau - s$ relationship for each series of specimens with an overlap length of 25 mm.

	s_m [mm]	τ_m [MPa]	Err [%]	K_τ [MPa/mm]
SF-L25	0.368	7.4	1.4	–
SD-L25	–	–	–	317.5
3M-L25	0.117	19.6	2.1	–

4.3. Effective bond length

In composite systems, the load is transferred to the reinforcement element by means shear stresses in the adhesive layer, mostly near the loaded end. When the applied load increases, the adhesive close to the loaded end is damaged and the active bond length shifts to a new zone, towards the free end, indicating that only part of the adhesive bond is effective.

Considering design purposes of glass-CFRP composite systems, the maximum load (F_{max}) as a function of the anchorage length of CFRP laminate was determined for the three adhesives. For this purpose, the computational programme abovementioned as well as the previously calibrated $\tau - s$ relationships were used. As presented in **Figure II.16**, F_{max} no longer increases when L_b is extended to values above the effective bond length (l_{eff}), which is approximately 400 mm and 150 mm for SikaForce and 3M adhesives, respectively. The $F_{max} - L_b$ curve was not depicted for glass-CFRP connections with SikaDur because their interfaces were analytically modelled using a linear $\tau - s$ relationship, neglecting any adhesive damage. Therefore, F_{max} is infinite for $L_b > 0$.

(a)   (b)
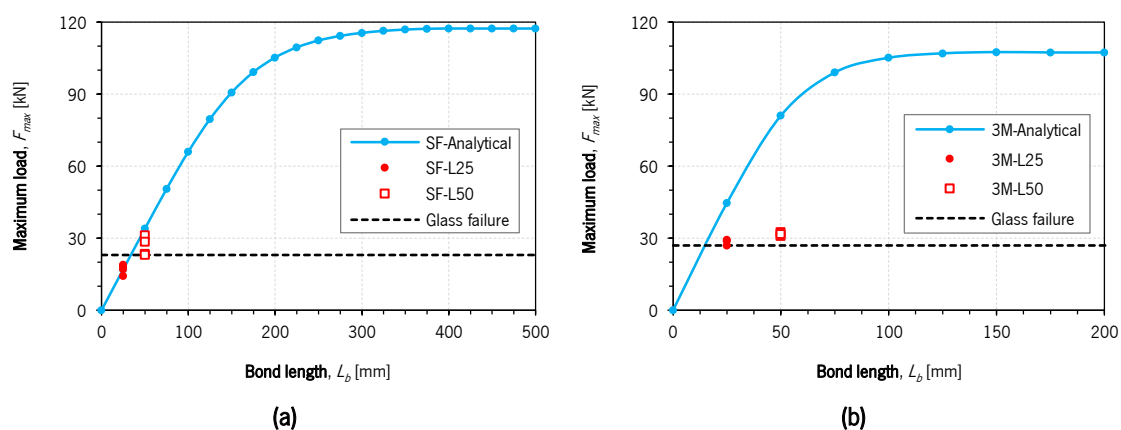
Figure II.16: Comparison of the experimentally obtained Maximum load (F_{max}) for each bonded length (L_b) with the expected one using the analytical model for (a) SikaForce and (b) 3M adhesives.

5   NUMERICAL ANALYSIS

5.1.   Initial considerations

Numerical analysis were performed using the finite element method, in order to verify the effectiveness of the local bond-slip laws determined in **Section 4** for the simulation of glass-CFRP composite structural elements and, in addition, to obtain the profile of shear stresses along the bond length. Therefore, cohesive elements were used to simulate the non-linear behaviour of the interfaces (CFRP/adhesive and adhesive/glass) and the adhesive itself. The results obtained from the numerical simulations provide additional information regarding the bond behaviour of glass-to-CFRP adhesively bonded joints. Moreover, the parameters determined from the analytical study (see **Section 4**) were recalibrated taking into account some aspects that influenced the experimental measurements in $F - s_{le}$ curves. Similarly to the analytical approach presented in **Section 4**, the results of the numerical results were compared with the experimental ones.

All numerical simulations were performed in ABAQUS/Standard software [24], using material models available in the software's library. ABAQUS/Explicit was not considered due to its mesh limitations, since only finite elements with reduced integration could be used and therefore would affect the accuracy of the numerical models in this particular case.

5.2.   FE model description

The double-lap joint tests were simulated with following assumptions: (i) two-dimensional (2D) problem, with different out-of-plane widths for the three elements, in order to consider the influence of the edges treatment on the adhesive layer's width; (ii) only one adhesive interface was considered, assuming symmetrical behaviour for both glass-to-CFRP interfaces with respect to the longitudinal axis of the specimen. **Figure II.17** shows the geometry, boundary conditions and load configuration.

The annealed glass and CFRP were simulated as an isotropic materials with linear elastic constitutive laws, both in tension and in compression. A Young's modulus (E_g) of approximately 70 GPa and a Poisson's ratio (v_g) of 0.23 should be used to describe the linear elastic behaviour of annealed glass, in accordance with the recommendations of the Guideline for European Structural Design of Glass Components [35]. Based on the results measured by the strain gauges from the double-lap joint tests, a Young's modulus (E_g) of 74 GPa was adopted (see **Table II.2**). Regarding the CFRP, a Young's modulus (E_{CFRP}) of 165.2 GPa was adopted (see **Table II.2**) and a Poisson's ratio (v_{CFRP}) of 0.28 was assumed, according to its technical data sheet.

(a)

(b)
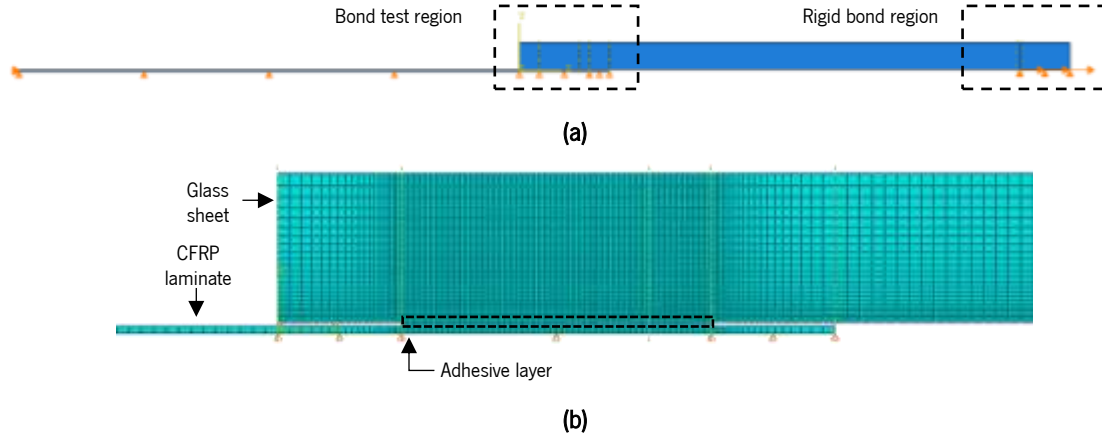
Figure II.17: Geometry, boundary conditions and load configuration used in the numerical simulation of the behaviour of double-lap joints (a), and detail of the bond test region showing the studied connection including the mesh and the boundary conditions(b).

5.2.1.   Adhesive interface

The glass-to-CFRP interfaces were modelled using "*cohesive elements*". Their constitutive response was defined using a "*traction-separation approach*". Although the traction-separation approach is more suitable to model delamination at bonded interfaces where the interface thickness is negligibly small, this option was used because the "*continuum approach*" only allows to simulate the material damage and failure in ABAQUS/Explicit [24], which was not considered at this stage.

The traction-separation approach assumes that failure of the cohesive elements is characterized by progressive degradation of the material stiffness driven by a damage process [24]. A linear elastic behaviour is initially considered by the abovementioned approach. An uncoupled behaviour between the normal and shear components was defined for these simulations. Therefore, the linear elastic normal stiffness (K_n) and the linear elastic tangential stiffness (K_s) were derived from the mechanical characterization (see **Section 3.1**) and double-lap joint tests (see **Section 3.2**), respectively. The adopted constitutive relationship to simulate glass-to-CFRP interfaces is governed by **Eq. (II.4)**, where $\Delta\sigma_n$ and Δu_n are increments of stress and displacement in the normal direction to the interface, while $\Delta\tau_s$ and Δs_s are increments of stress and displacement in the tangential direction to the interface, respectively.

$$\begin{bmatrix}\Delta\sigma_n \\ \Delta\tau_s\end{bmatrix} = \begin{bmatrix}K_n & 0 \\ 0 & K_s\end{bmatrix}\begin{bmatrix}\Delta u_n \\ \Delta s_s\end{bmatrix} \qquad\text{(II.4)}$$

According to ABAQUS [24], the failure mechanism is controlled by (i) the damaged initiation criteria and (ii) the damaged evolution law. For the former, a "*maximum nominal stress criterion*" was

adopted, i.e. the damage initiates when the maximum nominal stress ratio reaches either the normal strength ($\sigma_{n,max}$) or the shear strength ($\tau_{s,max}$), according to **Eq. (II.5)**. For the latter, the damage factor was specified as a function of the displacement in relation to the effective displacement at damage initiation, using the $\tau - s$ relationships derived in **Section 4.2**.

$$max\left\{\frac{\sigma_n}{\sigma_{n,max}}, \frac{\tau_s}{\tau_{s,max}}\right\} = 1 \tag{II.5}$$

5.2.2. Mesh strategy

Both glass sheets and the CFRP laminate were simulated using 4-node plane stress elements with a 2×2 integration scheme (CPS4). 4-node two-dimensional cohesive elements with two integration points (COH2D4) were used to simulate the adhesive layer. As shown in **Figure II.17**, special attention was paid to the mesh in the overlap zone to ensure a sufficient refinement. Therefore, finite elements ranging in size from 0.25 (width) $\times$ 0.25 (height), near the adhesive interface, to 1.0 (width) $\times$ 1.0 (height) [mm] were used in these numerical simulations.

5.3. Numerical results

In the experimental tests, the LVDTs used to measure the slip at the loaded end were placed on the external faces of the glass sheets, about 20 mm below the free end section (see **Figure II.2**). Thereby, the experimental measurements of the slip at the loaded end section (see **Figure II.5**) included also the longitudinal deformation of glass sheets between the loaded end section and the LVDTs section ($\approx$ 20 mm), as well as the three-dimensional effects that had occurred (e.g. lateral deflection of glass sheets). In contrast, the numerical model allows to take the measurement of the slip directly at the loaded end section, without the physical constrains that the experimental model imposes. Thus, in order to simulate the behaviour of the double-lap joints, an iterative procedure was initially adopted to find a s_{eff} corresponding to τ_m, where s_{eff} is the effective slip that would be experimentally obtained if the LVDTs could be physically placed on the inner faces of the glass sheets at the loaded end section. The initial stiffness was the criteria used to find s_{eff}. The iterative procedure ended when the initial stiffness obtained from the $\tau - s_{eff}$ law *versus* LVDTs section (outer face) reached the initial stiffness obtained from the $\tau - s$ law *versus* loaded end section (inner face). The maximum relative difference between these two initial stiffnesses was limited to 1.0 %. All numerical results presented later were obtained taking into account the $\tau - s_{eff}$ relationships based on the parameters shown in **Table II.6**.

Table II.6: Values of the parameters defining the $\tau - s_{eff}$ relationship for each series of specimens with an overlap length of 25 mm.

	s_{eff} [mm]	τ_m [MPa]	$K_{\tau,eff}$ [MPa/mm]
SF-L25	0.280	7.4	–
SD-L25	–	–	412.12
3M-L25	0.088	19.6	–

For the sake of simplicity, only the iterative procedure applied to the SF-L25 series is covered in detail in this paper, showing its initial ($\tau - s$ law) and final ($\tau - s_{eff}$ law) stages in **Figure II.18b** and **Figure II.18c**, respectively. According to **Figure II.18a**, $d_{CFRP,le-s}$ and $d_{g,le-s}$ are, respectively, the longitudinal displacements of CFRP laminate and glass (inner face) at the free end section and $d_{g,LVDT-s}$ is the longitudinal displacement of glass at the LVDTs section (outer face). Called "Ref." in **Figure II.18**, the reference $F - s_{le}$ curve to find s_{eff} was initially defined by subtracting $d_{CFRP,le-s}$ to $d_{g,le-s}$, both obtained from the $\tau - s$ law. On the other hand, the object $F - s_{le}$ curve, called "Obj." in **Figure II.18**, was determined at each iteration by subtracting $d_{CFRP,le-s}$ to $d_{g,LVDT-s}$, both derived from the bond stress – slip law considered in this iteration. **Figure II.18** shows that the longitudinal deformation of glass influenced significantly the experimental responses captured by LVDTs. However, due to the brittle nature of glass, it would be very difficult to implement another measurement strategy.

(a)

(b)

(c)
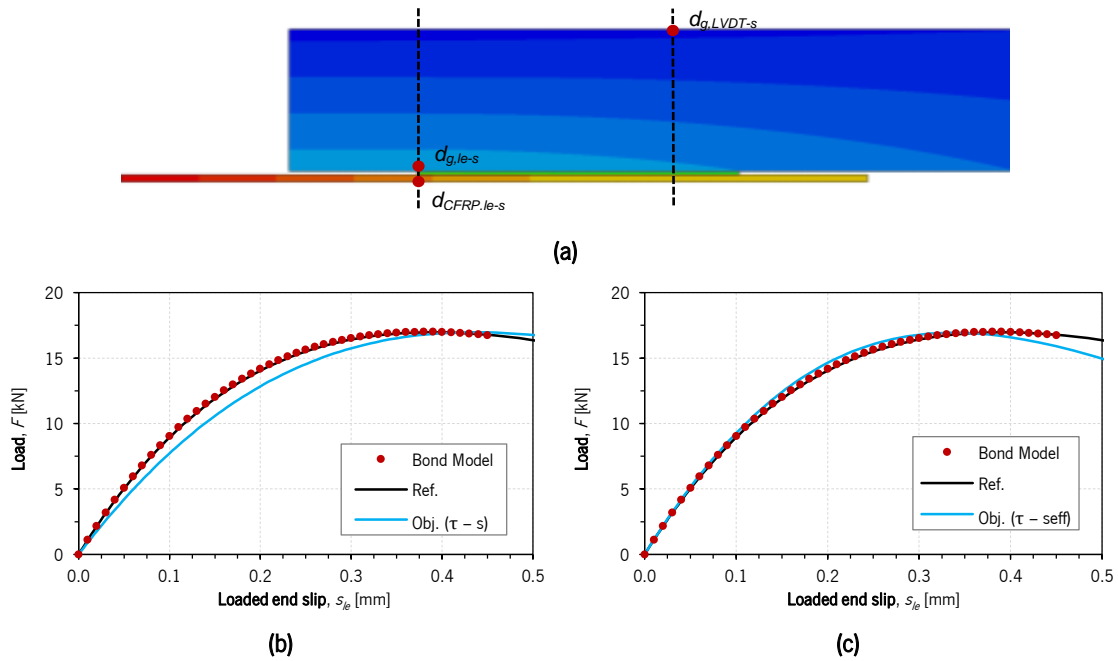
Figure II.18: Numerical model used in the iterative procedure applied to the SF-L25 series, showing the points where the displacements were measured (a) for the initial $\tau - s$ relationship (b) and for the numerically fitted $\tau - s_{eff}$ law.

As shown in **Figure II.19**, the numerical models simulated with great accuracy the experimental behaviour of each series of double-lap joints when the $\tau - s_{eff}$ relationships were used. This shows that the analytical parameters shown in **Table II.6** are effective when used in numerical simulations. Further studies of glass-to-CFRP interfaces, as well as numerical simulations of glass-CFRP composite systems (e.g. beams) are possible using this approach.
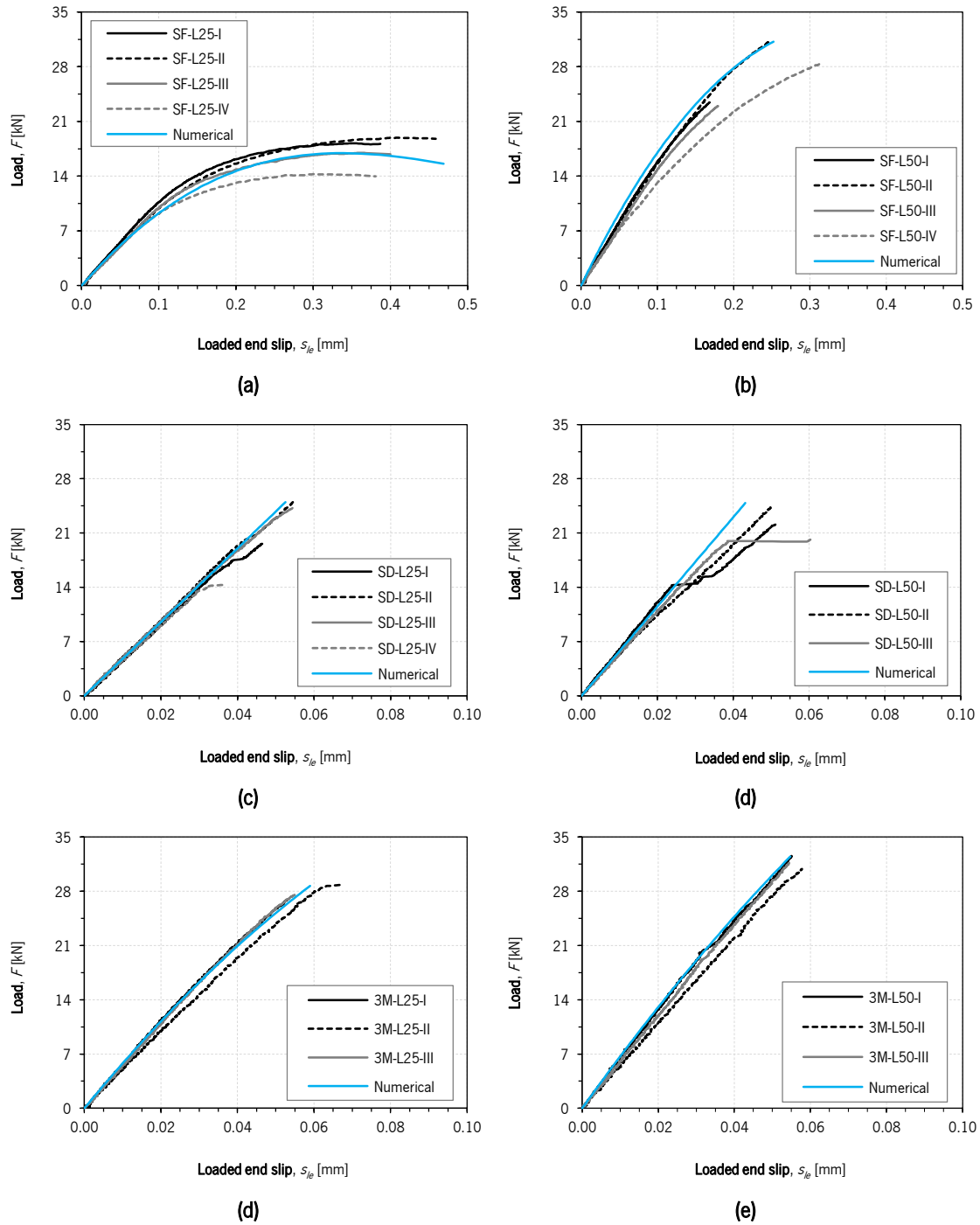
Figure II.19: Numerical and experimental load (F) *vs.* free end slip (s_{le}) responses for each series of double-lap joints: (a) SF-L25, (b) SF-L50, (c) SD-L25, (d) SD-L50, (e) 3M-L25 and (f) 3M-L50.

Furthermore, the relative slips along L_b extracted using the DIC method, $s_{DIC}(x)$, and the ones obtained from the numerical simulations, $s_{NS}(x)$, were compared for the specimens SF-L25-I, SD-L25-I and 3M-L25-I. The $s_{DIC}(x)$ and $s_{NS}(x)$ curves were defined using the last image captured and the maximum load step, respectively. Since the parameters presented in **Table II.6** were obtained using the average $F - s_{le}$ curve of each series and individual specimens are expected to show a scatter in the overall response magnitudes, the dimensionless curves $s_{NS}(x) / s_{NS}(x = 0)$ and $s_{DIC}(x) / s_{DIC}(x = 0)$ were considered. This strategy was also followed for other properties. Thus, this analysis was mainly focussed on the shape of $s(x)$ and, consequently, on the distribution of longitudinal strains in the CFRP laminate, $\varepsilon_{CFRP}(x)$, and shear stresses in the adhesive layer, $\tau(x)$.

The axial strain distributions in the CFRP laminate along L_b were previously determined using the differential equation that characterizes the local bond phenomenon (see more details in **Section 3.3**). According to Sena-Cruz [38], considering the linear elastic behaviour of the reinforcement and neglecting the deformability of adhesive and glass, $\varepsilon_{CFRP,DIC}(x)$ can be obtained thought **Eq. (II.6)**. $s_{DIC}(x)$ is shown in **Figure II.10** for the SF-L25-I and SD-L25-I specimens.

$$\varepsilon_{CFRP,DIC} = \frac{ds_{DIC}(x)}{dx} \tag{II.6}$$

As shown in **Figure II.20**, the DIC technique and the numerical models were able to capture the bond behaviour between the adherends, providing similar distributions in terms of either slip or longitudinal deformations in the CFRP laminate along the bond length. As $\varepsilon_{CFRP}(x)$ is linear in SF-L25-I (see **Figure II.20a**), $\tau(x)$ is approximately constant along L_b due to its flexibility. However, in SD-L25-I, $\varepsilon_{CFRP}(x)$ is governed by a quadratic equation (see **Figure II.20b**) and, consequently, $\tau(x)$ is not constant along L_b. High shear stresses occurred close to the loaded end of the double-lap joints using SikaDur, about 2 times greater than the shear stresses at the free end. As discussed in **Section 3.3**, when stiff adhesives showing linear elastic behaviour are used, the performance of glass-CFRP composite systems is more susceptible to the local features of glass (e.g. tensile strength, edge treatment and density of micro-cracking). On the other hand, the 3M adhesive shows an intermediate type of response that is characterized by being not flexible enough for $\tau(x)$ in 3F-L25-I to be constant, like in the case of SF-L25-I, although flexible enough to avoid high shear stress concentrations near the loaded end, as in the case of SD-L25-I.
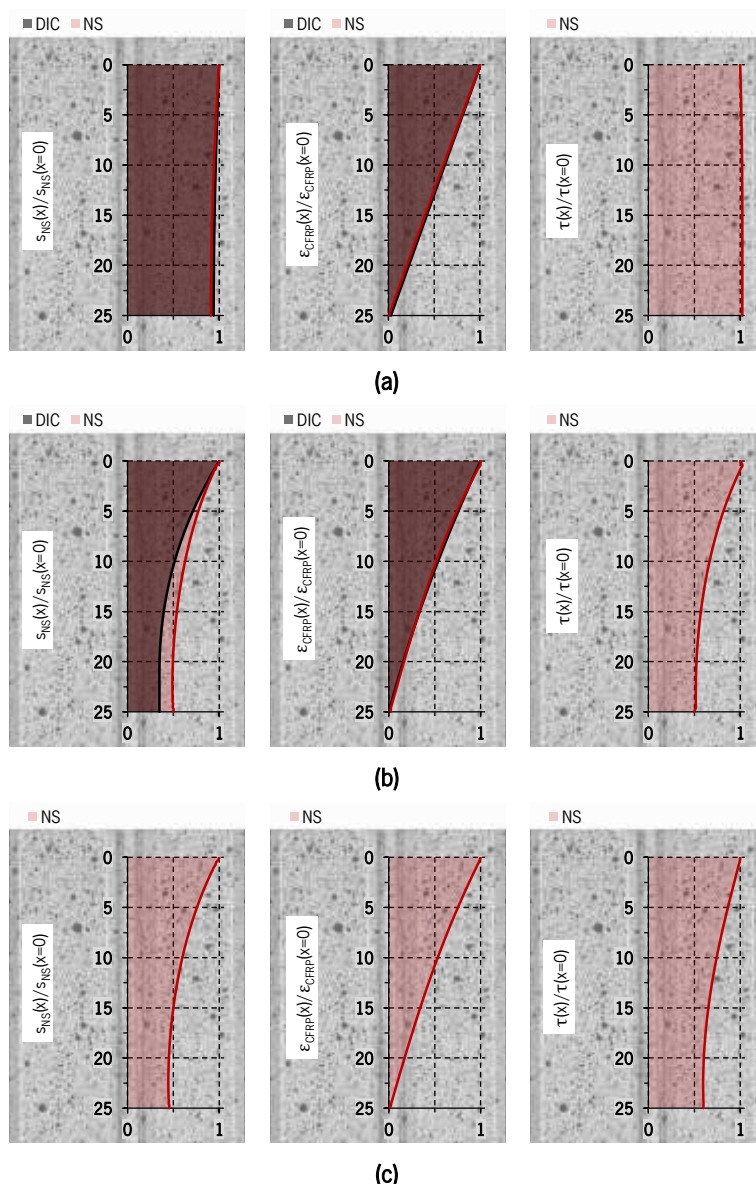
Figure II.20: Distribution of slip, CFRP strain and bond stress along the bond length obtained from DIC method (DIC) and numerical simulations (NS) for (a) SF-L25-I, (b) SD-L25-I and (c) 3M-L25-I specimens. Note: values extracted when the maximum load was reached in each of the specimens.

According to Machalická and Eliášová [17], the shear stresses pattern depends on (i) the geometry of the double-lap joints, that is, the overlap length and the adhesive thickness, (ii) the mechanical properties of the adhesive and (iii) the stiffness of adherend materials and their thicknesses. In order to evaluate the influence of the overlap length in each adhesive, the $\tau(x) / \tau(x=0)$ curves were compared in **Figure II.21** according to following criteria: (i) similar loads during pre-peak response were considered to extract the distribution patterns of both series of each adhesive; and (ii) the two $\tau(x)$ curves of each adhesive were normalized using $\tau(x=0)$ corresponding to L_b of 25 mm.

According to **Figure II.21**, when the stiff adhesives are used, the shape of the shear stress distribution diagrams are significantly influenced by L_b, but the bond stress at the loaded end remains almost constant, since the tensile stress transfer length is smaller. On the other hand, with the polyurethane adhesive, $\tau(x)$ is mainly influenced by L_b in terms of value, since for the investigated overlap lengths the shear stresses remains almost constant along L_b due to the flexibility of the adhesive.

(a)　　　　　　　　　(b)　　　　　　　　　(c)
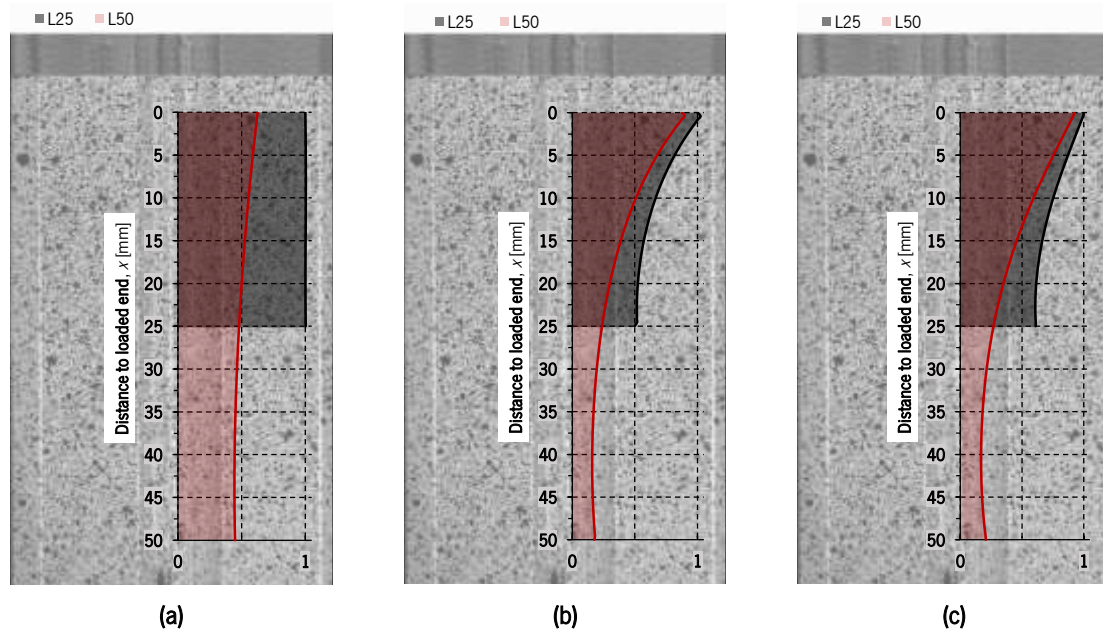
Figure II.21: Evolution of shear stress to shear strength ratio (horizontal axis) at different distances to the loaded end (vertical axis) along the ligament for both bond lengths of each adhesive: (a) SF, (b) SD and (c) 3M specimens. Note: values extracted from the numerical models for the average maximum load of the corresponding L25 series.

6   CONCLUSIONS

In this research work, the structural performance of glass-to-CFRP adhesively bonded joints using different adhesives was experimentally studied. For this purpose, double-lap joints with two bond lengths (25 and 50 mm) were produced and then tested in tension. Considering only structural adhesives that ensure high interaction between the glass and the CFRP, three adhesives were selected to comprise a wide range in terms of material stiffness: (i) the SikaForce L100 7100 (SF), flexible polyurethane adhesive; (ii) the SikaDur 330 (SD) stiff epoxy adhesive; (iii) the 3M DP490 (3M) stiff epoxy adhesive. In addition, analytical and numerical investigations were performed to determine the local bond stress-slip law for each adhesive type, and to extend the analysis of the experimental results.

The main conclusions can be summarized as follows:

- Comparing the experimental responses obtained with stiff and flexible adhesives, significant differences were found in terms of initial stiffness, maximum load and corresponding slip for the studied bond lengths. Due to the linear elastic behaviour of the SikaDur adhesive, the SD double-lap joints showed linear behaviour until failure of the glass, while in the other series of specimens a progressive loss of stiffness for increasing load was observed. A noticeable higher slip at maximum load was achieved in joints with SikaForce, the most flexible adhesive. The high deformation capacity of this adhesive can contribute to increase the ductility of glass-CFRP composite systems (e.g. beams). For these materials and specimen configuration, it was not possible to obtain post-peak (softening) behaviour.

- While debonding at the glass/adhesive interface and cohesive failure in glass occurred in all SF-L25 and SF-L50 joints, respectively, all 3M specimens failed due to the glass cohesive failure in tension, between the rigid and studied bond regions. In the case of the SD series, a mixed failure mode combining cohesive shear debonding in glass and fibre-tear failure in CFRP was observed, due to the high concentration of shear stresses close to the loaded end caused by high stiffness of the SikaDur adhesive. The failure modes could be deducted from the obtained distributions of shear stresses along the bond length which, in turn, were also clearly influenced by the adhesive type, with uniform patterns for the flexible adhesive and non-uniform patterns for the epoxy adhesives, mainly in joints with SikaDur.

- When stiff adhesives with linear elastic behaviour are used in glass-to-CFRP adhesively joints, their bond behaviour is much more susceptible to the local mechanical properties and features of glass (e.g. tensile strength, edge treatment quality, density of micro-cracking and localized damage during handling). As the glass is a heterogeneous material in terms of its tensile strength, the adhesives must combine two essential features to improve the structural performance of glass-to-CFRP connections: (i) high shear strength and (ii) considerable deformation capacity.

- Extremely stiff responses of the adhesives, e.g. SikaDur, can impair the ductile performance of glass-CFRP composite systems (e.g. beams) after cracking, since they are less effective in distributing the shear stresses throughout longer bond lengths and, therefore, do not promote stress redistribution mechanisms. However, this characteristic is also related to the type of reinforcement used.

- The adopted analytical model was capable of predicting the local bond-slip laws of glass-CFRP composite systems with good accuracy for all adhesives, using a linear $\tau - s$ relationship for stiff adhesives with linear behaviour until failure (e.g. SikaDur) and the Dimande's exponential $\tau - s$ relationship for flexible adhesives (e.g. SikaForce), as well as stiff adhesives with non-linear behaviour (e.g. 3M).

- Regardless the tensile strength of the CFRP laminates and glass used, the maximum load *vs.* bond length curves were defined for specimens with 3M and SikaForce adhesives and the effective bond lengths of approximately 150 and 400 mm were found, respectively. This allowed to define the required anchorage length as a function of the ultimate limit state conditions.

- The numerical model for glass-to-CFRP interfaces showed very good predictive performance for all the simulated double-lap joints. Furthermore, it allowed to determine the effective loaded end slip, as well as to quantify the effects of the longitudinal deformation of the glass sheets and three-dimensional effects (e.g. lateral deflection of the glass sheets) experimentally measured. Therefore, it was possible to determine the effective local bond-slip law for each adhesive.

- The approach followed in this study, including the experimental characterization of the bond behaviour of the adhesives, the derivation of the analytical local bond laws, and the numerical simulation of the glass-to-CFRP interfaces, was found useful for the modelling of glass-CFRP composite systems with good accuracy. This may contribute to the structural design of larger scale reinforced glass composite systems.

7   ACKNOWLEDGEMENTS

8   REFERENCES

[1]   Correia J, Valarinho L, Branco F. Post-cracking strength and ductility of glass-GFRP composite beams. Composite Structures 2011;93:2299–309.

[2]   Valarinho L, Correia JR, Branco F. Experimental study on the flexural behaviour of multi-span

transparent glass-GFRP composite beams. Construction and Building Materials 2013;49:1041–53. https://doi.org/10.1016/j.conbuildmat.2012.11.024.

[3]   Balan B, Achintha M. Experimental and Numerical Investigation of Float Glass-GFRP Hybrid Beams. In: Belis, Bos, Louter, editors. Challeging Glass 5 - Conference on Architectural and Structural Applications of Glass, vol. 97, Ghent: 2016, p. 281–96. https://doi.org/10.2514/6.2009-5462.

[4]   Biolzi L, Orlando M, Piscitelli LR, Spinelli P. Static and dynamic response of progressively damaged ionoplast laminated glass beams. Composite Structures 2016;157:337–47. https://doi.org/10.1016/j.compstruct.2016.09.004.

[5]   Cruz P, Pequeno J. Structural Timber-Glass Adhesive Bonding. Challenging Glass, 2008, p. 205–14.

[6]   Cruz P, Pequeno J. Timber-Glass Composite Beams: Mechanical Behaviour & Architectural Solutions. Challenging Glass, 2008, p. 439–48.

[7]   Belis J, Callewaert D, Delincé D, Impe R Van. Experimental failure investigation of a hybrid glass / steel beam. Engineering Failure Analysis 2009;16:1163–73. https://doi.org/10.1016/j.engfailanal.2008.07.011.

[8]   Bos F, Veer F, Hobbelman G, Louter C. Stainless steel reinforced and post-tensioned glass beams. ICEM12 - 12th International Conference on Experimental Mechanics, Bari, Italy: 2004, p. 1–9.

[9]   Louter C, Belis J, Veer F, Lebet J. Structural response of SG-laminated reinforced glass beams; experimental investigations on the effects of glass type, reinforcement percentage and beam size. Engineering Structures 2012;36:292–301. https://doi.org/10.1016/j.engstruct.2011.12.016.

[10]   Louter C, Cupać J, Lebet J. Exploratory experimental investigations on post-tensioned structural glass beams. Journal of Facade Design and Engineering 2014;2:3–18. https://doi.org/10.3233/FDE-130012.

[11]   Louter C, Cupać J, Debonnaire M. Structural glass beams prestressed by externally bonded tendons. GlassCon Global Conference Proceedings, Philadelphia, EUA: 2014, p. 450–9. https://doi.org/10.14296/deeslr.v5i0.1848.

[12]   Palumbo M. A New Roof for the XIIIth Century 'Loggia de Vicari' (Arquà Petrarca – PD Italy) Based on Structural Glass Trusses: A Case Study. Glass Processing Days, Tempere, Finland: 2005.

[13]   Neto P, Alfaiate J, Valarinho L, Correia J, Branco F, Vinagre J. Glass beams reinforced with GFRP laminates: Experimental tests and numerical modelling using a discrete strong discontinuity approach. Engineering Structures 2015;99:253–63. https://doi.org/10.1016/j.engstruct.2015.04.002.

178

[14] Valarinho L, Sena-Cruz J, Correia J, Branco F. Numerical simulation of the flexural behaviour of composite glass-GFRP beams using smeared crack models. Composites Part B: Engineering 2017;110:336–50. https://doi.org/10.1016/j.compositesb.2016.10.035.

[15] Achintha M, Balan B. Characterisation of the mechanical behaviour of annealed glass – GFRP hybrid beams. Construction and Building Materials 2017;147:174–84. https://doi.org/10.1016/j.conbuildmat.2017.04.086.

[16] Keller T, De Castro J. System ductility and redundancy of FRP beam structures with ductile adhesive joints. Composites Part B: Engineering 2005;36:586–96. https://doi.org/10.1016/j.compositesb.2005.05.001.

[17] Machalická K, Eliášová M. Adhesive joints in glass structures: effects of various materials in the connection, thickness of the adhesive layer, and ageing. International Journal of Adhesion and Adhesives 2017;72:10–22. https://doi.org/10.1016/j.ijadhadh.2016.09.007.

[18] Louter C, Belis J, Veer F, Lebet J. Durability of SG-laminated reinforced glass beams: Effects of temperature, thermal cycling, humidity and load-duration. Construction and Building Materials 2012;27:280–92. https://doi.org/10.1016/j.conbuildmat.2011.07.046.

[19] Nhamoinesu S, Overend M. The mechanical performance of adhesives for a steel-glass composite façade system. Challenging Glass 3: Conference on Architectural and Structural Applications of Glass, CGC 2012, Delft, Netherlands: 2012, p. 293–306. https://doi.org/10.3233/978-1-61499-061-1-293.

[20] Speranzini E, Agnetti S, Corradi M. Experimental analysis of adhesion phenomena in fibre-reinforced glass structures. Composites Part B: Engineering 2016;101:155–66. https://doi.org/10.1016/j.compositesb.2016.06.074.

[21] Bedon C, Machalická K, Eliášová M, Vokáč M. Numerical modelling of adhesive connections including cohesive damage. Challenging Glass 6: Conference on Architectural and Structural Applications of Glass, CGC 2018 - Proceedings, 2018, p. 309–20. https://doi.org/10.7480/cgc.6.2155.

[22] Speranzini E, Agnetti S. The technique of digital image correlation to identify defects in glass structures. Structural Control and Health Monitoring 2014:1015–1029. https://doi.org/10.1002/stc.

[23] GOM. Correlate Software and Online Documentation. Rev.121188. 2019.

[24] Simulia. ABAQUS computer software and Online Documentation. v6.12. 2012.

[25] ISO. Plastics - Determination of tensile properties - Part 5: Test conditions for unidirectional fibre-reinforced plastic composites. 527-5, Genève, Switzerland: International Organization for Standardization; 2009, p. 11.

[26] SIKA. Technical Data Sheet SikaForce ® -7710 L100. 2008.

[27]   SIKA. Technical Data Sheet Sikadur®-330. 2017.

[28]   3M. Technical Data Sheet 3M™ Scotch-Weld™ EPX™ Epoxy Adhesive DP490. 1996.

[29]   ISO. Plastics – Determination of tensile properties – Part 2: Test conditions for moulding and extrusion plastics. 527-2, Genève, Switzerland: International Organization for Standardization; 2012, p. 5.

[30]   ISO. Plastics – Determination of tensile properties – Part 1: General principles. 527-1, Genève, Switzerland: International Organization for Standardization; 2006, p. 13.

[31]   ISO. Glass in building — Determination of the bending strength of glass — Part 3: Test with specimen supported at two points (four point bending). 1288-3, Genève, Switzerland: International Organization for Standardization; 2016.

[32]   Machalická K, Vokáč M, Kostelecká M, Eliášová M. Structural behavior of double-lap shear adhesive joints with metal substrates under humid conditions. International Journal of Mechanics and Materials in Design 2019;15:61–76. https://doi.org/10.1007/s10999-018-9404-y.

[33]   Belis J, Van Hulle A, Out B, Bos F, Callewaert D, Poulis H. Broad screening of adhesives for glass-metal bonds. Proceedings of Glass Performance Days 2011, Tampere, Finlandia: 2011, p. 286–9.

[34]   Omairey S, Jayasree N, Kazilas M. Defects and uncertainties of adhesively bonded composite joints. SN Applied Sciences 2021;3. https://doi.org/10.1007/s42452-021-04753-8.

[35]   Feldmann M, Kasper R, Abeln B. Guidance for European Structural Design of Glass Components. Report EUR 26439 EN. Report EUR. Luxembourg: 2014. https://doi.org/10.2788/5523.

[36]   Rodrigues A. Caracterização do comportamento do adesivo estrutural SikaForce 7710. Universidade de Coimbra, 2017.

[37]   Haghani R, Al-Emrani M. A new design model for adhesive joints used to bond FRP laminates to steel beams: Part B: Experimental verification. Construction and Building Materials 2012;30:686–94. https://doi.org/10.1016/j.conbuildmat.2011.12.005.

[38]   Sena-Cruz J. Strengthening of concrete structures with near-surface mounted CFRP laminate strips. [PhD thesis]. Minho University, 2005.

[39]   Focacci F, Nanni A, Bakis CE. Local Bond-Slip Relationship for FRP Reinforcement in Concrete. Journal of Composites for Construction 2000;4(1):24–31.

[40]   Russo G, Zingone G, Romano F. Analytical Solution for Bond-SLip of Reinforcing Bars in R. C. Joints. Journal of Structural Engineering 1990;116:336–55.

[41]   Sena-Cruz J, Barros J. Modeling of bond between near-surface mounted CFRP laminate strips and concrete. Computers and Structures 2004;82:1513–21.

https://doi.org/10.1016/j.compstruc.2004.03.047.

[42]   Cunha V, Barros J, Sena-cruz J. Pullout Behavior of Steel Fibers in Self-Compacting Concrete. Journal of Materials in Civil Engineering 2010;22:1–9.

[43]   Biscaia H, Chastre C, Silva M. Linear and nonlinear analysis of bond-slip models for interfaces between FRP composites and concrete. Composites Part B 2013;45:1554–68. https://doi.org/10.1016/j.compositesb.2012.08.011.

[44]   Biscaia H, Chastre C, Viegas A. A new discrete method to model unidirectional FRP-to-parent material bonded joints subjected to mechanical loads. Composite Structures 2015;121:280–95. https://doi.org/10.1016/j.compstruct.2014.10.036.

[45]   Fernandes P. Bond behaviour of NSM CFRP-concrete systems: durability and quality control. Universdidade do Minho, 2016.

[46]   Ko H, Matthys S, Palmieri A, Sato Y. Development of a simplified bond stress – slip model for bonded FRP – concrete interfaces. Construction and Building Materials 2014;68:142–57. https://doi.org/10.1016/j.conbuildmat.2014.06.037.

[47]   Dimande A. Influência da Interface no Reforço à Flexão de Estruturas de Betão com Sistemas FRP. Universidade do Porto, 2003.

PAPER III

POST-CRACKING PERFORMANCE OF GLASS-CFRP COMPOSITE BEAMS

ABSTRACT: Reinforcement strategies have been developed to prevent catastrophic failures of glass structures after cracking. In this context, the composite action between glass and reinforcement plays a crucial role in the post-cracking performance of glass composite systems. Hence, this paper presents an experimental and numerical investigation on glass-CFRP composite beams manufactured using three different adhesives, with high, intermediate and low stiffness. The experimental programme comprised (i) mechanical characterization tests, (ii) tensile tests on double-lap joints and (iii) flexural tests on composite beams. Moreover, numerical simulations were carried out aiming at providing reliable numerical tools for the design of glass structural elements. Bending tests have shown that it is possible to obtain ductile failure modes in glass elements reinforced with CFRP laminates, sometimes attaining or surpassing the cracking load during the post-cracking phase, depending on the type of adhesive. On the other hand, glass-CFRP composite beams manufactured with stiff, moderate and flexible adhesives were well simulated (i) neglecting the physical existence of the

adhesive layer, (ii) assuming the linear elastic behaviour of the adhesive, and (iii) modelling the bond behaviour of the adhesive joint, respectively.

KEYWORDS: Ductility; CFRP laminate; Glass; Interface behaviour; Numerical Analysis; Residual Strength;

1   INTRODUCTION

Contemporary architecture is nowadays encouraging the structural application of glass due to its aesthetic possibilities and transparency [1, 2]. However, due to the brittle nature of glass, appropriate safety measures must be taken to prevent the sudden collapse of glass structural elements. In the last few decades, the glass industry has improved processing methods to boost its structural application [1,3], namely (i) by developing the lamination technique, which consists of joining glass plies to improve its post-failure performance and safety through the interlayer action, and (ii) by introducing the thermal treatment, commonly called "tempering", to increase the tensile strength of glass by creating favourable compression stresses on the external surfaces and edges. However, none of the mentioned methods provides sufficient toughness to prevent catastrophic collapse in structural applications.

In order to promote ductile failure modes in glass structural elements, several safety concepts have been developed combining glass with timber (e.g. [4,5]), steel (e.g. [6–9]), Carbon Fibre Reinforced Polymers, CFRP (e.g. [10–13]) and Glass Fibre Reinforced Polymers, GFRP (e.g. [1,2,14–17]). These strategies, closely following the ones employed for reinforced concrete, provide post-failure stiffness and ductility. Composite glass systems show the ability to still carry load after the glass breakage, due to the transfer of tensile stresses from the glass to the reinforcement through shear stresses in the adhesive joint. Aspects related to the geometry of the composite glass elements (e.g. [1]), the type of glass (e.g. [8]), the geometry and relative position of the reinforcement element (e.g. [18]) as well as the type of adhesive (e.g. [2]) have also been investigated.

In the last few decades, CFRP materials have been extensively applied for the strengthening of existing concrete structures. Two main distinct concepts have been widely used to apply CFRP reinforcement in construction industry: (i) firstly, the Externally Bonded Reinforcement (EBR) technique, in which the CFRP reinforcement is bonded on the tensile faces of the structural element to be strengthened; and (ii) secondly, the Near Surface Mounted (NSM) technique, in which the CFRP reinforcement is introduced inside pre-opened grooves located in the tensile region of the target structural element

[19,20]. In comparison with traditional reinforcement materials (e.g. steel), CFRP materials are lighter and have higher stiffness and tensile strength, as well as longer fatigue life and higher resistance to corrosion and other aggressive environmental effects [21]. However, the use of CFRP as reinforcement in glass structures is still relatively recent and, for this reason, needs further investigation.

A limited number of studies have addressed the structural behaviour of glass-CFRP composite systems, despite the application of CFRP materials shows great potential to create highly transparent glass structures, since their high strength and stiffness allow to reduce the amount of reinforcement needed to comply with the design requirements [22]. Palumbo [10] followed the concept behind the EBR technique, bonding the CFRP reinforcement to the tensile edge of glass beams. Subsequently, different reinforcement concepts were investigated to improve the structural performance of glass-CFRP composite beams, such as (i) embedding CFRP rods inside the interlayer (e.g. [13]); (ii) designing grooves during the production of laminated glass panels for later insertion of CFRP rods, according to the NSM technique (e.g. [12,23]); and (iii) prestressing the CFRP reinforcement before bonding it to increase the tensile strength of glass by producing favourable compression stresses at the tensile zone (e.g. [11]). In most of these experimental studies, it has been shown that glass-CFRP composite systems provide significant load carrying capacity and ductility after glass rupture. The adhesive type (e.g. resistance, stiffness and overall behaviour) plays a crucial role in the response of glass composite systems (e.g. [24–26]), as glass is a heterogeneous material, with surface flaws randomly distributed on its surfaces, and shows no softening behaviour. Nevertheless, the influence of different types of adhesive on the post-cracking behaviour of glass-CFRP composite systems was not sufficiently addressed by most of these studies. Considering its importance on the overall structural response, this topic needs further attention, considering also its relevance to the systematic design of glass structures.

On the other hand, few studies are found addressing the numerical modelling and design of glass-CFRP composite systems (e.g. [13,27,28]). Most studies have aimed at experimentally validating the structural concept of novel glass-CFRP composite systems, and their translation into reliable analysis and design tools is still insufficiently developed. Because glass behaviour is rather complex, numerical modelling is essential to investigate the structural behaviour of glass-CFRP composite systems and make them useful for industrial and large scale applications. In this regard, the brittle nature of glass and the bond behaviour of glass-to-CFRP adhesive connections are particularly challenging for numerical simulations. Among the various numerical approaches adopted to simulate glass fracture,

such as discrete crack (e.g. [29]), damaged elasticity (e.g. [30]) and rigid body spring (e.g. [31]), the smeared crack approach has been often used in most of the numerical studies found (e.g. [17,28,32]). Furthermore, a dynamic approach has also been adopted, in order to overcome convergence problems related to the low fracture energy of glass (e.g. [13,28]).

In this context, this research investigates the influence of the type of adhesive on the flexural behaviour of glass-CFRP composite beams. The reinforcement element was adhesively bonded to the bottom edge of annealed glass panels, according to the EBR technique, using three different commercial adhesives: two epoxy adhesives, with high and moderate stiffness, and one polyurethane adhesive, with low stiffness. The experimental programme comprised (i) mechanical characterization tests; (ii) tensile tests on double-lap joints; and (iii) full-scale bending tests on glass-CFRP composite beams. It should be noted that the results collected from the first two stages have already been published by Rocha *et al.* [26]. Moreover, the Digital Image Correlation (DIC) method was used to support the analysis of the post-cracking behaviour of the specimens under flexural loading.

In addition to the experimental programme carried out, this research also investigates the development of reliable approaches for the simulation of reinforced glass structures. In particular, it addresses the differences of the adhesives used and how these differences translate into the numerical simulation by adopting the finite elements software ABAQUS 6.14 [33]. Moreover, the bond stress – slip relationships previously calibrated by Rocha *et al.* [26] were used to numerically simulate glass-to-CFRP adhesive interfaces. In order to evaluate the efficiency of these approaches, the numerical results were analysed and compared with the experimental ones considering the following aspects: (i) initial stiffness; (ii) cracking load; (iii) post-cracking stiffness; (iv) crack pattern; and (v) failure mode.

2　EXPERIMENTAL PROGRAMME

2.1.　Materials

The mechanical properties of the glass and adhesives adopted in this study came from a previous one – Rocha *et al.* [26] – since the materials used were similar. Therefore, in the scope of this work, only CFRP materials were subjected to material characterization tests.

Since this investigation was particularly focused on the study of the influence of the composite action between the CFRP reinforcement and the glass substrate on the post-cracking response of glass-CFRP composite systems, single ply annealed glass elements were used, although in practice multi ply laminated glass is preferred for structural applications. On the other hand, heat-strengthened and fully

tempered glass were not adopted in these experiments because the post-cracking behaviour of composite beams would be strongly influenced by the fragmentation pattern of these types of glass, therefore necessarily distinct in terms of strengthening philosophy. **Table III.1** presents the modulus of elasticity (E_g) and the tensile strength ($f_{g,t}$) of the glass used in this investigation.

Table III.1: Average values of the mechanical properties of the involved materials.

Annealed glass				
	E_g [MPa]	$f_{g,t}$ [MPa]		
	74000.0 (2.6%) [1]	39.8 (3.1%) [1]		
CFRP laminate				
	E_r [MPa]	$f_{r,t}$ [MPa]	$\varepsilon_{r,ult}$ [%]	
	172400.0 (2.7%)	2489 (2.2%)	14.4 (3.1%)	
Adhesives				
	E_{adh} [MPa]	f_{adh} [MPa]	$\varepsilon_{adh,ult}$ [‰]	υ [-]
Soft [2]	48.4 (1.3%)	6.13 (1.7%)	250.5 (7.7%)	0.45
Intermediate [2]	1728.1 (3.3%)	32.8 (4.2%)	30.7 (2.8%)	0.38
Stiff [2]	4325.3 (3.1%)	32.34 (3.9%)	8.4 (5.4%)	0.30

Notes:
[1] Value derived from the cracking loads of the four-point bending tests through inverse analysis (see **Table III.3**)
[2] Mechanical properties previously assessed by Rocha *et al.* [26]
Coefficients of variation (CoV) are indicated in parenthesis

The CFRP laminates used in the composite beams, with a cross-section of 10×1.4 [mm], were produced by S&P® Clever Reinforcement Company. The CFRP laminates, with the trademark CFK 150/2000, are prefabricated by pultrusion with unidirectional carbon fibres agglutinated by an epoxy vinyl ester resin matrix. The external surface of the CFRP laminates is smooth and the content in fibres is about 70% in volume. The mechanical properties of the CFRP laminates have been characterized according to ISO 527-5:2009 [34]. Thus, five specimens of $250 \times 10 \times 1.4$ [mm] (length $\times$ width $\times$ thickness) were tested in tension in the longitudinal direction at ambient temperature and at a constant displacement rate of 1.0 mm/min until failure. A clip gauge (type: MFA 12; linearity: 0.1 %; sensitivity: 2.0 mV/V; resolution: 1.0 p.m.; precision: ± 1.5 μ m) with stroke of 50 mm was placed at the central region of each specimen to measure the deformation. The applied load was registered using a universal testing machine with a load cell with a maximum capacity of 200 kN and precision of 0.01 kN. Subsequently, the modulus of elasticity (E_r) of the CFRP material was determined from the slope of the linear trend line between the strain values of 0.05 % and 0.25 % of the stress – strain

response [34]. **Table III.1** presents the main mechanical properties of the CFRP laminates, namely E_r, tensile strength ($f_{r,t}$) and ultimate strain ($\varepsilon_{r,ult}$).

Three commercial adhesives suitable for glass-to-CFRP connections were chosen to cover a wide range of material stiffnesses, namely: (i) the two-component polyurethane adhesive SikaForce®-7710 L100, with low modulus of elasticity; (ii) the two-component epoxy resin-based adhesive (SikaDur®-330), with high modulus of elasticity; and (ii) the two-component epoxy resin-based adhesive (3M DP490), with an intermediate modulus of elasticity in relation to the two adhesives previously mentioned. They are from this point onwards designated as soft, stiff and intermediate, respectively. According to Rocha *et al.* [26], before the mechanical characterization tests, the adhesives were subjected to a post-curing treatment that comprised three thermal stages: (i) 12 h heating branch, from 20 °C to 50 °C; (ii) 24 h constant branch at 50 °C; and (iii) 12 h cooling branch, from 50 °C to 20 °C. The average values of the modulus of elasticity (E_{adh}), tensile strength (f_{adh}) and ultimate strain ($\varepsilon_{adh,ult}$) are presented in **Table III.1**, while **Figure III.1** shows the typical stress – strain curves obtained from tensile tests on five dumbbell shape specimens of each adhesive, according to EN ISO 527-2:2012 [35]. On the other hand, the Poisson's ratios adopted in numerical simulations for the soft, intermediate and stiff adhesives were assessed by Rodrigues [36], Nhamoinesu and Overend [37] and Haghani [38], respectively, and are also shown in **Table III.1**.
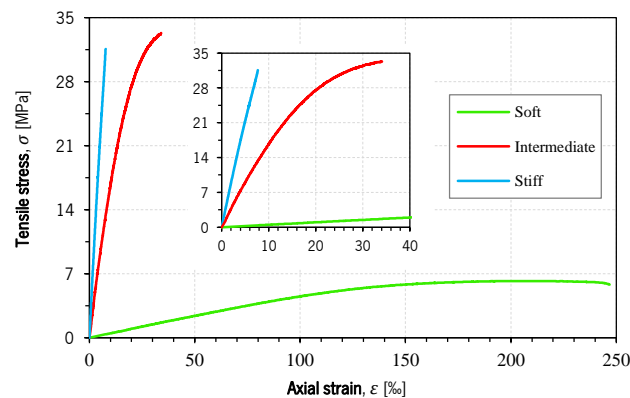
Figure III.1: Typical tensile stress-strain curves of the adhesives used in this investigation

2.2. Properties of the adhesive joints

The composite action between the adherends (level of shear interaction at bonded interfaces) depends on the adhesive used to bond them and plays a very important role after glass cracking in transferring tensile stresses from the glass to the reinforcement. In this sense, double-lap joint tests (see specimen geometry in **Figure III.2**) were previously performed by Rocha *et al.* [26] to characterize the bond behaviour of glass-to-CFRP adhesively bonded connections using the three adhesives referred in

Section 2.1. A bond length of 25 mm was investigated for all the adhesives. The adhesively bonded joints were produced with a layer thickness of 0.3 mm, for the two softer adhesives, and 1.0 mm, for the stiff adhesive, according to technical data sheets and/or suggestions of the suppliers. A total of 12 double-lap joints were manufactured and tested using the nomenclature *xx-i*, where *"xx"* is the type of adhesive (SF, 3M and SD for soft, intermediate and stiff adhesives, respectively), while *"i"* is the specimen of the same series. All test specimens were loaded in tension under displacement control at a constant rate of 1.0 mm/min (displacement between grips) until failure.
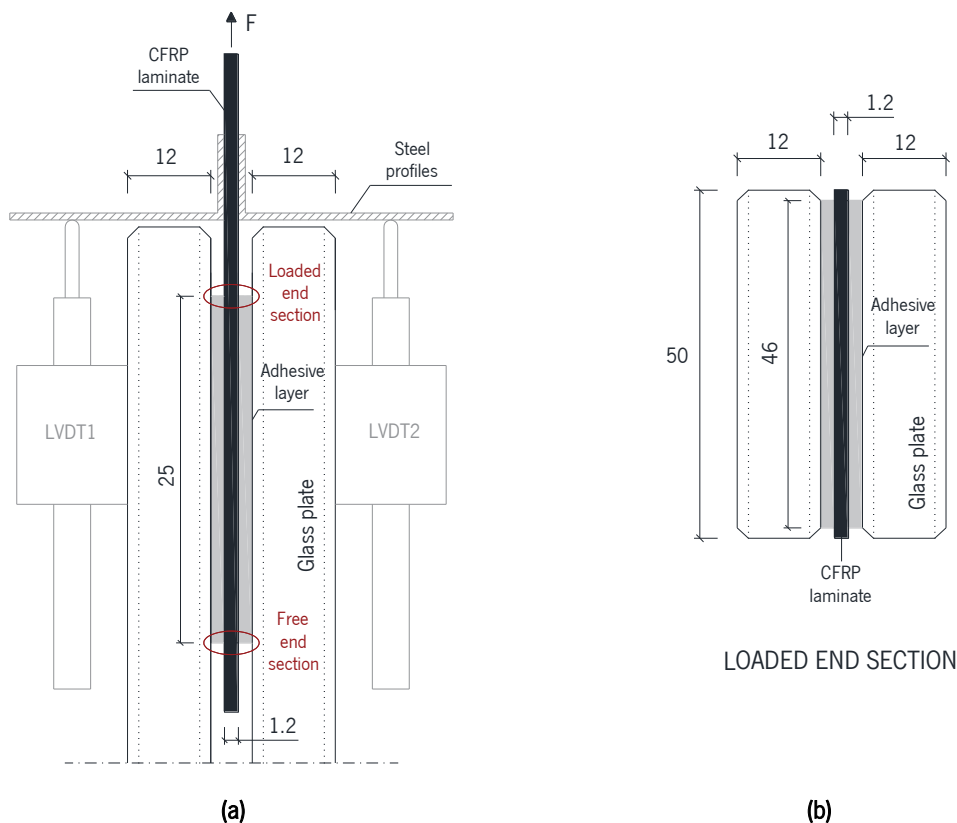
Figure III.2: Double-lap joint tests: (a) specimen's geometry; and (b) loaded end section. Units in [mm].

Figure III.3 shows the load (F) – loaded end slip (s_{el}) curves obtained from the double-lap joints manufactured with soft, intermediate and stiff adhesives. One of the 12 double-lap joint specimens (3M-IV) is not included because it showed premature failure, most likely due to a major surface flaw resulting from impact actions during transport and handing. **Table III.2** presents the average values for each series in terms of initial stiffness (K), peak load (F_p) and corresponding loaded end slip ($s_{le,p}$). Regardless of the adhesive type, no noticeable loss of stiffness occurred until the applied load attained a quarter of the F_p. Thus, the initial stiffness of the specimens was determined from the slope of the linear trend line between the values $F = 0$ and $F = \frac{1}{4} \times F_p$ of the $F - s_{el}$ responses. **Table III.2** also

indicates the failure modes observed in these experiments, using the following nomenclature: I-AG, for debonding at the adhesive/glass interface; FT-L, for fibre-tear failure in CFRP; CS-G, for glass substrate failure; and C-G, for tensile glass failure. Finally, **Figure III.4** shows the typical local failure modes observed in each specimen series.

(a)

(b)

(c)
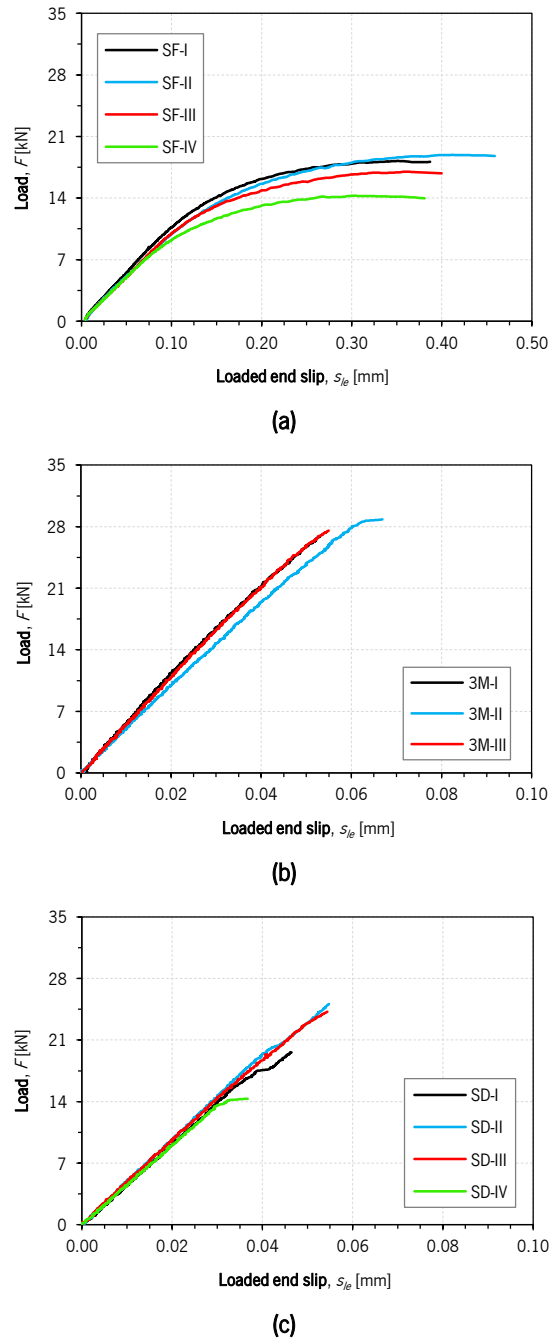
Figure III.3: Experimental load (F) *vs.* loaded end slip (s_{le}) responses obtained from tensile tests on double-lap joints with (a) soft, (b) intermediate and (c) stiff adhesives. Adapted from Rocha et al. [26].

Table III.2: Main properties obtained from double-lap joints for soft (SF), intermediate (3M) and stiff (SD) adhesives.

Series	Specimens	K [kN/mm]	F_p [kN]	$s_{le,p}$ [mm]	Failure mode
SF	4	102.6 (4.1%)	17.1 (10.4%)	0.410 (9.0%)	I-AG
3M	3	523.5 (4.9%)	28.4 (3.6%)	0.060 (9.4%)	C-G
SD	4	468.5 (3.7%)	23.0 (10.5%)	0.048 (15.3%)	FT-L + CS-G

Notes:
C-G, for tensile glass failure; I-AG, for debonding at the interface adhesive/glass; FT-L, for fibre-tear failure in CFRP laminate; and CS-G, for glass substrate failure
The values in brackets are the corresponding coefficients of variation (CoV).

(a)   (b)   (c)
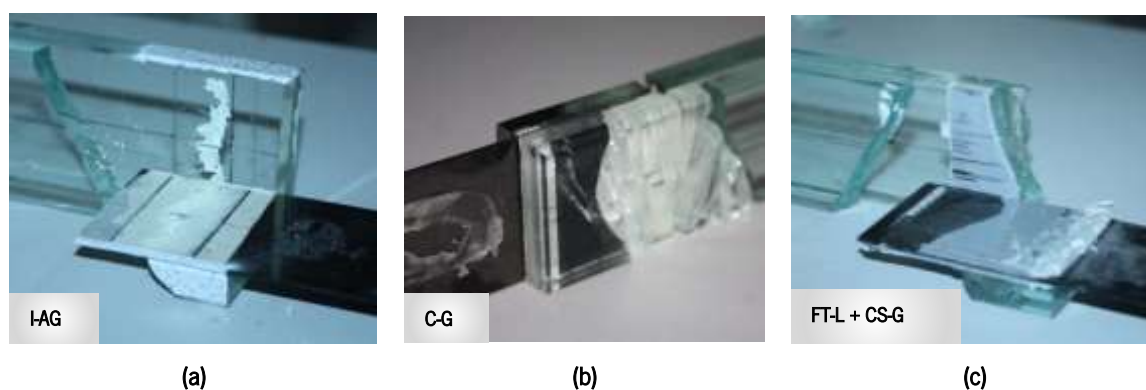
Figure III.4: Failure modes observed in double-lap joint tests: (a) debonding at the glass/adhesive interface in SF specimens; (b) tensile glass failure in 3M specimens; and (c) glass substrate failure and fibre-tear failure in CFRP in SD specimens.

2.3. Four-point bending tests

2.3.1. Geometry and fabrication

The glass-CFRP composite beams, with a length of 1.5 m, were manufactured according to the geometry shown in **Figure III.5**, which consisted of an annealed glass panel of 100 (height) × 12 (thickness) [mm] reinforced at the bottom edge with a CFRP laminate of 10 (width) × 1.4 (thickness) [mm]. The reinforcement was bonded to the glass using the adhesives previously mentioned in **Section 2.1**: (i) the soft adhesive – S*Force* beams; (ii) the intermediate adhesive – 3M beams; and (iii) the stiff adhesive – S*Dur* beams. Similarly to the previous research on double-lap joint specimens [26], adhesively bonded joints were produced with thicknesses of 0.3 mm (S*Force* and 3M series) and 1.0 mm (S*Dur* series). A total of 6 glass-CFRP composite beams were produced and tested, according to the following nomenclature: *i-j*, where *i* identifies the adhesive type (S*Force*, 3M and S*Dur*) and *j* is the test number within each series (I, II). In this case, a reference

glass beam without reinforcement was not considered for testing because sudden failure would be expected once the tensile strength of glass was first reached.

(a)

(b)

(c)
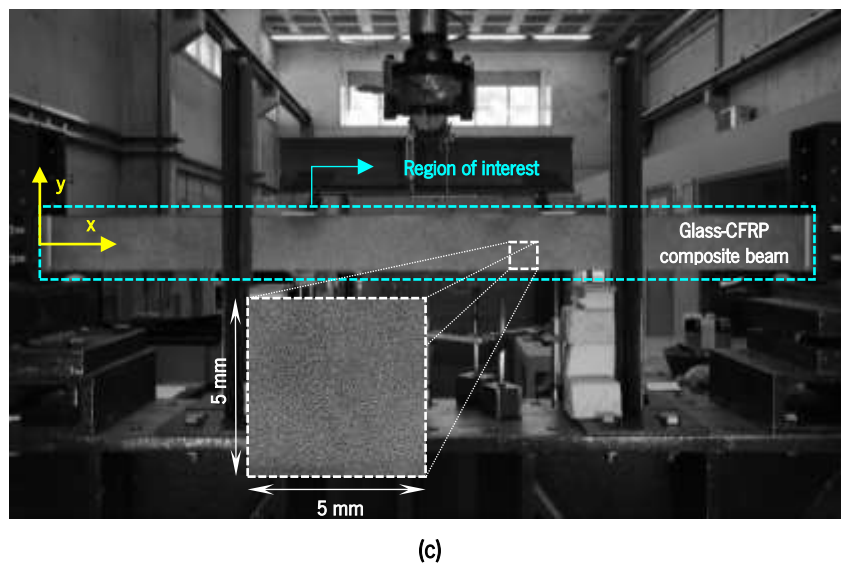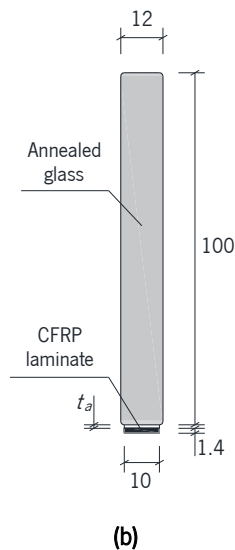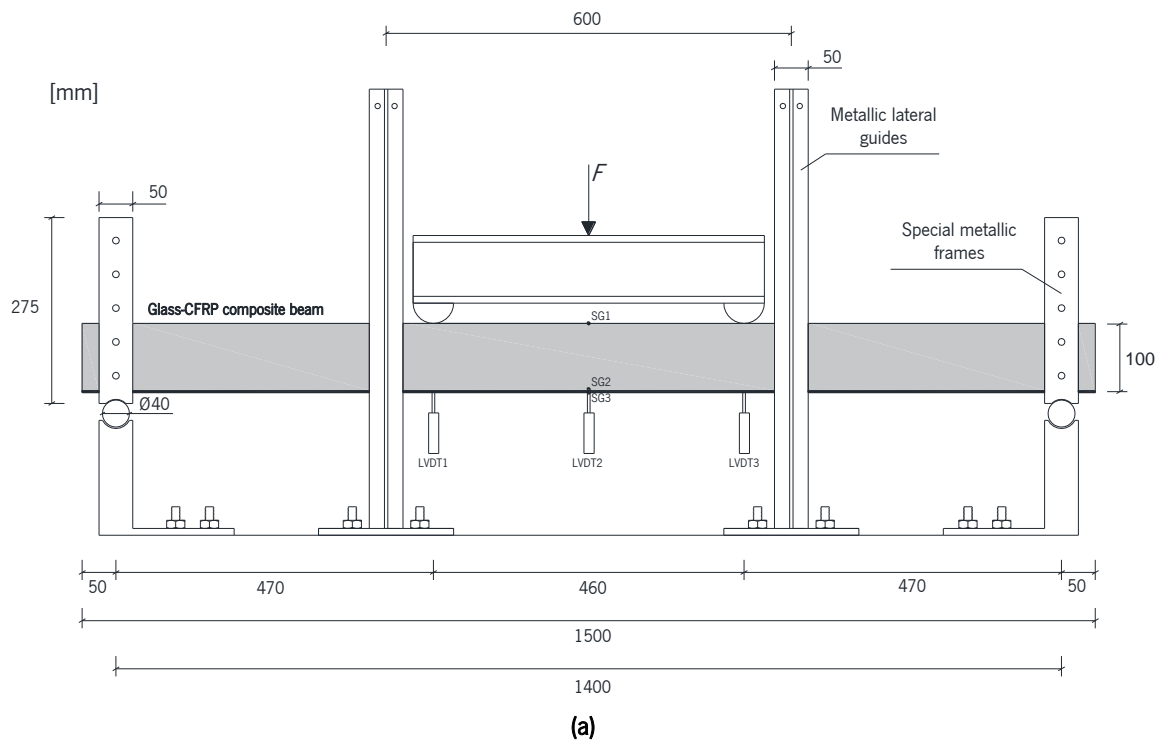
Figure III.5: Four point bending tests on glass-CFRP composite beams: (a) geometry and test configuration, including the lateral guides and the support frames used to guarantee the adequate support conditions; (b) cross-section of the beam specimens; and (c) experimental setup, including the region of interest defined to the DIC analysis of the specimens and detailing the speckle pattern. All units in [mm].

All beams were prepared according to the procedure described below. First, CFRP laminates and glass sheets were cut. The glass edges were subjected to grinding and polishing treatments to eliminate any

191

flaws and defects resulting from the cutting process, as well as to avoid any accidents during handling of the annealed glass beams. Then, the bonding surfaces were degreased and cleaned with acetone. After that, the adhesives were prepared according to the technical specifications and applied with the assistance of a spatula on the CFRP laminate and on the bottom edge of the glass panel. Thereafter, both adherends were carefully assembled using a special support system specifically built to guarantee the alignment between them. The thickness of the adhesive layer was controlled using commercial steel wires with a diameter of 0.3 mm (for the soft and intermediate adhesives) and 1.0 mm (for the stiff adhesive). Taking advantage of the glass transparency, a careful visual inspection of the adhesive layer was carried out to avoid voids. Subsequently, in order to guarantee the correct bonding conditions between adherends, gravity loads were applied on the top edge of the glass panels for 7 days. It is noteworthy to mention that no significant misalignments were observed after bonding, despite the slenderness of the composite beams. Finally, the composite beams were placed in a climatic chamber and subjected to the post-cure treatment described in **Section 2.1**. The post-curing conditions adopted were prescribed with the aim of increasing the glass transition temperature of the adhesives. As such, possible effects due to slightly different testing ages, or different ambient temperatures, could be avoided. These post-curing conditions also consider the typical service conditions, representing the expected range of temperature variations and aging in glass applications.

2.3.2. Experimental setup and test procedure

As shown in **Figure III.5**, all glass-CFRP composite beams, with a span of 1.4 m, were tested under symmetrical four-point bending configuration, with the load points 460 mm apart themselves. The load points were materialized by a metallic profile together with steel rollers. In order to avoid metal-glass contact, polytetrafluoroethylene (PTFE) plates were positioned between the steel rollers and the top edge of the beams (see **Figure III.6**). A steel roller was also placed between the hydraulic jack and the metallic profile in order to ensure its rotation and, therefore, equal loads at both load points during the test. In addition, to prevent lateral displacements (e.g. lateral-buckling effect), two pairs of vertical metallic guides were symmetrically positioned at 300 mm from the mid-span section, as shown in **Figure III.5a**. These lateral metallic guides were attached to the steel loading frame using screws and each pair was later joined using threaded rods to increase their lateral flexural stiffness. Finally, the inner surfaces of the lateral guides – in contact with the glass panel – were carefully wrapped using a thin film of polytetrafluoroethylene, in order to prevent frictional forces during the tests and to avoid direct metal-glass contact. In-plane flexural rotations were free at both supports, and one of the supports allowed also the longitudinal sliding of the beams. As illustrated in **Figure III.6**, special

metallic frames were used to restrain torsional rotation of the beams at the edge supports. These metallic frames were specifically designed to be placed above the rollers and their side faces were drilled to allow the beams to be fixed. Therefore, after positioning the beams, threaded screws were inserted into the holes of the metallic frames and carefully pressed against the glass, using intermediate PTFE plates to avoid glass-steel contact.

(a)   (b)
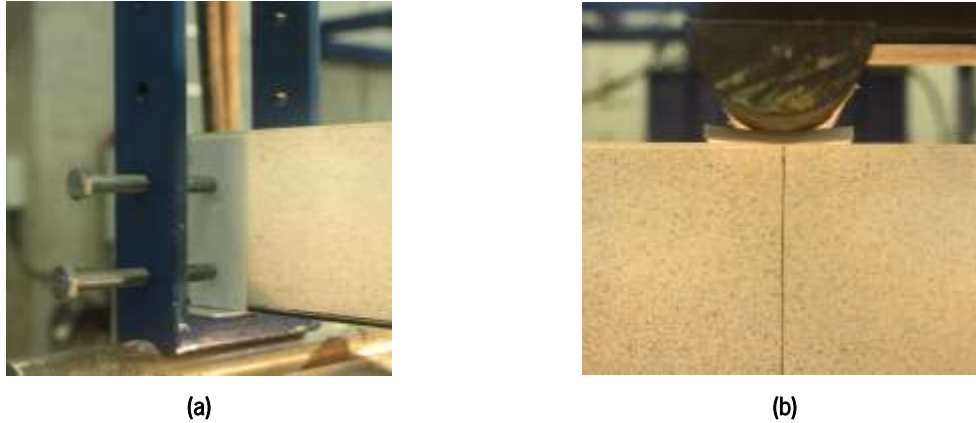
Figure III.6: Strategies adopted to mitigate undesirable affects during the tests: (a) metallic frame to prevent torsional rotations at the supports sections; and (b) PTFE plates to avoid metal-glass contact.

Displacement transducers – Linear Variable Differential Transformer (LVDT) – with stroke of 25 mm and 50 mm and precision of 0.01 mm were used to measure the deflection at the load point sections (LVDT1 and LVDT3) and at mid-span (LVDT2). The applied load was measured by means of a load cell with a maximum measuring capacity of 200 kN and precision of 0.01 kN. In addition, axial strains were measured at the mid-span section of all beams using three strain gauges (type: BFLA-5-3-3L by TML; measuring length: 5 mm; gauge factor: 2.08 ±1 %), positioned on the top edge of the beam (SG1), as close as possible to the bottom edge of the glass pane (SG2) and on the reinforcement (SG3). All beams were loaded monotonically under displacement control at a speed of 1 mm/min until failure. The applied load and the deflection were measured at an average frequency of 50 Hz, while the axial strain was measured at an average frequency of 3 Hz due to technical limitations on the data acquisition system. All tests were conducted in laboratory environment at an average temperature of 22 °C and relative humidity of 60 %. Before the tests, a plastic film was glued to one of the side faces of the beams to avoid the dispersion of fragments after crack initiation.

The DIC method was also used to document the evolution of the cracking mechanisms of the glass-CFRP composite beams and to complement the analysis of the structural responses obtained from the four-point bending tests. For this purpose, a thin spray of white matt paint was applied over the region of interest (ROI), followed by a spray of black dots using matt paint. The camera used to capture

the images had a full frame CMOS sensor (7360 × 4912 pixels), and the focal distance of the lens was 35 mm. A working distance (distance between the external face of the camera and the target surface) of approximately 1500 mm was adopted. All beams were monitored in order to apply the DIC technique using the GOM Correlate 2019 software [39]. The ROI of the S*Force*-I beam, the first beam to be tested, included only half of the span. However, due to the brittle nature of the annealed glass and its unpredictable behaviour, the cracking occurred only on the unmonitored half of the span. Thus, for the remaining tests, the ROI was extended to the entire span of the beams (see **Figure III.5c**). Images were recorded at 5 s intervals.

3   RESULTS AND DISCUSSION

Figure III.7, **Figure III.8** and **Figure III.9** show the load (F) – mid-span deflection (δ) responses of the S*Force*, 3M and S*Dur* series, respectively, as well as the crack patterns at different stages during the post-cracking stage, extracted from DIC technique. Although small parts of the crack patterns have been hidden by the metallic lateral guides, the DIC method was extremely useful to document and understand the post-cracking behaviour of the glass-CFRP composite beams. **Table III.3** summarizes the average results of each series in terms of initial stiffness (K), cracking load (F_{cr}) and corresponding deflection (δ_{cr}), maximum load (F_{max}) registered after initial glass cracking and ultimate deflection (δ_{ult}). **Table III.3** presents also the residual strength index, which is the relationship between F_{max} and F_{cr}, and the ductility index, which is the relationship between δ_{ult} and δ_{cr}, which measure the ability of each series to recover from the initial load drop and to deform during the post-cracking stage, respectively. These two parameters allowed to quantitatively assess the influence of the adhesive on the post-cracking behaviour of glass-CFRP composite beams, which is of great importance from a structural application perspective.

3.1.   S*Force* beams

Both S*Force* beams have shown similar experimental responses. A linear behaviour during the pre-cracking stage was followed by a sudden load drop associated to the appearance of a V-shaped crack in the pure bending zone (see **Figure III.7**). Subsequently another V-shaped crack appeared in both S*Force* beams, between the two branches of the first V-shaped crack. Finally, when the first shear crack appeared, the S*Force* beams failed by debonding of the CFRP laminate at the adhesive/glass interface (see **Figure III.10a**), as observed in double-lap joints with the soft adhesive (see **Figure III.4a**). Both S*Force* beams exhibited higher values of F_{max} than F_{cr} (average residual strength equal to 117 %

– see **Table III.3**), showing their ability to recover from the load drop experienced when the first crack formed.
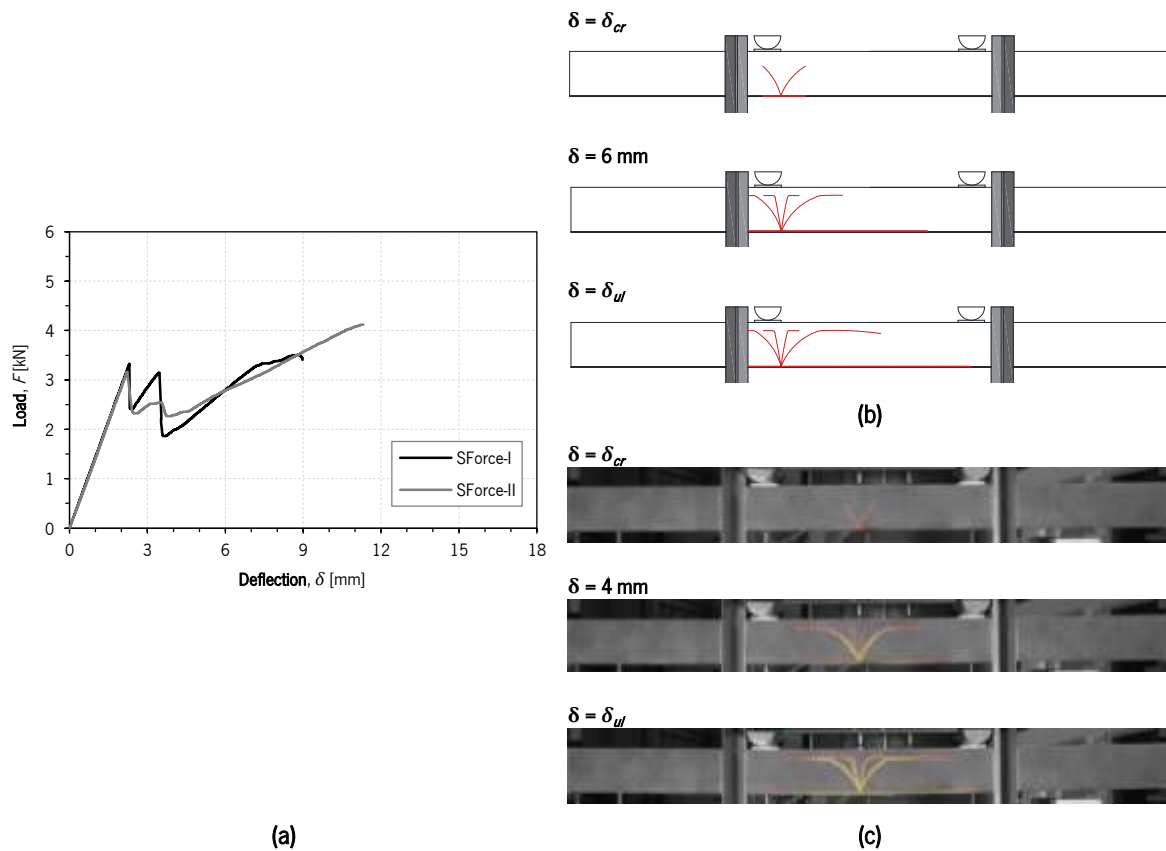
Figure III.7: Flexural behaviour of the S*Force* series: (a) load *versus* mid-span deflection curves; (b) illustration of the crack patterns observed in the S*Force*-I; and (c) DIC crack patterns of the S*Force*-II beam at different stages.

Cracks form very quickly in glass, causing sudden increases in shear stresses at the glass-to-reinforcement interfaces. Due to the low toughness of the soft adhesive, the first V-shaped crack caused partial debonding of the CFRP laminate in its vicinity (captured by the DIC crack patterns shown in **Figure III.7b** and **Figure III.7c**). Consequently, large crack opening displacements and extensive horizontal crack propagation (crack branching) occurred at the beginning of the post-cracking stage. After crack initiation, the neutral axis moves towards the top edge of the glass panel until a new balance of internal forces is achieved, with a compression force in the uncracked glass zone and a tensile force in the reinforcement. However, this did not happen between the branches of the first V-shaped crack, where the uncracked glass zone remained resisting both compression stress (above the neutral axis) and tensile stress (below the neutral axis). Hence, with increasing load, another V-shape crack appeared between the branches of the first one, in the stiffest section of the uncracked glass zone (near the crack bifurcation section). Thus, glass branching seems to provide additional

carrying capacity at the beginning of the post-cracking stage, before the appearance of the second V-shaped crack.

(a)

(b)

(c)
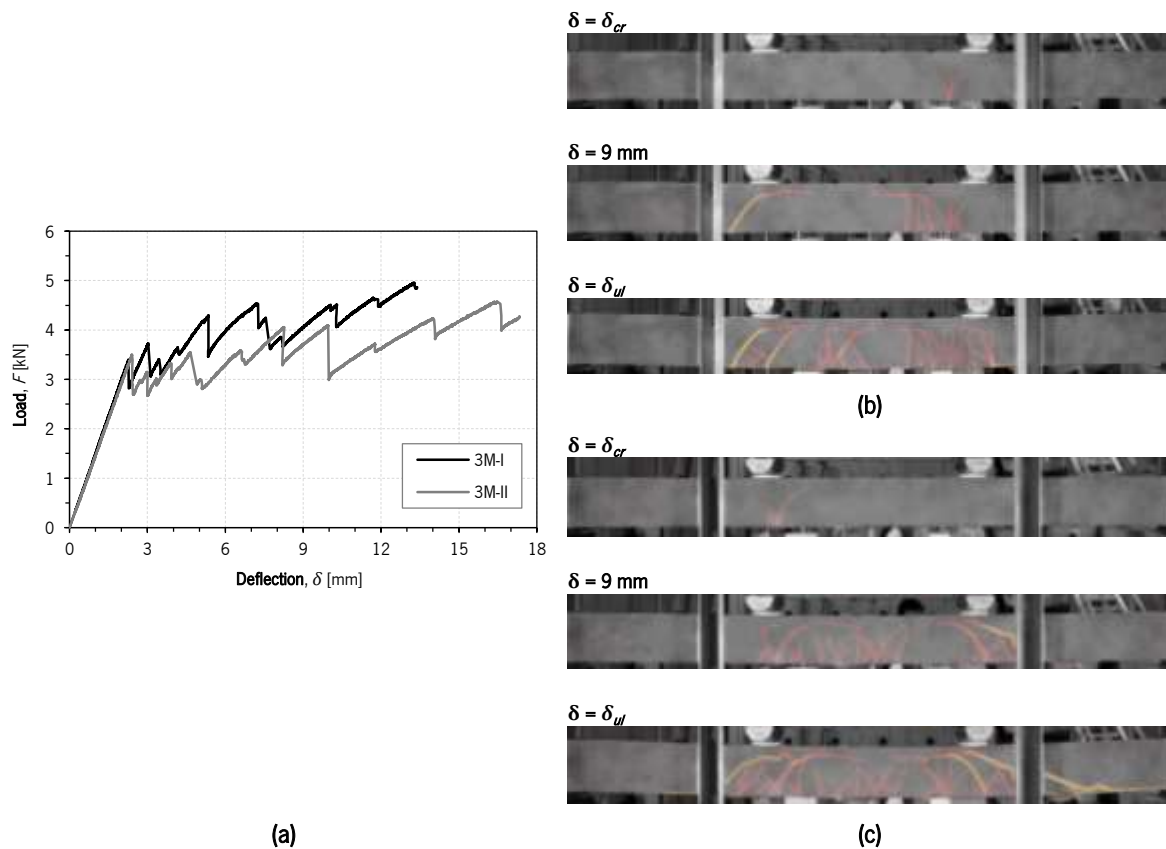
Figure III.8: Flexural behaviour of the 3M series: (a) load *versus* mid-span deflection curves; and DIC crack patterns of the beams (b) 3M-I and (c) 3M-II at different stages.

Similar responses have been obtained by other authors (e.g. [1,2,18]) when composite glass beams are produced using flexible adhesives (e.g. polyurethane or acrylic) to join the adherends. The crack pattern is formed by few (or eventually just one) large V-shaped cracks, typically more concentrated near the load point sections. The increase in deflection is associated to the progressive detachment of the reinforcement element towards the supports, as well as the horizontal propagation of the branches of the V-shaped cracks, separating the compression glass zone from the tensile glass zone and providing a certain level of ductility to the beams.

(a)

(b)

(c)
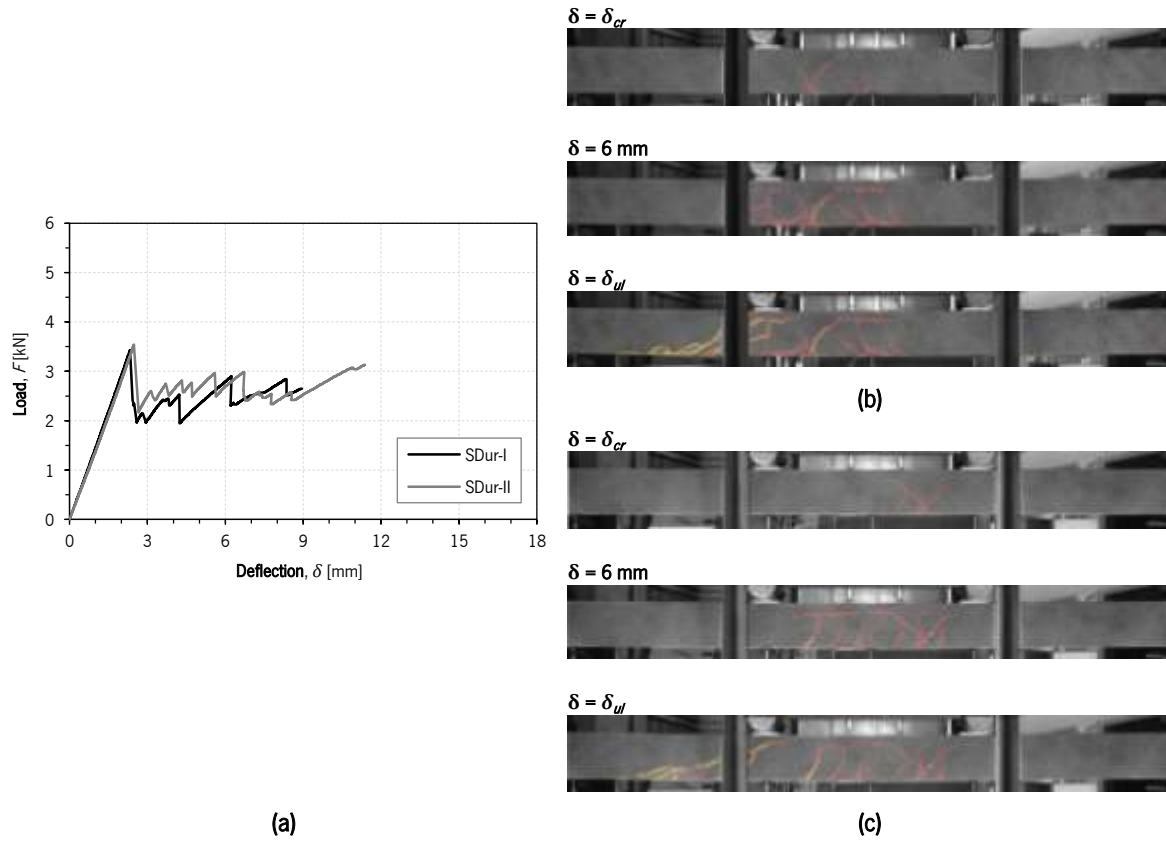
Figure III.9: Flexural behaviour of the S*Dur* series: (a) load *versus* mid-span deflection curves; and DIC crack patterns of the beams (b) S*Dur*-I and (c) S*Dur*-II at different stages.

Table III.3: Main properties of glass-CFRP composite beams with soft (S*Force*), intermediate (3M) and stiff (S*Dur*) adhesives, indicating the average results obtained for each series.

Specimen	K [kN/mm]	F_{cr} [kN]	δ_{cr} [mm]	F_{max} [kN]	δ_{ult} [mm]	Residual strength [%]	Ductility [%]
S*Force*-I	1.44	3.46	2.39	3.63	8.98	105	375
S*Force*-II	1.43	3.29	2.30	4.24	11.31	129	492
S*Force* series	**1.44**	**3.38**	**2.35**	**3.94**	**10.14**	**117**	**434**
3M-I	1.50	3.40	2.27	4.96	13.39	146	591
3M-II	1.45	3.35	2.40	4.58	17.34	131	721
3M series	**1.48**	**3.45**	**2.34**	**4.77**	**15.36**	**138**	**656**
S*Dur*-I	1.47	3.55	2.41	3.02	8.95	85	371
S*Dur*-II	1.43	3.67	2.56	3.26	11.38	89	444
S*Dur* series	**1.45**	**3.61**	**2.49**	**3.13**	**10.16**	**87**	**407**
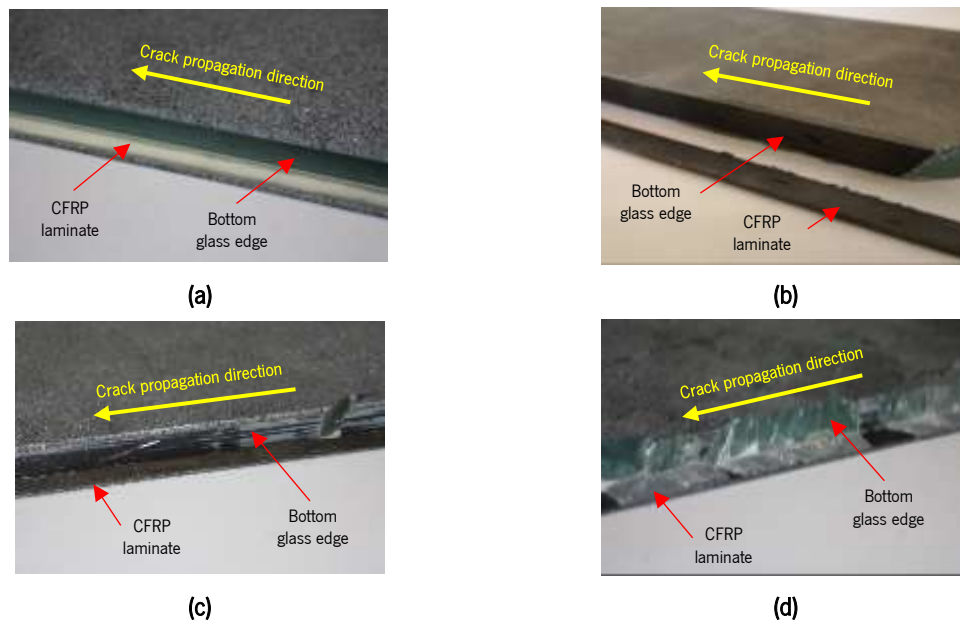
Figure III.10: Failure modes observed in the composite beams after four-point bending tests: (a) debonding at the adhesive/glass interface in S*Force* beams, (b) fibre-tear failure in CFRP in 3M beams; and (c) fibre-tear failure in CFRP and (d) glass substrate failure in S*Dur* beams.

3.2.   3M beams

3M beams also showed similar behaviour, both in the pre- and post-cracking stages. The experimental responses showed a linear elastic behaviour until first visible crack appeared. Thereafter, additional cracks started to form towards the supports, and each new crack appearing resulted in a new sudden load drop and subsequent non-linear load recovery in the experimental response, showing also a progressive loss of stiffness (see **Figure III.8**). The 3M-I beam failed abruptly due to the sudden detachment of the reinforcement element (shear span) by fibre-tear failure in CFRP (see **Figure III.10b**), while for the 3M-II beam the test was terminated before collapse was reached, due to excessive deformation. Possible explanations for fibre-tear failure in CFRP are discussed later in **Section 3.3**. In the case of the 3M-II beam, the adhesive visually showed a remarkable resistance to peel stresses induced by shear cracks. Both 3M beams demonstrated a clear ability to recover from the sudden load drop occurred at the first crack. After crack initiation, they have reached a maximum load of 4.77 kN, increasing 38 % with respect to the cracking load.

3.3.   S*Dur* beams

The two S*Dur* beams showed very similar flexural behaviours, both in the pre- and post-cracking stages. After a linear elastic response until the appearance of the first crack (see **Figure III.9**), a sequence of sudden drops in load occurred due to the initiation of new cracks. Each load drop was

followed by an approximately linear increase in load carrying capacity, but showing a progressive loss of stiffness after every new crack. Initially, the glass cracking occurred exclusively in the pure bending zone, with cracks showing an approximately vertical trajectory. In a subsequent stage, cracks started to form closer to the supports, in the shear span, and showed an increasing inclination towards the supports. Finally, the failure of the two S*Dur* beams was triggered by the appearance of successive shear cracks that gradually led to the detachment of the CFRP laminate towards the support (in the shear span).

In line with the failure modes observed in double-lap joint tests with stiff adhesive (see **Figure III.4c**), the beam collapse resulted from glass substrate failure and fibre-tear failure in CFRP (see **Figure III.10c** and **Figure III.10d**, respectively). Fibre-tear failure in CFRP can be explained by the low fracture energy of the glass, which caused (i) release of large amounts of strain energy during glass rupture, inducing dynamic forces at the CFRP/adhesive interface, and (ii) sudden increments of tensile force at the CFRP reinforcement after every new crack. Finally, unlike the previous beam series (S*Force* and 3M), the cracking load of S*Dur* beams (F_{cr} = 3.61 kN) was never attained or surpassed during the post-cracking stage ($F_{cr} > F_{max}$ = 3.13 kN). Probably the high stiffness of the adhesive resulted in higher stress gradients at the cracks and interfaces between the glass substrate and the reinforcement, leading to premature failure with respect to the previous two series using softer adhesives.

3.4. Influence of the adhesive stiffness

In general, all beams presented two distinct stages in their structural response. Before cracking, the flexural behaviour was clearly linear elastic. After cracking, the experimental responses were strongly influenced by the type of adhesive, and a progressive loss of stiffness was observed due to the propagation of cracks towards the supports and/or progressive detachment of the CFRP laminate. During the post-cracking stage, all beams showed to be able to maintain their integrity, which is not always the case for glass structures. The effective transferring of the tensile stresses from the cracked glass to the reinforcement was in general guaranteed by all adhesives studied.

All series presented similar values of initial stiffness and cracking load. The adhesive layer represents an almost negligible part of the cross-section, between 0.25 %, in S*Force* and 3M series, and 0.83 %, in S*Dur* series, with respect to the total cross-section area. Therefore, the type of adhesive did not influence significantly the values of K obtained before cracking. Furthermore, thinner layer thicknesses were adopted for adhesives with lower modulus of elasticity, mitigating any differences in the initial

stiffness caused by the adhesives (e.g. shear stiffness). In any case, the results of the flexural stiffness ($K_{SForce} < K_{SDur} < K_{3M}$) are consistent with the ones obtained from double-lap joint tests (see **Table III.2**), with a difference of 2.8 % (average value) between K_{SForce} and K_{3M}.

More significant differences between the beam series were observed in terms of cracking load. While the S*Force* series exhibited the lowest cracking load (F_{cr} = 3.38 kN), the S*Dur* series showed the highest one (F_{cr} = 3.61 kN), with a difference of 6.8 % between them. Although high scatter of tensile strength is generally expected for glass, these differences are clearly related to the composite action provided by each adhesive, as well as the layer thickness adopted in each series. According to the double-lap joint tests [26], epoxy adhesives provided greater composite action than the polyurethane one. Based on the Euler-Bernoulli theory, the bending stress is defined by **Eq. (III.1)** and depends on the bending moment (M_{cr}) corresponding to $F = F_{cr}$, the moment of inertia (I_{el}) and the distance (y_{el}) between the target fibre and the neutral axis. The thicker and stiffer the adhesive, the greater the moment of inertia and the shorter the distance from the bottom edge of the glass panel to the neutral axis, and according to **Eq. (III.1)**, the higher the beam cracking load. Accordingly, the 3M series presented an intermediate F_{cr} among the other tested series, which was 2.1 % higher than the one of the S*Force* series, since the intermediate adhesive provides greater composite action than the softest one, and 4.4 % lower than the one of the S*Dur* series, since the intermediate adhesive was applied in an adhesive layer 3 times thinner than the stiffest one.

$$f_{g,t} = \frac{M_{cr}}{I} \cdot y \qquad \text{(III.1)}$$

Regarding the post-cracking behaviour, the type of adhesive significantly influenced the cracking process and, in turn, the post-cracking performance of glass-CFRP composite beams. However, regardless of the adhesive type, all composite beams exhibited pseudo-ductile behaviour during the post-cracking stage, thus avoiding the catastrophic collapse typically observed in all-glass beams. When the first V-shaped crack appeared in S*Force* beams, their flexural stiffness decreased gradually due to the progressive debonding of the CFRP laminate at the adhesive/glass interface, preventing the formation of dense crack patterns. In contrast, a much greater number of flexural cracks appeared in beams with stiffer adhesives, distributing diffusely towards the supports and leading to the loss of flexural stiffness and later to the detachment of the CFRP laminate.

In S*Force* beams, the adhesive joint was damaged in the vicinity of the first V-shape crack, as previously observed by Louter *et al.* [18], due to (i) the shock load (dynamic effects) caused by glass

breakage and (ii) the low toughness of the soft adhesive. After the initial glass cracking, the adhesive damage gradually propagated towards the supports (see **Figure III.7**), developing an extended plastic zone that redistributed stresses and smoothed local stress concentrations in the glass substrate, as opposed to what was observed in the S*Dur* beams. Stress whitening of the adhesive normally occurs during the plastic zone development. However, this was not clearly observed in S*Force* beams probably due to the light colouring of the soft adhesive (beige). The resistant mechanism of the S*Force* beams was formed by the undamaged adhesive joint zone at the beam ends (anchorage effect), which provided sufficient post-cracking stiffness for both S*Force* beams to reach residual strength indexes higher than 100 %.

The 3M series have shown the highest residual strength and ductility among all the tested beam series, probably due to the moderate stiffness of the adhesive used. Unlike the soft adhesive, the high toughness of the intermediate one prevented the partial debonding of the CFRP laminate when the first flexural crack formed, creating stiffer post-cracking responses. On the other hand, in comparison with the stiff adhesive, the lower stiffness of the intermediate one smoothed the stress concentration at the tip of the delamination cracks, delaying the progressive detachment of the CFRP laminate towards supports.

Although S*Dur* beams were manufactured with the stiffest adhesive among all tested, they exhibited the lowest residual strength index (87 %) of all the tested beam series. Although many cracks are formed before beam collapse and the system adhesive-reinforcement seems to be able to effectively restrain the propagation of new cracks and allow the formation of additional ones, S*Dur* beams do not seem to be able to recover from the sudden load drop occurred at the beginning of the post-cracking stage and attain higher load levels ($F_{max} > F_{cr}$). As noticed in double-lap joint tests [26], the stiff adhesive promotes high stress concentrations near the loaded end, magnifying the dynamic response in glass-CFRP composite systems. Consequently, mode-II failure occurred in the glass substrate, promoting the premature debonding of the CFRP laminate and resulting in lower bond strength despite the higher resistance exhibited by the stiff adhesive. This unexpected behaviour has also been obtained by other authors (e.g. [24]) when stiff/brittle adhesives are used to produce glass composite systems. Theoretically, for short term loading and excluding time-dependent effects, the first crack forms at the section where the lowest tensile strength is found, and only for $F > F_{cr}$ should additional cracks appear in the pure bending zone. In contrast to the two softer adhesives, which have a non-linear response in tension with visible reduction in stiffness near the peak load and failure, the stiff adhesive presents

constant stiffness until failure and, as a consequence, has greater difficulty in accommodating the strain energy released during the formation of new cracks. This means that the stiff adhesive is not as capable of dampening the dynamic effects induced by glass cracking as the two softer adhesives. As a consequence, the shock load can lead to the growth of existing flaws in the surrounding areas (bottom edge of the glass panel), thus reducing the tensile stress required for the formation of new cracks. This explain why the S*Dur* series exhibited a much lower residual strength index (< 100 %) than the 3M series. Furthermore, dynamic effects also explain why shear cracks only appeared in one of the shear spans (unlike the 3M series). The appearance of a new crack was governed by the distance from the previous ones, since the tensile strength of glass is lower the closer the older cracks are.

The failure modes observed in bending tests presented features similar to those observed in double-lap joint tests [26], showing the agreement between the results obtained from both test configurations. As shown in **Figure III.10**, fibre-tear failure in CFRP occurred in both S*Dur* beams and the 3M-I beam, while interface debonding at the adhesive/glass interface was noticed in both S*Force* beams. Finally, it is noteworthy that the post-cracking performance and the failure mechanism of glass composite beams was significantly influenced by dynamic effects induced by glass breakage, as well as the elastic strain energy absorption capacity of the adhesives used to join the components [40].

4   NUMERICAL SIMULATIONS

4.1.   Simulation strategy

Considering the importance of establishing practical and reliable design approaches for glass structures, the following section is dedicated to the numerical simulation of the flexural tests conducted, based on the material properties and the bond behaviour previously characterized using double-lap joints [26]. The numerical simulations were performed using ABAQUS/Explicit software [33]. The main objective of this numerical study was to demonstrate that with simple mechanical tests, such as the double-lap bond and three point bending tests, it is possible to accurately estimate the structural response of complex glass structural systems (e.g. glass-CFRP composite systems) and support their safe design.

Three different hypotheses were studied to simulate the adhesive joint: (i) the *Perfect Bond* (*PB*) between the glass and CFRP laminate, neglecting the physical existence of the adhesive layer; (ii) the *Elastic Behaviour* (*EB*) of the adhesive, using plane stress elements for 2D models or solid elements for 3D models, and assuming perfect bond at the CFRP/adhesive and adhesive/glass interfaces; and

(iii) the *Interface Behaviour* (*IB*) of the adhesive joint, using zero thickness interface elements to simulate the non-linear behaviour of the adhesive bonded joints. Regarding the last two hypotheses, the input parameters to define the behaviour of the adhesive joints were obtained from different sources. For the *EB* hypothesis, the results retrieved from the mechanical characterization tests (see **Section 2.1**) were considered. In the case of the *IB* hypothesis, the adhesive joints were simulated using the bond stress (τ) – slip (s) relationships obtained from inverse analysis performed with the results obtained from double-lap joint tests [26].

In order to obtain the quasi-static responses, the dynamic effects of the numerical models in ABAQUS/Explicit needed to be controlled. In the present study, the recommendations proposed by Rocha *et al.* [32,41] in terms of loading time, loading scheme and damping ratio were considered. A loading time between $50\,T_1$ and $100\,T_1$ should be used to avoid significant dynamic effects, in which T_1 is the period of the fundamental vibration mode. Therefore, the loading time was set to 22.5 seconds. The mass-proportional damping was used, in order to guarantee lower computation effort and higher damping efficiency for low frequency vibration modes, and a linear loading scheme was assumed.

For the sake of simplicity, the numerical simulations were stopped when the largest mid-span deflection registered in each series was attained (11.38 mm for S*Force* beams; 17.34 mm for 3M beams; and 11.31 mm for S*Dur* beams – see **Table III.3**).

4.2. Model description

4.2.1. Annealed glass

The brittle behaviour of the annealed glass was properly considered by adopting the "*Brittle Cracking*" model, as well as the "*Brittle Shear*" and "*Brittle Failure*" options to simulate the crack evolution. According to ABAQUS [33], this constitutive model is suitable for brittle and quasi-brittle materials, having been adopted for the simulations of glass in previous numerical studies (e.g. [28,42–44]). For glass, the following assumptions were made: (i) the linear elastic behaviour was assumed before cracking, both in compression and in tension; (ii) Rankine's failure criterion was used for crack detection; and (iii) after cracking, the smeared crack model was adopted to model the non-linear tensile behaviour of cracked glass, while linear elastic behaviour was assumed in compression.

The value adopted for the modulus of elasticity is included in **Table III.1**. The Poisson's ratio (υ_g) which was set to 0.23, followed the recommendations of the Guideline for European Structural Design of

Glass Components [45]. Manipulating **Eq. (III.1)** and assuming full composite action between the adherends, the tensile strength of annealed glass was derived from the experimental results (cracking loads) of four-point bending tests through inverse analysis. A $f_{g,t}$ of 39.8 MPa was obtained and adopted, which is consistent with the literature [45].

The tensile strength ($f_{g,t}$), the mode-I facture energy (G_g) and the shear retention factor (β) are the main parameters required by "*Brittle Cracking*" and its sub-options. According to ABAQUS [33], by default, the crack band width (h) is equal to the square root of the finite elements, the threshold angle for a new crack is 90° (fixed concept) and the number of cracks per integration point is limited by the number of stress components, that is, 3 cracks in 3D models and 2 cracks in 2D models. A linear shape tension-softening diagram is assumed when the "*GFI*" option (facture energy cracking criterion) is used.

In order to avoid computational instabilities and convergence problems (e.g. snap-back instabilities) in smeared crack models, the mesh objectivity can be ensured by forcing the relationship between the crack band width and mesh size [46,47]. According to de Borst [48], the minimum facture energy (G_{min}) that guarantees the convergence of numerical models is given by **Eq. (III.2)**, where b typifies the shape of the tension-softening diagram (b = 0.5 for linear shape).

$$G_{min} \geq \frac{f_{g,t}^2 bh}{E_g} \tag{III.2}$$

In a smeared crack approach, the non-linear behaviour in shear can be accounted for through the shear retention factor law [49], according to **Eq. (III.3)**, where ε_n^{cr} and $\varepsilon_{n,ult}^{cr}$ are the crack normal strain and the ultimate crack normal strain, respectively, and p is a constant value (e.g. 1, 2 or 3). In analogy with concrete materials, the complete loss of aggregate interlock occurs when β is equal to 0.

$$\beta = \left(1 - \frac{\varepsilon_n^{cr}}{\varepsilon_{n,ult}^{cr}}\right)^p \tag{III.3}$$

The non-linear tensile behaviour of the cracked glass was simulated considering a quadratic shear retention factor law (p = 2) and the minimum mode-I fracture energy. Due to the dynamic approach used in ABAQUS/Explicit, fracture energies lower than the value provided by **Eq. (III.3)** have been used in previous studies, such as 3 J/m^2 (e.g. [28,30,42–44,50]). However, the minimum mode-I fracture energy was adopted in the present study. This strategy was successfully used by Rocha *et al.* [32] for

the numerical simulation of annealed glass, providing a good agreement between the experimental and numerical results, both in $F - \delta$ response and in terms of crack patterns.

4.2.2. CFRP

The CFRP reinforcement was simulated as an isotropic material with linear elastic behaviour, for both compression and tension. The CFRP laminates were mainly subjected to tensile stresses in the fibre direction during the flexural tests and, for the sake of simplicity, were simulated as an isotropic material. A more complex orthotropic approach would have a negligible influence on the numerical results because the out-of-plane shear stiffness was set to zero (more details in **Section 4.2.3**), avoiding additional shear stress at the bonded interfaces due to the Poisson's ratio effect on the CFRP laminate. On the other hand, the CFRP has a tensile strength ≈ 62 times higher than that of annealed glass and, therefore, no damage material models were implemented to describe possible failure modes. However, it should be noted that the maximum tensile stress in the CFRP laminates was monitored during the simulations. A modulus of elasticity of 172.4 GPa was adopted, according to **Table III.1**.

4.2.3. Adhesive joint

In the case of *PB* hypothesis, the rigid connection between the glass panel and the CFRP laminate was materialized by the "tie" constraint, which avoided relative translations and/or rotations between nodes.

For the case of the *EM* hypothesis, the adhesive joint was simulated as a linear elastic material, using the modulus of elasticity and the Poisson's ratio presented in **Table III.1** for each adhesive. A rigid connection at the CFRP/adhesive and adhesive/glass interfaces was assumed through the "tie" constraint.

Regarding the *IB* hypothesis, the bond behaviour of the glass-to-CFRP interfaces was modelled by adopting "*Surface-Based Cohesive Behaviour*". This interface model is appropriate when the interface thickness is negligible [33]; therefore, the thickness of the adhesive layer was not considered. With the *IB* hypothesis, the mechanical properties of the adhesive and the bond behaviour at the CFRP/adhesive and adhesive/glass interfaces are considered simultaneously. The interface model used requires as input parameters the linear elastic normal stiffness, K_n, and the linear elastic tangential stiffnesses, K_s and K_t. The values of K_n and K_s were assigned based on the modulus of elasticity of each adhesive (see **Table III.1**) and on the $\tau - s$ relationships previously derived by Rocha

et al. [26], respectively. In order to reduce any influence of the finite element model type (2D *versus* 3D models) on the numerical results, K_t was assumed to be zero to prevent out-of-plane shear stresses (mode-III loading), resembling a 2D model (like in *PB* and *EB* hypotheses).

The experimental responses of adhesive joints made with stiff adhesive were used by Rocha *et al.* [26] to derive a simple $\tau - s$ linear law (see **Eq. (III.4)**), which is governed by the elastic tangential stiffness (K_s). The ones of adhesive joints produced with the soft and intermediate adhesives were used to derive non-linear laws using the Dimade's $\tau - s$ exponential law (see **Eq. (III.5)**), which is governed by the bond strength (τ_m) and the corresponding slip (s_m) [51]. The parameters mentioned were previously obtained by Rocha *et al.* [26] and are summarized in **Table III.4**.

$$\tau(s) = K_s \cdot s \tag{III.4}$$

$$\tau(s) = \tau_m \cdot \frac{s}{s_m} \cdot e^{1 - \frac{s}{s_m}} \tag{III.5}$$

Table III.4: Bond behaviour parameters obtained from each series of double-lap joints, namely the shear bond strength (τ_m) and the corresponding shear slip (s_m) for the soft and intermediate adhesives, and the linear elastic tangential stiffness (K_s) for the stiff adhesive.

Adhesive type	s_m [mm]	τ_m [MPa]	K_s [MPa/mm]
Soft	0.280	7.4	-
Intermediate	0.088	19.6	-
Stiff	-	-	412.12

Notes:
The parameters of the local $\tau - s$ laws for the three types of adhesive were previously calibrate by Rocha *et al.* [26]

In opposition to the stiff adhesive ($\tau - s$ linear law without damage), the Dimade's $\tau - s$ exponential law adopted for the two softer adhesives considers damage propagation and consists of three distinct stages: (i) the elastic stage, for $s < s_m$, when the shear stress increases for increasing relative slip until the bond strength is reached; (ii) the softening stage, for $s > s_m$, when the shear stress decreases for increasing relative slip, i.e., after damage initiation; and (iii) the complete debonding stage, when there is no shear interaction between the bonded interfaces.

For both S*Force* and 3M beams the damage propagation in the adhesive joint was simulated using the "*Progressive Damage and Failure*" option. For this purpose, the normal strength, $\sigma_{n,max}$, and the shear strengths, $\tau_{s,max}$ and $\tau_{t,max}$ were prescribed for modelling the damage initiation. In four-point bending tests, the adhesive damage propagation in S*Force* (without shear cracking) and 3M beams

was mainly governed by mode-II fracture. In addition, double-lap joints were mainly subjected to mode-II loading. Nevertheless, in double-lap joint specimens, mainly those manufactured with the soft adhesive, the progression of adhesive damage from the loaded end to the free end section was governed by a mixed-mode-I+II due to the eccentricity between the middle plane of the glass plates and CFRP laminate [26]. Thus, it is reasonable to assume that the mixed-mode behaviour that governs the debonding process was, to some extent, taken into account by the experimentally derived $\tau - s$ relationships. Consequently, mode-I and -III fracture were not considered in this study and therefore extremely high values (= 10^6 MPa) were assigned to $\sigma_{n,max}$ and $\tau_{t,max}$.

The damage initiation was governed by a maximum nominal stress criterion, according to **Eq. (III.6)**, in which σ_n, τ_s and τ_t represent the stress state at the bonded interfaces at each time step. Based on the $\tau - s$ laws, the damage evolution was set as a tabular function, which defines the damage factor as a function of the relative displacement between bonded interfaces after damage initiation.

$$\left(\frac{\sigma_n}{\sigma_{n,max}}\right) + \left(\frac{\tau_s}{\tau_{s,max}}\right) + \left(\frac{\tau_t}{\tau_{t,max}}\right) = 1 \qquad \text{(III.6)}$$

4.2.4.   Mesh strategy and boundary conditions

Two-dimensional (2D) simulations were carried out when the *PB* and *EB* hypotheses were considered. On the other hand, ABAQUS/Explicit does not allow the edge-to-edge contact with cohesive interface models, thereby three-dimensional (3D) simulations were performed when the *IB* hypothesis was considered (see **Table III.5**). The bi-symmetrical behaviour of the glass-CFRP composite beams was assumed, in order to decrease the computational effort. Therefore, in 2D and 3D models, only half and a quarter of the beams were simulated, respectively. **Figure III.11** shows the geometry, boundary conditions, load configuration and the mesh.

While 8-node solid elements with reduced integration (C3D8R) were used in 3D models, 4-node plane stress elements with reduced integration (CPS4R) were used in 2D models. In addition, the adhesive interface in 3M models was simulated by 4-node zero thickness surface elements (SFM3D4), with 4 integration points (surface-to-surface). Finite elements of 5 (width) × 5 (height) [mm] were used in 2D models, while a mesh with finite elements of 5 (width) × 5 (height) × 6 (thickness) [mm] were adopted in 3D models. Based on the knowledge obtained from the mesh sensitivity analysis carried out by Rocha *et al.* [32], these finite element meshes were considered adequate to capture the experimental

responses, including the glass cracking at the glass-CFRP interface. Finer meshes would unnecessarily increase the computational cost.
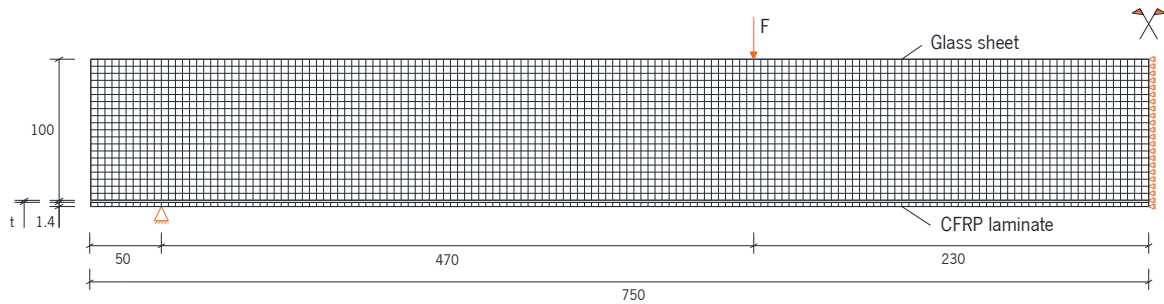
Figure III.11: Finite element model to simulate the glass-CFRP composite beams, including supports, symmetry conditions and mesh pattern. Notes: *t* may be non-existent (*PB* hypothesis), zero (*IB* hypothesis) or equal to the layer thickness (*EB* hypothesis), depending on the hypothesis adopted to simulate the adhesive joint. All units in [mm].

Table III.5: Approaches adopted for the numerical modelling of the glass-to-CFRP adhesive connections.

Premise in terms of	*PB* hypothesis	*EB* hypothesis	*IB* hypothesis
Adhesive joint	-	Linear elastic material	Bond stress (τ) – slip (s) law
Model type	2D	2D	3D

4.3. Discussion of numerical results

For each series of beams, **Figure III.12** shows the structural response obtained from each numerical hypothesis and the corresponding ultimate crack pattern. On the other hand, **Table III.6** allows to compare the numerical and experimental responses in terms of (i) initial stiffness, (ii) cracking load and (iii) corresponding deflection, (iv) applied load for $\delta_{num} = \delta_{ult}$, and, finally, (iv) an additional parameter called strain energy (E_t), which was defined as the area bounded by the $F - \delta$ responses, and represents the work done by the applied bending load. According to **Table III.6**, the three hypotheses used to simulate the adhesive joint accurately estimated the initial stiffness of the glass-CFRP composite beams and their cracking load, regardless of the simulated adhesive. However, small differences can be found between the three hypotheses due to the different model assumptions. While the *EB* hypothesis considered the thickness of the adhesive layer, the other two hypotheses neglected it. On the other hand, while the *IB* hypothesis considered the adhesive damage and its propagation, the other two hypotheses neglected it.

4.3.1.   S*Force* series

Figure III.12a shows that the *IB* hypothesis was the one that simulated better the post-cracking response and the crack pattern of S*Force* beams, since it captured the progression of adhesive damage towards the supports after crack initiation (gradual debonding of the CFRP laminate), which yielded numerical crack patterns with very low crack density, like the experimental ones. Nevertheless, in terms of strain energy, the *IB* hypothesis resulted in a difference of 11.7 % between the numerical and the experimental responses, which compares with 7.6 % and 19.3 % for the *PB* and *EB* hypotheses, respectively. This difference is larger than expected because quasi-static simulations were performed (see **Section 4.1**) and, consequently, the numerical model was not able to capture the partial debonding of the CFRP laminate due to the shock load caused by the appearance of the first V-shaped crack (previously discussed in **Section 3.1**). However, with purely dynamic simulations (e.g. without mass-proportional damping and/or shorter loading times), the overall response would be entirely affected by dynamic effects, certainly producing $F - \delta$ responses even more distinct from the experimental ones.

Table III.6: Comparison between the numerical results obtained from the hypotheses adopted to simulate the glass-to-CFRP adhesive connection and the experimental ones, indicating the difference between them in parentheses.

Hypothesis	K [kN/mm]	F_{cr} [kN]	δ_{cr} [mm]	$F(\delta_{ult})$ [kN] [1]	E_t [J]
S*Force* series	1.44	3.38	2.35	3.76	26.94 [2]
PB hypothesis	1.49 (3.6%)	3.69 (9.5%)	2.48 (5.7%)	2.95 (-21.5%)	24.89 (-7.6%)
EB hypothesis	1.38 (-4.3%)	3.61 (7.0%)	2.62 (11.8%)	4.67 (24.2%)	32.15 (19.3%)
IB hypothesis	1.45 (0.5%)	3.53 (4.6%)	2.44 (4.1%)	4.58 (21.8%)	30.08 (11.7%)
3M series	1.48	3.45	2.34	4.48	53.85 [2]
PB hypothesis	1.49 (0.9%)	3.69 (7.2%)	2.48 (6.2%)	-	27.41 (-49.1%)
EB hypothesis	1.47 (-0.3%)	3.65 (5.8%)	2.48 (6.1%)	4.78 (6.7%)	49.86 (-7.4%)
IB hypothesis	1.43 (-3.3%)	3.51 (1.7%)	2.46 (5.1%)	5.10 (13.8%)	57.06 (6.0%)
S*Dur* series	1.45	3.61	2.49	2.89	24.11 [2]
PB hypothesis	1.49 (2.7%)	3.69 (2.5%)	2.48 (-0.3%)	2.95 (2.1%)	24.95 (3.5%)
EB hypothesis	1.48 (2.1%)	3.68 (2.1%)	2.49 (0.1%)	3.57 (23.5%)	30.04 (24.6%)
IB hypothesis	1.46 (0.4%)	3.66 (1.5%)	2.51 (1.0%)	3.67 (27.0%)	29.30 (21.5%)

Notes:
[1] Applied load corresponding to the average experimental ultimate deflection (δ_{ult}) indicated in **Table III.3** for each series.
[2] Experimental average value of each beam series
The numerical strain energy was determined based on the mean experimental value of δ_{ult} recorded in each series (see **Table III.3**)

Due to the reasons mentioned, crack branching was not captured by the *IB* hypothesis. The load drop at first crack was greater in the numerical response than in the experimental one. Thus, as previously inferred in **Section 4.1**, the crack branching observed experimentally seems to have prevented a greater load drop. The uncracked tensile region between the branches of the V-shaped crack seems to provide additional load-bearing capacity and flexural stiffness at the beginning of the post-cracking stage.

(a)

(b)

(c)
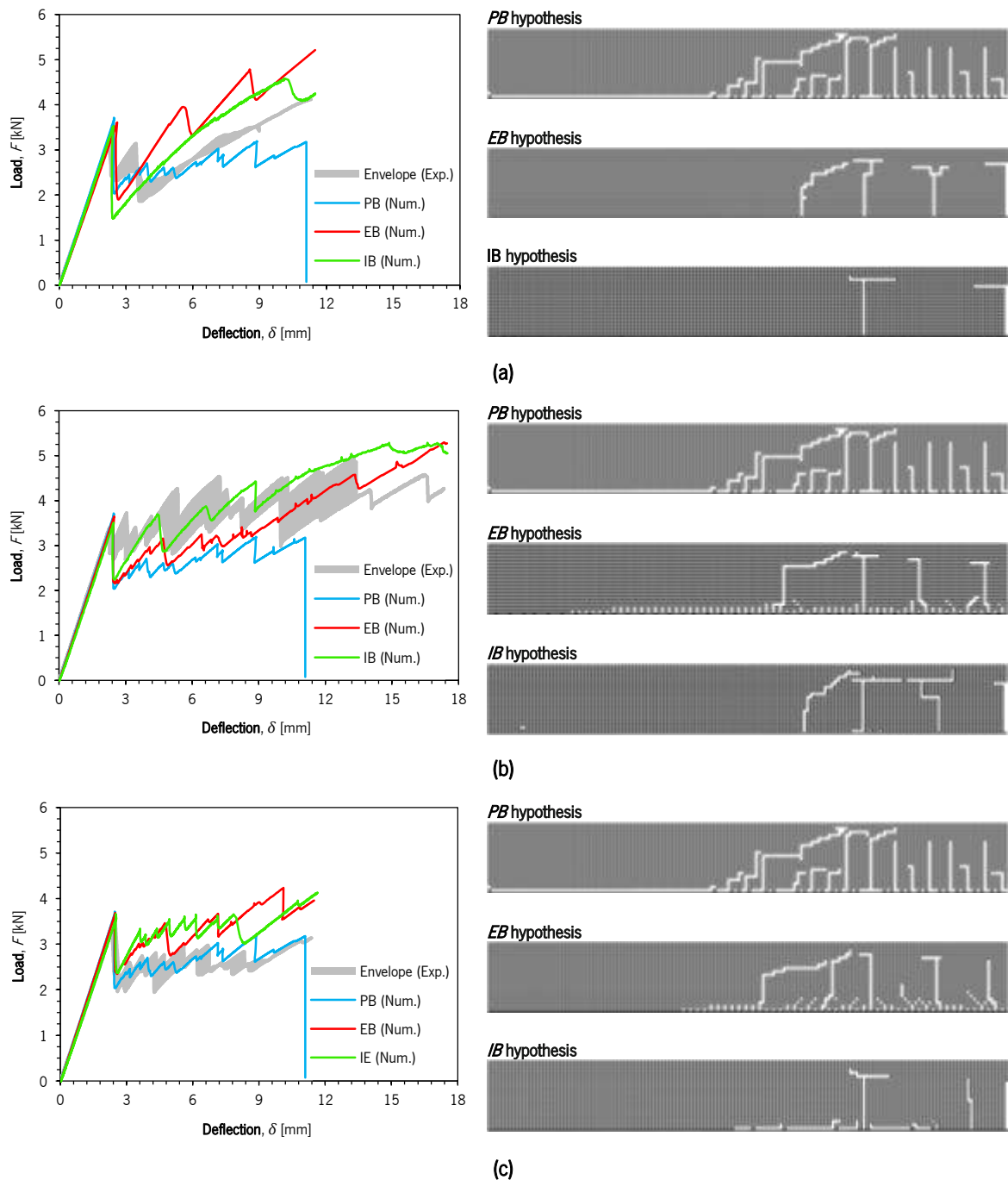
Figure III.12: Comparison between the experimental and numerical responses of the (a) S*Force*, (b) S*Dur* and (c) 3M series, considering the three hypotheses adopted to simulate the glass-to-CFRP adhesive connection.

With the *IB* hypothesis, the first crack appeared close to the load point section. Hence, the numerical post-cracking stiffness was initially similar to that recorded in the S*Force*-I beam, where the first V-shaped crack also appeared near one of the load points (see **Figure III.7b**). However, due to the damage propagation at the glass-to-CFRP interfaces, the numerical post-cracking stiffness decreased gradually and, for $\delta > 6.0$ mm, it resembled the experimental one recorded in the S*Force*-II beam. A second crack appeared later ($\delta \approx 10$ mm) at the mid-span section. As a result, the load carrying capacity of the numerical model dropped again, then resembling the one of the S*Force*-II beam (see **Figure III.12a**). As the *IB* hypothesis did not capture the initial adhesive damage (shock load) in the bonding areas around the first V-shaped crack, the numerical model overestimated the load carrying capacity of S*Force* beams until the appearance of the second crack. Two cracks were observed both experimentally (see **Figure III.7**) and numerically (see **Figure III.12a**), but their shape and relative location were significantly different due to the reasons previously discussed.

The *PB* hypothesis was inappropriate to simulate the post-cracking behaviour of the S*Force* beams because it underestimated their residual strength. The perfect bond between the glass and the CFRP does not represent well the non-linear behaviour of glass-to-CFRP adhesively bonded connections with soft adhesive, where debonding at the adhesive/glass interface was observed in double-lap joint tests (see **Figure III.4a**) and in four-point bending tests (see **Figure III.10a**). In contrast, the *EB* hypothesis overestimated the residual strength of the S*Force* beams, as well as their post-cracking stiffness. This is explained by several reasons: (i) first, the mechanical properties of the adhesive used in the *EB* hypothesis were obtained from tensile tests on dumbbell shape specimens (see mechanical characterization in **Section 2.1**), while the adhesive joints in four-point bending tests were mostly subjected to shear stresses; and (ii) second, the *EB* hypothesis did not simulate the adhesive damage and its propagation, neglecting the loss of composite action. Therefore, the *EB* hypothesis should not be used for flexible adhesives with viscoelastic behaviour.

4.3.2.   3M series

In contrast to the *PB* hypothesis, which underestimated the residual strength of 3M beams after crack initiation, the *EB* and *IB* hypotheses captured well their post-cracking behaviour, including the progressive loss of stiffness and the consecutive load drops after the first cracking. In general, **Figure III.12b** shows that the *EB* and *IB* hypotheses provided similar crack patterns, both in density and in shape. Taking into account that the *EB* hypothesis neglected the adhesive damage, shorter bond lengths were required to transfer the tensile stresses between the two components than in the

IB hypothesis, leading to the appearance of small cracks close to the bottom edge of the glass panel. This explains the difference between the aforementioned hypotheses at the beginning of the post-cracking stage, as these small cracks caused small load drops that led the *EB* hypothesis to underestimate the load carrying capacity of 3M beams.

On the other hand, the numerical post-cracking stiffness significantly decreased for $\delta > 11.0$ mm when the *IB* hypothesis was used, creating a plateau at the end of the $F - \delta$ response (see **Figure III.12b**). This occurred due to the progression of adhesive damage from the beam central part towards the supports which, in turn, led to the sudden horizontal propagation of the existing vertical cracks, similarly to what was observed for S*Force* beams. However, this phenomenon was not observed in experimental tests with the same intensity. As a result, the *IB* hypothesis underestimated the post-cracking stiffness at the final part of the post-cracking stage.

Concerning the numerical strain energy, the *EB* and *IB* hypotheses approximated well the experimental results, showing differences with respect to the experimental of 7.4 % and 6.0%, respectively. However, the former requires parameters that can be more easily determined, since the adhesive is simulated as an isotropic material with linear elastic behaviour. In addition, neglecting the adhesive damage can be an effective measure to reduce the computational cost.

4.3.3.   S*Dur* series

Among the different hypotheses, the *PB* hypothesis simulated with greater precision the post-cracking behaviour – with successive load drops and progressive loss of stiffness – and crack patterns – including the shear cracks that appeared toward the supports (see **Figure III.12c**) – of the S*Dur* beams. Furthermore, the *PB* hypothesis resulted in the lowest difference between the experimental and numerical strain energies (3.5 %, against 24.6 % and 21.5 % for the *EB* and *IB* hypotheses, respectively).

Unlike other hypotheses and/or series, the *PB* hypothesis captured the failure of S*Dur* beams, which occurred for $\delta \approx 11.1$ mm, which is 9.3 % higher than the experimental values of δ_{ult} obtained from the S*Dur* series (see **Figure III.12c**). Numerically, the collapse of S*Dur* beams resulted from the breakage of the bottom edge of the glass panel (glass substrate failure), which was triggered by the high interfacial stresses caused by shear cracks. Crack propagation at the bottom edge of the glass was mainly controlled by mode-II fracture (shear stresses) due to the stiffness mismatch between both adherends. In contrast to the experimental tests (see **Section 3.3**), fibre-tear failure in CFRP was not

observed numerically because this damage mode was not considered. As referred in **Section 4.1**, since the aim was to simulate quasi-static loading, mass-proportional damping was introduced in the models. Therefore, fibre-tear failure in CFRP, seen as a purely dynamic phenomenon associated to the sudden energy release resulting from cracking, could not be captured even if a more complex orthotropic approach was adopted to simulate the material behaviour of CFRP.

The *EB* and *IB* hypotheses did not capture the glass cracking at the bottom edge in S*Dur* beams, leading to higher residual strengths than the experimental ones (see **Figure III.12b**). Although the *EB* hypothesis showed to be able to simulate the progressive loss of stiffness and successive load drops, the numerical crack pattern obtained was less dense than the experimental ones (see **Figure III.9**). This can be explained by a smoother transfer of the tensile stresses between adherends when compared to the *PB* hypothesis, which may also explain the absence of glass cracking at the glass-to-CFRP interfaces (glass substrate failure).

In addition, the crack pattern produced by the *IB* hypothesis was significantly different from the experimental ones. This may be caused by the high tangential stiffness of the stiff adhesive and, at the same time, by the interfacial behaviour adopted to simulate the adhesive joint, which was assumed to be elastic and not damage dependent (see assumptions in **Section 4.2.3**). Due to the high shear stresses at the glass-to-CFRP interfaces, in the *IB* hypothesis, the crack propagation was mainly controlled by mode-II failure at the bottom edge of the glass panel near the first vertical crack.

Considering the results obtained, the stiffness, the overall behaviour and the tensile strength of the adhesive used seem to be important variables to consider on the definition of the simulation hypothesis. Therefore, in the case of the three adhesives adopted in this study, the behaviour of glass-CFRP composite beams was best simulated when: (i) the *IB* hypothesis was adopted in the case of the S*Force* beams, because it considered the flexible behaviour of the soft adhesive with greater precision, as well as the progression of adhesive damage towards the supports; (ii) the *PB* hypothesis was adopted in the case of S*Dur* beams, because it was more sensitive to high stress concentrations caused by the high stiffness of the stiff adhesive; and, (iii) the *EB* hypothesis was adopted for 3M beams, because the progression of adhesive damage towards the supports was not so relevant due to the high toughness of the intermediate adhesive and, on the other hand, high stress concentrations such as the ones experienced with the stiffest adhesive are not expected.

5   CONCLUSIONS

This investigation aimed to study the influence of different types of adhesive on the structural performance of glass-CFRP composite beams. Three different adhesives were used, namely (i) the SikaDur 330, with high stiffness, (ii) the 3M DP490 epoxy adhesive, with moderate stiffness, and (iii) the SikaForce L100 7100 polyurethane adhesive, with low stiffness. In addition, numerical simulations were performed in order to investigate the best approach to simulate the adhesive connection and, in turn, the structural response of the glass-CFRP composite beams, with particular emphasis on the post-cracking stage, which is typically challenging due to the calibration of the non-linear constitutive models to simulate cracked glass and the realistic definition of the structural interaction between components.

The main conclusions of this work may be summarized as follows:

- Experimental tests proved the advantages of strengthening annealed glass beams with externally bonded CFRP reinforcement. Relatively safe and ductile failure mechanisms were observed in all series. After the appearance of the first crack in glass, all composite beams were able to maintain their integrity, exhibiting a post-cracking stage that was strongly influenced by the mechanical properties of the adhesive;

- S*Dur* beams were not able to significantly recover from the load drop caused by the first crack because the stiff adhesive is too stiff to mobilize relatively long bond lengths, which induced high stress concentrations in the glass and promoted the premature detachment of the reinforcement;

- The soft adhesive was able to avoid high stress gradients at the glass-to-CFRP interfaces, promoting higher residual strength indexes than the stiff adhesive. However, the low resistance of this adhesive prevented the S*Force* beams from reaching higher ductility indexes than the S*Dur* beams. Furthermore, when cracks appeared in S*Force* beams, the soft adhesive was unable to withstand the sudden increase in tensile force in the CFRP laminate, damaging the adhesive connection in the surrounding areas and creating V-shaped cracks, which apparently provided additional load-bearing capacity and flexural stiffness to the S*Force* beams;

- Due to its moderate stiffness and high toughness, the intermediate adhesive was more efficient than the stiff adhesive in smoothing the stress gradients at the glass-to-CFRP

interfaces and more efficient than the soft adhesive in delaying the debonding of the CFRP laminate. As a result, the 3M beams presented the highest residual strength and ductility indexes of all tested beam series;

- Dynamic effects (e.g. shock load) influenced the post-cracking behaviour of S*Dur* and S*Force* beams. The stiff adhesive was apparently unable to damp the large amounts of strain energy released whenever cracks formed, weakening the glass in the surrounding areas due to the growth of surface flaws and promoting an asymmetric progression of new cracks towards the supports.

- Numerical models accurately simulated the flexural behaviour and crack pattern of glass-CFRP composite beams using different hypotheses to model the glass-to-CFRP adhesively bonded connection. The *IB* hypothesis was better at capturing the flexural behaviour of the S*Force* beams because the non-linear behaviour of the soft adhesive was taken into account. On the other hand, S*Dur* and 3M beams were better simulated using the *PB* and *EB* hypotheses, respectively;

- Using only material properties which can be easily obtained from simple mechanical characterization tests, the *PB* and *EB* hypotheses can accurately simulate the performance of glass-CFRP composite beams produced with stiff adhesives (e.g. stiff adhesive) or adhesives with moderate stiffness (e.g. intermediate adhesive). Nevertheless, these hypotheses are not appropriate for simulating glass-CFRP composite beams with a remarkable adhesive damage. In this case, the bond behaviour of the glass-to-CFRP connection should be previously characterized;

- The approach followed in this study, which included the experimental characterization of the flexural behaviour of glass-CFRP composite beams manufactured with different adhesives, as well as the choice of the best approach to simulate adhesive connections as a function of the type of adhesive, was found useful for the modelling of glass-CFRP composite systems with good accuracy and eventually for the design of reinforced composite glass systems.

6   ACKNOWLEDGEMENTS

7   REFERENCES

[1]   Correia J, Valarinho L, Branco F. Post-cracking strength and ductility of glass-GFRP composite beams. Composite Structures 2011;93:2299–309.

[2]   Valarinho L, Correia JR, Branco F. Experimental study on the flexural behaviour of multi-span transparent glass-GFRP composite beams. Construction and Building Materials 2013;49:1041–53. https://doi.org/10.1016/j.conbuildmat.2012.11.024.

[3]   Biolzi L, Orlando M, Piscitelli LR, Spinelli P. Static and dynamic response of progressively damaged ionoplast laminated glass beams. Composite Structures 2016;157:337–47. https://doi.org/10.1016/j.compstruct.2016.09.004.

[4]   Cruz P, Pequeno J. Structural Timber-Glass Adhesive Bonding. Challenging Glass, 2008, p. 205–14.

[5]   Cruz P, Pequeno J. Timber-Glass Composite Beams: Mechanical Behaviour & Architectural Solutions. Challenging Glass, 2008, p. 439–48.

[6]   Belis J, Callewaert D, Delincé D, Impe R Van. Experimental failure investigation of a hybrid glass / steel beam. Engineering Failure Analysis 2009;16:1163–73. https://doi.org/10.1016/j.engfailanal.2008.07.011.

[7]   Bos F, Veer F, Hobbelman G, Louter C. Stainless steel reinforced and post-tensioned glass beams. ICEM12 - 12th International Conference on Experimental Mechanics, Bari, Italy: 2004, p. 1–9.

[8]   Louter C, Belis J, Veer F, Lebet J. Structural response of SG-laminated reinforced glass beams; experimental investigations on the effects of glass type, reinforcement percentage and beam size. Engineering Structures 2012;36:292–301. https://doi.org/10.1016/j.engstruct.2011.12.016.

[9]   Louter C, Cupać J, Lebet J. Exploratory experimental investigations on post-tensioned structural glass beams. Journal of Facade Design and Engineering 2014;2:3–18. https://doi.org/10.3233/FDE-130012.

[10]   Palumbo M. A New Roof for the XIIIth Century 'Loggia de Vicari' (Arquà Petrarca – PD Italy) Based on Structural Glass Trusses: A Case Study. Glass Processing Days, Tempere, Finland: 2005.

[11]   Louter C, Cupać J, Debonnaire M. Structural glass beams prestressed by externally bonded tendons. GlassCon Global Conference Proceedings, Philadelphia, EUA: 2014, p. 450–9.

https://doi.org/10.14296/deeslr.v5i0.1848.

[12]   Cagnacci E, Orlando M, Spinelli P. Experimental campaign and numerical simulation of the behaviour of reinforced glass beams. Glass Performance Days, Tempere, Finland: 2009, p. 3–9.

[13]   Bedon C, Louter C. Structural glass beams with embedded GFRP, CFRP or steel reinforcement rods: Comparative experimental, analytical and numerical investigations. Journal of Building Engineering 2019;22:227–41. https://doi.org/10.1016/j.jobe.2018.12.008.

[14]   Achintha M, Balan B. Characterisation of the mechanical behaviour of annealed glass – GFRP hybrid beams. Construction and Building Materials 2017;147:174–84. https://doi.org/10.1016/j.conbuildmat.2017.04.086.

[15]   Bedon C, Louter C. Numerical investigation on structural glass beams with GFRP-embedded rods, including effects of pre-stress. Composite Structures 2018;184:650–61. https://doi.org/10.1016/j.compstruct.2017.10.027.

[16]   Neto P, Alfaiate J, Valarinho L, Correia J, Branco F, Vinagre J. Glass beams reinforced with GFRP laminates: Experimental tests and numerical modelling using a discrete strong discontinuity approach. Engineering Structures 2015;99:253–63. https://doi.org/10.1016/j.engstruct.2015.04.002.

[17]   Valarinho L, Sena-Cruz J, Correia J, Branco F. Numerical simulation of the flexural behaviour of composite glass-GFRP beams using smeared crack models. Composites Part B: Engineering 2017;110:336–50. https://doi.org/10.1016/j.compositesb.2016.10.035.

[18]   Louter C, Veer F, Hobbelman G. Reinforcing glass, effects of reinforcement geometry and bonding technology. Glass Processing Days, 2007, p. 2–6.

[19]   Sena-Cruz J, Barros J, Coelho M, Silva L. Efficiency of different techniques in flexural strengthening of RC beams under monotonic and fatigue loading. Construction and Building Materials 2012;29:175–82. https://doi.org/10.1016/j.conbuildmat.2011.10.044.

[20]   De Lorenzis L, Teng JG. Near-surface mounted FRP reinforcement: An emerging technique for strengthening structures. Composites Part B: Engineering 2007;38:119–43. https://doi.org/10.1016/j.compositesb.2006.08.003.

[21]   Baraldi D, Cecchi A, Foraboschi P. Broken tempered laminated glass: Non-linear discrete element modeling. Composite Structures 2016;140:278–95. https://doi.org/10.1016/j.compstruct.2015.12.050.

[22]   Martens K, Caspeele R, Belis J. Development of Reinforced and Posttensioned Glass Beams: Review of Experimental Research. Journal of Structural Engineering 2016;142:4015173. https://doi.org/10.1061/(asce)st.1943-541x.0001453.

[23]   Cagnacci E, Orlando M, Salvatori L, Spinelli P. Four-point bending tests on laminated glass

beams reinforced with FRP bars adhesively bonded to the glass. Glass Structures and Engineering 2021;6:211–32. https://doi.org/10.1007/s40940-021-00147-9.

[24]   Katsivalis I, Thomsen OT, Feih S, Achintha M. Failure prediction and optimal selection of adhesives for glass/steel adhesive joints. Engineering Structures 2019;201:109646. https://doi.org/10.1016/j.engstruct.2019.109646.

[25]   Katsivalis I, Thomsen OT, Feih S, Achintha M. Development of cohesive zone models for the prediction of damage and failure of glass/steel adhesive joints. International Journal of Adhesion and Adhesives 2020;97:102479. https://doi.org/10.1016/j.ijadhadh.2019.102479.

[26]   Rocha J, Sena-Cruz J, Pereira E. Tensile behaviour of CFRP-glass adhesively bonded connections: double-lap joint tests and numerical modelling. Engineering Structures 2022;260:114212. https://doi.org/10.1016/j.engstruct.2022.114212.

[27]   Foti D, Lerna M, Carnimeo L, Vacca V. Finite element models and numerical analysis of a structural glass beam reinforced with embedded carbon fibre rod. International Journal of Mechanics 2020;14:163–7. https://doi.org/10.46300/9104.2020.14.22.

[28]   Bedon C, Louter C. Numerical analysis of glass-FRP post-tensioned beams – Review and assessment. Composite Structures 2017;177:129–40. https://doi.org/10.1016/j.compstruct.2017.06.060.

[29]   Baraldi D, Cecchi A, Foraboschi P. Broken tempered laminated glass: Non-linear discrete element modeling. Composite Structures 2016;140:278–95. https://doi.org/10.1016/j.compstruct.2015.12.050.

[30]   Bedon C, Louter C. Finite-element analysis of post-tensioned SG-laminated glass beams with mechanically anchored tendons. Glass Structures & Engineering 2016;1:39–59. https://doi.org/10.1007/s40940-016-0020-7.

[31]   Biolzi L, Casolo S, Orlando M, Tateo V. Modelling the response of a laminated tempered glass for different configurations of damage by a rigid body spring model. Engineering Fracture Mechanics 2019;218:106596. https://doi.org/10.1016/j.engfracmech.2019.106596.

[32]   Rocha J, Pereira E, Sena-Cruz J, Valarinho L, Correia JR. Numerical simulation of GFRP-reinforced glass structural elements under monotonic load. Engineering Structures 2021;234:111968. https://doi.org/10.1016/j.engstruct.2021.111968.

[33]   Simulia. ABAQUS computer software and Online Documentation. v6.12. 2012.

[34]   ISO. Plastics - Determination of tensile properties - Part 5: Test conditions for unidirectional fibre-reinforced plastic composites. 527-5, Genève, Switzerland: International Organization for Standardization; 2009, p. 11.

[35]   ISO. Plastics – Determination of tensile properties – Part 2: Test conditions for moulding and

extrusion plastics. 527-2, Genève, Switzerland: International Organization for Standardization; 2012, p. 5.

[36]   Rodrigues A. Caracterização do comportamento do adesivo estrutural SikaForce 7710. Universidade de Coimbra, 2017.

[37]   Nhamoinesu S, Overend M. The mechanical performance of adhesives for a steel-glass composite façade system. Challenging Glass 3: Conference on Architectural and Structural Applications of Glass, CGC 2012, Delft, Netherlands: 2012, p. 293–306. https://doi.org/10.3233/978-1-61499-061-1-293.

[38]   Haghani R. Finite element modelling of adhesive bonds joining fibre-reinforced polymer (FRP) composites to steel. In Rehabilitation of Metallic Civil Infrastructure Using Fiber Reinforced Polymer (FRP) Composites, Woodhead Publishing; 2014, p. Pages 60-95. https://doi.org/https://doi.org/10.1533/9780857096654.1.60.

[39]   GOM. Correlate Software and Online Documentation. Rev.121188. 2019.

[40]   Bos F. Elastic strain energy release at failure and its consequence for structural glass testing and design. Challenging Glass 2 - Conference on Architectural and Structural Applications of Glass, Delft, The Netherlands: 2010, p. 287–96.

[41]   Rocha J, Pereira E, Sena-cruz J. Alternative Approaches for the Numerical Simulation of Glass Structural Beams Reinforced with GFRP Laminates. In: Louter, Bos, Belis, Veer, Nijsse, editors. Challenging Glass 6 - Conference on Architectural and Structural Applications of Glass, vol. 14, Delft: 2018.

[42]   Bedon C, Louter C. Finite Element analysis of post-tensioned SG-laminated glass beams with adhesively bonded steel tendons. Composite Structures 2017;167:238–50. https://doi.org/10.1016/j.compstruct.2017.01.086.

[43]   Bedon C, Louter C. Exploratory numerical analysis of SG-laminated reinforced glass beam experiments. Engineering Structures 2014;75:457–68. https://doi.org/10.1016/j.engstruct.2014.06.022.

[44]   Bedon C, Louter C. Finite-Element Numerical Simulation of the Bending Performance of Post-Tensioned Structural Glass Beams with Adhesively Bonded CFRP Tendons. American Journal of Engineering and Applied Sciences 2016;9(3):680–91. https://doi.org/10.3844/ajeassp.2016.680.691.

[45]   Feldmann M, Kasper R, Abeln B. Guidance for European Structural Design of Glass Components. Report EUR 26439 EN. Report EUR. Luxembourg: 2014. https://doi.org/10.2788/5523.

[46]   Rots J, Blaauwendraad J. Cracks Models for Concrete: Discrete or Smeared? Fixed, Multi-directional or Rotating? Heron 1989;34.

[47]   Sena-Cruz J. Strengthening of concrete structures with near-surface mounted CFRP laminate strips. [PhD thesis]. Minho University, 2005.

[48]   de Borst R. Computational methods in non-linear solid mechanics. Part 2: physical non-linearity. Netherlands: 1991.

[49]   Rots J, Nauta P, Kusters G, Blaauwendraad J. Smeared Crack Approach and Fracture Localization in Concrete. Heron 1985;30.

[50]   Kozłowski M, Kadela M, Hulimka J. Numerical Investigation of Structural Behaviour of Timber-Glass Composite Beams. Procedia Engineering 2016;161:990–1000. https://doi.org/10.1016/j.proeng.2016.08.838.

[51]   Dimande A. Influência da Interface no Reforço à Flexão de Estruturas de Betão com Sistemas FRP. Universidade do Porto, 2003.

PAPER IV

MECHANICAL POST-TENSIONING OF FE-SMA REINFORCED GLASS BEAMS

ABSTRACT: The structural concept of post-tensioned glass systems has been investigated to minimize the unpredictable response of structural glass in tension. The Fe-SMAs have been successfully explored for strengthening existing structures due to their advantages in comparison with the conventional reinforcement materials. In particular, the recently developed Fe-17Mn-5Si-10Cr-4Ni-1VC (mass-%) alloy seems sustainable and shows promising properties for the construction industry. This study investigates the feasibility of post-tensioning glass beams by activating externally bonded Fe-SMA strips. The investigation is mainly focussed on (i) the activation process of Fe-SMA strips, with temperatures ranging between 120 °C and 160 °C, and (ii) the advantages of this reinforcement for post-tensioning of glass structural elements, in terms of applicability and structural response. Flexural tests show that it is possible to obtain ductile failure modes when glass beams are reinforced with passive or activated Fe-SMA strips. Activation of Fe-SMA strips resulted in an increase of up to 30 % of the cracking load.

1   INTRODUCTION

Although the theoretical tensile strength of glass is exceptionally high at the molecular scale, its effective tensile strength is much lower due to mechanical flaws resulting from the production, cutting, polishing and handling operations [1,2]. The tensile strength of glass is influenced by (i) surface conditions, i.e., the number and depth of initial flaws, (ii) size of the glass elements, (iii) loading history, i.e., intensity and duration, and (iv) residual stresses and environmental conditions [3]. The glass industry has developed improved processing methods, namely the tempering and the lamination [4,5]. A favourable stress field is created by the tempering, which restrains the propagation of existing surface flaws and increases the apparent tensile strength of glass. Glass lamination, on the other hand, uses a transparent polymeric interlayer to join glass plies in a single panel – following the concept of redundancy – to ensure the integrity of the structural element after cracking. Nevertheless, glass remains an extremely fragile material.

1.1.   Glass composite systems

Several safety concepts have been developed based on the composite action between glass and reinforcement materials, such as timber (e.g. [6,7]), steel (e.g. [8–11]), Carbon Fibre Reinforced Polymers, CFRP (e.g. [12–14]) and Glass Fibre Reinforced Polymers, GFRP (e.g. [5,15–19]) have been investigated. Due to the transfer of tensile stresses from the glass to the reinforcement through shear stresses in the adhesive joint, these composite glass systems show the ability to carry load even after glass cracking.

The tensile strength of annealed glass is unpredictable because surface flaws grow when exposed to long-term loads under environmental conditions. The higher the tensile stress, longer the loading duration and deeper the surface flaws, the lower the tensile strength of annealed glass [3]. Tempering has been successful at preventing this unpredictability. However, tempered glass failure is catastrophic and results in small shards, compromising its structural integrity and, consequently, the post-failure residual strength/reserve and ductility of composite systems [4,5,18]. Heat-strengthened glass provides an interesting compromise between fairly high tensile strength and sufficiently large fragmentation patterns. In any case, annealed glass has obvious economic and structural benefits for the construction industry [20].

In order to overcome the unpredictability of the tensile strength of annealed glass and make it safer for structural applications, the structural concept of post-tensioned glass systems has been recently investigated, using steel (e.g. [9,11,21]), CFRP (e.g. [12]) and SMA (e.g. [22]) as reinforcement. These studies, yet reduced in number, have addressed different strategies concerning (i) the relative position of the reinforcement element; (ii) the post-tensioning setup; and (iii) the anchorage strategy to transfer the post-tensioning force from the reinforcement to the glass. While Bos *et al.* [9] and Louter *et al.* [11] positioned the reinforcement within the glass panel, Jordão *et al.* [21] and Louter *et al.* [12] placed it externally. In relation to the post-tensioning setup, the reinforcement has been positioned as a straight line along the glass panel (e.g. [12]) or adopting a layout resembling the bending moment curve shape (e.g. [21]). Concerning the anchorage strategy, the reinforcement has been mechanically anchored (e.g. [11]) and/or adhesively bonded to the glass (e.g. [12]).

Although the post-tensioned glass systems were proved to be effective, the procedure for applying post-tensioning is sometimes challenging because (i) heavy equipment is required, e.g. hydraulic actuators; and (ii) high stress concentrations are induced in the glass substrate when the prestressed reinforcement is released. As the tensile strength of annealed glass depends on the surface conditions and loading history [3], appropriate safety measures must be taken to ensure that the post-tensioning force is smoothly transferred from the reinforcement to the glass, preventing the premature failure of the glass due to the growth of existing surface flaws [23].

1.2.   SMAs in civil engineering

Shape Memory Alloys (SMAs) have been used in civil engineering applications (e.g. buildings and bridges), reducing the effort and time involved in post-tensioning actions in comparison to conventional reinforcement materials (e.g. steel and CFRP). SMAs have shown to be advantageous due to two main characteristics [24,25]: (i) the *shape memory effect*, which is the capability of the deformed material to partially return to its initial shape when heated above the activation temperature; and (ii) the *superelasticity*, which refers to the property in which the material undergoes large mechanical deformations, but can still recover its initial shape after unloading and without the need for any thermal activation.

SMAs have been used for different fields of the civil engineering. While the superelasticity effect is used to increase the damping and energy dissipation of reinforced concrete structures during earthquakes (e.g. [26,27]), the shape memory effect is appropriate for the post-tensioned strengthening of structural elements (e.g. [28–33]). When the SMA reinforcement is properly anchored

(e.g. adhesively bonded and/or mechanically anchored) to the structural element prior to its activation, recovery stresses (post-tensioning forces) are developed by heating and subsequent cooling of the SMA material. The simplicity of this post-tensioning technique has enhanced the applicability of SMAs for the post-tensioned strengthening of existing structures, where the conventional procedure with hydraulic jacks is often difficult to implement due to lack of space [25,34].

The most recognized SMA is the nickel-titanium (Ni-Ti) alloy, which has been used in the automotive, aerospace, robotic, biomedical and construction industries for both sensory and structural (e.g. damper and reinforcement) purposes [24]. However, the Ni-Ti alloy may hardly be considered as a sustainable solution for generalized applications in the construction industry [31]. In construction, the material usage is several orders of magnitude larger when compared to other industries and, therefore, low-cost and less resource-intensive SMAs have been applied in this case, namely the iron-based (Fe-SMAs) and the copper-based (Cu-SMAs) alloys. Fe-SMAs are relatively low cost and easy to process, machine and weld, thus making them the most promising candidates for the application in the construction industry, whether for repairing existing structures or for reinforcing new ones [25,35].

In 1982, Sato *et al.* [36] discovered shape memory effect in Fe-Mn-Si alloys. Since then, the chemical composition of Fe-SMAs has been improved to increase their corrosion resistance, training effect, cyclic deformation and strength [37]. In this context, a new Fe-SMA, suitable for the construction industry, was developed in 2009 by Dong *et al.* [38] at the Swiss Federal Laboratories for Materials Science and Technology (Empa), Switzerland. This Fe-SMA, which can be activated by resistive heating, was especially developed for the post-tensioned strengthening of existing concrete structures. In addition, it is produced at atmospheric conditions, without the need for expensive high-vacuum processing facilities and thermomechanical training, making the large-scale production feasible [31,39]. Research studies have shown the potential of this Fe-SMA for the post-tensioned strengthening of concrete, using strips (e.g. [30,31,40,41]) or ribbed bars (e.g. [42,43]), and metallic (e.g. [28,29,34]) structural elements. Further research studies have been conducted to show the potential of the developed Fe-SMA for structural engineering applications, investigating aspects related to the fatigue behaviour (e.g. [39]), phase transformation (e.g. [41]), creep and stress relaxation (e.g. [44]), electrochemical and corrosion behaviour (e.g. [45]) and recovery stress (e.g. [46]).

The application of SMAs as reinforcement material in glass composite systems is a very recent research field and, consequently, very few studies are found in the literature addressing this topic. They have focused on the bond behaviour of glass-to-SMA adhesively bonded joints (e.g. [47,48]). In

addition, Silvestru *el at.* [22] proved, for the first time, the feasibility of activating Fe-SMA reinforcement to introduce an initial compressive pre-stress in laminated glass beams. Furthermore, the results showed that SMA reinforced glass elements can exhibit ductile failure modes.

1.3. Research significance

This study investigates the feasibility of the post-tensioning of monolithic glass beams by activating Fe-SMA strips previously bonded to the bottom edge, according to the External Bonded Reinforcement (EBR) technique, as well as the influence of the activation temperature on their post-cracking performance. After being bonded with an epoxy adhesive to glass structural elements, Fe-SMA strips were heated at temperatures ranging between 120 °C and 160 °C to activate them and introduce post-tensioning in the glass elements. The experimental programme comprised (i) mechanical characterization tests and (ii) full-scale bending tests. This study also addresses the opportunity to adapt the Fe-SMA reinforcement activation procedure in order to take advantage of initially deleterious effects, such as the degradation of the adhesive due to temperature exposure, in favour of an optimized anchorage and the gradual stress transfer from the reinforcement to the glass substrate.

2   EXPERIMENTAL PROGRAMME

Two different types of experimental tests were carried out in the scope of this work: (i) first, material characterization tests were conducted to determine the mechanical properties of the Fe-SMA material and (ii) second, four-point bending tests were carried out to assess the flexural behaviour of annealed glass beams strengthened with passive Fe-SMA strips (reference beams) and activated Fe-SMA strips (post-tensioned beams).

2.1. Materials

2.1.1.   Iron-based shape memory alloy (Fe-SMA)

In this research, the Fe-17Mn-5Si-10Cr-4Ni-1(V,C) (mass%) alloy with shape memory effect, developed by Dong *et al.* [38], was used as a reinforcement material for glass beams. Its detailed production procedure is described by Leinenbach *et al.* [49]. The industrial production of this Fe-SMA is ensured by re-fer AG Company, which offers two distinct products: (i) ribbed bars; and (ii) plates with thicknesses of 0.5 and 1.5 mm and widths of 50 and 100 mm. In this study, Fe-SMA plates of 100 (width) × 1.5 (thickness) [mm] were used to extract strips of 1500 (length) × 10 (width) × 1.5 (thickness) [mm]. The Fe-SMA strips were cut using the water jet technique to avoid overheating the Fe-SMA material. Specimens were also extracted to characterize the Fe-SMA's tensile behaviour.

Five specimens of 250 (length) × 10 (width) [mm] were tested in tension at ambient temperature and at a constant displacement rate of 1.0 mm/min until failure. Prior to testing, 50 mm long tabs were glued to the edges of the Fe-SMA strips to avoid premature failure of the specimen due to stress concentrations introduced by the clamping equipment. The longitudinal deformation of each specimen was measured using a clip gauge (type: MFA 12; linearity: 0.1 %; sensitivity: 2.0 mV/V; resolution: 1.0 p.m.; precision: ±1.5 µm) with stroke of 50 mm, which was placed at the central region of the specimens (see **Figure IV.1a**). A universal testing machine and a load cell with a maximum capacity of 200 kN (precision of 0.01 kN) were used to record the load. Furthermore, some specimens were monitored with the Digital Image Correlation (DIC) technique and using the GOM Correlate 2019 software [50] for processing the images. A thin spray of white matt paint was applied over a region of interest, followed by a spray of black dots using black paint. The camera used to capture the images included a full frame CMOS sensor (7360 × 4912 pixels). The images of the ROI were collected at an acquisition frequency of 0.1 Hz.

(a) (b)
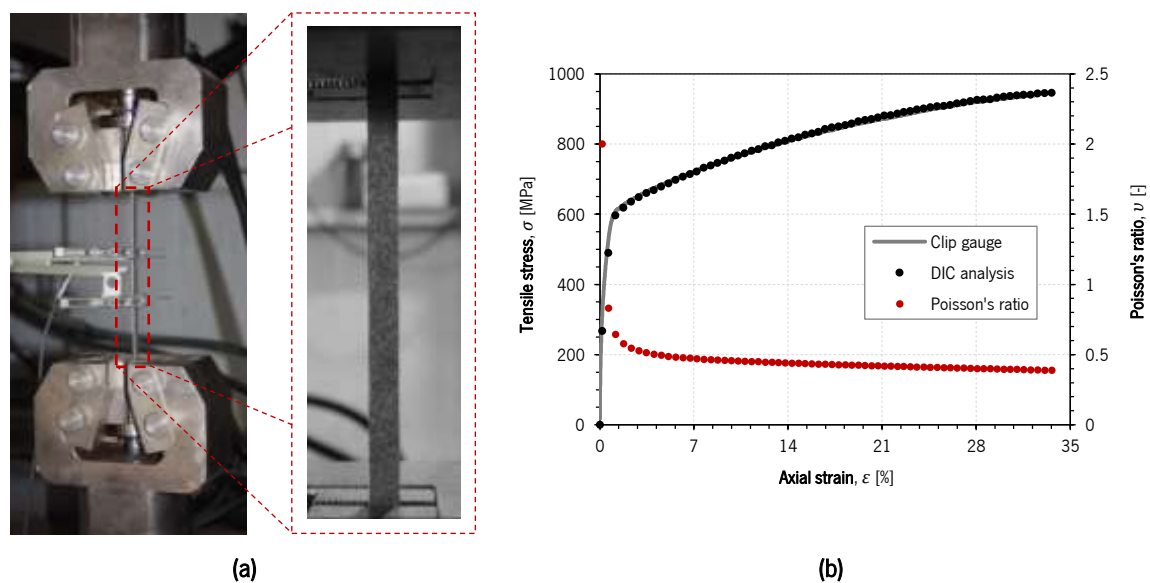
Figure IV.1: Tensile tests on Fe-SMA strips: (a) experimental setup and DIC pattern; and (b) stress-strain response obtained from both measurements methods, as well as evolution of the Poisson's ratio.

Table IV.1 includes the average values obtained for the modulus of elasticity (E_r), tensile strength ($f_{r,t}$) and ultimate strain ($\varepsilon_{r,ult}$). As the Fe-SMA shows a highly non-linear behaviour, E_r was determined from the linear portion of the stress-strain response between stress values of 0 MPa and 200 MPa. The mechanical properties indicated in **Table IV.1** compare very well with values found in the literature for this Fe-SMA. The modulus of elasticity of 172 GPa is in the range of previously published values, from 160 GPa [46] to 175 GPa [39]. With respect to the tensile strength, 948.1 MPa is also an

intermediate value between 939.3 MPa by Silvestru *et al.* [48] and 1015 MPa by Ghafoori *et al.* [39]. However, the ultimate strain of 31.0 % is lower when compared to the values reported in the literature, usually higher than 40 %. The main reason for this difference seems to be displacement speed between clamps, which in this study was set to 1.0 mm/s while literature values range from 0.012 mm/s [48] and 0.075 mm/s [39].

Table IV.1: Mechanical properties of the Fe-SMA material, annealed glass and 3M adhesive (average values).

Material	E_r [GPa]	$f_{r,t}$ [MPa]	$\varepsilon_{r,ult}$ [%]	υ [-]
Fe-SMA	172.0 (1.7%)	948.1 (0.6%)	32.5 (2.3%)	0.39
Material	E_g [GPa]	$f_{g,t}$ [MPa]		υ [-]
Annealed glass [1]	74.0 (2.6%)	40		0.23
Material	E_{adh} [MPa]	f_{adh} [MPa]	$\varepsilon_{adh,ult}$ [‰]	υ [-]
Adhesive [1]	1728.1 (3.3%)	32.8 (4.2%)	30.7 (2.8%)	0.38

Notes:
[1] Results collected from Rocha *et al.* [51]
Coefficients of variation (CoV) are indicated in parenthesis

Figure IV.1b shows the typical stress – strain experimental response obtained from both measurement methods. Given the good agreement between the DIC and clip gauge measurements, the Poisson's ratio was determined from the deformation fields at the surface of the specimens and assuming plane stress state. **Figure IV.1b** shows the obtained Poisson's ratio as a function of the axial strain. Unexpectedly, at the beginning of loading, the Poisson's ratio reached values of approximately 2.0, which gradually decreased to 0.39 at the end of the stress – strain response. Such response seems to be related to the phase change behaviour of the SMA materials. During the martensitic transformation, at the beginning of the stress – strain response, axial deformation is associated to the lattice detwinning. On the other hand, after martensitic transformation, at the end of the stress – strain response, further axial deformation is associated to the permanent and irreversible slip between atomic planes (yielding). Hence, at this final stage, the Fe-SMA Poisson's ratio converges to values exhibited by traditional materials (e.g. steel).

2.1.2. Glass and adhesive

All specimens used in the experimental programme were made of annealed glass. Laminated glass was not considered at this stage of the research because the interlayer may be significantly damaged during the heating of Fe-SMA strips, leading to layering of the glass plies. This effect, which is difficult to measure experimentally, may introduce uncertainty in the structural response of post-tensioned beams. The edges of the annealed glass panels were polished to minimize the flaws resulting from

the cutting process and to prevent accidents during handling. The mechanical properties of the annealed glass shown in **Table IV.1** were previously assessed by Rocha *et al.* [51], with the tensile strength ($f_{g,t}$) and the modulus of elasticity (E_g) equal to 40 MPa and 74.0 GPa, respectively.

An epoxy adhesive, the two-component adhesive 3M Scotch-Weld DP490, suitable for glass-to-steel bonded connections was used in these experiments. The tensile behaviour of this adhesive was previously characterized by Rocha *et al.* [51]. Its mechanical properties are presented in **Table IV.1**, including the Poisson's ratio determined by Nhamoinesu and Overend [52]. The adhesive presents a non-linear behaviour in tension until failure, combining a high tensile strength (f_{adh}) of 32.8 MPa with a relatively low modulus of elasticity (E_{adh}) of 1728.1 MPa, as well as an ultimate strain ($\varepsilon_{adh,ult}$) of 30.7 ‰.

2.2. Production and testing of the specimens

As schematically shown in **Figure IV.2**, the application of Fe-SMA strips for post-tensioning of structural elements consists of three main phases: (i) pre-straining; (ii) activation; and (iii) service loading. The post-tensioning procedure will be briefly explained in this section. First, the Fe-SMA strip is mechanically loaded (path (1) in **Figure IV.2**) at room temperature, between M_s (martensite start temperature) and A_s (austenite start temperature), modifying the lattice from austenite to detwinned martensite (i.e., martensitic transformation). When the target strain is attained, the Fe-SMA is then completely unloaded (path (2) in **Figure IV.2**), then presenting a permanent macroscopic deformation. Second, the Fe-SMA strip is mechanically anchored and/or adhesively bonded to the structural element. Third, the Fe-SMA strip is activated through resistive heating (path (3) in **Figure IV.2**) and, when A_s is surpassed, the restrained Fe-SMA strip tends to shrink due to the reverse transformation from detwinned martensite to austenite. Consequently, tensile stresses (i.e., recovery stresses) are developed in the Fe-SMA strip, recovering the thermal expansion observed at the beginning of the thermal cycle. When the target temperature is attained, heating of the Fe-SMA strip is stopped and the recovery stress gradually increases during the cooling phase, until the ambient temperature is reached again (path (4) in **Figure IV.2**). Further details related to the behaviour of Fe-SMA during the activation can be found in the literature (e.g. [39,53]).

Taking into account the procedure mentioned above, the post-tensioned glass beams were prepared considering the following steps: (i) cutting the Fe-SMA strips; (ii) pre-straining the Fe-SMA strips; (iii) bonding the Fe-SMA strips to the bottom edge of the glass panels; and (iv) activating the Fe-SMA strips using a resistive heating device. The reference beams were manufactured considering only the first

and third steps. On the other hand, the bonding of Fe-SMA strips – the third step of the general procedure – involved additional paths. First, the bonding surfaces were carefully degreased and cleaned with acetone. Subsequently, the adhesive was prepared and applied according to the requirements included in the manufacturer specifications. After that, both adherends were assembled and then slightly pressed against each other in order to reach a pre-defined adhesive layer thickness. Finally, all specimens were placed in a climatic chamber at 30 °C during 7 days.
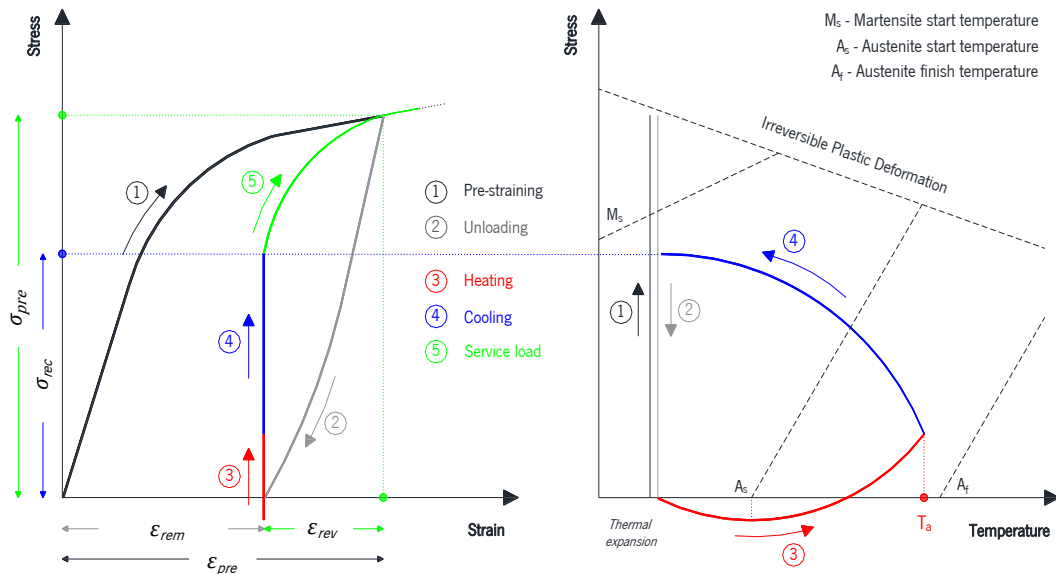
Figure IV.2: Schematic representation of the activation procedure of Fe-SMAs under strain recovery constraint (red colour) adapted from Shahverdi *et al.* [31].

The glass-SMA composite beams were manufactured considering the geometry shown in **Figure IV.3**, which consisted of an annealed glass panel of 100 (height) × 12 (thickness) [mm] reinforced at the bottom edge with a Fe-SMA strip of 10 (width) × 1.5 (thickness) [mm]. The components were joined using the epoxy adhesive presented in **Section 2.1**. The thickness of the adhesive joint (t_a in **Figure IV.3**) was set to 0.3 mm. A total of 6 glass-SMA composite beams were produced, namely two reference beams with passive Fe-SMA strips and four post-tensioned beams with activated Fe-SMA strips. They were identified following the nomenclature *i-j-z*, where *i* was adopted to distinguish reference beams (R) from post-tensioned beams (P), *j* refers to the activation temperature (T0 for reference beams and T120, T140 and T160 for post-tensioned beams – further details in **Section 2.2.2**) and *z* identifies the specimens of each series with the same activation temperature (I and II).
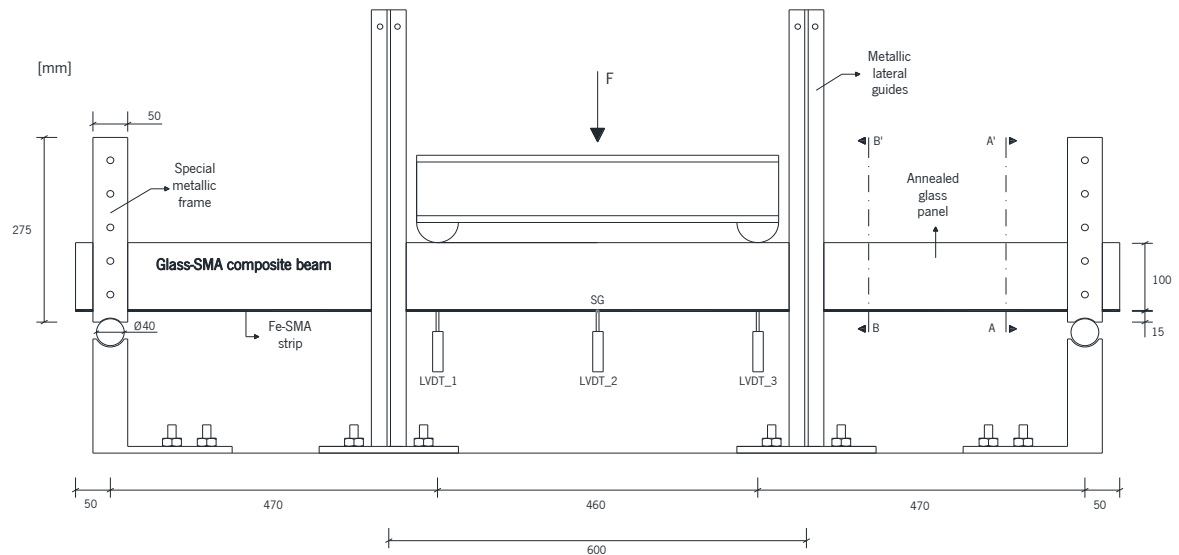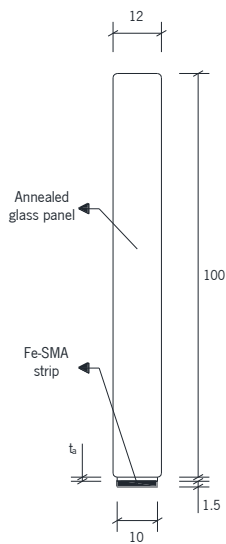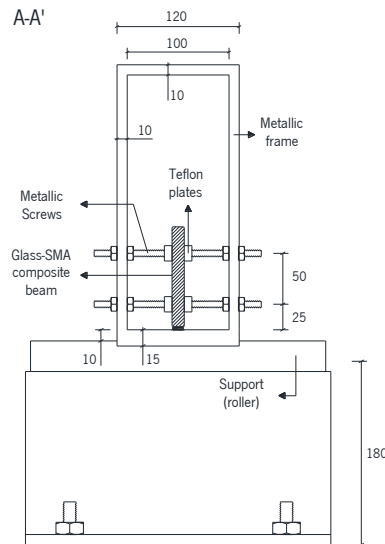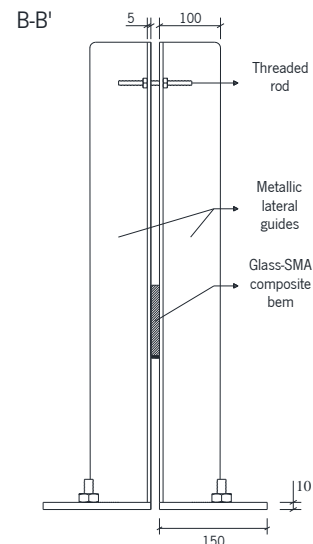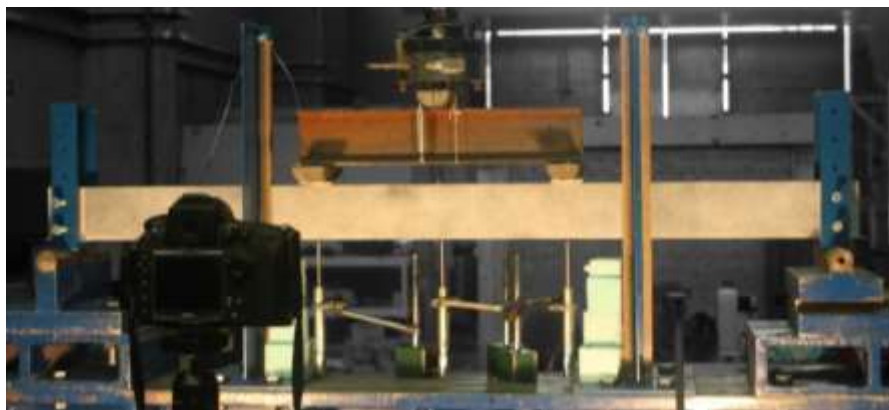
Figure IV.3: Glass-SMA composite beams: (a) beam geometry and instrumentation adopted for the bending tests; (b) cross-section geometry; (c) metallic frames placed at the support sections; (d) lateral guides to prevent lateral instability; and (e) experimental setup. All units in [mm].

2.2.1. Pre-straining of Fe-SMA strips

The amount of recovery stress depends on the amount of martensite in the Fe-SMA. Investigations conducted by Shahverdi *et al.* [31] on the Fe-SMA used in this study showed that a pre-strain (ε_{pre}) of 2.0 % is sufficient to achieve the maximum possible recovery stress. Therefore, before bonding the Fe-SMA strips to the glass substrate, these were pre-strained up to 2.25 % at room temperature. After unloading, the Fe-SMA strips showed a permanent remaining deformation (ε_{rem}) of approximately 1.25 %. Only a portion of the ε_{rem} could be recovered by activation (recovery strain) since the non-linear behaviour exhibited during pre-straining was a consequence of the phase transformation from austenite to martensite, as well as the plastic deformation (irreversible slippage between atoms) [46]. As shown in **Figure IV.4**, the deviation from the linear elastic unloading is called pseudo-elastic strain, indicating that the reverse transformation from martensite to austenite occurred partially during unloading [46]. The longitudinal deformation in the Fe-SMA strips was measured using a clip gauge (the same used for the characterization of the Fe-SMA described in **Section 2.1.1**) with a gauge length of 100 mm. A universal testing machine was used to apply the load.

(a)　　　　　　　　　　　　　(b)
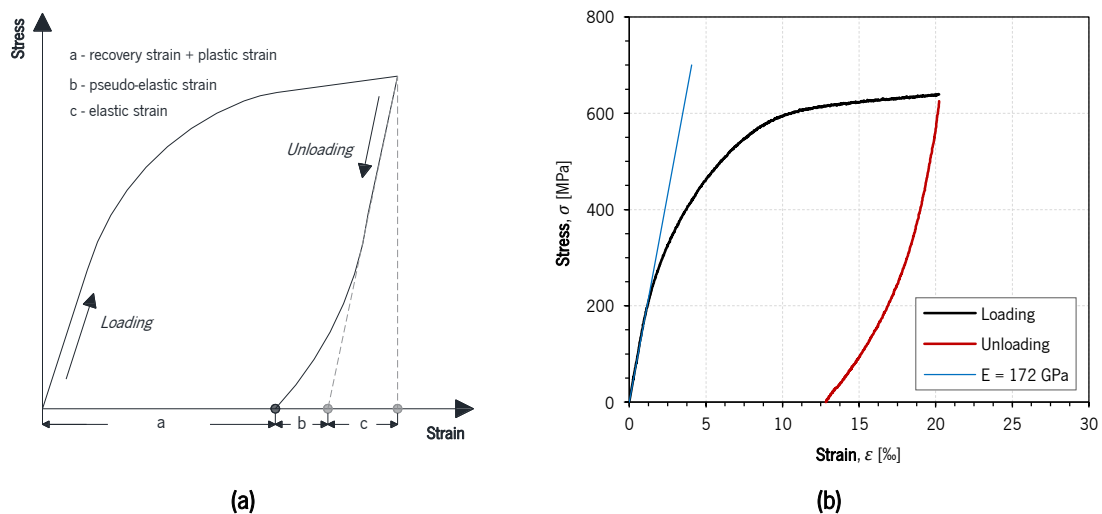
Figure IV.4: Pre-straining of Fe-SMAs: (a) schematic diagram (b) stress-strain diagram retrieved from the experiments.

2.2.2. Activation procedure

Glass contains numerous surface flaws that result from the production, cutting, polishing and handling processes [1]. In addition, glass edges typically have lower tensile strength than glass surfaces [54]. Accordingly, a smooth transfer of the post-tensioning force from the reinforcement to the glass panel must be guaranteed to avoid the growth of existing surface flaws over time, especially near the glass corners, which are usually weaker than the glass surfaces due to the handling operations. In addition,

based on previous studies on the activation of adhesively bonded SMA reinforcement (e.g. [48,55]), an undamaged bond region (anchorage zone) should be guaranteed on both sides of the activated Fe-SMA strip zone to transfer the post-tensioning force from the reinforcement to the glass substrate. These anchorage zones prevent premature debonding of the Fe-SMA strip during activation due to the loss of shear interaction at the bonded interfaces caused by heating. Accordingly, the Fe-SMA strips should not be activated throughout its entire length.

As shown in **Figure IV.5a**, the activated length (l_a) was set to 700 mm (half of the beam span), creating an undamaged bond length of 400 mm at both beam ends (non-activated Fe-SMA strip zones). A welding machine was used to supply the electrical power (see **Figure IV.5b**). Two metallic pieces were symmetrically positioned at 350 mm from the mid-span section and subsequently pressed against the bottom edge of the Fe-SMA strip by means of metal clamps (see **Figure IV.5c** and **Figure IV.5d**). After that, the electrode holder and the ground clamp were connected to these metallic pieces, creating a circuit where the electrical current flowed from the former to the latter. Polytetrafluoroethylene (teflon) plates were positioned between the metallic pieces and the metal clamps, for safety.

A relatively high current density of ≈ 4.0 A/mm^2 was adopted to shorten the heating phase as much as possible, in order to reduce the heat flow into the non-activated Fe-SMA strip zones. Different activation temperatures (T_a) were adopted to activate the Fe-SMA: (i) 120 °C for the P_T120 beams, (ii) 140 °C for the P_T140 beam, and (iii) 160 °C for the P_T160 beam. The power supply was interrupted when the target temperature was attained. The activation process was assumed complete when the temperature on the Fe-SMA strip reached the room temperature again.

Figure IV.5a shows the instrumentation adopted for the activation process. The deflection at mid-span section of the Fe-SMA reinforced glass beams was measured using a displacement transducer – Linear Variable Differential Transformer (LVDT) – with stroke of 50 mm and precision of 0.01 mm. Furthermore, a strain gauge (type: BFLA-5-3-3L by TML; gauge length: 5 mm; gauge factor: 2.08 ± 1 %) was placed at the top edge of the glass panel. On the other hand, an infrared camera (Type: FLIR T420; temperature range: -20 °C to 650 °C; spectral range: 7.5 μm to 13 μm) was used to monitor the temperature evolution in the Fe-SMA strip during the activation process. User-defined parameters required by the infrared camera (e.g. emissivity) were previously calibrated using a type K thermocouple (see **Figure IV.6**). For the sake of simplicity, only a small part of the Fe-SMA strips (≈ 20 mm in length) was monitored by the infrared camera (control region), therefore assuming a constant temperature along the activated length. The infrared camera was positioned so that only the

Fe-SMA strip was captured by the control region (see **Figure IV.7**), in order to avoid de influence of the emissivity of other components on the maximum temperature registered within the control region, which was taken as the effective activation temperature.

(a)

(b)

(c)

(d)
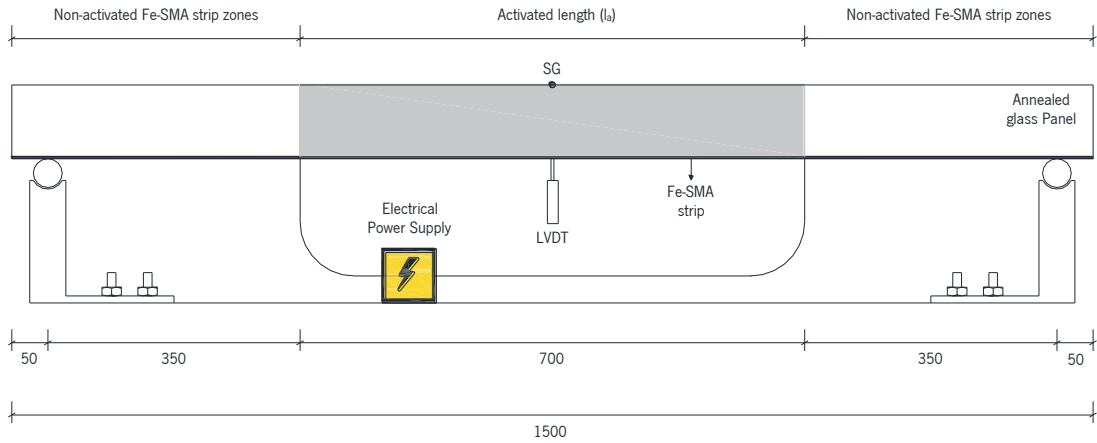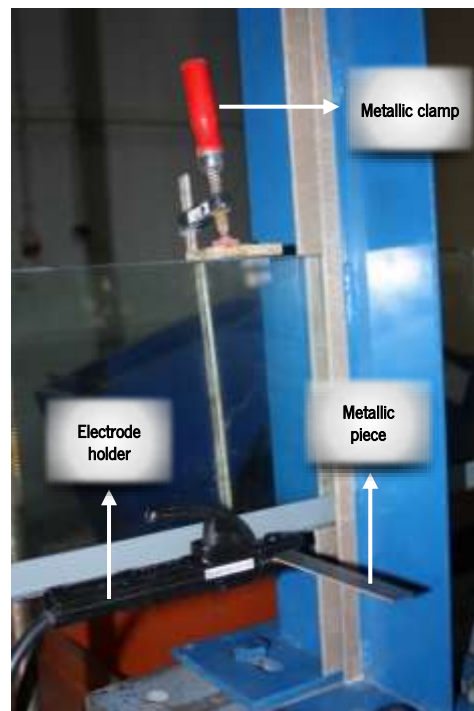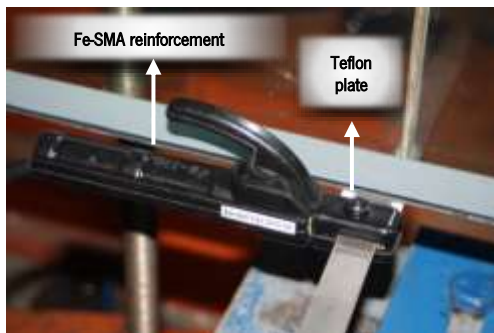
Figure IV.5: Activation of the Fe-SMA strips: (a) activated region and adopted strategy; (b) welding machine used to supply electrical power for the activation process; and (c) and (d) connection between the welding machine clamps and the Fe-SMA reinforcement. All units in [mm].
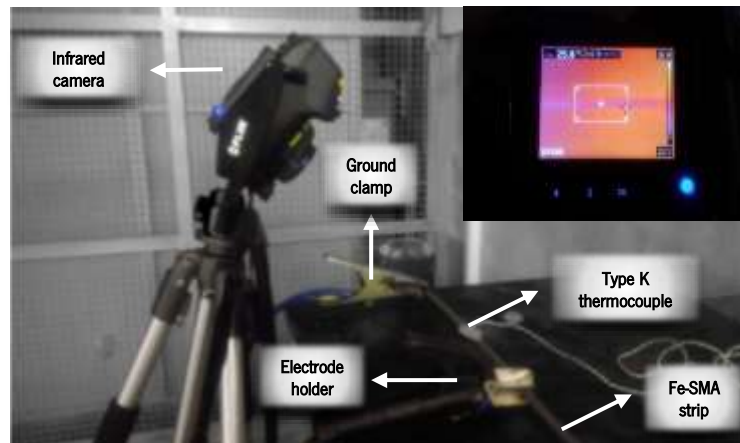
Figure IV.6: Preliminary experiments conducted to determine the user-defined variables required by the thermographic camera.
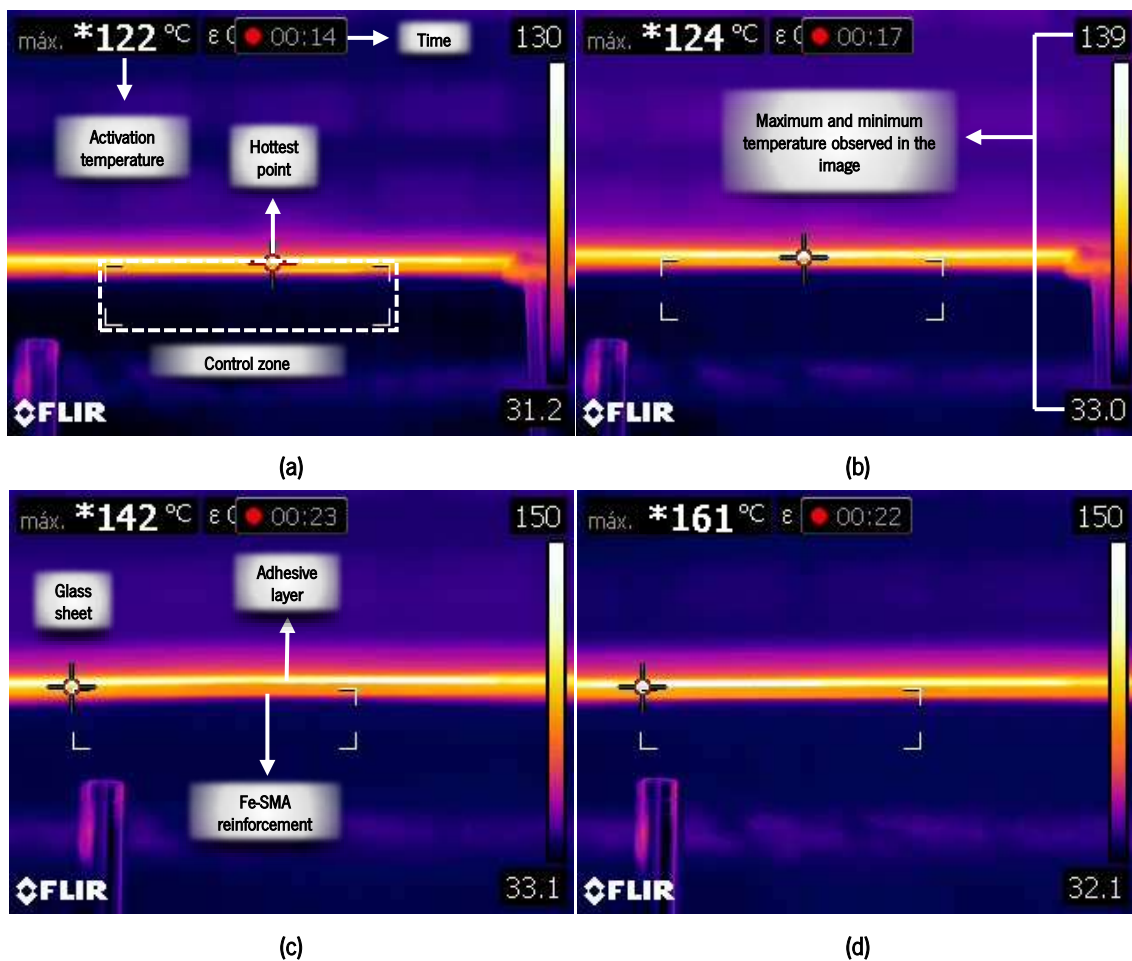
Figure IV.7: Images retrieved by the infrared camera corresponding to $T = T_a$ in each of the post-tensioned beams: (a) P_T120-I, (b) P_T120-II, (c) P_T140 and (d) P_T160.

2.2.3.   Bending tests

As shown in **Figure IV.3**, the glass-SMA composite beams, with a span of 1.4 m, were tested adopting a symmetrical four-point bending configuration, with load points 460 mm apart. In order to avoid the direct metal-glass contact and the premature failure of composite beams, teflon plates were positioned between the steel pieces and the glass. As shown in **Figure IV.3c**, two pairs of vertical metallic guides were symmetrically positioned at 300 mm from the mid-span section to prevent lateral displacements (e.g. lateral-buckling effect). Each pair was joined by means of threaded rods to enhance the out-of-plane flexural stiffness. The surfaces of these lateral guides were carefully wrapped with a thin teflon film to prevent frictional forces during tests, as well as direct metal-glass contact.

In-plane flexural rotations were free at both supports, and one of the supports allowed the longitudinal sliding of the beams. As illustrated by **Figure IV.3a**, metallic frames specially designed were placed overhead the supports to restrain out-of-plane rotations at the support sections. After positioning the composite beams, the threaded screws of metallic boxes were carefully pressed against the glass, using intermediate teflon plates to avoid glass-steel contact.

Figure IV.3a shows the LVDTs used in these experiments: LVDT_1 and LVDT_3 measured the deflections at loading point sections, while the LVDT_2 measured the mid-span deflection. These LVDTs have equal characteristics to the ones referred in **Section 2.2.2**. Axial strains in the Fe-SMA strips were also measured at the mid-span section using a strain gauge (type: PFL-10-11-3LJC-F by TML; gauge length: 10 mm; gauge factor: 2.12 ± 1 %). A load cell with a maximum measuring capacity of 200 kN and a linearity error of ± 0.05 % was used to measure the applied load. All test specimens were loaded monotonically under displacement control at a speed of 1.0 mm/min (internal LVDT of the actuator). While the applied load and the deflections were measured using a relatively high acquisition frequency of 50 Hz to capture sudden phenomena resulting from the low fracture energy of the glass, axial strains were recorded at a frequency of 3 Hz due to limitations on the acquisition system. The tests were conducted in laboratory environment at an average temperature of 26 °C and relative humidity of 65 %.

The Digital Image Correlation (DIC) method was also used to document the evolution of cracking and the formation of resisting mechanisms in glass-SMAs composite beams. Further details about the DIC method can be found in **Section 2.1.1**, including the characteristics of the camera used.

3   ACTIVATION OF FE-SMA STRIPS

3.1.   Experimental measurements

Figure IV.7 shows the images captured by the infrared camera during the activation of Fe-SMA reinforcement, when the peak temperature was reached. **Figure IV.8** depicts the evolution of the vertical displacement at the mid-span section (d_{exp}), the tensile strain at the top edge of the glass panel ($\varepsilon_{g,t}$) and the temperature in the Fe-SMA strip (T) during the activation process. It is noteworthy to mention that positive values correspond to tensile strains and therefore downward displacements. Finally, the values of d_{exp} and $\sigma_{g,t} = \varepsilon_{g,t} \times E_g$ registered at the end of the cooling phase are summarized in **Table IV.2**, as well as the maximum temperature (T_a) achieved in the Fe-SMA strip. The heating phase of each beam, which lasted between 10 and 18 seconds, was much shorter than the subsequent cooling phase (≈ 3000 seconds). It is noteworthy to mention that no detachment of the Fe-SMA strip from the glass substrate was observed for any of the post-tensioned beams, showing that the used adhesive performed well when exposed to the high temperatures experienced.

As shown in **Figure IV.8**, due to the thermal expansion of the Fe-SMA strips, all beams deformed downwards between 0.067 mm and 0.086 mm at the beginning of the heating phase, leading to the appearance of compression stresses at the top region of the glass panel. A few seconds later, yet during the heating phase, these initial deformations were completely suppressed by the shape memory effect of Fe-SMAs. Due to the reverse transformation from martensite to austenite, the Fe-SMA strips developed recovery stresses and, consequently, the beams deformed upwards between 0.433 mm and 0.752 mm.

3.2.   Recovery stress

Based on the strain gauge measurements, the recovery stress developed in Fe-SMA strips ($\sigma_{rec,sg}$) may be estimated by performing numerical simulations. In this study ABAQUS 6.14 finite elements software was used [56]. Both the glass and the Fe-SMA were simulated as an isotropic material with linear elastic behaviour. The mechanical properties adopted for the glass were taken from **Table IV.1**. Based on the experiments conducted by Shahverdi *et al.* [31], the relationship between the recovery stress (restrained Fe-SMA strip) and the recovery strain (non-restrained Fe-SMA strip) was simulated using an equivalent modulus of elasticity ($E_{r,a}$) equal to 95 GPa. In addition, within the non-activated region, the non-linear behaviour of the Fe-SMA material in tension was simulated using a USDFLD subroutine to select the modulus of elasticity as a function of the axial stress, based on the response

shown in **Figure IV.1**. A Poisson's ratio of 0.39 (see **Table IV.1**) was adopted for these numerical simulations.
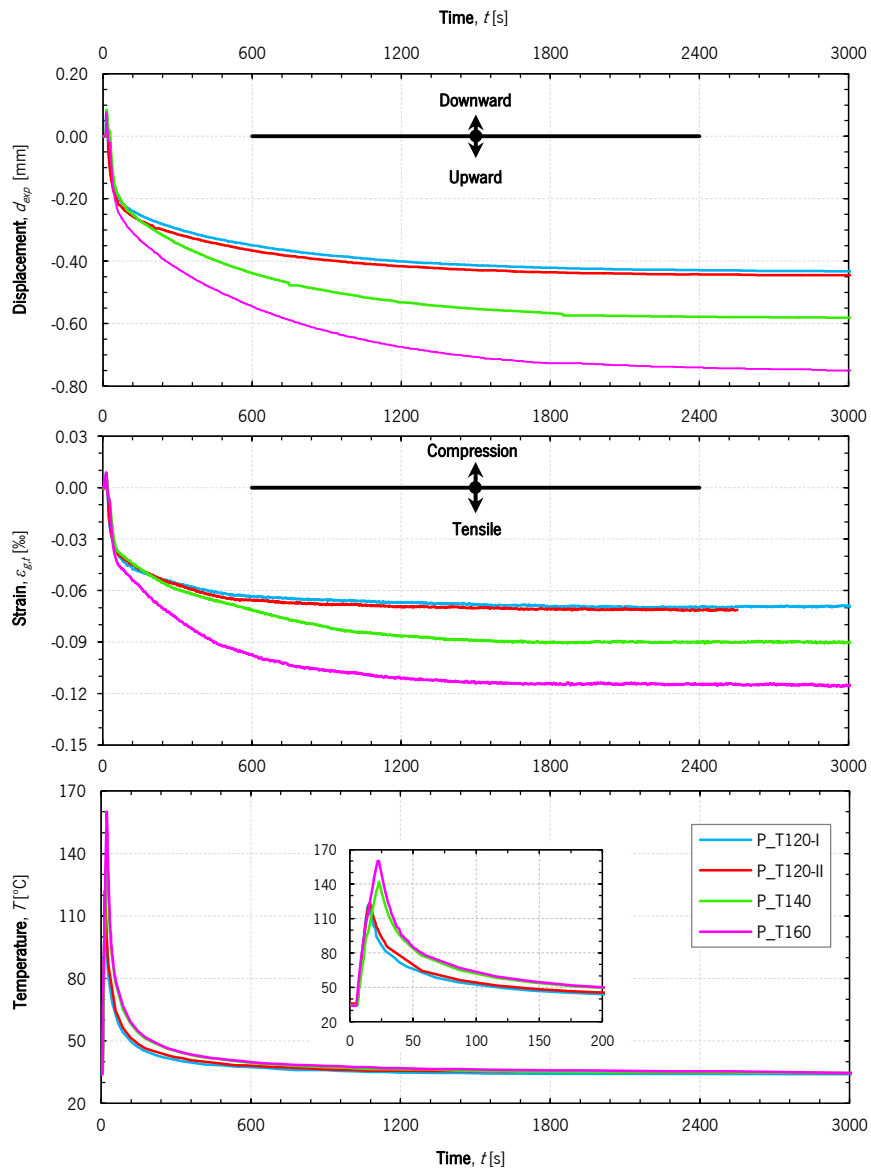
Figure IV.8: Activation process of the externally bonded Fe-SMA strips: displacement at mid-span (d_{exp}), strain at the top edge of the glass panel ($\varepsilon_{g,t}$) and temperature in the Fe-SMA (T).

Typically, polymeric adhesives do not perform well at high temperatures. After reaching the glass transition temperature, the polymers lose their ability to transfer shear stress between adherends. Thereby, the activation process and resulting heating effect of the Fe-SMA strips certainly reduced the shear interaction at the bonded interfaces during the activation process, and likely damaged the adhesive afterwards. A maximum working temperature of 120 °C is indicated by the adhesive's technical data sheet, but it is expectable that a considerable degradation of the mechanical properties exists at temperatures of this magnitude. Accordingly, the complete absence of shear interaction within

the activated region (shaded in **Figure IV.5a**) – no composite action – was considered in these numerical simulations. Thus, the beams were simulated by setting E_{adh} to zero in the activated length, while the remaining length of the adhesive was considered as undamaged and simulated as an isotropic material with linear elastic behaviour (E_{adh} = 1728 MPa). In the non-activated region, the numerical model assumed that the relative slippage at the reinforcement/adhesive and adhesive/glass interfaces was not possible. For the sake of simplicity, the adopted approach did not consider the thermo-mechanical behaviour of the components and neglected any heat flow into the non-activated region.

Table IV.2: Experimental measurements retrieved from the activation of the Fe-SMA reinforcement and comparison with results extracted from numerical simulations performed to determine the recovery stress.

Experimental measurements			
Beam	T_a [°C]	d_{exp} [mm]	$\sigma_{g,t}$ [MPa]
P_T120-I	122	0.433	5.11
P_T120-II	124	0.445	5.25
P_T140	142	0.584	6.70
P_T160	161	0.752	8.51
Numerical results			
Beam	d_{num} [mm]	$\sigma_{g,b}$ [MPa]	$\sigma_{rec,sg}$ [MPa]
P_T120-I	0.412 (-4.8%)	-10.16	201.7
P_T120-II	0.423 (-4.9 %)	-10.43	207.0
P_T140	0.539 (-7.7 %)	-13.29	263.8
P_T160	0.685 (-8.9%)	-16.89	335.2

Note:
The values between parentheses are the difference in percentage between d_{num} and d_{exp}.

Regarding the finite element modelling, two-dimensional simulations were carried out assuming the symmetrical behaviour of SMA reinforced glass beams with respect to the mid-span vertical axis. A finite element mesh with an element size of 5 (width) × 5 (height) [mm] was adopted, using 4-node plane stress elements (CPS4) with 2 × 2 integration points for all components. **Figure IV.9** shows the geometry, boundary conditions, load configuration and the mesh pattern. In addition, the rigid connection at the Fe-SMA/adhesive and adhesive/glass interfaces were materialized setting these as a "tie" constraint, which avoids relative translations and/or rotations between adjacent nodes. Recovery stresses were simulated as an imposed temperature variation along the l_a. Finally, for each specimen, iterative numerical simulations were run until the numerical axial stress at the top edge of the glass panel attained the experimental one (see $\sigma_{g,t}$ in **Table IV.2**).
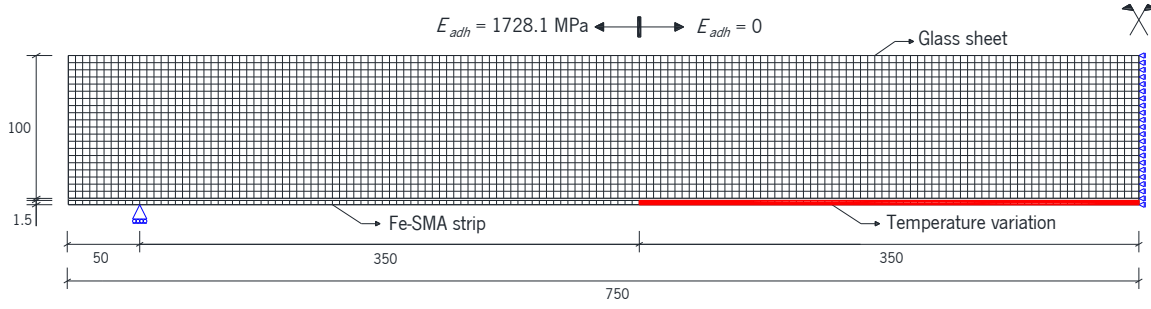
Figure IV.9: Finite element model used to determine the recovery stress in the Fe-SMA strips, identifying the length (red colour) that was subjected to temperature variation. All units in [mm].

Table IV.2 presents the results extracted from the numerical simulations, namely the $\sigma_{rec,sg}$, the numerical displacement at the mid-span section (d_{num}) and the compression stress at the bottom edge of the glass panel ($\sigma_{g,b}$). Recovery stresses ranged between 201.7 MPa ($T_a = 120\ ^\circ$C) and 335.2 MPa ($T_a = 160\ ^\circ$C). As expected, beams with the lowest T_a (e.g. P_T120 beams) exhibited the lowest $\sigma_{rec,sg}$.

Concerning the beams P_T120-I and -II, d_{num} was 4.8 % to 4.9 % lower than d_{exp}, respectively. Higher differences can be found in the beams P_T140 and P_T160, where d_{num} was 7.7 % and 8.9 % lower than d_{exp}, respectively. Neglecting minor deviations in beam geometry (e.g. height), these differences seem to be related to the propagation of damage at the adhesive to the non-activated region (near the loaded end sections), which was disregarded in the numerical model. Typically, the bond behaviour of adhesively bonded connections consists of three distinct stage: (i) the elastic stage, before bond strength is attained; (ii) the softening stage, where the adhesive is still able to transfer shear stress that decreases with increasing relative slip; and (iii) the debonding stage, when there is no shear interaction between the bonded interfaces. Due to premises adopted in these numerical simulations, only the elastic (non-activated regions) and debonding (activated region) stages were modelled, respectively setting E_{adh} equal to 1728 MPa and zero. However, the underestimation of the mid-span deflection provided by the numerical model, i.e. the difference between d_{num} and d_{exp}, seems to indicate that $l_{b,d}$ – which is defined as the bond length damaged by the activation of the Fe-SMA strips – was in fact longer than l_a, even in post-tensioned specimens with the lowest activation temperature. Accordingly, it is reasonable to assume that no shear interaction exists between adherends within the activated region, providing further validation to the numerical simulations.

Adhesive damage propagation in the non-activated region was a result of the heat flow into the non-activated region, as well as the high stress concentrations at the glass-to-SMA interfaces near the

loaded end sections of the non-activated Fe-SMA strip zones. As expected, the $d_{num} - d_{exp}$ relationship suggests that the adhesive damage propagation into the non-activated region was significantly influenced by the activation temperature. The application of higher T_a extended the heating phase, increasing the heat flow into the non-activated zone, and developed greater $\sigma_{rec,sg}$, increasing the stress concentrations in the anchorage zones. The combination of these two effects increased the $l_{b,d}$ and, as a consequence, the stress transfer zone between adherends shifted towards the beam ends. In practical terms, a similar effect would be obtained if a longer length of the beam was activated and post-tensioned ($l_{b,d} > l_a$), thus promoting d_{exp} slightly larger than d_{num}.

The recovery strain – recovery stress ratio depends on the restraint conditions of the anchorage zone. When assuming that the glass panel behaves as an infinitely rigid substrate, the maximum recovery stress ($\sigma_{rec,max}$) can be fully mobilized if the anchorage zones do not allow any deformation (e.g. slip at the bonded interfaces). Nevertheless, in reality, elastic deformation of the adhesive joint along the stress transfer length, as well as the adhesive damage propagation into the non-activated region (softening and debonding stages), both occur. As a consequence, the non-activated Fe-SMA strip zones located between $l_{b,d}$ and l_a were tensioned ($\sigma \approx \sigma_{rec,sg}$) and elongated. Therefore the activated Fe-SMA strip zone was allowed to contract slightly (recovery strain) and, consequently, the potential recovery stress was reduced ($\sigma_{rec,sg} \leq \sigma_{rec,max}$). Nevertheless, due to the heat flow into the non-activated region, these Fe-SMA strip zones were to some extent activated ($T < T_a$), reducing the shrinkage of the activated Fe-SMA strip zone. Therefore, it is reasonable to assume that the experimental $\sigma_{rec,sg}$ were not significantly affected by the adhesive damage propagation and resemble well the numerical ones.

The activation process was well captured when assuming no composite action between adherends within the activated region. Furthermore, it should be noted that the recovery stresses are a function of the activation temperature, the substrate stiffness and the anchorage restraint conditions. If the glass panel and the adhesive joint were infinitely stiff in flexure and shear, respectively, the $\sigma_{rec,sg}$ would have varied between 231.1 MPa (T_a = 120 °C) and 379.2 MPa (T_a = 160 °C), which compares very well with the values commonly found in the literature for this Fe-SMA material (e.g. [31]). Assuming $f_{g,t}$ = 40 MPa (see **Table IV.1**) and neglecting its inherent variability, it would be expected that the first cracking load of the post-tensioned beams would be 1.25 to 1.42 times higher than that obtained from R_T0 beams (increment of cracking load – ΔF_{cr}). It is noteworthy that these values do

not consider any influence of the activation procedure on the mechanical properties of the Fe-SMA reinforcement.

4   RESULTS AND DISCUSSION

Figure IV.10 and **Figure IV.11** and **Figure IV.12** show the applied load (F) *versus* mid-span deflection (δ) experimental responses of the reference and post-tensioned beams, respectively, as well as the crack patterns obtained using the DIC technique at different stages. On the other hand, **Table IV.3** summarizes the experimental responses in terms of initial stiffness (K), cracking load (F_{cr}) and corresponding deflection (δ_{cr}), maximum load (F_{max}), and ultimate deflection (δ_{ult}). **Table IV.3** lists two additional parameters: (i) the residual strength index (RSi), which was defined as the F_{max} / F_{cr} ratio, quantifying the load carrying capacity after crack initiation; and (ii) the ductility index at failure (Di), which was defined as the δ_{ult} / δ_{cr} ratio, quantifying the capacity of the beams to deform after the appearance of the first crack.

4.1.   Reference beams

As shown in **Figure IV.10**, both reference beams presented similar structural responses, exhibiting linear behaviour during the pre-cracking stage with K = 1.53 kN/mm. Thereafter, successive sudden load drops occurred due to the appearance of cracks appearing from the mid-span section towards the supports, creating non-linear branches with progressive loss of stiffness due to the yielding of the Fe-SMA. The large crack openings attained and the extensive horizontal crack propagation generated crack branching (V-shaped cracks). The high deformation capacity of the reinforcement material delayed the appearance of shear cracks, as well as the debonding of the Fe-SMA strip. The R_T0-I beam failed due to debonding of the Fe-SMA strip at the reinforcement/adhesive interface (see **Figure IV.13**) due to cracks that formed in the shear span (failure mode: critical shear crack). In contrast, the R_T0-II beam was unloaded prior to collapse because the maximum deflection allowed by the experimental setup was reached. In general, both R_T0 beams showed the ability to recover the load carrying capacity after initial cracking, exceeding F_{cr} during the post-cracking stage. These results show that glass structural elements can present safe and ductile responses when Fe-SMA is used as reinforcement, as previously observed by Silvestru *et al.* [22].
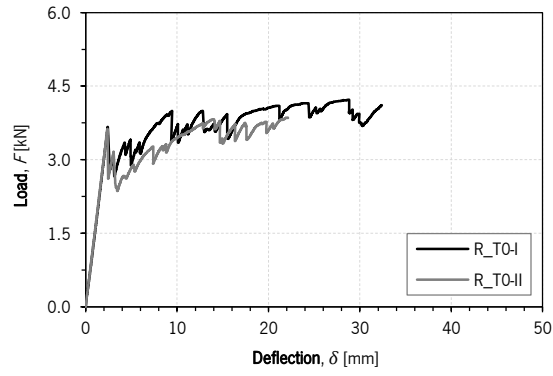
(a)
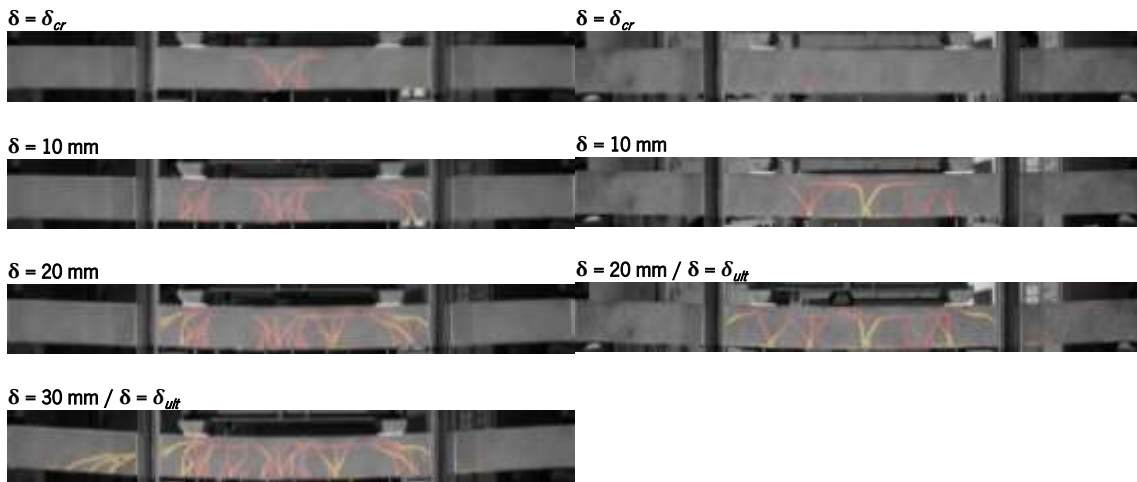
(b)   (c)

Figure IV.10: Results of the flexural tests with the reference beams: (a) structural responses and crack pattern of the beams (b) R_T0-I and (c) R_T0-II at different stages.
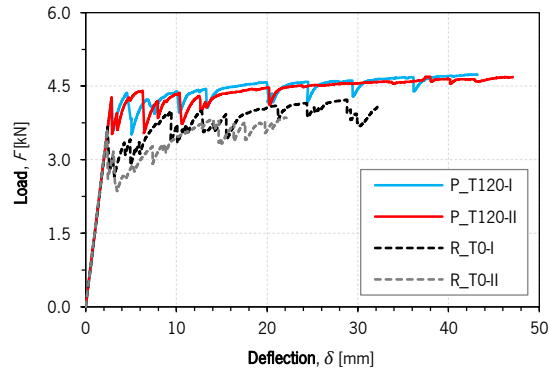
(a)
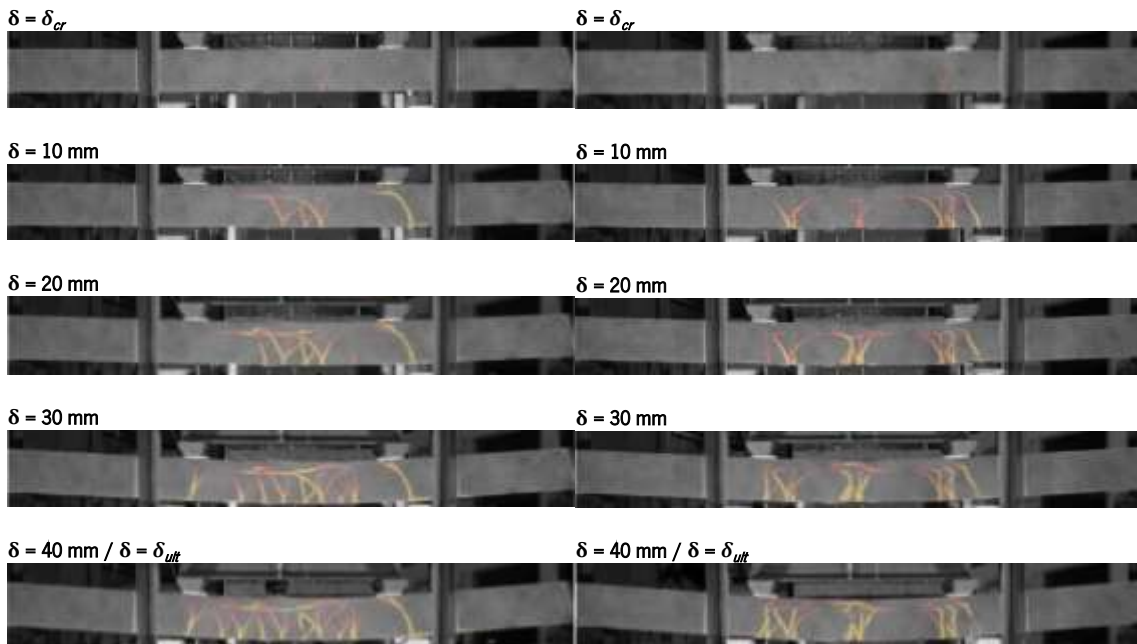
(b)　　　　　　　　　　　　　　　　　　　(c)

Figure IV.11: Results of the flexural tests with the post-tensioned beams: (a) comparison between the structural responses of both P_T120 beams with those of the reference series, as well as the crack pattern of the beams (c) P_T120-I (c) and (d) P_T120-II at different stages.
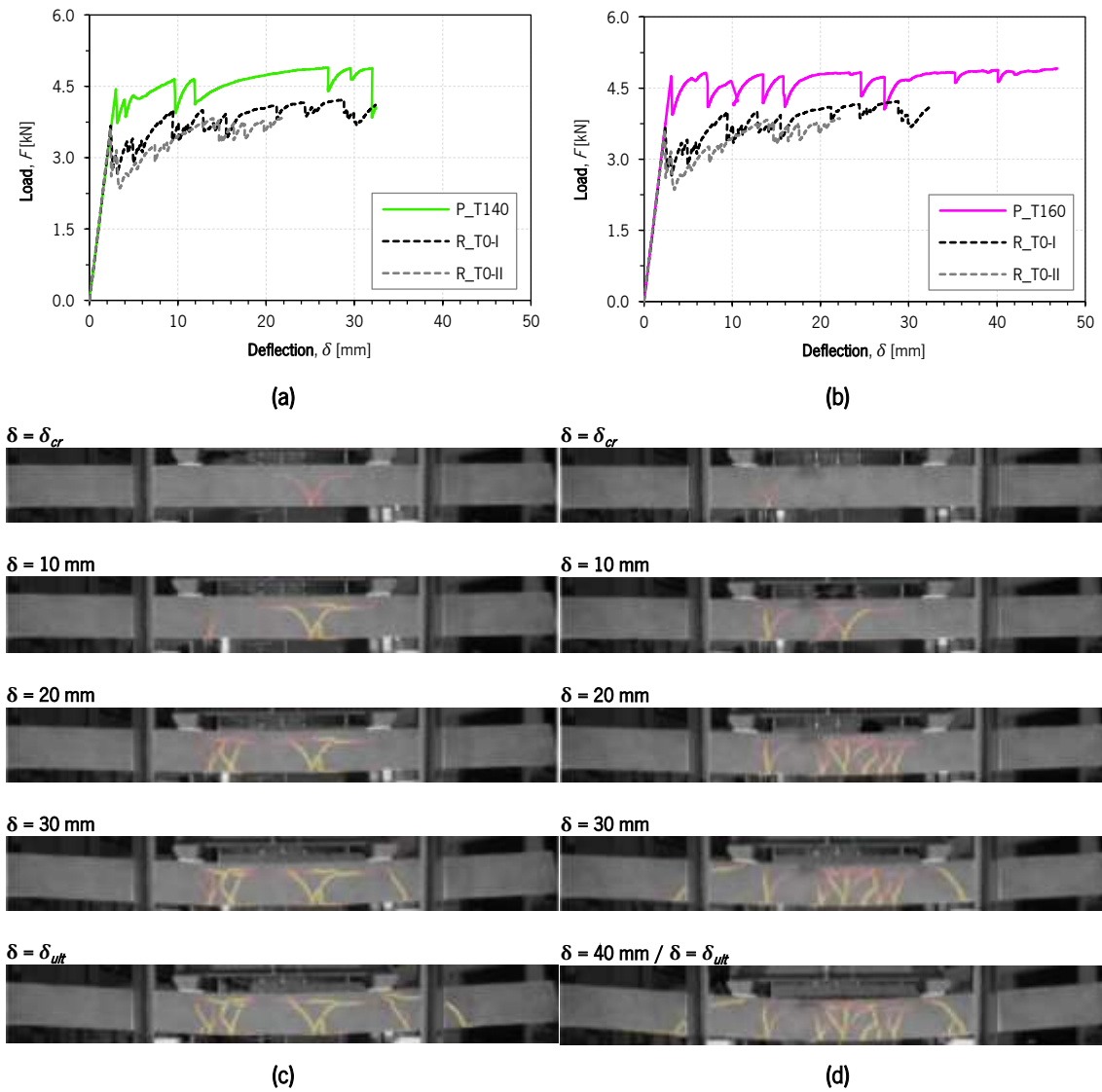
Figure IV.12: Results of the flexural tests with the post-tensioned beams: comparison between the structural responses of the beams (a) P_T140 and (b) P_T160 and those obtained from the reference series, as well as the crack pattern of the beams (c) P_T140 and (d) P_T160 at different stages.

Table IV.3: Main properties of the reference (R_T0) and post-tensioned (P_T120, P_T140 and P_T160) SMA reinforced glass beams extracted from the flexural tests.

Reference beams				
Property	R_T0-I	R_T0-II	R_T0 series	
K [kN/mm]	1.53	1.53	1.53	
F_{cr} [kN]	3.67	3.63	3.65	
δ_{cr} [mm]	2.40	2.38	2.39	
F_{max} [kN]	4.22	3.86	4.04	
δ_{ult} [mm]	32.9	22.1	27.5	
Di [%]	1370	931	1151	
RSi [%]	115	106	111	
Post-tensioned beams				
Property	P_T120-I	P_T120-II	P_T140	P_T160
T_a [°C]	122	124	142	161
K [kN/mm]	1.50 (-1.8%)	1.50 (-1.9%)	1.49 (-2.7%)	1.54 (0.7%)
F_{cr} [kN]	4.26 (16.8%)	4.28 (17.2%)	4.44 (21.8%)	4.75 (30.3%)
δ_{cr} [mm]	2.84 (19.0%)	2.86 (19.5%)	2.99 (25.2%)	3.09 (29.5%)
F_{max} [kN]	4.74 (17.2%)	4.69 (16.2%)	4.89 (21.1%)	4.92 (21.7%)
δ_{ult} [mm]	43.2 (56.8%)	47.1 (71.0%)	32.5 (17.8%)	46.8 (70.0%)
Di [%]	1519 (31.9%)	1648 (43.2%)	1085 (-5.7%)	1512 (31.5%)
RSi [%]	111 (0.4%)	110 (-0.8%)	110 (-0.6%)	103 (-6.6%)

Notes:
The values indicated in parentheses represents the difference between the property of the post-tensioned beams with the one of the reference beams

4.2.   Post-tensioned beams

4.2.1.   Initial stiffness

Similarly to the reference beams, all post-tensioned beams exhibited linear behaviour during the pre-cracking stage. Excluding the P_T160 beam, all post-tensioned beams showed lower initial stiffness than the reference beams, between 1.8 % (P_T120-I beam) and 2.7 % (P_T140 beam). This reduction is explained by two main aspects: (i) first, heating the Fe-SMA strips partially damaged the adhesive joint of post-tensioned beams, reducing the composite action between adherends; and (ii) second, the tensile stiffness of the Fe-SMA strips decreased after activation [31]. Thereby, the reduction of the initial stiffness of post-tensioned beams showed to be proportional to T_a. Unexpectedly, the P_T160 beam showed the highest initial stiffness among the post-tensioned beams, being 0.7 % higher than the one obtained from the R_T0 series. This can be explained by minor geometric deviations, as well as residual frictional forces between the glass panel and the lateral guides.

245
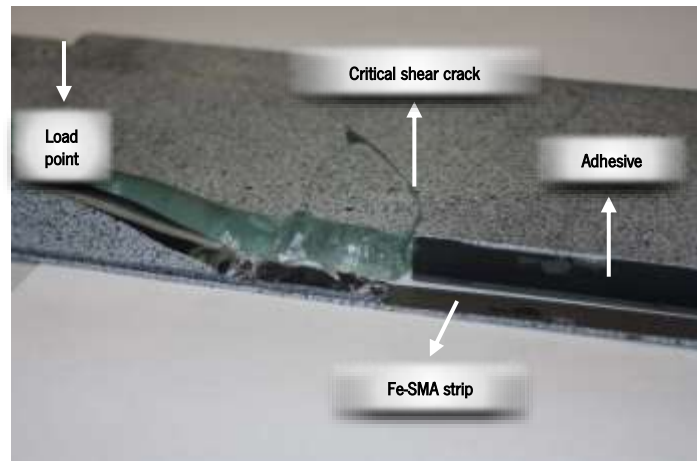
(a)
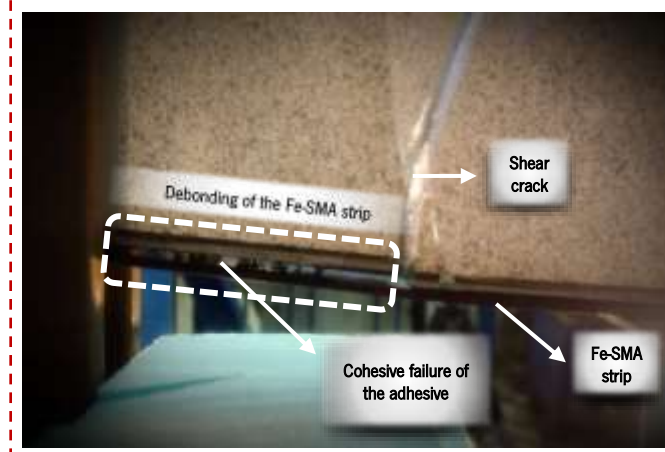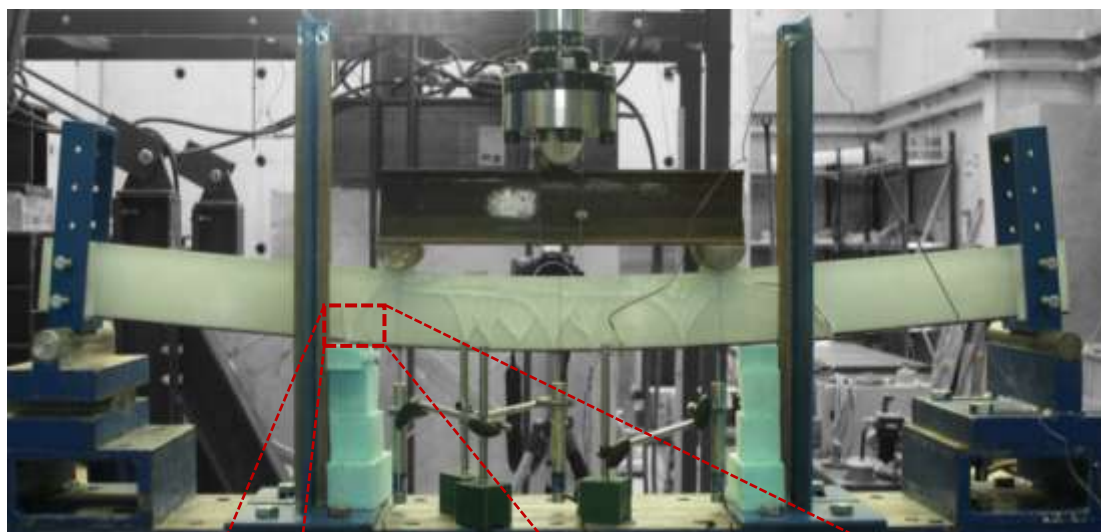
(b)

Figure IV.13: Failure modes: (a) debonding of the Fe-SMA strip at the adhesive/reinforcement interface observed in the beams R_T0-II and P_T140; and (b) cohesive failure of the 3M adhesive due to the appearance of shear cracks.

4.2.2. First cracking load

When comparing the post-tensioned beams with the R_T0 series, it is possible to observe that the activation of the Fe-SMA reinforcement increased the glass fracture strength between 16.8 % – in the P_T120-I beam (with the lowest T_a) – and 30.3 % – in the P_T160 beam (with the highest T_a). According to **Table IV.3**, the first cracking loads obtained from bending tests (F_{cr} (P_T120-I beam) < F_{cr} (P_T120-II beam) < F_{cr} (P_T140 beam) < F_{cr} (P_T160 beam) are consistent with the results obtained from the activation process. However, the estimated values of ΔF_{cr} for post-tensioned beams (see **Section 3.2**) were not reached, being the experimental ΔF_{cr} (see **Table IV.3**) between 6.8 % (P_T120-I beam) and 8.4 % (P_T140 beam) lower than the former. Despite the inherent variability of the tensile strength of glass, as well as the decrease in tensile stiffness of the Fe-SMA material after activation (see **Section 4.2.1**), the loss of post-tensioning force (stress relaxation in Fe-SMA) seems to be the main explanation for this difference, as observed in previous studies on the long term-behaviour of activated Fe-SMA reinforcement (e.g. [31,42]).

Based on the F_{cr} obtained from flexural tests, the analytical model presented in **APPENDIX A** was used to determine the decrease in post-tensioning force over time, assuming linear elastic behaviour for all components, as well as the strain distribution shown in **Figure IV.14**. Based on previous studies (e.g. [29,30]), the stress – strain curve shown by activated Fe-SMA strips resembles the one shown by passive Fe-SMA strips after the former achieve an increase in axial strain (ε_{rev}) of ≈ 1.0 % (see **Figure IV.2**). Thus, the reversal stress (σ_{rev}) was assumed equal to σ (ε_{pre}) = 638.5 MPa (maximum stress reached during the pre-straining process).

Table IV.4 compares the recovery stresses obtained from cracking loads ($\sigma_{rec,cr}$) and strain gauges measurements ($\sigma_{rec,sg}$). Values of $\sigma_{rec,cr}$ lower than $\sigma_{rec,sg}$ were obtained in all beams, varying between 4.9 % (P_T120-I beam) and 10.1 % (P_T140 beam). It is noteworthy to mention that, for the sake of simplicity, the analytical procedure did not take into account several aspects that obviously influenced the first cracking load of post-tensioned beams, mainly the permanent adhesive damage after the activation of the Fe-SMA strips and its effect on the composite action reduction. According to **Eq. (IV.8)** in **APPENDIX A**, lower values of I_{el} would result in higher recovery stresses. Therefore, if the adhesive damage would have been introduced in the analytical procedure, the difference between $\sigma_{rec,cr}$ and $\sigma_{rec,sg}$ would be smaller, mainly in the beams whose Fe-SMA strips were activated at higher temperatures.
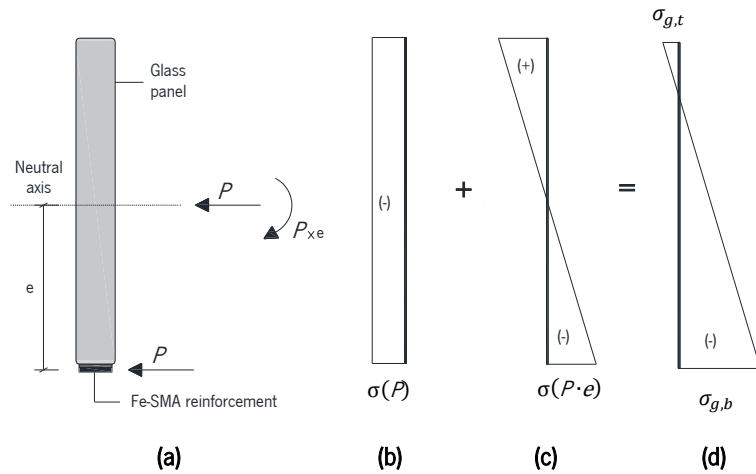
Figure IV.14: Stress distribution over the cross-section due to the post-tensioning: (a) compression and flexural forces; (b) compression stress distribution; (c) flexural stress distribution; and (d) final stress distribution.

Table IV.4: Parameters used to determine the recovery stresses from cracking loads and comparison with the ones derived from the strain gauges measurements.

Beam	I_{el} [mm^4]	I_a [mm^4]	$\sigma_{rec,sg}$ [MPa] [1]	$\sigma_{rec,cr}$ [MPa]
P_T120-I	973645.3		201.7	191.8 (-4.9%)
P_T120-II	973386.9	951294.1	207.0	195.3 (-5.6%)
P_T140	970587.7		263.8	237.3 (-10.1%)
P_T160	967071.0		335.2	313.4 (-6.5%)

Notes:
[1] Values retrieved from **Table IV.2** considering no composite action between adherends
Post-tensioning force loss is indicated in parentheses and represents the difference between $\sigma_{rec,cr}$ and $\sigma_{rec,sg}$

Disregarding small temperature variations, which may have slightly reduced the post-tensioning force due to the thermal expansion of the Fe-SMA reinforcement, the stress relaxation of Fe-SMA material is the main explanation for why the $\sigma_{rec,cr}$ were consistently lower than the $\sigma_{rec,sg}$. The post-tensioned beams were tested up to 48 hours after activation of the Fe-SMA strips. According to the tensile relaxation tests conducted by Shahverdi *et al.* [31], activated Fe-SMA strips with an initial recovery stress of 350 MPa ($\approx \sigma_{rec,sg}$ for the P_T160 beam) experienced a relaxation of $\approx$ 6.0 % during this time period. It should be noted that the relaxation behaviour depends on the amount of recovery stress and, in line with the experimental results, stress relaxation in Fe-SMA increases for increasing recovery stress. Nevertheless, according to Hosseini *et al.* [53], a significant part of the losses in the recovery stress can be retrieved by reactivating the Fe-SMA reinforcement, providing a possible solution to restore the initial recovery stresses in practical applications.

4.2.3. Post-cracking behaviour

In general, the post-cracking behaviour is characterized by a series of sudden load drops which create non-linear branches, with progressive loss of stiffness due to the martensitic transformation in the Fe-SMA reinforcement (see **Figure IV.11** and **Figure IV.12**). Like in the R_T0 series, crack propagation towards the supports was delayed by the extremely ductile behaviour of the Fe-SMA after the martensitic transformation. The post-tensioned beams presented high deformation capacity, reaching ductility values above 1000 %. In terms of residual strength, all post-tensioned beams were able to exceed the first cracking load during the post-cracking stage.

Compared to the R_T0 series, the post-tensioned beams achieved higher values of F_{max}, between 16.2 % (P_T120-I beam) and 21.7 % (P_T160 beam). However, in general, the post-tensioned beams showed lower RSi values than the reference ones. The activation of the Fe-SMA reinforcement reduced its tensile strength reserve (difference between σ_{rev} and $\sigma_{rec,sg}$) before the forward transformation, thus reducing significantly the post-cracking stiffness of the post-tensioned beams, as well as their load carrying capacity. Therefore, as experimentally observed, the residual strength tended to be lower in beams with higher T_a. Nevertheless, the P_T140 beam displayed an unexpectedly high RSi value among the post-tensioned beams. The high scatter of the tensile strength of glass seems to be the main reason for this result, having produced a lower F_{cr} than expected. This also justifies why the P_T140 beam showed a greater difference between $\sigma_{rec,cr}$ and $\sigma_{rec,sg}$ (see **Section 4.2.2**) than the P_T160 beam.

Glass structures are safe only when the resisting mechanism generated after the initial glass cracking is capable of assuring a load carrying capacity that is higher than the F_{cr}. Therefore, a maximum recovery stress ($\sigma_{rec,max}$) should be estimated to ensure $F_{ult} > F_{cr}$. After cracking, the load carrying mechanism is formed by a compression force in the uncracked glass zone and a tensile force in the reinforcement element, identified as $F_{c,g}$ and $F_{r,t}$ in **Figure IV.15**, respectively. Two failure mechanism were considered: (i) tensile failure in the Fe-SMA reinforcement and (ii) crushing of the cross-section area where compression stresses are maximum. Lateral instability and debonding of the Fe-SMA strip were neglected because they can be postponed or avoided by changing the beam geometry and choosing adhesives with greater shear resistance, respectively. The compression strength of glass ($f_{g,c}$) was not experimentally characterized in this investigation. A $f_{g,c}$ = 500 MPa was adopted in this study [57].

Based on **APPENDIX B**, the maximum recovery stress obtained when the beam collapse is governed by glass crushing and tensile failure in Fe-SMA is equal to 379.7 MPa and 612.4 MPa, respectively (see **Table IV.5**). Considering the lowest value, F_{cr} ($\sigma_{rec,max}$ = 379.7 MPa) is equal to 5.07 kN, which represents a maximum increment of ≈ 40.0 % in cracking load taking the R_T0 series as a reference. In any case, the recovery stress – activation temperature relationship reaches a maximum for which an increase in temperature no longer results in an increase in the recovery stress, which according to Shahverdi *et al.* [31] is equal to approximately 450 MPa. As discussed in **Section 4.2.2**, the recovery stress reduces over time due to stress relaxation of the Fe-SMA material. Therefore, recovery stresses slightly higher than $\sigma_{rec,max}$ can be introduced. However, further investigation to determine the amount of stress relaxation over time is particularly important.
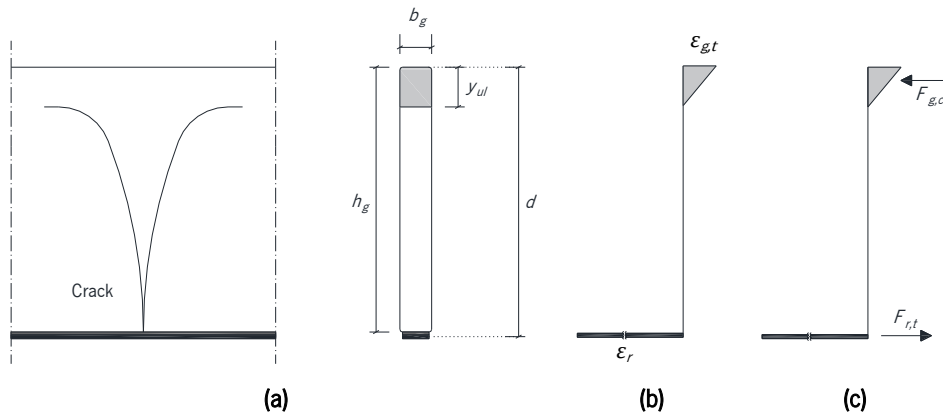
Figure IV.15: Resistant mechanism after glass cracking: (a) and (b) cracked cross-section and (c) strain and (d) stress distributions.

Table IV.5: Main parameters used to determine the maximum recovery stress that guarantees the safe collapse of composite beams.

Fe-SMA tensile failure				
ε_r [‰]	$\sigma_{g,t}$ [MPa]	y_{ult} [mm]	$\sigma_{rec,max}$ [MPa]	$F_{cr} = F_{ult}$ [kN]
324.9	755.8 > $f_{g,c}$	3.20	612.4	5.99
Glass crushing				
ε_r [‰]	$\sigma_{g,t}$ [MPa]	y_{ult} [mm]	$\sigma_{rec,max}$ [MPa]	$F_{cr} = F_{ult}$ [kN]
174.3 < $\varepsilon_{r,ult}$	500.0	4.02	379.7	5.07

4.2.4. Failure modes

Excluding the P_T140 beam, which failed due to debonding of the Fe-SMA strip at the reinforcement/adhesive interface (see **Figure IV.13a**), all post-tensioned beams were unloaded before collapse when the maximum deformation allowed by the experimental setup was exceeded. In the

P_T140 beam, the detachment of the Fe-SMA strip was triggered by a critical shear crack that appeared in the non-activated region. Due to the low fracture energy of glass, strain energy is suddenly released during the crack formation, damaging the adhesive joint around the crack. Then, shear cracks induce high interfacial stresses (mode-I and -II) at the bonded interfaces, causing progressive debonding of the reinforcement.

Figure IV.13b shows a close up of the partial detachment of the Fe-SMA strip observed in the post-tensioned beams after unloading, which seems to have resulted from the cohesive failure of the adhesive used. Nevertheless, the adhesive was able to keep the reinforcement bonded to the glass, probably because shear cracks did not appear sufficiently close to the supports, as occurred in the case of the P_T140 beam. Therefore, further investigation is necessary to understand in detail this failure mechanism and to develop an analytical model to predict the collapse due to critical shear crack in passive and post-tensioned composite glass systems.

5 CONCLUSIONS

This research was focused on the structural performance of post-tensioned glass beams using Fe-SMA as reinforcement. First, Fe-SMA strips were mechanically deformed to induce the martensitic transformation. Second, pre-strained Fe-SMA strips were adhesively bonded to the bottom edge of glass panels using an epoxy adhesive. Third, the Fe-SMA strips were activated by resistive heating at temperatures between 120 °C and 160 °C, approximately. Finally, the post-tensioned beams were experimentally tested until failure under a four-point bending configuration. In addition, based on the strain gauge measurements, numerical investigations were performed to determine the initial stress-state generated by the activation of Fe-SMA strips.

The main conclusions of this research may be summarized as follows:

- Post-tensioning of glass beams by activating Fe-SMA strips adhesively bonded is a relatively quick and easy process. Partial activation of Fe-SMA strips proved to be a suitable strategy to avoid the concentration of high shear stresses in weaker zones of the glass panel (e.g. beam ends), ensuring an undamaged bond region able to transfer the post-tensioning force from the reinforcement element to the glass substrate;

- Numerical models showed that the loss of composite action was directly correlated to the activation temperature; higher activation temperature resulted smoother post-tensioning force transfer, significantly reducing the possibility of premature glass breakage. In addition, the

251

propagation of adhesive damage into the non-activated region increased the vertical displacement at the mid-span section;

- Four-point bending tests proved the feasibly of SMA strengthening of glass beams. All beams were able to maintain their integrity during the cracking process, exhibiting a post-cracking behaviour that was strongly influenced by the mechanical properties of the adhesive and reinforcement. Relatively safe and ductile failure mechanisms were achieved in the strengthened glass beams;

- In general, the activation of the Fe-SMA strips was an advantageous strategy to enhance the overall response of glass composite systems. The post-tensioning resulted in first cracking loads ranging between 17 % and 30 % higher than those obtained with reference beams (passive Fe-SMA reinforcement);

- Due to the stress relaxation behaviour of the Fe-SMA, the post-tensioning stress decreased over time between 4.9 % and 10.1 %, depending on the recovery stress. However, for practical applications, the initial recovery stresses could be retrieved by reactivating the Fe-SMA reinforcement;

- All beams were able to exceed the first cracking load during the post-cracking stage. The post-cracking behaviour of the post-tensioned beams was mainly influenced by the recovery stress developed in Fe-SMA strips. Compared to the reference beams, the post-tensioned beams showed lower residual strength indexes for increasing activation temperatures, since the activation of the Fe-SMA strips reduced the tensile strength reserve before the austenite-martensite transformation;

- In order to avoid catastrophic collapses, it is recommendable that a maximum recovery stress is not exceeded so that the ultimate load is at least equal to the first cracking load, considering all possible failure mechanisms.

The results obtained from the experimental tests showed that the post-tensioning of annealed glass beams using adhesively bonded Fe-SMA strips is a feasible and promising strengthening strategy, capable of generating safe and ductile failure mechanisms. However, additional investigation is required to address aspects that can promote post-tensioning losses over time, whether related to the post-tensioning procedure (e.g. structural performance of glass-to-SMA adhesive joints at high temperatures and adhesive damage propagation) or long-term behaviour (e.g. relaxation behaviour of

the Fe-SMA, creep in the adhesive joint due to permanent shear stresses imposed by the post-tensioning). In addition, the effect of different environmental conditions (e.g. temperature, moisture and UV radiation) should also be considered in future studies. As glass is a transparent material, special attention should be paid to the influence of the solar radiation, especially the UV radiation and thermal cycling, on the bond behaviour of adhesive connections over time. Thus, in order to promote the use of Fe-SMA reinforced glass elements in a wide spectrum of applications, additional experimental studies should focus on the aspects mentioned above, as well as on the development of reliable analytical/numerical methodologies to simulate the activation procedure (e.g. thermo-mechanical analysis) and predict the structural response of post-tensioned glass-SMA composite systems.

6   ACKNOWLEDGEMENTS

7   REFERENCES

[1]   Yankelevsky DZ. Strength prediction of annealed glass plates - A new model. Engineering Structures 2014;79:244–55. https://doi.org/10.1016/j.engstruct.2014.08.017.

[2]   Veer FA, Rodichev YM. The structural strength of glass: Hidden damage. Strength of Materials 2011;43:302–15. https://doi.org/10.1007/s11223-011-9298-5.

[3]   Haldimann M, Luible A, Overend M. Structural use of glass. LABSE - Lanka Association of Building Services Engineers; 2008.

[4]   Biolzi L, Orlando M, Piscitelli LR, Spinelli P. Static and dynamic response of progressively damaged ionoplast laminated glass beams. Composite Structures 2016;157:337–47. https://doi.org/10.1016/j.compstruct.2016.09.004.

[5]   Correia J, Valarinho L, Branco F. Post-cracking strength and ductility of glass-GFRP composite beams. Composite Structures 2011;93:2299–309.

[6]   Cruz P, Pequeno J. Structural Timber-Glass Adhesive Bonding. Challenging Glass, 2008, p. 205–14.

[7]   Cruz P, Pequeno J. Timber-Glass Composite Beams: Mechanical Behaviour & Architectural Solutions. Challenging Glass, 2008, p. 439–48.

[8]   Belis J, Callewaert D, Delincé D, Impe R Van. Experimental failure investigation of a hybrid glass / steel beam. Engineering Failure Analysis 2009;16:1163–73. https://doi.org/10.1016/j.engfailanal.2008.07.011.

[9]   Bos F, Veer F, Hobbelman G, Louter C. Stainless steel reinforced and post-tensioned glass beams. ICEM12 - 12th International Conference on Experimental Mechanics, Bari, Italy: 2004, p. 1–9.

[10]   Louter C, Belis J, Veer F, Lebet J. Structural response of SG-laminated reinforced glass beams; experimental investigations on the effects of glass type, reinforcement percentage and beam size. Engineering Structures 2012;36:292–301. https://doi.org/10.1016/j.engstruct.2011.12.016.

[11]   Louter C, Cupać J, Lebet J. Exploratory experimental investigations on post-tensioned structural glass beams. Journal of Facade Design and Engineering 2014;2:3–18. https://doi.org/10.3233/FDE-130012.

[12]   Louter C, Cupać J, Debonnaire M. Structural glass beams prestressed by externally bonded tendons. GlassCon Global Conference Proceedings, Philadelphia, EUA: 2014, p. 450–9. https://doi.org/10.14296/deeslr.v5i0.1848.

[13]   Palumbo M. A New Roof for the XIIIth Century 'Loggia de Vicari' (Arquà Petrarca – PD Italy) Based on Structural Glass Trusses: A Case Study. Glass Processing Days, Tempere, Finland: 2005.

[14]   Rocha J, Sena-Cruz J, Pereira E. Influence of adhesive stiffness on the post-cracking behaviour of CFRP-reinforced structural glass beams. Composites Part B: Engineering 2022;110293. https://doi.org/https://doi.org/10.1016/j.compositesb.2022.110293.

[15]   Achintha M, Balan B. Characterisation of the mechanical behaviour of annealed glass – GFRP hybrid beams. Construction and Building Materials 2017;147:174–84. https://doi.org/10.1016/j.conbuildmat.2017.04.086.

[16]   Bedon C, Louter C. Numerical investigation on structural glass beams with GFRP-embedded rods, including effects of pre-stress. Composite Structures 2018;184:650–61. https://doi.org/10.1016/j.compstruct.2017.10.027.

[17]   Neto P, Alfaiate J, Valarinho L, Correia J, Branco F, Vinagre J. Glass beams reinforced with GFRP laminates: Experimental tests and numerical modelling using a discrete strong discontinuity approach. Engineering Structures 2015;99:253–63. https://doi.org/10.1016/j.engstruct.2015.04.002.

[18]   Valarinho L, Correia JR, Branco F. Experimental study on the flexural behaviour of multi-span transparent glass-GFRP composite beams. Construction and Building Materials

2013;49:1041–53. https://doi.org/10.1016/j.conbuildmat.2012.11.024.

[19]   Valarinho L, Sena-Cruz J, Correia J, Branco F. Numerical simulation of the flexural behaviour of composite glass-GFRP beams using smeared crack models. Composites Part B: Engineering 2017;110:336–50. https://doi.org/10.1016/j.compositesb.2016.10.035.

[20]   Martens K, Caspeele R, Belis J. Development of composite glass beams - A review. Engineering Structures 2015;101:1–15. https://doi.org/10.1016/j.engstruct.2015.07.006.

[21]   Jordão S, Pinho M, Martin J, Santiago A, Neves L. Behaviour of laminated glass beams reinforced with pre-stressed cables. Steel Construction 2014;7:204–7. https://doi.org/10.1002/stco.201410027.

[22]   Silvestru V, Deng Z, Michels J, Taras A. Enabling a Ductile Failure of Laminated Glass Beams with Iron-Based Shape Memory Alloy (Fe-SMA) Strips. The International Colloquium on Stability and Ductility of Steel Structures, Aveiro, Portugal: Ernst & Sohn GmbH; 2022. https://doi.org/https://doi.org/10.1002/cepa. 1839.

[23]   Cupać J, Louter C, Nussbaumer A. Post-tensioning of glass beams: Analytical determination of the allowable pre-load. Glass Structures and Engineering 2021;6:233–48. https://doi.org/10.1007/s40940-021-00150-0.

[24]   Jani JM, Leary M, Subic A, Gibson MA. A review of shape memory alloy research, applications and opportunities. Materials and Design 2014;56:1078–113. https://doi.org/10.1016/j.matdes.2013.11.084.

[25]   Cladera A, Weber B, Leinenbach C, Czaderski C, Shahverdi M, Motavalli M. Iron-based shape memory alloys for civil engineering structures: An overview. Construction and Building Materials 2014;63:281–93. https://doi.org/10.1016/j.conbuildmat.2014.04.032.

[26]   Asgarian B, Moradi S. Seismic response of steel braced frames with shape memory alloy braces. Journal of Constructional Steel Research 2011;67:65–74. https://doi.org/10.1016/j.jcsr.2010.06.006.

[27]   Dieng L, Helbert G, Chirani SA, Lecompte T, Pilvin P. Use of shape memory alloys damper device to mitigate vibration amplitudes of bridge cables. Engineering Structures 2013;56:1547–56. https://doi.org/10.1016/j.engstruct.2013.07.018.

[28]   Hosseini A, Michels J, Izadi M, Ghafoori E. A comparative study between Fe-SMA and CFRP reinforcements for prestressed strengthening of metallic structures. Construction and Building Materials 2019;226:976–92. https://doi.org/10.1016/j.conbuildmat.2019.07.169.

[29]   Izadi M, Hosseini A, Michels J, Motavalli M, Ghafoori E. Thermally activated iron-based shape memory alloy for strengthening metallic girders. Thin-Walled Structures 2019;141:389–401. https://doi.org/10.1016/j.tws.2019.04.036.

[30]   Michels J, Shahverdi M, Czaderski C. Flexural strengthening of structural concrete with iron-

based shape memory alloy strips. Structural Concrete 2017;19:876–91. https://doi.org/10.1002/suco.201700120.

[31] Shahverdi M, Michels J, Czaderski C, Motavalli M. Iron-based shape memory alloy strips for strengthening RC members: Material behavior and characterization. Construction and Building Materials 2018;173:586–99. https://doi.org/10.1016/j.conbuildmat.2018.04.057.

[32] Shin M, Andrawes B. Experimental investigation of actively confined concrete using shape memory alloys. Engineering Structures 2010;32:656–64. https://doi.org/10.1016/j.engstruct.2009.11.012.

[33] Rojob H, El-Hacha R. Self-prestressing using iron-based shape memory alloy for flexural strengthening of reinforced concrete beams. ACI Materials Journal 2017;114:523–32. https://doi.org/10.14359/51689455.

[34] Izadi MR, Ghafoori E, Shahverdi M, Motavalli M, Maalek S. Development of an iron-based shape memory alloy (Fe-SMA) strengthening system for steel plates. Engineering Structures 2018;174:433–46. https://doi.org/10.1016/j.engstruct.2018.07.073.

[35] Kajiwara S. Characteristic features of shape memory effect and related transformation behavior in Fe-based alloys. Materials Science and Engineering A 1999;273–275:67–88. https://doi.org/10.1016/s0921-5093(99)00290-7.

[36] Sato A, Chishima E, Soma K, Mori T. Shape memory effect in $\gamma \rightleftarrows \epsilon$ transformation in Fe-30Mn-1Si alloy single crystals. Acta Metallurgica 1982;30:1177–83. https://doi.org/10.1016/0001-6160(82)90011-6.

[37] Sato A, Kubo H, Maruyama T. Mechanical properties of Fe-Mn-Si based SMA and the application. Materials Transactions 2006;47:571–9. https://doi.org/10.2320/matertrans.47.571.

[38] Dong Z, Klotz UE, Leinenbach C, Bergamini A, Czaderski C, Motavalli M. A novel Fe-Mn-Si shape memory alloy with improved shape recovery properties by VC precipitation. Advanced Engineering Materials 2009;11:40–4. https://doi.org/10.1002/adem.200800312.

[39] Ghafoori E, Hosseini E, Leinenbach C, Michels J, Motavalli M. Fatigue behavior of a Fe-Mn-Si shape memory alloy used for prestressed strengthening. Materials and Design 2017;133:349–62. https://doi.org/10.1016/j.matdes.2017.07.055.

[40] Shahverdi M, Czaderski C, Motavalli M. Iron-based shape memory alloys for prestressed near-surface mounted strengthening of reinforced concrete beams. Construction and Building Materials 2016;112:28–38. https://doi.org/10.1016/j.conbuildmat.2016.02.174.

[41] Czaderski C, Shahverdi M, Brönnimann R, Leinenbach C, Motavalli M. Feasibility of iron-based shape memory alloy strips for prestressed strengthening of concrete structures. Construction and Building Materials 2014;56:94–105. https://doi.org/10.1016/j.conbuildmat.2014.01.069.

[42] Michels J, Shahverdi M, Czaderski C, El-Hacha R. Mechanical performance of iron-based shape-memory alloy ribbed bars for concrete prestressing. ACI Materials Journal 2018;115:877–86. https://doi.org/10.14359/51710959.

[43] Shahverdi M, Czaderski C, Annen P, Motavalli M. Strengthening of RC beams by iron-based shape memory alloy bars embedded in a shotcrete layer. Engineering Structures 2016;117:263–73. https://doi.org/10.1016/j.engstruct.2016.03.023.

[44] Leinenbach C, Lee WJ, Lis A, Arabi-Hashemi A, Cayron C, Weber B. Creep and stress relaxation of a FeMnSi-based shape memory alloy at low temperatures. Materials Science and Engineering A 2016;677:106–15. https://doi.org/10.1016/j.msea.2016.09.042.

[45] Lee WJ, Partovi-Nia R, Suter T, Leinenbach C. Electrochemical characterization and corrosion behavior of an Fe-Mn-Si shape memory alloy in simulated concrete pore solutions. Materials and Corrosion 2016;67:839–46. https://doi.org/10.1002/maco.201508701.

[46] Lee WJ, Weber B, Feltrin G, Czaderski C, Motavalli M, Leinenbach C. Stress recovery behaviour of an Fe–Mn–Si–Cr–Ni–VC shape memory alloy used for prestressing. Smart Materials and Structures 2013;22:125037. https://doi.org/10.1088/0964-1726/22/12/125037.

[47] Deng Z, Silvestru V, Michels J, Li L, Ghafoori E, Taras A. Performance of Glass to Iron-based Shape Memory Alloy Adhesive Shear Joints with Different Geometry. In: Belis B& L (Eds. ., editor. Challenging Glass Conference Proceedings, vol. 8, Ghent, Belgium: 2022, p. 1–12. https://doi.org/10.47982/cgc.8.397.

[48] Silvestru V, Deng Z, Michels J, Li L, Ghafoori E, Taras A. Application of an iron-based shape memory alloy for post-tensioning glass elements. Glass Structures and Engineering 2022;7:187–210. https://doi.org/10.1007/s40940-022-00183-z.

[49] Leinenbach C, Kramer H, Bernhard C, Eifler D. Thermo-mechanical properties of an Fe-Mn-Si-Cr-Ni-VC shape memory alloy with low transformation temperature. Advanced Engineering Materials 2012;14:62–7. https://doi.org/10.1002/adem.201100129.

[50] GOM. Correlate Software and Online Documentation. Rev.121188. 2019.

[51] Rocha J, Sena-Cruz J, Pereira E. Tensile behaviour of CFRP-glass adhesively bonded connections: double-lap joint tests and numerical modelling. Engineering Structures 2022;260:114212. https://doi.org/10.1016/j.engstruct.2022.114212.

[52] Nhamoinesu S, Overend M. The mechanical performance of adhesives for a steel-glass composite façade system. Challenging Glass 3: Conference on Architectural and Structural Applications of Glass, CGC 2012, Delft, Netherlands: 2012, p. 293–306. https://doi.org/10.3233/978-1-61499-061-1-293.

[53] Hosseini E, Ghafoori E, Leinenbach C, Motavalli M, Holdsworth SR. Stress recovery and cyclic behaviour of an Fe-Mn-Si shape memory alloy after multiple thermal activation. Smart Materials and Structures 2018;27. https://doi.org/10.1088/1361-665X/aaa2c9.

[54]   Veer F, Riemslag T, Romein T. The failure strength of glass, a non transparent value. Glass Performance Days, Tempere, Finland: 2007, p. pages 610–614.

[55]   Wang W, Li L, Hosseini A, Ghafoori E. Novel fatigue strengthening solution for metallic structures using adhesively bonded Fe-SMA strips: A proof of concept study. International Journal of Fatigue 2021;148:106237. https://doi.org/10.1016/j.ijfatigue.2021.106237.

[56]   Simulia. ABAQUS computer software and Online Documentation. v6.12. 2012.

[57]   Feldmann M, Kasper R, Abeln B. Guidance for European Structural Design of Glass Components. Report EUR 26439 EN. Report EUR. Luxembourg: 2014. https://doi.org/10.2788/5523.

APPENDIX A

The recovery stress ($\sigma_{rec,cr}$) can be derived from the first cracking load. For the sake of simplicity, the tensile behaviour of activated Fe-SMA strips was assumed to be bilinear (see **Figure IV.2**), with the first branch including $\varepsilon \leq \varepsilon_{rev}$ and the second $\varepsilon > \varepsilon_{rev}$. An equivalent modulus of elasticity ($E_{r,rec}$), defined as the slope of the first linear branch (see **Eq. (IV.1)**), was conservatively used in these calculations.

$$E_{r,rec} = (\sigma_{rev} - \sigma_{rec})/\varepsilon_{rev}$$

(IV.1)

Neglecting the adhesive damage, the moment of inertia (I_{el}) is given by **Eq. (IV.2)**, in which b_i, h_i and E_i correspond to the width, height and modulus of elasticity of each component, and z_i determines the distance between the centroid and the neutral axis. In turn, the position of neutral axis (y_{el}) can be determined by means of **Eq. (IV.3)**, where $z_{i,t}$ represents the distance between the centroid of each component and the beam's top edge.

$$I_{el} = \sum \left(\frac{b_i h_i^3}{12} \cdot \frac{E_i}{E_g} + b_i h_i z_i^2 \cdot \frac{E_i}{E_g} \right)$$

(IV.2)

$$y_{el} = \frac{\sum b_i h_i z_{i,t} \cdot E_i / E_g}{\sum b_i h_i \cdot E_i / E_g}$$

(IV.3)

Cracking initiates when $f_{g,t}$ is attained at the bottom edge of the glass panel. Therefore, the initial compression stress at the bottom edge of the glass panel ($\sigma_{g,b}$) can be determined from **Eq. (IV.4)**, where F_{cr} is the cracking load, l_1 is the length of the shear span and h_g is the height of the glass panel.

$$\sigma_{g,b} = \frac{F_{cr}l_1}{2I_{el}} \cdot \left(h_g - y_{el}\right) - f_{g,t} \tag{IV.4}$$

Considering **Figure IV.14**, $\sigma_{g,b}$ can be written as a function of $\sigma_{rec,cr}$ using **Eq. (IV.5)**, in which A_r is the cross-section area of the Fe-SMA strip, d is the distance between the intermediate fibre of the Fe-SMA strip and the top glass edge, and A_a is the cross-section area of the composite beam. I_a and A_a are given by **Eq. (IV.6)** and **Eq. (IV.7)**, respectively while y_a can be determined through **Eq. (IV.3)**, like y_{el}, but in this case considering only the contribution of the glass panel and the Fe-SMA strip (no composite action). According to **Section 3.2**, these parameters were calculated assuming $E_{r,a}$ = 95 GPa and E_{adh} = 0.

$$\sigma_{g,b} = \frac{\sigma_{rec,cr} \cdot A_r}{A_a} + \frac{\sigma_{rec,cr} \cdot A_r \cdot (d - y_a)}{I_a} \cdot \left(h_g - y_a\right) \tag{IV.5}$$

$$I_a = \sum \left(\frac{b_i h_i^3}{12} \cdot \frac{E_i}{E_g}\right) \tag{IV.6}$$

$$A_a = \sum b_i h_i \cdot E_i / E_g \tag{IV.7}$$

Finally, equating **Eq. (IV.4)** and **Eq. (IV.5)**, $\sigma_{rec,cr}$ can be determined as a function of F_{cr} using the following expression:

$$\sigma_{rec,cr} = \left(\frac{F_{cr} \cdot l_1}{2I_{el}} \cdot \left(h_g - y_{el}\right) - f_{g,t}\right)/J \tag{IV.8}$$

Where,

$$J = \left(\frac{A_r}{A_a} + \frac{A_r \cdot (d - y_a)}{I_a} \cdot \left(h_g - y_a\right)\right)$$

APPENDIX B

Tensile failure in Fe-SMA

Considering the strain distribution shown in **Figure IV.15**, the beam collapse is governed by **Eq. (IV.9)** in which $\varepsilon_{g,t}$ is the axial strain at the top edge of glass and y_{ult} represents the position of the neutral axis at failure.

$$\varepsilon_{g,t} = \frac{(\varepsilon_{r,ult} - \varepsilon_{rem}) \cdot y_{ult}}{(d - y_{ult})} \leq \frac{f_{g,c}}{E_g} \tag{IV.9}$$

With,

$$y_{ult} = \frac{2A_r \cdot f_{r,t}}{t \cdot \varepsilon_{g,t} \cdot E_g}$$

By enforcing the equilibrium of internal forces, the ultimate load (F_{ult}) is provided by **Eq. (IV.10)**.

$$F_{ult} = \frac{2 \cdot A_r \cdot f_{r,t} \cdot (d - y_{ult}/3)}{l_1} \tag{IV.10}$$

From the rearrangement of **Eq. (IV.8)**, F_{cr} can be determined from **Eq. (IV.11)**.

$$F_{cr} = \frac{2I_{el}}{(h_g - y_{el}) \cdot l_1} \cdot (J \cdot \sigma_{rec,max} + f_{g,t}) \tag{IV.11}$$

No composite action between the adherends was considered to determine I_a, and A_a (see **Section 3.2**). Thereby, equating **Eq. (IV.10)** and **Eq. (IV.11)**, $\sigma_{rec,max}$ can be calculated through the following expression:

$$\sigma_{rec,max} \leq \frac{A_r \cdot f_{r,t} \cdot (d - y_{ult}/3) \cdot (h_g - y_{el})}{J \cdot I_{el}} - \frac{f_{g,t}}{J} \tag{IV.12}$$

Glass crushing

Assuming glass crushing, the tensile strain in the Fe-SMA strip (ε_r) at failure is given by **Eq. (IV.13)**, considering by default $\varepsilon_r > \varepsilon_{rem} + \varepsilon_{rev}$.

$$\varepsilon_r = \frac{f_{g,c} \cdot (d - y_{ult})}{E_g \cdot y_{ult}} + \varepsilon_{rem} \leq \varepsilon_{r,ult} \tag{IV.13}$$

With,

$$y_{ul} = \frac{2A_r \cdot \left(\sigma_{rev} + (\varepsilon_r - \varepsilon_{rem} - \varepsilon_{rev}) \cdot E_{r,rev}\right)}{t \cdot f_{g,c}}$$

F_{ult} is given by the following expression:

$$F_{ult} = \frac{t \cdot f_{g,c} \cdot y_{ult} \cdot (d - y_{ult}/3)}{l_1} \tag{IV.14}$$

In order to determine $\sigma_{rec,max}$ corresponding to the glass crushing, **Eq. (IV.11)** and **Eq. (IV.14)** were equated and **Eq. (IV.15)** was obtained.

$$\sigma_{rec,max} \leq \frac{t \cdot f_{g,c} \cdot y_{ult} \cdot (d - y_{ult}/3) \cdot \left(h_g - y_{el}\right)}{2I_{el} \cdot J} - \frac{f_{g,t}}{J} \tag{IV.15}$$

PAPER V

HYBRID STRENGTHENING SYSTEMS

ABSTRACT: The fracture strength of glass is often an unreliable parameter and post-tensioning strategies have been investigated to mitigate this uncertainty. Glass composite systems with EBR strengthening systems often fail due to premature debonding. In concrete structures, the NSM technique has been successful in preventing peeling-off failure due to the crack propagation. CFRP and Fe-SMA reinforcement have been explored for the post-tensioned strengthening of existing structures. By combining NSM and EBR techniques, this study explores the benefits of applying hybrid strengthening systems to glass structures. Thus, five large-scale laminated glass beams were tested in flexure. Different strengthening systems (reinforcement material *versus* application technique) were adopted in each specimen, using CFRP and/or Fe-SMA as reinforcement. Flexural tests showed that hybrid strengthening systems are better than EBR systems at preventing crack-induced debonding. The best strengthening system includes NSM-CFRP and EBR-SMA reinforcements. Both can be safely post-tensioned, preventing stress concentrations in the glass substrate, and the NSM-CFRP reinforcement can still carry load after the possible debonding of the EBR-SMA reinforcement.

1   INTRODUCTION

However, in recent decades, glass has also been used with structural functions (e.g. floors, beams and frames), being generally designed to withstand flexural loads. Unlike other building materials (e.g. reinforced concrete, steel and timber), the glass brittleness and the lack of appropriate European standardization – Eurocodes – makes the design and application of glass structural elements very challenging. Following the design methodologies used in the aeronautic industry, glass structures have been designed according to the concepts of hierarchy, robustness and redundancy [1]. For structural applications, laminated glass is preferred because it satisfies the concept of redundancy by dividing the glass panel into thinner glass plies joined by transparent interlayers.

1.1.   Post-tensioned glass systems

The design of glass structural elements consists of verifying whether the tensile strength of glass is sufficient to withstand the anticipated actions. However, its long-term tensile strength is unreliable due to the growth of surface flaws under humidity conditions [2]. Hence, glass requires sufficient redundancy after breakage to accomplish the robustness requirements. However, glass lamination is not sufficient to provide the desirable robustness for unpredictable actions (e.g. vandalism and earthquakes) and/or imperfections derived from design, fabrication and assembly procedures (e.g. stress concentrations). A secondary load carrying mechanism is therefore essential to provide ductility and residual strength capacity after glass cracking. Several reinforcement materials, such as timber (e.g. [3,4]), steel (e.g. [5–8]), Carbon Fibre Reinforced Polymers, CFRP (e.g. [9–11]), and Glass Fibre Reinforced Polymers, GFRP (e.g. [12–17]), have been used with the aim of enhancing the post-failure structural redundancy of glass structural elements. However, the tensile strength of annealed glass is still unpredictable. Although the glass industry has successfully developed thermal toughening to improve its fracture strength, annealed glass presents obvious economic, structural and technical benefits for the construction industry [18].

In analogy to prestressed concrete, post-tensioned strategies have been recently tested to improve the overall performance of glass structural elements, both before and after glass cracking. Like tempering, the mechanical post-tensioning introduces beneficial compressive pre-stress in the glass tensile zones that avoid existing flaws from growing under service loading. However, the latter does not affect the nature of glass fragmentation. A limited number of studies have tested post-tensioning methodologies

using steel (e.g. [6,8,19,20]) and CFRP (e.g. [9]). In these studies, the reinforcement has been mechanically anchored (e.g. [8]) and/or adhesively bonded (e.g. [19]) to the glass. A reinforcement layout resembling the bending moment diagram has also been adopted to decrease the deformation of glass elements under service loading (e.g. [6,20]).

1.2. CFRP in glass industry

CFRP materials have been widely used to strengthen existing concrete structures adopting two distinct techniques. While the Externally Bonded Reinforcement (EBR) technique is based on adhesively bonding the reinforcement to the tensile face of the structural element to be strengthened, the Near Surface Mounted (NSM) technique consists of inserting the reinforcement inside pre-opened grooves in the tensile zone. The premature debonding of the CFRP reinforcement triggered by a critical shear crack has often been observed in EBR systems, both in reinforced concrete (e.g. [21]) and glass (e.g. [22]). Compared to the EBR, the NSM system is less prone to premature debonding due to the larger bonded surface area between adherends, as well as the confinement effect provided by the grooves [23]. Furthermore, the groove is completely filled with adhesive, thus protecting the reinforcement against corrosion, fire, vandalism actions, mechanical damage and aging [24].

Some studies have addressed the structural behaviour of CFRP reinforced glass structural elements, both experimentally (e.g. [9–11,25]) and numerically (e.g. [11,26]). These have shown that such reinforcement is efficient in producing glass composite systems showing relatively ductile failure modes due to the sequential failure of materials and/or connections, the so-called pseudo-ductility behaviour [27]. CFRP has been applied according to the EBR technique (e.g. [22,25]), embedded into the interlayer (e.g. [11]) or introduced inside recessed grooves designed during the glass lamination (e.g. [10]). It is noteworthy to mention that the feasibility of prestressing CFRP reinforcement before bonding it to the glass has also been addressed (e.g. [9]).

1.3. SMA in glass industry

Unlike the traditional reinforcement materials, Shape Memory Alloys (SMA) exhibit (i) shape memory effect, which is the ability to retrieve its initial shape by heating after mechanical deformation, and (ii) superelasticity, which is the ability to fully retrieve its initial shape after unloading under certain temperature conditions. Due to the shape memory effect, SMAs have been used for post-tensioning existing structural elements (e.g. [28–33]). In opposition to the traditional materials, whose post-tensioning procedure is often difficult due to the lack of space to install hydraulic jacks for prestressing the reinforcement, activation of SMA materials is simple [34,35]. In the case of glass structures, the

shape memory effect of SMAs can be used in two distinct scenarios: (i) before glass rupture, to increase the initial fracture strength by inducing favourable compressive pre-stresses in the tensile zones, or (ii) after glass rupture, to temporarily enhance the post-failure performance until the cracked glass element is replaced, reducing the deformation, preventing the crack progression and, ultimately, restraining or partially closing existing cracks.

Nickel-titanium (Ni-Ti) alloy is the most recognized SMA, but it is not considered suitable for the construction industry due to its expensive nature [31]. Hence, low-cost SMAs were recently developed and investigated, with emphases on iron-based alloys (Fe-SMA). Compared to the Ni-Ti alloy, Fe-SMAs show (i) lower cost, (ii) easier manufacturing process, (iii) higher modulus of elasticity, and (iv) lower activation temperature [36]. They are suitable for a wide range of applications in the construction industry. In this context, the Fe-17Mn-5Si-10Cr-4Ni-1(V, C) alloy, a promising Fe-SMA for the construction industry, was developed by Dong *et al.* [37] at the Swiss Federal Laboratories for Materials Science and Technology (Empa), Switzerland. This novel Fe-SMA is produced at atmospheric conditions and without expensive high-vacuum processing facilities and thermomechanical training [31,38]. Some studies have focused on the post-tensioned strengthening of concrete (e.g. [30,33,39–41]) and steel (e.g. [28,29,35]) structural elements using this Fe-SMA.

Few studies (e.g. [42–46]) have addressed the structural behaviour of SMA reinforced glass elements, probably due to the relative novelty of both materials in the civil engineering. Bedon *et al.* [42] performed an exploratory numerical study on the feasibility of activating embedded Ni-Ti wires to reduce out-of-plane deformations in laminated glass panels. Rocha *et al.* [44] and Silvestru *et al.* [46] investigated the feasibility of activating externally bonded Fe-SMA strips to increase the initial fracture strength of annealed glass beams and improve its post-failure performance. Compared to traditional prestressing methodologies, the activation of Fe-SMA strips is advantageous for smoothing the transfer of post-tensioning force to the glass substrate because heating the Fe-SMA induces a favourable adhesive damage gradient within the activation region and nearby regions [44]. Recently, the bond behaviour of glass-to-SMA adhesively bonded joints has also been investigated (e.g. [47,45]).

1.4. Research significance

Taking into account the challenges associated to the long-term tensile strength, lack of ductility and reliability of glass as a structural material, as well as the scarcity of research works focusing on the feasibility of strengthening glass elements with CFRP and Fe-SMA reinforcements, this research is aimed at investigating the post-tensioning of laminated glass beams by prestressing CFRP laminates

and/or activating pre-strained SMA strips. Five laminated glass beams were tested using a four-point bending configuration. In order to assess the influence of the reinforcement material and application technique on the post-cracking performance, different strengthening systems were adopted (CFRP and/or Fe-SMA *versus* EBR and/or NSM). Moreover, two epoxy adhesives were used to join the components. The finite elements software ABAQUS 6.14 [48] was used to numerically simulate the activation of the Fe-SMA strips. Digital Image Correlation (DIC) method was used to support the analysis of results obtained from flexural tests.

2   MATERIALS AND SPECIMENS

As stated in the introductory section, this study comprises an extensive experimental investigation on the flexural behaviour of laminated glass beams reinforced with CFRP and/or Fe-SMA. The first stage of this experimental study involves the material characterization (see **Section 2.1**) and the design of the beam geometry (see **Section 2.2**).

2.1.   Mechanical characterization

2.1.1.   Annealed glass

This work aims to investigate the feasibility of mechanically post-tensioning the annealed glass as an alternative to the thermal toughening to increase its initial fracture strength, but without compromising its post-failure performance. Thus, annealed glass layers were used to manufacture tailored laminated glass panels. The modulus of elasticity (E_g) and tensile strength($f_{g,t}$) of the annealed glass indicated in **Table V.1** were assessed by Rocha *et al.* [49].

2.1.2.   CFRP laminate

The CFRP laminates used in this study, with a cross section of 20×1.2 [mm], were produced by S&P® Clever Reinforcement Company by pultruding unidirectional carbon fibres with a vinyl ester resin matrix. The mechanical properties of the CFRP laminates were characterized according to ISO 527-5:2009 [50], by testing five specimens of $250 \times 20 \times 1.2$ [mm] (length × width × thickness) in tension at ambient temperature and at a constant tensile displacement rate of 1.0 mm/min until failure. The longitudinal deformation of the specimens was measured installing a clip gauge (type: MFA 12; linearity: 0.1 %; sensitivity: 2.0 mV/V; resolution: 1.0 pm; precision: ±1.5 μm) with stroke of 50 mm at the central region of each specimen, while the applied load was registered using a load cell with a maximum capacity of 200 kN and precision of 0.01 kN. Subsequently, the modulus of elasticity was determined from the slope of the linear trend line of the stress-strain response between strain

values of 0.05 % and 0.25 % [50]. **Table V.1** presents the average properties of the CFRP laminate, namely the modulus of elasticity (E_r), tensile strength ($f_{r,t}$) and ultimate strain ($\varepsilon_{r,ult}$).

Table V.1: Mechanical properties (average values) of the Fe-SMA strips, CFRP laminates, annealed glass and 3M and SD adhesives.

Material	E_r [GPa]	$f_{r,t}$ [MPa]	$\varepsilon_{r,ult}$ [%]	v[-]
Fe-SMA [1]	172.0 (1.7%)	948.1 (0.6%)	32.5 (2.3%)	0.39
CFRP	179.6 (1.9%)	2561.4 (2.9 %)	14.26 (3.6 %)	-
Material	E_g [GPa]	$f_{g,t}$ [MPa]	-	v[-]
Annealed glass [2]	74.0 (2.6%)	40	-	0.23
Material	E_{adh} [MPa]	f_{adh} [MPa]	$\varepsilon_{adh,ult}$ [‰]	v[-]
3M [2]	1728.1 (3.3%)	32.8 (4.2%)	30.7 (2.8%)	0.38
SD [2]	4325.3 (3.1%)	32.34 (3.9%)	8.4 (5.4%)	0.30

Notes:
The coefficients of variation (CoV) are indicated in parenthesis
[1] The mechanical properties of the Fe-SMA were assessed by Rocha *et al.* [44]
[2] The mechanical properties of the annealed glass and adhesives were assessed by Rocha *et al.* [49]

2.1.3.   Fe-SMA strip

The Fe-17Mn-5Si-10Cr-4Ni-1(V,C) (mass%) alloy is commercialized by re-fer AG Company and its production process is detailed by Leinenbach *et al.* [36]. The tensile behaviour of the Fe-SMA was previously characterized by Rocha *et al.* [44], including the average values of the modulus of elasticity (E_r), tensile strength ($f_{r,t}$) and ultimate strain ($\varepsilon_{r,ult}$), as presented in **Table V.1**.

2.1.4.   Adhesives

Based on previous studies on glass composite systems with CFRP [22] and Fe-SMA [44], the two-component epoxy adhesives SikaDur®-330 and 3M Scotch-Weld DP490 – later called as SD and 3M – were adopted to bond CFRP and Fe-SMA to glass, respectively. Compared to 3M adhesive, which must be used when the adhesive layer is thinner than 0.5 mm, according to the supplier, the SD adhesive can be used to produce adhesive layers up to 3 times thicker. The long-term performance of both adhesives was not considered in this study. **Table V.1** presents the modulus of elasticity (E_{adh}), tensile strength (f_{adh}) and ultimate strain ($\varepsilon_{adh,ult}$)of each adhesive, obtained by Rocha *et al.* [49]. In contrast to the SD adhesive, which exhibits linear elastic behaviour until failure, 3M adhesive shows a slight loss of stiffness with increasing load.

2.2. Geometry of beam elements

This study is the last phase of a wider research project aimed at investigating the flexural behaviour of composite glass systems with CFRP and Fe-SMA reinforcements. Experimental and numerical results were previously obtained by Rocha *et al.* [22] and Rocha *et al.* [44], addressing the flexural behaviour of monolithic glass beams with externally bonded CFRP and Fe-SMA reinforcements, respectively. **Table V.2** details the characteristics of the specimens tested in the scope of these research works, such as the beam geometry, the involved materials (adhesive and reinforcement) and the reinforcement ratio (ρ_r). Excluding the beams unloaded before the collapse due to excessive deformation, all the others failed due to premature debonding of the reinforcement when a critical shear crack appeared near the supports.

Table V.2: Summary of the main characteristics of glass monolithic beams reinforced with CFRP laminates [22] and Fe-SMA strips [44] previously tested.

Properties		Units	Glass-CFRP beams	Glass-SMA beams
Series designation			SDur	P_T120
	Series designation		SDur	P_T120
	Number of specimens		2	2
Glass panel				
	Type of glass	-	Annealed	Annealed
	Cross-section	[mm]	100 × 12	100 × 12
	Length	[mm]	1500	1500
Reinforcement				
	Material	-	CFRP	Fe-SMA
	Cross-section	[mm]	10 × 1.4	10 × 1.5
	Reinforcement ratio (ρr)	[%]	1.17	1.25
Adhesive layer				
	Adhesive	-	SD	3M
	Layer thickness (ta)	[mm]	0.9	0.3
Post-tensioning level				
	Activation temperature	[°C]	-	120
	Prestressing level	[MPa]	0	-
Testing				
	Span length	[mm]	1400	
	Configuration	-	Four-point bending tests	
	Load application	-	Displacement control with speed of 1.0 mm/s	

The NSM technique has recently been used for strengthening laminated glass elements (e.g. [7,10]). However, glass structural elements are typically very thin (slender), which poses challenges for

inserting the reinforcement inside the glass panel. Furthermore, externally bonded reinforcement can also be useful to protect the glass tensile zones from accidental actions and aggressive environmental conditions, thus preventing the undesired growth of existing flaws over time. Therefore, all tested specimens were strengthened using two reinforcement elements. One of them was introduced inside the laminated glass panel, according to the NSM technique, while the other was externally bonded to the bottom edge.

Five laminated glass panels were manufactured according to the geometry shown in **Figure V.1**. All panels consisted of joining three layers of annealed glass with polished edges using two polyvinyl butyral (PVB) interlayers with a thickness of 0.76 mm. The difference in height between the two outer layers – 220 (height) × 10 (thickness) [mm] – and the inner layer – 198 (height) × 3 (thickness) [mm] – created a groove of 22 (depth) × 4.5 (thickness) [mm] for subsequent insertion of the NSM reinforcement.
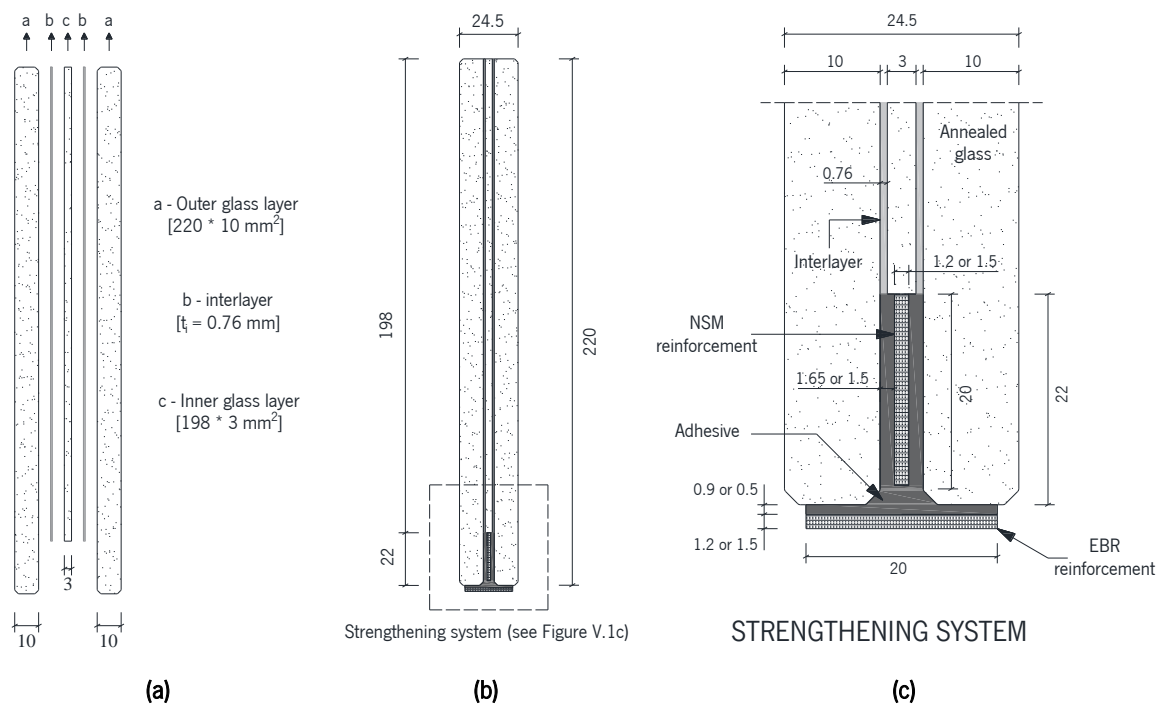
Figure V.1: Schematic representation of the cross section of the laminated glass beams: (a) exploited view; (b) assembled view after the lamination process; and (c) detailing the glass groove for inserting the reinforcement. Units in [mm].

Different strengthening systems were adopted in terms of reinforcement material *versus* application technique. **Table V.3** summarizes the main characteristics of all specimens, including the post-tensioning level adopted in each one. A total of 5 specimens were produced and tested according to the nomenclature *n-i-j*, where *i* and *j* identify the reinforcement material applied according to the NSM

and EBR techniques, respectively. The parameter n was adopted to distinguish specimens strengthened with NSM- and EBR-CFRP laminates, representing the prefixes "R" or "P" the cases where passive or prestressed reinforcement were applied, respectively.

3 TEST METHODS

3.1. General procedure

All composite glass beams were reinforced according to the scheme shown in **Figure V.1c**, by bonding CFRP laminates – 20 (width) × 1.2 (thickness) [mm] – and/or Fe-SMA strips – 20 (width) × 1.5 (thickness) [mm] – to the glass using the two adhesives mentioned in **Section 2.1.4**. Small PVC spacers were used to guarantee the symmetrical positioning of the NSM reinforcement inside the longitudinal groove, occupying less than 1.0 % of the bonding surface area to avoid a significant interference with the test results. Considering the suggestions provided by manufacturers, the EBR reinforcement was bonded to the glass adopting adhesive layers with a thickness of 0.9 mm and 0.3 mm for the SD and 3M adhesives, respectively. **Table V.3** describes the main characteristics of the beams tested in this work, including the adhesives used for each strengthening system and the respective layer thickness.

The specimens were prepared according to the following general procedure:

i. Cutting of the reinforcement elements and manufacturing of the laminated glass panels;

ii. Prestressing of the CFRP laminate against the reaction frame *versus* pre-straining the Fe-SMA strip (further details in **Section 3.2** and **Section 3.3**, respectively);

iii. Bonding of the reinforcement to the glass. First, the bonding surfaces were cleaned with acetone. Then, the adhesive was prepared and applied according to the manufacturer's specifications. Afterwards, the components were carefully assembled. Finally, in order to obtain a further cure of the adhesives and to avoid effects of different ambient temperature among the tested beams during curing, all specimens were subjected to post-curing conditions before releasing the CFRP laminate or activating the Fe-SMA strip. The post-curing was achieved by using heating fans aimed at the specimens (zones in the vicinity of the loaded end section), producing the rise of the temperature measured in the specimens to approximately 45 °C for 2 hours (see **Figure V.2a**);

iv.   Releasing of the CFRP laminate by removing the prestressing hydraulic jacks *versus* activating the Fe-SMA strip by resistive heating. This step took place at least 96 hours after bonding to guarantee sufficient adhesive toughness to transfer the post-tensioning force from the reinforcement to the glass.
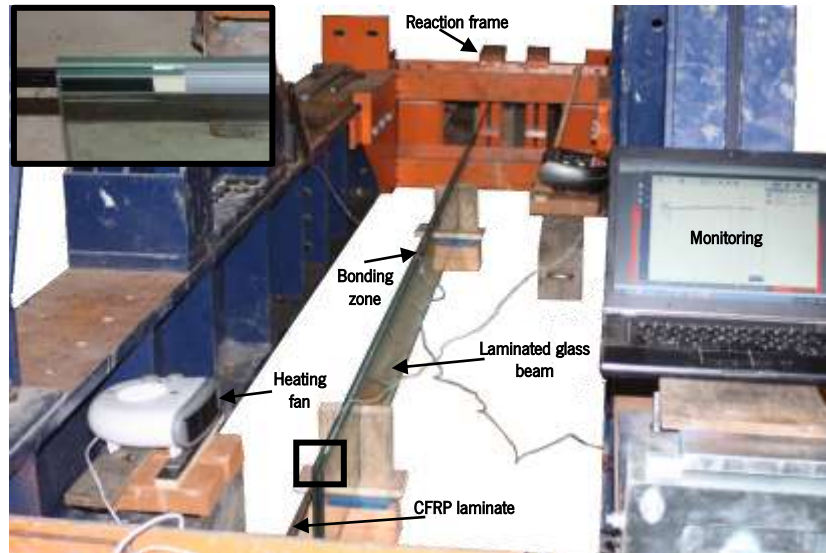
(a)
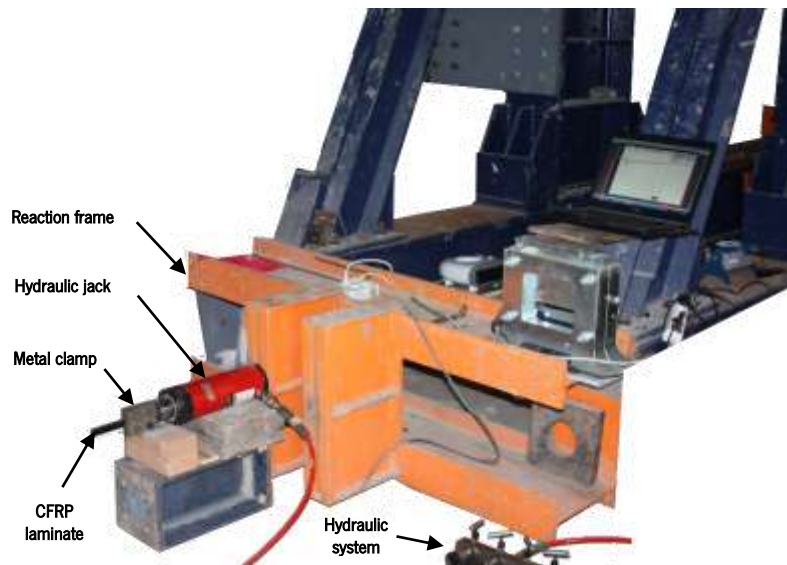
(b)

Figure V.2: Overview of the experimental setup used for prestressing the CFRP laminates: (a) prestressing bed; and (b) external reaction frame, hydraulic jack and metal clamps used to fix the CFRP laminates.

Table V.3: Characteristics of the laminated glass beams tested in this study, including geometry, reinforcement materials and respective application technique, adhesives and respective thickness, and post-tensioning level adopted in each beam.

Property	Units	Beam designation				
		R_CFRP_CFRP	P_CFRP_CFRP	CFRP_SMA	SMA_CFRP	SMA_SMA
Glass panel						
Type of glass	-	Annealed	Annealed	Annealed	Annealed	Annealed
Cross-section						
Outer layers	[mm]	220 × 10	220 × 10	220 × 10	220 × 10	220 × 10
Inner layer	[mm]	198 × 3	198 × 3	198 × 3	198 × 3	198 × 3
Length	[mm]	2900	2900	2900	2900	2900
Interlayer						
Material	-	PVB	PVB	PVB	PVB	PVB
Thickness	[mm]	0.76	0.76	0.76	0.76	0.76
Strengthening system						
NSM reinforcement						
Material	-	CFRP	CFRP	CFRP	Fe-SMA	Fe-SMA
Cross-section	[mm]	20 × 1.2	20 × 1.2	20 × 1.2	20 × 1.5	20 × 1.5
EBR reinforcement						
Material	-	CFRP	CFRP	Fe-SMA	CFRP	Fe-SMA
Cross-section	[mm]	20 × 1.2	20 × 1.2	20 × 1.5	20 × 1.2	20 × 1.5
Reinforcement ratio	[%]	0.96	0.96	1.08	1.08	1.20

Table V.3 (Cont.): Characteristics of the laminated glass beams tested in this study, including geometry, reinforcement materials and respective application technique, adhesives and respective thickness, and post-tensioning level adopted in each beam.

Property	Units	Beam designation				
		R_CFRP_CFRP	P_CFRP_CFRP	CFRP_SMA	SMA_CFRP	SMA_SMA
Adhesively bonded connections						
NSM reinforcement						
Adhesive	-	SD	SD	SD	3M	3M
Layer thickness (t_a)	[mm]	1.65	1.65	1.65	1.50	1.50
EBR reinforcement						
Adhesive	-	SD	SD	3M	SD	3M
Layer thickness (t_a)	[mm]	1.0	1.0	0.5	1.0	0.5
Post-tensioning						
NSM reinforcement						
Target temperature	[°C]	-	-	-	200	200
Initial pre-strain	[‰]	-	2.0	2.0	-	-
EBR reinforcement						
Target temperature	[°C]	-	-	120	-	120
Initial pre-strain	[‰]	-	-	-	-	-

In the specimens R_CFRP_CFRP and P_CFRP_CFRP, the two reinforcement elements were simultaneously bonded to the glass, since only the SD adhesive was used for this purpose. Regarding the R_CFRP_CFRP beam, it was prepared by executing only the first and third steps. For the remaining specimens, each reinforcement element was bonded individually and in a separate stage, either because different adhesives were used to bond each reinforcement, or because in the case of the Fe-SMA strips these were not entirely activated, as further explained in **Section 3.3**. Therefore, all specimens strengthened with Fe-SMA were manufactured by applying twice the general procedure described above, for each of the reinforcement elements individually.

3.2. Prestressing of CFRP

Glass edges show lower apparent tensile strength than the glass surfaces, because the former contain deeper surface flaws induced during the production, cutting, polishing and handling operations [51,52]. In addition, it is reasonable to assume that the glass corners show an even lower tensile strength, as they are typically the most unprotected zones when glass pieces are handled. As a result, preliminary studies (e.g. [53]) have shown that prestressing externally bonded reinforcement is often unsuccessful because the glass fails due to the stress concentration at the loaded end sections. Accordingly, in this case, only the NSM-CFRP laminates were prestressed.

After being mechanically anchored at both ends using metal clamps (see **Figure V.2b**), the NSM-CFRP laminates were prestressed up to an average strain of 2.0 ‰ ($\sigma \approx 367.7$ MPa) using a hydraulic jack. The axial strain was recorded by means of a strain gauge (type: PFL-10-11-3LJC-F by TML; measuring length: 10 mm; gauge factor: 2.12 ± 1 %) previously installed in the middle of the CFRP laminate. The prestressing level was continuously monitored until the NSM-CFRP laminate was released.

3.3. Activation of Fe-SMA

Fe-SMAs have two distinct crystal structures, called (i) austenite phase, which is stable at higher temperatures, and (ii) martensite phase, which is stable at lower temperatures. The martensitic transformation consists of modifying the lattice from austenite to detwinned martensite through mechanical deformation or temperature variation. As schematized in **Figure V.3**, the martensitic transformation does not involve any slippage between atoms (neighbors remain neighbors). It takes place at temperatures between M_s (martensite start temperature) and A_s (austenite start temperature). When the Fe-SMA is heated at temperatures above A_s, the detwinned martensite is reversed to austenite and its initial shape is retrieved.

Post-tensioning of structural elements with Fe-SMAs involves three phases: (i) pre-straining, (ii) activation and (iii) service loading (see **Figure V.3**). In the first phase, the Fe-SMA is mechanically loaded at room temperature ($M_s < T < A_s$) until reaching a target strain. Once unloaded, the Fe-SMA shows a permanent deformation that can be partially recovered through heating ($T > A_s$). When the Fe-SMA is adhesively bonded to the target structural element, recovery stress is generated during the activation (rise in temperature to a specific peak value) and, as a result, the target structural element is post-tensioned. Stress recovery ends when the Fe-SMA reaches the room temperature again.
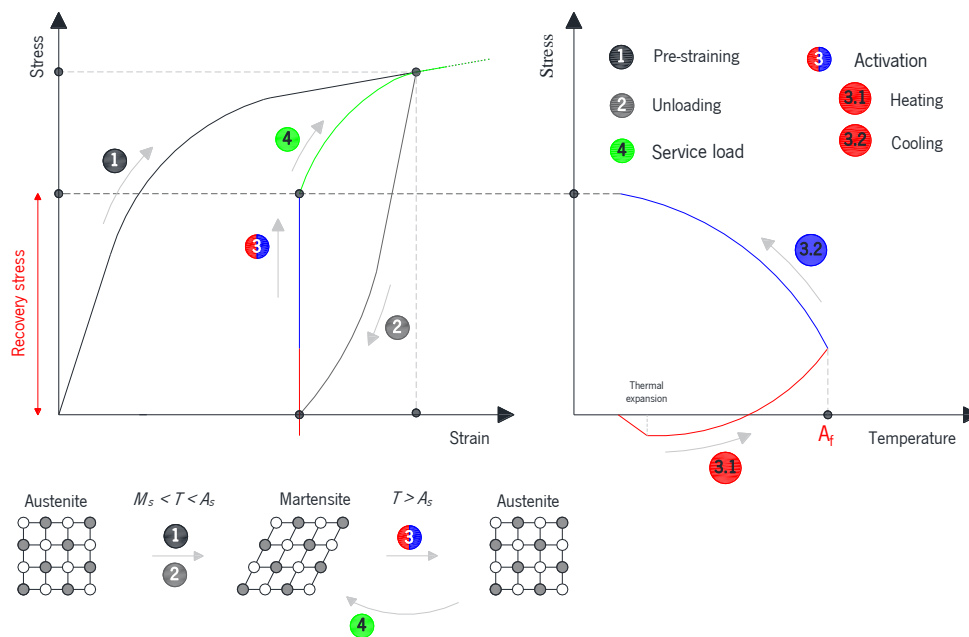
Figure V.3: Schematic activation procedure of Fe-SMAs under constraint strain recovery, also including the phase behaviour. Adapted from Michels *et al.* [30].

According to the technical specifications provided by the producer, Fe-SMA strips were pre-strained to 2.0 % at room temperature. A hydraulic jack was used to apply the load and a clip gauge (technical specifications described in **Section 2.1.1**) to measure the longitudinal deformation.

Adhesive damage is an inevitable consequence of activating the Fe-SMA reinforcement. However, this apparently deleterious effect can be used to prevent stress concentrations in the glass substrate. A favourable damage gradient is produced along the adhesive connection, on both sides of the activated Fe-SMA strip zone, which helps to smooth the stress transfer between adherends. Desirably, the adhesive bond regions closest the beam ends should remain undamaged to efficiently transfer the post-tensioning force between the adherends. Following the recommendations proposed by Rocha *et al.* [44], the Fe-SMA strips were heated symmetrically with respect to the mid-span section and the activated length (l_a) was set to 1400 mm, as schematized in **Figure V.4a**.
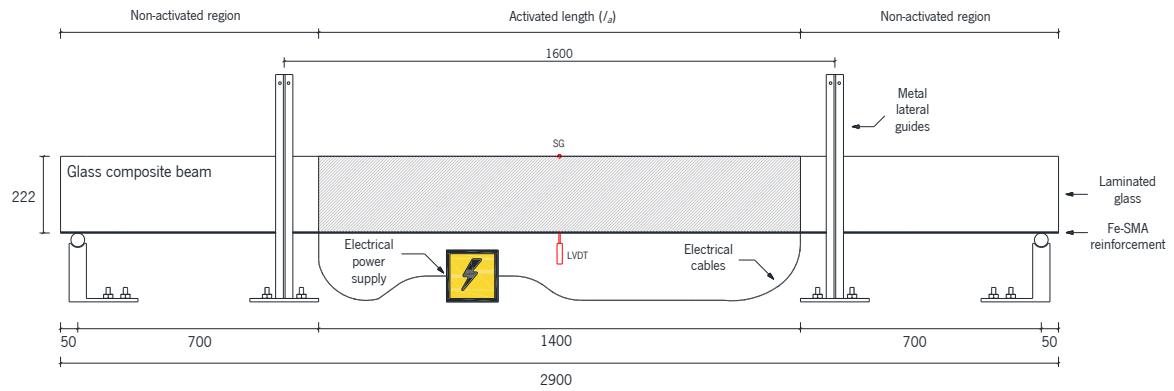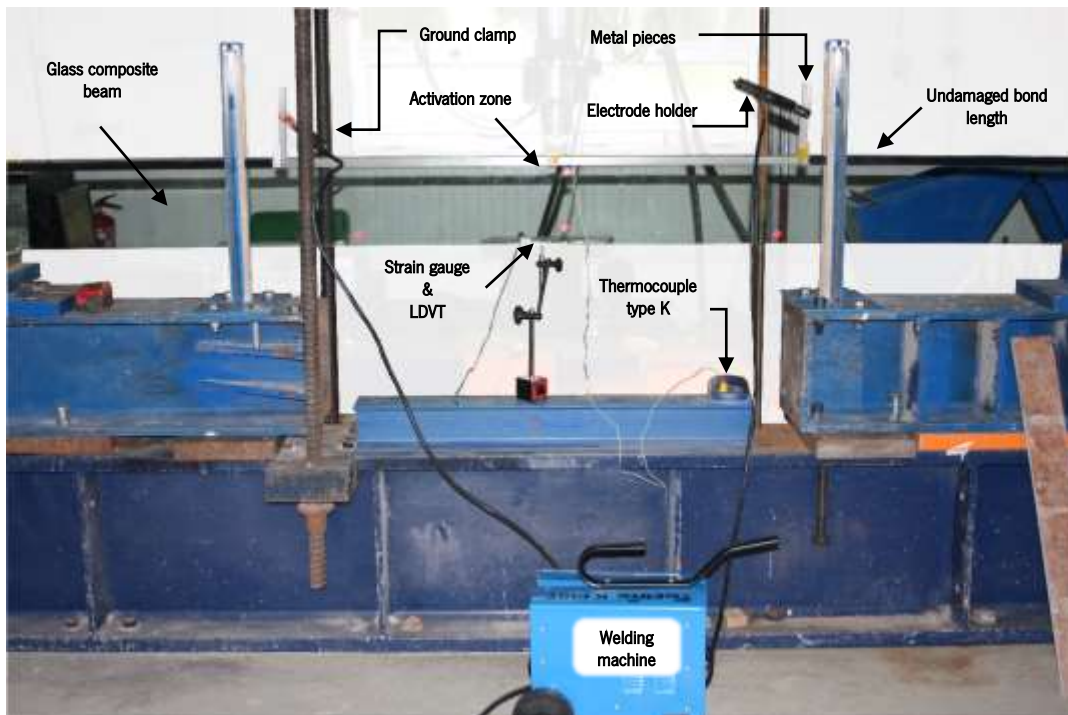
Figure V.4: Activation of the Fe-SMA reinforcement: (a) schematic representation of the experimental procedure; (b) overview of the experimental setup adopted; and connection between the power supply clamps and the (c) NSM-SMA and (d) EBR-SMA strips, respectively.

Accordingly, the non-activated NSM-SMA strip zones were first bonded to the glass. After that, the unbonded Fe-SMA zone ($l = l_a$) was activated. Then, the unbonded groove zone was filled with adhesive and, finally, the EBR reinforcement was bonded to the glass and subsequently activated in some of the specimens.

Electric power was supplied to the Fe-SMA reinforcement using two small metal pieces placed 700 mm apart from the mid-span section, in order to connect the electrode holder and the ground clamp (see **Figure V.4**) and induce a current at the Fe-SMA. To activate the NSM-SMA strip, the metal pieces were inserted into the groove, between the reinforcement and the outer glass sheets (see **Figure V.4b**). Metal clamps were used to press the metal pieces against the EBR-SMA strip (see **Figure V.4c**). A relatively high current density of approximately ≈ 4.0 A/mm^2 was applied. The Fe-SMA strips were heated at different temperatures: (i) 200 °C for NSM-SMA strips; and (ii) 120 °C for EBR-SMA strips (see **Table V.3**). Due to a brief power outage during the activation process, in the SMA_CFRP beam, the NSM-SMA strip was only heated at ≈ 180 °C.

Figure V.4b shows the instrumentation adopted during the activation of the Fe-SMA strips, which included the measurement of (i) the mid-span deflection by means of a displacement transducer – linear variable differential transformer (LVDT) – with stroke of 25 mm and precision of 0.01 mm; (ii) the axial strain at the top edge of the glass panel using a strain gauge (technical specifications indicated in **Section 3.2**) and (iii) the temperature in the Fe-SMA through a type K thermocouple. All measurements were recorded at an average frequency of 5 Hz.

3.4. Four-point bending tests

As shown in **Figure V.5**, five laminated glass beams with a span of 2.8 m were tested adopting a symmetrical four-point bending configuration, with two central load points 700 mm apart. In these tests, the ratio between the shear span length and the beam height (≈ 4.8 times) was the same as that one adopted for the monolithic glass beams previously tested [22,44]. To prevent lateral-buckling, two pairs of vertical metal guides were symmetrically positioned at 700 mm from the mid-span section and metal frames were placed at the beams supports. In these supports, threaded screws were inserted into the holes and carefully pressed against the glass to maintain the alignment of the specimens during the test. Furthermore, polytetrafluoroethylene (teflon) was placed between the threaded screws and the glass beams to prevent premature failure by direct metal-glass contact due to stress concentrations. Lateral guides were also wrapped with a thin teflon film to avoid frictional forces during the test.
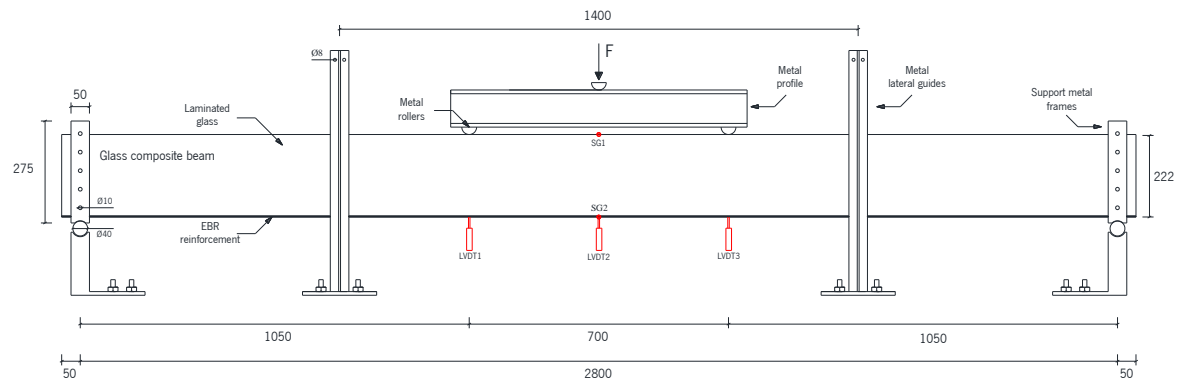
(a)

(b)

Figure V.5: Four-point bending tests carried out in this study: (a) general layout; and (b) experimental setup.

As shown in **Figure V.5**, displacement transducers with stroke of 50 mm (linearity of 0.15 %) were used to measure the deflection at the load point (LVDT1 and LVDT3) and mid-span (LVDT2) sections. Axial strains were recorded by placing strain gauges on the top edge of the glass (SG1) and on the bottom edge of the EBR reinforcement (SG2). Their technical specifications were indicated above, in **Section 3.2**. A load cell with a maximum capacity of 200 kN and precision of 0.01 kN was used to measure the applied load. The beams were loaded monotonically under displacement control at a displacement rate of 1.0 mm/min (internal LVDT control of the actuator). A relatively high acquisition frequency of 25 Hz was adopted for all experimental measurements. Finally, the tests were conducted in laboratory environment at an average temperature of 24 °C and relative humidity of 65 %.

All experimental tests were monitored also adopting the Digital Image Correlation (DIC) technique, in order to document the crack evolution and complement the understanding of the structural behaviour

obtained from flexural tests until failure. The camera used to capture the images was equipped with a full frame CMOS (7360 × 4912 pixels), and the focal distance of the lens was 35 mm. The GOM Correlate 2019 software [54] was used for image processing. Images were recorded at 10-second intervals. Due to the large dimension of the specimens tested (length of 2900 mm), the region of interest (ROI) included only half of the span, in order to optimize resolution.

4   RESULTS

4.1.   Post-tensioning

Table V.4 presents the pre-strain ($\varepsilon_{r,p}$) and the corresponding post-tensioning force (F_p) measured after the NSM-CFRP laminates were released by the hydraulic jacks. **Figure V.6** shows the evolution of the pre-strain and temperature over time for the P_CFRP_CFRP beam. In the beams P_CFRP_CFRP and CFRP_SMA, the $\varepsilon_{r,p}$ recorded by strain gauges decreased about 4.5 % and 4.9 % when the NSM-CFRP laminate was released, respectively. The eccentricity of the post-tensioning force in relation to the neutral axis generated camber in the laminated glass beams, which slightly reduced the prestress.

Table V.4: Results obtained during the prestressing procedure of the NSM-CFRP reinforcement in the P_CFRP_CFRP and CFRP_SMA beams.

Beam	Reinforcement	$\varepsilon_{r,p}$ [‰]	F_p [kN]
P_CFRP_CFRP	NSM	1.926	8.50
CFRP_SMA	NSM	1.923	8.49

Figure V.7 and **Figure V.8** show the evolution of the vertical displacement at the mid-span section (d_{exp}), the tensile strain at the top edge of the glass panel ($\varepsilon_{g,t}$) and the temperature in the Fe-SMA strip (T) during the activation process. It should be noted that the positive values correspond to downward displacements and tensile strains. **Table V.5** summarizes the values of d_{exp} and $\varepsilon_{g,t}$ registered at the end of the cooling phase, as well as the maximum temperature (T_a) attained in the Fe-SMA strip. At the beginning of the heating phase, for temperatures below A_s ($\approx$ 60 °C), all specimens deformed downwards due to the thermal expansion of the Fe-SMA. Since the Fe-SMA strips were restrained by the glass, the beams deformed upwards between 0.413 mm (CFRP_SMA beam) and 1.058 mm (SMA_SMA beam), depending on the activation temperature and number of activated Fe-SMA strips in each specimen.
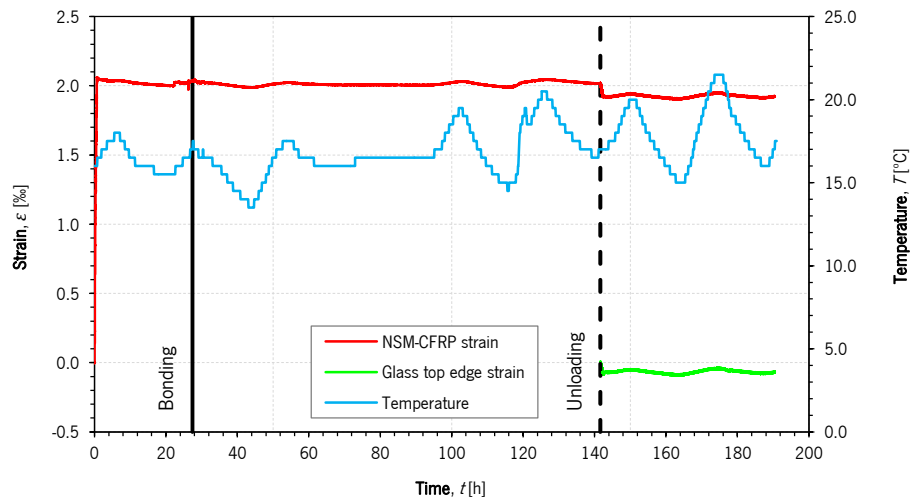
Figure V.6: Post-tensioning of the P_CFRP_CFRP beam, namely the evolution of the pre-strain in the CFRP laminate, of the compressive pre-stress at the bottom glass edge and the temperature over the time.

4.1.1.   Numerical modelling

The recovery stress (σ_{rec}). developed in the Fe-SMA strips was determined based on the experimental measurements (see **Table V.5**) by performing numerical simulations using the finite elements software ABAQUS 6.14 [48]. They were carried out based on the recommendations proposed by Rocha *et al*. [44]. All components were simulated as an isotropic material with linear elastic behaviour. The activated Fe-SMA strip zone was simulated by adopting a modulus of elasticity ($E_{r,a}$) equal to 95 GPa. In addition, the absence of shear interaction along l_a was considered by setting E_{adh} to zero. Finally, in the non-activated beam regions, all components, including the adhesive, were simulated using the mechanical properties indicated in **Table V.1**.

In the beams CFRP_SMA and SMA_SMA, the post-tensioning procedure entailed two phases (see **Section 3**) that were precisely reflected in the numerical simulations. A phased analysis with an incremental-iterative procedure was employed in the calculations. The first phase simulated the prestressing/activation of the NSM reinforcement involving the following components: (i) the laminated glass panel; (ii) the NSM reinforcement; (iii) the adhesive bonding of the non-activated Fe-SMA strip zones to the glass; and (iv) the boundary conditions. The second phase consisted of activating the EBR-SMA reinforcement. In this phase, the EBR reinforcement and corresponding adhesive layer were added to the numerical model from the first phase. **Figure IV.9** schematizes the numerical simulation of these specimens.

Figure V.7: Experimental measurements recorded during the activation of the NSM-SMA strips in the SMA_SMA and SMA_CFRP beams: (a) displacement at the mid-span section (d_{exp}), (b) axial strain at the top edge of the glass panel ($\varepsilon_{g,t}$) and (c) temperature in the Fe-SMA (T).

Three-dimensional simulations were carried out using 8-node cubic elements (C3D8) of 10×10 [mm]. **Figure IV.9** shows the geometry, boundary conditions, load configuration and the mesh pattern. Adhesive damage propagation into the non-activated region was neglected and the "tie" constraint was assigned to the Fe-SMA/adhesive and adhesive/glass interfaces. The recovery stress was simulated as a temperature variation along the l_a and was extracted when the numerical axial stress at the top edge of glass attained $\varepsilon_{g,t}$ (see **Table V.5**). In specimens where the prestressing of the CFRP laminate was also included in the numerical simulations (e.g. CFRP_SMA beam), a temperature

variation was applied along the entire length of the CFRP laminate until reaching the final $\varepsilon_{r,p}$ (see
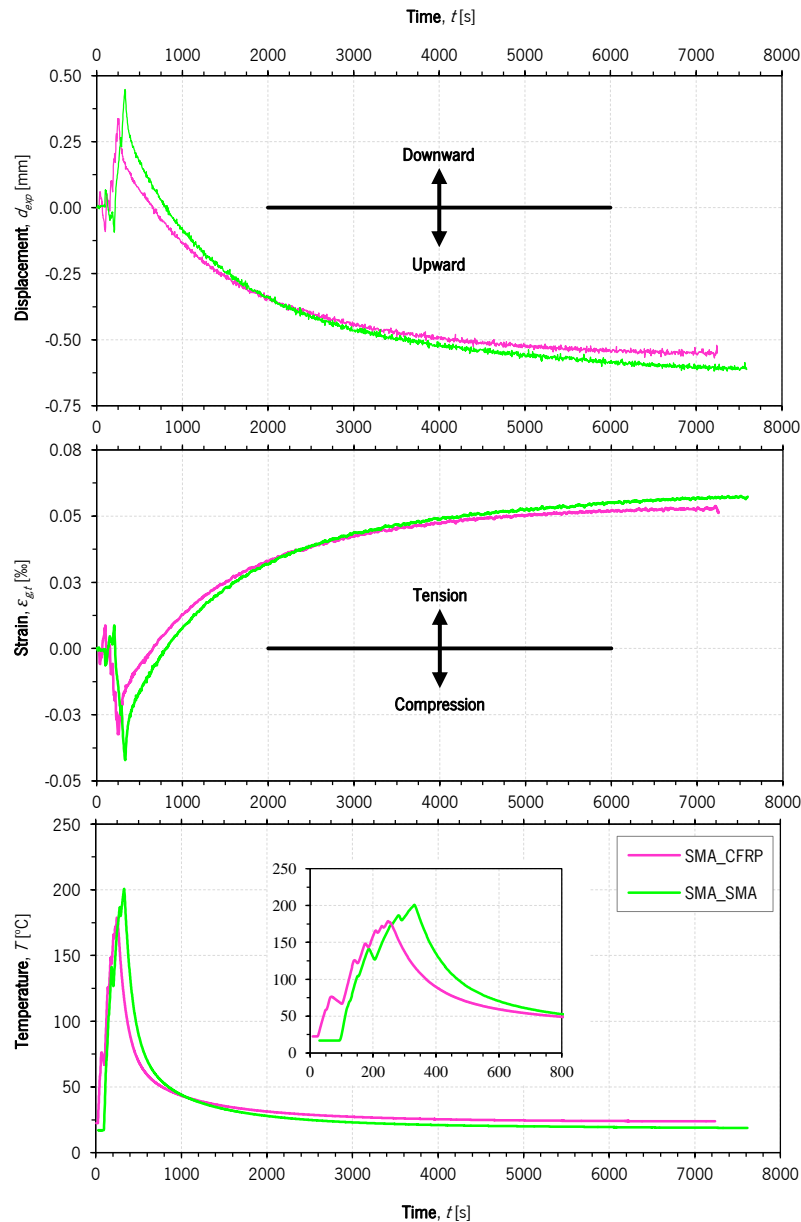
Table V.4).
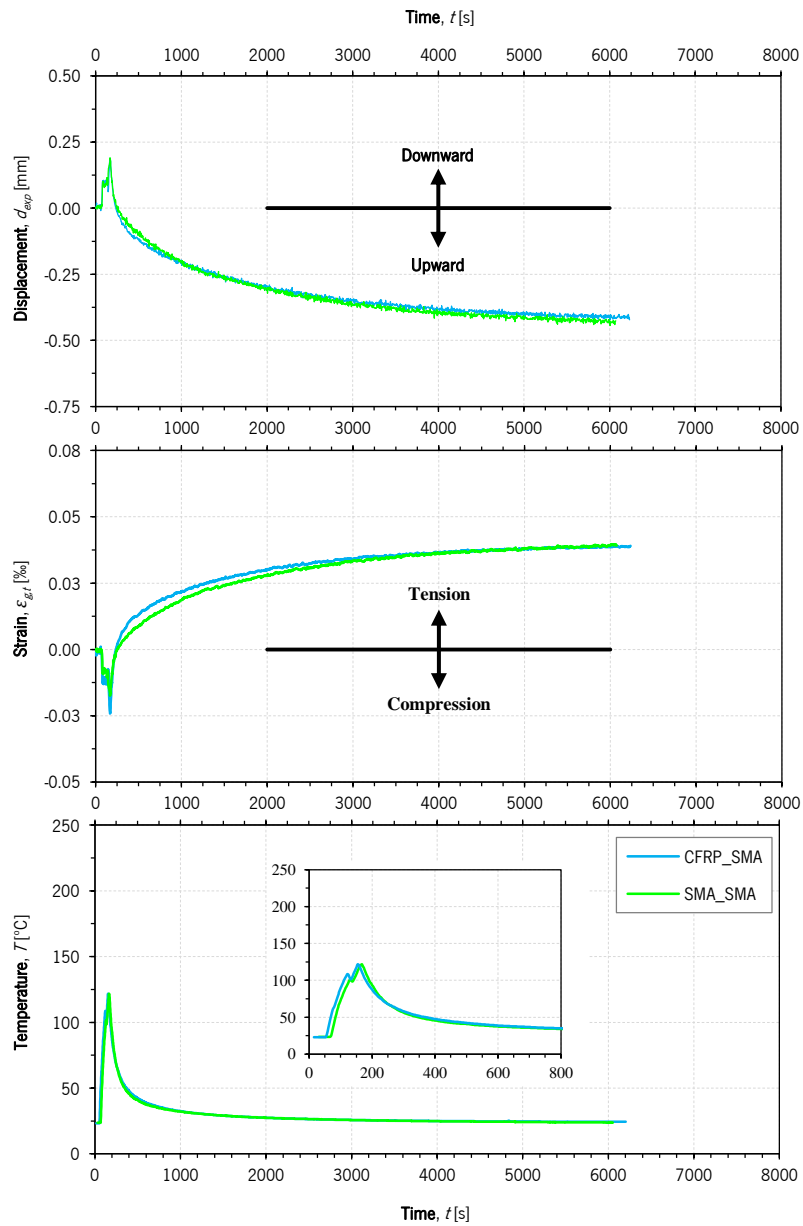
Figure V.8: Experimental measurements recorded during the activation of the EBR-SMA strips in the CFRP_SMA and SMA_SMA beams: (a) displacement at the mid-span section (d_{exp}), (b) axial strain at the top edge of the glass panel ($\varepsilon_{g,t}$) and (c) temperature in the Fe-SMA (T).
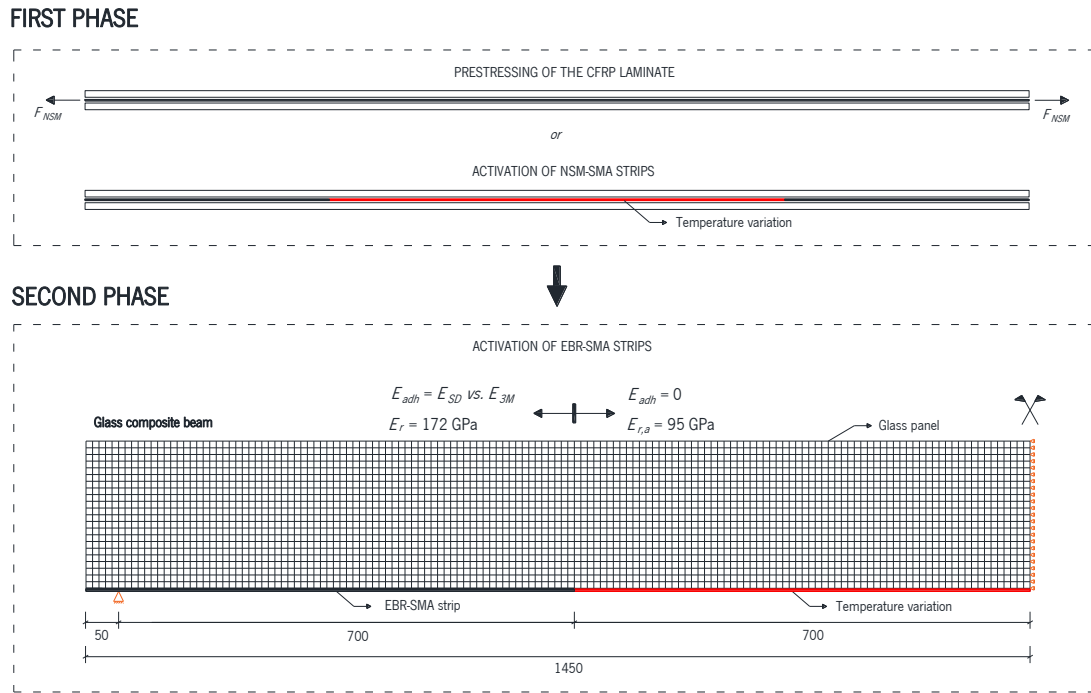
Figure V.9: Phased analysis adopted in numerical simulation to model the post-tensioning procedure and determine the recovery stress in the Fe-SMA strips, including the finite element model and the Fe-SMA strip length (red colour) that was subjected to temperature variation.

Table V.5: Results obtained during the activation of Fe-SMA strips, as well as the comparison between the experimental measurements and the numerical results.

Experimental measurements				
Beam	Reinforcement	T_a [°C]	d_{exp} [mm]	$\sigma_{g,t}$ [MPa]
CFRP_SMA	EBR	121.9	0.413	-2.997
SMA_CFRP	NSM	178.9	0.552	-3.759
SMA_SMA	NSM	200.8	0.615	-4.174
	EBR	122.0	0.443	-3.138
Numerical results				
Beam	Reinforcement	d_{num} [mm]	σ_{rec} [MPa]	F_p [kN]
CFRP_SMA	EBR	0.418 (1.2%)	257.3	7.12
SMA_CFRP	NSM	0.557 (0.9%)	373.5	11.21
SMA_SMA	NSM	0.619 (0.7%)	414.6	12.44
	EBR	0.439 (-0.9%)	268.2	8.05

Note:
The difference between d_{num} and d_{exp} is indicated in parentheses

4.1.2. Recovery stress

Table V.5 presents the results obtained from the numerical simulations, namely the displacement at mid-span (d_{num}), the recovery stress in the Fe-SMA strip (σ_{rec}) and the respective post-tensioning

force (F_p). The numerical displacements at mid-span are very similar to the experimental ones (differences below 1.2 %), providing further validation to the numerical models. Fe-SMA strips developed recovery stresses between 257.3 MPa ($T_a \approx 120\ °C$) and 414.6 MPa ($T_a \approx 200\ °C$), in line with the values found in the literature (e.g. [31]).

The post-tensioning level in the NSM reinforcement decreased when the EBR-SMA strip was activated. In this sense, based on the superposition principle, the final post-tensioning force in each specimen is indicated in **Table V.6**. In the beams CFRP_SMA and SMA_SMA, the activation of EBR-SMA strips reduced the F_{NSM} by 4.2 % and 1.6 %, respectively. **Table V.6** presents the compressive pre-stress at the glass bottom edge ($\sigma_{g,b}$) resulting from the post-tensioning procedure.

Table V.6: Final post-tensioning force applied to the NSM (F_{NSM}) and EBR (F_{EBR}) reinforcement elements, as well as the compressive pre-stress at the bottom edge of glass, both estimated from the numerical simulations.

Beam	F_{NSM} [kN]	F_{EBR} [kN]	$\sigma_{g,b}$ [MPa]
P_CFRP_CFRP	8.50	-	-6.17 (+15.4 %)
CFRP_SMA	8.14	7.12	-12.16 (+30.4 %)
SMA_CFRP	11.21	-	-8.28 (+20.7 %)
SMA_SMA	12.24	8.05	-15.21 (+38.0 %)

Note:
The theoretical increase in initial cracking load considering $f_{g,t}$ = 40 MPa (see **Table V.1**) is indicated in parentheses.

4.2.   Flexural tests

Figure IV.10, **Figure V.11** and **Figure V.12** show the applied load (F) *versus* mid-span deflection (δ) responses of the tested specimens, as well as the experimental crack patterns extracted from the DIC technique at different stages. Although, the region of interest (ROI) has included only half of the span, all specimens showed crack patterns approximately symmetrical in relation to the mid-span section, both in terms of crack density and shape. Therefore, to facilitate the understanding of the crack propagation towards the supports, all crack patterns extracted from the DIC technique were mirrored, thus providing an overview of the entire crack pattern observed in each specimen. It should be noted that only the cracks that appeared on the outer layer facing the camera were documented using the DIC technique.

(a)

(b)
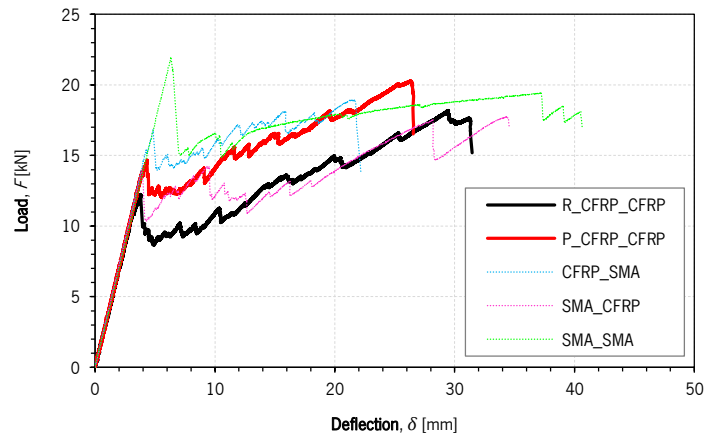
(c)

Figure V.10: Flexural behaviour of the beams R_CFRP_CFRP and P_CFRP_CFRP: (a) load deflection curves; and (b-c) DIC crack patterns at different stages.
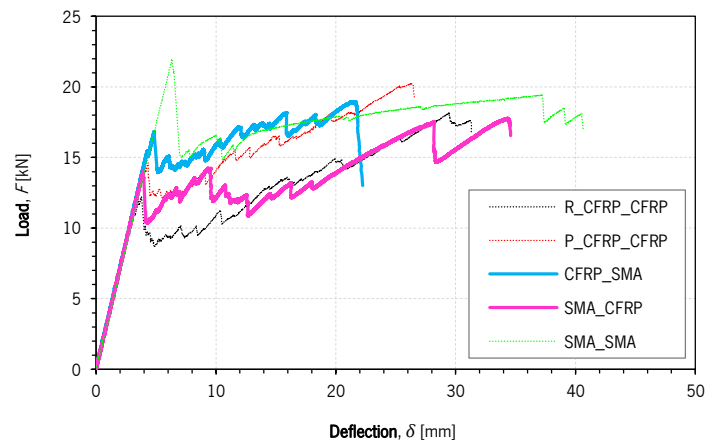
(a)
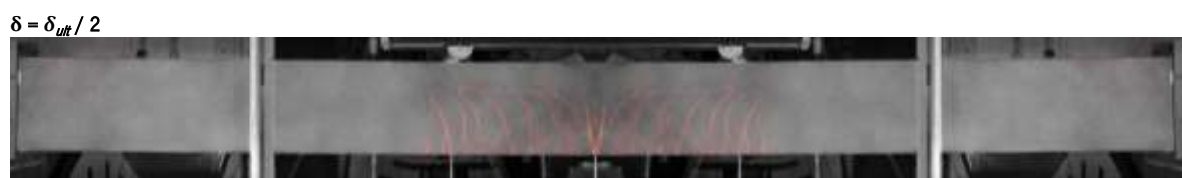
(b)

(c)

Figure V.11: Flexural behaviour of the beams CFRP_SMA and SMA_CFRP: (a) load deflection curves; and (b-c) DIC crack patterns at different stages.

(a)
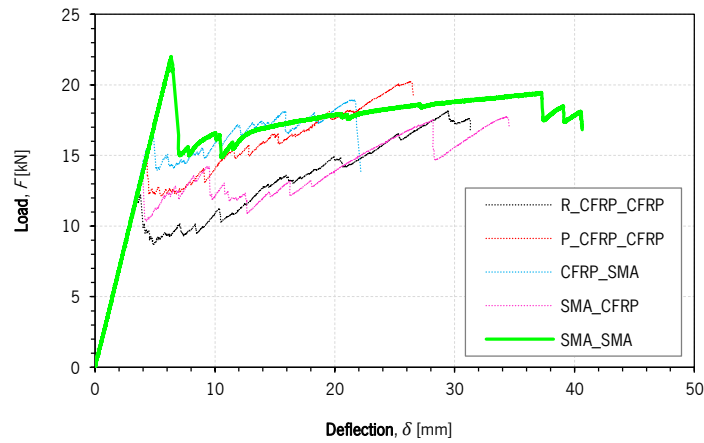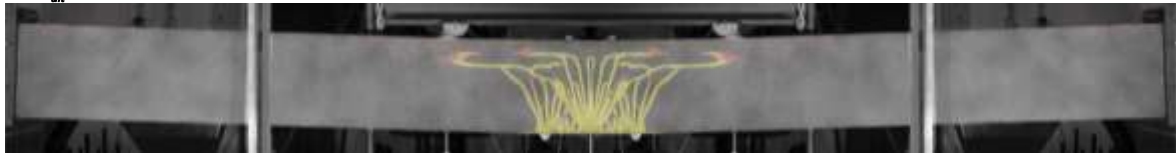
(b)

Figure V.12: Flexural behaviour of the SMA_SMA beam: (a) load deflection curves; and (b) DIC crack patterns at different stages.

Table V.7 summarizes the $F - \delta$ responses in terms of initial stiffness (K), first cracking load (F_{cr}) and corresponding deflection (δ_{cr}), maximum load after first cracking (F_{max}), load at failure (F_{ult}) and corresponding deflection (δ_{ult})., as well as the residual strength index (RSi) – defined as the ratio between F_{max} and F_{cr} – and the ductility index (Di) – defined as the ratio between δ_{ult} and δ_{cr}. In addition, **Table V.7** also presents the axial strain measured at the top edge of the glass panel ($\varepsilon_{g,t}$) and at the EBR element (ε_r) corresponding to F_{ult}, as well as the identification of the failure mode observed in each specimen according to the nomenclature: CSC, for critical shear crack formation; and GC, for shear-compression failure and consequent crushing at compression glass zone.

As expected, the structural response of the glass composite beams was composed of two different stages: (i) the pre-cracking stage, during which the glass panel was the main responsible for withstanding the applied bending load; and (ii) the post-cracking stage, starting with the appearance of the first crack, which involved the appearance of new cracks towards the support, as well as the propagation of existing ones. During the second stage, additional load carrying capacity was provided by the resisting mechanism formed by the compression force in the upper uncracked glass zone and the tensile force in the reinforcement element. As a consequence, all specimens presented a relatively ductile failure. Crack propagation towards the supports resulted in successive load drops during the post-cracking stage, leading to a progressive loss of stiffness of the beams. At the end of the post-cracking stage, all specimens ruptured when explosive failure occurred at the compression zone of glass beams.

Table V.7: Summary of the main properties extracted from the $F - \delta$ experimental responses of laminated glass beams, as well as the failure mode observed and the strain gauge measurements when $F = F_{ult}$.

Property	Units	Beam designation				
		R_CFRP_CFRP	P_CFRP_CFRP	CFRP_SMA	SMA_CFRP	SMA_SMA
Structural response						
K	[kN/mm]	3.49	3.53	3.63	3.57	3.47
F_{cr}	[kN]	11.31	13.88	15.48	14.02	22.02
δ_{cr}	[mm]	3.24	3.93	4.26	3.93	6.34
F_{max}	[kN]	18.19	20.27	18.95	17.79	19.30
F_{ult}	[kN]	17.65	20.27	18.95	17.79	18.13
δ_{ult}	[mm]	31.45	26.54	22.24	34.59	35.21
Di	[%]	971.2	675.3	521.7	881.2	555.0
RSi	[%]	160.8	146.0	122.4	126.9	87.6
Failure modes						
-	-	GC	GC	GC	GC	GC
Strain gauge measurements						
$\varepsilon_{g,t}$	[‰]	-1.09	-1.43	-1.22	-1.25	-2.65
ε_r	[‰]	4.45	4.35	4.72	4.71	48.72

For comparison, **Figure V.13** presents the $F - \delta$ responses of monolithic glass beams previously tested, namely the S*Dur* [22] and P_T120 series [44], as well as the crack patterns observed in each series before collapse. In order to assess the efficiency of the hybrid strengthening systems tested, **Table V.8** summarizes the *RSi, Di* and ε_r obtained from these specimen series, as well as the observed failure modes.

5   DISCUSSION

5.1.   Before first cracking

5.1.1.   Initial stiffness

All specimens showed similar values of initial stiffness, between 3.47 kN/mm (SMA_SMA beam) and 3.63 kN/mm (CFRP-SMA beam). Although the reinforcement ratio of the SMA_SMA beam was the highest among all the specimens tested, with a value of 1.20 %, it also presented the lowest K. This may be the result of the modulus of elasticity reduction of the Fe-SMA when it is activated [31]. The higher the T_a, the lower the modulus of elasticity of the Fe-SMA observed after activation. Accordingly and as experimentally observed, both specimens reinforced with two CFRP laminates exhibited the highest initial stiffness values.

(c)   (d)
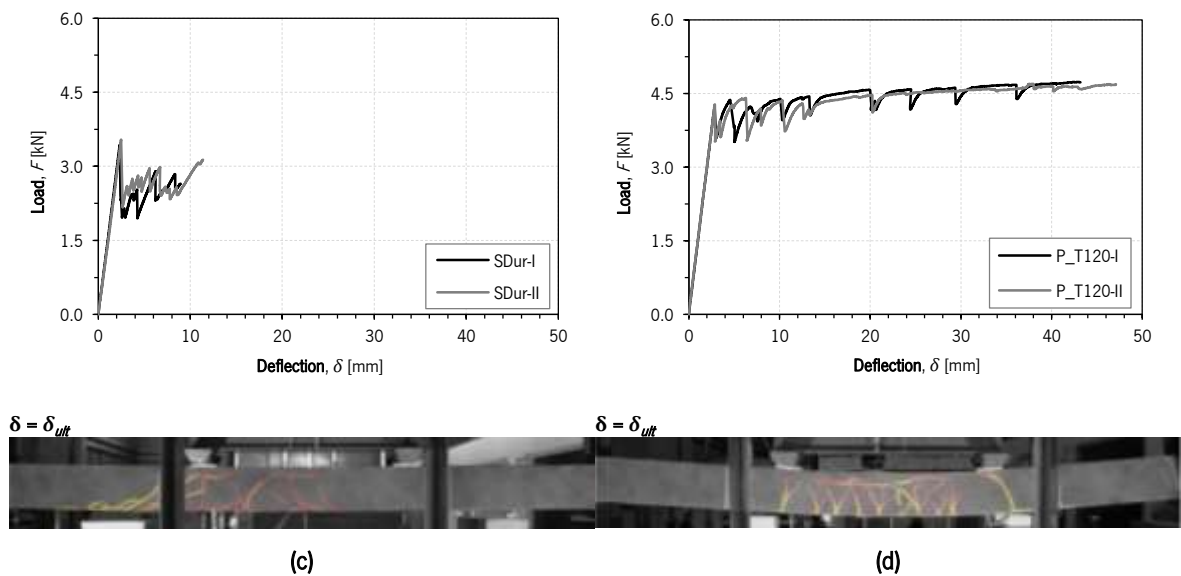
Figure V.13: Flexural responses and crack patterns at failure of monolithic glass beams reinforced with (a) CFRP and (b) Fe-SMA.

Table V.8: Main properties related to the post-cracking performance of the S*Dur* [22] and P_T120 [44] series, as well as the respective failure modes.

Series	Di [%]	RSi [%]	Failure mode	ε_r [‰]
SDur	407	87	CSC	3.22
P_T120	1584	111	Unloaded	40.3

5.1.2. First cracking load

According to **Table V.7**, the first cracking loads obtained from the flexural tests (F_{cr} (R_CFRP_CFRP) < F_{cr} (P_CFRP_CFRP) ≈ F_{cr} (SMA_CFRP) < F_{cr} (CFRP_SMA) < F_{cr} (SMA_SMA) are consistent with the compressive pre-stress induced by the post-tensioning at the bottom edge of the glass (see **Table V.6**). Taking the R_CFRP_CFRP beam as a reference, all post-tensioned beams showed first cracking loads between 22.7 % (P_CFRP_CFRP beam) to 94.7 % (SMA_SMA beam) higher.

The mechanical behaviour of the Fe-SMA material after activation was not characterized in this investigation. However, based on the stress-strain response in tension, its modulus of elasticity after activation ($E_{r,rec}$) was estimated from the slope of the tangent line when $\sigma = \sigma_{rec}$ (see values in **Table V.9**). Assuming linear elastic behaviour for all components and assuming the Euler-Bernoulli hypothesis to determine the moment of inertia prior to glass rupture (I_{el}) and the neutral axis position (y_{el}) from the top edge of glass, the analytical cracking load ($F_{cr,a}$) can be calculated from **Eq. (V.1)**, with l_1 = 1050 mm (shear span length) and h_g = 220 mm (glass panel height).

$$F_{cr,a} = \frac{2I_{el} \cdot \left(f_{g,t} + \sigma_{g,p}\right)}{l_1 \cdot \left(h_g - y_{el}\right)} \tag{V.1}$$

Table V.9: Modulus of elasticity adopted for each reinforcing element, as well as the comparison between the experimental cracking loads and those calculated analytically considering the $f_{g,t}$ obtained from the mechanical characterization and the $f_{g,eff}$ derived from the bending tests.

Property	Units	Beam designation				
		R_CFRP_CFRP	P_CFRP_CFRP	CFRP_SMA	SMA_CFRP	SMA_SMA
Reinforcement tensile stiffness						
E_{NSM}	[GPa]	183.87	183.87	183.87	59.94	52.13
E_{EBR}	[GPa]	183.87	183.87	101.68	183.87	99.18
Cracking load						
F_{cr}	[kN]	11.31	13.88	15.48	14.02	22.02
$F_{cr,a}$ ($f_{g,t}$)	[kN]	14.73 (30.2 %)	17.16 (23.6 %)	19.05 (23.1 %)	17.39 (24.0 %)	19.81 (10.0%)
$F_{cr,a}$ ($f_{g,eff}$)	[kN]	11.40 (0.8 %)	13.79 (-0.6 %)	15.74 (1.7 %)	14.13 (0.8 %)	16.56 (24.8 %)

Note:
Values in parenthesis correpond to the difference between the theoretical values in relation to the experimental ones

Assuming $f_{g,t}$ = 40 MPa (see **Table V.1**) and adopting this analytical procedure, higher F_{cr} were expected during the flexural tests, between 14.73 kN – with the R_CFRP_CFRP beam – and 19.81 kN – with the SMA_SMA beam (see details in **Table V.9**). The difference to the experimental results seems

to be related to the large size of the tested specimens. The tensile strength of glass in not a constant property. It depends on many aspects, including the element size [2]. In addition, handling large glass panels is difficult, leading to the growth of surface flaws and, sometimes, the formation of new ones. Thereby, from the manipulation of **Eq. (V.1)** and considering only the beams R_CFRP_CFRP and P_CFRP_CFRP, since the CFRP composite behaves linear elastically until failure, an effective tensile strength of glass ($f_{g,eff}$) was estimated from **Eq. (V.2)**. With an average value of 31.0 MPa, $f_{g,eff}$ was 22.6 % lower than $f_{g,t}$.

$$f_{g,eff} = \frac{F_{cr} \cdot l_1}{2 I_{el}} \cdot \left(h_g - y_{el} \right) - \sigma_{g,p} \qquad \text{(V.2)}$$

The SMA_SMA beam presented an F_{cr} that was 33.0 % higher than the $F_{cr,a}$ ($f_{g,eff}$). Due to the lack of evidences in the $F - \delta$ response for this unexpected difference (e.g. higher initial stiffness due to frictional forces between the composite beam and the metal lateral guides), the inherent variability of the tensile strength of glass seems to be the main reason.

5.2. After first cracking

After the first crack appeared in glass, all composite beams showed to be able to maintain their integrity because the reinforcement restrained crack propagation and the interlayer held the fragments in place. Furthermore, all specimens excluding the SMA_SMA beam, achieved $F_{max} > F_{cr}$, which denotes the notorious ability of the studied strengthening system to provide additional load carrying capacity and prevent premature failure. Both the strengthening system and the post-tensioning level played an important role in the post-cracking performance. Among the specimens tested, the R_CFRP_CFRP beam showed the highest Di (971.2 %) and RSi (160.8 %) values. On the other hand, the lowest Di (122.4 %) and RSi (87.6 %) values were observed in the beams CFRP_SMA and SMA_SMA, respectively. Specimens strengthened with NSM-CFRP laminates showed lower Di for increasing post-tensioning level, with $Di_{CFRP\_SMA} < Di_{P\_CFRP\_CFRP} < Di_{R\_CFRP\_CFRP}$.

5.2.1. Strengthening system

In comparison to the monolithic beams previously tested (SDur series presented in **Table V.8**), the R_CFRP_CFRP beam exhibited a much better post-cracking performance. In spite of a slight reduction in the reinforcement ratio from 1.17 % in the SDur series to 0.96 % in the R_CFRP_CFRP beam, the RSi increased from 87 % to 160.8 %, respectively. Such results indicate that the post-cracking performance of glass composite systems can be significantly enhanced when the tensile reinforcement

is applied according to the NSM technique. Therefore, the hybrid strengthening systems adopted in this study are clearly more efficient than EBR systems in delaying premature debonding of the reinforcement after the formation of large shear cracks. Unlike the SDur series, which presented asymmetric crack propagation governed mainly by dynamic effects arising from glass cracking (see **Figure V.13b**), the R_CFRP_CFRP beam showed a uniform and dense crack pattern, with vertical cracks in the pure bending zone and increasingly inclined shear cracks towards the supports. As a result, Di increased from 407 %, in the SDur series, to 971 %, in the R_CFRP_CFRP beam ($\approx$ 2.5 times higher). Finally, taking the monolithic beams (P_T120 series) as a reference, ε_r (F_{ult}) was 38.1 % higher in the case of the R_CFRP_CFRP beam (4.45 ‰). Thus, hybrid strengthening systems are better at exploiting the tensile capacity of the CFRP, allowing to reduce the reinforcement percentage and, simultaneously, to obtain better flexural responses in comparison to the EBR systems.

Although the SMA_SMA beam did not show the ability to exceed the F_{cr} during the post-cracking stage, as opposed to the monolithic beams (P_T120 series in **Table V.8**), some improvements in the post-cracking performance were observed. Even slightly, the tensile capacity of the Fe-SMA was better exploited in the SMA_SMA beam (ε_r = 48.7 ‰) than in the P_T120 series (ε_r = 40.3 ‰). Moreover, unlike the monolithic beams, the progressive debonding of the SMA reinforcement towards the support was not observed before the collapse.

The hybrid strengthening system adopted in this study showed to be able to avoid premature debonding of the reinforcement before the beam failure. As a result, it was more efficient than EBR systems at taking advantage of the tensile capacity of the reinforcement materials. Moreover, in case debonding occurs of the EBR reinforcement, it is reasonable to assume that the NSM reinforcement can still transfer load to the supports. Following the principle behind the laminated glass, when the strengthening systems includes two or more reinforcement elements, the premature debonding and/or failure of one of can be offset by the others, thus preventing a sudden failure of the glass composite element. Such behaviour is crucial to prevent catastrophic collapses, such as in beams entirely made of glass without reinforcement. Given the extremely brittle nature of glass and its unreliable tensile strength, redundancy at different levels is required to fulfil the ductility and safety requirements. Alongside the reinforcement material and adhesive type, the strengthening system also plays a critical role in the post-cracking response of glass structural elements.

5.2.2.   Load bearing capacity

The beams R_CFRP_CFRP and P_CFRP_CFRP showed quite similar flexural responses during the post-cracking stage. For similar mid-span deflections in both beams, the prestressing of the NSM-CFRP laminate resulted in a shift of the $F - \delta$ response upwards, to higher load levels. This increase of load carrying capacity is equal to the additional bending moment generated by the eccentricity between the post-tensioning force and the neutral axis (cracked section analysis). However, by prestressing the NSM-CFRP laminate the RSi reduced from 971 % (P_CFRP_CFRP beam) to 675 % (R_CFRP_CFRP beam) and the Di reduced from 161 % to 146 %, respectively. Neglecting the tensile pre-stress imposed at the top edge of glass due to the post-tensioning, the F_{ult} depends only on the material properties. Thus, the higher the post-tensioning level, the higher the F_{cr} and, consequently, the lower the RSi and Di values. Hence, the R_CFRP_CFRP beam (passive reinforcement) exhibited the highest RSi and Di among the specimens tested.

After glass cracking, the flexural stiffness of the CFRP_SMA beam gradually decreased due to the progression of cracks towards the supports. At the end of the post-cracking stage, its $F - \delta$ response was unexpectedly similar to that of the P_CFRP_CFRP beam. The main reason for this relies on the non-linear behaviour of the Fe-SMA in tension. As the CFRP presents linear elastic behaviour until failure, when it is prestressed, the increment of loading carrying capacity is approximately constant throughout the post-cracking stage (e.g. P_CFRP_CFRP *versus* R_CFRP_CFRP). As the Fe-SMA exhibits plastic behaviour, the post-tensioning effect (shifting of the $F - \delta$ response upwards) seems to have been lost when the yield strength was attained. Additionally, the higher stiffness of the CFRP also seems to have contributed to a more efficient restraining effect of crack propagation. On the other hand, due to the yielding of the Fe-SMA, the neutral axis gradually moved upwards, towards the top edge of glass, increasing the compression stress in the upper uncracked zone. Hence, F_{ult} (CFRP_SMA beam) was lower than F_{ult} (P_CFRP_CFRP beam), as experimentally observed.

A series of consecutive load drops occurred in the SMA_CFRP beam for 9.5 mm $< \delta <$ 13.0 mm (see **Figure V.11**), and two phases may be distinguished in the post-cracking response. During the first phase, with $\delta <$ 9.5 mm, flexural cracks appeared between the load points. Then, for 9.5 mm $< \delta <$ 13.0 mm, increasingly inclined shear cracks formed suddenly, but only towards one of the supports, appearing in the non-activated region when $\delta_{out,exp} \approx$ 13.0 mm and $F_{out,exp} \approx$ 14.0 kN. This non-symmetrical behaviour is explained by minor deviations in the cross-section geometry of the laminated glass panel. New cracks appeared first towards the stiffer support section (monitored by

the DIC technique), since the beam height ranged between 219.2 mm and 222.6 mm. Adapting Eq. (V.1) and assuming mode-I failure, the minimum load ($F_{cr,out}$) required for glass cracking in non-activated regions is equal to 17.21 kN, according to Eq. (V.3). This value is 18.8% higher than the $F_{out,exp}$, probably due to the inherent variability of the tensile strength of glass. Subsequently, for $\delta > 13.0$ mm, additional shear cracks formed in the non-activation region and, consequently, the strengthening system shifted to a passive-like behaviour (no post-tensioning effect), which explains the similarity between the $F - \delta$ responses of the beams SMA_CFRP and R_CFRP_CFRP at this stage. This shows that the EBR-CFRP composite systems are not as efficient for restraining the crack propagation as the NSM-CFRP ones. The strengthening systems show great difficulty in restraining the crack opening when NSM systems are not adopted (e.g. monolithic glass beams) or relatively flexible materials are used as reinforcement (e.g. Fe-SMA after activation). Hence, NSM systems with low tensile stiffness promote damage concentration and, consequently, high interfacial stress (mixed mode-I+II) between the EBR reinforcement and the glass substrate, causing the growth of existing flaws.

$$F_{cr,out} = \frac{2f_{g,eff} \cdot I_{el}}{((l - l_a)/2) \cdot (h_g - y_{el})} \tag{V.3}$$

Concerning the SMA_SMA beam, it did not achieve the F_{cr} again during the post-cracking stage ($RSi < 100$ %), in contrast to other specimens. Considering the $F_{cr,a}$ ($f_{g,eff}$) indicated in Table V.9, the RSi of the SMA_SMA beam would be equal to 116.5 % (F_{ult} vs. $F_{cr,a}$ ratio), which, in any case, would still be the lowest value among the five beams, despite being significantly higher than the experimental value of 87.6 %. In crack patterns captured from the SMA_SMA beam, the V-shaped cracks in the pure bending zone were predominantly identified (see Figure V.12b), unlike those observed in the other specimens. Both aspects emphasized above are a result of the mechanical behaviour of the Fe-SMA. The higher the activation temperature, the higher the recovery stress and the lower the tensile strength reserve of the Fe-SMA before the yielding (martensitic transformation). When the first crack appeared, the tensile stress in the reinforcement suddenly increased, resulting in yielding in the Fe-SMA and significantly reducing the flexural stiffness of the SMA_SMA beam. This sudden loss of tensile stiffness in the strengthening system resulted in large crack opening and extensive horizontal crack propagation (crack branching), as observed in Figure V.12. Thereafter, the further yielding of the Fe-SMA prevented crack propagation towards the supports.

In general, the post-tensioning resulted in obvious improvements in the overall structural response of the composite glass beams, both before and after crack initiation. Some aspects observed in this investigation are highlighted below: (i) unlike the Fe-SMA, the CFRP reinforcement can be entirely prestressed and it does not damage the adhesive connection; in addition, it prevents significant load drops when the cracking progresses towards the non-activated regions (e.g. SMA_CFRP beam); (ii) heating the Fe-SMA smoothens the post-tensioning force transfer from the reinforcement element to the glass, reducing the risk of peeling-off failure of the strengthening system and allowing the post-tensioning of externally bonded reinforcement; (iii) a significant tensile strength reserve before the yielding must be ensured when Fe-SMA reinforcement is activated, to create sufficiently stiff post-cracking responses (e.g. SMA_SMA beam); and (iv) the post-tensioning level must be defined by balancing the glass fracture strength and the post-cracking performance, ensuring in any case a residual strength capacity above 100 %, with $F_{ult} > F_{cr}$.

Based on the referred requirements, the best strengthening system seems to be the one adopted in the CFRP_SMA beam. As experimentally observed, premature debonding of the reinforcement is much less likely when NSM strengthening systems are adopted. Therefore, the stiffer reinforcement material must be introduced into the groove in order to prevent high interfacial stresses and minimize stress concentrations, as well as to guarantee sufficient post-failure stiffness, even if premature debonding of the externally bonded reinforcement occurs. When CFRP reinforcement is applied according to the NSM technique, it can be safely prestressed, inducing a favourable compression pre-stress in the glass tensile zone along the entire beam length. On the other hand, externally bonded Fe-SMA reinforcement can be safely activated because the inevitable adhesive damage generates a damage gradient in the stress transfer zone and prevents high stress concentrations at the glass substrate.

5.2.3.   Failure modes

All composite beams ruptured by shear-compression failure and showed the typical glass crushing in the compression zone (see **Figure V.14**). According to **Table V.7**, $\varepsilon_{g,t}$ ranged between 1.15 ‰ (R_CFRP_CFRP beam) and 2.65 ‰ (SMA_SMA beam), with the latter being 2.3 times higher than the former. Despite this variability, all beams presented almost similar F_{ult}, which varied between 17.65 kN (SMA_CFRP beam) and 20.27 kN (P_CFRP_CFRP beam), being the difference between these equal to 14.8 %. The scatter in $\varepsilon_{g,t}$ is probably related to the properties of each strengthening system (e.g. tensile stiffness and post-tensioning level). The stiffer the strengthening system, the deeper the neutral axis and, consequently, the lower the compression strain at the top edge of glass

when F_{ult} is achieved. As the post-tensioning induced favourable tensile pre-stresses in the upper glass zone, the stiffer the strengthening system and the higher the post-tensioning level, the higher the ultimate load should be, in line with the experimental observations.
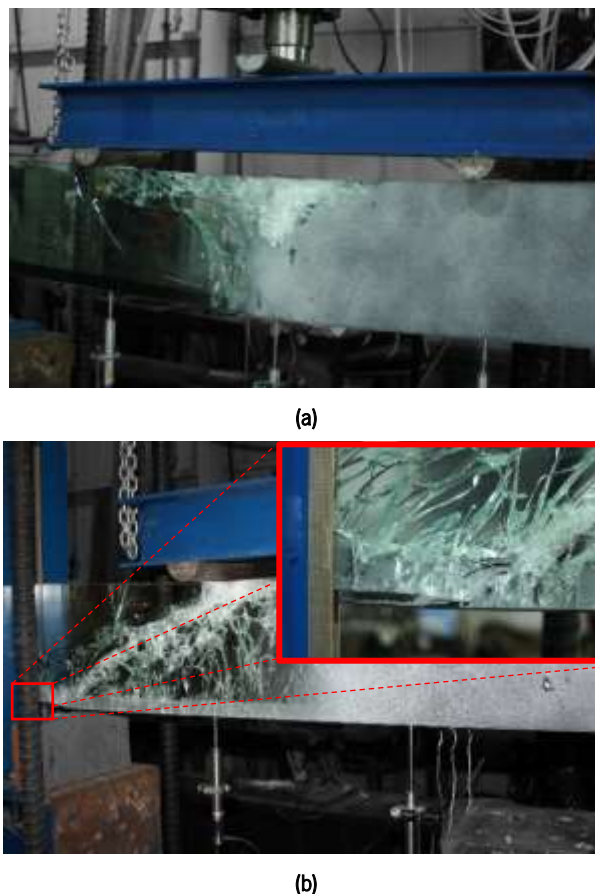

(a)

(b)

Figure V.14: Typical failure modes observed in (a) SMA_SMA beam and (b) in all other glass composite beams.

Excluding the SMA_SMA beam, where the compression failure by crushing occurred approximately at mid-span section (see **Figure V.14a**), in the other beams glass crushing was observed in the vicinity of the load point sections. In the SMA_SMA beam, it is clear that the height of the compression glass zone progressively decreased during the post-cracking stage due to the yielding of the Fe-SMA and the resulting beam deflection. In the remaining specimens, the deformation was a result of the progressive crack propagation towards the supports. In the absence of transverse reinforcement or stirrups, shear cracks inevitably propagated towards the load point sections (see **Figure V.12**), later causing shear-compression failure in glass. This failure mode is commonly observed in reinforced concrete (e.g. [55]). The shear cracks induced shear and compression stresses around the load application zones and, when the maximum principal stress reached the compression strength of glass ($f_{g,c}$), glass crushing occurred above the tip of the critical shear crack. As a result, shear cracks penetrated into the glass compression zone, which was accompanied by the spalling of the glass zones around the

load introduction points. It should be noted that this failure mode was already observed in glass composite systems (e.g. [56]).

Regarding the SMA_SMA beam, where no shear cracks appeared before the beam collapse, it is reasonable to assume that glass crushing occurred only when the $f_{g,c}$ was achieved at the top edge of glass. However, lateral-torsional buckling may have also influenced the F_{ult}, as noticed in other studies on glass composite systems (e.g. [57]). This explains why the SMA_SMA beam exhibited a much higher $\varepsilon_{g,t}$ than its counterparts. The $f_{g,c}$ was not experimentally assessed in this investigation. According to Haldiman [2], the compression strength of glass is generally much higher than the tensile strength and DIN 1249-10:1990 [58] indicates values between 700 and 900 MPa. However, Campione et al. [59] found values of ≈ 200 MPa, in line with the experimentally measured $\varepsilon_{g,t}$ ($\sigma_{g,t}$ = 196.1 MPa).

6   CONCLUSIONS

This research work focused on the structural performance of laminated glass beams post-tensioned with Fe-SMA and CFRP reinforcements, both applied according to the NSM and EBR techniques. First, laminated glass panels were designed to create a groove on the tensile zone. Then, both reinforcement elements were adhesively bonded to the tensile zone of the glass panels using two epoxy adhesives. After that, Fe-SMA and CFRP reinforcements were activated and released, respectively, inducing compressive pre-stress in the tensile glass zone. Finally, all specimens were tested under a four-point bending configuration. In addition, numerical investigations were performed to determine the recovery stresses in the Fe-SMA strips from the strain gauge measurements.

The main conclusions may be summarized as follows:

- Post-tensioning significantly increased the glass first cracking strength, between 22.7 % and 94.7 %. Mechanical post-tensioning of annealed glass by prestressing CFRP or activating FE-SMA materials seems to be a promising alternative to tempering to increase its first cracking strength and prevent the growth of surface flaws under service loading;

- The activation strategy of externally bonded Fe-SMA strips prevented stress concentrations along the bonded interfaces and, in turn, reduced the risk of premature peeling-off failure of the strengthening system due to rupture of the glass substrate;

- The activation procedure adopted did not require the application of mechanical anchorages at the beam ends for fixing the Fe-SMA strips, thus maximizing the transparency of glass structures. Furthermore, the activation layout can be optimized and adapted to the distribution of loads;

- For relatively high prestressing levels, NSM-CFRP reinforcement can be safely prestressed without premature peeling-off failure during the application of prestressing. Unlike the EBR-CFRP, the NSM-CFRP reinforcement is bonded to the glass surfaces, which usually have higher resistance than glass edges, further reducing the risk of premature failure of the glass substrate during the application of prestressing. In addition, in NSM systems, thicker adhesive layers can be easily adopted as a simple approach to smooth the transfer of the post-tensioning force to the glass substrate;

- All specimens maintained their integrity after crack initiation, exhibiting pseudo-ductile behaviour thereafter. Relatively safe and ductile failure mechanisms were observed in all glass composite beams. Hybrid strengthening systems showed to be much more effective in preventing the premature failure typically observed when EBR systems are adopted and progressive detachment of the reinforcement occurs due to the high interface stresses induced at the bonded interfaces by a critical shear crack;

- Hybrid strengthening systems adopted in this study were efficient in taking advantage of the tensile capacity of the reinforcement materials, outperforming EBR systems. Compared to the latter, hybrid strengthening systems allowed to obtain better flexural behaviours (residual strength capacity and utility) even with lower reinforcement ratios;

- Post-cracking performance was significantly influenced by the strengthening system and post-tensioning level (recovery stress). Specimens reinforced with Fe-SMA presented lower post-cracking flexural stiffness than those reinforced with two CFRP laminates. In addition, the higher the activation temperature, the higher the recovery stress and, in turn, the lower the tensile strength reserve before yielding of the Fe-SMA material;

- High stress concentrations in the vicinity of the load application zones seem to have triggered glass crushing in all beams, excluding in SMA_SMA. Due to the lack of transverse reinforcement in glass, shear cracks suddenly propagated towards the load points, inducing

high shear and compression stresses that crushed the glass above the tip of the critical shear crack;

- First cracking strength of glass can be maximized by applying CFRP and Fe-SMA reinforcements according to the NSM and EBR techniques, respectively, because both can be safely post-tensioned without inducing relatively high stress concentrations in the glass substrate. The NSM reinforcement, which is less prone to premature debonding, must be stiff enough to avoid damage concentrations and carry load after the possible debonding of the EBR reinforcement. Therefore, the best strengthening layout in terms of structural performance for the post-cracking behaviour of the laminated glass beams is the one where CFRP is introduced inside the groove and Fe-SMA is externally bonded.

The results obtained from this exploratory study show the advantages of post-tensioning laminated glass beams using CFRP and Fe-SMA reinforcements, both before and after crack initiation. Besides an economic feasibility study focusing on the application of hybrid strengthening systems, further studies are required to investigate aspects such as (i) the influence of the reinforcement ratio on the failure mechanisms of the composite beams, as well as the ratio between both reinforcement materials; (ii) the influence of the tensile strength reserve of the Fe-SMA reinforcement after activation; (iii) the long-term behaviour of the post-tensioning force transfer zones; and (iv) new strategies to increase the prestressing level without causing the premature peeling-off failure of the CFRP reinforcement, in order to better exploit the high tensile strength of this material.

7 ACKNOWLEGMENTS

8 REFERENCES

[1]   CNR-DT 2010/2013. Guide for the Design, Construction and Control of Buildings with Structural Glass Elements. CNR - Advisory Committee on Technical Recommendations for Construction, Rome: National Research Council of Italy; 2013.

[2]   Haldimann M, Luible A, Overend M. Structural use of glass. LABSE - Lanka Association of Building Services Engineers; 2008.

[3]   Cruz P, Pequeno J. Structural Timber-Glass Adhesive Bonding. Challenging Glass, 2008, p. 205–14.

[4]   Cruz P, Pequeno J. Timber-Glass Composite Beams: Mechanical Behaviour & Architectural Solutions. Challenging Glass, 2008, p. 439–48.

[5]   Belis J, Callewaert D, Delincé D, Impe R Van. Experimental failure investigation of a hybrid glass / steel beam. Engineering Failure Analysis 2009;16:1163–73. https://doi.org/10.1016/j.engfailanal.2008.07.011.

[6]   Bos F, Veer F, Hobbelman G, Louter C. Stainless steel reinforced and post-tensioned glass beams. ICEM12 - 12th International Conference on Experimental Mechanics, Bari, Italy: 2004, p. 1–9.

[7]   Louter C, Belis J, Veer F, Lebet J. Structural response of SG-laminated reinforced glass beams; experimental investigations on the effects of glass type, reinforcement percentage and beam size. Engineering Structures 2012;36:292–301. https://doi.org/10.1016/j.engstruct.2011.12.016.

[8]   Louter C, Cupać J, Lebet J. Exploratory experimental investigations on post-tensioned structural glass beams. Journal of Facade Design and Engineering 2014;2:3–18. https://doi.org/10.3233/FDE-130012.

[9]   Louter C, Cupać J, Debonnaire M. Structural glass beams prestressed by externally bonded tendons. GlassCon Global Conference Proceedings, Philadelphia, EUA: 2014, p. 450–9. https://doi.org/10.14296/deeslr.v5i0.1848.

[10]   Cagnacci E, Orlando M, Spinelli P. Experimental campaign and numerical simulation of the behaviour of reinforced glass beams. Glass Performance Days, Tempere, Finland: 2009, p. 3–9.

[11]   Bedon C, Louter C. Structural glass beams with embedded GFRP, CFRP or steel reinforcement rods: Comparative experimental, analytical and numerical investigations. Journal of Building Engineering 2019;22:227–41. https://doi.org/10.1016/j.jobe.2018.12.008.

[12]   Correia J, Valarinho L, Branco F. Post-cracking strength and ductility of glass-GFRP composite beams. Composite Structures 2011;93:2299–309.

[13]   Achintha M, Balan B. Characterisation of the mechanical behaviour of annealed glass – GFRP hybrid beams. Construction and Building Materials 2017;147:174–84. https://doi.org/10.1016/j.conbuildmat.2017.04.086.

[14]   Bedon C, Louter C. Numerical investigation on structural glass beams with GFRP-embedded rods, including effects of pre-stress. Composite Structures 2018;184:650–61.

https://doi.org/10.1016/j.compstruct.2017.10.027.

[15]   Neto P, Alfaiate J, Valarinho L, Correia J, Branco F, Vinagre J. Glass beams reinforced with GFRP laminates: Experimental tests and numerical modelling using a discrete strong discontinuity approach. Engineering Structures 2015;99:253–63. https://doi.org/10.1016/j.engstruct.2015.04.002.

[16]   Valarinho L, Correia JR, Branco F. Experimental study on the flexural behaviour of multi-span transparent glass-GFRP composite beams. Construction and Building Materials 2013;49:1041–53. https://doi.org/10.1016/j.conbuildmat.2012.11.024.

[17]   Valarinho L, Sena-Cruz J, Correia J, Branco F. Numerical simulation of the flexural behaviour of composite glass-GFRP beams using smeared crack models. Composites Part B: Engineering 2017;110:336–50. https://doi.org/10.1016/j.compositesb.2016.10.035.

[18]   Martens K, Caspeele R, Belis J. Development of composite glass beams - A review. Engineering Structures 2015;101:1–15. https://doi.org/10.1016/j.engstruct.2015.07.006.

[19]   Cupać J, Louter C, Nussbaumer A. Flexural behaviour of post-tensioned glass beams: Experimental and analytical study of three beam typologies. Composite Structures 2021;255. https://doi.org/10.1016/j.compstruct.2020.112971.

[20]   Engelmann M, Weller B. Post-tensioned glass beams for a 9 m Spannglass Bridge. Structural Engineering International 2016;26:103–13. https://doi.org/10.2749/101686616X14555428759000.

[21]   Sena-Cruz J, Barros J, Coelho M, Silva L. Efficiency of different techniques in flexural strengthening of RC beams under monotonic and fatigue loading. Construction and Building Materials 2012;29:175–82. https://doi.org/10.1016/j.conbuildmat.2011.10.044.

[22]   Rocha J, Sena-Cruz J, Pereira E. Influence of adhesive stiffness on the post-cracking behaviour of CFRP-reinforced structural glass beams. Composites Part B: Engineering 2022;247. https://doi.org/https://doi.org/10.1016/j.compositesb.2022.110293.

[23]   Bilotta A, Ceroni F, Di Ludovico M, Nigro E, Pecce M, Manfredi G. Bond Efficiency of EBR and NSM FRP Systems for Strengthening Concrete Members. Journal of Composites for Construction 2011;15:757–72. https://doi.org/10.1061/(asce)cc.1943-5614.0000204.

[24]   Dias SJE, Barros JAO. Performance of reinforced concrete T beams strengthened in shear with NSM CFRP laminates. Engineering Structures 2010;32:373–84. https://doi.org/10.1016/j.engstruct.2009.10.001.

[25]   Palumbo M. A New Roof for the XIIIth Century 'Loggia de Vicari' (Arquà Petrarca – PD Italy) Based on Structural Glass Trusses: A Case Study. Glass Processing Days, Tempere, Finland: 2005.

[26]   Bedon C, Louter C. Numerical analysis of glass-FRP post-tensioned beams – Review and

assessment. Composite Structures 2017;177:129–40. https://doi.org/10.1016/j.compstruct.2017.06.060.

[27] Keller T, De Castro J. System ductility and redundancy of FRP beam structures with ductile adhesive joints. Composites Part B: Engineering 2005;36:586–96. https://doi.org/10.1016/j.compositesb.2005.05.001.

[28] Hosseini A, Michels J, Izadi M, Ghafoori E. A comparative study between Fe-SMA and CFRP reinforcements for prestressed strengthening of metallic structures. Construction and Building Materials 2019;226:976–92. https://doi.org/10.1016/j.conbuildmat.2019.07.169.

[29] Izadi M, Hosseini A, Michels J, Motavalli M, Ghafoori E. Thermally activated iron-based shape memory alloy for strengthening metallic girders. Thin-Walled Structures 2019;141:389–401. https://doi.org/10.1016/j.tws.2019.04.036.

[30] Michels J, Shahverdi M, Czaderski C. Flexural strengthening of structural concrete with iron-based shape memory alloy strips. Structural Concrete 2017;19:876–91. https://doi.org/10.1002/suco.201700120.

[31] Shahverdi M, Michels J, Czaderski C, Motavalli M. Iron-based shape memory alloy strips for strengthening RC members: Material behavior and characterization. Construction and Building Materials 2018;173:586–99. https://doi.org/10.1016/j.conbuildmat.2018.04.057.

[32] Shin M, Andrawes B. Experimental investigation of actively confined concrete using shape memory alloys. Engineering Structures 2010;32:656–64. https://doi.org/10.1016/j.engstruct.2009.11.012.

[33] Rojob H, El-Hacha R. Self-prestressing using iron-based shape memory alloy for flexural strengthening of reinforced concrete beams. ACI Materials Journal 2017;114:523–32. https://doi.org/10.14359/51689455.

[34] Cladera A, Weber B, Leinenbach C, Czaderski C, Shahverdi M, Motavalli M. Iron-based shape memory alloys for civil engineering structures: An overview. Construction and Building Materials 2014;63:281–93. https://doi.org/10.1016/j.conbuildmat.2014.04.032.

[35] Izadi MR, Ghafoori E, Shahverdi M, Motavalli M, Maalek S. Development of an iron-based shape memory alloy (Fe-SMA) strengthening system for steel plates. Engineering Structures 2018;174:433–46. https://doi.org/10.1016/j.engstruct.2018.07.073.

[36] Leinenbach C, Kramer H, Bernhard C, Eifler D. Thermo-mechanical properties of an Fe-Mn-Si-Cr-Ni-VC shape memory alloy with low transformation temperature. Advanced Engineering Materials 2012;14:62–7. https://doi.org/10.1002/adem.201100129.

[37] Dong Z, Klotz UE, Leinenbach C, Bergamini A, Czaderski C, Motavalli M. A novel Fe-Mn-Si shape memory alloy with improved shape recovery properties by VC precipitation. Advanced Engineering Materials 2009;11:40–4. https://doi.org/10.1002/adem.200800312.

[38] Ghafoori E, Hosseini E, Leinenbach C, Michels J, Motavalli M. Fatigue behavior of a Fe-Mn-Si shape memory alloy used for prestressed strengthening. Materials and Design 2017;133:349–62. https://doi.org/10.1016/j.matdes.2017.07.055.

[39] Shahverdi M, Czaderski C, Motavalli M. Iron-based shape memory alloys for prestressed near-surface mounted strengthening of reinforced concrete beams. Construction and Building Materials 2016;112:28–38. https://doi.org/10.1016/j.conbuildmat.2016.02.174.

[40] Shahverdi M, Czaderski C, Annen P, Motavalli M. Strengthening of RC beams by iron-based shape memory alloy bars embedded in a shotcrete layer. Engineering Structures 2016;117:263–73. https://doi.org/10.1016/j.engstruct.2016.03.023.

[41] Czaderski C, Shahverdi M, Brönnimann R, Leinenbach C, Motavalli M. Feasibility of iron-based shape memory alloy strips for prestressed strengthening of concrete structures. Construction and Building Materials 2014;56:94–105. https://doi.org/10.1016/j.conbuildmat.2014.01.069.

[42] Bedon C, Amarante dos Santos F. FE Exploratory Investigation on the Performance of SMA-Reinforced Laminated Glass Panels. Advanced Engineering Materials 2016;18:1478–93. https://doi.org/10.1002/adem.201600096.

[43] Dieng L, Helbert G, Chirani SA, Lecompte T, Pilvin P. Use of shape memory alloys damper device to mitigate vibration amplitudes of bridge cables. Engineering Structures 2013;56:1547–56. https://doi.org/10.1016/j.engstruct.2013.07.018.

[44] Rocha J, Pereira E, Sena-Cruz J. Feasibility of mechanical post-tensioning of annealed glass beams by activating externally bonded Fe-SMA reinforcement. Construction and Building Materials 2022;365. https://doi.org/10.1016/j.conbuildmat.2022.129953.

[45] Silvestru V, Deng Z, Michels J, Li L, Ghafoori E, Taras A. Application of an iron-based shape memory alloy for post-tensioning glass elements. Glass Structures and Engineering 2022;7:187–210. https://doi.org/10.1007/s40940-022-00183-z.

[46] Silvestru V, Deng Z, Michels J, Taras A. Enabling a Ductile Failure of Laminated Glass Beams with Iron-Based Shape Memory Alloy (Fe-SMA) Strips. The International Colloquium on Stability and Ductility of Steel Structures, Aveiro, Portugal: Ernst & Sohn GmbH; 2022. https://doi.org/https://doi.org/10.1002/cepa. 1839.

[47] Deng Z, Silvestru V, Michels J, Li L, Ghafoori E, Taras A. Performance of Glass to Iron-based Shape Memory Alloy Adhesive Shear Joints with Different Geometry. In: Belis B& L (Eds. ., editor. Challenging Glass Conference Proceedings, vol. 8, Ghent, Belgium: 2022, p. 1–12. https://doi.org/10.47982/cgc.8.397.

[48] Simulia. ABAQUS computer software and Online Documentation. v6.12. 2012.

[49] Rocha J, Sena-Cruz J, Pereira E. Tensile behaviour of CFRP-glass adhesively bonded connections: double-lap joint tests and numerical modelling. Engineering Structures

2022;260:114212. https://doi.org/10.1016/j.engstruct.2022.114212.

[50]   ISO. Plastics - Determination of tensile properties - Part 5: Test conditions for unidirectional fibre-reinforced plastic composites. 527-5, Genève, Switzerland: International Organization for Standardization; 2009, p. 11.

[51]   Veer F, Riemslag T, Romein T. The failure strength of glass, a non transparent value. Glass Performance Days, Tempere, Finland: 2007, p. pages 610–614.

[52]   Yankelevsky DZ. Strength prediction of annealed glass plates - A new model. Engineering Structures 2014;79:244–55. https://doi.org/10.1016/j.engstruct.2014.08.017.

[53]   Cupać J, Louter C, Nussbaumer A. Post-tensioning of glass beams: Analytical determination of the allowable pre-load. Glass Structures and Engineering 2021;6:233–48. https://doi.org/10.1007/s40940-021-00150-0.

[54]   GOM. Correlate Software and Online Documentation. Rev.121188. 2019.

[55]   Qassim H, AL-Saraj W. Shear compression failure in reinforced self-compacted lightweight concrete beams subjected to axial load. Materials Today: Proceedings 2022;60:1179–85. https://doi.org/10.1016/j.matpr.2021.08.035.

[56]   Wang Z, Shi Y, Wang Q, Wu Y, He M. In-plane shear compression behaviour of steel-glass composite beams with laminated glass webs. Engineering Structures 2017;150:892–904. https://doi.org/10.1016/j.engstruct.2017.07.076.

[57]   Louter C, Veer F, Hobbelman G. Reinforcing glass, effects of reinforcement geometry and bonding technology. Glass Processing Days, 2007, p. 2–6.

[58]   DIN 1249-10:1990. Glass for use in building construction - Part 10: Chemical and physical properties. Deutsches Institut für Normung, Deutsches Institut fur Normung E.V. (DIN); 1990.

[59]   Campione G, Cannella F, Scibilia N. Shear-to-Moment Interaction in Glass Beams with Open Cross Sections. Journal of Structural Engineering 2018;144:4018038. https://doi.org/10.1061/(asce)st.1943-541x.0002033.